Universität Hamburg
DER FORSCHUNG | DER LEHRE | DER BILDUNG

Thermodynamic Behavior of Nanoconfined Water in Surface-Engineered Periodic Mesoporous Organosilicas

Dissertation

with the aim of achieving the doctoral degree

doctor rerum naturalium (Dr. rer. nat.)

at the Faculty of Mathematics, Informatics and Natural Sciences

Department of Chemistry

University of Hamburg

submitted by

Philip Lenz

Hamburg, 2026

This dissertation was carried out from September 2020 to June 2026 at the Institute of Inorganic and Applied Chemistry, University of Hamburg, under the supervision of Professor Dr. Michael Fröba and the co-supervision of Professor Dr. Michael Steiger.

This work was funded by the Cluster of Excellence ’Advanced Imaging of Matter’ of the Deutsche Forschungsgemeinschaft (DFG) – EXC 2056 - project ID 390715994 and FR 1372/26-1.

Reviewers of the Dissertation:

1. Prof. Dr. Michael Fröba
2. Prof. Dr. Tobias Beck
3. Prof. Dr. Matthias Thommes

Members of the examination committee:

1. Prof. Dr. Michael Fröba
2. Prof. Dr. Alf Mews
3. Prof. Dr. Simone Mascotto

Date of disputation: 11.09.2026

Date of approval for publication: 02.10.2026

List of Publications

1. Niels C. Gießelmann, **Philip Lenz**, Sophia-Marie Meinert, Tamás Simon, Wonhyuk Jo, Nele N. Striker, Michael Fröba*, Felix Lehmkühler*, “Structure of Water under Confinement in Periodic Mesoporous Organosilicas Investigated by X-ray Scattering”, *The Journal of Physical Chemistry C* **2024**, *128* (1), 499–507. DOI: 10.1021/acs.jpcc.3c06491, **Impact Factor** at the time of publication: **3.2**.

2. Niels C. Gießelmann, **Philip Lenz**, Sophia-Marie Meinert, Tamás Simon, Robert P. C. Bauer, Wonhyuk Jo, Sarah Claas, Christian Köhn, Nele N. Striker, Michael Fröba*, Felix Lehmkühler*, “The Structure of Ice under Confinement in Periodic Mesoporous Organosilicas (PMOs)”, *The Journal of Chemical Physics* **2024**, *161*, 034508.
DOI: 10.1063/5.0216697, **Impact Factor** at the time of publication: **3.8**.

3. **Philip Lenz**, Sophia-M. Meinert, Sandra König, Michael Steiger*, and Michael Fröba*, “Influence of Surface Chemistry on *t*-Layer Dimension and Density of Nanoconfined Water by Fine-Tuning the Functional Groups of Periodic Mesoporous Organosilicas”, *The Journal of Physical Chemistry C* **2025**, *129* (27), 12536–12550.
DOI: 10.1021/acs.jpcc.5c02277, **Impact Factor** at the time of publication: **3.2**.

4. Armin Mozhdehei, **Philip Lenz**, Stella Gries, Sophia-Marie Meinert, Ronan Lefort, Jean-Marc Zanotti, Quentin Berrod, Markus Appel, Mark Busch, Patrick Huber*, Michael Fröba*, Denis Morineau*, “Colossal Effect of Nanopore Surface Ionic Charge on the Dynamics of Confined Water”, *The Journal of Physical Chemistry C* **2025**, *129* (40), 18311–18324.
DOI: 10.1021/acs.jpcc.5c04787, **Impact Factor** at the time of publication: **3.2**.

5. **Philip Lenz**, Uta Sazama, Michael Steiger*, and Michael Fröba*, “Periodic Mesoporous Organosilicas as Host Materials for Studying Surface Chemistry Effects on the Freezing and Melting Behavior of Nanoconfined Water”, *The Journal of Physical Chemistry C* **2025**, 129 (45), 20373–20386.
DOI: 10.1021/acs.jpcc.5c05595, **Impact Factor** at the time of publication: **3.2**.

6. **Philip Lenz**, Uta Sazama, Sandra König, Michael Steiger*, and Michael Fröba*, “The Role of Fine-Tuned Surface Functionality on Adsorption Thermodynamics of Nanoconfined Water within Periodic Mesoporous Organosilicas” *The Journal of Physical Chemistry C* **2025**, 130 (9), 3472–3485.
   DOI: 10.1021/acs.jpcc.5c07495, **Impact Factor** at the time of publication: **3.2**.

Table of Contents

List of Abbreviations IX

1. Zusammenfassung 13

2. Summary 17

3. Introduction 21

3.1. The Special Behavior of Water in Nanoconfinement 21

3.2. Periodic Mesoporous Organosilica: A Host Material with Fine-Tunable Surface Chemistry 30

3.3. Analytical Methods for Investigating Water Behavior in Nanoconfinement with Different Surface Hydrophilicity 36

3.3.1. Water from Adsorbed Layers to Confined Liquids: Probing Water–Surface Interactions via Vapor Sorption 37

3.3.2. Energetics of Adsorption: Deconstructing the Influence of Surface Chemistry on Water–Surface Interactions via Isothermal Calorimetry and Isosteric Enthalpy Method 43

3.3.3. Nanoconfined Ice: Investigating the Impact of Surface Chemistry on Water's Freezing Behavior via Differential Scanning Calorimetry 49

4. Aim of the Work 57

5. Cumulative Part of the Dissertation 59

5.1. Influence of Surface Chemistry on *t*-Layer Dimension and Density of Nanoconfined Water by Fine-Tuning the Functional Groups of Periodic Mesoporous Organosilicas 59

5.2. The Role of Fine-Tuned Surface Functionality on Adsorption Thermodynamics of Nanoconfined Water within Periodic Mesoporous Organosilicas 79

5.3. Structure of Water under Confinement in Periodic Mesoporous Organosilicas Investigated by X-ray Scattering 94

5.4. Colossal Effect of Nanopore Surface Ionic Charge on the Dynamics of Confined Water 104

5.5. Periodic Mesoporous Organosilicas as Host Materials for Studying Surface Chemistry Effects on the Freezing and Melting Behavior of Nanoconfined Water 119

5.6. The Structure of Ice under Confinement in Periodic Mesoporous Organosilicas (PMOs) 134

6. Discussion 147

7. References 157

8. Appendix 177

8.1. List of Chemicals Used in This Work 177

8.2. Supporting Information for “Influence of Surface Chemistry on *t*-Layer Dimension and Density of Nanoconfined Water by Fine-Tuning the Functional Groups of Periodic Mesoporous Organosilicas” 188

8.3. Synthesis of Bifunctional Amide–Acid PMOs 220

8.3.1. BTEPA-Based PMOs 220

8.3.2. Aspartic-Acid-Based PMOs 238

8.3.3. BTEVA-Based Bifunctional Amide–Acid PMOs 246

8.3.4. Porosity Characteristics of Bifunctional Amide–Acid PMOs 267

8.4. Supporting Information for “The Role of Fine-Tuned Surface Functionality on Adsorption Thermodynamics of Nanoconfined Water within Periodic Mesoporous Organosilicas” 269

8.5. Supporting Information for “Structure of Water under Confinement in Periodic Mesoporous Organosilicas Investigated by X-ray Scattering” 281

8.6. Supporting Information for “Colossal Effect of Nanopore Surface Ionic Charge on the Dynamics of Confined Water” 287

8.7. Supporting Information for “Periodic Mesoporous Organosilicas as Host Materials for Studying Surface Chemistry Effects on the Freezing and Melting Behavior of Nanoconfined Water” 297

8.8. Supporting Information for “The Structure of Ice under Confinement in Periodic Mesoporous Organosilicas (PMOs)” 314

9. Acknowledgment 323

10. Declaration on Oath 325

List of Abbreviations

-AA	-aspartic acid
$AlCl_3$	aluminium chloride
BET	Brunauer, Emmett and Teller
BOC	tert-butyloxycarbonyl
BTEB	1,4-bis(triethoxysilyl)benzene
BTEPA	bis(3-triethoxysilylpropyl)amine
BTEPSA	(*S*)-2-amino-*N*1,*N*4-bis(3-(triethoxysilyl)propyl)succinamide
BTEVA	2,5-bis[(*E*)-2-(triethoxysilyl)vinyl]aniline
BTEVB	1,4-bis[(*E*)-2-(triethoxysilyl)vinyl]benzene
BTEVClB	2-chloro-1,4-((*E*)-2'-bis(triethoxysilyl)vinyl)benzene
BTEVFB	2,5-bis((*E*)-2(triethoxysilyl)vinyl)-2-fluorobenzene
BTEVP	2,5-bis[(*E*)-2-(triethoxysilyl)vinyl]pyridine
C	climate chamber
Cbz	benzyl chloroformate
cf	completely functionalized
CMC	critical micelle concentration
CTAB	cetyltrimethylammonium bromide
CPG	controlled pore glasses
D_2O	deuterium oxide
DMSO-d_6	hexadeuterodimethylsulfoxid
DSC	differential scanning calorimetry
DTA	differential thermal analysis
e.g.	*exempli gratia* (for example)
EA	elemental analysis

end	endset
et al.	*et alii* (and others)
exp	experimental
(FT-) IR	(fourier transform) infrared
HBr	hydrobromic acid
HCl	hydrochloric acid
HDL	high-density liquid
HI	hydrophilicity index
hp	homopolymeric
HWHM	half width at half maximum
i.e.	*id est* (that is to say)
IW	incipient wetness
KBr	potassium bromide
LDL	low-density liquid
LLCP	liquid–liquid critical point
MA	maleic anhydride
MCM-41	Mobil Composition of Matter no. 41
MOF	metal-organic framework
MS	mass spectrometry
N-MBTEVP^{+}I^{-}	*N*-methyl-2,5-bis((*E*)-2-(triethoxysilyl)vinyl)pyridinium iodide
N,*N*-DMBTEVA	*N*,*N*-dimethyl-2,5-bis((E)-2-(triethoxysilyl)vinyl)aniline
NaOD	sodium deuteroxide
NaOH	sodium hydroxide
nf	not functionalized
NFL	non-freezable layer

NLDFT	nonlocal density functional theory
NMR	nuclear magnetic resonance
-OBA	-oxobutanoic acid
-OBenA	-oxobut-2-enoic acid
on	onset
pH	*potentia hydrogenii* (potential of hydrogen)
PMO	periodic mesoporous organosilica
PS	post-synthetic
PT	pseudomorphic transformation
(P)XRD	(powder) X-ray diffraction
QENS	quasi-elastic neutron scattering
QLL	quasi-liquid layer
RU	repeating-unit
SA	succinic anhydride
SAXS	small-angle X-ray scattering
SBA-15	Santa Barbara Amorphous-15
SDA	structure-directing agent
SHS	surface hydration sites
TEM	transmission electron microscopy
TEOS	tetraethyl orthosilicate
TGA	thermogravimetric analysis
TLCT	true liquid crystal templating
VHDA	very high-density amorphous
wt%	weight percent
WVS	water vapor sorption

1. Zusammenfassung

Wasser ist eine der am intensivsten untersuchten Substanzen, doch sein Verhalten unter Nanoconfinement ist nach wie vor nicht vollständig verstanden. Obwohl zahlreiche Studien Wasser in porösem Silica untersucht haben, bestehen weiterhin Widersprüche darüber, wie Oberflächenhydrophilie und spezifische chemische Funktionalitäten die Struktur und das Phasenverhalten von eingeschlossenem Wasser beeinflussen. Diese Unterschiede ergeben sich unter anderem aus der Verwendung unterschiedlicher Analysemethoden, uneinheitlicher Messbedingungen und verschiedener poröser Systeme, was zu schwer vergleichbaren oder sogar widersprüchlichen Ergebnissen führt.

Periodisch mesoporöse Organosilicas (PMOs) eignen sich hervorragend als Modellsysteme zur Untersuchung von Wasser im Nanoconfinement. PMOs sind poröse Hybridmaterialien aus einem Siliciumdioxidgerüst mit kovalent eingebauten organischen Brückeneinheiten, bei denen unter geeigneten Synthesebedingungen und mit entsprechenden Vorläufern kristallartig angeordnete Porenwände entstehen können. Ihre Synthese mittels Tensid-Templating ermöglicht hochgeordnete, stabile Porenstrukturen mit einstellbarer Größe und enger Porengrößenverteilung. Durch die Kombination aus großer spezifischer Oberfläche, hoher Porosität und gezielt einstellbarer Oberflächenchemie bieten PMOs eine ideale Plattform, um systematisch den Einfluss von Confinement und Oberflächenfunktionalität auf die Eigenschaften von Wasser zu untersuchen. Im Vergleich zu porösen Silicas erlauben sie eine direkte Kontrolle der Oberflächenpolarität und damit vielseitige Möglichkeiten zur Erforschung von Confinementeffekten. Zur Untersuchung des oberflächenchemieabhängigen Verhaltens von Wasser im Nanoconfinement wurden neben literaturbekannten PMOs auch neuartige PMOs mit vergleichbarer Basisstruktur entwickelt, die stark hydrophobe, positiv geladene sowie aminosäure- und amid–carbonsäurebasierte Funktionalitäten besitzen. Durch Variation der Synthesebedingungen und der Tensidkettenlänge konnte ein breites Spektrum an PMOs mit hydrophilen und hydrophoben Oberflächen sowie Porendurchmessern im Bereich von etwa 2.5–6 nm erzeugt werden. Divinylanilin-basierte Vorläufer (BTEVA) mit ihrer Aminfunktion bieten großes Potenzial, da sie sowohl post-synthetisch als auch *in situ* mit einer breiten Palette an Funktionalitäten modifiziert werden können. Diese Studie zeigt zudem, dass Verunreinigungen im BTEVA-Vorläufer die Ausbildung eines reinen PMO-Gerüsts nicht

beeinträchtigen, da sie während der Synthese entfernt werden. Dies spart Zeit und Material, da aufwändige Aufreinigungsschritte entfallen. Während dies für post-synthetische Modifikationen unkritisch ist, wird für Vorläufermodifikationen jedoch hochreines BTEVA benötigt, insbesondere für die analytische Bestimmung des Funktionalisierungsgrades. Aufbauend auf BTEVA und weiteren aminfunktionalisierten Organosilicas wurden im nächsten Schritt Amid-Carbonsäure-Funktionen auf Basis von Malein-, Bernstein- und Asparaginsäure eingeführt.

Wasserdampfsorptionsmessungen wurden bei 298.15 K durchgeführt, um die MCM-41 Silicas und PMOs hinsichtlich ihrer Hydrophilie zu charakterisieren. Hierzu wurden verschiedene Hydrophilie-Indizes verwendet, darunter ein eigens entwickelter Index, der auf dem Vergleich des relativen Drucks am Wendepunkt der Kapillarkondensation bzw. der Porenentleerung aus Wasser- und Stickstoff-sorptionsisothermen basiert. Zudem wurde der Einfluss der Oberflächenchemie auf die adsorbierte und flüssige Phase des Wassers im Confinement anhand geometrischer Berechnungen untersucht. Im Allgemeinen besitzt das Wasser im Confinement mittlere Dichten (0.4 bis 0.8 g cm^{-3}), die niedriger sind als die Dichte von Wasser in der Volumenphase, wobei hydrophobe Materialien tendenziell geringere Dichten aufweisen als hydrophile. Zudem wurde beobachtet, dass die mittlere Dichte stark von der Größe und Dichte der Adsorptionsschicht abhängt, die wiederum hauptsächlich durch die Anzahl der Oberflächenhydratisierungsstellen beeinflusst wird. Für hydrophobere Materialien wurde eine geringere Dichte sowie ein größeres Verhältnis von Adsorptionsschichtdicke zu Porenradius beobachtet, was auf wasserfreie Zonen nahe der hydrophoben Oberflächenbereiche hinweist, die durch an Hydratisierungsstellen gebundenes Wasser überbrückt werden. PMOs mit Oberflächenladung zeigten aufgrund veränderter Wasser-Wand-Wechselwirkungen größere Adsorptionsschichten und höhere adsorbierte Wasserdichten. Amid–Säure-funktionalisierte PMOs weisen aufgrund der modifizierten Oberflächenchemie und der erhöhten Dichte der Hydratationsstellen, die mit dem Funktionalisierungsgrad zunimmt, eine hohe Wasserbeständigkeit auf. Die Trends im Verhalten der *t*-Schicht in Abhängigkeit von der Oberflächenhydrophilie entsprechen denen klassischer PMOs, zeigen jedoch deutlich höhere durchschnittliche Porenwasserdichten und eine dichtere Adsorptions-schicht, was auf die erhöhte Dichte der Oberflächenhydratationsstellen zurück-zuführen ist. Zudem zeigte sich, dass eingeschlossenes Wasser hinsichtlich seiner strukturellen und dynamischen Eigenschaften stark von der Oberflächenchemie

beeinflusst wird. Röntgenstreudaten zeigen systematische Verschiebungen struktureller Merkmale, die mit Änderungen der effektiven Dichte und der lokalen Ordnung konsistent sind: hydrophile und kleinere Poren begünstigen ein ausgeprägteres, wenn auch verzerrtes, tetraedrisches Netzwerk, während hydrophobe und größere Poren zu einer Strukturierung führen, die der des Wassers in der Volumenphase ähnlicher ist. Ergänzende Ergebnisse der quasi-elastischen Neutronenstreuung (QENS) zeigen, dass ionisch geladene Oberflächen einen dominanten Einfluss auf die Dynamik haben, indem sie die Translationsbewegung drastisch verlangsamen und die Verweildauer erhöhen, wobei die Ergebnisse darauf hindeuten, dass sich diese Verlangsamung über die Grenzschicht hinaus auf das gesamte Porenvolumen erstreckt.

Zur Untersuchung des adsorbierten Zustands des Wassers, d. h. ohne flüssigen Kern, wurden die Adsorptionsenergien mittels zweier komplementärer Ansätze untersucht: (i) der isosteren Methode, basierend auf drei Wasserdampfsorptions-isothermen bei unterschiedlichen Temperaturen, und (ii) der Kalorimetrie unter Verwendung eines speziell entwickelten isothermen Differenz-Scanning-Kalorimeters (DSC), gekoppelt mit einem Thermogravimeter und einem modularen Feuchtigkeitsgenerator. Bei höheren relativen Luftfeuchtigkeiten ergaben beide Methoden größtenteils konsistente Ergebnisse für die Wasseradsorption. Dabei zeigten hydrophobere Materialien aufgrund schwächerer Wasser–Oberflächen-Wechselwirkungen geringere Adsorptionsenergien, bevor Wasser–Wasser-Wechsel-wirkungen dominieren und Kondensation einsetzt. Nach der Kapillarkondensation deutet die isostere Methode darauf hin, dass bei hydrophilen Materialien die Kondensationsenthalpien weiterhin beeinflusst werden, was auf einen Einfluss der Oberfläche auf das Wasser in nachfolgenden Adsorptionsschichten hinweist. Die Kalorimetrie ermöglicht eine detaillierte Analyse bei sehr niedrigen Bedeckungen und zeigte, dass sowohl hydrophile als auch hydrophobe Materialien zu Beginn hohe Adsorptionsenthalpien aufweisen, da Silanolgruppen stark mit Wasser interagieren können, bis diese gesättigt sind. Zusätzlich wurde die Temperaturabhängigkeit der Wasserdampfsorptions-isothermen auf unterschiedlich funktionalisierten Oberflächen analysiert. Die Clustergröße bei der Kapillarkondensation erwies sich als temperaturunabhängig. Hingegen wurde eine Temperaturabhängigkeit der Adsorptions–Desorptions-Hysterese beobachtet, die hauptsächlich durch die Desorption bestimmt wird.

Der Einfluss der Oberflächenchemie auf die Gefrier- und Schmelzübergänge wurde mittels DSC untersucht. Oberflächeneffekte auf die Phasenübergangstemperatur treten nur bei Porenradien unter 1.8 nm auf, wobei Wasser in hydrophoben Materialien eine stärkere Schmelzpunkterniedrigung mit abnehmender Porengröße aufweist. In diesen hydrophoben Confinements weist Wasser zudem geringere spezifische Gefrier- und Schmelzenthalpien sowie größere berechnete kritische Porenradien auf, was auf kleinere Eiskerne und dickere nicht gefrierbare Wasserschichten hinweist. Geometrische Berechnungen bestätigen diese Trends und zeigen zudem, dass größere Poren und geladene PMOs zu dickeren nicht gefrierbaren Wasserschichten führen. Über alle Materialien hinweg sind die Dichten der nicht gefrierbaren Wasserschichten höher als die der Adsorptionsschichten, was auf den Kristallisationsdruck zurückgeführt werden kann, der Wasser in hydrophobe Bereiche hineinpresst. In hydrophoben Materialien ist die Dichte der nicht gefrierbaren Wasserschichten jedoch generell geringer, mit Ausnahme von PMOs mit Divinylbenzol-Brücken. Darüber hinaus wurden Röntgenmessungen durchgeführt, um die Abhängigkeit der Struktur von eingeschlossenem Eis von der Oberflächenchemie zu untersuchen. Das eingeschlossene Eis zeigt sowohl hexagonale als auch kubische Strukturanteile sowie Verschiebungen der Gitterparameter der hexagonalen Phase, die von Porengröße und Oberflächenfunktionalität abhängen. Die Röntgen-Kreuzkorrelationsanalyse weist zudem auf nicht-zufällige Winkelkorrelationen der Eiskristallite hin, was darauf hindeutet, dass das Confinement und die Oberflächen-chemie auch deren bevorzugte Orientierung innerhalb der Poren beeinflussen.

Insgesamt zeigt sich ein Einfluss der Oberflächenchemie auf Wasser in allen untersuchten Phasen. Zwischen Kondensation und Gefrieren lassen sich vergleichbare Trends hinsichtlich der Auswirkungen der Oberflächenchemie beobachten, wobei beim Übergang von Dampf zu Flüssigkeit der Oberflächeneinfluss stärker ausgeprägt ist als beim Übergang von Flüssigkeit zu Feststoff. Schichtdicke und Dichte zeigen in beiden Fällen, sowohl für den flüssigen als auch für den gefrorenen Kern, ähnliche von der Oberflächenfunktionalität abhängige Trends. In Anwesenheit eines gefrorenen Kerns sind jedoch sowohl die Dichte als auch die Dicke der Oberflächenwasserschicht insgesamt höher, wobei die Schichtdicke nahezu doppelt so groß ist wie bei einem flüssigen Kern. Während die Oberflächenhydrophilie ein nützliches Konzept zur Beschreibung dieser Zusammenhänge darstellt, spielen auch der Typ und die Größe der funktionellen Gruppen eine bedeutende Rolle.

2. Summary

Water is one of the most intensively studied substances, yet its behavior under confinement remains far from fully understood. Although numerous studies have examined water in porous silica, discrepancies persist regarding how surface hydrophilicity and specific chemical functionalities influence the structure and phase behavior of confined water. These inconsistencies stem partly from the use of different analytical methods, varying measurement conditions, and diverse porous systems, which often produce results that are difficult to compare or even contradictory.

Periodic mesoporous organosilicas (PMOs) are highly suitable model systems for studying water under nanoconfinement. PMOs are porous hybrid materials composed of a silica framework with covalently incorporated organic bridging units, and under appropriate synthesis conditions and with suitable precursors, they can form pore walls with a crystal-like structural arrangement. Their synthesis via surfactant-templating enables highly ordered pore structures with tunable pore size and narrow pore size distributions. The combination of large surface area, high porosity, and precisely adjustable surface chemistry, from strongly hydrophobic to highly hydrophilic, makes PMOs particularly well-suited to systematically investigate how confinement and surface functionality influence the properties of water. Compared to conventional porous silica materials, they allow direct control over surface polarity and thus offer a more versatile and robust platform for studying confinement effects.

To understand the surface-chemistry-dependent behavior of confined water, a variety of PMOs, including literature-known ones and additional novel PMOs with similar backbone structures but with strongly hydrophobic, positively charged, hydrophilic, and bifunctional amide–acid functionalities, were employed. By adjusting the synthesis conditions and the surfactant chain length, a broad set of PMOs with hydrophilic or hydrophobic surfaces and pore diameters ranging from roughly 2.5 to 6 nm were obtained.

Divinylaniline-based precursors (BTEVA), with their amino functionality, offer substantial potential because they can be modified with a broad range of functional groups both post-synthetically and *in situ*. This study also shows that, despite impurities in the BTEVA precursor, a pure PMO framework forms during synthesis, as these impurities are removed in the process. This eliminates the need for extensive purification steps, saving time and material. While these impurities are not critical for

post-synthetic modifications, precursor modifications require highly pure BTEVA, particularly for accurate determination of the functionalization degree. Based on BTEVA and other amine-functionalized organosilicas, amide-carboxylic acid groups derived from maleic acid, succinic acid, and aspartic acid were introduced in the next step.

Water vapor sorption studies were conducted at 298.15 K to characterize the MCM-41 silica and PMOs according to their hydrophilicity by applying several hydrophilicity indices, including one developed in this work, that is based on the comparison of the relative pressure at the inflection point of capillary condensation or pore emptying of water vapor sorption isotherms with that in nitrogen physisorption isotherms. Additionally, the impact of surface chemistry on both the adsorbed and liquid phases of confined water was investigated using a geometric calculation approach. In general, lower average densities of confined water (in the range of 0.4–0.8 g cm^{-3}) than in its bulk state were observed, with hydrophobic materials leading to a lower density than hydrophilic ones. It was found that the average density is strongly governed by the size and density of the adsorption layer, which itself is mainly influenced by the number of surface hydration sites. For more hydrophobic materials, a lower density and a larger adsorption-layer-to-pore-radius ratio were observed, supporting the concept of water-free cavities near surface regions with low water affinity that are bridged by water adsorbed at hydration sites. PMOs with a surface charge exhibit altered water–wall interactions, resulting in a thicker adsorption layer and higher adsorbed water density. Amide–acid functionalized PMOs show high resistance to water due to the modified surface chemistry and the increased density of hydration sites, which rises with the functionalization degree. The trends in *t*-layer behavior with respect to surface hydrophilicity follow those observed for classical PMOs, but with notably higher average confined-water densities and a denser adsorption layer, driven by the higher density of surface hydration sites.

Additionally, confined water was found to be strongly impacted by surface chemistry with respect to its structural and dynamic properties. X-ray scattering indicates systematic shifts in structural features consistent with variations in effective density and local ordering, with hydrophilic and smaller pores promoting a more pronounced, though distorted, tetrahedral network, while hydrophobic and larger pores lead to more bulk-like structuring. Complementary quasi-elastic neutron scattering (QENS) results reveal that charged surfaces have a dominant effect on the dynamics, drastically

slowing translational motion and increasing residence times, with the results indicating that this slowdown extends beyond the interfacial layer into the entire pore volume.

To study water in its adsorbed state, i.e., without a liquid core, adsorption energetics were investigated using two complementary approaches: (i) the isosteric method, based on three water vapor isotherms at different temperatures, and (ii) calorimetry, employing a custom isothermal differential scanning calorimeter coupled to a thermogravimeter and a modular humidity generator. At higher relative humidities, both methods produce consistent results, showing that more hydrophobic materials have lower adsorption energies due to weaker water–surface interactions until water–water interactions dominate and condensation sets in. After capillary condensation, isosteric enthalpy analysis shows that surface chemistry still affects the condensation enthalpy in hydrophilic materials, indicating its influence on water in subsequent adsorption layers. Calorimetry allows a detailed analysis at very low coverages and shows that both hydrophilic and hydrophobic materials exhibit high initial adsorption enthalpies, as surface silanol groups strongly interact with water until these sites are saturated. In addition, using the isotherms measured for the isosteric method, we analyzed the temperature dependence of water adsorption on surfaces with different functionalities. The cluster size at capillary condensation was found to be temperature-independent, whereas the temperature dependence of the adsorption–desorption hysteresis is primarily governed by desorption.

The impact of surface chemistry on the freezing and melting transitions of water was investigated using differential scanning calorimetry (DSC). Surface effects on the phase transition temperature are only observed for pore radii below 1.8 nm, where water confined in hydrophobic materials shows a stronger melting temperature depression with decreasing pore size. Water in these hydrophobic confinements also exhibits lower specific freezing and melting enthalpies and larger calculated critical pore radii, indicating smaller ice cores and thicker non-freezable layers. Geometric calculations corroborate these trends and further show that larger pores and charged PMOs lead to thicker non-freezable water layers. Across all materials, the density of the non-freezable water layer is higher than that of the adsorption layer, which may be attributed to crystallization pressure forcing water into hydrophobic regions. However, non-freezable layer densities are generally lower in hydrophobic materials, except for divinylbenzene-bridged PMOs.

Moreover, X-ray measurements were used to study the surface chemistry dependence of confined ice structure. The confined ice shows contributions from both hexagonal and cubic stacking sequences as well as shifts in the lattice parameters of the hexagonal component, depending on pore size and surface functionality. X-ray cross-correlation analysis further reveals non-random angular correlations of the ice crystallites, indicating that confinement and surface functionality also influence their preferred orientation within the pores.

Overall, surface chemistry was found to influence water in all phases studied. Between condensation and freezing, comparable trends in the effect of surface chemistry can be observed, although the surface impact is more pronounced for the vapor–liquid transition than for the liquid–solid transition. Layer thickness and density show similar trends for both the liquid and the frozen core, depending on the surface functionality. In the presence of a frozen core, however, both the density and the thickness of the surface water layer are higher, with the latter being nearly twice as large as for a liquid core. While surface hydrophilicity provides a useful framework to describe these relationships, the type and possibly the size of the functional groups also play a significant role.

3. Introduction

3.1. The Special Behavior of Water in Nanoconfinement

Water, a key molecule for life and climate on Earth, naturally occurs in all three phases of matter and is known for its numerous anomalies. The most familiar are the density maximum at 4 °C and its expansion upon freezing.[1,2] In its solid form, water exhibits pronounced polymorphism, with 20 ice phases identified to date.[3–6] Some of these are shown in the *p*–*T* phase diagram of water in Figure 1 (top). With decreasing temperature, reaching the deeply supercooled zone, water's anomalous properties become increasingly pronounced.[7] A comprehensive overview of these properties and anomalies is provided by Martin Chaplin on the *Water Structure and Science* website at London South Bank University (LSBU),[8] as well as in other literature.[1,2] The origin of many anomalies is linked to water's complex, dynamic hydrogen-bonding network, which can involve up to four hydrogen bonds, allowing for various local structural arrangements.[9,10] Despite extensive studies, a conclusive explanation for these anomalous behaviors remains elusive. A leading hypothesis, particularly relevant in the supercooled regime, is the existence of a liquid–liquid critical point (LLCP), which proposes two distinct liquid states with a density difference of about 20 %, separated by a liquid–liquid phase transition line: a low-density liquid (LDL) with tetrahedral coordination and a high-density liquid (HDL) with a distorted or collapsed structure.[7,11] This second critical point of water is assumed to be located in the so-called "no-man's-land", a region in the *p*–*T* phase diagram between the homogeneous nucleation temperature (≈ −41 °C) and the crystallization temperature of ultraviscous water (≈ −123 °C). In this region, rapid ice nucleation prevents experimental access (see Figure 1).[12] In addition to the LLCP hypothesis, three alternative scenarios have been proposed to explain the origin of water's anomalies: the singularity-free,[13] the critical-point-free,[14,15] and the stability-limit conjecture.[16] These and other aspects of water behavior at low temperatures are described in detail elsewhere.[7,17–19] Additionally, water clusters that fluctuate between high- and low-density forms have been proposed to explain many of water's anomalies.[7,8,20–23]

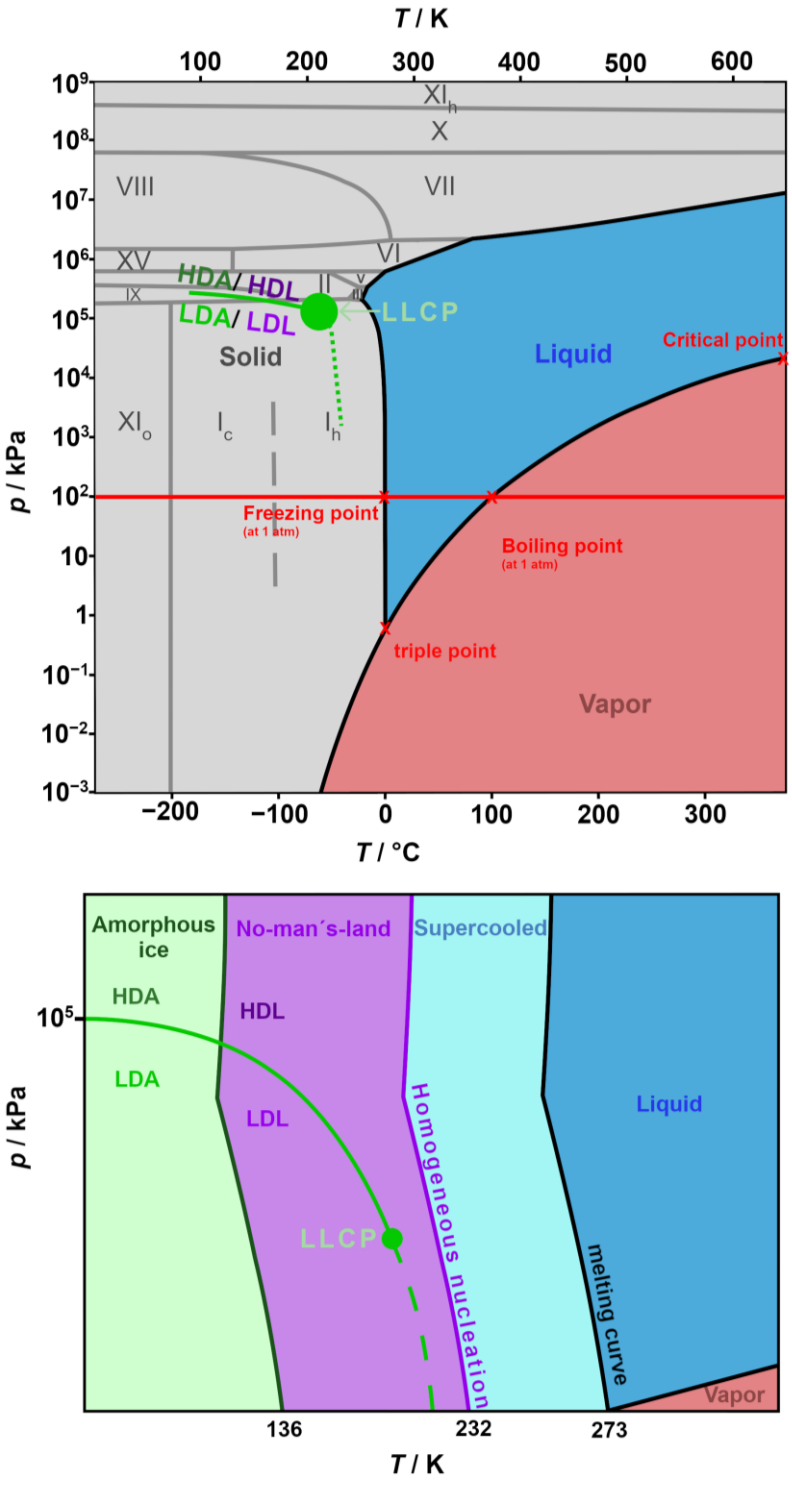


Figure 1: *p*–*T* phase diagram of water (top) showing the three phases and various ice polymorphs, and an illustrative *p*–*T* phase diagram of liquid water during supercooling (bottom). The coexistence line (green) separates the amorphous states into high- and low-density forms of amorphous ice, and the liquid state within the "no-man's-land" region into high- and low-density liquid water. The line terminates at the liquid–liquid critical point (green dot), followed by the Widom line (dashed), which delineates regions dominated by fluctuations between the two liquid forms and their transient species. This conceptual context is projected onto the upper *p*–*T* phase diagram. The upper figure is a modified derivative of *Phase diagram of water*;[24] licensed under CC BY-SA 3.0. This version was colour-corrected and supplemented with additional data points.[7] The lower figure is reproduced from Miller, J. L. Supercooled water goes supercritical. *Physics Today* **2018**, *71* (3), 18–20,[25] with permission of the American Institute of Physics.

Due to experimental limitations in studying water's behavior within the no-man's-land, various alternative approaches, besides computer simulations, have been employed, including aqueous solutions, nano- and micrometer-sized water droplets, stretched water, and confined water.[7,26–30] Furthermore, combining the colligative effects of aqueous solutions with confinement can lead to even lower melting temperatures than those observed for confined water alone.[31–35] The smaller the pore, the stronger the effect of the solute on the melting temperature depression. Using a 0.24 mol kg^{-1} aqueous sodium chloride solution leads to a melting transition at −47.89 °C, which is 9.75 °C lower than that of pure confined water.[31] Confinement alone already alters the structural and dynamical behavior of water,[27,36] but the additional presence of solutes raises doubts about whether such observations can be applied to describe bulk water in the no-man's-land. In this work, we therefore focus on pure water under confinement.

In nature, water in confinement is common, occurring in clays, rocks, zeolites, and biological systems such as proteins, including aquaporins,[37,38] and cells, where it constitutes 70–80 % of the total mass.[1,39] Water adsorption in porous materials is a fundamental process with broad relevance for applications such as gas separation,[40,41] water desalination,[42–46] humidity regulation,[47] and energy storage.[48,49] Under confinement, water exhibits pronounced deviations from bulk behavior, including shifts in freezing and melting points,[50–57] changes in density,[50,58–62] dielectric constant,[63–65] and surface tension,[60] as well as alterations in both liquid[66–68] and ice structures.[69–77] Confinement also influences microphase separation,[78–80] solvation capacity,[81] and other physicochemical properties, offering new opportunities to control chemical processes at the nanoscale.[50,51,82,83] The present study focuses on the combined effects of surface chemistry and confinement on water in its various phases and during phase transitions.

In general, the p–T phase diagram of water is altered under confinement (see Figure 2, left). Under isothermal conditions, the liquid–vapor curve of water is shifted to lower pressures with stronger confinement, whereas under isobaric conditions, the solid–liquid curve is shifted to lower temperatures, meaning that water remains liquid below the bulk melting point. Both processes are pore-size (d_P) dependent, as illustrated by the confinement-induced melting temperature (T_m) depression (Figure 2, right), and can be described by the Kelvin[84,85] and Gibbs–Thomson[57] relations for the vapor–liquid and solid–liquid transitions, respectively. A more detailed discussion is

provided in Chapter 3.3. It has also been reported that under liquid intrusion conditions in hydrophobic metal–organic frameworks (MOFs), the supercritical transition temperature of water can be reduced by ~250 K.[86] This effect has been attributed primarily to the higher density of the vapor phase rather than a reduction in the number of hydrogen bonds in the liquid phase. Calorimetric measurements[57] indicate that no freezing occurs in MCM-41 silica pores smaller than 3 nm, with the lowest observed phase transition temperature being 217 K. These findings are in agreement with other studies,[87–90] which showed that water in pores with a diameter of 2–3 nm does not freeze, suggesting that 2–3 molecular layers are insufficient to form stable ice crystals.

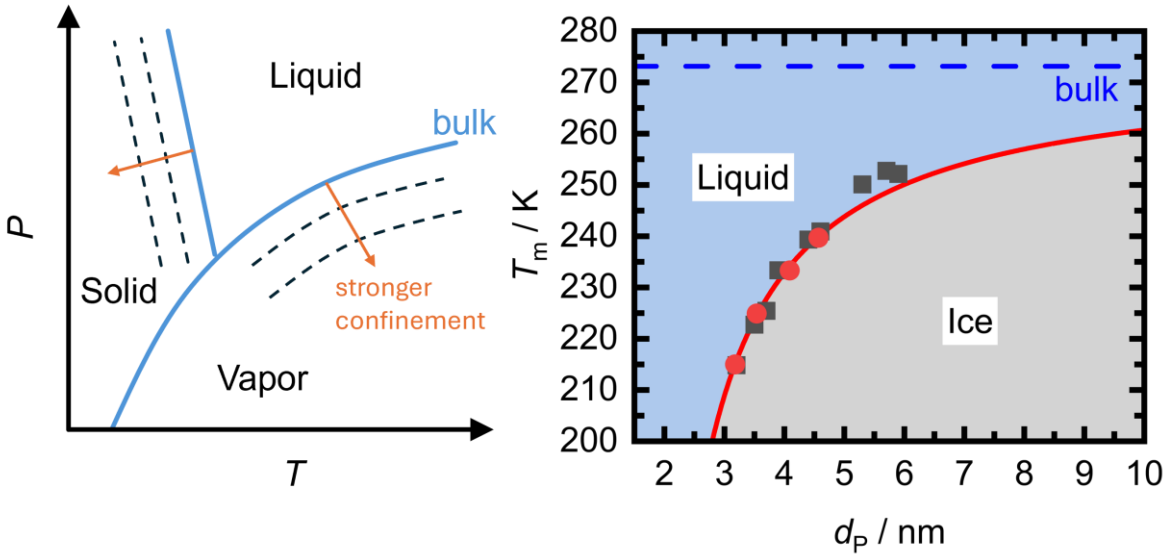


Figure 2: Left: Schematic *p*–*T* phase diagram of bulk water (blue solid line) and the effect of increasing confinement on the fusion and vaporization curves (dotted lines). Right: Dependence of the melting transition temperature on pore diameter (d_P) for water confined in MCM-41 silica. Data points from this work (black squares) are shown alongside literature data reported by Jähnert *et al.*[57] (red circles). The red line represents a Gibbs–Thomson fit based on their reported parameters.

In addition to surface roughness,[91] pore size[50–59] and geometry,[92–96] surface hydrophilicity and chemical functionality also affect the thermodynamic behavior of confined water and aqueous solutions. However, the effect of surface chemistry on the solid–liquid and vapor–liquid transitions remains debated.[97]

In contrast to the liquid-like water in the pore core,[61,98–103] water at interfaces deviates from its bulk behavior. Surface properties strongly influence the structure of interfacial water. For hydrophilic materials, highly structured, solid-like water was observed, whereas weakly organized, liquid-like water was found on hydrophobic surfaces.[104,105] While hydrophobic materials show only a thin adsorption layer, the thicker, ice-like water in hydrophilic materials can extend over 3–4 monolayers.[106]

Additionally, the entropy of surface water on hydrophilic surfaces has been reported to be lower than that of bulk water, and its dynamics were slower than those of water at hydrophobic surfaces.[107] Moon *et al.*[108] described this behavior as enthalpy-dominated interfacial hydration, as observed for SBA-15 silica with heterogeneously distributed silanol groups, which, with decreasing density, leads to fewer water–wall hydrogen bonds and consequently to increased surface water dynamics. For PMOs, they observed entropically driven surface hydration, in which low-entropy regions form due to the organization of hydrogen-bonded water structures around nanometer-scale hydrophobic domains, stabilized by nearby silanol groups. With increasing hydrophobic content, this structuring leads to a reduction in interfacial water dynamics.

Based on simulations[109,110] and a variety of experimental methods,[111–116] it was observed that interfacial water arranges in distinct layers, as illustrated by the density profile in Figure 3. For water confined in nanoslits of hexagonal boron nitride and graphene, an anomalously low dielectric constant of around 2 (compared to 80 for bulk water) has been reported, corresponding to an electrically "dead" water layer.[63] The extent of this reduction in dielectric constant was reported to span two to three water layers before reaching bulk values.[64,107]

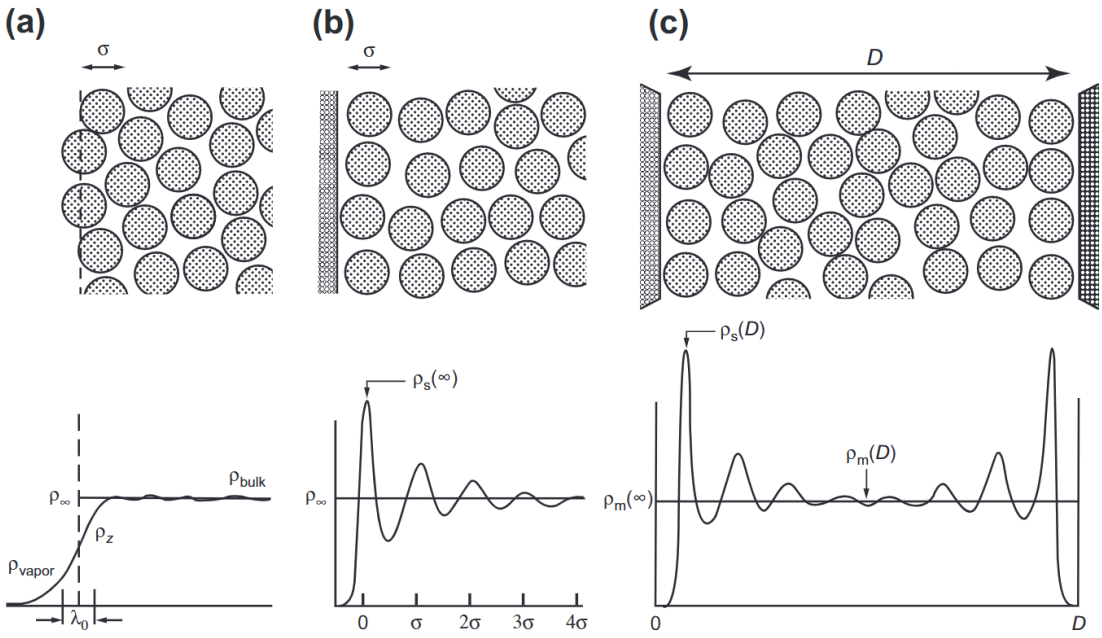


Figure 3: Density profile of water at the liquid–vapor interface with molecular-scale roughness (λ_0) (a), the liquid–solid interface (b), and the solid–liquid–solid configuration of confined water shown as a function of distance (D). Different densities (ρ) are assigned to the bulk (∞), surface contact (s), and midplane (m). These figures were originally published by Israelachvili[113] in *Intermolecular and Surface Forces* and are reused with permission from Elsevier.

Although water in the pore core is often considered bulk-like, with the influence of the surface diminishing after a few water layers, effects extending beyond these layers have been observed in hydrophilic materials.[68] In general, for porous silica such as MCM-41, water dynamics in confinement are reduced and decrease further with decreasing pore size.[74,117–120] The translational diffusion of interfacial water strongly depends on the water–surface interaction strength, with stronger interactions leading to slower diffusivities, whereas water in the pore center remains largely unaffected by surface chemistry.[100]

For bulk ice, the most stable structure is hexagonal ice (I_h). Under confinement, water crystallizes into a mixed structure of I_h and cubic ice (I_c), referred to as stacking-disordered ice (I_{sd}).[73–75,121,122] The corresponding crystal structures and calculated X-ray diffraction patterns are shown in Figure 4.

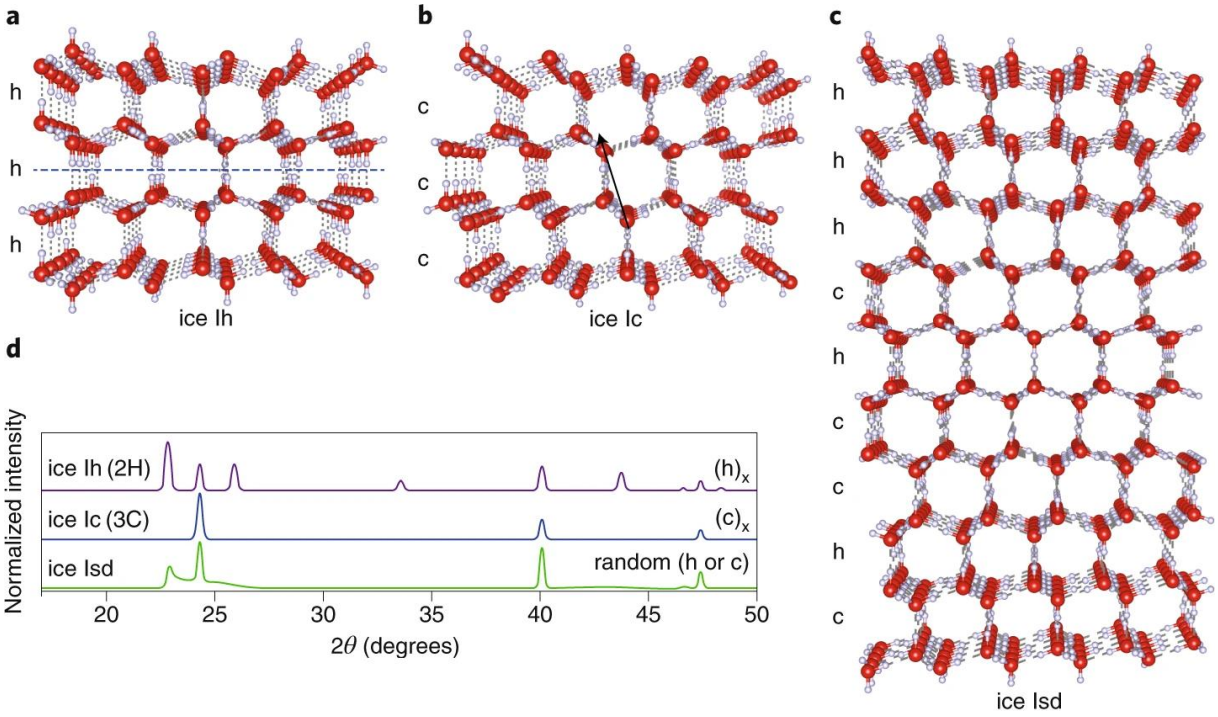


Figure 4: Water molecules, with oxygen atoms in red and hydrogen atoms in white, arranged in different ice structures (hexagonal (I_h), cubic (I_c), and stacking-disordered ice (I_{sd})) and their calculated X-ray diffractograms. These figures were originally published by Salzmann *et al.*[123] in *Nature Materials* and are reproduced with permission from Springer Nature. The image has been slightly modified.

The mechanism of nucleation during freezing is still not fully understood. Based on molecular simulations, Moore *et al*. proposed a pore-wall-independent homogeneous nucleation mechanism for hydrophilic, open cylindrical pores with a diameter of 3 nm.[124] Several simulation studies likewise suggest that ice formation occurs away from the interface, in regions where water exhibits bulk-like behavior. The ice nucleus

itself was found to behave similarly in confinement and in bulk, with both systems showing a critical nucleus diameter of about 1 nm, below which the cluster becomes unstable and melts. Up to pore diameters of ≥ 4.5 nm, the critical diameter is pore size independent. Only for pores < 4.5 nm was an increase in the critical ice cluster size observed.[125] Sometimes, the freezing process is described as a layer-by-layer mechanism, leading to a distinction between shell and core solidification, whereas melting typically proceeds as a single-phase transition. In an experimental study[126] of water confined in a millimeter-sized glass tube, the freezing temperature was found to depend on the cooling rate and the interfacial water–solid area, indicating a heterogeneous nucleation mechanism. A recent molecular dynamics simulation study[127] of water confined between platinum plates with water film thicknesses ranging from 4 to 25 nm suggested that both homogeneous and heterogeneous nucleation can occur. However, the probability of heterogeneous nucleation increases as the film becomes thinner, due to the growing influence of interfacial effects. In zeolites of the type $AlPO_4$-54, where the pore diameter is only 1.3 nm, no freezing takes place. Instead, the confined water exhibits plastic behavior, forming a dense and highly disordered amorphous state at temperatures below 240 K.[128]

In our previous study,[129] periodic mesoporous organosilicas (PMOs) were used in X-ray scattering experiments to study the influence of surface chemistry and pore size on ice structure. By applying X-ray cross-correlation analysis, it was observed that PMOs with strong water–wall interactions showed pronounced angular correlations, indicating that elongated ice unit cells tend to orient along the pore axis, as seen for the charged surface of $BTEVP^+$-PMO in Figure 5. Pore walls carrying an aniline functionality (BTEVA-PMO) exhibit more bulk-like lattice parameters with a pronounced orthogonal (90°) orientational contribution. Hydrophilicity alone does not appear to be the sole factor governing angular correlation, as the more hydrophobic BTEVB-PMO,[62] in which only cubic ice features are observed, also exhibits several correlation peaks. In contrast, PMOs bearing hydrophobic functionalities such as fluorine or chlorine, oriented toward the pore center, show only weak or no correlations.

An X-ray study[130] demonstrated that the filling degree influences the type of ice crystals formed upon freezing. When MCM-41 silica pores are fully filled, the ice can grow out of the pores, forming a mixture of hexagonal and cubic structures. In contrast, partially filled pores do not exhibit ice formation outside the pores, with predominantly cubic ice remaining confined inside. From this observation, the authors concluded that

ice nucleation occurs in the bulk-like core region of the pore, as external ice growth was only observed in fully filled samples. Since partially filled samples still form an ice core, crystallization is assumed to originate from quasi-free water located near the liquid–vapor interface and farther from the pore wall.

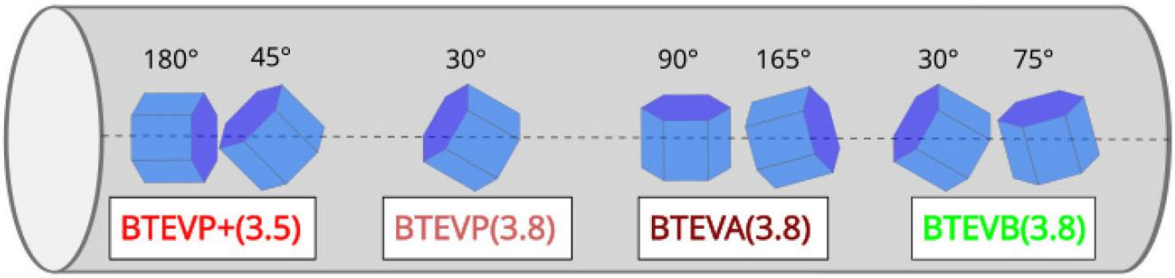


Figure 5: Illustration of the dominant hexagonal ice orientation inside the pores (gray tube) of PMOs with different surface functionalities. The pore sizes are indicated in brackets for each PMO type. This figure was published by Gießelmann *et al*.[129] in *The Journal of Chemical Physics* under a CC-BY 4.0 license.

In a recent simulation study, a new ice phase, the bilayer penta-hexa ice (BL-PHI), consisting of interlocking pentagonal and hexagonal rings, was found to form in hydrophobic slits with a width of 0.86 nm under moderate to high pressures. Its formation is kinetically hindered, exhibiting a significantly slower freezing rate due to the high activation energy for diffusion.[131] These findings demonstrate that confinement not only shifts melting points but also affects the structural organization of water.

In both states, liquid and solid, a water layer mediates the interaction between the condensed or frozen water in the pore core and the surface (Figure 6). The structure, dynamic behavior, and thickness of this layer are not fixed but strongly depend on surface chemistry, roughness, and temperature. The dimension of this so-called adsorption layer in adsorption studies with a liquid core, or of the non-freezable layer (NFL), sometimes referred to as quasi-liquid layer (QLL) or δ-layer in systems with a solid core, significantly influences the measurable condensation pressure and the freezing/melting temperature of confined water, particularly under strong nanoconfinement. While both interfacial water films are bound to and affected by the surface, they differ in origin and properties. The adsorption layer forms upon the first contact with water, i.e., before liquid water is present in the core, whereas the NFL develops around the solid–liquid transition temperature of the freezable water (typically about 20 K below the melting point).[132] Water in the adsorption layer strongly interacts

with the surface functionalities, leading to the formation of a structured layer in which two water molecules form hydrogen bonds to surface silanol groups, resulting in preferred arrangements and altered dynamical behavior. On hydrophilic surfaces (e.g., MCM-41 silica and divinylaniline-bridged PMO), slower dynamics are observed compared to hydrophobic ones (e.g., benzene-bridged PMO).[59,100] At lower temperatures, when a frozen core is present, surface chemistry appears to be of secondary importance due to dominant water–water interactions, so that the dynamics of both the ice core and the non-freezable layer seem unaffected by surface hydrophilicity.[133,134] In a dielectric spectroscopy study, Banys *et al*.[135] observed a freezing temperature of the NFL on MCM-41 silica at around 26 K, which lies within the range typically found for hydrogen-bonded systems in a glass-like state. The analytical methods used in the present work to investigate the solid–liquid and liquid–vapor phase behavior, as well as their implications for the surface water layer, are described in detail in Chapters 3.3.1 to 3.3.3. This ability to control the surface water layer properties based on surface chemistry offers a direct pathway for material scientists to engineer surfaces with specific functionalities. This fundamental understanding is crucial for developing advanced anti-icing coatings, low-friction surfaces, and membranes for water purification, by enabling the rational design of surface–water interactions.

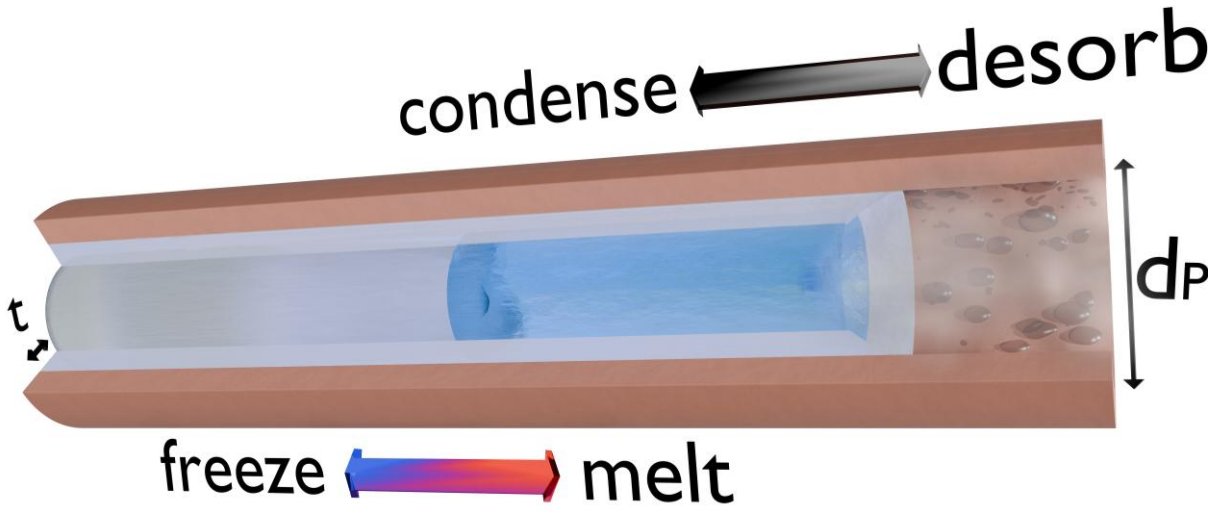


Figure 6: Illustration of water in its vapor, liquid, and solid states confined inside a pore (orange pore walls) with a diameter d_P, showing an interfacial water layer of thickness t between the pore wall and the liquid or solid water core.

3.2. Periodic Mesoporous Organosilica: A Host Material with Fine-Tunable Surface Chemistry

A broad range of host materials has been used to study confined water, including porous carbons,[61,75,77,95,97] MOFs,[67,136] zeolites,[128,137] and porous silicas,[54,57,62,77,95] yet comparing the effects of hydrophilicity remains difficult because these systems differ in pore structure, pore connectivity, chemical composition and arrangement of the pore walls, surface polarity, hydration-site distribution, and pore-size range. Additional approaches have focused on modifying surface polarity, for example, by hydrophilizing carbon materials or hydrophobizing silica, in order to isolate the effect of surface hydrophilicity on the thermodynamic behavior of confined water.[138–141] However, such modifications typically result in non-uniform functional group distributions across the surface.

Periodic mesoporous organosilicas represent a hybrid material class capable of bridging the gap between hydrophilic and hydrophobic materials and overcoming most of the aforementioned limitations. These materials feature a silica-based framework interconnected by organic bridging units, enabling the formation of ordered, in some cases crystal-like, pore wall structures depending on the synthesis conditions.[142–145] A central characteristic of PMOs is their tunable pore size and surface chemistry, which can be precisely adjusted through the choice of organic bridging units in the precursors. This versatility makes them ideal for studying how nanoconfined water and ice respond to variations in surface polarity and pore size. As a result, PMOs serve as powerful model systems for investigating the dynamic, structural, and adsorption behavior of water, including its temperature dependence under confinement.[61,68,100,101,129,133,146]

The synthesis of PMOs is based on sol-gel chemistry[147,148] combined with the endo-templating method.[142,149] This approach, first reported in 1999 by the groups of Inagaki,[150] Ozin,[151] and Stein,[152] enables the formation of hybrid materials with highly ordered mesopores and chemically tunable pore walls through the direct incorporation of organic bridging groups into the silica framework. In contrast to purely inorganic mesoporous silica, PMOs provide a wide range of chemical functionalities and structural versatility, making them ideal for applications that demand both stability and molecular specificity. A schematic representation of the synthesis concept is shown in Figure 7.

The sol–gel process involves the hydrolysis and condensation of bis-silylated precursors of the type $(R'O)_3Si–R–Si(OR')_3$, where R represents an organic bridging group and R' is typically an ethoxy or methoxy group. During hydrolysis, the alkoxy groups are replaced by hydroxyl groups, forming silanol groups that subsequently condense to generate the three-dimensional organosiloxane network. The quality of the resulting product depends on several synthesis parameters, including the water-to-precursor ratio, pH, the number and steric bulk of alkoxy groups, and the electronic properties of the bridging moiety. These factors govern reaction rates, network connectivity, and the resulting pore structure.[147,148]

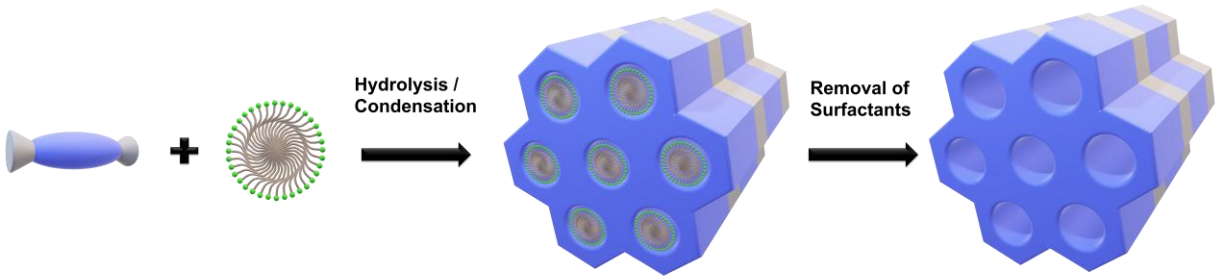


Figure 7: Schematic synthesis route of PMOs via the endo-templating method using bis-silylated precursors of the form $(R'O)_3Si–R–Si(OR')_3$, with the organic bridge shown in blue and Si–O units in gray, in the presence of surfactants (carbon chains illustrated as brown lines and head groups in green). Schematic inspired by concepts from the referenced work.[142]

To obtain highly ordered pores with narrow size distributions, PMO synthesis employs the endo-templating method using surfactants as structure-directing agents (SDAs). These include ionic surfactants, such as cetyltrimethylammonium bromide (CTAB), or nonionic ones, such as the polyalkylene glycol ethers (Brij). Above the critical micelle concentration (CMC), surfactants self-assemble into micelles or higher-order lyotropic mesophases (hexagonal, cubic, or lamellar structures), depending on the concentration, temperature, pH, and surfactant architecture. These aggregates serve as templates around which the organosilane framework forms. The interaction strength between surfactant head groups and the forming pore walls depends on the type of precursor and affects the micelle arrangement. Under basic synthesis conditions with cationic quaternary ammonium surfactants, stronger interactions, as in SiO_2-based systems, lead to stronger adsorption of the head groups and more ordered tail arrangements, whereas in divinylbenzene-bridged PMOs, hydrophobic interactions with the surfactant tails weaken head group adsorption. Consequently, different

surfactant conformations and structural arrangements can arise for different PMO types.[153]

The templating mechanisms can be distinguished into two types: true liquid crystal templating (TLCT), where surfactants with sufficiently high concentrations form mesophases independently of the precursor, and cooperative self-assembly, where the precursor and surfactant interact during structure formation. The latter mechanism, typically involving surfactant concentrations below those required to form mesophases, is more common in PMO synthesis. Under acidic conditions, protonated silanol groups interact with anionic or neutral surfactants via electrostatics or hydrogen bonding. Under basic conditions, deprotonated silanols interact with cationic surfactants such as CTAB. These interactions direct the organization of the mesostructure during gelation.[142,149] After network formation, the final porous material is obtained by removing the surfactant. Since PMOs contain thermally sensitive Si–C bonds, calcination is typically avoided. Instead, mild extraction using an ethanol/HCl solution is employed to preserve the organic groups and maintain framework integrity.[142]

As shown in Figure 8, different experimental methods can be used to characterize the porosity of a material. In this study, the PMOs were primarily characterized by gas adsorption, specifically nitrogen physisorption, to determine BET surface area, pore volume, and pore size distribution using nonlocal density functional theory (NLDFT). Nowadays, the NLDFT method has become the standard approach for determining pore sizes. It uses theoretical isotherms, called kernels, which include specifications regarding pore geometry, branch used (adsorption or desorption), adsorptive type, and the material analyzed, correlating them with the experimental isotherms. Depending on the software provided by the instrument manufacturer, only a limited number of kernels are available. Since no kernels exist specifically for hybrid materials like PMOs, the kernel for cylindrical silica pores was applied in this study. A comprehensive description of gas adsorption technology and its interpretation is provided elsewhere.[154–158]

Using powder X-ray diffraction (PXRD), a porous material can be analyzed with regard to pore order, which, for the PMOs used here, is a 2D hexagonal structure, and the crystallinity of the pore walls, which are amorphous in conventional silica materials but can be crystal-like in PMOs.[142,159,160] Transmission electron microscopy (TEM) can further visualize the pores, domain sizes, pore orientations, and particle sizes.

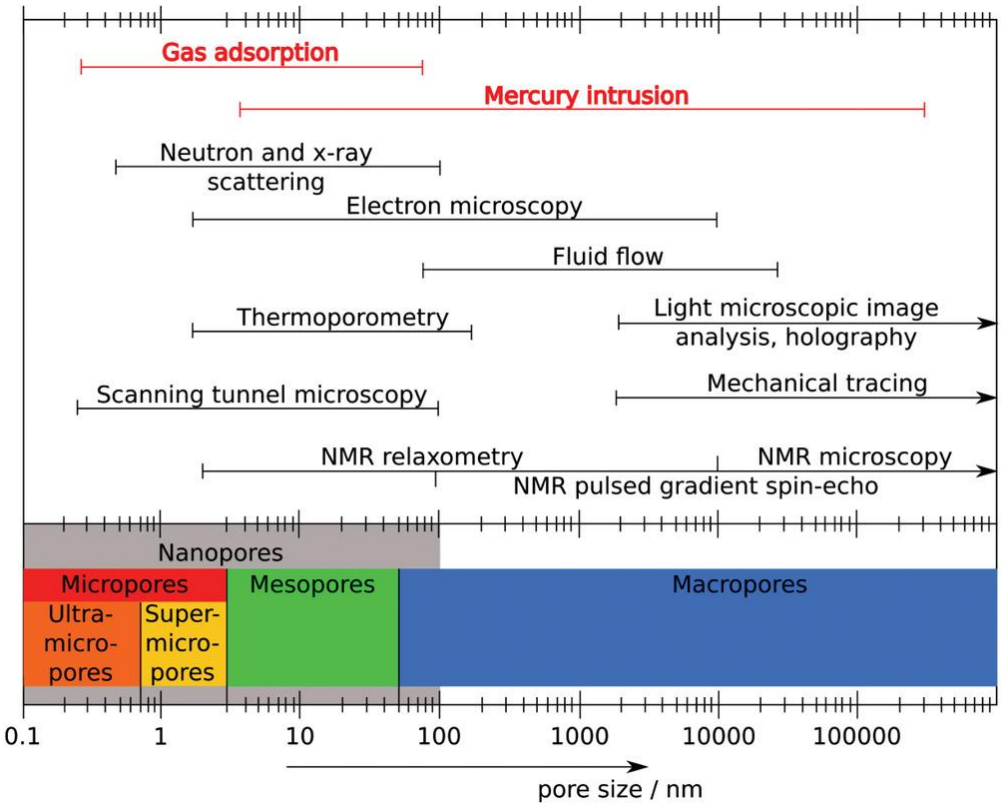


Figure 8: Application ranges of various characterization methods for pore size determination. This figure was originally published by Schlumberger *et al*.[154] in *Advanced Materials Interfaces* under a CC BY-NC-ND 4.0 license.

An exemplary porosity characterization of a BTEVP-PMO with ordered mesopores, high surface area, and a crystal-like pore wall arrangement is shown in Figure 9. The chemical integrity of PMOs after synthesis or post-synthetic functionalization can be assessed using infrared spectroscopy to identify characteristic functional groups, solid-state nuclear magnetic resonance (NMR) to examine framework integrity and the degree of condensation, and thermogravimetric analysis to evaluate the stability of organic moieties and functional groups. Since the condensation process is reversible, PMOs can also be dissolved in aqueous sodium hydroxide and analyzed by solution-state NMR, yielding higher-resolution information on functional group composition and concentration.

The pore structure and the degree of pore ordering in PMOs are closely tied to the precursor structure and the synthesis conditions. Unlike conventional porous silica, PMOs can be produced with amorphous as well as crystal-like pore walls. Aromatic or conjugated bridging groups such as 1,4-bis(triethoxysilyl)benzene (BTEB) and vinyl-functionalized analogs like 1,4-bis[(*E*)-2-(triethoxysilyl)vinyl]benzene (BTEVB), 2,5-bis[(*E*)-2-(triethoxysilyl)vinyl]-aniline (BTEVA), and 2,5-bis[(*E*)-2-(triethoxysilyl)vinyl]-pyridine (BTEVP), developed by Wang *et al*.,[144] Fröba *et al*.[145,161] and Inagaki *et*

al.,[162] support pseudo-crystalline pore walls, most likely due to π–π stacking. PMOs synthesized under basic conditions often exhibit wide-angle XRD reflections indicative of short-range molecular order, whereas acidic conditions typically produce amorphous walls, despite retaining ordered pore arrangements.[142,149]

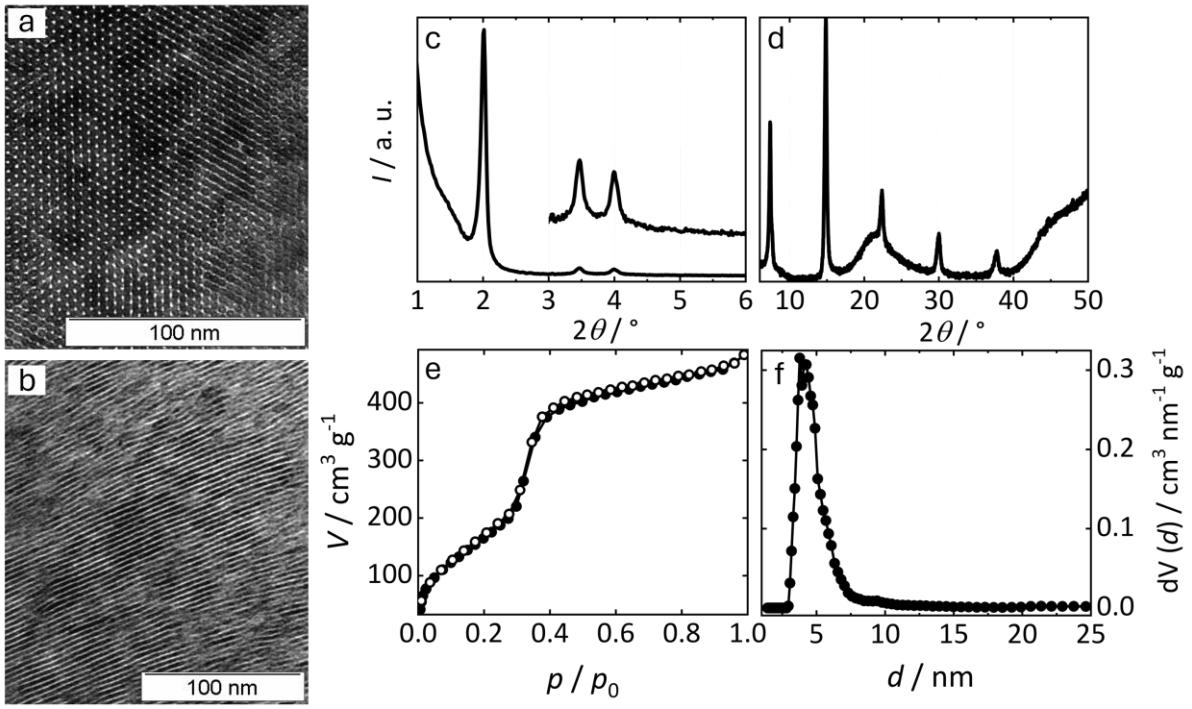


Figure 9: An exemplary BTEVP-PMO with hexagonally ordered pores as shown by TEM images from top view (a) and side view (b), along with the corresponding normalized PXRD patterns in the range of 1–6° 2*θ* (c). The normalized PXRD pattern in the range of 6–50° 2*θ* (d) shows a crystal-like arrangement of the pore walls. Nitrogen physisorption isotherms at 77 K (e) with adsorption (filled circles) and desorption (hollow circles) branches, and the corresponding pore size distribution curves (f), calculated using the NLDFT kernel "N_2 at 77 K on silica, cylindrical pores" based on the adsorption branch, are also shown. This figure was published by Lenz *et al*.[62] in *The journal of Chemical Physics* under a CC-BY 4.0 license. The image has been modified.

The PMOs used in this study are shown in Figure 10. In addition to literature-known precursors for PMO synthesis such as BTEB,[143] BTEVB,[144,145] BTEVA[161,163] and a significantly optimized BTEVP,[162] two newly developed PMO types were employed, one based on the 2-chloro-1,4-((*E*)-2'-bis(triethoxysilyl)vinyl)benzene (BTEVClB) precursor, and another derived from an *in situ* methylation of BTEVA with iodomethane, yielding the twice-methylated *N*,*N*-dimethyl-2,5-bis((*E*)-2-(triethoxysilyl)vinyl)aniline (*N*,*N*-DMBTEVA)-PMO.[62,129] Both the BTEVClB- and *N*,*N*-DMBTEVA-PMOs are considered more hydrophobic materials. Because water in nature frequently occurs at charged interfaces that affect its structure, dynamics, viscosity, and interfacial interactions, which are relevant for biological, geological, and technological

systems,[164,165] a post-synthetically modified, salt-like *N*-MBTEVP^{+}I^{-}-PMO was developed based on the BTEVP-PMO framework.

PMOs are attractive for stimulus-responsive drug or compound delivery, catalysis, chemical separations, sensing, and CO_2 capture due to their advanced porosity, high loading capacity, and mechanical and hydrothermal stability, as well as their versatile surface modification.[142,166,167] Amino acids and their derivatives have been used to introduce pH-responsive functionalities with high potential for drug delivery and enzyme immobilization.[168] For this purpose, histidine-,[168] alanine-,[161,169] aspartic-acid-,[170] tyrosine-,[171,172] serine-,[173] and chiral-functionalized PMOs[174] were introduced into the PMO framework. Because water is always present in biological environments, water–amino-acid interfacial interactions and water dynamics under controlled confinement have been investigated.[175] In this work, PMOs functionalized with amide–acid and aspartic acid groups were used to study their influence on confined water behavior (see Figure 10).

Besides the homopolymeric PMOs described so far, two different precursors can be used to synthesize co-polymeric PMOs. This approach is particularly useful when a precursor alone cannot condense into a stable framework or interact sufficiently with the surfactant to form an ordered PMO under given synthesis conditions. Introducing a second precursor that readily forms a PMO under those conditions can assist the assembly and condensation of the desired precursor. To achieve this, tetraethyl orthosilicate (TEOS) or other PMO-forming precursors are often used as secondary silica sources.[142,167,176] Furthermore, this method allows the systematic investigation of surface chemistry effects on confined guest molecules by gradually varying the ratio of two precursors with distinct surface functionalities, rather than comparing separate homopolymers. For instance, co-condensation of the hydrophobic, functional-group-free divinylbenzene bridge of BTEVB-PMO with the amine-containing BTEVA at different ratios allows detailed insight into the influence of amine functionalities on water behavior. However, this method also has limitations, as the spatial distribution of the two components is generally random and poorly controlled. In addition, identifying synthesis conditions suitable for both precursors is challenging, often resulting in materials with inferior porosity characteristics, such as reduced pore order and broader pore size distributions compared to the homopolymers. Furthermore, the actual composition of the resulting material can deviate from the intended precursor ratio.[142]

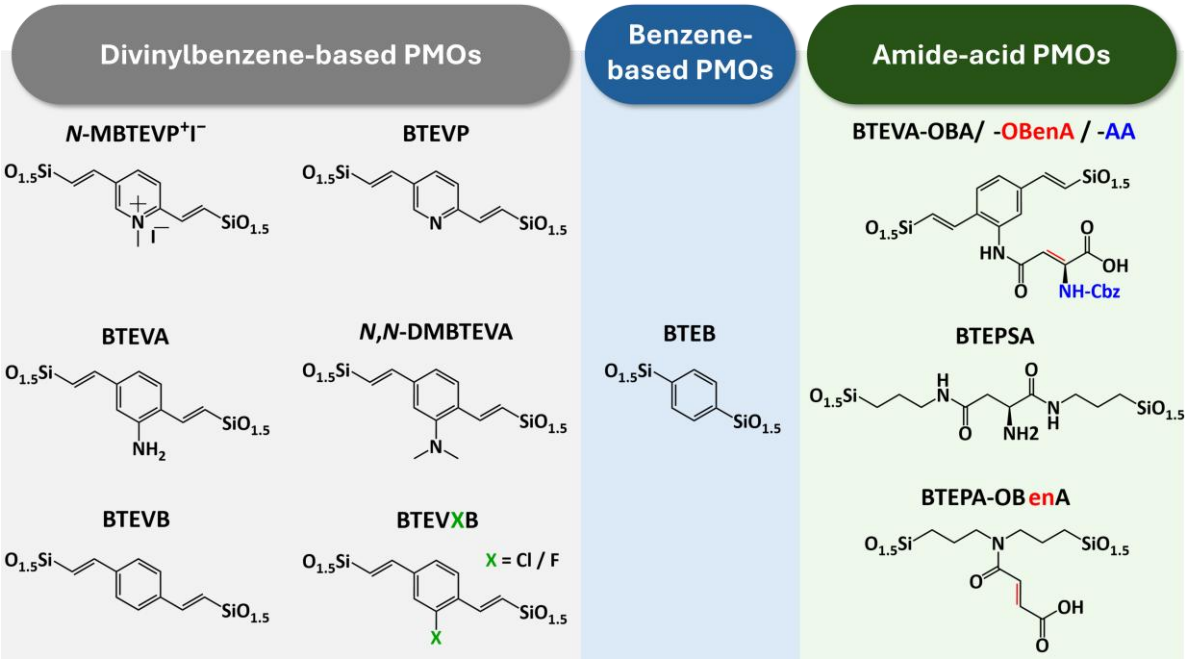


Figure 10: Overview of PMOs used in this study.

3.3. Analytical Methods for Investigating Water Behavior in Nanoconfinement with Different Surface Hydrophilicity

To investigate the behavior of confined water across its various phases, a wide range of analytical techniques has been employed, complementing molecular dynamics simulations.[74,98,102,109,110,124,131,177–182] These include infrared (IR),[35,50,66,67,183–186] Raman,[50,89,101,187] and NMR spectroscopy,[28,55,70,141,146,175,188–192] X-ray[53,68,74,75,97,120,122,129,193] and neutron experiments,[35,68,71,76,100,117–120,194–199] calorimetric methods such as differential scanning calorimetry (DSC),[54,57,75,87,120,141,188,192,198] water vapor sorption (WVS),[58,59,61,137,200] and dielectric spectroscopy.[133,175,192,198,201]

Despite extensive research on confined water, the combined influence of pore size and surface chemistry on its interfacial and confined states is still not fully resolved.[27,28,104] To determine the impact of surface chemistry on confined liquid water and its adsorbed surface layer, on thermodynamic properties during adsorption, and on freezing and melting behavior, including the remaining non-freezable layer between the frozen core and the pore wall, water vapor sorption (including temperature-dependent measurements), gravimetric adsorption calorimetry, and low-temperature DSC were employed in this work. While the following chapters focus primarily on these analytical approaches, complementary experiments, including X-ray scattering and quasielastic neutron scattering, were conducted to investigate the structural and

dynamic properties of nanoconfined water. The theoretical background and data evaluation of these methods are described in detail in the respective original publications, the doctoral thesis of the first author, or the relevant literature.[68,79,129,199,202–204] In many studies, surfaces are treated as ideally flat, assuming that water forms a homogeneous, well-ordered monolayer. While such simplifications help to identify general principles, real-world environments such as biomolecules are far more complex, with nanoscale roughness and heterogeneous chemical functionalities in close proximity, both complicating interfacial water structuring. PMOs, featuring alternating hydrophilic silanol groups and organic bridges with tunable chemistry, offer a practical middle ground. They retain structural simplicity through periodic and geometrically simple cylindrical pores while introducing controlled chemical complexity, making them ideal model systems that bridge the gap between idealized and biologically relevant surfaces.

3.3.1. Water from Adsorbed Layers to Confined Liquids: Probing Water–Surface Interactions via Vapor Sorption

As outlined in Chapter 3.1, water nanoconfined by surfaces with different interaction strengths exhibits distinct structural and thermodynamic behavior. Water vapor sorption is a suitable method to study adsorption and desorption, as well as condensation and pore-emptying behavior, providing information on water–wall interaction strength, the density of confined water and of hydrophilic surface sites, adsorption layer dimensions, and the material's water resistance.

Two measurement approaches are commonly used: volumetric and gravimetric. In volumetric water vapor sorption, the sample is first evacuated and then exposed to a defined water vapor pressure. Adsorption by the sample causes a measurable pressure drop. With the system's temperature, volume, and pressure known, the corresponding amount of adsorbed water can be determined. In gravimetric water vapor sorption, the mass change is monitored at controlled relative humidity. At each humidity step, the sample is allowed to equilibrate before the next increase (adsorption) or decrease (desorption), and the associated mass change is measured. Gravimetric measurements typically employ a carrier gas such as nitrogen. Despite these methodological differences, a good agreement between the resulting isotherms has been reported.[61] In this study, water vapor sorption experiments were performed volumetrically using VSTAR instruments from Quantachrome.

For cylindrical porous materials with identical surface chemistry, decreasing pore size leads to a shift of the gas–liquid transition to lower relative pressures. This pore-size-dependent shift is well described by the Kelvin equation for cylindrical pores:[84,85]

$$\ln\left(\frac{p}{p_0}\right) = -\frac{2\, v_l\, \gamma \cos(\theta)}{R\, T\, (r_P - t_a)} \tag{1}$$

with the relative pressure at which the phase transition takes place (p/p_0), the surface tension of confined water (γ), the molar volume of water in confinement (v_l), the universal gas constant (R), the temperature (T), the adsorption-layer thickness (t_a) and the pore radius (r_P), determined from nitrogen physisorption using a cylindrical pore NLDFT kernel.

Hydrophilicity reflects the interaction strength between water and a surface, which can be quantified using various parameters. These parameters are essential for understanding water's behavior in different states on various surfaces. A widely used measure is the contact angle (θ), which describes the wettability of a surface by a liquid. For confined water, the contact angle can be estimated using a modified Kelvin equation introduced by Kocherbitov and Alfredsson:[205,206]

$$\theta = \arccos\left(\frac{r_P\, R\, T\, ln\left(\frac{p}{p_0}\right)}{-\sqrt{\frac{V_P}{V_P - V_a}}\, 2\, \gamma\, v_l}\right)\frac{\pi}{180} \tag{2}$$

where V_P is the total pore volume and V_a is the volume of adsorbed water. Both γ and v_l are temperature dependent. For water at 273.15 K under confinement, values of 71.69 mJ m^{-2} and $20.5 \cdot 10^{-6}$ m^3 mol^{-1}, respectively, were used.[205]

From the slope of the adsorption branch at low pressures (< 340 Pa) in a plot of the specific water amount (in mol g^{-1}) against the absolute pressure (in Pa), the Henry adsorption constant (K_H) can be determined. In the adsorption of water vapor on a solid surface, K_H quantifies the strength of the water–surface interaction at low vapor pressures, with higher values indicating greater affinity of water for the surface. Using this approach, Canivet *et al.*[136] were able to rank different MOFs according to their hydrophilicity. The Henry adsorption constant is temperature dependent and can be used to calculate the energy change associated with the adsorption of a gas molecule onto the surface.[207,208]

By comparing the adsorption of water, which is sensitive to surface chemistry and readily forms hydrogen bonds with specific functional groups, to that of non-surface-sensitive adsorbates such as nitrogen (which interacts only weakly via its quadrupole moment) or argon, hydrophilicity indices (*HI*s) can be determined. Using mesoporous zeolites, Thommes *et al*.[137] developed a hydrophilicity index (HI_T) that compares the volume of water and nitrogen adsorbed during sorption experiments after micropore filling (p/p_0 = 0.15) and mesopore filling (p/p_0 = 0.92). In this volumetric comparison, highly hydrophilic materials are readily wetted by water, resulting in HI_T values approaching 1.

An alternative approach was proposed by Fröba *et al*.[200] with the introduction of HI_{BET}, which is based on comparing the specific BET surface areas obtained from water vapor sorption and nitrogen or argon physisorption. Since this hydrophilicity index is determined at low pressures, where water strongly interacts with surface functional groups, it is highly surface-sensitive. More recently, another hydrophilicity index was introduced, calculated from the ratio of water to nitrogen relative pressure at the inflection point of the capillary condensation (HI_{ia}) or pore emptying (HI_{id}) step, using the following equation:[62]

$$HI_i = \frac{\ln\left(\frac{p}{p_0}\right)_{i,w}}{\ln\left(\frac{p}{p_0}\right)_{i,n}} \tag{3}$$

The relative pressure at the inflection point for nitrogen physisorption (i,n) is predominantly determined by the pore size, whereas for water sorption (i,w) it is influenced by both pore size and surface chemistry. Since the expressions in Equation (3) are linked to the Kelvin Equation (1), this HI_i has the advantage of retaining information on the contact angle, providing a direct measure of hydrophilicity while also accounting for pore radius and adsorption-layer thickness.

Beyond the hydrophilicity indices presented, additional parameters are continually being developed.[62,209,210] The slope of the adsorption branch before capillary condensation (s_a) or after pore emptying (s_d) has also proven useful for reliably assessing a material's hydrophilicity.[62,211] For materials of similar class and identical pore size, the relative pressures at the onset or inflection points of capillary condensation allow a reliable distinction between different degrees of hydrophilicity.[62]

The primary origin of surface hydrophilicity lies in its surface chemistry, more precisely in the density of surface hydration sites (*SHS*). Using the adsorption branch of water vapor sorption isotherms, the specific BET surface area from water sorption ($S_{BET,w}$), the specific BET surface area from nitrogen physisorption (S_{BET}), and the cross-sectional area of water (0.125 nm^2)[58], the *SHS* can be determined using the following equation:

$$SHS = \frac{S_{BET,w}}{0.125\ S_{BET}} \tag{4}$$

Compared to S_{BET}, the $S_{BET,w}$ is typically considerably smaller, as is the case for all materials used in this study. This difference arises from the preferential adsorption of water molecules at hydration sites and their absence in hydrophobic regions. For MCM-41 type porous silicas, *SHS* densities between 1.2 and 3.4 nm^{-2} (depending on the sample pretreatment conditions)[58] have been reported, which is consistent with ^{15}N-NMR experiments[212] and other reports.[50,57,205,213] While only silanol groups serve as adsorption sites for water in MCM-41 silica, PMOs additionally contain hydrophilic functional groups in the organic regions that contribute to the *SHS*. An exemplary water vapor sorption isotherm (see Figure 11) illustrates the ranges used to determine the various hydrophilicity parameters.

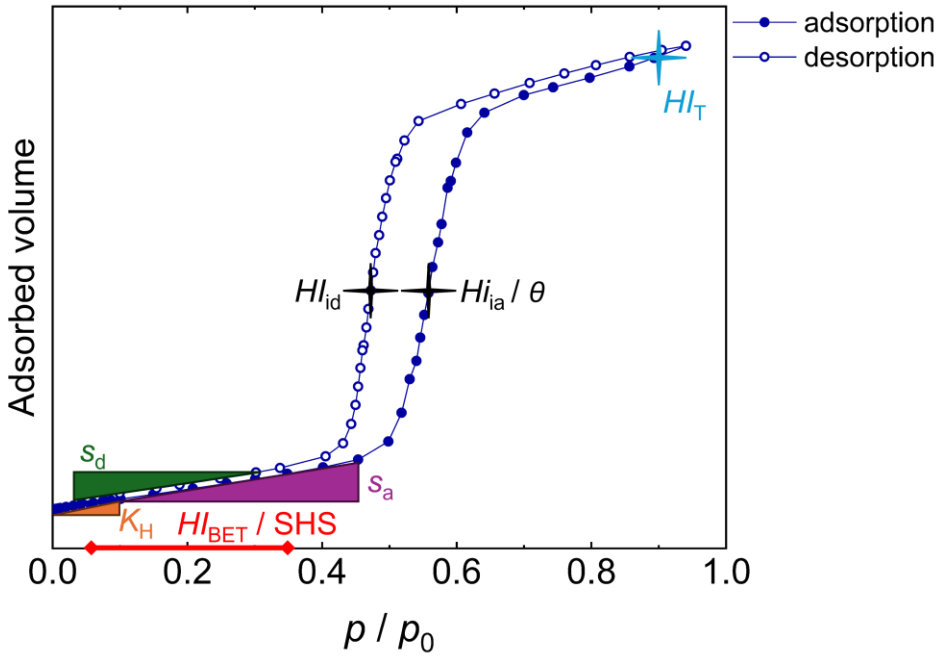


Figure 11: An exemplary volumetric water vapor sorption isotherm at 25 °C, showing the relative pressure regions used to determine different hydrophilicity parameters.

Using a range of hydrophilicity parameters provides a comprehensive assessment of a material's water affinity and allows for a detailed classification of hydrophilicity. Since each parameter is derived from a different region of the isotherm, hydrophilicity can be evaluated at various filling levels. Comparisons of different hydrophilicity parameters for PMOs and MCM-41 silica reveal similar overall trends, while also highlighting the effects of specific functional groups, such as the dual hydrophobic–hydrophilic behavior of fluorinated PMOs.[62] Additionally, the parameters complement each other when individual methods face limitations. For example, the HI_T is less reliable for materials with hydrophobic surfaces and/or large pore sizes, where incomplete condensation prevents plateau formation, and comparisons are ideally made with materials of similar porosity. With increasing pore size, the surface-to-volume ratio decreases, reducing the sensitivity to hydrophilicity, particularly for parameters that rely on fully filled pores.[62] Therefore, employing multiple *HI*s enables more robust hydrophilicity comparisons across different material classes. Additionally, the hydrophilicity of porous materials can be divided into an internal component, referring to water vapor adsorption at the pore surface, and an external component, describing the interaction of liquid water with the surface, commonly characterized by the contact angle.[214] For water confined inside pores, hydrophilicity depends not only on the properties of the pore surface but also on confinement effects.[62,215]

The presence of an adsorption layer, sometimes referred to as the *t*-layer (here t_a-layer), which behaves differently from the core water, was described in Chapter 3.1. It is well established that the *t*-layer imposes an additional restriction on the effective pore dimension. In the lower mesoporous range, its thickness significantly contributes to the confinement effects described by the Kelvin Equation (1), making it essential to understand its surface chemistry-dependent dimensions and its influence on confined water. Using water vapor sorption, Rother *et al*.[58,59] developed a geometrical approach to determine the t_a-layer thickness and density in porous silicas with hydraulic pore radii ranging from 1.19–32.1 nm. By exposing materials such as MCM-41 silica to water vapor and regenerating them under various conditions, they achieved different surface silanol densities and, consequently, varying hydrophilicities. The adsorption-layer thickness can be calculated using the hydraulic pore radius (r_h) and the liquid core radius (r_c), which is derived from the liquid water volume uptake during capillary condensation ($V_{pc,w}$) assuming the bulk water density (0.997 g cm^{-3})[58] (see Equation (5)–(7)).

$$r_h = \frac{2\,V_P}{S_{BET}} \tag{5}$$

$$r_c = \sqrt{\frac{V_{pc,w}\,r_h^2}{V_P}} \tag{6}$$

$$t_a = r_h - r_c \tag{7}$$

Contrary to the common assumption, when applying the Kelvin equation, it was found that the adsorption-layer thickness is not constant but scales with the pore size.[58,59] As the pore size increases, the condensation step shifts to higher pressures, allowing a thicker adsorption layer to form. Conversely, in smaller pores, curvature effects may influence the t_a-layer dimensions and modify the interaction behavior of neighboring water molecules.

The density of the adsorbed water layer can be calculated by dividing the amount of water at the onset of capillary condensation (m_a) by the adsorption-layer volume (V_a), as described by the following equation:

$$\rho_a = \frac{m_a}{V_a} = \frac{m_a}{V_P - V_{pc,w}} \tag{8}$$

It was observed that values of ρ_a are significantly lower (for MCM-41 silica about 0.5–0.7 g cm^{-3}) than the bulk density and scale with *SHS*.[58,59] The density defined in Equation (8) does not reflect the actual microscopic water density but represents an average over the entire surface volume. Water preferentially adsorbs at *SHS*, forming small aggregates of a few water molecules with bulk-like or potentially even higher densities,[146,216,217] hereafter referred to as water clusters, while avoiding more hydrophobic regions.[146,186,205] The presence of these voids in the water layer reduces the average density of the adsorption layer, leading to a lower overall density of confined water. In materials with fewer *SHS*, i.e., higher hydrophobicity, the distances between water clusters are larger, further lowering ρ_a and the average confined water density, as illustrated in Figure 12.

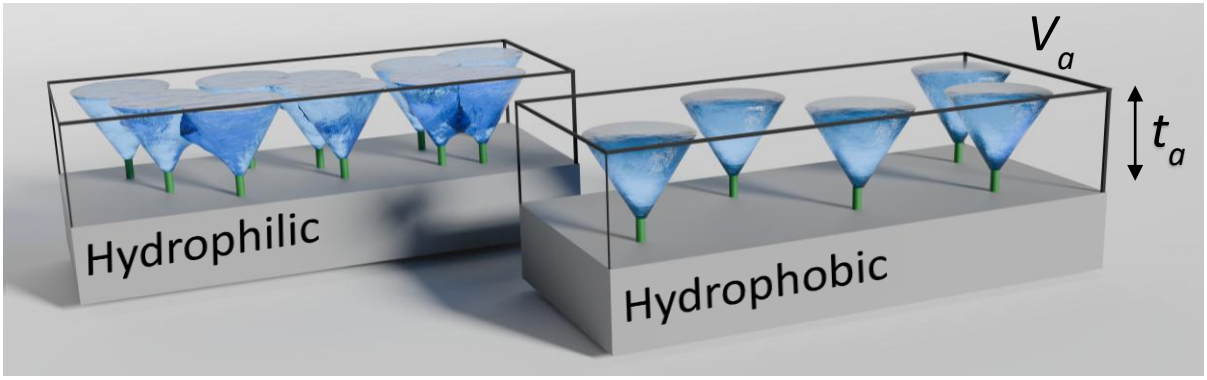


Figure 12: Schematic illustration of water (blue cone) density in the adsorption layer (t_a) with volume (V_a) in a fully water-filled pore (core water would be located above the t_a-layer and is not illustrated here) at the pore wall (gray rectangular cuboid), showing a higher density of surface hydration sites (green sticks) for hydrophilic surfaces and a lower density for hydrophobic surfaces.

3.3.2. Energetics of Adsorption: Deconstructing the Influence of Surface Chemistry on Water–Surface Interactions via Isothermal Calorimetry and the Isosteric Enthalpy Method

The interaction strength between a surface and water is established at the first contact, where water either strongly interacts with and adsorbs onto available hydration sites, or, if such sites are not available on hydrophobic surfaces, interacts weakly via van der Waals forces or avoids surface adsorption to a certain extent. A key thermodynamic parameter describing the strength of water–material interactions and the energetics of the adsorption process is the enthalpy of adsorption. During adsorption, the adsorbate loses translational degrees of freedom and adopts a more ordered state than in the vapor phase, resulting in a negative entropy change (ΔS). Since adsorption is a spontaneous process, the Gibbs free energy change (ΔG) is also negative, which, according to Equation (9), requires a negative enthalpy change (ΔH), making adsorption an exothermic process.[156]

$$\Delta G = \Delta H - T\Delta S \tag{9}$$

Strong hydrogen bonding and polar interactions on hydrophilic surfaces lead to higher adsorption enthalpies, whereas hydrophobic surfaces, with weaker water–surface interactions, typically show lower adsorption enthalpies.[218–223]

Two main experimental approaches can be used to determine the adsorption enthalpy: the indirect isosteric method and the direct calorimetric method.[155,224–228] The isosteric method determines the isosteric enthalpy of adsorption ($\Delta H_{a,st}$),

sometimes also referred to (though not recommended) as the isosteric heat of adsorption ($Q_{a,st}$),[155,227] by applying the Clausius–Clapeyron equation to adsorption isotherms measured at different temperatures. This involves plotting the natural logarithm of pressure ln(p) against the reciprocal temperature (T^{-1}) at a constant surface coverage. This method is widely used because it can be performed with standard sorption equipment and a straightforward experimental setup. However, it relies on the assumption of ideal gas behavior, requires multiple isotherms to be measured at closely spaced temperatures (ideally about 10 K apart) to minimize errors, and is highly sensitive to inaccuracies in the measured equilibrium pressure. The isosteric method is generally not recommended at low surface coverages (< 0.5), as phase transitions or measurement errors in this range can lead to substantial inaccuracies in the calculated values.[155,225,229,230] Figure 13 shows an exemplary determination of the isosteric enthalpy of adsorption using three water vapor sorption isotherms measured at 25, 35, and 45 °C.

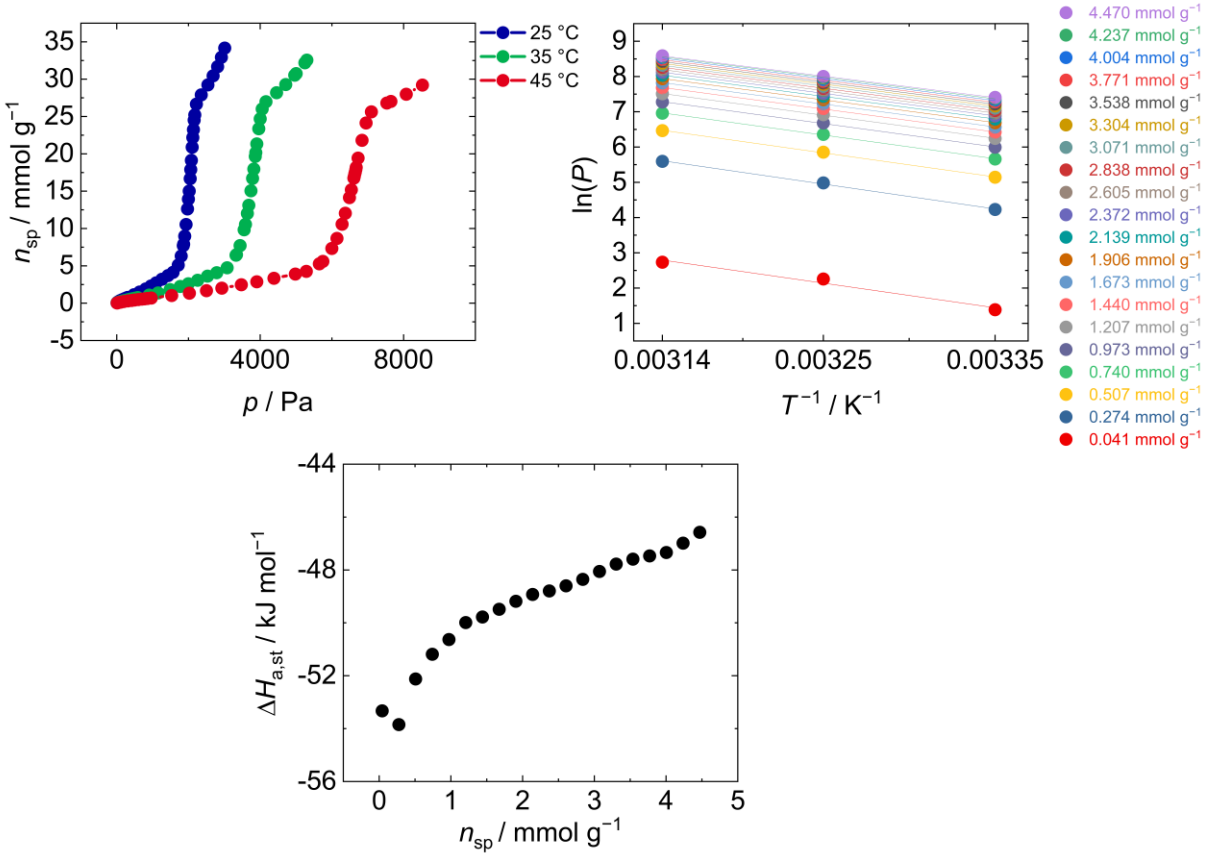


Figure 13: Determination of the isosteric enthalpy of adsorption based on three water vapor sorption isotherms measured at different temperatures (top left) for a BTEVA-PMO with a pore diameter of 3.8 nm. The pressure at constant loading (interpolated specific water amount (n_{sp}) from the isotherms) is used to construct a Van't Hoff plot (top right) , from which the enthalpy is determined. The resulting enthalpy is then plotted as a function of n_{sp} (bottom).

At a constant specific water amount (n_{sp}), the corresponding absolute pressures are extracted from all three isotherms and plotted as ln(p) against T^{-1} in a Van't Hoff plot (Figure 13, right). The analysis is based on the Clausius–Clapeyron relation in the integrated form:

$$\ln(p) = -\frac{\Delta H_{a,st}}{R} \cdot \frac{1}{T} + C \tag{10}$$

If the pressure p is replaced by an equilibrium constant (K), the same expression corresponds to the Van't Hoff equation.[207] $\Delta H_{a,st}$ can be determined from the slope and plotted as a function of the corresponding n_{sp} (Figure 13, bottom).[230] The constant C is related to the entropy change (ΔS) of the adsorption process and can be determined from the intercept.[231–233]

The absolute entropy of adsorption ($S_{a,st}$) for each adsorbed water amount can be calculated using the following equation:[223,234,235]

$$\ln\left(\frac{p_0}{p}\right) = -\frac{\Delta H_b - \Delta H_{a,st}}{RT} - \frac{S_b - S_{a,st}}{R} \tag{11}$$

with the bulk water condensation enthalpy (ΔH_b = −44 kJ mol^{-1} at 298 K) and the entropy of bulk liquid (S_b = 69.9 J mol^{-1} K^{-1} at 298 K).

Since adsorption is an exothermic process, the enthalpy of adsorption is inherently negative and reflects the interaction strength between water and the solid surface. For clarity, adsorption enthalpies are reported in this work as absolute values ($|\Delta H_a|$), so that larger values correspond directly to stronger water–wall interactions. At low surface coverage, hydrophilic materials often show a maximum or initially high $|\Delta H_{a,st}|$, which decreases with loading and eventually approaches the condensation enthalpy of bulk water. This reflects the higher energy release from stronger water–surface interactions compared to water–water interactions.[219,220,236] For example, a silica surface with silanol groups as hydration sites shows higher $|\Delta H_{a,st}|$ values than partially methylated (hydrophobized) silica, for which $|\Delta H_{a,st}|$ increases with loading.[223] It was found that for $|\Delta H_{a,st}|$ values higher than the bulk condensation enthalpy, combined with low isosteric adsorption entropy values, solid-like structures in the adsorption layer are dominant.[223,236]

In contrast, hydrophobic materials show less structuring of water, with entropies closer to bulk values. For hydrophobic surfaces, $|\Delta H_{a,st}|$ is initially lower and reaches

bulk values only at higher water loadings, where surface effects are less significant. This surface dependence of $|\Delta H_{a,st}|$ is illustrated in Figure 14 for a hydrophilic MCM-41 silica and a hydrophobic BTEVB-PMO.

In Chapter 3.3.1, the Henry adsorption constant and its use for categorizing different materials according to their hydrophilicity were discussed. Since K_H is determined at low pressures of the adsorption isotherms, it provides a sensitive measure of the water–wall interaction. By determining K_H from isotherms measured at different temperatures, the average absolute value of the adsorption enthalpy of the first water layer ($|\Delta H_{a,K}|$) can be calculated analogously to the isosteric method by replacing p by K_H in Equation (10).[155,207,208,237]

In the BET equation,[238] the BET constant (C_{BET}) is an energetic term that can be used to approximate the absolute adsorption enthalpy of the first water layer ($|\Delta H_{a,BET}|$) according to the relation:[155,239,240]

$$\Delta H_{a,BET} = T\,R\,\ln(C_{BET}) + \Delta H_b \qquad (12)$$

The calorimetric method directly measures the enthalpy released during adsorption, providing a model-independent and highly accurate determination of $|\Delta H_{a,c}|$, especially at low coverage and on heterogeneous surfaces. Calorimetry is considered the gold standard for probing adsorption energetics, particularly in studies of micropore filling and high-energy adsorption sites. Its application, however, is limited by the requirement for highly sensitive and costly equipment, as well as tightly controlled experimental conditions.[155,225–227] Further details on calorimetric principles, mainly for DSC, are provided in Chapter 3.3.3.

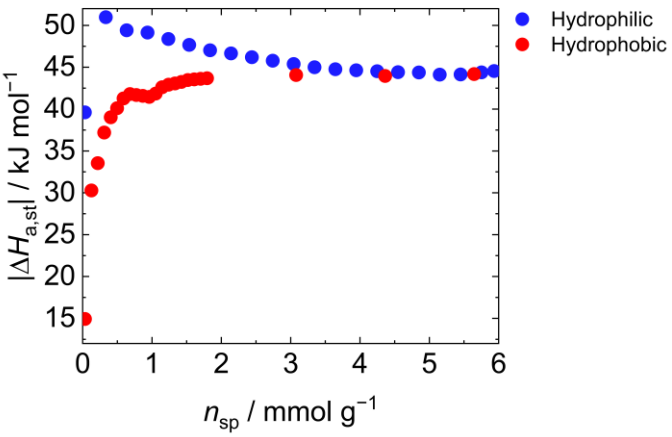


Figure 14: Comparison of the absolute values of isosteric enthalpy of adsorption ($|\Delta H_{a,st}|$) as a function of specific water amount (n_{sp}) for water adsorption in the pores of hydrophilic MCM-41 silica and hydrophobic BTEVB-PMO.

To investigate the enthalpy of water adsorption, several calorimetric methods have been applied in the past, including Tian–Calvet calorimetry[221,241–245] and humidity titration calorimetry.[224,246] In this work, a hybrid approach combining thermogravimetric analysis (TGA) and differential scanning calorimetry (DSC) with a humidity generator was employed. A schematic of the experimental setup is shown in Figure 15. Samples were exposed to a nitrogen stream with stepwise increasing relative humidity at constant temperature (25 °C), allowing simultaneous monitoring of mass uptake and heat flow during sorption. Reliable DSC detection requires a sufficiently high absolute surface area. As shown in Figure 15, mesoporous MCM-41 silica (1118 $m^2\ g^{-1}$, ~5 m^2 absolute surface area) produces the strongest signals, whereas CPG (18 $m^2\ g^{-1}$) and non-porous glass exhibit much weaker signals. Based on experimental experience, an absolute surface area of 3–6 m^2 is optimal for resolving water uptake and enthalpy changes, whereas values below ~2 m^2 result in poor signal quality and pronounced balance drift errors. This setup represents a variant of isothermal sorption calorimetry, analogous to humidity titration calorimetry,[246] but operated in continuous-flow mode[247,248] on a standard DSC-TGA system. It allows direct determination of hydration enthalpies together with adsorption isotherms, providing precise control of RH and stable equilibration at each step. Similar concepts have been applied in studies of water desorption from hygroscopic fibers during heating,[249] capillary condensation of propane in mesoporous silica,[250] water vapor adsorption on coal at elevated temperature,[247] and sorption processes in zeolites and MOFs.[251] Despite the well-established nature of thermal analysis and adsorption methods, applications using this combined setup remain limited. Most previous studies have focused on desorption, whereas adsorption experiments with fine relative humidity resolution and very low coverage, particularly relevant for materials with diverse surface functionalities, as in the present study, remain largely unexplored.

The adsorption enthalpy change can be calculated by determining the area of the DSC adsorption signal (A), together with the gravimetrically measured adsorbed water amount ($n_{w,a}$) obtained from stepwise humidity increases, and applying a calibration factor ($k_{c,f}$). The calibration factor, determined in this study using the organic reference material Micronal (BASF), converts the DSC signal from Vs to J. The adsorption enthalpy is then calculated using the following equation:

$$\Delta H_{a,c} = \frac{A\ k_{cf}}{n_{w,a}} \tag{13}$$

Further, $\Delta H_{a,c}$, together with the absolute vapor pressure (p) and a reference pressure (p_r = 10^5 Pa), can be used to calculate the entropy change upon adsorption ($\Delta S_{a,c}$):[252]

$$\Delta S_{a,c} = \frac{\Delta H_{a,c} - R\,T \ln\left(\frac{p}{p_r}\right)}{T} \tag{14}$$

A comprehensive understanding of adsorption thermodynamics across different surface chemistries is critical for optimizing porous materials in applications such as water harvesting,[253,254] adsorption-driven heat pumps,[255–257] and separation processes,[41,258,259] as well as for elucidating fundamental adsorption mechanisms. While surface hydrophilicity is a primary factor, surface roughness[91] also significantly influences adsorption behavior. Notably, in contrast to typical hydrophobic trends, fluorinated surfaces show increasing adsorption enthalpies with higher fluorine concentration.[260] Understanding these adsorption energetics provides insight into the initial adsorption layer, where water first interacts with the surface, and clarifies how surface effects propagate into subsequent layers of adsorbed or condensed water.

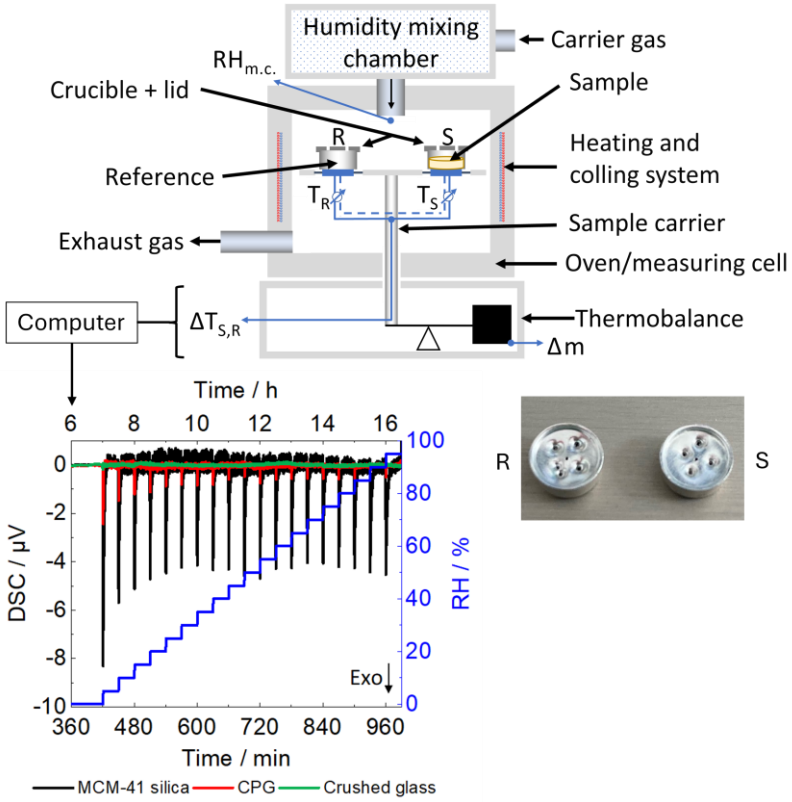


Figure 15: Schematic illustration of the experimental setup used for calorimetric water vapor adsorption measurements under controlled temperature and humidity conditions, including an image of aluminum crucibles with perforated lids. In addition, baseline-corrected water vapor adsorption data under isothermal conditions are presented for three silica materials with different surface areas. This figure was published by Lenz *et al.*[211] in *The Journal of Chemical Physics* under a CC-BY 4.0 license. The image has been modified.

3.3.3. Nanoconfined Ice: Investigating the Impact of Surface Chemistry on Water's Freezing Behavior via Differential Scanning Calorimetry

Water confined in pores freezes and melts below its bulk transition temperature. As previously discussed, this depression of freezing and melting points has attracted attention because it allows experimental access to the no-man's-land.[28,201] Furthermore, controlling crystallization in confined spaces requires a detailed understanding of how surface chemistry, confinement dimensions, and pore geometry influence transition temperatures, nucleation rates, crystal structure and orientation, as well as molecular dynamics. To investigate the melting and freezing behavior of confined water, a range of methods has been applied, including NMR spectroscopy,[70,76,188–192,261] DSC,[54,70,75,188,192,262] XRD,[74,75,97,122,129,193] neutron experiments,[71,76,194,195] and Raman spectroscopy.[89]

In this work, DSC was used to investigate how surface chemistry influences the melting and freezing behavior of nanoconfined water. According to ISO 11357-1, Differential Scanning Calorimetry is a thermoanalytical method that records the heat-flow difference between a sample and a reference. During a measurement, both follow the same controlled temperature program, and the resulting heat-flow difference is monitored as a function of temperature and/or time. Any endothermic or exothermic event, such as melting, freezing, or a glass transition, creates a temperature difference (ΔT) between the sample and reference. This ΔT is proportional to the heat flow rate (Φ) and is measured as an electrical voltage. The heat flow rate, defined as the heat exchanged per unit time ($\Phi = \mathrm{d}Q / \mathrm{d}t$), is related to the measured temperature difference through a calibration factor (K):[263]

$$\Phi = -K \cdot \Delta T \tag{15}$$

For bulk materials, transition temperatures are typically taken from the onset of the DSC signal, because this point marks the start of the transition and is independent of the heating rate. For liquids confined in nanometer-sized pores, the DSC peaks broaden due to higher sensitivity to the pore size distribution, making the onset less reliable. In this case, using the peak maximum is a practical way to determine the transition temperature.[57] Since the maximum can shift with heating rate and water loading, comparisons must be made at identical heating rates and similar sample amounts. In MCM-41 silicas and PMOs, the water content is only in the microliter range, so the heating rate needs to be high enough to generate a clear signal, yet low

enough to resolve closely spaced peaks. Heating rates between 1–10 K min^{-1} give reliable signals, with 3 Kmin^{-1} being particularly well-suited.

Two filling methods are commonly used: the incipient wetness (IW) and the climate chamber (C) method. In the IW approach, water is dosed based on the sample mass and the pore volume determined from nitrogen physisorption, aiming to achieve full theoretical pore filling. In practice, this often results in excess bulk water, most likely due to the reduced density of confined water and uncertainties when dosing very small volumes. In Figure 16 (left), a BTEVA-PMO was filled to various degrees, with bulk freezing and melting signals observed at 100 % and 150 % filling. Using less water than the calculated pore volume avoids bulk water formation, as observed for the 60 % filling. The absence of bulk water indicates that the added water droplets are entirely confined within the pores. Across these three filling degrees, mass-related thermal lag effects in the DSC melting transitions are evident, with the melting temperature shifting to higher values at higher water loadings (150 %), whereas the freezing process is less affected. The signal intensity associated with confined water differs because the heat flow is normalized to the total water amount used in the DSC experiment. In further analysis, the bulk water contribution can be subtracted using the determined enthalpy values. In contrast to the IW approach, the C method exposes the samples to water vapor at 25 °C and 90 % relative humidity for at least 24 h, allowing the pores to fill without forming bulk water, similar to the WVS approach.

All low-temperature DSC measurements of confined water exhibited reproducible melting and freezing cycles (see Figure 16, right). This contrasts with bulk water, where freezing is delayed by the kinetic barrier of ice nucleation, keeping water in a metastable state until spontaneous crystallization occurs, whereas melting proceeds under thermodynamic equilibrium.[87] This leads to unpredictable freezing temperatures for bulk water. A similar mechanism can help explain the hysteresis observed between melting and freezing in confined water.

It was found that hysteresis strongly depends on pore size and diminishes with decreasing diameter, disappearing at around 3 nm (see Figure 17). This corresponds to the same range below which no melting or freezing transitions are observed, indicating the absence of a first-order phase transition.[53,57] Jähnert *et al*.[57] interpreted this behavior as a critical-like phenomenon in confined water, reporting a linear decrease of the melting enthalpy with the inverse pore radius, which vanishes at

approximately 2.8 nm. The narrowing hysteresis was attributed to the increasing structural disorder of ice under confinement and the enhanced short-range order of liquid water upon cooling, which make the solid and liquid phases locally more similar and lower the activation barrier for ice nucleation, resulting in less distinct freezing and melting processes.

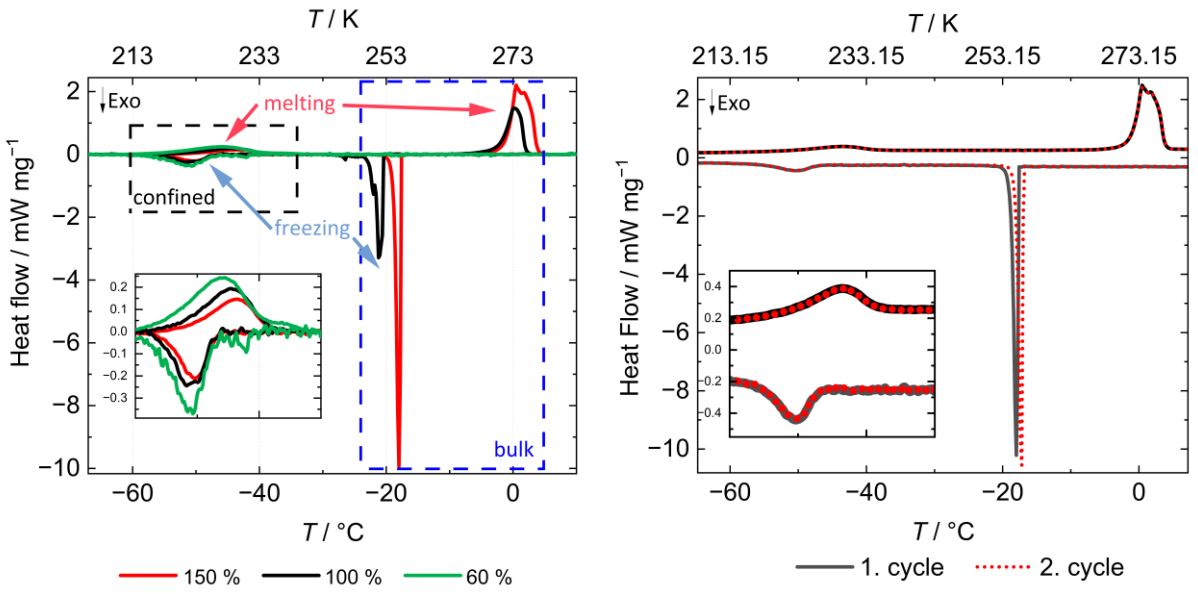


Figure 16: DSC curves of water confined in a BTEVA-PMO with a pore diameter of 3.8 nm, prepared using the incipient wetness method and measured at a heating rate of 3 K min^{-1}. Left: Baseline-corrected DSC thermograms at different filling degrees. Right: Raw cyclic thermograms at 150 % pore filling.

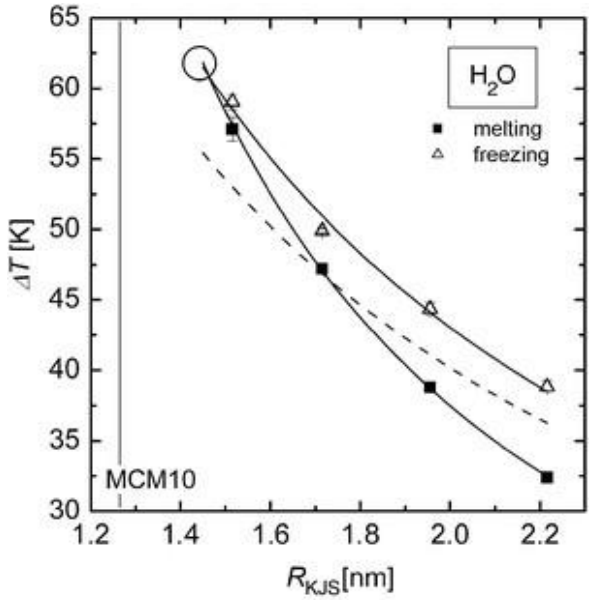


Figure 17: Melting and freezing point depression (ΔT) of water confined in MCM-41 silica as a function of pore radius. The fit curves (solid lines), based on the Gibbs–Thomson equation, show a crossover between freezing and melting behavior at a pore diameter of approximately 3 nm. The figure was originally published by Jähnert *et al.*[57] in *Physical Chemistry Chemical Physics* and is reproduced with permission from the Royal Society of Chemistry.

While nanoconfined water exhibits a shift of the capillary condensation to lower relative pressures under isothermal conditions compared to bulk water, its melting and freezing transitions occur at lower temperatures under isobaric conditions. Analogous to the Kelvin Equation (1), which describes the dependence of the relative phase transition pressure on pore radius and contact angle in water vapor sorption, the melting temperature shift (ΔT) can be described by the Gibbs–Thomson equation:[52,54,264]

$$\Delta T = \frac{2\, T_b \left(\gamma_{ws} - \gamma_{wl}\right) v}{(r_P - t)\, \Delta H_b} = \frac{C_{GT}}{(r_P - t_{nf})} \tag{16}$$

with the bulk melting point of water (T_b), the interfacial free energies of wall–solid (γ_{ws}) and wall–liquid (γ_{wl}), the molar volume of liquid water (v), and the bulk melting enthalpy (ΔH_b). By applying Young's equation ($\gamma_{ws} - \gamma_{wl} = \gamma_{sl} \cos(\theta)$), where γ_{sl} is the solid–liquid interfacial energy, the ice–water contact angle (θ, with $\theta = 0°$ for complete wetting) can be introduced into Equation (16). For practical use, the relation is often expressed through the Gibbs–Thomson constant (C_{GT}).[54,87] Numerous studies have shown that the phase transition behavior of confined water is well described by the Gibbs–Thomson equation.[53–55,57,87] Based on this relation, melting transitions of confined water are used in NMR cryoporometry and DSC thermoporometry to extract pore-size information.[261,265] Analogous to the adsorption layer that mediates the interaction between the pore wall and the condensed liquid core, a non-freezable water layer (t_{nf}) forms at the interface between the pore wall and the frozen ice core. This so-called non-freezable layer is hereinafter referred to as the t_{nf}-layer and is defined as a thin, disordered water film that forms on the surface of ice at temperatures below its bulk melting point of 0 °C and is reported to consist of one to three water monolayers.[265] Using water-filled MCM-41 silicas in DSC experiments, the group of Findenegg[57,87] obtained a NFL thickness of 0.6 nm, either by fitting the melting-point depression as a function of pore radius or through the linear correlation between normalized melting enthalpy and the reciprocal ice-core radius. Using PMOs in dielectric relaxation spectroscopy experiments, Malfait *et al.*[133] found indications of larger interfacial water fractions in materials with higher hydrophilicity. The dynamics of confined ice and of the interfacial layer appear largely insensitive to surface chemistry and are instead dominated by water–water interactions. It was observed that the non-freezable layer is

amorphous and has a density (1.25 g cm^{-3}) close to very high-density amorphous ice (VHDA).[266,267] Its hydrogen-bond network is weak and lacks tetrahedral order.[89]

For a given surface chemistry, the NFL thickness is commonly treated as a fixed value, assuming it has universal applicability across different pore structures, sizes, and temperatures. In practice, however, this approach neglects the dependence of the NFL thickness on the phase transition temperature and pore size, with studies showing that smaller pores and lower temperatures result in a thinner NFL.[89,180–182,191,267–269] As noted earlier, t_{nf} is typically obtained by fitting the phase-transition temperature as a function of pore radius across a series of materials with identical composition but varying pore sizes, which yields a single averaged value. A geometric approach analogous to the adsorption-layer calculation (see Equation (6) to (7)) can also be used to determine t_{nf}, using the following relation:

$$V_{c,ice} = \frac{\Delta H_m}{\Delta H_T} \cdot \frac{1}{\rho_{ice}} \tag{17}$$

where the volume of the core ($V_{c,ice}$) is calculated using the melting enthalpy of water inside the pore (ΔH_m, in kJ), the temperature-dependent bulk melting enthalpy (ΔH_T), and the bulk ice density (ρ_{ice} = 0.917 g cm^{-3}).[270] The t_{nf} can then be calculated using Equations (6) and (7) by applying the specific ice core volume ($V_{c,ice}$ divided by the sample mass) instead of V_c. This approach allows calculation of t_{nf} for each individual sample, avoiding the assignment of a fixed layer thickness to an entire sample class. Additionally, Equation (17) accounts for the impact of the transition temperature on the melting enthalpy, which is often neglected in other studies. Assuming ice I_h, the temperature-dependent melting enthalpy can be derived from the heat capacities of ice and supercooled water reported by Murphy and Koop.[271] The temperature dependence of ΔH_T and the difference in specific heat capacity (ΔC_p) are shown in Figure 18. For confined water in MCM-41 silica with a pore diameter of 3.2 nm and a melting temperature of 219 K,[57] the melting enthalpy of the frozen core corresponds to almost 50 % of the melting enthalpy of ice at standard conditions.

In hydrophobic confinement, a lower fraction of liquid-like water is found in the NFL compared to hydrophilic pores, indicating a reduced water density in pores with weaker water–surface interactions, similar to observations for the adsorption layer with a condensed liquid core.[272]

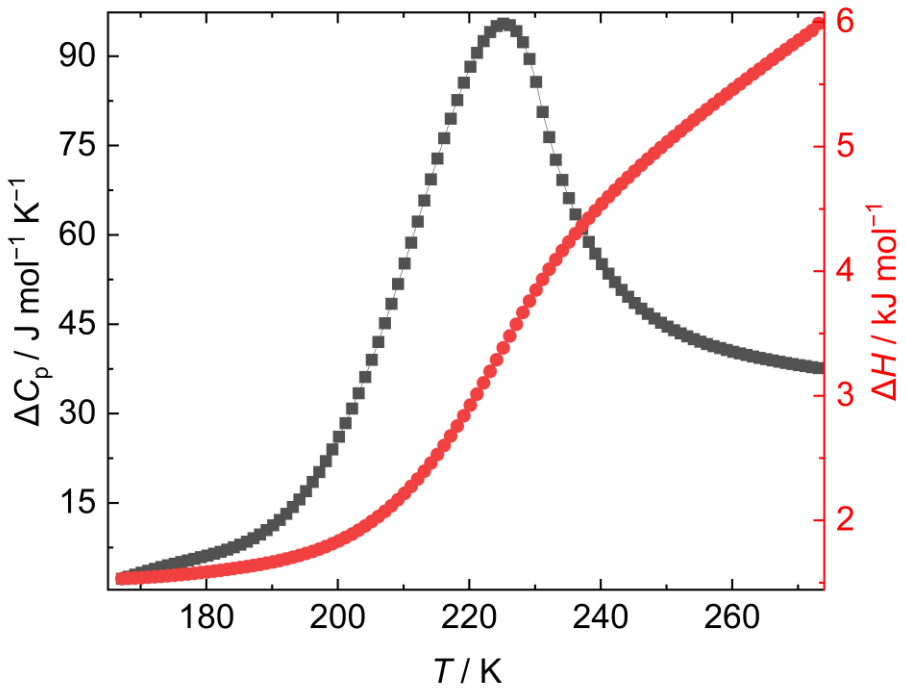


Figure 18: Temperature dependence of the difference in specific heat capacity (ΔC_p) and melting enthalpy of water (ΔH_T).[271]

Many studies have used porous silica to investigate the effect of pore size and geometry on nanoconfined water. Although various groups have studied the impact of surface hydrophilicity on the freezing and melting behavior of nanoconfined water, discrepancies remain as to whether surface chemistry has an effect and, if so, how it influences the melting temperatures.[97] The use of different material types with varying pore size ranges, determined using different pore size calculation approaches, together with differences in pore filling degree, analytical methods, and measurement parameters such as DSC heating rates and peak evaluation procedures, likely contributes to these discrepancies.[87,97,138–141,198] Figure 19 shows results for various materials and pore sizes. Aso *et al.*[120] investigated a benzene-bridged PMO with a pore diameter of 3.9 nm and compared the melting and freezing behavior of confined water to that in MCM-41 silica with a pore diameter of 2.8 nm. They observed that water in the more hydrophobic PMO exhibited slightly higher phase transition temperatures than in MCM-41 silica. However, because the comparison involved different pore sizes and DSC measurements performed at different heating rates, these differences cannot be unambiguously attributed to surface effects. Similar trends were observed in other studies with limited numbers of samples. A more systematic investigation by Deschamps *et al.*[138] and Osta-Rangel[139] compared water melting in hydrophilic MCM-41 silica to hydrophobically modified MCM-41 silica, reporting

significantly lower melting temperatures for the more hydrophobic materials. Morishige[97] used three hydrophilic SBA-15 silica/CPGs and compared them with ordered mesoporous carbon, concluding that surface hydrophilicity does not affect the solid–liquid phase transition behavior. Given the large pore sizes studied (d_P = 6–16 nm), these results suggest that surface chemistry effects on melting transitions may only be relevant for pore diameters below 6 nm. Furthermore, for materials that were post-synthetically treated to tune surface hydrophilicity, the effects of functional group size, which adds an additional roughness to the surface, the degree of functionalization, and their distribution across the surface are not fully understood and could produce misleading results. To resolve this, a material class with fine-tunable surface chemistry, ideally featuring periodically ordered hydration sites in the pore walls, and a wide range of pore sizes with narrow size distributions is required. Since confinement effects become most pronounced in mesopores below approximately 5 nm due to the high surface-to-volume ratio, the influence of hydrophilicity on NFL thickness requires closer investigation in this pore size regime.[50,273]

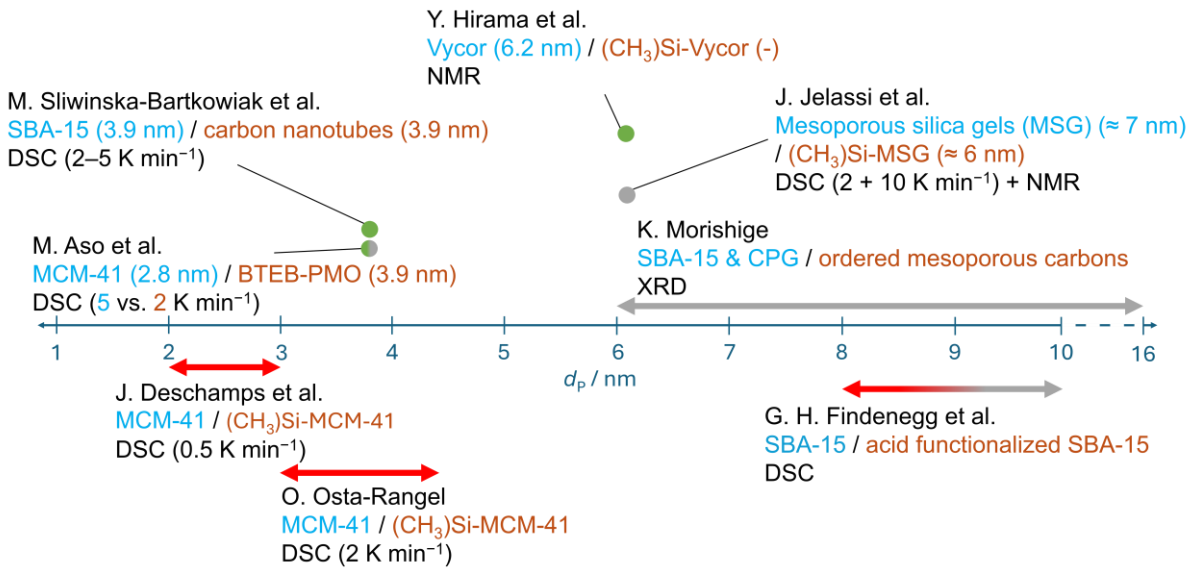


Figure 19: Overview of reported observations on the influence of surface hydrophilicity on the melting temperature of nanoconfined water. Results from different studies are categorized by pore diameter (d_P) and include various materials and characterization methods under different experimental conditions. Hydrophilic materials are shown in blue and hydrophobic materials in brown. A stronger melting temperature depression is indicated in red for hydrophobic materials and in green for hydrophilic materials, while gray denotes no observable surface effect.

4. Aim of the Work

Water is the basis of life on Earth and one of the most intensively studied substances. Despite its simple chemical structure, water exhibits numerous properties and anomalies that remain unresolved. The crystallization mechanism of water in the so-called “no-man’s-land” is a particular mystery. Due to rapid nucleation below the homogeneous nucleation temperature, this region is difficult to access with current experimental methods. The crystallization of water can be delayed by confining liquid water within porous solids.[27] Although water in porous silica has been extensively studied, the influence of surface hydrophilicity and, more specifically, distinct chemical functionalities on confined water phases is not fully understood. Inconsistent measurement conditions across analytical techniques and the use of diverse porous systems have led to differing and sometimes contradictory results.

The aim of this study is to address the remaining open questions[274–276] regarding the fundamental properties of water under confinement by providing a platform consisting of a wide range of materials with adjustable surface chemistry and pore diameters, and by systematically studying their impact on water’s adsorbed, condensed, and frozen states. As a porous medium, PMOs are particularly suitable due to their fine-tunable surface chemistry, which can be periodically ordered along the pore walls, and pore sizes that fall within the range where surface effects are especially pronounced. Additionally, the pores are highly ordered, with the possibility of forming cylindrical pores with 2D hexagonal order, providing a simple model system. They also possess high surface areas and pore volumes, which enhance the observable confinement effects on water. Beyond the use of established PMOs, novel PMOs with similar backbone structures, functionalized with strongly hydrophobic, positively charged, and amide–acid groups, are designed and optimized. Since MCM-41 silica materials are widely used in water studies, they are employed both for comparison with PMO results and to reinforce previously published findings.

To classify the different PMOs and MCM-41 silica according to their hydrophilicity and to study the impact of surface chemistry on water adsorption–desorption processes as well as on its condensed state, water vapor sorption experiments are conducted. A major focus is placed on the size and density of the adsorption layer, as these initial water layers are most strongly influenced by the surface and, in turn, affect the overall behavior of the confined water. A thermodynamic perspective on the

adsorption process, which is important for understanding the mechanism and energetics of water adsorption on different surfaces, is obtained through temperature-dependent isosteric water vapor sorption measurements. Additionally, a calorimetric method, coupled to a thermogravimeter and humidity generator, is developed to investigate the adsorption enthalpy and entropy at very low relative humidities and to compare these results with those from the isosteric method. Using low-temperature differential scanning calorimetry, the dependence of freezing and melting behavior on surface hydrophilicity under confinement is systematically investigated to resolve existing discrepancies. Additionally, different filling methods are compared.

PMOs with different surface chemistries and pore sizes are also studied at large research facilities such as DESY and ILL using X-ray and neutron techniques to investigate both the structural properties and the dynamic behavior of water. Understanding the fundamental properties of water in its vapor, liquid, and solid phases under confinement in materials with different surface chemistries is of broad relevance for numerous natural and industrial processes.[274–276]

5. Cumulative Part of the Dissertation

5.1. Influence of Surface Chemistry on *t*-Layer Dimension and Density of Nanoconfined Water by Fine-Tuning the Functional Groups of Periodic Mesoporous Organosilicas

Philip Lenz, Sophia-M. Meinert, Sandra König, Michael Steiger*, Michael Fröba*

Synopsis

In nature, water frequently occurs in confined environments, where its properties are strongly affected by surface interactions due to the high surface-to-volume ratio. These effects are studied and mimicked by designing artificial or biomimetic environments. Since the first few water layers at a substrate surface exhibit distinct behavior and are strongly influenced by the surface properties, various porous model systems have been used to understand the surface impact on confined water. The most common systems with cylindrical pores are silica- or carbon-based materials, representing two extremes in terms of hydrophilicity.

In this publication, periodic mesoporous organosilicas with finely tuned surface functionalities, based on either a divinylbenzene backbone or benzene as the organic bridging unit, were used to study the impact of different functional groups and their hydrophilicity on the adsorption–desorption behavior, the adsorption-layer thickness, and density by means of water vapor sorption measurements. Various parameters were used to define the hydrophilicity of the different PMOs. Using a geometric calculation approach for cylindrical pores, the adsorption-layer thickness and its density were determined. Water in hydrophobic materials tends to form a larger adsorption layer relative to the pore radius, as well as lower average and adsorption-layer densities, which can be attributed to the smaller number of surface hydration sites and the presence of hydrophobic regions where water is absent. PMOs based on methylated divinylpyridine with a surface charge showed, despite their hydrophilic behavior, a larger *t*-layer and a higher adsorbed water density, probably due to modified water–wall interactions associated with the chaotropic nature of the ions. In addition to the influence of surface functionality, curvature effects on the adsorption-layer properties were confirmed, with smaller pores leading to an increasing relative adsorption-layer thickness.

Unpublished Additional Results

Water adsorption behavior in bifunctional amide–acid PMOs

The ability of PMOs to fine-tune their surface chemistry makes them ideal materials for studying the interaction of defined biological functionalities with water and aqueous solutions. Proteins, as the fundamental building blocks of life, exhibit a wide range of functions and are composed of amino acids. Incorporating functional groups found in nature to create biomimetic or artificial water channels can aid in understanding the natural function of protein channels and may provide pathways toward the design of highly selective, advanced water purification systems.[277–280]

In this study, several bifunctional amide–acid PMOs were synthesized based on amine-containing backbone precursors (BTEPA, BTEVA) that were functionalized with maleic anhydride (OBenA), succinic anhydride (OBA), Cbz-protected aspartic anhydride (AA), or contained a fully integrated L-aspartic acid unit within the backbone (BTEPSA-PMO). Due to their relatively flexible and extended organic bridges, the BTEPA- and BTEPSA-based materials have difficulty forming stable and highly porous frameworks, and were therefore co-condensed with the shorter, more rigid BTEB precursor in varying ratios. Detailed synthesis and characterization procedures are provided in the appendix (Section 8.3).

Cyclical volumetric water vapor sorption measurements were performed for selected materials (see Figure S9, Figure S15, Figure S23, and Figure S40). In general, the reproducibility of the water vapor sorption isotherms of all PMOs indicates structural stability upon water exposure, which can be attributed to the relatively thick pore walls (5.8–9.9 nm) of the BTEPA-based PMOs. In contrast, the functionalized BTEVA-based materials, whose unfunctionalized analogs typically lose porosity during desorption, likely due to strong water–amine interactions, the basicity of the amine groups, and capillary forces, showed improved resistance to water despite having only marginally thicker pore walls (up to 1.1 nm) compared to the pristine BTEVA-PMO (≈ 1.0 nm). Notably, the BTEVA-OBA_PT-PMO synthesized via the pseudomorphic transformation route, which possesses the thinnest pore walls, exhibited one of the highest cyclic water sorption stabilities (Figure S40). This improved stability can be explained by the reduced basicity resulting from the amine-to-amide conversion, the steric hindrance and rotational freedom of the bulky amide-acid groups, and possible neutralization of residual amines by the acid functionalities in partially unfunctionalized regions.

The influence of the functionalization degree (F_{NMR}) of co-condensed and homopolymeric PMOs on their hydrophilicity, characterized by *SHS* and HI_{ia} parameters, is shown in Figure 20.

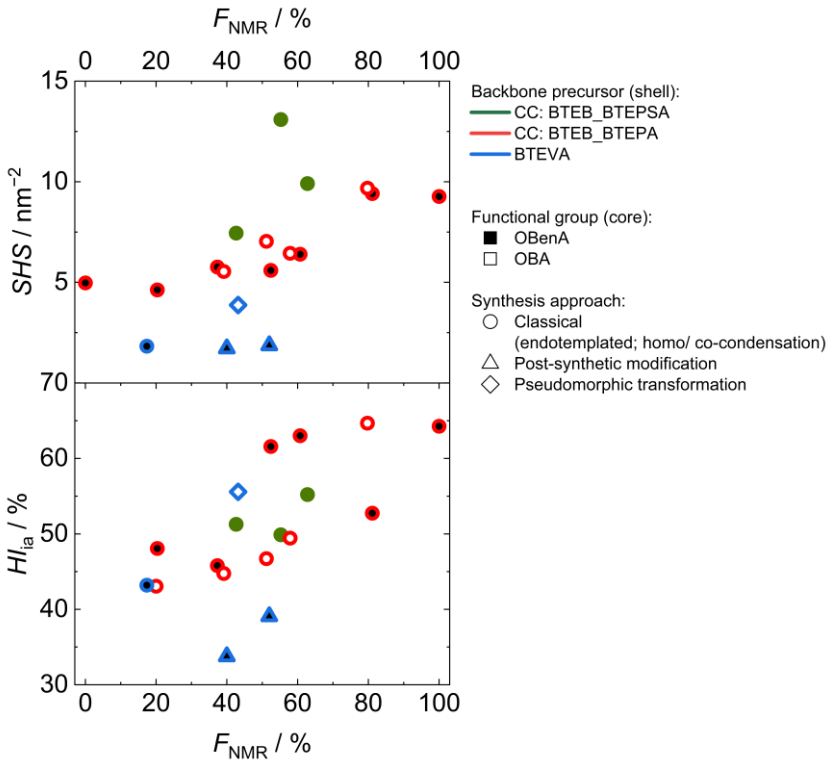


Figure 20: Comparison of the functionalization degree determined from the ^{1}H-NMR spectra (F_{NMR}), which for co-condensed (CC) PMOs includes the functionalization degrees of amine and bifunctional amide–acid species, with hydrophilicity parameters such as the surface hydration site (*SHS*) density and the hydrophilicity index derived from the relative pressure at the inflection point of condensation in water vapor sorption isotherms compared to nitrogen physisorption isotherms (HI_{ia}).

Due to the short repetition-unit length of the co-condensed materials (BTEB_BTEPA: 0.78–1.31 nm, BTEB_BTEPSA: 0.78–0.88 nm) and the presence of multiple functional groups capable of acting as adsorption sites for water, these materials exhibit higher *SHS* densities and larger HI_{ia} values than the functionalized BTEVA-PMOs and neutral PMOs with divinylbenzene backbones (*SHS* = 0.28–1.5 nm^{-2}; HI_{ia} = 9–37 %).[62] With increasing BTEPA content, and consequently a higher degree of amide–acid functionalization, the *SHS* increases by roughly a factor of two, while HI_{ia} rises from approximately 45 to 65 %. Although the BTEB_BTEPSA PMOs show the highest *SHS* (up to 13 nm^{-2}), their HI_{ia} values remain within the same range as those of the BTEB_BTEPA co-condensates. Functionalization of BTEVA with OBA or OBenA leads to higher *SHS* densities (1.7–3.9 nm^{-2}) and HI_{ia} values (34–56 %) compared to the pristine BTEVA-PMO (*SHS* ≈ 0.9 nm^{-2}, HI_{ia} ≈ 32 %). In general, the amide–acid functionalized BTEVA-PMOs exhibit less hydrophilic behavior than the co-

condensed PMOs, with the exception of the BTEVA-OBA-PMO synthesized via pseudomorphic transformation, which shows a distinctly higher hydrophilicity.

Following the approach presented in the literature,[62] the relative *t*-layer thickness (t_a/r_h) and density (ρ_{t1}) were calculated using Equations (7) and (8) and are presented in Figure 21.

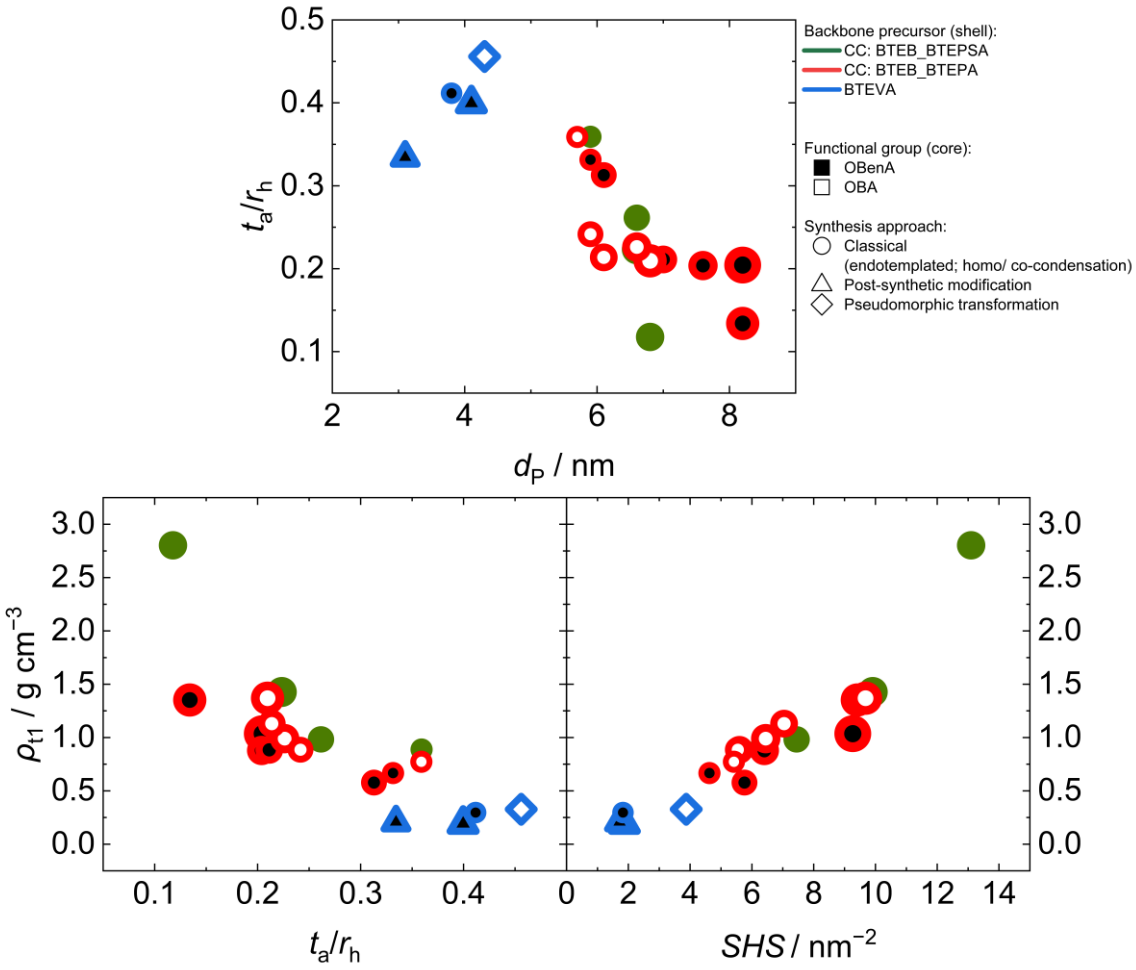


Figure 21: Plot of the relative *t*-layer thickness (t_a/r_h) against the pore diameter (d_P) (top), and the *t*-layer density (ρ_{t1}) against the relative *t*-layer thickness (bottom, left) and the *SHS* density (bottom, right). Symbol size corresponds to the amine/amide–acid bridge content for co-condensed PMOs and to the OBA/OBenA functionalization degree for BTEVA-bridged PMOs.

Consistent with previous observations,[62] the t_a/r_h decreases as pore size increases, reaching values as low as 0.1 at a pore diameter of 8 nm (see Figure 21, top). The less hydrophilic amide–acid-functionalized BTEVA shows the highest t_a/r_h of around 0.4. For the co-condensed materials, t_a/r_h decreases with increasing amine/ amide–acid content, and thus with increasing hydrophilicity. The density of the adsorption layer scales with both t_a/r_h and *SHS* (see Figure 21, bottom). As previously reported for divinylbenzene-bridged PMOs,[62] more hydrophilic materials (those with higher *SHS*

values) exhibit a thinner and denser adsorption layer. In that earlier study, even at a maximum *SHS* of 2.2 nm^{-2} for charged PMOs, the density did not exceed 0.3 g cm^{-3}. In contrast, the co-condensed PMOs investigated here exhibit *SHS* values up to 13 nm^{-2} and considerably higher adsorption-layer densities. The OBA- or OBenA-functionalized BTEPA-PMOs show an increase in ρ_{t1} with higher amine/amide–acid content, reaching up to 1.5 g cm^{-3} and thus exceeding the density of bulk water. The observation of increased water density is consistent with findings for hydration layers at protein surfaces.[281,282] The aspartic-acid-bridged PMO with 55 % content exhibits the highest hydrophilicity and a ρ_{t1} of 2.8 g cm^{-3}. Such high densities, as observed for other co-condensed materials, could indicate a restructuring of water beyond the adsorption layer, resulting in a pore-core density exceeding the assumed bulk density. Additionally, surface charges can arise from deprotonated carboxylic acid groups and protonated amine groups, around which water forms tightly bound hydration layers. These findings are consistent with previous observations for PMOs bearing surface charges,[62] which exhibited thicker adsorption layers with higher densities. It should also be noted that most co-condensed PMOs possess a fraction of smaller interconnecting pores, which likely influence the results. Therefore, the reported values should be considered as averages over the main pore size and the additional connecting pores (> 2 nm).

In comparison, the BTEVA-PMOs show ρ_{t1} = 0.1–0.2 g cm^{-3} and t_a/r_h = 0.2–0.4,[62] while the functionalized BTEVA-PMOs exhibit higher ρ_{t1} (0.2–0.3 g cm^{-3}) and t_a/r_h (0.3–0.45). The higher adsorption-layer density originates from the greater number of surface hydration sites. Moreover, the increased t_a/r_h values, together with the higher *SHS*, indicate that, in addition to hydrophilicity, the spatial dimensions of the functional groups extending toward the pore center significantly influence the *t*-layer size.

THE JOURNAL OF PHYSICAL CHEMISTRY C
A JOURNAL OF THE AMERICAN CHEMICAL SOCIETY

Open Access
This article is licensed under CC-BY 4.0

pubs.acs.org/JPCC
Article

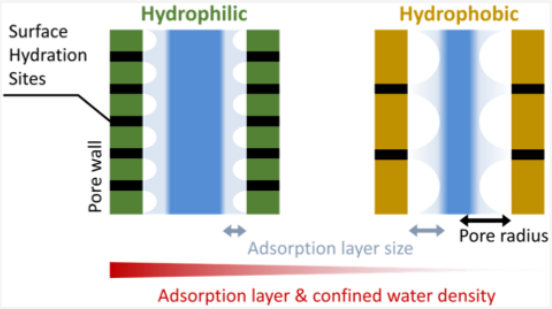
Influence of Surface Chemistry on *t*-Layer Dimension and Density of Nanoconfined Water by Fine-Tuning the Functional Groups of Periodic Mesoporous Organosilicas

Philip Lenz, Sophia-M. Meinert, Sandra König, Michael Steiger,* and Michael Fröba*

Cite This: *J. Phys. Chem. C* 2025, 129, 12536−12550
Read Online

ACCESS | Metrics & More | Article Recommendations | Supporting Information

ABSTRACT: This study investigates the behavior of water confined in cylindrical nanopores with hydrophilic, charged, and hydrophobic surfaces using water vapor sorption at 298.15 K. MCM-41 silica and periodic mesoporous organosilicas (PMOs) serve as host materials, with PMOs featuring a silica backbone linked by organic bridging units, allowing precise control over surface chemistry. Using a consistent divinylbenzene-based structure, the study assesses how functional groups influence confined water properties. A novel hydrophilicity index is introduced, incorporating contact angle data and adsorption layer thickness to quantify surface chemistry effects. Hydrophilic materials exhibit distinct adsorption profiles compared to hydrophobic PMOs, where surface chemistry and confinement influence water density, adsorption behavior, and *t*-layer proportions. In hydrophobic materials, such as divinylbenzene- and *N*,*N*-dimethyldivinylaniline-bridged PMOs, thicker water adsorption layers with lower average density are observed, which can be attributed to the localization of water near silanol groups and its absence near hydrophobic regions. Fluorinated PMOs fluctuate between hydrophobic and hydrophilic tendencies depending on water saturation. Introduction of surface charges enhances water adsorption, leading to a larger *t*-layer and higher adsorbed water density. These findings provide critical insights into how surface chemistry and pore size collectively govern water behavior, offering a framework for future studies on nanoconfined water.



1. INTRODUCTION

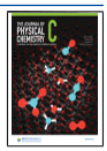
Water exhibits unique behaviors, including its density maximum at 4 °C, expansion upon freezing and ice polymorphism, driven by its intricate hydrogen bonding network.[1−5]

These anomalies, along with water's fundamental role in life, being essential for stabilizing structures, modulating dynamics, and supporting the functions of proteins and biomolecules,[6] as well as comprising 70−80% of cell mass,[7,8] and its key role in earth's geology and chemistry,[9] emphasize its extraordinary significance. Liquid water is in permanent contact with solid, liquid or gaseous environments. Interfacial water exhibits distinct properties compared to bulk water, with its structure and dynamics influenced by surface chemistry and interaction type.[10−13] Water in confinement is common in nature, occurring in rocks, clays, zeolites, and biological systems such as cells and proteins (e.g. aquaporins).[14,15] It is also present in artificial porous materials, including water purification membranes and MCM-41 silica. Due to the increasing surface to volume ratio with decreasing spatial dimensions, the influence of interfacial water increases.

Nanoporous systems are often used to investigate the influence of the surrounding matrix on the properties of the confined water. Due to its highly ordered pores and pronounced porosity, SBA-15 or MCM-41 silica are often used to study phase transition[16−23] and adsorption behavior[23−26] of water or D_2O in more hydrophilic confinement. In contrast, hydrophobic confinement is explored using porous carbons, such as ordered mesoporous carbons or carbon nanotubes.[27−31]

MCM-41 silica and porous carbons represent opposite extremes in hydrophilicity, with one being highly hydrophilic and the other distinctly hydrophobic. While postsynthetic modifications have been used to adjust the hydrophobicity of MCM-41 and SBA-15 silica, uncertainties remain regarding the extent of functionalization, the uniformity of functional group distribution, and their impact on confined water properties.[18,32,33] Existing silanol groups are assumed to catalyze the hydroxylation of neighboring siloxane groups, forming silanol

Received: April 4, 2025
Revised: June 9, 2025
Accepted: June 18, 2025
Published: June 27, 2025



ACS Publications
© 2025 The Authors. Published by American Chemical Society

https://doi.org/10.1021/acs.jpcc.5c02277
J. Phys. Chem. C 2025, 129, 12536−12550

clusters on the surface. These clusters, rather than the overall silanol density, likely play a key role in adsorption behavior and hydration dynamics.[34]

Periodic mesoporous organosilicas are well-suited for studying confined water due to their high porosity and tunable surface polarity. As nanoporous hybrid materials, PMOs feature a silica backbone linked by organic bridging units and, under certain synthesis conditions, can develop crystal-like pore walls.[35−39] They are characterized by a narrow pore size distribution, large surface area, and highly ordered pore structure. Their adjustable surface chemistry and pore size make PMOs particularly valuable for studying confined water. Research has explored their role in determining the structure, dynamics, adsorption behavior, and temperature dependence of confined water.[40−47]

In a recent study,[40] we used various PMOs with organic bridging units of similar length but different functional groups in X-ray scattering experiments to examine how surface hydrophilicity influences the structure of confined water. Structural analysis revealed that higher hydrophilicity and smaller pore diameters result in lower density and more pronounced tetrahedral structuring of water. Conversely, in more hydrophobic PMOs with larger pores, water exhibits a bulk-like tetrahedral structure. This confirms that the structural properties of confined water are strongly influenced by surface hydrophilicity, with the effect becoming more pronounced as pore size decreases.

Since the point of zero charge differs between surfaces, water in nature is often found on charged surfaces. These charged surfaces significantly influence water structure, dynamics, viscosity and water-surface interaction, yet their effects remain not fully understood, making their study essential.[48,49] Organofluorine is notable for its anomalous properties[50−52] and potential for halogen bonding.[53,54] It can act as a dipolar rotor,[55] and can form weak hydrogen bonds.[56,57]

This study examines how surface hydration site densities, encompassing both charged and uncharged hydrophilic functionalities, influence water behavior by employing PMOs with different surface chemistries, including fluorinated and charged pyridinium surfaces, alongside pure MCM-41 silica. A water vapor sorption study is conducted to assess their impact on adsorption layer size and density. Rother et al.[24,25] carried out a similar water vapor sorption study, applying a geometrical approach to determine the thickness and density of the adsorption layer. By analyzing nanoporous silica with varying pore sizes and morphologies, they identified a correlation between surface silanol group density and sorption layer density. To vary the surface silanol density, the MCM-41 silica materials were exposed to water vapor and regenerated under different conditions. However, it is important to consider the potential dissolution and recondensation of the silica walls during this process, as it can lead to deformation and ultimately block the pores.[58,59]

By using the adsorbed phase model (APM), Rother et al. observed a decrease of adsorption layer density with decreasing surface silanol density. Regarding the adsorption layer thickness, their initial study observed a decrease in *t*-layer thickness with lower OH group density using two MCM-41 silica materials with different pore sizes.[24,25] In later studies, they expanded the porous silica system to cover a broader range of pore radii (1.19−32.1 nm), but due to nonideal cylindrical pore shape, an adapted method was necessary. They found that sorption layer thickness scales with pore size, as the condensation step shifts to higher relative pressures for larger pores, allowing for an additional adsorption layer.[25]

Along with the surface silanol density (as defined by Rother et al.), or in case of PMOs, the surface hydration site (SHS) density, which includes both silanol and organic bridge functional groups as bonding sites, we introduce additional hydrophilicity indices (*HI*). We also propose a novel *HI* that compares the relative pressure at which capillary condensation (HI_{ia}) or desorption (HI_{id}) occurs in the water vapor sorption and nitrogen physisorption isotherms. The various *HI*s are used to compare different PMOs and MCM-41 silica with respect to their water affinity and to establish a correlation between their surface hydrophilicity and the properties of interfacial water.

Besides MCM-41 silica and the PMOs known from the literature using precursors such as 1,4-bis[(*E*)-2-(triethoxysilyl)vinyl]benzene (BTEVB),[37,38] 2,5-bis[(*E*)-2-(triethoxysilyl)vinyl]aniline (BTEVA)-PMO,[39,60] 1,4-bis-(triethoxysilyl)benzene (BTEB),[36] 2,5-bis((*E*)-2-(triethoxysilyl)vinyl)-2-fluorobenzene (BTEVFB)[55] as well as a significantly optimized 2,5-bis[(*E*)-2-(triethoxysilyl)vinyl]-pyridine (BTEVP)-PMO,[61] the materials presented in this work also include PMOs based on the precursor 2-chloro-1,4-((*E*)-2'-bis(triethoxysilyl)vinyl)benzene (BTEVClB), *N*,*N*-dimethyl-2,5-bis((*E*)-2-(triethoxysilyl)vinyl)aniline (*N*,*N*-DMBTEVA) and 1-methyl-2,5-bis((*E*)-2-(triethoxysilyl)-vinyl)pyridinium iodide (*N*-MBTEVP$^+$I$^-$)-PMOs, which were recently presented for the first time by our group and are described in more detail here (Figure 1).[47]

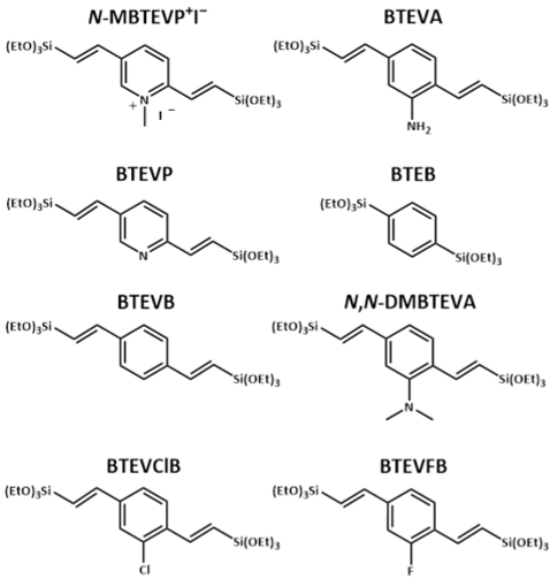


Figure 1. Different PMO precursors.

2. EXPERIMENTAL SECTION

2.1. Materials. The synthesis of the PMO precursors is based on the double Heck cross-coupling reaction,[62,63] as used for BTEVB, BTEVClB, BTEVFB and BTEVA. In contrast, BTEVP is synthesized using in a first step a Heck type dehydrohalogenation reaction[64] and in a final step a Rhodium-

https://doi.org/10.1021/acs.jpcc.5c02277
J. Phys. Chem. C 2025, 129, 12536−12550

catalyzed hydrosilylation.[61] PMOs using *N*-MBTEVP$^+$I$^-$ or *N*,*N*-DMBTEVA were produced via a postsynthetic route or the latter via an in situ approach using BTEVP or BTEVA and methyl iodide.

The synthesis of the different PMOs and MCM-41 silicas are based on a soft-matter templating using cationic quaternary ammonium surfactant of the type C_nTAB with a different number of carbon atoms (n) in the alkyl chain. Pore sizes of roughly 3 to 5 nm were achieved with surfactant alkyl chain length of n = 12−20. Detailed synthesis instructions for the precursors and the PMOs, as well as for the MCM-41 silica materials, are described in the Supporting Information.

The different porous materials are identified according to their material class and the pore size. For example, a PMO produced from the precursor BTEVClB with a pore diameter of 3.8 nm is labeled as BTEVClB_3.8.

2.2. Characterization Methods. To investigate the materials regarding their mesostructure and molecular ordering within the pore walls, X-ray powder diffractograms (PXRD) were recorded with a PANalytical X'Pert Pro PW3040/60 (Cu−Kα). The evaluation was performed using Origin Pro 2024 from OriginLab and X'Pert Highscore Plus from PANalytical.

Nitrogen physisorption measurements were performed to characterize the porosities of the different materials. At first, the samples were activated at 100 °C for 20 h under reduced pressure in a degasser (Quantachrome Masterprep). The N_2 physisorption measurements were performed at a temperature of 77 K (Quantachrome Quadrasorb-SI-MP and Quadrasorb evo). Using the program QuadraWin 6.0, the pore size distribution according to density functional theory (DFT) calculation with the model N_2 on silica (cylindr. pores), nonlocal DFT (NLDFT) at the adsorptions branch, and the specific surface area with the Brunauer−Emmett−Teller (BET) method (p/p_0 range from 0.05 to 0.3) were determined from the obtained measurement.[65−67] In cases where the BET region intersects with the condensation step of the isotherms, the BET range was reduced to ensure it remained within the plateau region before condensation (p/p_0 < 0.3).

To perform the water vapor sorption measurements, the samples were first degassed at 100 °C for 20 h under reduced pressure (Quantachrome MasterPrep Degasser). The water vapor sorption isotherms were recorded at 25 °C (Quantachrome VSTAR). Additionally, the evaluation was performed with the software Origin Pro 2024 from OriginLab and VstarWin 2.0.1 from Quantachrome.

The purity of the PMOs was characterized using NMR, IR, and partially TG-DTA-MS. For the NMR measurements, the PMOs were dissolved at room temperature in 2 mL of 1 M NaOD/D_2O solution and filtered prior to analysis. NMR spectra were recorded on a Bruker Avance III HD 600 MHz spectrometer (base frequency: 600.13 MHz), and the data were processed using MestReNova software. The Fourier transform infrared (FT-IR) spectra were measured at room temperature using the FT-IR spectrometer Vertex 70 from Bruker with 64 scans per measurement and a resolution of 3 cm^{-1}. The samples were measured as KBr pellets. The analysis was carried out using the OPUS 8.5 software from Bruker. Thermal analysis (TG-DTA-MS) measurements were carried out under an argon and oxygen (4:1) atmosphere with a heating rate of 5 K min^{-1}, using a simultaneous thermal analyzer NETZSCH STA 449 F3 Jupiter equipped with a silicon carbide furnace. The flow rate was set to 20 mL min^{-1}, and a DTA-Corundum 0.3 mL crucible was used. Volatile decomposition products were qualitatively detected during thermal analysis with a capillary-coupled Aëolos QMS 403 quadrupole mass spectrometer. Data analysis was performed using Netzsch Proteus Thermal Analysis 8.0.3.

Transmission electron microscopy (TEM) images were acquired using a JEOL JEM-2200FS microscope operating at an acceleration voltage of 200 kV.

3. RESULTS AND DISCUSSION

3.1. Material Characterization. The different materials were characterized with regard to their pore order, pore wall structure and porosity using PXRD and nitrogen physisorption.

In Figure S4 diffractograms of the different materials are shown. Reflections in the range of 1−6° 2θ of the PXRD indicate a periodic arrangement of the pores of both MCM-41 silica and PMOs.

Unlike the amorphous MCM-41 silica, PMOs show reflection patterns in the range of 6−50° 2θ, suggesting a crystal-like arrangement at the molecular level in the pore walls. Using the pyridine-bridged PMO with a pore size of 3.8 nm (BTEVP_3.8) as a representative example, the high pore order is evidenced by TEM imaging (Figure 2(a)) as well as by the low-angle reflections in the PXRD pattern (Figure 2(b)), while additional reflections in the wider 2θ range indicate a crystal-like arrangement of the pore walls(Figure 2(c)). This material exhibits a d_{100}-spacing of 4.40 nm and a periodicity of the repetition units d_{RU} of 1.19 nm. The TEM image confirms the hexagonally ordered pores in top view. Side-view TEM images of the pore channels and the preserved porosity of the postsynthetically methylated, charged PMO (*N*-BTEVP$^+$I$^-$) are shown in Figure S6.

The d_{100}-spacing values and d_{RU} of all materials are summarized in Table S2. Except for BTEB-PMOs, the various PMOs have comparable lengths of the periodically arranged organic bridges of roughly 1.2 nm.

Porosity characteristics such as pore size (d_P), pore volume at a relative pressure of 0.8 ($V_{P,n,0.8}$)[23] and specific BET surface area (S_{BET}) can be determined using the nitrogen physisorption isotherms (Figure S7) and are listed in Table S2.

The nitrogen physisorption data of all materials can be described with a type IV isotherm. As a representative example, the pyridine-bridged PMO (BTEVP_3.8) exhibits a pore diameter of 3.8 nm and a specific BET surface area of 740 m^2/g, derived from the isotherm and pore size distribution curve shown in Figure 2. The corresponding distribution confirms the narrow mesopore size and uniform porosity. The pore diameters were obtained using the maximum of the pore size distribution curves (Figure S7) that were calculated using DFT. Additionally, the hydraulic radii (r_h) were calculated via the pore volume and the specific surface area using following equation[24]

$$r_h = \frac{2V_{P,n,0.8}}{S_{BET}} \quad (1)$$

The charged *N*-MBTEVP$^+$I$^-$-PMOs were prepared by postsynthetic functionalization of BTEVP-PMOs with iodomethane. Porosity analysis indicates a decrease in pore volume, specific BET surface area, and pore size from BTEVP_4.4 to *N*-BTEVP$^+$I$^-$_3.8 and from BTEVP_3.5 to *N*-MBTEVP$^+$I$^-$_3.2. Another interesting observation is that the d_{RU} of BTEVP-PMO (1.19 nm) is slightly smaller (1.17 nm) after

https://doi.org/10.1021/acs.jpcc.5c02277
J. Phys. Chem. C 2025, 129, 12536−12550

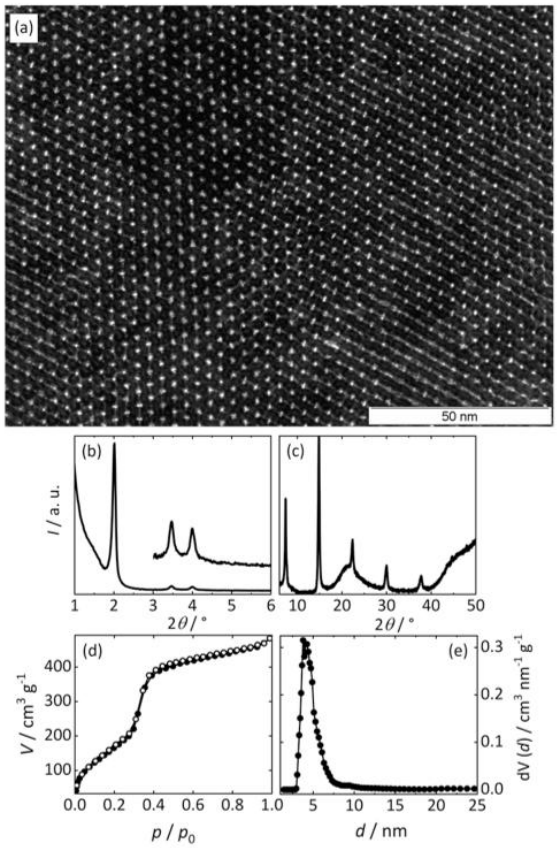


Figure 2. Highly ordered hexagonal cylindrical pores of (BTEVP_3.8) as shown by (a) TEM image (top view); (b) normalized PXRD patterns in the low-angle range (1 to 6° 2θ), indicating long-range pore order; (c) normalized PXRD patterns in the wide-angle range (6 to 50° 2θ), reflecting the crystal-like structure of the pore walls; (d) nitrogen physisorption isotherms at 77 K with adsorption (filled circles) and desorption (hollow circles) branch; (e) corresponding pore size distribution curves (calculated using the kernel: N_2 at 77 K on silica, cylindrical pores NLDFT at adsorptions branch).

methylation to the charged *N*-MBTEVP$^+$I$^-$. The other (00l) reflections (see Figure S8 and Table S5) also indicate a functionalization-related shrinkage of the system.

3.2. Water Vapor Sorption Measurements. In order to investigate the influence of surface chemistry on the behavior of intraporous water, water vapor sorption measurements were carried out. In contrast to nitrogen physisorption, the water vapor sorption isotherms show a type V curve, as can be seen in the exemplary isotherms of BTEVFB-PMOs in Figure 3. The water vapor sorption isotherms for all other samples are presented in Figure S9 and the parameters used for various calculations are listed in Table S3. When comparing the isotherms of cylindrical porous materials with the same surface chemistry but different pore sizes, a shift in the gas–liquid or liquid–gas transition to lower relative pressures can be observed for smaller pores (see Figure 3). This pore size-dependent shift in the relative pressure at which the phase transition takes place can be described by the Kelvin eq 2 for cylindrical pores[68,69]

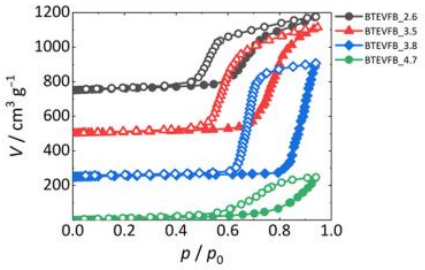


Figure 3. Water vapor sorption isotherms at 25 °C of BTEVFB-PMOs with pore diameters of 2.6 to 4.7 nm (from top to bottom). The adsorption branch is represented by filled symbols and the desorption branch by hollow symbols. The isotherms are shifted along the *y*-axis by the value +250 cm^{3}g^{-1} from bottom to top.

$$\ln\left(\frac{p}{p_0}\right) = -\frac{2\,\nu_l\gamma\,\cos(\theta)}{RT(r_p - t_a)} \tag{2}$$

where p/p_0 is the relative pressure at which the phase transition takes place, γ the surface tension of water in confinement, θ the contact angle, ν_l the molar volume of water in confinement, R the universal gas constant, T the temperature, t_a the thickness of the adsorption layer and r_p is the pore radius determined by nitrogen physisorption.

However, if materials are compared that have the same pore size but differ in surface chemistry, a shift in the relative pressure of capillary condensation can also be observed. Adsorption isotherms of MCM-41 silica and different PMOs with a pore diameter of ≈3.8 nm are compared in Figure 4. By

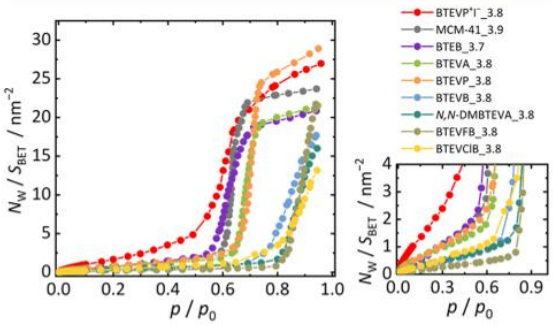


Figure 4. Adsorption branch of water vapor sorption measurement at 25 °C of MCM-41 silica and various PMOs with a pore diameter of about 3.8 nm. The isotherms were normalized with the specific BET surface area of the respective materials to show the number of water molecules per surface unit at a certain relative pressure. Bottom right an enlarged section of the isotherms in the adsorption area is shown.

applying the Gurvich rule[70−72] and using S_{BET} the adsorption isotherms shown here are expressed as the number of water molecules per nm^2. This approach allows for a direct, surface-area-independent comparison of the amount of water adsorbed per nm^2 at a given relative pressure. Based on the position of the capillary condensation, the materials can be roughly categorized according to their hydrophilicity.[31,45] For the different materials with pore diameters of 3.8 nm shown in Figure 4, those exhibiting capillary condensation at relative pressures of 0.7 and below are categorized as more hydrophilic,

https://doi.org/10.1021/acs.jpcc.5c02277
J. Phys. Chem. C 2025, 129, 12536−12550

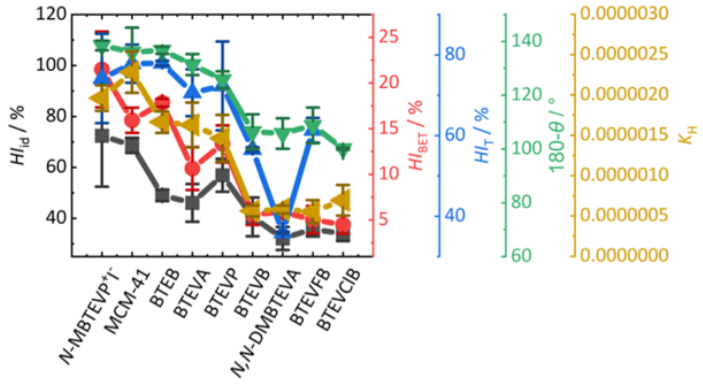


Figure 5. Comparison of the different water affinity values to rank the different PMOs and MCM-41 silica according to their hydrophilicity. The error bars represent the mean values of the calculated hydrophilicity parameters for all samples within each material class.

while hydrophobic materials generally exhibit the gas−liquid transition at higher relative pressures.

The magnification of the area before capillary condensation (Figure 4(bottom, right)) also shows that the curves of the more hydrophilic materials have a greater slope than the hydrophobic samples. The charged *N*-MBTEVP$^+$I$^-$_3.8 in particular takes up a lot of water in the adsorption area and has around 4 water molecules per nm^2 before capillary condensation. In comparison, the very hydrophobic BTEVFB has 0.65 water molecules per nm^2 at the onset of capillary condensation. Furthermore, what can be observed in Figure 3, Figure 4(left) and in Figure S9 is that particularly hydrophobic materials, especially those with larger pore diameters, do not exhibit a plateau at the end of adsorption. This means that the pores are not completely filled, which is why these materials cannot be used for certain calculations in the later sections.

3.3. Hydrophilicity Index. In the previous section, we made a rough classification of the materials into hydrophobic and hydrophilic based on the position of the relative pressure range at which capillary condensation occurs and on the number of water molecules adsorbed at the onset of the phase transition. Here we aim to apply and compare various hydrophilicity indices (*HI*) and other parameters known from the literature, as well as our own, on PMOs and then use these to explain some phenomena.

Since water is known to be sensitive to surface chemistry and can form hydrogen bonds with certain functionalities, while nitrogen does not or only interact weakly via its quadrupole moment, the comparison of the two can be used to calculate a *HI*. Thommes et al. have presented an HI_T in which the adsorbed volumes of water and argon isotherms at a relative pressure of 0.92 were compared with regard to the degree of pore filling.[73] A material is considered more hydrophilic the more its surface is wetted with water and the closer the contact angle is to 0°, which would result in matching pore volume between water vapor sorption and nitrogen physisorption, as well as a filling level close to 100%. While the HI_T gives a tendentially consistent picture of the hydrophilicity ranking (except for the BTEVFB, see Figure 5), it has a practical problem especially for the hydrophobic materials. As discussed in the previous section, for hydrophobic materials, especially with larger pores, no plateau is observed in the adsorption branch of the water vapor isotherms. This means that the condensation is incomplete, making this volume-based method unsuitable for these samples. Additionally, as pore radius increases, the surface-to-volume ratio decreases, leading to a reduced sensitivity to surface hydrophilicity using this volumetric approach.

Our group has also introduced a hydrophilicity index (HI_{BET}), which compares the specific BET surface area (S_{BET}) calculated from water vapor sorption and nitrogen physisorption isotherms.[74] This method is highly surface-sensitive, as at low pressures water only attaches to hydrophilic binding sites and hydrophobic areas are not occupied, while nitrogen or argon are completely wetting as adsorptive. A similar approach is often used to calculate the surface silanol group density, where the number of water molecules adsorbed, derived from S_{BET} of water vapor sorption ($S_{BET,w}$), is equated with the number of Si−OH groups under the assumption that one water molecule adsorbs per silanol group.[24−26,40,75] Since the organic bridging units in PMOs have functional groups that can also interact with water, we use the term surface hydration site (SHS) density.

In the previous section we have shown that the position of the condensation step of the water vapor sorption isotherms varies for different materials with the same pore diameter. But also in the desorption branch, the position of the pore emptying depends on the surface chemistry (see Figure S10). Since this relationship can be described by the Kelvin eq 2, we have developed a hydrophilicity index based on the comparison of the inflection point of desorption (HI_{id}) or adsorption (HI_{ia}) from water vapor sorption and nitrogen physisorption and can be calculated using eq 3.

$$HI_i = \frac{\ln\left(\frac{p}{p_0}\right)_{i,w}}{\ln\left(\frac{p}{p_0}\right)_{i,n}} \tag{3}$$

The advantage of this HI_i is that it retains information on the contact angle and thus directly on the hydrophilicity and also takes into account the *t*-layer thickness, which, as we will see in the next sections, is also influenced by the surface chemistry.

Figure 5 illustrates the mean values of various hydrophilicity parameters for each material class. While averaging may introduce errors due to size dependencies, curvature effects, or variations in SHS densities within a material class, this figure serves as a clear comparison of different hydrophilicity

https://doi.org/10.1021/acs.jpcc.5c02277
J. Phys. Chem. C 2025, 129, 12536−12550

classifications. In later chapters, individual samples are analyzed separately.

There seems to be a good trend match between the three *HI* presented (especially between HI_{id} and HI_{BET}). In the case of HI_{BET} and HI_T, however, the BTEB-PMOs appear to be more hydrophilic than in HI_{id}. According to Thommes's calculation method, the *N*,*N*-DMBTEVA-PMOs show a significant drop in hydrophilicity. This may be because the hydrophobic organic bridges and additional hydrophobic functionalities extend into the pores, creating a larger hydrophobic gap, an area where water is not in direct contact with the surface. Consequently, the volume of water in a fully filled pore would be smaller relative to the total pore volume. Only the BTEVFB-PMOs exhibit increased hydrophilicity, a phenomenon that will be discussed in the following sections.

In Figure 5, further parameters such as contact angle (θ) and Henry's constant (K_H) are shown, which can give an indication of the hydrophilicity. Canivet et al. used the Henry constant to sort metal−organic frameworks (MOFs) according to their water affinity and determined it from the slope of the water vapor adsorption isotherm at low pressures ($p/p_0 < 0.1$).[76]

Kocherbitov and Alfredsson introduced a modified Kelvin equation[26] that can be used to calculate the contact angle (θ).[77] As with the *HI* presented, these two parameters also indicate the following ranking of the MCM-41 silica and PMOs regarding the increasing water-pore wall affinity

$$\begin{aligned}\text{BTEVClB} \leq \text{BTEVFB} \approx \textit{N}, \textit{N}\text{-DMBTEVA} \approx \text{BTEVB}\\ < \text{BTEVP} \approx \text{BTEVA} < \text{BTEB} \leq \text{MCM-41 silica}\\ < \textit{N}\text{-MBTEVP}^{+}\text{I}^{-}\end{aligned}$$

This demonstrates that estimating hydrophilicity based on the relative pressure of capillary condensation is valid, but only when comparing materials with the same pore diameter. Using the *HI*, however, eliminates this pore size limitation.

The example of BTEB-PMO highlights the significant influence of organic bridge length on hydrophilicity. Despite lacking functional groups on the benzene ring, BTEB-PMOs exhibit greater hydrophilicity than PMOs with hydrogen-bonding functionalities, such as divinylaniline or divinylpyridine, probably due to BTEB's shorter organic unit.

An interesting observation arises when comparing the amount of water adsorbed at the onset of capillary condensation ($n_{o,a}$) with the amount of water remaining after pore emptying ($n_{e,d}$) (see Figure S11). While $n_{o,a}$ and $n_{e,d}$ for PMOs have a linear trend that goes through the origin, the MCM-41 silica have almost twice as much or more water at $n_{e,d}$ than at $n_{o,a}$. Additional silanol groups can be formed from siloxane on the surface of MCM-41 silica when it comes into contact with water.[41,78−80] This increases the hydrophilicity and number of SHS, which means that more water remains on the surface at the $n_{e,d}$. For the PMOs, this result means that there is a negligible or no formation of new silanol groups.

Alongside the presented hydrophilicity indices or parameters that indicate the hydrophilic behavior, others are also being further developed.[81,82]

3.4. Investigation of the Adsorption Layer. The calculation of the size and density of the adsorption layer is based on a geometric approach that was introduced by Rother et al.[24,25]

With the assumption of a bulk density of the liquid core water, the Kelvin radius (r_K) can be calculated from the amount of water adsorbed during capillary condensation. Samples whose isotherms do not reach a plateau at the end of adsorption cannot be used for this calculation. The *t*-layer size is obtained by subtracting r_K from r_h. In addition to determining the *t*-layer size from the adsorption branch (t_a), it is also derived from the desorption branch (t_d). The comparison of both *t*-layers is shown in Figure 6.

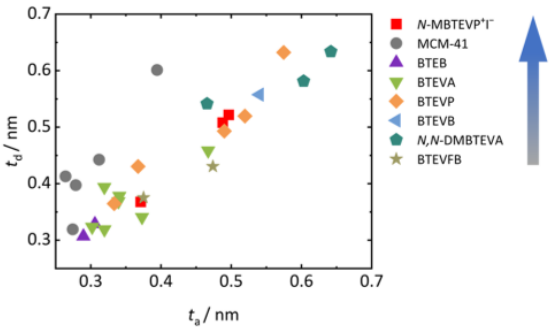


Figure 6. Comparison of the *t*-layer thicknesses, calculated from adsorption (t_a) and desorption (t_d) isotherms, for different materials with varying pore sizes. An arrow in the legend denotes the order of increasing hydrophilicity for the listed materials.

For the MCM-41 silica materials, the t_a values are roughly in the range of 0.25 to 0.4 nm and agree with the literature values.[24,25] While t_a and t_d for the PMOs are in the same order of magnitude, the *t*-layers for the MCM-41 silica materials differ from each other, with t_d reaching higher values than t_a. This may also be due to the formation of surface silanol groups and the alteration of the material by water. The wide range of values in Figure 6 also indicates that no fixed size of adsorption layer can be specified for the respective material classes. The reason for the differences within a material class can be seen in the pore size. When looking at the isotherms of a material type, capillary condensation is shifted to higher relative pressures as the pore size increases and for similar slopes in the range before the capillary condensation, therefore, more water is adsorbed within larger pores. In Figure 7(top) the *t*-layer sizes of materials with similar pore diameters are compared in order to obtain a pore size/curvature effect independent view. Except for the charged *N*-MBTEVP^{+}I^{-} and the fluorinated material, there is a correlation between the *t*-layer size and the hydrophilicity. It appears that materials with decreasing water affinity have an increase in the adsorption layer size. The charged PMOs feature a methyl group oriented toward the pore interior, which can shift the equilibrium *t*-layer size to higher values. The effects of charged and fluorinated surfaces will be explored in greater detail later in this section. The size of the *t*-layer is calculated according to the method of Rother et al.[24,25] using the situation of a completely filled pore. Similar to the nonfreezable layer in the frozen state of the core water the *t*-layer can act as a mediator between the pore surface and the core water. The result that the *t*-layer thickness is greater for hydrophobic PMOs in order to increase the distance between the surface and the core water appears to make sense. Given the pore size dependence of adsorption layer dimensions, the ratio t_a/r_h is used for comparison with hydrophilicity HI_{id} (Figure 7, bottom). This also reveals that hydrophilic materials, such as MCM-41 silica, BTEVP-, BTEB- or BTEVA-PMOs, have smaller *t*-layer sizes relative to their

https://doi.org/10.1021/acs.jpcc.5c02277
J. Phys. Chem. C 2025, 129, 12536−12550

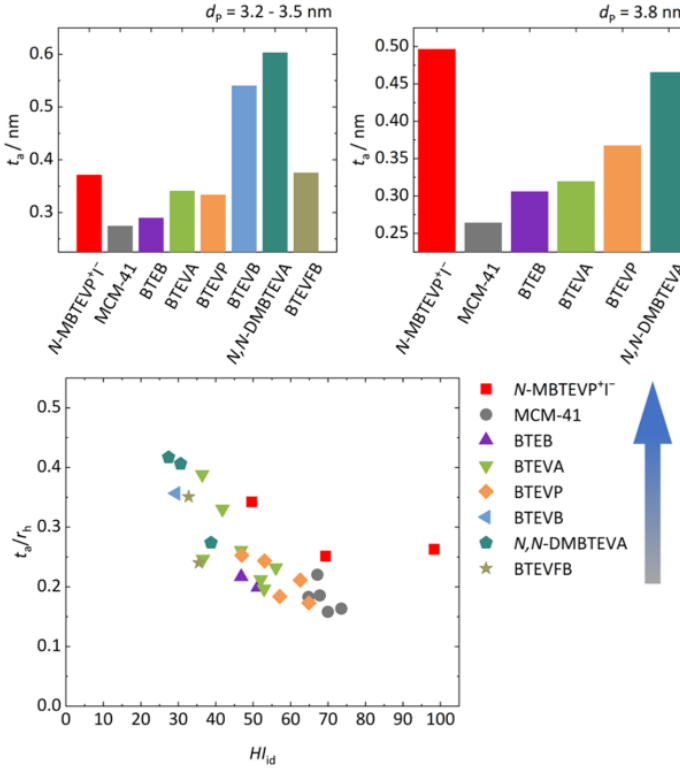


Figure 7. Adsorption layer size for materials with a pore diameter of 3.2−3.5 nm (top, left) and 3.8 nm (top, right). Correlation of the ratio t_a/r_h and HI_{id} (bottom). An arrow in the legend denotes the order of increasing hydrophilicity for the listed materials.

pore radius. An overlap between hydrophilic and hydrophobic materials is observed, particularly for BTEVA-PMOs, as the t_a content increases and the pore size decreases. This suggests a pore size dependence of hydrophilicity. From the point of view that the attractiveness of water is expressed by how much water can be adsorbed on the surface, confinement effects would limit water adsorption before condensation, so that in this context hydrophilicity is pore size dependent.

The other hydrophilicity indices also indicate a trend where materials appear more hydrophobic as the t_a/r_h ratio increases. The contact angles (Figure S12) further support this, showing a decrease in contact angle with smaller pore sizes for each material class. However, the charged *N*-MBTEVP$^+$I$^-$-PMO is an exception, with contact angles remaining stable or even slightly increasing.

A measure of the amount of water adsorbed with increasing relative pressure, for a given total pore volume, is the pore volume-normalized slope of the adsorption area prior to capillary condensation ($s_{a,V}$). This relative slope scales with SHS (see Figure S13a) and appears to follow an exponential trend with the relative pressure at which capillary condensation occurs (see Figure S13b). This correlation indicates that, for a given increase in p/p_0, a higher water uptake at a fixed pore volume shifts capillary condensation to lower relative pressures. In other words, faster pore filling promotes the formation of metastable water clusters, lowering the relative pressure required for capillary condensation. This relationship allows for an estimation of the inflection point based on the adsorption slope and vice versa.

As the pore size decreases, $s_{a,V}$ increases (see Figure S13c), though this behavior is material-dependent. For pores larger than ∼3.8 nm, $s_{a,V}$ flattens, whereas for smaller pores, particularly in BTEVA-PMOs, it rises more sharply. When comparing relative slope and t_a/r_h, a material-specific linear trend emerges, where $s_{a,V}$ approaches zero as t_a/r_h decreases (see Figure S13d). This implies that water uptake decreases with increasing pore size and/or decreasing *t*-layer thickness. Hydrophobic samples such as BTEVB-, BTEVFB- and *N*,*N*-DMBTEVA-PMOs exhibit the lowest slopes, followed by BTEVP- and BTEVA-PMOs, which show similar values, while more hydrophilic samples like MCM-41 silica, BTEB- and *N*-MBTEVP$^+$I$^-$-PMOs have the highest slopes. Additionally, a relationship between $s_{a,V}$ and contact angle is observed, with a linear fit showing a contact angle of approximately 90° at the *X*-axis intercept (see Figure S13e).

Based on all the observations described above, it is essential to distinguish between intrinsic and effective hydrophilicity. Intrinsic hydrophilicity is determined solely by surface chemistry and functional groups interacting with water and is observed in the absence of confinement effects, such as curvature, *t*-layer fraction of pore radius, and surface-to-volume ratio, typical for large pores or planar surfaces.

However, within confined environments, water affinity (expressed in various *HI*s, adsorption slope, Henry constant and contact angle) is influenced not only by intrinsic hydrophilicity but also by geometric factors. Thus, in nanoporous systems, we refer to an effective hydrophilicity, which accounts for both the chemical nature of the surface and

https://doi.org/10.1021/acs.jpcc.5c02277
J. Phys. Chem. C 2025, 129, 12536−12550

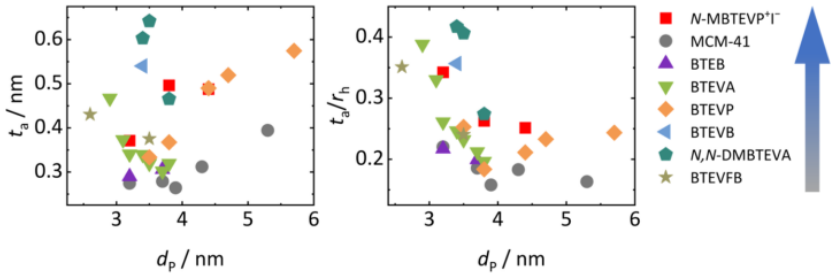


Figure 8. Pore size dependence of the adsorption layer (left) and the *t*-layer fraction (right). An arrow in the legend denotes the order of increasing hydrophilicity for the listed materials.

the confinement effects. Figure 7(bottom) illustrates the correlation between HI_{id} and t_a/r_h, showing that as hydrophilicity increases, the *t*-layer occupies a smaller fraction of the pore radius. This trend, characterized by decreasing t_a/r_h, may result from the reduced surface-to-volume ratio at larger pore diameters. Figure S14 highlights a material-specific correlation between pore size and the difference in relative pressures at the inflection points of capillary condensation in water vapor sorption and nitrogen physisorption isotherms ($\Delta(p/p_0)_{i,w\text{-}n}$). As the pore diameter increases, capillary condensation in water and nitrogen adsorption occurs at progressively similar relative pressures, suggesting that surface effects become less significant. In a linear relationship, the inflection points of both isotherms align at a pore size of approximately 8 to 15 nm (6.3 nm for the charged PMO) at the same relative pressures. Only the fluorine-functionalized PMO shows a contrasting trend. However, due to the limited number of measurement points, the results should be interpreted with caution.

The pore size dependence of the adsorption layer for each material type is illustrated in Figure 8(left). A material-dependent trend seems to exist. An interesting observation is that for PMOs with a functional group protruding into the pore center, such as the amine in BTEVA, the fluorine in BTEVFB or the dimethylated amine in *N,N*-DMBTEVA, an increase in the *t*-layer occurs with decreasing pore size. An exception to this is the charged *N*-MBTEVP$^+$I$^-$-PMO.

In contrast, the adsorption layer of the other porous materials appears to decrease with decreasing pore size. For instance, reducing the pore size of BTEVP-PMO from about 6 to 3.5 nm leads to a 50% reduction in the adsorption layer size. With MCM-41 silica, a similar trend can be observed for d_p = 4 to 6 nm, except that a constant adsorption layer thickness of around 0.3 nm is reached for pores smaller than 4 nm. This value is in the same order of magnitude as the results of Rother et al. and indicates a formation of a water monolayer (0.23–0.35 nm).[25,83−86]

As pore diameter decreases, the surface-to-volume ratio is expected to increase, leading to a larger proportion of the *t*-layer relative to the pore radius, or a smaller ratio of core water to surface water. Conversely, as the pore diameter increases, approaching that of a planar surface, the *t*-layer is expected to become increasingly negligible compared to the core water. In Figure 8(right), this behavior is evident for both MCM-41 silica and the majority of PMOs. At approximately 4 nm, both BTEVP-PMOs and MCM-41 silicas exhibit a minimum. However, the increase in t_a/r_h appears to level off around a pore diameter of 6 nm and will probably decrease again at even larger pores (as indicated for MCM-41 silica). This happens because the size of the adsorption layer increases at pores larger than 4 nm for both materials. This trend suggests the presence of counteracting effects. While the relative size of the adsorption layer (t_a/r_h) decreases with increasing pore size due to reduced confinement, a reversal of this trend beyond ∼4 nm can be attributed to curvature effects. As the pore walls become less curved at larger diameters, the adsorption layer grows disproportionately due to increased layering and weaker geometric restriction, resulting in a slight relative increase of t_a with respect to r_h. This behavior reflects a balance between geometric confinement and surface curvature, where reduced wall curvature enables a thicker multilayer adsorption structure. Since no PMOs with a pore size of 4 nm and larger are available for BTEVA, *N,N*-DMBTEVA and BTEB or the *t*-layer cannot be determined due to the incomplete condensation in the adsorption isotherm at larger pores, no statement can be made as to whether these also have a minimum or whether the curve progresses with a continuous decrease in the slope with increasing pore sizes (as it appears with the charged *N*-MBTEVP$^+$I$^-$-PMOs). Nevertheless, when drawing a straight line for the respective PMO class, these materials seem to indicate an alignment in the direction of this minimum. The adsorption layer size of the relatively hydrophobic BTEVFB exhibits a pore size dependence that is more similar to that of hydrophilic materials.

As observable in Figure S15, a larger *t*-layer does not automatically mean that the amount of adsorbed water is higher. For example, with hydrophobic materials such as BTEVB and *N,N*-DMBTEVA-PMO with a pore diameter of around 3.5 nm, the *t*-layer are almost twice as large (0.5 and 0.6 nm respectively) as for more hydrophilic materials such as the BTEVA-PMO (0.3 nm) with the same pore size (see Figure 8). Despite the larger *t*-layer, the hydrophobic materials have a similar amount of water per unit surface area ($N_{w,SBET}$) of around 1 nm^{-2}. For adsorption layers of the same size, the hydrophilic materials even have several times as many water molecules on the surface. Such behavior could only be explained by the existence of different adsorption layer densities.

The average density of water ($\rho_{w,avg}$) was calculated using the amount of water adsorbed after condensation and the pore volume obtained from nitrogen physisorption. A correlation between $\rho_{w,avg}$ and surface chemistry emerges when compared with HI_{id} (Figure S16, left), showing a decline in density for materials with lower hydrophilicity. $\rho_{w,avg}$ decreases from 0.8 g/cm^3 in the highly hydrophilic MCM-41 silica to 0.4 g/cm^3 in the more hydrophobic *N,N*-DMBTEVA-PMO. In addition, the density also decreases with the pore size in a material-specific

https://doi.org/10.1021/acs.jpcc.5c02277
J. Phys. Chem. C 2025, 129, 12536−12550

manner (Figure S16, right). These findings align with previous reports in the literature.[13,31,32]

It is often suggested and for some calculation assumed that the water in the pore center of hydrophilic as well as hydrophobic systems has a bulk like density.[31,87,88] If this is the case, then a lower density is caused by the adsorption layer, as the average density is composed of the density of the core water and the *t*-layer. As discussed above, the adsorption layer size depends not only on the pore surface hydrophilicity but also on the pore size, therefore in Figure 9 the average density

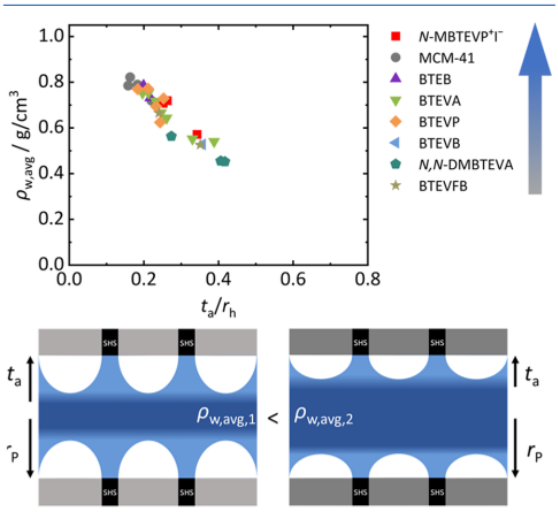


Figure 9. Top: Dependence of total density on the fraction of the *t*-layer in the pore radius. An arrow in the legend indicates the order of increasing hydrophilicity for the listed materials. Bottom: Schematic illustration of a cross-section of water-filled pores, showing variations in *t*-layer thickness and density (left: larger *t*-layer, lower density; right: smaller *t*-layer, higher density). Gray areas indicate more hydrophobic regions on the surface, with lighter gray representing more hydrophobic bridging groups (left) compared to darker gray (right), while black areas correspond to surface hydration sites (SHS).

is plotted as a function of t_a/r_h. A pronounced relationship can be observed for all materials, in which hydrophilic materials with a smaller *t*-layer-to-pore ratio, such as MCM-41 silica, BTEB-PMOs, as well as, in some cases, BTEVA- and BTEVP-PMOs, have higher water densities compared to PMOs with a larger adsorption layer fraction. As t_a decreases and the pore diameter increases, approaching flat-surface conditions, water density becomes more bulk-like, following the trend until $t_a/r_h = 0$, where it intersects the *y*-axis at the bulk water density. This indicates that the density reduction of water in cylindrical pores is governed by the proportion of the adsorption layer within the pore radius, as illustrated in the schematic at the Figure 9(bottom).

There are two ways to calculate the density of the adsorption layer in a geometrical manner. One way is to take the adsorbed water amount at the onset of the condensation step and divide it by the difference between the total pore volume from nitrogen physisorption and the water pore condensation volume (ρ_{t1}).[24,25] A second possibility to calculate the adsorbed phase density (ρ_{t2}) is to use the adsorbed amount of water and divide by the product of *t*-layer size and the S_{BET} to receive the volume of the adsorption layer. Figure S17 shows that both methods exhibit a strong linear correlation with each other, yielding nearly identical results, though ρ_{t1} values are slightly higher. For better comparability with the literature, ρ_{t1} is used for further analysis. Rother et al. identified a correlation between the density of surface hydration sites and the adsorption layer density in MCM-41 silicas.[24,25] Here, we extend this approach with the use of PMOs with different surface chemistries to investigate SHS of less than 1 nm^{-2} (see Figure 10). A distinct correlation across all materials indicates

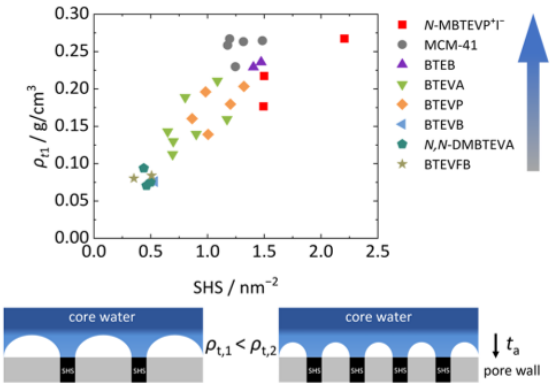


Figure 10. Top: Dependence of ρ_{t1} on surface hydration site density. An arrow in the legend denotes the order of increasing hydrophilicity for the listed materials. Bottom: Schematic representation of the relationship between SHS density and water *t*-layer density, based on a section of water near the pore wall. Gray areas indicate more hydrophobic regions of the surface, while black areas represent surface hydration sites (SHS).

that hydrogen bond interactions with the SHS play a dominant role in water adsorption on the pore surface. For SHS of 0.5 nm^{-2}, like for the BTEVB-, BTEVFB- and *N*,*N*-DMBTEVA-PMOs, a density as low as 0.075 g/cm^3 can be observed. As the SHS density increases, the density of the *t*-layer also increases, as evident in the comparison between BTEVB- and BTEB-PMOs. Due to its shorter repetition unit (0.76 nm vs 1.2 nm for BTEVB), BTEB-PMOs exhibit a higher SHS density while maintaining similar surface chemistry, resulting in a correspondingly higher *t*-layer density. The correlation between SHS density and ρ_{t1} is illustrated in Figure 10(bottom), where ρ_t refers to the water density in the adsorption layer. A higher SHS in situation 2 results in an increased density $\rho_{t,2}$ compared to $\rho_{t,1}$. The d_{RU} from the X-ray measurements and the SHS density can be used to get an indication of how much water is adsorbed per repetition unit or per nm^2 of the respective materials. Since the BTEVB-PMO has no other hydration sites apart from the silanol groups, the SHS density and number of water molecules per repetition unit normalized to a BTEVB-PMO are listed in Table S4. To exclude curvature effects, materials with a pore diameter of 3.8 nm are considered. Materials such as *N*,*N*-DMBTEVA- and BTEVClB-PMO show comparable values for SHS and for the number of hydration sites per repetition unit ($RUHS_B$) as the BTEVB-PMO, resulting in a *t*-layer density of similar magnitude. This suggests that in all three materials, water adsorption occurs only via the silanol groups, and that the organic bridging unit is probably not in direct contact with water molecules. This observation is consistent with findings from NMR studies of PMOs.[45]

https://doi.org/10.1021/acs.jpcc.5c02277
J. Phys. Chem. C 2025, 129, 12536−12550

In Figure 11(top), the water density of the adsorption layer for BTEVB, *N*,*N*-DMBTEVA and BTEVFB-PMOs was

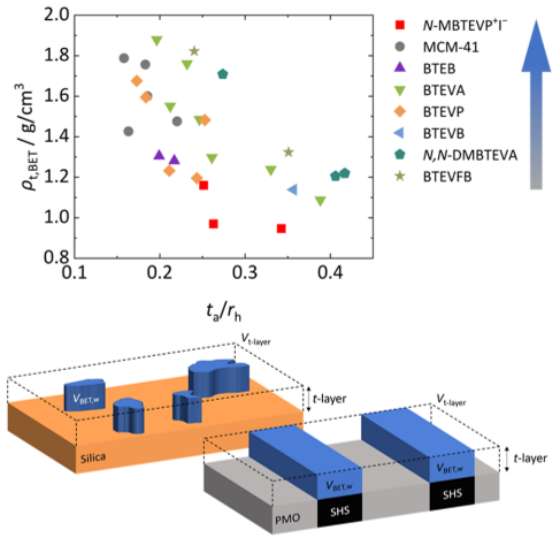


Figure 11. Top: Density of water in the adsorption layer, assuming it is confined to the SHS region with an volume of $V_{BET,w}$ plotted against the proportion of the *t*-layer in the pore radius. Bottom: Schematic illustration of water volume in the *t*-layer localized only at the SHS for two scenarios: On a silica surface and a PMO surface.

calculated for the case that water accumulates exclusively near the SHS, covering a surface area of $S_{BET,w}$ (see Figure 11, bottom), using following equation

$$\rho_{t,BET} = \frac{m_{w,a}}{(V_{P,n,0.8} - V_{PC,w})\frac{S_{BET,w}}{S_{BET}}} \quad (4)$$

Where $m_{w,a}$ is the mass of water adsorbed before capillary condensation (determined at the onset) and $V_{PC,w}$ is the volume of liquid water adsorbed during capillary condensation (determined from the difference between the endset and onset of capillary condensation) assuming a bulk water density of 0.997 g/cm^3. The calculated $\rho_{t,BET}$ of all materials ranges from 0.9 to 1.9 g/cm^3 and exhibits a material-specific increase as t_a/r_h decreases. A possible explanation for the increasing water density is that in larger pores, capillary condensation shifts to higher relative pressures, leading to a higher water uptake. The increased water density likely does not reflect the actual microscopic density but instead suggests an overestimation due to water extending beyond the defined volume. This is especially the case for water layers farther from the pore surface, where the interaction with the surface diminishes, and the hydrophobic regions may be bridged by water. Previous studies also report a higher water density near silica surfaces.[89,90] When adsorption occurs dominantly via SHS, the water molecules are forced into a more compact arrangement, avoiding hydrophobic regions. At a fixed t_a/r_h value, more hydrophobic materials, particularly BTEVFB and *N*,*N*-DMBTEVA, exhibit higher $\rho_{t,BET}$ values, indicating surface chemistry-dependent water structuring.[40]

The fluorinated PMO demonstrates hydrophobicity, with 60% of the hydration sites compared to BTEVB (see Table S4). This suggests that fluorine not only hinders water adsorption at the organic bridge but also at nearby silanol groups, assuming both PMO types have a similar surface silanol density. Notably, its hydrophobicity varies with pore filling. In this study, BTEVFB-PMO appears hydrophobic upon first water contact. However, in fully saturated pores, as seen in *t*-layer size, average density, and HI_T calculations, it exhibits characteristics of more hydrophilic materials, including a smaller *t*-layer and higher HI_T. This may result from differences in water structuring and interactions between these two conditions.[91] In fully saturated pores, water may accumulate more densely near fluorine,[92] resulting in a higher-than-expected pore volume from water vapor adsorption relative to nitrogen physisorption. Additionally, water may interact with fluorine-bound carbon atoms.[93] The dual hydrophobic−hydrophilic behavior of BTEVFB-PMO, hydrophobic at low water content but less so at higher filling states, can be explained by weak fluorine-water interactions, kinetic barriers, and water clustering. At low humidity, high energy barriers hinder water adsorption on the fluorinated surface, enhancing apparent hydrophobicity.[94,95] At high humidity, water stabilization through hydrogen bonding, clustering, and weak fluorine-stabilized dangling OH defects may enhance hydrophilicity.[94,96,97]

Given the observed rotation of organic bridges in BTEVFB-PMO walls,[55] at low humidity, water likely cannot adsorb onto these rotating regions and instead binds to silanol groups via hydrogen bonds. As water clusters grow around silanol groups and capillary condensation occurs, more water molecules come into proximity with the fluorinated surface. Dipole−dipole interactions between water and fluorine, which have been reported to slow water motion,[98] become more frequent. This growing interaction may enhance water−fluorine coupling, potentially slowing fluorine rotation. PMOs such as BTEVA and BTEVP-PMO contain an aromatic primary or heterocyclic amine in their organic bridge, enabling hydrogen bonding with water. In its nonprotonated state, aniline can theoretically form three H-bonds (two as a donor, one as an acceptor), whereas pyridine can form only one as an acceptor.

Both are weak bases, with pyridine (pK_b = 8.77) exhibiting slightly stronger basicity than aniline (pK_b = 9.38).[99] Upon contact with water, both amines can generate protonated sites, with hydroxide acting as the counterion. Due to the higher basicity of BTEVP-PMOs, a greater concentration of protonated sites may result, leading to a slightly higher water adsorption site density, 2.5 times higher than the 2.0 times increase in $RUHS_B$ observed for BTEVA-PMOs. Compared to other materials, BTEVP-PMOs exhibit a distinct effect on water properties in the *t*-layer, especially in pores larger than 4 nm. Other studies have also demonstrated that water behaves differently in this type of PMO.[40] While MCM-41 silica has a lower adsorbed water quantity ($RUHS_B$ = 0.8 per SiO_2 repeating unit) compared to BTEVB-PMO, its SHS density is three times higher. This value aligns well with its relative density, $\rho_{t,MB}$.

Despite possessing a hydrophobic organic bridging unit, BTEB-PMOs were found to be more hydrophilic, as indicated by their relative SHS_B of 3.5. They also contain 2.2 times more hydration sites per repeating unit than BTEVB-PMOs. One possible explanation is the smaller dimensions of the organic bridge. Once the free silanol groups are saturated, additional water molecules may adsorb in the organic phenylene region, forming water bridges stabilized by hydrogen bonds with water bound to silanol groups. This could result in a denser

https://doi.org/10.1021/acs.jpcc.5c02277
J. Phys. Chem. C 2025, 129, 12536−12550

adsorption layer, similar to that observed in MCM-41 silica, leading to a higher average water density. When comparing the relative surface hydration sites and relative adsorption layer density for the materials discussed above, a good correlation is observed (see Table S4). Notably, the fact that $\rho_{t,MB}$ for BTEB-PMOs is lower than the SHS_B, which assumes one water molecule adsorbs per hydration site, indicates that water also adsorbs onto surface-bound water. This suggests that water bridges the organic components of the PMO even at low loadings.

The salt-like *N*-MBTEVP$^+$I$^-$-PMO shows in many cases the highest *HI*s, with SHS and adsorption layer densities comparable to or even higher than MCM-41 silica, reaching SHS_B and $RUHS_B$ values around 5.5. However, its relative adsorption layer density ($\rho_{t,MB}$ = 2.9) does not align with the SHS, likely due to the presence of the iodide counterion. The iodide ion is likely located near the pore surface, attracted to the pyridinium cation due to electrostatic forces, or it may stay near less polar or hydrophobic regions due to its chaotropic nature, which weakens hydration and disrupts the structure of the surrounding water.[100−103] With an ion radius of 0.22 nm,[104,105] iodide could span the entire adsorption layer thickness, which ranges from 0.4 to 0.5 nm. Furthermore, both iodide and, to a lesser extent, the *N*-methylpyridinium bridge could disrupt the water structure in the *t*-layer due to their chaotropic behavior, allowing water to adsorb at hydrophobic sites.[106] This may explain why $\rho_{t,MB}$ is lower than expected for the given SHS_B. However, SHS_B is likely higher because, in addition to free silanol groups and pyridinium, iodide itself serves as an additional adsorption site for water.

When comparing *N*-MBTEVP$^+$I$^-$-PMOs with the non-functionalized BTEVP-PMOs from the same batch, the introduction of charge results in a significant increase in hydrophilicity, along with a larger *t*-layer, a greater proportion of the pore radius occupied by the *t*-layer, and higher *t*-layer density, while the average density of the confined water is lower (Table S5). Also, slight structural changes in the material occur due to the postsynthetic methylation of BTEVP-PMOs. The increase in water adsorption layer density can also be attributed to the chaotropic nature of the pyridinium iodide surface function, as described earlier. This disrupts the water structure and facilitates adsorption at hydrophobic sites. The hydration shell of iodide also contributes to the water density in the adsorption layer, increasing ρ_{t1}.[107,108] Despite this, the adsorption layer density remains significantly lower than bulk density, and the t_a/r_h ratio is higher in charged systems, leading to a lower overall density in *N*-MBTEVP$^+$I$^-$-PMOs compared to nonfunctionalized BTEVP-PMOs. Additionally, the degree of functionalization varies across *N*-MBTEVP$^+$I$^-$-PMO, resulting in different charge densities. The methylation degree was determined using ^{1}H NMR analysis (Figure S1) of PMO dissolved in 1 M NaOD/D_2O. The higher degree of functionalization in *N*-MBTEVP$^+$I$^-$_3.8 (18%) compared to *N*-MBTEVP$^+$I$^-$_3.2 (7%) may be due to its larger pore size. After functionalization, the inward orientation of the methyl group and the bulky iodide counterion may partially block the pore channels, particularly in smaller pores, likely limiting further diffusion of methyl iodide vapor into the full pore system. Surface area does not appear to be a determining factor, as the *N*-MBTEVP$^+$I$^-$_3.2 precursor has a larger surface area.

The lower density and increased adsorption layer size observed in hydrophobic materials suggest the presence of water-free cavities, likely located in the area of the organic bridge in PMOs or in nonhydroxylated regions of MCM-41 silica.[26,45,109] In gravimetric water vapor sorption or other methods using carrier gases like nitrogen or where samples are exposed to air during preparation, molecules other than water might deposit as nanobubbles.[109] However, in the volumetric water vapor sorption as conducted in this study, where the sample filling begins under reduced pressure, the likelihood of other molecules being present is minimized, suggesting that the cavities are most likely empty.

4. CONCLUSIONS

In this study, the hydrophilicity of various PMOs and MCM-41 silica materials was characterized using multiple hydrophilicity indices (*HI*s), including the newly introduced HI_i, which follows the trends of established *HI*s while incorporating contact angle information and accounting for adsorption layer thickness, both influenced by surface chemistry.

Using the geometric approach, the adsorption layer size can be calculated from both adsorption and desorption, yielding similar values. However, this is only valid if the material's hydrophilicity remains unchanged after contact with water. For MCM-41 silica, hydration induces the formation of new silanol groups. Hydrophobic materials, such as BTEVB- and *N*,*N*-DMBTEVA-PMOs, tend to exhibit larger *t*-layers with lower water density, which can be attributed to water being concentrated near silanol groups and being absent in hydrophobic regions. The behavior of BTEVFB-PMOs differ, showing both hydrophobic and partially hydrophilic tendencies depending on the hydrophilicity index used. These differences may stem from the distinct hydration scenarios of the fluorine atoms: in fully saturated pores, the increased water content results in a greater number of water−fluorine interactions, whereas in partially filled pores, the fluorinated organic bridge appears to shield the surface more effectively, possibly due to its rotational dynamics, reducing water adsorption.

A correlation exists between t_a/r_h and total water density, effective hydrophilicity, and volume-normalized, pressure-dependent water uptake. Hydrophobic materials tend to have a larger t_a relative to pore radius. Adsorbed water density depends on hydration site density but remains significantly below bulk density (0.05−0.3 g/cm^3). Consequently, a higher t_a/r_h leads to a lower average density of confined water.

The introduction of surface charge on BTEVP-PMOs through methylation of the pyridine nitrogen induces structural changes, including reduced pore size, repeating unit shrinkage, increased pore wall thickness, and altered water-wall interactions, which result in a larger *t*-layer and increased adsorbed water density ρ_{t1}.

The aim of this study is to analyze water behavior in both established and novel PMOs, offering a reference for future research on similar materials. PMOs are well-suited as model systems for exploring interactions between functional groups and guest molecules in confined spaces.

■ ASSOCIATED CONTENT

Supporting Information

The Supporting Information is available free of charge at https://pubs.acs.org/doi/10.1021/acs.jpcc.5c02277.

https://doi.org/10.1021/acs.jpcc.5c02277
J. Phys. Chem. C 2025, 129, 12536−12550

Synthesis details for PMO precursors, PMOs, and MCM-41 silica, including synthesis parameters; powder X-ray diffraction, porosity data, ^{1}H NMR, FT-IR, and thermogravimetric analysis of porous materials; water vapor sorption isotherms and additional adsorption layer behavior (PDF)

AUTHOR INFORMATION

Corresponding Authors

Michael Steiger − *Institute of Inorganic and Applied Chemistry, University of Hamburg, 20146 Hamburg, Germany*; Phone: +49-40-42838-2895; Email: michael.steiger@uni-hamburg.de

Michael Fröba − *Institute of Inorganic and Applied Chemistry, University of Hamburg, 20146 Hamburg, Germany; The Hamburg Centre for Ultrafast Imaging, 22761 Hamburg, Germany*; orcid.org/0000-0001-6927-0509; Phone: +49-40-42838-3100; Email: michael.froeba@uni-hamburg.de

Authors

Philip Lenz − *Institute of Inorganic and Applied Chemistry, University of Hamburg, 20146 Hamburg, Germany; The Hamburg Centre for Ultrafast Imaging, 22761 Hamburg, Germany*

Sophia-M. Meinert − *Institute of Inorganic and Applied Chemistry, University of Hamburg, 20146 Hamburg, Germany*

Sandra König − *Institute of Inorganic and Applied Chemistry, University of Hamburg, 20146 Hamburg, Germany*

Complete contact information is available at: https://pubs.acs.org/10.1021/acs.jpcc.5c02277

Notes

The authors declare no competing financial interest.

ACKNOWLEDGMENTS

This work was funded by the Cluster of Excellence "Advanced Imaging of Matter" of the Deutsche Forschungsgemeinschaft (DFG)—EXC 2056—project ID 390715994 and it was supported in the frame of the LFF-project "Control of the special properties of water in nanopores" (LFF-FV68-2019), financed by the BWFGB. Scientific exchange and support of the Center for Molecular Water Science (CMWS) is also acknowledged. We would like to thank Isabelle Nevoigt for measuring our PXRDs, Uta Sazama for the TG-MS measurements, Claudia Wontorra for measuring the NMR spectra, and Dr. Charlotte Ruhmlieb and Andrea Köppen for obtaining the HRTEM images of our samples.

REFERENCES

(1) Pettersson, L. G. M.; Henchman, R. H.; Nilsson, A. Water-the most anomalous liquid. *Chem. Rev.* **2016**, *116* (13), 7459−7462.

(2) Gallo, P.; Amann-Winkel, K.; Angell, C. A.; Anisimov, M. A.; Caupin, F.; Chakravarty, C.; Lascaris, E.; Loerting, T.; Panagiotopoulos, A. Z.; Russo, J.; et al. Water: A tale of two liquids. *Chem. Rev.* **2016**, *116* (13), 7463−7500.

(3) Brini, E.; Fennell, C. J.; Fernandez-Serra, M.; Hribar-Lee, B.; Lukšič, M.; Dill, K. A. How water's properties are encoded in its molecular structure and energies. *Chem. Rev.* **2017**, *117* (19), 12385−12414.

(4) Nilsson, A.; Pettersson, L. G. M. The structural origin of anomalous properties of liquid water. *Nat. Commun.* **2015**, *6*, No. 8998.

(5) Salzmann, C. G. Advances in the experimental exploration of water's phase diagram. *J. Chem. Phys.* **2019**, *150* (6), No. 060901.

(6) Bellissent-Funel, M.-C.; Hassanali, A.; Havenith, M.; Henchman, R.; Pohl, P.; Sterpone, F.; van der Spoel, D.; Xu, Y.; Garcia, A. E. Water determines the structure and dynamics of proteins. *Chem. Rev.* **2016**, *116* (13), 7673−7697.

(7) Lynden-Bell, R. M.; Morris, S. C.; Barrow, J. D.; Finney, J. L.; Harper, C. *Water and life: The unique properties of H_2O*; CRC Press, 2010.

(8) Mentré, P. Water in the orchestration of the cell machinery. Some misunderstandings: a short review. *J. Biol. Phys.* **2012**, *38* (1), 13−26.

(9) Ni, H.; Zheng, Y.-F.; Mao, Z.; Wang, Q.; Chen, R.-X.; Zhang, L. Distribution, cycling and impact of water in the Earth's interior. *Natl. Sci. Rev.* **2017**, *4* (6), 879−891.

(10) Björneholm, O.; Hansen, M. H.; Hodgson, A.; Liu, L.-M.; Limmer, D. T.; Michaelides, A.; Pedevilla, P.; Rossmeisl, J.; Shen, H.; Tocci, G.; et al. Water at interfaces // Water at Interfaces. *Chem. Rev.* **2016**, *116* (13), 7698−7726.

(11) Brovchenko, I.; Oleinikova, A. *Interfacial and Confined Water*; Elsevier, 2008.

(12) Nishida, K.; Anada, T.; Tanaka, M. Roles of interfacial water states on advanced biomedical material design. *Adv. Drug Delivery Rev.* **2022**, *186*, No. 114310.

(13) Knight, A. W.; Kalugin, N. G.; Coker, E.; Ilgen, A. G. Water properties under nano-scale confinement. *Sci. Rep.* **2019**, *9* (1), No. 8246.

(14) Agre, P.; Kozono, D. Aquaporin water channels: molecular mechanisms for human diseases. *FEBS Lett.* **2003**, *555* (1), 72−78.

(15) Agre, P. Aquaporin water channels (Nobel lecture) // Aquaporin water channels (Nobel Lecture). *Angew. Chem., Int. Ed.* **2004**, *43* (33), 4278−4290.

(16) Webber, B.; Dore, J. Structural and dynamic studies of water in mesoporous silicas using neutron scattering and nuclear magnetic resonance. *J. Phys.: Condens. Matter* **2004**, *16* (45), S5449−S5470.

(17) Yoshida, K.; Yamaguchi, T.; Kittaka, S.; Bellissent-Funel, M.-C.; Fouquet, P. Thermodynamic, structural, and dynamic properties of supercooled water confined in mesoporous MCM-41 studied with calorimetric, neutron diffraction, and neutron spin echo measurements. *J. Chem. Phys.* **2008**, *129* (5), No. 054702.

(18) Deschamps, J.; Audonnet, F.; Brodie-Linder, N.; Schoeffel, M.; Alba-Simionesco, C. A thermodynamic limit of the melting/freezing processes of water under strongly hydrophobic nanoscopic confinement. *Phys. Chem. Chem. Phys.* **2010**, *12* (7), 1440−1443.

(19) Morishige, K.; Nobuoka, K. X-ray diffraction studies of freezing and melting of water confined in a mesoporous adsorbent (MCM-41). *J. Chem. Phys.* **1997**, *107* (17), 6965−6969.

(20) Findenegg, G. H.; Jähnert, S.; Akcakayiran, D.; Schreiber, A. Freezing and melting of water confined in silica nanopores. *ChemPhysChem* **2008**, *9* (18), 2651−2659.

(21) Liu, E.; Dore, J. C.; Webber, J. B. W.; Khushalani, D.; Jähnert, S.; Findenegg, G. H.; Hansen, T. Neutron diffraction and NMR relaxation studies of structural variation and phase transformations for water/ice in SBA-15 silica: I. The over-filled case. *J. Phys.: Condens. Matter* **2006**, *18* (44), 10009−10028.

(22) Schreiber, A.; Ketelsen, I.; Findenegg, G. H. Melting and freezing of water in ordered mesoporous silica materials. *Phys. Chem. Chem. Phys.* **2001**, *3* (7), 1185−1195.

(23) Jähnert, S.; Vaca Chávez, F.; Schaumann, G. E.; Schreiber, A.; Schönhoff, M.; Findenegg, G. H. Melting and freezing of water in cylindrical silica nanopores. *Phys. Chem. Chem. Phys.* **2008**, *10* (39), 6039−6051.

(24) Rother, G.; Stack, A. G.; Gautam, S.; Liu, T.; Cole, D. R.; Busch, A. Water uptake by silica nanopores: Impacts of surface hydrophilicity and pore size. *J. Phys. Chem. C* **2020**, *124* (28), 15188−15194.

(25) Rother, G.; Gautam, S.; Liu, T.; Cole, D. R.; Busch, A.; Stack, A. G. Molecular structure of adsorbed water phases in silica nanopores. *J. Phys. Chem. C* **2022**, *126* (5), 2885−2895.
(26) Kocherbitov, V.; Alfredsson, V. Hydration of MCM-41 studied by sorption calorimetry. *J. Phys. Chem. C* **2007**, *111* (35), 12906−12913.
(27) Morishige, K. Influence of pore wall hydrophobicity on freezing and melting of confined water. *J. Phys. Chem. C* **2018**, *122* (9), 5013−5019.
(28) Ito, K.; Faraone, A.; Tyagi, M.; Yamaguchi, T.; Chen, S.-H. Nanoscale dynamics of water confined in ordered mesoporous carbon. *Phys. Chem. Chem. Phys.* **2019**, *21* (16), 8517−8528.
(29) Chatzichristos, A.; Hassan, J. Current understanding of water properties inside carbon nanotubes. *Nanomaterials* **2022**, *12* (1), No. 174.
(30) Alexiadis, A.; Kassinos, S. Molecular simulation of water in carbon nanotubes. *Chem. Rev.* **2008**, *108* (12), 5014−5034.
(31) Thommes, M.; Morell, J.; Cychosz, K. A.; Fröba, M. Combining nitrogen, argon, and water adsorption for advanced characterization of ordered mesoporous carbons (CMKs) and periodic mesoporous organosilicas (PMOs). *Langmuir* **2013**, *29* (48), 14893−14902.
(32) Weinberger, C.; Zysk, F.; Hartmann, M.; Kaliannan, N. K.; Keil, W.; Kühne, T. D.; Tiemann, M. The structure of water in silica mesopores − influence of the pore wall polarity. *Adv. Mater. Interfaces* **2022**, *9* (20), No. 2200245.
(33) Collados, C. C.; Huber, C.; Söllner, J.; Grass, J.-P.; Inayat, A.; Durdyyev, R.; Smith, A.-S.; Wisser, D.; Hartmann, M.; Thommes, M. Assessment of hydrophilicity/hydrophobicity in mesoporous silica by combining adsorption, liquid intrusion, and solid-state NMR spectroscopy. *Langmuir* **2024**, *40* (25), 12853−12867.
(34) Schrader, A. M.; Monroe, J. I.; Sheil, R.; Dobbs, H. A.; Keller, T. J.; Li, Y.; Jain, S.; Shell, M. S.; Israelachvili, J. N.; Han, S. Surface chemical heterogeneity modulates silica surface hydration. *Proc. Natl. Acad. Sci. U.S.A.* **2018**, *115* (12), 2890−2895.
(35) Hoffmann, F.; Cornelius, M.; Morell, J.; Fröba, M. Silica-based mesoporous organic-inorganic hybrid materials. *Angew. Chem., Int. Ed.* **2006**, *45* (20), 3216−3251.
(36) Inagaki, S.; Guan, S.; Ohsuna, T.; Terasaki, O. An ordered mesoporous organosilica hybrid material with a crystal-like wall structure. *Nature* **2002**, *416* (6878), 304−307.
(37) Sayari, A.; Wang, W. Molecularly ordered nanoporous organosilicates prepared with and without surfactants. *J. Am. Chem. Soc.* **2005**, *127* (35), 12194−12195.
(38) Cornelius, M.; Hoffmann, F.; Fröba, M. Periodic mesoporous organosilicas with a bifunctional conjugated organic unit and crystal-like pore walls. *Chem. Mater.* **2005**, *17* (26), 6674−6678.
(39) Beretta, M.; Morell, J.; Sozzani, P.; Fröba, M. Towards peptide formation inside the channels of a new divinylaniline-bridged periodic mesoporous organosilica. *Chem. Commun.* **2010**, *46* (14), 2495−2497.
(40) Gießelmann, N. C.; Lenz, P.; Meinert, S.-M.; Simon, T.; Jo, W.; Striker, N. N.; Fröba, M.; Lehmkühler, F. Structure of water under confinement in periodic mesoporous organosilicas investigated by X-ray scattering. *J. Phys. Chem. C* **2024**, *128* (1), 499−507.
(41) Mietner, J. B. Visiting Nanopores: The Great Potential of PMOs for Studying the Properties of Water in Nanopores of Different Polarity. Ph.D. Thesis, University of Hamburg: Germany, 2018.
(42) Mietner, B. J.; Fröba, M.; Valiullin, R. Water transport in periodic mesoporous organosilica materials. *J. Phys. Chem. C* **2018**, *122* (24), 12673−12680.
(43) Malfait, B.; Jani, A.; Mietner, J. B.; Lefort, R.; Huber, P.; Fröba, M.; Morineau, D. Influence of pore surface chemistry on the rotational dynamics of nanoconfined water. *J. Phys. Chem. C* **2021**, *125* (30), 16864−16874.
(44) Jani, A.; Busch, M.; Mietner, J. B.; Ollivier, J.; Appel, M.; Frick, B.; Zanotti, J.-M.; Ghoufi, A.; Huber, P.; Fröba, M.; Morineau, D. Dynamics of water confined in mesopores with variable surface interaction. *J. Chem. Phys.* **2021**, *154* (9), No. 094505.
(45) Mietner, J. B.; Brieler, F. J.; Lee, Y. J.; Fröba, M. Properties of water confined in periodic mesoporous organosilicas: Nanoimprinting the local structure. *Angew. Chem., Int. Ed.* **2017**, *56* (40), 12348−12351.
(46) Aso, M.; Ito, K.; Sugino, H.; Yoshida, K.; Yamada, T.; Yamamuro, O.; Inagaki, S.; Yamaguchi, T. Thermal behavior, structure, and dynamics of low-temperature water confined in mesoporous organosilica by differential scanning calorimetry, X-ray diffraction, and quasi-elastic neutron scattering. *Pure Appl. Chem.* **2012**, *85* (1), 289−305.
(47) Gießelmann, N. C.; Lenz, P.; Meinert, S.-M.; Simon, T.; Bauer, R. P. C.; Jo, W.; Claas, S.; Köhn, C.; Striker, N. N.; Fröba, M.; et al. The structure of ice under confinement in periodic mesoporous organosilicas (PMOs). *J. Chem. Phys.* **2024**, *161* (3), No. 034508, DOI: 10.1063/5.0216697.
(48) Gonella, G.; Backus, E. H. G.; Nagata, Y.; Bonthuis, D. J.; Loche, P.; Schlaich, A.; Netz, R. R.; Kühnle, A.; McCrum, I. T.; Koper, M. T. M.; et al. Water at charged interfaces. *Nat. Rev. Chem.* **2021**, *5* (7), 466−485.
(49) Horner, A.; Siligan, C.; Cornean, A.; Pohl, P. Positively charged residues at the channel mouth boost single-file water flow. *Faraday Discuss.* **2018**, *209* (0), 55−65.
(50) Politzer, P. Anomalous properties of fluorine. *J. Am. Chem. Soc.* **1969**, *91* (23), 6235−6237.
(51) O'Hagan, D. Understanding organofluorine chemistry. An introduction to the C-F bond. *Chem. Soc. Rev.* **2008**, *37* (2), 308−319.
(52) Smart, B. E. Fluorine substituent effects (on bioactivity). *J. Fluorine Chem.* **2001**, *109* (1), 3−11.
(53) Legon, A. C. The halogen bond: an interim perspective. *Phys. Chem. Chem. Phys.* **2010**, *12* (28), 7736−7747.
(54) Politzer, P.; Lane, P.; Concha, M. C.; Ma, Y.; Murray, J. S. An overview of halogen bonding. *J. Mol. Model.* **2007**, *13* (2), 305−311.
(55) Bracco, S.; Beretta, M.; Cattaneo, A.; Comotti, A.; Falqui, A.; Zhao, K.; Rogers, C.; Sozzani, P. Dipolar rotors orderly aligned in mesoporous fluorinated organosilica architectures. *Angew. Chem., Int. Ed.* **2015**, *54* (16), 4773−4777.
(56) Champagne, P.; Desroches, J.; Paquin, J.-F. Organic fluorine as a hydrogen-bond acceptor: Recent examples and applications. *Synthesis* **2015**, *47* (03), 306−322.
(57) Jia, Q.; Li, Q.; Luo, M.; Li, H.-B. Understanding the effects of vicinal carbon substituents and configuration on organofluorine hydrogen-bonding interaction. *RSC Adv.* **2018**, *8* (68), 38980−38986.
(58) Galarneau, A.; Nader, M.; Guenneau, F.; Di Renzo, F.; Gedeon, A. Understanding the stability in water of mesoporous SBA-15 and MCM-41. *J. Phys. Chem. C* **2007**, *111* (23), 8268−8277.
(59) Gouze, B.; Cambedouzou, J.; Parrès-Maynadié, S.; Rébiscoul, D. How hexagonal mesoporous silica evolves in water on short and long term: Role of pore size and silica wall porosity. *Microporous Mesoporous Mater.* **2014**, *183*, 168−176.
(60) Martens, S.; Ortmann, R.; Brieler, F. J.; Pasel, C.; Joo Lee, Y.; Bathen, D.; Fröba, M. Periodic mesoporous organosilicas as adsorbents of toxic trace gases out of the ambient air. *Z. Anorg. Allg. Chem.* **2014**, *640* (3−4), 632−640.
(61) Waki, M.; Mizoshita, N.; Ohsuna, T.; Tani, T.; Inagaki, S. Crystal-like periodic mesoporous organosilica bearing pyridine units within the framework. *Chem. Commun.* **2009**, *46* (43), 8163−8165.
(62) Mizoroki, T.; Mori, K.; Ozaki, A. Arylation of olefin with aryl iodide catalyzed by palladium. *Bull. Chem. Soc. Jpn.* **1971**, *44* (2), No. 581.
(63) Heck, R. F.; Nolley, J. P. Palladium-catalyzed vinylic hydrogen substitution reactions with aryl, benzyl, and styryl halides. *J. Org. Chem.* **1972**, *37* (14), 2320−2322.
(64) Dieck, H. A.; Heck, F. R. Palladium catalyzed synthesis of aryl, heterocyclic and vinylic acetylene derivatives. *J. Organomet. Chem.* **1975**, *93* (2), 259−263.
(65) Brunauer, S.; Emmett, P. H.; Teller, E. Adsorption of gases in multimolecular layers. *J. Am. Chem. Soc.* **1938**, *60* (2), 309−319.

(66) Landers, J.; Gor, G. Y.; Neimark, A. V. Density functional theory methods for characterization of porous materials. *Colloids Surf., A* **2013**, *437*, 3−32.
(67) Thommes, M.; Kaneko, K.; Neimark, A. V.; Olivier, J. P.; Rodriguez-Reinoso, F.; Rouquerol, J.; Sing, K. S. Physisorption of gases, with special reference to the evaluation of surface area and pore size distribution (IUPAC Technical Report). *Pure Appl. Chem.* **2015**, *87* (9−10), 1051−1069.
(68) Thomson, W. LX. On the equilibrium of vapour at a curved surface of liquid. *London Edinburgh Philos. Mag. J. Sci.* **1871**, *42* (282), 448−452.
(69) Cohan, L. H. Sorption hysteresis and the vapor pressure of concave surfaces. *J. Am. Chem. Soc.* **1938**, *60* (2), 433−435.
(70) Gurvich, L. G. Physio-Chemical Attractive Force. *J. Russ. Phys.-Chem. Soc.* **1915**, No. 47, 805−827.
(71) Rouquerol, F.; Rouquerol, J.; Sing, K. S. W.; Llewellyn, P.; Maurin, G. *Adsorption by Powders and Porous Solids: Principles, Methodology and Applications*, 2nd ed.; Elsevier/Academic Press, 2014.
(72) Lowell, S.; Shields, J. E.; Thomas, M. A.; Thommes, M. *Characterization of Porous Solids and Powders: Surface Area, Pore Size and Density*, Particle Technology Series; Springer, 2004; Vol. *16*.
(73) Thommes, M.; Mitchell, S.; Pérez-Ramírez, J. Surface and pore structure assessment of hierarchical MFI Zeolites by advanced water and argon sorption studies. *J. Phys. Chem. C* **2012**, *116* (35), 18816−18823.
(74) Fried, D. I.; Bednarski, D.; Dreifke, M.; Brieler, F. J.; Thommes, M.; Fröba, M. Influence of the hydrophilic-hydrophobic contrast of porous surfaces on the enzymatic performance. *J. Mater. Chem. B* **2015**, *3* (11), 2341−2349.
(75) Naono, H.; Fujiwara, R.; Yagi, M. Determination of physisorbed and chemisorbed waters on silica gel and porous silica glass by means of desorption isotherms of water vapor. *J. Colloid Interface Sci.* **1980**, *76* (1), 74−82.
(76) Canivet, J.; Bonnefoy, J.; Daniel, C.; Legrand, A.; Coasne, B.; Farrusseng, D. Structure−property relationships of water adsorption in metal−organic frameworks. *New J. Chem.* **2014**, *38* (7), 3102−3111.
(77) David, R. O.; Fahrni, J.; Marcolli, C.; Mahrt, F.; Brühwiler, D.; Kanji, Z. A. The role of contact angle and pore width on pore condensation and freezing. *Atmos. Chem. Phys.* **2020**, *20* (15), 9419−9440.
(78) Matsumoto, A.; Sasaki, T.; Nishimiya, N.; Tsutsumi, K. Evaluation of the hydrophobic properties of mesoporous FSM-16 by means of adsorption calorimetry. *Langmuir* **2001**, *17* (1), 47−51.
(79) Matsumoto, A.; Tsutsumi, K.; Schumacher, K.; Unger, K. K. Surface functionalization and stabilization of mesoporous silica spheres by silanization and their adsorption characteristics. *Langmuir* **2002**, *18* (10), 4014−4019.
(80) Zhuravlev, L. T. The surface chemistry of amorphous silica. Zhuravlev model. *Colloids Surf., A* **2000**, *173* (1−3), 1−38.
(81) Dallin, B. C.; Kelkar, A. S.; van Lehn, R. C. Structural features of interfacial water predict the hydrophobicity of chemically heterogeneous surfaces. *Chem. Sci.* **2023**, *14* (5), 1308−1319.
(82) Nguyen, H. L.; Darù, A.; Chheda, S.; Alawadhi, A.; Neumann, S. E.; Wang, L.; Bai, X.; Alawad, M. O.; Borgs, C.; Chayes, J. T.; et al. Pinpointing the onset of water harvesting in reticular frameworks from structure. *ACS Cent. Sci.* **2025**, *11* (5), 665−671.
(83) Lin, X.; Hu, Q.; Chen, Z.; Wang, Q.; Zhang, T.; Sun, M. Changes in water vapor adsorption and water film thickness in clayey materials as a function of relative humidity. *Vadose Zone J.* **2020**, *19* (1), No. e20063.
(84) Israelachvili, J. N.; Pashley, R. M. Molecular layering of water at surfaces and origin of repulsive hydration forces. *Nature* **1983**, *306* (5940), 249−250.
(85) Antognozzi, M.; Humphris, A. D. L.; Miles, M. J. Observation of molecular layering in a confined water film and study of the layers viscoelastic properties. *Appl. Phys. Lett.* **2001**, *78* (3), 300−302.
(86) Möhlmann, D. T. The influence of van der Waals forces on the state of water in the shallow subsurface of Mars. *Icarus* **2008**, *195* (1), 131−139.
(87) Lerbret, A.; Lelong, G.; Mason, P. E.; Saboungi, M.-L.; Brady, J. W. Water confined in cylindrical pores: A molecular dynamics study. *Food Biophys.* **2011**, *6* (2), 233−240.
(88) Soper, A. K. Radical re-appraisal of water structure in hydrophilic confinement. *Chem. Phys. Lett.* **2013**, *590*, 1−15.
(89) Erko, M.; Wallacher, D.; Hoell, A.; Hauss, T.; Zizak, I.; Paris, O. Density minimum of confined water at low temperatures: a combined study by small-angle scattering of X-rays and neutrons. *Phys. Chem. Chem. Phy.* **2012**, *14* (11), 3852−3858.
(90) Gallo, P.; Ricci, M. A.; Rovere, M. Layer analysis of the structure of water confined in vycor glass. *J. Chem. Phys.* **2002**, *116* (1), 342−346.
(91) Roy, S.; Biswas, B.; Ghosh, N.; Singh, P. C.; Mondal, J. A. Hydrophobic hydration of fluoroalkyl (C−F) is distinctly different from that of its hydrogenated counterpart (C−H), as observed by raman difference with simultaneous curve fitting analysis. *J. Phys. Chem. C* **2019**, *123* (44), 27012−27019.
(92) Shibuta, S.; Imamura, H.; Shibuta, K.; Judai, K. Water depletion enhanced by halogenation of benzene. *J. Phys. Chem. B* **2021**, *125* (31), 8855−8861.
(93) Yang, Y.; Liu, F.; Kawazoe, Y. Adsorption of water on fluorinated graphene. *J. Phys. Chem. Solids* **2019**, *124*, 54−59.
(94) Nijem, N.; Canepa, P.; Kaipa, U.; Tan, K.; Roodenko, K.; Tekarli, S.; Halbert, J.; Oswald, I. W. H.; Arvapally, R. K.; Yang, C.; et al. Water cluster confinement and methane adsorption in the hydrophobic cavities of a fluorinated metal-organic framework. *J. Am. Chem. Soc.* **2013**, *135* (34), 12615−12626.
(95) Farmahini, A. H.; Sholl, D. S.; Bhatia, S. K. Fluorinated carbide-derived carbon: more hydrophilic, yet apparently more hydrophobic. *J. Am. Chem. Soc.* **2015**, *137* (18), 5969−5979.
(96) Zhang, J.; Tan, J.; Pei, R.; Ye, S.; Luo, Y. Ordered water layer on the macroscopically hydrophobic fluorinated polymer surface and its ultrafast vibrational dynamics. *J. Am. Chem. Soc.* **2021**, *143* (33), 13074−13081.
(97) Robalo, J. R.; Streacker, L. M.; de Oliveira, D. M.; Imhof, P.; Ben-Amotz, D.; Verde, A. V. Hydrophobic but water-friendly: Favorable water-perfluoromethyl interactions promote hydration shell defects. *J. Am. Chem. Soc.* **2019**, *141* (40), 15856−15868.
(98) Kwon, O.-H.; Yoo, T. H.; Othon, C. M.; van Deventer, J. A.; Tirrell, D. A.; Zewail, A. H. Hydration dynamics at fluorinated protein surfaces. *Proc. Natl. Acad. Sci. U.S.A.* **2010**, *107* (40), 17101−17106.
(99) Tshepelevitsh, S.; Kütt, A.; Lõkov, M.; Kaljurand, I.; Saame, J.; Heering, A.; Plieger, P. G.; Vianello, R.; Leito, I. On the basicity of organic bases in different media. *Eur. J. Org. Chem.* **2019**, *2019* (40), 6735−6748.
(100) Lund, M.; Jungwirth, P. Patchy proteins, anions and the Hofmeister series. *J. Phys.: Condens. Matter* **2008**, *20* (49), No. 494218.
(101) Liu, L.; Kou, R.; Liu, G. Ion specificities of artificial macromolecules. *Soft Matter* **2017**, *13* (1), 68−80.
(102) Lee, E.; Choi, J.-H.; Cho, M. The effect of Hofmeister anions on water structure at protein surfaces. *Phys. Chem. Chem. Phys.* **2017**, *19* (30), 20008−20015.
(103) Assaf, K. I.; Nau, W. M. The chaotropic effect as an assembly motif in chemistry. *Angew. Chem., Int. Ed.* **2018**, *57* (43), 13968−13981.
(104) Marcus, Y. Ionic radii in aqueous solutions. *Chem. Rev.* **1988**, *88* (8), 1475−1498.
(105) Babu, C. S.; Lim, C. Theory of ionic hydration: insights from molecular dynamics simulations and experiment. *J. Phys. Chem. B* **1999**, *103* (37), 7958−7968.
(106) Zhao, H. Are ionic liquids kosmotropic or chaotropic? An evaluation of available thermodynamic parameters for quantifying the ion kosmotropicity of ionic liquids. *J. Chem. Technol. Biotechnol.* **2006**, *81* (6), 877−891.

(107) Levin, Y.; dos Santos, A. P. Ions at hydrophobic interfaces. *J. Phys.: Condens. Matter* **2014**, *26* (20), No. 203101.
(108) Bastos-González, D.; Pérez-Fuentes, L.; Drummond, C.; Faraudo, J. Ions at interfaces: the central role of hydration and hydrophobicity. *Curr. Opin. Colloid Interface Sci.* **2016**, *23*, 19−28.
(109) Kocherbitov, V. Properties of water confined in an amphiphilic nanopore. *J. Phys. Chem. C* **2008**, *112* (43), 16893−16897.

https://doi.org/10.1021/acs.jpcc.5c02277
J. Phys. Chem. C 2025, 129, 12536−12550

5.2. The Role of Fine-Tuned Surface Functionality on Adsorption Thermodynamics of Nanoconfined Water within Periodic Mesoporous Organosilicas

Philip Lenz, Uta Sazama, Sandra König, Michael Steiger*, Michael Fröba*

Synopsis

Building on the previously established differences in surface hydration site densities, water–wall interactions, and adsorption-layer properties determined by water vapor sorption at 298.15 K, the present study investigates the thermodynamic characteristics of water adsorption in periodic mesoporous organosilicas with finely tuned surface functionality. Adsorption enthalpies were determined using the indirect isosteric method at different temperatures and a direct calorimetric approach based on combined DSC–TGA measurements under controlled humidity flow, enabling a detailed analysis of adsorption energetics, particularly in the low-coverage regime.

Hydrophilic materials exhibit high absolute adsorption enthalpies at low surface coverage, reflecting strong water–surface interactions at surface hydration sites. Hydrophobic PMOs likewise show pronounced initial interactions at isolated silanol groups, followed by a marked decrease in adsorption enthalpy after saturation of these preferred sites. In this regime, the decreasing adsorption enthalpy reflects a shift from surface-dominated interactions to water–water interactions and aggregate growth before capillary condensation. The correlation between Henry-derived adsorption enthalpies and surface hydration site density further confirms that the initial adsorption energetics are primarily governed by the density and accessibility of hydration sites.

Calorimetric measurements reveal distinct enthalpic maxima for selected functionalized PMOs, indicating cooperative effects between silanol groups and organic bridge functionalities. Furthermore, temperature-dependent sorption measurements show that, within the range of 298–318 K, neither the water amount at the onset of capillary condensation nor the corresponding relative pressure exhibit a pronounced temperature dependence, whereas hysteresis behavior is largely controlled by the desorption branch.

Overall, this study extends the structural hydrophilicity classification derived from water vapor sorption by providing a quantitative thermodynamic framework for water–surface interactions in periodic mesoporous organosilicas.

THE JOURNAL OF PHYSICAL CHEMISTRY C
A JOURNAL OF THE AMERICAN CHEMICAL SOCIETY

Open Access
This article is licensed under CC-BY 4.0

pubs.acs.org/JPCC
Article

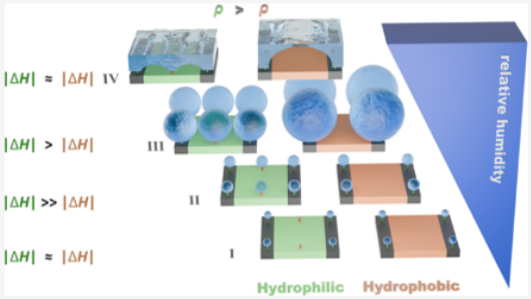
The Role of Fine-Tuned Surface Functionality on Adsorption Thermodynamics of Nanoconfined Water within Periodic Mesoporous Organosilicas

Philip Lenz, Uta Sazama, Sandra König, Michael Steiger,* and Michael Fröba*

Cite This: J. Phys. Chem. C 2026, 130, 3472−3485
Read Online

ACCESS | Metrics & More | Article Recommendations | Supporting Information

ABSTRACT: In this study, the adsorption enthalpy and entropy of water in the nanoconfinement of periodic mesoporous organosilicas with fine-tuned surface chemistry were investigated by integrating thermogravimetric analysis (TGA) and differential scanning calorimetry (DSC) with a continuous-flow humidity generator, providing a direct method to better understand the water adsorption process at very low surface coverage. For comparison, the commonly used indirect isosteric method was employed, yielding generally comparable results to the simultaneous DSC-TGA measurements despite differing experimental conditions. Only the calorimetric method revealed that not only more hydrophilic materials exhibit high absolute values of adsorption enthalpy of water at the first surface contact but also hydrophobic materials, as they contain surface silanol groups that can strongly interact with water until these sites are saturated. Beyond this initial humidity region of water-surface contact, both methods yield largely consistent results at higher relative humidity, clearly distinguishing between hydrophilic and hydrophobic surface behavior. More hydrophobic materials have lower absolute values of adsorption enthalpy, reflecting weaker interaction strength and less structuring before reaching the condensation enthalpy of water (−44 kJ mol^{-1}), while hydrophilic materials exhibit higher absolute values of adsorption enthalpy before water−water interactions dominate. Additionally, results from the isosteric method indicate that, at higher surface coverage, hydrophilic materials exert a long-range structural influence extending into distant water layers. Furthermore, the influence of surface functionality and temperature on water vapor sorption isotherms was analyzed, revealing the temperature independence of both the water aggregate size prior to, and the relative pressure at, the inflection point of capillary condensation. In contrast, the desorption branch primarily governs the temperature dependence of the adsorption−desorption hysteresis. This study presents the first detailed enthalpic analysis of water adsorption in PMOs using a continuous-flow calorimetric method, providing a foundation for future research on water-surface functionality interactions either at different loadings under isothermal conditions or across varying temperatures.



1. INTRODUCTION

The adsorption of water in porous materials is a fundamental process with broad implications for applications including gas separation,[1,2] humidity control,[3] thermal energy storage,[4,5] and water desalination.[6−10] Periodic Mesoporous Organosilicas (PMOs), characterized by tunable surface chemistry, well-defined pore structures, and the ability to form crystal-like pore walls,[11−15] serve as an ideal model system to study confined water and ice behavior within nanopores, as well as water adsorption processes.[16−25] By using different precursors with similar sized backbone structures, the influence of specific functional groups on the water adsorption−desorption behavior can be systematically investigated. A key thermodynamic parameter in this context is the enthalpy of adsorption, which provides insights into the strength of water-material interactions and the energetics of the adsorption process. Hydrophilic surfaces typically exhibit higher adsorption enthalpies due to strong hydrogen bonding and polar interactions, while hydrophobic surfaces with weaker water interactions generally show lower adsorption enthalpies.[26−31] Understanding these differences is essential for optimizing porous materials in applications such as water harvesting,[32,33] adsorption-driven heat pumps,[34−36] and separation processes[2,37,38] as well as for unraveling the underlying adsorption mechanisms. However, it has been shown that not only surface hydrophilicity, but also surface roughness[39] plays a role. Notably, even fluorinated surfaces, which are typically considered more hydrophobic, exhibit increasing adsorption enthalpies with higher degrees of fluorination.[40]

Received: November 1, 2025
Revised: January 17, 2026
Accepted: February 16, 2026
Published: February 24, 2026



© 2026 The Authors. Published by American Chemical Society

The adsorption enthalpy (ΔH_{ads}) is a fundamental parameter characterizing adsorbate−adsorbent interactions. It can be determined by two main experimental approaches: the indirect isosteric method and the direct calorimetric method.[41−46]

The isosteric method derives ΔH_{ads} by analyzing adsorption isotherms measured at different temperatures using the Clausius−Clapeyron equation, plotting the natural logarithm of absolute pressure ln$p$ at constant coverage against reciprocal temperature (T^{-1}). This approach is widely used because it relies on standard sorption equipment and relatively simple experimental setup. The method assumes ideal gas behavior as well as temperature independence of enthalpy, and requires multiple isotherms measured at closely spaced temperatures (typically ∼10 K) to minimize uncertainty. While reliable across a broad range of coverages, it is more sensitive to errors in equilibrium pressure at very low coverage (<0.5), where phase transitions or data inaccuracies can introduce significant deviations.[42,45,47,48]

The calorimetric method directly measures the enthalpy released during adsorption, providing a model-independent and more accurate determination of ΔH_{ads}, especially at low coverage and on heterogeneous surfaces. However, it requires sensitive, costly equipment and tightly controlled experimental conditions, limiting its routine use.[42−45]

Both methods target the same thermodynamic property, but differences in assumptions, data quality, and experimental conditions often lead to discrepancies. For reliable isosteric enthalpy values, using at least three isotherms within a narrow temperature range is recommended. Calorimetry remains the gold standard for detailed adsorption energetics, particularly in studies of micropore filling or high-energy adsorption sites.[44,45]

To measure the enthalpy of adsorption with water as adsorbate, different calorimetric approaches, including Tian-Calvet-type calorimetry[29,49−53] and humidity titration calorimetry,[54] had been used.[41] In this work, we employed a technique combining thermogravimetric analysis (TGA) and differential scanning calorimetry (DSC) with a humidity generator to study water adsorption. The sample was exposed to a nitrogen stream with stepwise increasing relative humidity at constant temperature (25 °C), enabling simultaneous measurement of mass uptake and heat flow during water sorption. This setup represents a variant of sorption calorimetry under isothermal conditions, analogous to humidity titration calorimetry[54] but operated in continuous flow mode,[55,56] utilizing a standard DSC-TGA method. Through simultaneous recording, this technique enables direct determination of hydration enthalpies alongside sorption isotherms, with precise relative humidity (RH) control and stable conditions during each adsorption step. Variants of this method have been applied to measure desorption enthalpy of water on hygroscopic fibers while heated at 10 °C/min,[57] capillary condensation of propane by isothermal compression in mesoporous silica SBA-15,[58] water vapor adsorption on coal at 107 °C,[55] as well as on zeolites and metal−organic frameworks (MOFs).[59] Although the underlying principles and instrumentation are well established in thermal analysis and adsorption science, publications applying this approach remain scarce. Most existing studies focus on desorption, whereas adsorption measurements at very fine RH increments and very low surface coverage, especially for materials with variable surface functionalities as in our study, have not yet been reported.

In this study, we investigate the influence of temperature on water sorption isotherms and adsorption enthalpy of water in PMOs with hydrophilic and hydrophobic surface functionalities, using two complementary approaches: the isosteric method and direct calorimetric measurements. The isosteric method, derived from adsorption isotherms at different temperatures, provides a macroscopic view on the energy changes during adsorption. In contrast, calorimetry directly quantifies the heat released or absorbed, offering detailed insight into interaction energetics. By combining these approaches, we aim to provide a comprehensive characterization of water adsorption in PMOs with different surface chemistries, clarifying underlying mechanisms and their relevance for material design.

2. EXPERIMENTAL SECTION

2.1. Materials

The synthesis of the PMO and MCM-41 silica materials employed a soft-templating approach using cationic quaternary ammonium surfactants (C_nTAB) with varying alkyl chain lengths (n). This study primarily focuses on materials with a pore diameter of 3.8 nm to study the impact of surface chemistry and to minimize any geometrical confinement effects on adsorption and condensation. Some measurements were performed using materials with different pore sizes to evaluate their influence on adsorption behavior. Detailed synthesis procedures for PMO precursors and most PMO and MCM-41 materials are reported in our previous work.[24]

2.2. Characterization Methods

X-ray powder diffraction (PXRD) patterns were recorded using a PANalytical X'Pert Pro PW3040/60 instrument with Cu−Kα radiation to analyze the mesostructure and molecular ordering in the pore walls of the materials. Data evaluation was performed using OriginPro 2024 from OriginLab and X'Pert Highscore Plus from PANalytical.

Nitrogen physisorption measurements were conducted to characterize the porosities of the materials. Before measurement, samples were activated at 100 °C for 20 h under reduced pressure using a Quantachrome Masterprep degasser. The N_2 physisorption experiments were carried out at 77 K using a Quantachrome Quadrasorb-SI-MP and Quadrasorb evo. The pore size distribution was calculated using density functional theory (DFT) with the kernel: N_2 on silica (cylindrical pores), nonlocal DFT (NLDFT) using the adsorption branch. The specific surface area was determined using the Brunauer−Emmett−Teller (BET) method within the p/p_0 range of 0.05 to 0.3.[60] In cases where the BET range intersected with the condensation step of the isotherms, the range was reduced to ensure measurements remained within the plateau region before condensation ($p/p_0 < 0.3$). Data analysis was performed using QuadraWin 6.0 software from Quantachrome.

Water vapor sorption measurements were performed after degassing the samples at 100 °C for 20 h under reduced pressure using a Quantachrome MasterPrep Degasser. Isotherms were recorded at 25, 35, and 45 °C, using a fresh sample for each temperature, with a Quantachrome VSTAR sorption analyzer. Data evaluation was carried out using OriginPro 2024 (OriginLab) and VstarWin 2.0.1 (Quantachrome). The isosteric enthalpy of adsorption was determined from the adsorption isotherms measured at the three temperatures mentioned above using Van't Hoff-type plots generated with the VstarWin software. Interpolation was used to determine the pressures at constant loading for all three temperatures.

For simultaneous differential scanning calorimetry-thermogravimetry (DSC-TGA) experiments under defined humidity in continuous flow mode, the copper furnace of an STA 449 F3 Jupiter (NETZSCH-Gerätebau GmbH, Germany), equipped with a liquid nitrogen cooling system and DSC-TGA sensor type E, was modified by integrating a mixing chamber connected to a humidity generator (MHG32, proUmid GmbH, Germany), using nitrogen as the carrier

https://doi.org/10.1021/acs.jpcc.5c07495
J. Phys. Chem. C 2026, 130, 3472−3485

gas at a flow rate of 100 mL/min. For DSC-TGA measurements, aluminum crucibles (80 μL, Ø 6.8 mm, NETZSCH-Gerätebau GmbH) were filled to three-quarters of their volume with 3−5 mg of sample and using 4-fold-perforated aluminum lids. A schematic illustration of the experimental setup is shown in Figure 1. All

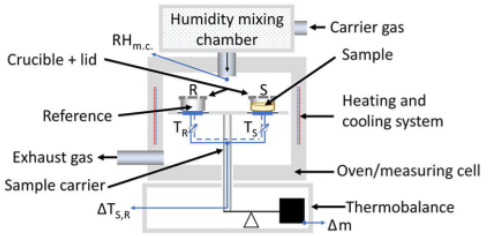


Figure 1. Schematic representation of the setup for calorimetric water vapor adsorption measurements under controlled temperature and humidity.

measurements were carried out isothermally at 298 K to capture adsorption and condensation enthalpies, which are reported per mole of adsorbed water (kJ mol^{-1} H_2O). The temperature and sensor calibration were performed manually using Micronal, an organic phase change material specified by the BASF-company, with a melting point of 23 °C and a melting enthalpy of 110 J g^{-1} at a slow heating rate of 0.1 K min^{-1}. The accuracy of the calibration was validated by comparison with the known condensation enthalpy of water (−44 kJ mol^{-1} at 298 K), further confirmed by the consistency of the experimental data presented in the subsequent sections. Additionally, measurements using indium were conducted to verify the calibration.

The program for the isothermal calorimetric measurement of the adsorption enthalpy was structured as follows:

In the first step, residual water was removed by heating the sample to 100 °C at a rate of 5 K min^{-1}, followed by an isothermal hold at 100 °C for 2 h under dry conditions (0% RH). The system was then cooled to 25 °C at 5 K min^{-1}.

Subsequently, an isothermal adsorption phase was conducted at 25 °C. The duration of this step depended on the target relative humidity range and the corresponding filling degree. For experiments reaching up to 95% RH, the isothermal phase lasted 90 h; for experiments limited to 35% RH, the duration was 28 h.

During the isothermal phase, relative humidity was increased in defined steps:

For full-range experiments (0−95% RH), RH was increased in 5% increments. Each step was held for 1 h in the range 0−45% RH, 1.5 h between 45−55% RH, and 7 h from 55−95% RH. The extended equilibration times at higher RH were necessary due to slower kinetics associated with capillary condensation and pore filling. Equilibration times were determined from the adsorption kinetics of water vapor sorption measurements and by performing DSC-TGA test runs on the analyzed materials until the thermal signal returned to baseline, thereby establishing a measurement protocol suitable for all materials.

For experiments limited to the subcondensation (adsorption-only) regime (0−35% RH), RH was increased in 1% increments from 0−10% RH and in 5% increments from 10−35% RH, with each step held for 1 h. An example of a typical measurement cycle is shown in Figure S1.

For reliable detection of DSC water vapor adsorption signals, a sufficiently high absolute surface area is required. This is demonstrated in the measurements of different silica types with varying surface areas (Figure 2).

The mesoporous MCM-41 silica, with a specific BET surface area (S_{BET}) of 1118 m^2 g^{-1}, exhibits the most intense DSC signals, followed by CPG with 18 m^2 g^{-1} and nonporous crushed glass. Owing to its high specific surface area and the sample mass used in the DSC experiments (typically 3−5 mg), MCM-41 silica provides a high absolute surface area, defined here as $A = S_{BET} \cdot m$, which amounts to

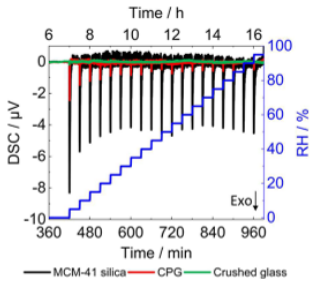


Figure 2. Example of raw water vapor adsorption measurement on three silica materials with different surface areas, conducted using DSC-TGA coupled to a humidity generator under isothermal conditions. DSC curves have been baseline corrected.

approximately 5 m^2. Based on experience, an absolute surface area in the range of 3−6 m^2 is well-suited for simultaneous detection of water uptake and associated enthalpy changes with sufficient resolution. Below ∼2 m^2, the combination of low water uptake and long-term balance drift can introduce significant errors. Since water adsorption primarily occurs at surface hydration sites (SHS),[61,62] a high absolute number of SHS enhances signal quality. Due to the longer measurement time, a drift in the balance occurs. This is accounted for in the mass determination by averaging the baseline slope before and after each adsorption step (induced by increasing humidity), specifically in the regions where thermal equilibrium is observed in the DSC signal.

Since adsorption is an exothermic process, the enthalpy of adsorption is inherently negative and reflects the interaction strength between water and the solid surface.[63] For clarity, in this work we report adsorption enthalpies as absolute values ($|\Delta H|$), so that larger values directly indicate stronger water-wall interactions.

3. RESULTS AND DISCUSSION

3.1. Material Characterization

Most of the materials investigated here were previously characterized in our recent studies.[24,25] Table 1 summarizes

Table 1. Material Properties Determined by Nitrogen Physisorption and Water Vapor Sorption: NLDFT Pore Diameter (d_P), Pore Volume (V_P), Specific BET Surface Area (S_{BET}), and Surface Hydration Sites at 25 °C (SHS_{25})

material	d_P/nm	V_P/cm^3 g^{-1}	S_{BET}/m^2 g^{-1}	SHS_{25}/nm^{-2}
MCM-41	3.9	0.887	1032	1.66
BTEVA	3.8	0.817	1158	1.17
BTEVP	3.8	0.649	783	1.02
BTEVB	3.8	0.638	752	0.45
N,*N*-DMBTEVA	3.8	0.647	808	0.67
BTEVClB	3.7	0.780	1053	0.69

key properties derived from nitrogen physisorption and water vapor sorption measurements. To exclude pore curvature effects on adsorption behavior, this work focuses primarily on materials with a uniform pore diameter of approximately 3.8 nm. Only these materials are listed in Table 1; all others are provided in the Supporting Information. The surface hydration site density (SHS_{25}) was derived from a combined evaluation of nitrogen physisorption and water vapor sorption data as described in the literature.[61,62,64] The calculation is based on comparing the surface area accessible to nitrogen with that accessible to water, using the molecular cross-sectional area for H_2O of 0.125 nm^2.[61,62] In the low-relative-pressure regime,

https://doi.org/10.1021/acs.jpcc.5c07495
J. Phys. Chem. C 2026, 130, 3472−3485

where adsorption is dominated by specific surface sites, each accessible hydroxyl group is assumed to accommodate a single water molecule. This approach yields the number of hydration sites per unit surface area, expressed in nm^{-2}. For porous silica materials, SHS_{25} values typically fall in the range of ≈1−3 nm^{-2}.[61,62,65,66] The SHS_{25} value obtained for MCM-41 silica in the present study (1.66 nm^{-2}) lies within this range and is consistent with literature reports, for example those by Rother et al. (1.54 and 1.18 nm^{-2})[61,62] or Kocherbitov and Alfredsson (1.6 nm^{-2}).[64]

3.2. Influence of Temperature on Water Vapor Sorption Isotherms

To investigate the combined effects of surface chemistry and temperature on water vapor sorption behavior, as well as to enable calculation of the isosteric enthalpy of adsorption (discussed in the following section), sorption measurements were conducted at 25, 35, and 45 °C (Figure 3). All measured

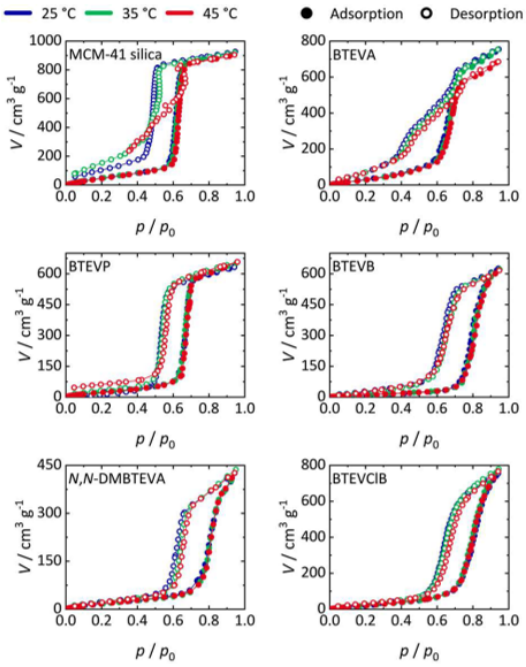


Figure 3. Water vapor sorption isotherms of different materials recorded at 25, 35, and 45 °C.

isotherms exhibit type V characteristics according to the IUPAC classification,[67,68] indicating a generally hydrophobic nature. Water adsorption via hydrogen bonding in these materials can occur at hydrolysis-generated silanol groups on the surface or, where present, at polar functional groups within the organic bridge. Regions of the organic bridges lacking such hydration sites likely remain inaccessible to water molecules.[18,24,64] Differences in functional groups result in varying degrees of hydrophilicity, as reflected by the slope of the adsorption step and by shifts in the relative pressure at the inflection point of capillary condensation when comparing materials with identical pore diameters. A more detailed discussion is provided in our previous publication.[24]

Analysis of the adsorption branches in Figure 3 shows that the relative pressure at which capillary condensation occurs is unaffected by temperature. Only minor shifts toward higher relative pressures are observed at elevated temperatures for more hydrophilic materials such as MCM-41 silica and BTEVA-PMO.

Both materials exhibit atypical desorption behavior, with MCM-41 primarily at elevated temperatures, likely due to material alteration caused by a combined effect of increased hydrolysis and capillarity,[69,70] and BTEVA-PMO across all investigated temperatures. Since this is observed exclusively in the desorption branch, a partial collapse of the pore structure during pore emptying is assumed. This effect likely results from a combination of strong water-surface interactions and capillary forces. Supporting measurements show unchanged pore diameters but a pronounced reduction in pore volume, indicating either a collapse of individual pore channels or blockage at pore entrances (see Figure S2). A similar desorption profile, as observed for BTEVA-PMOs, has been reported for MOFs[71] and may be attributed to capillary stress-induced pore collapse during emptying.[70] As the inflection points of the desorption branch cannot be reliably determined for BTEVA-PMOs across all temperatures or for MCM-41 silica at 45 °C, associated parameters such as hysteresis width and the desorption-based hydrophilicity index are not reported in this work.

Changes in porosity due to water exposure at room temperature or above have been reported and analyzed,[69,72−75] with indications that structural alterations predominantly occur during desorption rather than adsorption.[76] Hydrophilicity, reflecting the strength of water-surface interactions, plays a key role, as all hydrophobic materials demonstrate water stability.

The desorption branches in all materials shift to higher relative pressures with increasing temperature (Figure 3), indicating a temperature-dependent pore emptying behavior. This trend is consistent with previous observations for porous carbons[67] and will be discussed in more detail below. Since water uptake prior to capillary condensation remains consistent across temperatures, condensation likely initiates from the formation of water aggregates reaching a certain size rather than continuous multilayer buildup.[67,77]

To determine the water content prior to condensation, the specific number of water molecules (N_w) at the onset of capillary condensation was related to the specific number of surface hydration sites (N_{SHS}). Figure 4 shows the relationship between the ratio of water molecules per surface hydration site (N_w/N_{SHS}) at the onset of capillary condensation and (i) the hydrophilicity index HI_{ia}, derived from the relative pressure at the inflection point of capillary condensation in nitrogen and

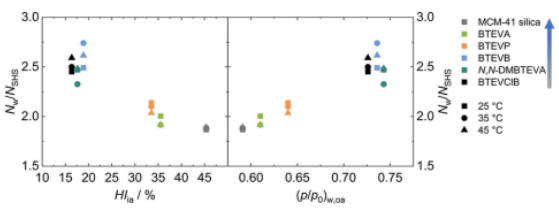


Figure 4. Plot of the adsorbed number of water molecules per surface hydration site (N_w/N_{SHS}) at the onset of capillary condensation against the hydrophilicity index (HI_{ia}, left) and the relative pressure at the onset of capillary condensation ($(p/p_0)_{w,oa}$, right). An arrow in the legend denotes the order of increasing hydrophilicity for the listed materials, based on our previous study.[24]

https://doi.org/10.1021/acs.jpcc.5c07495
J. Phys. Chem. C 2026, 130, 3472−3485

water vapor isotherms (Figure 4, left),[24] and (ii) the relative pressure at the onset of capillary condensation $(p/p_0)_{w,oa}$ (Figure 4, right). Normalization to surface hydration sites enables comparison across materials with different surface areas and surface chemistries, while the influence of vapor pressure is explicitly reflected in the relative pressure defining the inflection point and the onset of capillary condensation. With increasing hydrophilicity, the N_w/N_{SHS} ratio decreases, indicating that hydrophobic materials require more water molecules to reach the aggregate size necessary for condensation. Similar observations have been reported and discussed in the literature.[78−81] This behavior can be rationalized by the following hypothesis: On more hydrophilic surfaces, a higher density of surface hydration sites (SHS) reduces the spacing between water molecules adsorbed at these sites. This leads to a higher overall surface coverage and may promote interactions between adjacent water aggregates, thereby facilitating capillary condensation at lower overall water loadings. Conversely, on less hydrophilic surfaces with fewer SHS, adsorbed water molecules are more likely to remain spatially isolated, forming smaller and more weakly interacting water aggregates. Further adsorption may therefore preferentially occur on these aggregates until a certain size is reached, triggering condensation. Based on data from our previous study[24] (Figure S3), the characteristic size of these water aggregates appears to depend not only on surface hydrophilicity but also on pore diameter. In agreement with literature reports, larger pore sizes are associated with larger aggregate sizes.[82] It should be noted that hydrophilicity is not the sole parameter governing this behavior, as vapor pressure and pore geometry also influence the adsorption process.

Although previous studies have demonstrated that temperature can affect water aggregate size,[82−85] the data in Figure 4 show only minor fluctuations without a clear temperature-dependent trend. This could be due to the relatively narrow temperature range investigated, which may render any changes too subtle to detect. Moreover, the fixed spatial arrangement of hydration sites in PMOs likely imposes structural constraints on aggregate development. Within the examined temperature window, aggregates may only grow to a certain size before merging with neighboring aggregates, as illustrated in Figure S4.

The origin of hysteresis between water adsorption and desorption has long been debated and has recently gained renewed attention. Distinct differences between hydrophilic and hydrophobic surfaces have been observed.[78,81,86,87] Water vapor sorption experiments by Weinberger et al.[78] showed increased hysteresis in hydrophobically functionalized MCM-41 silica compared to its more hydrophilic, pristine counterpart. In a study of two PMOs with divinylbenzene and benzene bridges, both having the same pore size, Thommes et al.[67] observed a narrower hysteresis in the more hydrophilic, benzene-bridged PMO. This behavior was attributed to differences in surface chemistry and wettability. Figure 5 presents various sorption parameters, that are described in detail in our recent study,[24] for materials with comparable pore sizes, measured at different temperatures. Consistent with previous findings, our results also show larger adsorption−desorption hysteresis for more hydrophobic materials such as BTEVB-, *N*,*N*-DMBTEVA-, and BTEVClB-PMOs, with hysteresis widths at half height (fwhm) ranging from 0.15 to 0.2 at room temperature.

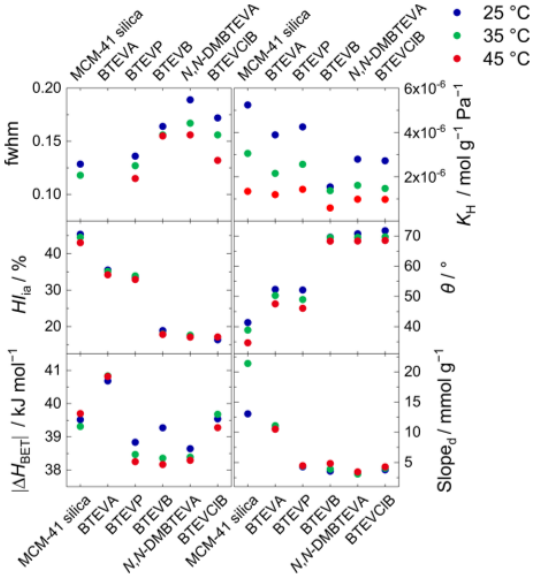


Figure 5. Material and temperature dependence of the hysteresis width at half height (fwhm), Henry's constant (K_H), hydrophilicity index based on relative pressure at the inflection point of capillary condensation in the adsorption branch (HI_{ia}), contact angle (θ), adsorption enthalpy of the first water layer (absolute value of ΔH_{BET}, calculated from the BET constant), and the slope of desorption after pore emptying (slope$_d$).

Hysteresis in water sorption isotherms has been attributed to the formation of water clusters, with the underlying mechanism depending on surface hydrophilicity, often described by the contact angle (θ).[81] The contact angle was calculated using established approaches,[24,88] accounting for the temperature dependence of water's density[89] and surface tension.[90] A correlation is observed between hysteresis width and θ (see Figure S5), with larger contact angles corresponding to broader hysteresis.

Additionally, all materials exhibit a general decrease in hysteresis width with increasing temperature. The amount of water adsorbed at the onset of capillary condensation, where water aggregates approach sizes sufficient for condensation, and the relative pressure of the condensation step are not significantly affected by temperature. This indicates that in PMOs the desorption process predominantly governs the hysteresis width. In hydrophilic materials, adsorption contributes only marginally. As previously discussed, in the adsorption regime, water aggregates growth is limited by curvature effects and the fixed spatial distribution of hydration sites in PMOs. These spatial constraints promote aggregate coalescence and ultimately trigger capillary condensation once a certain aggregate size is reached, as illustrated in Figure S4. In contrast, within the studied temperature range, a more pronounced effect is observed on the position of the pore emptying step. Similar temperature-dependent shifts in the desorption branch toward higher relative pressures with increasing temperature were reported by Thommes et al.[67] for CMK carbons, which were attributed to a capillary evaporation mechanism involving a receding meniscus, consistent with the Kelvin equation.

https://doi.org/10.1021/acs.jpcc.5c07495
J. Phys. Chem. C 2026, 130, 3472−3485

The temperature dependence of hydrophilicity indicators, including the contact angle and Henry's constant (K_h), is shown in Figure 5. For all materials, K_h decreases with increasing temperature, indicating reduced adsorption capacity at very low pressures and at elevated temperatures,[91] with a more pronounced reduction observed in hydrophilic samples. The stronger water-surface interaction on hydrophilic materials (larger exothermic adsorption enthalpies) make their Henry's constants more sensitive to temperature. In the van't Hoff relation, detailed more in the next chapter, $\ln K_h \propto -\Delta H/(RT)$, so larger $|\Delta H|$ yields a steeper slope of $\ln K_h$ vs $1/T$ and thus a more pronounced decrease with temperature. As a result, K_h values at 45 °C converge and thereby diminishing the distinction between hydrophilic and hydrophobic surfaces. Similarly, the contact angle decreases with increasing temperature, again more significantly for hydrophilic materials. Similar observation in contact angle measurements were made in literature.[92,93] The contact angle changes with temperature because interfacial tensions are temperature-dependent. For a liquid drop on a solid surface, the contact angle is described by the Young eq 1[94,95]:

$$\frac{\gamma_{sv} - \gamma_{sl}}{\gamma_{lv}} = \cos\theta \tag{1}$$

with interfacial tensions solid−vapor (γ_{sv}), solid−liquid (γ_{sv}) and the liquid−vapor (γ_{lv}). Increasing the temperature the liquid−vapor surface tension γ_{lv} decreases, which alone would result in a lower contact angle. In addition, several studies suggest that the solid−liquid interfacial tension γ_{sl} increases with temperature due to the weakening of intermolecular forces and hydrogen bonding in water.[90,93,96] Together, these changes are consistent with the observed decrease of contact angle, which occurs when the reduction of γ_{lv} with temperature contributes more strongly than the decrease of $(\gamma_{sv} - \gamma_{sl})$. On hydrophilic surfaces, where water-surface interaction are strong, this effect is amplified, while on hydrophobic surfaces, the weaker interaction results in much smaller temperature dependence of contact angle.[93,97] Unlike K_h, however, the contact angle at 45 °C still clearly distinguishes between hydrophilic and hydrophobic surfaces. While K_h is sensitive to subtle environmental changes, the contact angle reflects the state after water aggregates have reached certain size and condensation has initiated, meaning water is already partially in the liquid state. Consequently, temperature changes within the investigated range (298.15, 308.15, 318.15 K, with bulk water densities of 0.997, 0.994 0.990 g cm^3, respectively)[89] have only a limited impact on the contact angle. The differing temperature responses between hydrophilic and hydrophobic materials may result from variations in aggregate size: hydrophobic surfaces tend to form larger water aggregates that already approach the condensation threshold, limiting further growth with increasing temperature. In contrast, hydrophilic surfaces typically support smaller water aggregates, allowing additional water accumulation at elevated temperatures, which shifts condensation to lower relative pressures.

The hydrophilicity index (HI), defined by the relative pressure at the inflection point of capillary condensation in the adsorption branch (HI_{ia})[24] (Figure 5), is affected by temperature to a certain extent, which is more pronounced for hydrophilic materials. In contrast HI_{id} exhibits a higher temperature dependence (Figure S6).

As shown in Figures 5 and S6, both the SHS and the slope of the desorption branch after pore emptying ($slope_d$) appear largely unaffected by temperature. An exception is observed for MCM-41 silica, which displays a steeper slope at elevated temperatures. This behavior may be due to thermally induced hydrolysis of siloxane bridges, leading to the formation of additional silanol groups.[26,98,99] As a result, more water remains adsorbed on the surface and desorbs at lower relative pressures.

Using the BET constant (C_{BET})[45,100,101] the adsorption enthalpy of the first water layer (ΔH_{BET}) can be approximated. As shown in Figure 5, hydrophilic materials exhibit higher absolute values of ΔH_{BET}, indicating stronger water-surface interactions. Outliers include BTEVP-PMO, which shows comparatively weak surface affinity, and BTEVClB-PMO, which aligns more closely with the hydrophilic behavior of MCM-41 silica. For broader comparison, additional data from our previous work[24] are plotted against the contact angle (at 25 °C) in Figure S7. Materials with larger contact angles generally show lower $|\Delta H_{BET}|$ values. Increasing temperature results in lower absolute values of adsorption enthalpies for more hydrophobic materials, while MCM-41 silica and BTEVA-PMO show no significant temperature dependence. The reliability of the obtained enthalpy values is assessed in the following section through comparison with isosteric enthalpies.

3.3. Impact of Surface Functionality on Water Adsorption Enthalpy

To elucidate the nature of water−solid interactions, the adsorption enthalpy of water was determined for materials with varying degrees of hydrophilicity. This thermodynamic parameter directly reflects the interaction strength between water molecules and surface sites, thereby complementing macroscopic indicators such as the contact angle and Henry's constant. It serves as a key descriptor for distinguishing adsorption mechanisms and assessing material performance under humid conditions.

Using water vapor isotherms measured at three temperatures (25, 35 and 45 °C), the isosteric enthalpy of adsorption was calculated for different materials at defined water loadings based on the Clausius−Clapeyron equation in its integrated form[102]:

$$\ln p = -\frac{\Delta H_{a,st}}{RT} + C \tag{2}$$

If the pressure (p) is replaced by an equilibrium constant (K), the same expression corresponds to the van't Hoff equation.[103] The classical plot of isosteric enthalpy over the full loading range is provided in Figure S8. In this study the recommended term isosteric enthalpy of adsorption ($\Delta H_{a,st}$) instead of isosteric heat of adsorption ($Q_{a,st}$) is used.[44,45] As previously mentioned, adsorption enthalpies are reported throughout this work as absolute values ($|\Delta H|$) for clarity and consistency, allowing a more direct interpretation of adsorption strength and exothermicity. It should be noted that, as adsorption is an exothermic process, the actual enthalpy values are negative. In Figure 6, $|\Delta H_{a,st}|$ is plotted against the relative number of water molecules per surface hydration site (N_w/N_{SHS}). In the low loading regime (N_w/N_{SHS} = 0−3), a clear distinction between hydrophobic and hydrophilic materials becomes apparent. Hydrophilic samples such as MCM-41 silica, BTEVA-, and BTEVP-PMOs show significantly higher absolute values of $\Delta H_{a,st}$ at low relative water

https://doi.org/10.1021/acs.jpcc.5c07495
J. Phys. Chem. C 2026, 130, 3472−3485

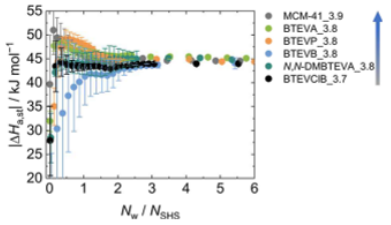


Figure 6. Plot of absolute values of isosteric enthalpy of adsorption ($|\Delta H_{a,st}|$) versus the number of adsorbed water molecules per surface hydration site (N_w/N_{SHS}) for various materials. An arrow in the legend denotes the order of increasing hydrophilicity for the listed materials, based on our previous study.[24]

contents ($N_w/N_{SHS} \approx 0.5$), exceeding the enthalpy of condensation of water ($|\Delta H| = 44$ kJ mol^{-1} at 298.15 K). Maxima of approximately 49 kJ mol^{-1} are observed, or around 48 kJ mol^{-1} for BTEVA-PMO. These peak values represent the maximum interaction strength between water and isolated SHS, as indicated by a sharp decrease in $|\Delta H_{a,st}|$ at lower coverages ($N_w/N_{SHS} < 0.5$); for instance, MCM-41 silica shifts steeply from around 39 kJ mol^{-1} at $N_w/N_{SHS} \approx 0$. The trend of higher isosteric enthalpies on hydrophilic surfaces at low water coverage is consistent with previous reports.[31,41,104−107] For silica surfaces, $|\Delta H_{a,st}|$ values of 50−60 kJ mol^{-1} have been observed at low coverage.[31,64,76] In the range $N_w/N_{SHS} = 0.5-3$, absolute values of $\Delta H_{a,st}$ progressively decreases as adsorption shifts from surface sites to preadsorbed water, reducing surface influence. At around 2−3 water molecules per site, the enthalpy approaches the bulk condensation value. Similar trends have been reported for cementitious substrates[107] or SiO_2 surfaces,[26,27,31] where the initially high enthalpy values are attributed to the formation of a highly ordered, solid-like monolayer with low entropy.

Hydrophobic materials such as BTEVB-, *N,N*-DMBTEVA-, or BTEVClB-PMOs do not exceed the condensation enthalpy of water, except slightly for *N,N*-DMBTEVA-PMO (~45 kJ mol^{-1}). At low coverage, they show low absolute values of isosteric adsorption enthalpy, though with the larger error (mostly for data points $N_w/N_{SHS} < 0.2$). For BTEVB-PMO, the error remains large until $|\Delta H_{a,st}|$ approaches bulk condensation value ($N_w/N_{SHS} \approx 0.2$), so the very low absolute values of adsorption enthalpy should be interpreted with caution. Between 0.5 and 1.6 water molecules per surface site, a shallow plateau with a slight negative slope is observed, followed by a gradual increase in $|\Delta H_{a,st}|$, reaching the bulk condensation enthalpy at around 3−4 water molecules per hydration site. This trend aligns with the observations from the previous chapter and our study,[24] which indicate that hydrophobic materials form larger water aggregates. After saturation of all SHS, water adsorption mainly occurs on preadsorbed molecules with limited surface interaction, until the growth of water aggregates enhances water−water interactions, culminating in liquefaction. Similar isosteric enthalpy trends have been reported for water adsorption on functional group-free porous carbons[77] or activated carbon with different surface oxidation,[28,108] where metastable water aggregate formation governs the adsorption process. Comparing the $|\Delta H_{a,st}|$ values in the range of $N_w/N_{SHS} = 0-1$ with the calculated $|\Delta H_{BET}|$ values of the previous chapter, which is associated with the enthalpic adsorption process of the first water layer, shows that $|\Delta H_{BET}|$ yields values that are too low, especially for hydrophilic materials, and can therefore only be used for a rough comparison between materials.

Using the K_H values from the low-pressure region of the adsorption isotherms at different temperatures, the adsorption enthalpy ($\Delta H_{a,K}$) can be calculated using the van't Hoff eq 3[45,103,109,110]:

$$\ln K_H = -\frac{\Delta H_{a,K}}{RT} + C \tag{3}$$

where T is the temperature, R is the universal gas constant, and C a constant. Plotting $\ln K_H$ against $1/T$ yields $\Delta H_{a,K}$ from the slope.[111] This enthalpy reflects the interaction strength of the first adsorbed water molecules with the surface, primarily at surface hydration sites. As shown in Figure 7, $|\Delta H_{a,K}|$ strongly

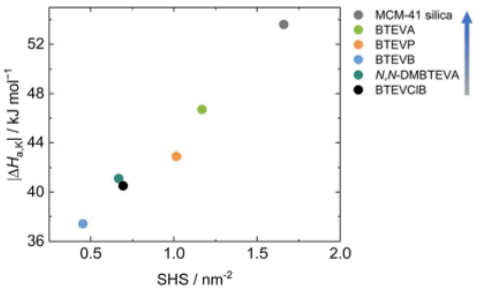


Figure 7. Dependence of the Henry's constant−based adsorption enthalpy (absolute value of $\Delta H_{a,K}$) on the density of surface hydration sites (SHS). An arrow in the legend denotes the order of increasing hydrophilicity for the listed materials, based on our previous study.[24]

correlates with the SHS density, with lower SHS densities leading to lower absolute values of adsorption enthalpies. It also correlates with HI_{ia}, the amount of water adsorbed at the onset of capillary condensation, and the slopes of desorption and adsorption branches (Figure S9). These correlations indicate that stronger water-surface interactions influence not only initial adsorption but also the structuring and growth of water aggregates before condensation. While HI_{ia} serves as a complementary measure of overall hydrophilicity, the adsorption enthalpy analysis presented in this work is primarily interpreted in terms of surface hydration site density, using the normalized loading N_w/N_{SHS} as the central descriptor. In this context, the K_H-based enthalpy provides an initial energetic reference derived from the low-pressure adsorption regime.

Since surface effects on adsorption enthalpies are most pronounced at low surface coverage, we employed a direct calorimetric approach to obtain more accurate and better-resolved data in this regime. This method also complements the isosteric approach, allowing validation of water-surface interaction trends across materials with varying surface chemistries. To ensure comparability with previous results, we first conducted a full-range screening up to 95% RH in 5% RH increments (see Figure 8 (bottom)). As in the isosteric analysis (Figure 6), the ratio N_w/N_{SHS} is used in Figure 8 (top) to describe how the calorimetrically measured absolute values of adsorption enthalpy ($|\Delta H_{a,c}|$) varies with the number of water molecules per surface hydration site. Error bars account for analytical uncertainties in both the integrated heat flow and the measured water uptake. Gravimetric water uptake data are provided in Figure S10.

https://doi.org/10.1021/acs.jpcc.5c07495
J. Phys. Chem. C 2026, 130, 3472−3485

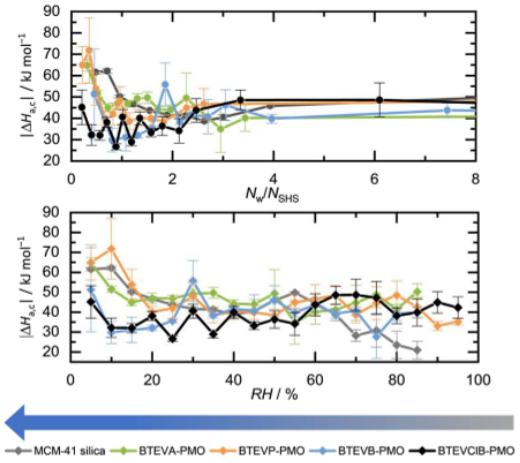


Figure 8. Calorimetrically determined absolute values of adsorption enthalpy ($|\Delta H_{a,c}|$) under isothermal conditions plotted against: Top: the number of water molecules per surface hydration site (N_w/N_{SHS}); Bottom: relative humidity (RH). The measurements were conducted using increments of 5% RH over a range of 0−95% RH. An arrow in the legend denotes the order of increasing hydrophilicity for the listed materials, based on our previous study.[24]

Similar to the isosteric enthalpy results (Figure 6), hydrophilic materials initially show high absolute values of adsorption enthalpies of 60 to 70 kJ mol^{-1}, consistent with literature values for silica.[64,106,112] These values persist until roughly one water molecule occupies each surface hydration site. For these materials, the condensation enthalpy of water is reached already at a surface coverage of 1−2 water molecules per SHS. This observation is in agreement with experimental results reported by Rother et al.,[61,62] who introduced a geometrical calculation method, namely the adsorbed-phase model, to determine the density and thickness of the adsorption layer from water vapor sorption measurements, and found that capillary condensation in MCM-41 silica occurs at around two water molecules per SHS. It should be noted that the amount of water per SHS, and thus the thickness of the surface water layer, additionally depends on pore curvature and pore size.[24,25,61,62]

In contrast, hydrophobic materials follow a comparable trend to the isosteric method for $N_w/N_{SHS} > 1$, although the initial $|\Delta H_{a,c}|$ is higher: around 45 kJ mol^{-1} for *N,N*-DMBTEVA-PMO and approximately 50 kJ mol^{-1} for BTEVB-PMO. This suggests a stronger interaction at the first water contact, likely due to adsorption at isolated silanol groups before complete SHS saturation.

To achieve higher resolution in the low water coverage regime, adsorption measurements were conducted using finer RH increments (Figure 9). Corresponding specific water uptake values, determined gravimetrically, are provided in Figure S10. Additionally, the adsorption entropy was calculated from the adsorption enthalpy data using the following equation[113]:

$$\Delta S = \frac{\Delta H - RT\ln\left(\frac{p}{p_r}\right)}{T} \quad (4)$$

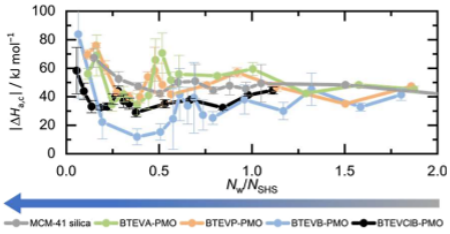


Figure 9. Calorimetrically determined absolute values of adsorption enthalpy ($|\Delta H_{a,c}|$) under isothermal conditions plotted against the number of water molecules per surface hydration site (N_w/N_{SHS}). The measurements were conducted using increments of 1% RH over a range of 0−10% RH and increments of 5% RH over a range of 10−35%. An arrow in the legend denotes the order of increasing hydrophilicity for the listed materials, based on our previous study.[24]

where R is the ideal gas constant, T the temperature, p the absolute vapor pressure, and p_r the reference pressure (10^5 Pa). The corresponding entropy changes (ΔS) upon adsorption, derived from the calorimetric measurements at 35 and 95% RH, are shown in Figure 10. Entropy values calculated via the isosteric method are provided in Figure S11.

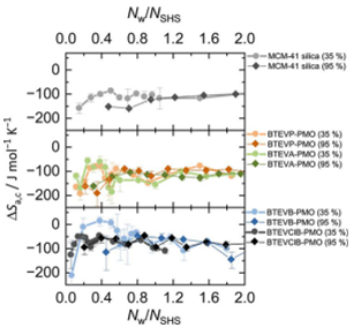


Figure 10. Dependence of the entropy change ($\Delta S_{a,c}$) during adsorption on the number of water molecules per surface hydration site (N_w/N_{SHS}) for different materials with a pore diameter of approximately 3.8 nm. The percentages in parentheses indicate the conditions used: full-range experiments (95% RH) and subcondensation, adsorption-only regime (35% RH).

Despite notable measurement uncertainty in Figure 9, even at fine RH increments, hydrophobic samples exhibit initial high adsorption enthalpies, followed by a sharp decrease with slight increases in surface coverage. Notably, BTEVB-PMO reaches enthalpy values comparable to those of hydrophilic materials, though at significantly lower water loadings. Similarly, the chlorinated PMO starts with a higher initial absolute value of enthalpy of approximately 60 kJ mol^{-1}, which drops to around 30 kJ mol^{-1}. The initial high absolute values of enthalpy, combined with the strong decrease in entropy upon first water contact (Figure 10), indicate favorable adsorption at isolated silanol sites. Subsequently, $|\Delta H_{a,c}|$ decreases while $\Delta S_{a,c}$ increases markedly, particularly for BTEVB-PMO, with enthalpy values of roughly 17 kJ mol^{-1} and entropy values close to zero. This behavior may be attributed to entropically favored π−hydrogen bonding between water and the aromatic moieties, which could explain the increase of entropy values, in addition to weak water−water interactions on silanol sites after saturation of the preferred hydration sites.[114] For non- or

https://doi.org/10.1021/acs.jpcc.5c07495
J. Phys. Chem. C 2026, 130, 3472−3485

weakly functionalized carbons, absolute values of isosteric adsorption enthalpy of 17 or 22 kJ mol^{-1} at zero or low surface coverage have been reported.[28,108] Calorimetric measurements of mesoporous FSM-16 with hydrophobic surface properties showed initial $|\Delta H_a|$ of 20 kJ mol^{-1}.[26] The chlorine-based PMO behaves similarly to the BTEVB-PMO, with the key difference that $|\Delta H_{a,c}|$ does not drop below 30 kJ mol^{-1}, while $\Delta S_{a,c}$ does not exceed −50 J mol^{-1} K^{-1}. This suggests that chlorine in the BTEVClB-PMO stabilizes adsorbed water more effectively, possibly via weak hydrogen bond acceptance,[115] than the π-system of the nonfunctionalized divinylbenzene bridge in BTEVB-PMO. Beyond initial adsorption, further water uptake occurs mainly through the growth of water aggregates and eventual capillary condensation, resulting in decreasing enthalpy and increasing entropy values characteristic of confined or bulk-like water. Based on the observations of Moon et al.,[116] this could proceed via the formation of an ordered hydrogen-bonded bridge across the organic units, creating low-entropy regions with reduced water dynamics.

The differences in initial adsorption enthalpies for hydrophobic samples between the coarse (5% RH) and fine (1% RH) step measurements likely result from averaging effects in the 5% RH increments, which cover the same range as the first five steps in the finer-resolved 1% RH data (Figure 9). For hydrophilic materials, both step protocols yield generally consistent enthalpy profiles. However, the higher-resolution 1% RH steps reveal additional features: after the initial maximum, the absolute values of enthalpy for BTEVA-PMO and BTEVP-PMO attain the condensation enthalpy of bulk water, with values around 40 kJ mol^{-1} at a surface hydration site (SHS) saturation of around 0.3. This is followed by a pronounced second maximum at $N_w/N_{SHS} \approx 0.5$, with $|\Delta H_{a,c}|$ values of 70 kJ mol^{-1} for BTEVA-PMO and 60 kJ mol^{-1} for BTEVP-PMO. The presence of two distinct maxima suggests the existence of two types of adsorption sites with differing affinities for water. At low surface coverage, the observed strong and energetically favorable adsorption, seen for pure silica MCM-41 and BTEVB-PMO, which carry only silanol groups as SHS, can be attributed to water binding at isolated silanol sites. MD simulations for MCM-41 silica suggest that at isolated silanol sites, two water molecules adopt preferred orientations, forming distinct hydrogen bonds with the hydroxyl oxygen and hydrogen, which gives rise to intralayer structuring of the adsorbed monolayer.[61]

The pronounced second maxima in enthalpy and minima in entropy suggest a second, distinct and highly specific interaction, likely involving the functional groups of the organic bridges. Alternatively, a cooperative hydration mechanism may be involved, where already adsorbed water molecules enhance the binding of additional molecules via strong water−water hydrogen bonding.

These interactions, in conjunction with surface hydrogen bonds, promote the formation of a highly ordered first hydration layer with low entropy. Beyond this point, as full hydration is approached ($N_w/N_{SHS} = 1$), $\Delta H_{a,c}$ gradually shifts toward values characteristic of bulk water. This behavior is consistent with the trends observed in the isosteric enthalpy data (Figure 6).

For MCM-41 silica, $|\Delta H_{a,c}|$ decreases while $\Delta S_{a,c}$ increases continuously with surface coverage, starting from $|\Delta H_{a,c}| \approx 70$ kJ mol^{-1} at low coverage, as reported in the literature[26,27] and gradually approaching the condensation enthalpy and entropy change (−119 J mol^{-1} K^{-1},[117] see as well eq 4 with $\Delta H = -44$ kJ mol^{-1} at 298.15 K) of bulk water. Additionally, the same experiment was performed on samples with smaller and larger pores (2.9−4.4 nm) compared to the previously discussed 3.8 nm material (excluding chlorinated samples, see Figure S12). The overall $|\Delta H_{a,c}|$ trend remained consistent across this range. However, slightly lower absolute values of enthalpy at low coverage were observed for materials with larger pores, suggesting weaker initial water-surface interactions. This could be attributed to the lower surface curvature in wider pores, which may reduce cooperative effects between water molecules adsorbed at adjacent SHS.

Isosteric entropy (Figure S11, bottom) reveals that even at higher surface coverage, hydrophilic materials retain structural ordering, while hydrophobic systems approach bulk water behavior, consistent with our prior X-ray scattering results.[16]

To assess desorption behavior across all materials, including those with different pore sizes, samples were subjected to a reduction in RH down to 0% following the regular adsorption experiments. The resulting endothermic DSC signal, accompanied by mass loss, was used to calculate the desorption enthalpy (ΔH_d), which is inherently positive and therefore reported directly rather than as absolute values. Data were obtained for both fully loaded ($\Delta H_{d,95\%}$) and partially loaded ($\Delta H_{d,35\%}$) states. A correlation between the calculated $\Delta H_{d,35\%}$ and the inflection point of capillary condensation ($(p/p_0)_{w,ia}$) was observed (Figure 11(left)). As $(p/p_0)_{w,ia}$, which reflects

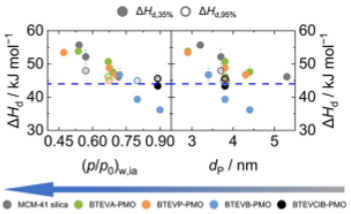


Figure 11. Plot of the enthalpy of desorption ($\Delta H_{d,35\%}$) against the relative pressure at the inflection point of capillary condensation ($(p/p_0)_{w,ia}$) (left), and against the pore diameter (d_p) (right). The blue dotted line marks the evaporation enthalpy of bulk water at 25 °C. An arrow in the legend denotes the order of increasing hydrophilicity for the listed materials, based on our previous study.[24]

increasing hydrophobicity, increases, $\Delta H_{d,35\%}$ gradually drops from approximately 55 kJ mol^{-1} to around 35 kJ mol^{-1}. This trend highlights the weaker binding of water in hydrophobic materials. An exception is the chlorinated PMO, which shows a desorption enthalpy of 43 kJ mol^{-1}, higher than that of BTEVB-PMO, despite a similar $(p/p_0)_{w,ia}$ values. This may point to specific water-chlorine interactions, as previously suggested for the adsorption process.

In contrast, this correlation is absent, or only weakly pronounced, for samples desorbed from 95% RH. This is attributed to the dominance of bulk-like core water over surface-bound water at higher filling levels. As a result, desorption enthalpies converge around 45 kJ mol^{-1} (approximately 48 kJ mol^{-1} for MCM-41 silica), approaching the latent heat of vaporization of bulk water. In Figure 11(right), a material-specific correlation between pore diameter and $\Delta H_{d,35\%}$ is observed, suggesting that both surface chemistry and pore curvature influence the desorption enthalpy.

For materials with a pore diameter of 3.8 nm, desorption enthalpy reveals a clear distinction between hydrophilic and

https://doi.org/10.1021/acs.jpcc.5c07495
J. Phys. Chem. C 2026, 130, 3472−3485

hydrophobic surfaces: hydrophilic samples show higher $\Delta H_{d,35\%}$ than $\Delta H_{d,95\%}$, whereas hydrophobic samples exhibit the opposite trend.

Although the isosteric and calorimetric approaches yield consistent trends overall, differences between them likely stem from variations in absolute pressure and measurement conditions. The isosteric method begins under vacuum with stepwise water vapor dosing, while DSC-TGA measurements are conducted at ambient pressure with continuous humidity flow. Moreover, the use of nitrogen as a carrier gas in calorimetry may lead to coadsorption effects, especially in hydrophobic regions of the organic bridge, where nitrogen could occupy unhydrated cavities.[80]

4. CONCLUSIONS

This study employed a straightforward approach for characterizing water adsorption by combining thermogravimetric analysis (TGA) and differential scanning calorimetry (DSC) with a continuous-flow humidity generator. This setup enabled direct and accurate measurement of differential molar adsorption enthalpies across varying water loadings under isothermal conditions, with the continuous flow ensuring short equilibrium times. A key advantage of this approach is its consistency with values obtained from the traditional isosteric method, thereby validating its reliability. Furthermore, the experimental configuration is simple, requiring only standard DSC-TGA instrumentation combined with an accessible humidity supply system. The continuous-flow calorimetric approach also closely mimics industrial adsorption conditions, providing relevant thermodynamic data for applications such as drying, purification, and energy storage.

While differences between the isosteric and calorimetric methods were expected, due to fundamental distinctions in theoretical approaches (indirect versus direct methods), differences in starting conditions (vacuum versus nonvacuum), and the presence of a carrier gas in the calorimetric setup, which itself can interact with the surface, results remain largely consistent. This agreement enables confident conclusions regarding materials with varying hydrophilicity:

Hydrophobic materials show, after an initial strong interaction of water with energetically favored surface silanol groups, a distinct drop in interaction strength. It is suggested that only weak water−water interactions take place, leading to the formation of larger aggregates than in hydrophilic materials, until a liquid-like state is reached, where the enthalpy of adsorption approaches the condensation enthalpy of bulk water. The other hydrophobic materials show similar behavior, with the difference that functional groups, such as the chlorine in BTEVClB-PMO or the dimethylamino group in *N*,*N*-DMBTEVA, appear to interact with water and stabilize it to some extent, despite their overall hydrophobic character.

Hydrophilic materials are characterized by strong initial water-surface interactions and pronounced structuring of adsorbed water, with high exothermic adsorption enthalpies around −70 kJ mol^{-1} and a significant decrease in entropy. While MCM-41 silica gradually reaches the condensation enthalpy of water with increasing loading, reflecting reduced surface water interaction at higher coverage, the hydrophilic BTEVA- and BTEVP-PMOs show two distinct enthalpic maxima and entropic minima. This behavior can only be explained by a complex cooperative interplay between water-silanol and water-functional group interactions.

In addition, data from the isosteric method at higher surface coverage show that the enthalpic and entropic behavior of adsorbed water in hydrophilic materials deviates more strongly from bulk water than in hydrophobic ones, indicating a long-range structural influence even in distant water layers. Hydrophobic materials, in contrast, tend to form a more bulk-like core at higher coverages.

The impact of hydrophilicity on the temperature dependence of water vapor sorption isotherms was also evident. It was confirmed that the pore emptying step is primarily responsible for the decreasing hysteresis width with increasing temperature across all materials. Nevertheless, more hydrophilic materials generally exhibit a larger hysteresis. Additionally, Henry's constant (an indicator of surface hydrophilicity at very low coverage) drops more steeply for highly hydrophilic materials with increasing temperature, indicating lower surface hydrophilicity dependence at higher temperatures. To date, such detailed enthalpic analysis of water adsorption in PMOs, particularly combining the rarely applied continuous-flow calorimetric method, has not been reported. This study provides a comprehensive view of the adsorption processes in PMOs and establishes a solid foundation for future investigations into materials with varying surface properties.

■ ASSOCIATED CONTENT

Supporting Information

The Supporting Information is available free of charge at https://pubs.acs.org/doi/10.1021/acs.jpcc.5c07495.

PMO synthesis conditions; porosity data of different materials; exemplary raw DSC-TGA adsorption measurement; DSC-TGA adsorption isotherms; calorimetrically determined adsorption enthalpy of water in various materials with differing pore sizes; and additional correlation water adsorption enthalpy (PDF)

■ AUTHOR INFORMATION

Corresponding Authors

Michael Steiger − *Institute of Inorganic and Applied Chemistry, University of Hamburg, 20146 Hamburg, Germany*; orcid.org/0000-0002-7527-1097; Phone: +49-40-42838-2895; Email: michael.steiger@uni-hamburg.de

Michael Fröba − *Institute of Inorganic and Applied Chemistry, University of Hamburg, 20146 Hamburg, Germany; The Hamburg Centre for Ultrafast Imaging, 22761 Hamburg, Germany*; orcid.org/0000-0001-6927-0509; Phone: +49-40-42838-3100; Email: michael.froeba@uni-hamburg.de

Authors

Philip Lenz − *Institute of Inorganic and Applied Chemistry, University of Hamburg, 20146 Hamburg, Germany; The Hamburg Centre for Ultrafast Imaging, 22761 Hamburg, Germany*

Uta Sazama − *Institute of Inorganic and Applied Chemistry, University of Hamburg, 20146 Hamburg, Germany*

Sandra König − *Institute of Inorganic and Applied Chemistry, University of Hamburg, 20146 Hamburg, Germany*

Complete contact information is available at: https://pubs.acs.org/10.1021/acs.jpcc.5c07495

https://doi.org/10.1021/acs.jpcc.5c07495
J. Phys. Chem. C 2026, 130, 3472−3485

Notes

The authors declare no competing financial interest.

■ ACKNOWLEDGMENTS

This work is funded by the Cluster of Excellence 'Advanced Imaging of Matter' of the Deutsche Forschungsgemeinschaft (DFG) – EXC 2056 – project ID 390715994 and DFG-Projekt: FR 1372/26-1). Scientific exchange and support of the Center for Molecular Water Science (CMWS) is also acknowledged. We would like to thank Isabelle Nevoigt for measuring our PXRDs.

■ REFERENCES

(1) Wu, X.; Bao, Z.; Yuan, B.; Wang, J.; Sun, Y.; Luo, H.; Deng, S. Microwave synthesis and characterization of MOF-74 (M = Ni, Mg) for gas separation. *Microporous Mesoporous Mat* **2013**, *180*, 114–122.
(2) Sircar, S. Basic research needs for design of adsorptive gas separation processes. *Ind. Eng. Chem. Res.* **2006**, *45* (16), 5435–5448.
(3) AbdulHalim, R. G.; Bhatt, P. M.; Belmabkhout, Y.; Shkurenko, A.; Adil, K.; Barbour, L. J.; Eddaoudi, M. A fine-tuned metal-organic framework for autonomous indoor moisture control. *J. Am. Chem. Soc.* **2017**, *139* (31), 10715–10722.
(4) Zhang, Y.; Wang, R. Sorption thermal energy storage: Concept, process, applications and perspectives. *Energy Storage Mater.* **2020**, *27*, 352–369.
(5) Frazzica, A.; Brancato, V.; Palomba, V.; Vasta, S. Sorption thermal energy storage. In *Recent advancements in materials and systems for thermal energy storage*; Frazzica, A.; Cabeza, L. F., Eds.; Green Energy and Technology; Springer International Publishing, 2019; 33–54.
(6) Riaz, N.; Sultan, M.; Miyazaki, T.; Shahzad, M. W.; Farooq, M.; Sajjad, U.; Niaz, Y. A review of recent advances in adsorption desalination technologies. *Int. Commun. Heat Mass Transfer* **2021**, *128*, No. 105594.
(7) Thu, K.; Chakraborty, A.; Kim, Y.-D.; Myat, A.; Saha, B. B.; Ng, K. C. Numerical simulation and performance investigation of an advanced adsorption desalination cycle. *Desalination* **2013**, *308*, 209–218.
(8) Ng, K. C.; Thu, K.; Kim, Y.; Chakraborty, A.; Amy, G. Adsorption desalination: An emerging low-cost thermal desalination method. *Desalination* **2013**, *308*, 161–179.
(9) Mitra, S.; Srinivasan, K.; Kumar, P.; Murthy, S. S.; Dutta, P. Solar driven adsorption desalination system. *Energy Procedia* **2014**, *49*, 2261–2269.
(10) Alsaman, A. S.; Askalany, A. A.; Harby, K.; Ahmed, M. S. Performance evaluation of a solar-driven adsorption desalination-cooling system. *Energy* **2017**, *128*, 196–207.
(11) Inagaki, S.; Guan, S.; Ohsuna, T.; Terasaki, O. An ordered mesoporous organosilica hybrid material with a crystal-like wall structure. *Nature* **2002**, *416* (6878), 304–307.
(12) Sayari, A.; Wang, W. Molecularly ordered nanoporous organosilicates prepared with and without surfactants. *J. Am. Chem. Soc.* **2005**, *127* (35), 12194–12195.
(13) Cornelius, M.; Hoffmann, F.; Fröba, M. Periodic mesoporous organosilicas with a bifunctional conjugated organic unit and crystal-like pore walls. *Chem. Mater.* **2005**, *17* (26), 6674–6678.
(14) Hoffmann, F.; Cornelius, M.; Morell, J.; Fröba, M. Silica-based mesoporous organic-inorganic hybrid materials. *Angew. Chem., Int. Ed.* **2006**, *45* (20), 3216–3251.
(15) Beretta, M.; Morell, J.; Sozzani, P.; Fröba, M. Towards peptide formation inside the channels of a new divinylaniline-bridged periodic mesoporous organosilica. *Chem. Commun.* **2010**, *46* (14), 2495–2497.
(16) Gießelmann, N. C.; Lenz, P.; Meinert, S.-M.; Simon, T.; Jo, W.; Striker, N. N.; Fröba, M.; Lehmkühler, F. Structure of water under confinement in periodic mesoporous organosilicas investigated by X-ray scattering. *J. Phys. Chem. C* **2024**, *128* (1), 499–507.
(17) Aso, M.; Ito, K.; Sugino, H.; Yoshida, K.; Yamada, T.; Yamamuro, O.; Inagaki, S.; Yamaguchi, T. Thermal behavior, structure, and dynamics of low-temperature water confined in mesoporous organosilica by differential scanning calorimetry, X-ray diffraction, and quasi-elastic neutron scattering. *Pure Appl. Chem.* **2012**, *85* (1), 289–305.
(18) Mietner, J. B.; Brieler, F. J.; Lee, Y. J.; Fröba, M. Properties of water confined in periodic mesoporous organosilicas: Nanoimprinting the local structure. *Angew. Chem., Int. Ed.* **2017**, *56* (40), 12348–12351.
(19) Mietner, J. B. *Visiting nanopores: The great potential of PMOs for studying the properties of water in nanopores of different polarity*; Ph.D. Thesis, University of Hamburg: Germany, **2018**.
(20) Mietner, B. J.; Fröba, M.; Valiullin, R. Water transport in periodic mesoporous organosilica materials. *J. Phys. Chem. C* **2018**, *122* (24), 12673–12680.
(21) Malfait, B.; Jani, A.; Mietner, J. B.; Lefort, R.; Huber, P.; Fröba, M.; Morineau, D. Influence of pore surface chemistry on the rotational dynamics of nanoconfined water. *J. Phys. Chem. C* **2021**, *125* (30), 16864–16874.
(22) Jani, A.; Busch, M.; Mietner, J. B.; Ollivier, J.; Appel, M.; Frick, B.; Zanotti, J.-M.; Ghoufi, A.; Huber, P.; Fröba, M.; Morineau, D. Dynamics of water confined in mesopores with variable surface interaction. *J. Chem. Phys.* **2021**, *154* (9), 94505.
(23) Gießelmann, N. C.; Lenz, P.; Meinert, S.-M.; Simon, T.; Bauer, R. P. C.; Jo, W.; Claas, S.; Köhn, C.; Striker, N. N.; Fröba, M.; Lehmkühler, F. The structure of ice under confinement in periodic mesoporous organosilicas (PMOs). *J. Chem. Phys.* **2024**, *161* (3), 34508.
(24) Lenz, P.; Meinert, S.-M.; König, S.; Steiger, M.; Fröba, M. Influence of surface chemistry on t-layer dimension and density of nanoconfined water by fine-tuning the functional groups of periodic mesoporous organosilicas. *J. Phys. Chem. C* **2025**, *129* (27), 12536–12550.
(25) Lenz, P.; Sazama, U.; Steiger, M.; Fröba, M. Periodic mesoporous organosilicas as host materials for studying surface chemistry effects on the freezing and melting behavior of nano-confined water. *J. Phys. Chem. C* **2025**, *129* (45), 20373–20386.
(26) Matsumoto, A.; Sasaki, T.; Nishimiya, N.; Tsutsumi, K. Evaluation of the hydrophobic properties of mesoporous FSM-16 by means of adsorption calorimetry. *Langmuir* **2001**, *17* (1), 47–51.
(27) Matsumoto, A.; Sasaki, T.; Nishimiya, N.; Tsutsumi, K. Thermal stability and hydrophobicity of mesoporous silica FSM-16. *Colloids Surf. A: Physicochem. Eng. Asp.* **2002**, *203* (1–3), 185–193.
(28) Salame, I. I.; Bandosz, T. J. Study of water adsorption on activated carbons with different degrees of surface oxidation. *J. Colloid Interface Sci.* **1999**, *210* (2), 367–374.
(29) Furmaniak, S.; Wiśniewski, M.; Werengowska-Ciećwierz, K.; Terzyk, A. P.; Hata, K.; Gauden, P. A.; Kowalczyk, P.; Szybowicz, M. Water at curved carbon surface: mechanisms of adsorption revealed by first calorimetric study. *J. Phys. Chem. C* **2015**, *119* (5), 2703–2715.
(30) Cauvel, A.; Brunel, D.; Di Renzo, F.; Garrone, E.; Fubini, B. Hydrophobic and hydrophilic behavior of micelle-templated mesoporous silica. *Langmuir* **1997**, *13* (10), 2773–2778.
(31) Asay, D. B.; Barnette, A. L.; Kim, S. H. Effects of surface chemistry on structure and thermodynamics of water layers at solid–vapor interfaces. *J. Phys. Chem. C* **2009**, *113* (6), 2128–2133.
(32) Bilal, M.; Sultan, M.; Morosuk, T.; Den, W.; Sajjad, U.; Aslam, M. M.; Shahzad, M. W.; Farooq, M. Adsorption-based atmospheric water harvesting: A review of adsorbents and systems. *Int. Commun. Heat Mass Transfer* **2022**, *133*, No. 105961.
(33) Kim, H.; Yang, S.; Rao, S. R.; Narayanan, S.; Kapustin, E. A.; Furukawa, H.; Umans, A. S.; Yaghi, O. M.; Wang, E. N. Water harvesting from air with metal-organic frameworks powered by natural sunlight. *Science* **2017**, *356* (6336), 430–434.
(34) Ülkü, S. Adsorption heat pumps. *J. Heat. Recov. Syst.* **1986**, *6* (4), 277–284.

https://doi.org/10.1021/acs.jpcc.5c07495
J. Phys. Chem. C 2026, 130, 3472–3485

(35) Demir, H.; Mobedi, M.; Ülkü, S. A review on adsorption heat pump: Problems and solutions. *Renew. Sustain. Energy Rev.* **2008**, *12* (9), 2381−2403.
(36) Saren, S.; Mitra, S.; Miyazaki, T.; Ng, K. C.; Thu, K. Adsorption heat transformer cycle using multiple adsorbent + water pairs for waste heat upgrade. *J. Therm. Anal. Calorim.* **2023**, *148* (8), 3059−3071.
(37) Akhtar, M. S.; Ali, S.; Zaman, W. Innovative adsorbents for pollutant removal: Exploring the latest research and applications. *Molecules* **2024**, *29* (18), 4317.
(38) Wang, Y.-S.; Zhang, X.-J.; Ba, Y.-Q.; Li, T.-Y.; Hao, G.-P.; Lu, A.-H. Recent Advances in Carbon-Based Adsorbents for Adsorptive Separation of Light Hydrocarbons. *Research* **2022**, *2022*, No. 9780864.
(39) Wang, M.; Wang, J.; Jiang, J. Membrane Fouling: Microscopic Insights into the Effects of Surface Chemistry and Roughness. *Adv. Theory Simul.* **2022**, *5* (1), No. 2100395.
(40) Farmahini, A. H.; Sholl, D. S.; Bhatia, S. K. Fluorinated carbide-derived carbon: more hydrophilic, yet apparently more hydrophobic. *J. Am. Chem. Soc.* **2015**, *137* (18), 5969−5979.
(41) Khan, M. A.; Thu, K.; Mitra, S. Experimental evaluation of Adsorption Heat for Water vapour/Silica gel pair for chiller application. *Applied Thermal Engineering* **2024**, *249*, No. 123289.
(42) Giraldo, L.; Rodriguez-Estupiñán, P.; Moreno-Piraján, J. C. Isosteric heat: Comparative study between Clausius−Clapeyron, CSK and adsorption calorimetry methods. *Processes* **2019**, *7* (4), 203.
(43) Tian, Y.; Wu, J. Differential heat of adsorption and isosteres. *Langmuir* **2017**, *33* (4), 996−1003.
(44) Nuhnen, A.; Janiak, C. A practical guide to calculate the isosteric heat/enthalpy of adsorption via adsorption isotherms in metal-organic frameworks, MOFs. *Dalton trans.* **2020**, *49* (30), 10295−10307.
(45) Rouquerol, J.; Rouquerol, F.; Llewellyn, P.; Maurin, G.; Sing, K. *Adsorption by powders and porous solids:Principles, methodology and applications*, Second ed.; Academic Press, 2014.
(46) Azahar, F. H. M.; Mitra, S.; Yabushita, A.; Harata, A.; Saha, B. B.; Thu, K. Improved model for the isosteric heat of adsorption and impacts on the performance of heat pump cycles. *Appl. Therm. Eng.* **2018**, *143*, 688−700.
(47) Siperstein, F. R.; Avendaño, C.; Ortiz, J. J.; Gil-Villegas, A. Analytic expressions for the isosteric heat of adsorption from adsorption isotherm models and two-dimensional SAFT-VR equation of state. *AIChE J.* **2021**, *67* (3), No. e17186.
(48) Ott, J. B.; Boerio-Goates, J. Chapter 8 - The Equilibrium Condition Applied to Phase Equilibria. In *Chemical Thermodynamics: Principles and Applications*; Ott, J. B.; Boerio-Goates, J., Eds.; Academic Press, 2000; 383−433.
(49) Demir, H.; Mobedi, M.; Ülkü, S. Microcalorimetric investigation of water vapor adsorption on silica gel. *J. Therm. Anal. Calorim.* **2011**, *105* (1), 375−382.
(50) Ushakov, S. V.; Navrotsky, A. Direct measurements of water adsorption enthalpy on hafnia and zirconia. *Appl. Phys. Lett.* **2005**, *87* (16), 164103.
(51) Mazeina, L.; Navrotsky, A. Enthalpy of water adsorption and surface enthalpy of goethite (α-FeOOH) and hematite (α-Fe_2O_3). *Chem. Mater.* **2007**, *19* (4), 825−833.
(52) Hayun, S.; Shvareva, T. Y.; Navrotsky, A. Nanoceria − Energetics of surfaces, interfaces and water adsorption. *J. Am. Ceram. Soc.* **2011**, *94* (11), 3992−3999.
(53) Gouvêa, D.; Ushakov, S. V.; Navrotsky, A. Energetics of CO2 and H2O adsorption on zinc oxide. *Langmuir* **2014**, *30* (30), 9091−9097.
(54) Binder, H.; Kohlstrunk, B.; Heerklotz, H. H. A humidity titration calorimetry technique to study the thermodynamics of hydration. *Chem. Phys. Lett.* **1999**, *304* (5−6), 329−335.
(55) Muangthong-on, T.; Wannapeera, J.; Ohgaki, H.; Miura, K. TG-DSC study to measure heat of desorption of water during the thermal drying of coal and to examine the role of adsorption of water vapor for examining spontaneous heating of coal over 100 °C. *Energy Fuels* **2017**, *31* (10), 10691−10698.
(56) Wang, C.; Zhang, Y.; Wang, J.; Fan, Y.; Tang, Y. A study on the influence of air humidity on the characteristic parameters and thermal effect of coal spontaneous combustion. *Combust. Sci. Technol.* **2024**, *196* (12), 1957−1972.
(57) Cui, Y.; Gao, S.; Zhang, R.; Cheng, L.; Yu, J. Study on the moisture absorption and thermal properties of hygroscopic exothermic fibers and related interactions with water molecules. *Polymers* **2020**, *12* (1), 98.
(58) Yang, H.; Jayaatmaja, K.; Qiu, X.; Fan, M.; Dejam, M.; Tan, S. P.; Adidharma, H. Accurate measurement of the isothermal heat of capillary condensation in nanopores using differential scanning calorimetry and adsorption/desorption experiments. *J. Phys. Chem. C* **2023**, *127* (45), 21980−21988.
(59) Kim, H.; Cho, H. J.; Narayanan, S.; Yang, S.; Furukawa, H.; Schiffres, S.; Li, X.; Zhang, Y.-B.; Jiang, J.; Yaghi, O. M.; Wang, E. N. Characterization of adsorption enthalpy of novel water-stable zeolites and metal-organic frameworks. *Sci. Rep.* **2016**, *6*, 19097.
(60) Brunauer, S.; Emmett, P. H.; Teller, E. Adsorption of gases in multimolecular layers. *J. Am. Chem. Soc.* **1938**, *60* (2), 309−319.
(61) Rother, G.; Gautam, S.; Liu, T.; Cole, D. R.; Busch, A.; Stack, A. G. Molecular structure of adsorbed water phases in silica nanopores. *J. Phys. Chem. C* **2022**, *126* (5), 2885−2895.
(62) Rother, G.; Stack, A. G.; Gautam, S.; Liu, T.; Cole, D. R.; Busch, A. Water uptake by silica nanopores: Impacts of surface hydrophilicity and pore size. *J. Phys. Chem. C* **2020**, *124* (28), 15188−15194.
(63) Lowell, S.; Shields, J. E.; Thomas, M. A.; Thommes, M. *Characterization of porous solids and powders: Surface area, pore size and density*. Particle Technology Series; Springer Netherlands, 2004.
(64) Kocherbitov, V.; Alfredsson, V. Hydration of MCM-41 studied by sorption calorimetry. *J. Phys. Chem. C* **2007**, *111* (35), 12906−12913.
(65) Knight, A. W.; Kalugin, N. G.; Coker, E.; Ilgen, A. G. Water properties under nano-scale confinement. *Sci. Rep.* **2019**, *9* (1), 8246.
(66) Saliba, S.; Ruch, P.; Volksen, W.; Magbitang, T. P.; Dubois, G.; Michel, B. Combined influence of pore size distribution and surface hydrophilicity on the water adsorption characteristics of micro- and mesoporous silica. *Microporous Mesoporous Mater.* **2016**, *226*, 221−228.
(67) Thommes, M.; Morell, J.; Cychosz, K. A.; Fröba, M. Combining nitrogen, argon, and water adsorption for advanced characterization of ordered mesoporous carbons (CMKs) and periodic mesoporous organosilicas (PMOs). *Langmuir* **2013**, *29* (48), 14893−14902.
(68) Thommes, M.; Kaneko, K.; Neimark, A. V.; Olivier, J. P.; Rodriguez-Reinoso, F.; Rouquerol, J.; Sing, K. S. Physisorption of gases, with special reference to the evaluation of surface area and pore size distribution (IUPAC Technical Report). *Pure Appl. Chem.* **2015**, *87* (9−10), 1051−1069.
(69) Galarneau, A.; Nader, M.; Guenneau, F.; Di Renzo, F.; Gedeon, A. Understanding the Stability in Water of Mesoporous SBA-15 and MCM-41. *J. Phys. Chem. C* **2007**, *111* (23), 8268−8277.
(70) López Pérez, L.; van Eck, E. R.; Melián-Cabrera, I. On the hydrothermal stability of MCM-41. Evidence of capillary tension-induced effects. *Microporous Mesoporous Mater.* **2016**, *220*, 88−98.
(71) Liu, J.; Prelesnik, J. L.; Patel, R.; Kramar, B. V.; Wang, R.; Malliakas, C. D.; Chen, L. X.; Siepmann, J. I.; Hupp, J. T. A nanocavitation approach to understanding water capture, water release, and framework physical stability in hierarchically porous MOFs. *J. Am. Chem. Soc.* **2023**, *145* (51), 27975−27983.
(72) Ribeiro Carrott, M. M. L.; Estêvão Candeias, A. J.; Carrott, P. J. M.; Unger, K. K. Evaluation of the stability of pure silica MCM-41 toward water vapor. *Langmuir* **1999**, *15* (26), 8895−8901.
(73) Broyer, M.; Valange, S.; Bellat, J. P.; Bertrand, O.; Weber, G.; Gabelica, Z. Influence of aging, thermal, hydrothermal, and mechanical treatments on the porosity of MCM-41 mesoporous silica. *Langmuir* **2002**, *18* (13), 5083−5091.

https://doi.org/10.1021/acs.jpcc.5c07495
J. Phys. Chem. C 2026, 130, 3472−3485

(74) Kim, J. M.; Ryu, R. Disintegration of mesoporous structures of MCM-41 and MCM-48 in water. *Bull. Korean Chem. Soc.* **1996**, *17* (1), 66−68.
(75) Shindo, T.; Nakazawa, Y.; Shima, K.; Ikeuchi, T.; Ozawa, S. Post-synthesis of thick wall mesoporous silica with wormhole framework structure using surfactant micelles and silica source incorporated inside the channels of silica precursor with large-mesopores. *Int. J. Soc. Mater. Eng. Resour* **2012**, *18* (2), 33−37.
(76) Kocherbitov, V.; Alfredsson, V. Assessment of porosities of SBA-15 and MCM-41 using water sorption calorimetry. *Langmuir* **2011**, *27* (7), 3889−3897.
(77) Ohba, T.; Kanoh, H.; Kaneko, K. Cluster-growth-induced water adsorption in hydrophobic carbon nanopores. *J. Phys. Chem. B* **2004**, *108* (39), 14964−14969.
(78) Weinberger, C.; Zysk, F.; Hartmann, M.; Kaliannan, N. K.; Keil, W.; Kühne, T. D.; Tiemann, M. The structure of water in silica mesopores − influence of the pore wall polarity. *Adv. Mater. Interfaces* **2022**, *9* (20), No. 2200245.
(79) Baumgartner, B.; Hayden, J.; Loizillon, J.; Steinbacher, S.; Grosso, D.; Lendl, B. Pore size-dependent structure of confined water in mesoporous silica films from water adsorption/desorption using ATR-FTIR spectroscopy. *Langmuir* **2019**, *35* (37), 11986−11994.
(80) Kocherbitov, V. Properties of water confined in an amphiphilic nanopore. *J. Phys. Chem. C* **2008**, *112* (43), 16893−16897.
(81) Viisanen, Y.; Lbadaoui-Darvas, M.; Alvarez Piedehierro, A.; Welti, A.; Nenes, A.; Laaksonen, A. Water vapor adsorption-desorption hysteresis due to clustering of water on nonporous surfaces. *Langmuir* **2024**, *40* (38), 20311−20321.
(82) Horikawa, T.; Sekida, T.; Hayashi, J.; Katoh, M.; Do, D. D. A new adsorption−desorption model for water adsorption in porous carbons. *Carbon* **2011**, *49* (2), 416−424.
(83) Horikawa, T.; Yuasa, R.; Yoshida, K.; Do, D. D. Temperature dependence of water cluster on functionalized graphite. *Carbon* **2021**, *183*, 380−389.
(84) Horikawa, T.; Tan, S.; Do, D. D.; Sotowa, K.-I.; Alcántara-Avila, J. R.; Nicholson, D. Temperature dependence of water adsorption on highly graphitized carbon black and highly ordered mesoporous carbon. *Carbon* **2017**, *124*, 271−280.
(85) Liu, X.; Zhang, L.; El Fil, B.; Díaz-Marín, C. D.; Zhong, Y.; Li, X.; Lin, S.; Wang, E. N. Unusual temperature dependence of water sorption in semicrystalline hydrogels. *Adv. Mater.* **2023**, *35* (22), No. e2211763.
(86) Factorovich, M. H.; Gonzalez Solveyra, E.; Molinero, V.; Scherlis, D. A. Sorption isotherms of water in nanopores: Relationship between hydropohobicity, adsorption pressure, and hysteresis. *J. Phys. Chem. C* **2014**, *118* (29), 16290−16300.
(87) Inagaki, S.; Fukushima, Y.; Kuroda, K.; Kuroda, K. Adsorption isotherm of water vapor and its large hysteresis on highly ordered mesoporous silica. *J. Colloid Interface Sci.* **1996**, *180* (2), 623−624.
(88) David, R. O.; Fahrni, J.; Marcolli, C.; Mahrt, F.; Brühwiler, D.; Kanji, Z. A. The role of contact angle and pore width on pore condensation and freezing. *Atmos. Chem. Phys.* **2020**, *20* (15), 9419−9440.
(89) Wagner, W.; Pruß, A. The IAPWS formulation 1995 for the thermodynamic properties of ordinary water substance for general and scientific use. *J. Phys. Chem. Ref. Data* **2002**, *31* (2), 387−535.
(90) Vargaftik, N. B.; Volkov, B. N.; Voljak, L. D. International Tables of the Surface Tension of Water. *J. Phys. Chem. Ref. Data.* **1983**, *12* (3), 817−820.
(91) Wang, Y. X.; Liu, B. S.; Zheng, C. Preparation and adsorption properties of corncob-derived activated carbon with high surface area. *J. Chem. Eng. Data* **2010**, *55* (11), 4669−4676.
(92) Villa, F.; Marengo, M.; Coninck, J. de A new model to predict the influence of surface temperature on contact angle. *Sci. Rep.* **2018**, *8* (1), 6549.
(93) Song, J.-W.; Fan, L.-W. Temperature dependence of the contact angle of water: A review of research progress, theoretical understanding, and implications for boiling heat transfer. *Adv. Colloid Interface Sci.* **2021**, *288*, No. 102339.
(94) Adam, N. K. Use of the term 'Young's equation' for contact angles. *Nature* **1957**, *180* (4590), 809−810.
(95) Young, T., III. An essay on the cohesion of fluids. *Philos. Trans. R. Soc.* **1805**, *95*, 65−87.
(96) Song, J.-W.; Zeng, D.-L.; Fan, L.-W. Temperature dependence of contact angles of water on a stainless steel surface at elevated temperatures and pressures: In situ characterization and thermodynamic analysis. *J. Colloid Interface Sci.* **2020**, *561*, 870−880.
(97) Song, J.-W.; Ma, M.-C.; Fan, L.-W. Understanding the temperature dependence of contact angles of water on a smooth hydrophobic surface under pressurized Conditions: An Experimental Study. *Langmuir* **2020**, *36* (32), 9586−9595.
(98) Zhuravlev, L. T. The surface chemistry of amorphous silica. Zhuravlev model. *Colloids Surf. A Physicochem. Eng. Asp.* **2000**, *173* (1−3), 1−38.
(99) Pérez-Hermosillo, I. J.; Ojeda-López, R.; Domínguez-Ortiz, A.; Marcos Esparza-Schulz, J. Hydrothermal rehydroxylation of SBA-15 material: Effect of initial silanol concentration and pore size on the textural properties. *Materialia* **2023**, *28*, No. 101725.
(100) Triyono, T.; Trisunaryanti, W.; Sidjabat, O. Calculation of nitrogen heat adsorption on various catalysts using bet-constant (BET-C) data. *Sci. Contrib. Oil Gas* **2008**, *31* (3), 21−25.
(101) Lu, N.; Khorshidi, M. Mechanisms for Soil-Water Retention and Hysteresis at High Suction Range. *J. Geotech. Geoenviron. Eng.* **2015**, *141* (8), No. 04015032.
(102) Pan, H.; Ritter, J. A.; Balbuena, P. B. Examination of the approximations used in determining the isosteric heat of adsorption from the Clausius−Clapeyron equation. *Langmuir* **1998**, *14* (21), 6323−6327.
(103) Carrero, J. I. Application of the van't Hoff equation to phase equilibria. *ChemTexts* **2024**, *10* (3), 4.
(104) Cantrell; Ewing, G. E. Thin film water on muscovite mica. *J. Phys. Chem. B* **2001**, *105* (23), 5434−5439.
(105) Ketteler, G.; Yamamoto, S.; Bluhm, H.; Andersson, K.; Starr, D. E.; Ogletree, D. F.; Ogasawara, H.; Nilsson, A.; Salmeron, M. The nature of water nucleation sites on TiO_2(110) surfaces revealed by ambient pressure X-ray photoelectron spectroscopy. *J. Phys. Chem. C* **2007**, *111* (23), 8278−8282.
(106) Takahara, S.; Nakano, M.; Kittaka, S.; Kuroda, Y.; Mori, T.; Hamano, H.; Yamaguchi, T. Neutron scattering study on dynamics of water molecules in MCM-41. *J. Phys. Chem. B* **1999**, *103* (28), 5814−5819.
(107) Poyet, S.; Charles, S. Temperature dependence of the sorption isotherms of cement-based materials: Heat of sorption and Clausius−Clapeyron formula. *Cem. Concr. Res.* **2009**, *39* (11), 1060−1067.
(108) Salame, I. I.; Bandosz, T. J. Experimental study of water adsorption on activated carbons. *Langmuir* **1999**, *15* (2), 587−593.
(109) Dávila-Jiménez, M. M.; Elizalde-González, M. P.; García-Díaz, E.; González-Perea, M.; Guevara-Villa, M. R. Using akaike information criterion to select the optimal isotherm equation for adsorption from solution. *Adsorpt. Sci. Technol.* **2014**, *32* (7), 605−622.
(110) Frías-Ureña, P. M.; Bárcena-Soto, M.; Soto, V.; Chávez, K.; Orozco-Guareño, E.; Badillo-Camacho, J.; Robledo-Ortiz, J. R.; Fernández-Cervantes, I.; Gómez-Salazar, S. CO2 capture on prussian blue analogues (PBAs): Modeling equilibrium, kinetics, and Iisosteric heats of adsorption. *ACS omega* **2025**, *10* (11), 11421−11438.
(111) Brandani, S.; Mangano, E.; Sarkisov, L. Net, excess and absolute adsorption and adsorption of helium. *Adsorption* **2016**, *22* (2), 261−276.
(112) Puibasset, J.; Pellenq, R. J.-M. Water adsorption on hydrophilic mesoporous and plane silica substrates: A grand canonical Monte Carlo simulation study. *J. Chem. Phys.* **2003**, *118* (12), 5613−5622.
(113) Li, T.; Tian, H.; Xiao, X.; Cheng, P.; Zhou, Q.; Wei, Q. Geochemical characterization and methane adsorption capacity of overmature organic-rich lower cambrian shales in northeast guizhou region, southwest china. *Mar. Pet. Geol.* **2017**, *86*, 858−873.

https://doi.org/10.1021/acs.jpcc.5c07495
J. Phys. Chem. C 2026, 130, 3472−3485

(114) Gierszal, K. P.; Davis, J. G.; Hands, M. D.; Wilcox, D. S.; Slipchenko, L. V.; Ben-Amotz, D. π-Hydrogen bonding in liquid water. *J. Phys. Chem. Lett.* **2011**, *2* (22), 2930−2933.
(115) Robertson, P. A.; Villani, L.; Dissanayake, U. L. M.; Duncan, L. F.; Abbott, B. M.; Wilson, D. J. D.; Robertson, E. G. Halocarbons as hydrogen bond acceptors: A spectroscopic study of haloethylbenzenes (PhCH2CH2X, X = F, Cl, Br) and their hydrate clusters. *Phys. Chem. Chem. Phys.* **2018**, *20* (12), 8218−8227.
(116) Moon, H.; Collanton, R. P.; Monroe, J. I.; Casey, T. M.; Shell, M. S.; Han, S.; Scott, S. L. Evidence for entropically controlled interfacial hydration in mesoporous organosilicas. *J. Am. Chem. Soc.* **2022**, *144* (4), 1766−1777.
(117) Wagman, D. D., Ed. The NBS tables of chemical thermodynamic properties: Selected values for inorganic and C1 and C2 organic substances in SI units; *Journal of physical and chemical reference data*; American Chemical Society, 1982, *11*, 2.

https://doi.org/10.1021/acs.jpcc.5c07495
J. Phys. Chem. C 2026, 130, 3472−3485

5.3. Structure of Water under Confinement in Periodic Mesoporous Organosilicas Investigated by X-ray Scattering

Niels C. Gießelmann, **Philip Lenz**, Sophia-Marie Meinert, Tamás Simon, Wonhyuk Jo, Nele N. Striker, Michael Fröba*, Felix Lehmkühler*

Synopsis

The previous publications described the adsorption thermodynamics, density, and hydrophilicity of PMOs with different pore sizes and surface chemistries and provided a basis for understanding the interaction between water and various pore walls. To further investigate the influence of surface chemistry and pore size on the structure of confined water at different temperatures, X-ray scattering measurements were performed at PETRA III (beamline P02.1) at DESY in Hamburg (Germany) using the same divinylbenzene-type PMOs that were analyzed in the water adsorption studies.

As in the water adsorption studies, a strong influence of surface chemistry was observed in the X-ray scattering experiments on confined liquid water. Comparison of the first structure factor peak of water inside the different PMOs shows that water in confinement generally exhibits lower values than in bulk water. Furthermore, water inside more hydrophobic PMOs displays a first structure factor peak closer to bulk water, whereas in more hydrophilic materials, the first structure factor peak becomes increasingly similar to that of low-density amorphous ice (LDA). With decreasing temperature, the first structure factor peak approaches the LDA value in all materials, with a stronger temperature dependence in more hydrophobic samples. Analysis of the pair distribution functions reveals that confined water differs from bulk water in exhibiting two to three peaks in the second-neighbor region instead of a single broad peak. The occurrence of two peaks can be attributed to a distorted tetrahedral bonding structure and is mainly observed for more hydrophilic materials with smaller pores, whereas three peaks are found in more hydrophobic materials or materials with larger pores, which may indicate a tendency toward more bulk-like behavior. From the results of this study, it can be concluded that the structural properties of liquid water are altered under confinement and can be controlled by tuning the surface chemistry of the PMOs.

The author of this PhD thesis, who is also a co-author of the publication (Philip Lenz), participated in the PETRA III measurements, synthesized and characterized the PMOs (including porosity and hydrophilicity), wrote the section on material properties, and contributed to the discussion of the structural behavior of confined water.

THE JOURNAL OF PHYSICAL CHEMISTRY C
A JOURNAL OF THE AMERICAN CHEMICAL SOCIETY

Open Access
This article is licensed under CC-BY 4.0

pubs.acs.org/JPCC
Article

Structure of Water under Confinement in Periodic Mesoporous Organosilicas Investigated by X-ray Scattering

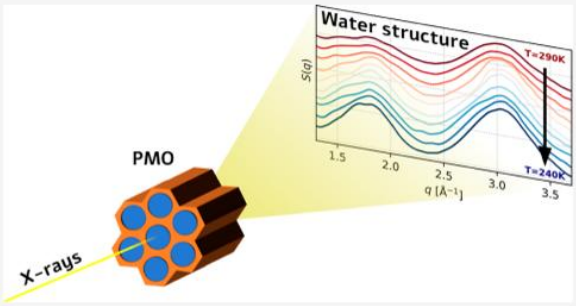
Niels C. Gießelmann, Philip Lenz, Sophia-Marie Meinert, Tamás Simon, Wonhyuk Jo, Nele N. Striker, Michael Fröba,* and Felix Lehmkühler*

Cite This: J. Phys. Chem. C 2024, 128, 499−507

Read Online

ACCESS | Metrics & More | Article Recommendations | Supporting Information

ABSTRACT: The effect of pore wall chemistry and pore diameter on the structure of confined water was studied by X-ray scattering on water confined in periodic mesoporous organosilicas (PMOs). A shift in the first structure factor peak at $q \approx 1.8$ Å^{-1} reveals a variation in the density of the confined water depending on the hydrophilicity and pore size. Smaller and more hydrophilic pores induce a lower density in the water. In contrast to bulk water, the pair distribution functions (PDFs) of confined water show a splitting of the second-neighbor peak into either two, in the case of smaller and more hydrophilic pores, or three separate peaks, in larger and more hydrophobic pores. From the running coordination number, we conclude that a smaller and more hydrophilic confinement leads to a stronger developed tetrahedral network in confined water, while confinement in larger and hydrophobic pores gives tetrahedral arrangements that are bulk-like or even less pronounced than in bulk water.



INTRODUCTION

Liquid water is known to show different equilibrium and dynamical properties in spatial confinement compared to bulk.[1−9] One particular example of this is a lower melting temperature compared to bulk water in dependence of the dimensions of the confining space.[1−4]

When confined in nanometer-sized pores, it has been found that the structure of water is not homogeneous throughout the pore: at the interface between the water and the surrounding material, a layer of a thickness of two to three molecules forms, which has a higher density than the water in the pore center.[10−13] This interfacial layer is also sometimes called the nonfreezing layer, as it does not form a crystalline structure upon freezing.[1,3] A remarkable finding by Soper et al.[12,14] has been that, while the interfacial layer in MCM-41 shows a higher and the core water a lower density than bulk water, the average density throughout the whole pore cross-section is lower than that of bulk water. This could be explained by the high negative pressure that the water experiences inside the pore. Soper[14] suggests that this negative pressure is caused by the formation of a concave meniscus where the liquid water inside the pore meets the water vapor on the outside.

Studies considering the molecular structuring of water under nanoscale confinement have also previously been conducted using methods such as X-ray and neutron scattering[15−17] as well as Raman spectroscopy.[18,19] There are also a number of simulation studies on the topic.[10,12,14] Authors employing different methods arrive at varying conclusions, in particular with regard to the effect of the confinement on the amount of tetrahedral structuring. Crupi et al.[18] and Malfait et al.,[19] for example, found a decrease in strongly hydrogen-bonded tetrahedral structures in the confined water, while previous studies using scattering techniques observed an increase of these structures.[15,17] Simulation studies, for example, by Soper et al.,[12,14] also found an increase of tetrahedrally structured water under confinement.

In order to investigate the influence of different parameters on the structure of confined water, we analyze its structure in materials with varying pore diameters and pore wall chemistry. This is achieved by the use of periodic mesoporous organosilicas (PMOs). These are a class of material consisting of a SiO_2 base lattice with periodically arranged organic moieties in the pore walls, forming a crystal-like wall structure.[20−27] The organic moieties can furthermore host functional components of various kinds, which can alter the interaction between the pore walls and the confined material.[28,29] PMOs provide a high stability due to the inorganic part

Received: September 28, 2023
Revised: November 27, 2023
Accepted: December 1, 2023
Published: December 21, 2023



See https://pubs.acs.org/sharingguidelines for options on how to legitimately share published articles.

© 2023 The Authors. Published by American Chemical Society

and at the same time a wide variety of possible functionalities in the organic bridging unit and can therefore be tuned to various intended applications, such as catalysis,[30,31] drug delivery,[32,33] or light harvesting.[34−36] Tuning the pore−water interaction and polarity of the pore wall has an influence on the structure and dynamics of water confined in PMOs.[19,27,29,37,38]

For instance, using Raman spectroscopy to investigate the hydrogen bonding behavior in water confined in PMOs, a reduction of tetrahedrally H-bonded was found in both MCM-41 and a more hydrophobic, phenylene-bridged BTEB-PMO with the effect being more pronounced in the latter.[19]

Another study by Jani et al.[29] claims that the dynamics of water are slowed down in the case of PMO confinement. Here, the diffusivity of water molecules close to the PMO interface is slower in the case of hydrophilic groups in the pore wall compared to hydrophobic ones.

With the study at hand, we want to expand the insights into the behavior of water in these systems by conducting X-ray scattering experiments on a variety of PMO materials, covering several pore sizes and pore wall functionalizations. This technique grants us direct access to the structural information on PMO-confined water, while a large selection of PMO materials allows us to study the impact of varying hydrophilicity over pore diameters between 3.4 and 5 nm. By studying the structure factors, pair distribution functions, and coordination numbers of water confined in PMOs, we find indications for a lower density and more strongly developed tetrahedral network under hydrophilic confinement when compared to bulk. This effect is strongly material-dependent and is amplified by confinement in smaller pores.

Sample Characterization. We used a variety of PMOs, as well as pure mesoporous silica (MCM-41), in order to cover variations in the pore diameter and pore wall functionalization. The precursors used for the PMO synthesis are 2,5-bis[(*E*)-2-(triethoxysilyl)vinyl]fluorobenzene (BTEVFB), 1,4-bis[(*E*)-2-(triethoxysilyl)vinyl]benzene (BTEVB), 2,5-bis[(*E*)-2-(triethoxysilyl)vinyl]aniline (BTEVA), and 2,5-bis[(*E*)-2-(triethoxysilyl)vinyl]pyridine (BTEVP). The chemical structure of the precursors is shown in Figure 1 and a list of the porous materials and their most important properties for this study is given in Table 1. More details on the material properties are found in the Supporting Information. In this study, the notation of the PMOs will be the precursor followed by the pore diameter in nanometers, written in parentheses. For example, BTEVA(3.4) denotes the PMO prepared with the BTEVA precursor with a pore diameter of 3.4 nm.

Details of the PMO synthesis, including a table with the synthesis parameters, are given in the Supporting Information (Table S1). In short, the synthesis of the BTEVB,[27,39] BTEVA,[27] and BTEVFB[25,39] precursors and their reaction to the corresponding PMOs were carried out according to the synthesis instructions given in literature. The synthesis of the BTEVP precursor is a modified form of literature synthesis.[24] Deviating from the three-step synthesis in the second step, the preparation of 2,5-diethynylpyridine, was carried out in a modified way.[40]

Nitrogen physisorption measurements were performed to characterize the porosities of the different materials. At first, the samples were activated at 100 °C for 20 h under reduced pressure in a degasser (*Quantachrome Masterprep*). The N_2-physisorption measurements were performed at a temperature of 77 K (*Quantachrome Quadrasorb-SI-MP* and *Quadrasorb evo*). Using the program *QuadraWin 6.0*, the pore size

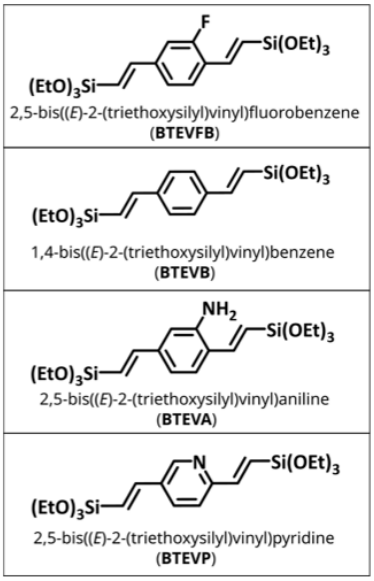


Figure 1. Chemical structures of the precursors.

distribution according to density functional theory (DFT) calculation with the model N_2 on silica (cylindr. pores), nonlocal DFT (NLDFT) at adsorptions branch, and the specific surface area with the Brunauer−Emmett−Teller (BET) method (p/p_0 range from 0.05 to 0.3) were determined from the obtained measurement.[41−43] In case of the intersection of the BET region with the condensation step of the isotherms, the BET range was reduced in order to be in the plateau region before the condensation ($p/p_0 < 0.3$). The measured nitrogen physisorption isotherms and the calculated pore size distributions of all materials are shown in Figure 2A. A type IV(b)-N_2 physisorption isotherm can be observed for all materials except for BTEVFB(4.9), which has hysteresis caused by cavitation or pore blocking effects and thus shows a type IV(a) isotherm.[43] Some of the porosity data of the different materials determined from the N_2 isotherms are listed in Table 1.

For the investigation of materials with regard to their hydrophilicity, the use of water as an adsorptive is suitable due to its sensitivity to surface chemistry.[27,37,44−46] To perform the water vapor sorption measurements, the samples were first degassed at 100 °C for 20 h (*Quantachrome MasterPrep Degasser*). Water vapor sorption isotherms were recorded at 25 °C (*Quantachrome VSTAR*).

Information on hydrophilicity can be obtained from water vapor sorption isotherms using the onset before the capillary condensation step, as well as the slope of the isotherm in the region of $p/p_0 < 0.5$. Since the relative pressure region of the onset is determined not only by the chemistry of the material surface but also by the pore radius, materials with similar pore diameters should be compared for the determination of hydrophilicity (see Figure 2B). For materials with the same pore diameter, more hydrophilic materials take more water at lower relative pressures, so capillary condensation occurs at lower relative pressures than for more hydrophobic materials.[27]

In the relative pressure range $p/p_0 < 0.5$, the pure silica MCM-41(3.9) has the steepest slope. As can be seen in Table

https://doi.org/10.1021/acs.jpcc.3c06491
J. Phys. Chem. C 2024, 128, 499−507

Table 1. List of the Porous Materials Used in the Experiment[a]

	precursor	d_P [nm]	$V_{P,0.9}$ [cm^3 g^{-1}]	S_{BET} [m^2 g^{-1}]	d_{org} [nm]	$(p/p_0)_{onset}$	N_w [nm^{-2}]	$s_{<0.5}$ [cm^3 g^{-1}]
■	MCM-41	3.9 ± 0.3	0.85	956		0.52	3.7	232
+	BTEVB	3.8 ± 0.7	0.54	762	1.19	0.75	0.96	31
●	BTEVFB	4.9 ± 1.4	0.83	632	1.20			
▶	BTEVFB	4.4 ± 0.7	1.04	976	1.20	0.88	0.66	24
▲	BTEVA	4.3 ± 0.3	0.83	966	1.18			
◀	BTEVA	3.8 ± 0.4	0.67	948	1.18	0.67	2.0	104
◆	BTEVA	3.4 ± 0.4	0.64	929	1.18			
×	BTEVP	3.5 ± 0.8	0.63	851	1.19	0.56	1.7	90

[a]Shown are the synthesis precursor, the pore diameter d_P (where the uncertainty is given by the half width at half maximum of the pore size distribution), the pore volume at 90% relative pressure $V_{P,0.9}$, the BET surface area S_{BET}, the organic unit periodicity d_{org} and where applicable the capillary condensation onset $(p/p_0)_{onset}$, the number of water molecules per area N_w, and the slope of the water adsorption isotherm for $p/p_0 < 0.5$.

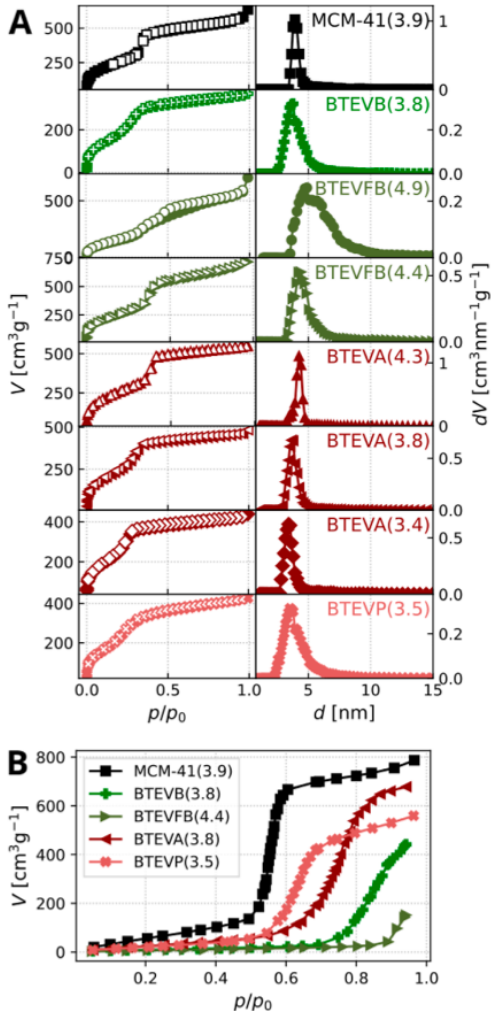


Figure 2. (A) N_2 physisorption isotherms (77 K) of the samples (left), showing adsorption (filled symbols) and desorption (hollow symbols). On the right, the pore size distribution curves, calculated using DFT. (B) Water vapor sorption isotherms at 25 °C of the adsorption branch from the materials with a pore diameter of about 3.8 nm. Additionally, the fluorinated BTEVFB sample with a pore diameter of 4.4 nm is shown.

1, the onset of pore condensation of MCM-41(3.9) has the smallest value. BTEVB(3.8) has by far the lowest slope and the highest onset position of the capillary condensation, indicating a comparatively higher hydrophobicity. In addition, it does not reach a plateau level after condensation; thus, the pores are not completely filled even at higher relative pressures. BTEVA(3.8) and BTEVP(3.5) are found between the samples mentioned above. While both have a similar slope, BTEVP(3.5) has a lower onset position with $p/p_0 = 0.56$ than the BTEVA(3.8) with $p/p_0 = 0.67$.

The amount of water adsorbed at the onset can be used to calculate the number of water molecules per surface area (N_w).[1,27] Comparing the different values for N_w (see Table 1) MCM-41 has $N_w = 3.7$ water molecules per square nanometer, which is also in agreement with the literature value.[1] The divinylaniline and pyridine materials show similar values with $N_w = 2.0$ and $N_w = 1.7$ nm^{-2}, respectively. Among the materials with pores about 3.8 nm in size, divinylbenzene bridged PMO has the lowest density of water molecules on the surface with $N_w = 0.96$ nm^{-2}. Additionally, a fluorine-containing PMO with a slightly larger pore diameter of 4.4 nm is shown. As with the divinylbenzene bridged PMOs, no plateau of the condensation step is achieved even at higher relative pressures. Since this material has the lowest slope and water density on the surface, it can be classified as the most hydrophobic among the presented materials. From the water vapor sorption analysis, the following series can be established, in which the hydrophilicity increases from left to right:

BTEVFB < BTEVB < BTEVA ≤ BTEVP < MCM-41.

Experiment and Analysis. The total X-ray scattering measurement was performed at beamline P02.1[47] at PETRA III (DESY, Hamburg, Germany) with a beam diameter of approximately 1 mm and at an energy of 60 keV. The powder samples were filled into glass capillaries with a diameter of 1.5 mm and a wall thickness of 10 μm (*Hilgenberg GmbH*). Scattering patterns were taken at temperatures between 290 and 245 K. At each temperature, 30 patterns were taken, with an exposure time of 1 s each. LaB_6 was used as a calibration sample for the measurements. The cooling was controlled by a nitrogen cryostream surrounding the sample capillary. We estimated the error of the temperature conservatively at 5 K, which is implied in all temperature data that we measured.

The water was adsorbed into the PMOs by means of a humidity chamber, where the humidity was gradually increased, thereby achieving a complete filling of the pores. Both the water-filled and -empty PMOs were investigated. This way, the water signal could be isolated by subtracting the signal of the empty PMO from that of the filled one. Note that the

https://doi.org/10.1021/acs.jpcc.3c06491
J. Phys. Chem. C 2024, 128, 499−507

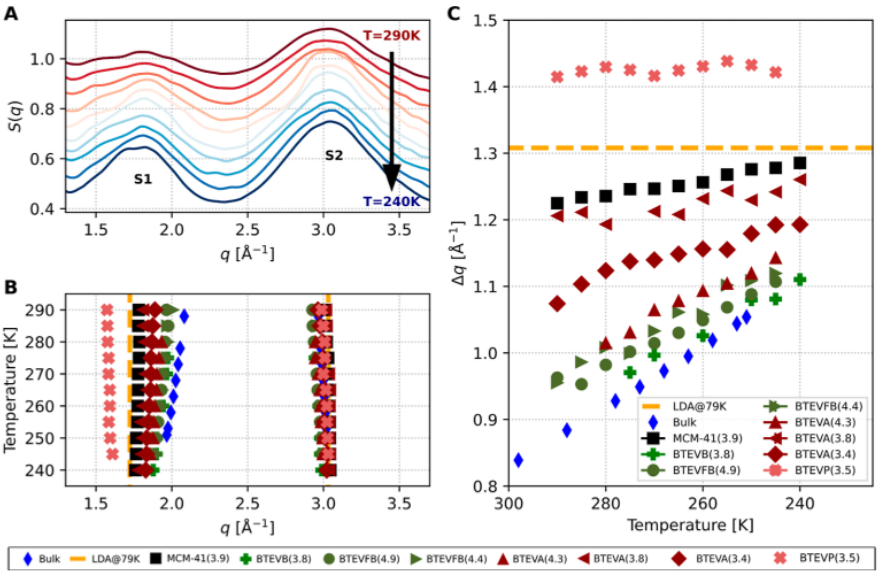


Figure 3. (A) Structure factor $S(q)$ of water in BTEVA(3.8)-PMO from 290 K (top) to 240 K (bottom) as an example of the typical form of the structure factor. (B) The structure factor peaks over different temperatures for water in different PMOs as well as in bulk. The bulk data were obtained from Sellberg et al.[51] (C) The splitting Δq between the $S(q)$ peaks. The LDA value was obtained from Mariedahl et al.[53]

result of this subtraction not only contains water−internal interactions but also those of water molecules with the pore wall, which contribute, for example, to the pair distribution functions.[15,16] This issue is further discussed in the Results and Discussion section. Because the electron density of the water molecule is mostly located at the oxygen atom, this is the dominant contributor to the X-ray scattering signal. As typical for X-ray studies, the quantities we compute do therefore not contain information about the bonding between the oxygen and hydrogen atoms but only about the oxygen structure.[48] To discuss the structure of the confined water, we make use of the (total) structure factor $S(q)$, which can be computed as described by Juhás et al.[49]

$$S(q) = \frac{I_c(q) - \langle f(q)^2\rangle + \langle f(q)\rangle^2}{\langle f(q)\rangle^2} \quad (1)$$

Here, I_c is the coherent scattering intensity and $f(q)$ is the atomic scattering factor. In order to compute the coherent contribution of the scattering intensity, corrections have to be applied which are further described by Juhás et al.,[49] as well as Egami and Billinge.[50] For the discussion of $S(q)$, we will focus on the region of q between 1.5 to about 4 Å^{-1}. In this region, bulk water typically shows two peaks, the first of which shifts to smaller q upon cooling. The subsequent spread of the two peaks can be used as a measure of the amount of tetrahedrally structured water in bulk.[51,52] However, in confinement, other factors must also be taken into account, such as interface interactions and geometric constraints, as these also affect the structuring of confined water.[10−12,14−16] From the structure factor the pair distribution functions (PDFs) can be computed as

$$G(r) = \frac{2}{\pi}\int_{q_{min}}^{q_{max}} q[S(q) - 1]\sin qr\,dq \quad (2)$$

$S(q)$ and the PDFs were computed using *PDFGetX3* software.[49] Another interesting quantity is the running coordination number n_{OO}.[14,53,54] It is calculated via the r-weighted integral of the reduced PDF

$$n_{OO}(r) = \int_0^r r' g(r')\,dr' \quad (3)$$

with $g(r) = G(r) - 1$. n_{OO} gives the coordination number at a distance of r from the origin atom.

RESULTS AND DISCUSSION

Structure Factor. Figure 3A exemplary shows the structure factor of water confined in BTEVA(3.8)-PMO at temperatures between 290 and 240 K. During cooling, both a spread and a growth of the two peaks is observed. This is a typical behavior reported for water. In bulk water this peak spread is often attributed to a more pronounced formation of a tetrahedral and hydrogen-bonded structure between the water molecules.[51,52] However, in confinement other interactions, like those between the water molecules and the pore wall, also have a considerable influence on the structuring of the molecules.[10−12,14,15]

Figure 3B shows the position of the structure factor peaks for different PMOs, as well as bulk water. The peak spread occurs in almost all samples, with the exception of BTEVP(3.8). Here, the lower-q peak (S1) seems to shift to larger q rather than lower ones.

The spread of the peaks during cooling, i.e., the difference between the two peak positions, can be observed in Figure 3C. A strong dependence of peak spread Δq on the confining material is found. Bulk water consistently shows the smallest values for Δq, while also giving rise to the strongest increase in the spread during the cooling process. The hydrophobic samples, which are shown with green markers in the figures, show a slightly larger spread and smaller increase for lowering temperature. The hydrophilic PMOs, as well as MCM-41(3.9),

https://doi.org/10.1021/acs.jpcc.3c06491
J. Phys. Chem. C 2024, 128, 499−507

marked in red and black, respectively, show the largest Δq value but cause a smaller change during cooling. BTEVP(3.5) shows the most extreme behavior compared to bulk water by staying at almost a constant value for Δq throughout the cooling process.

In the further discussion of the structure factor, we will focus only on the position of the first peak (S1), as the second peak does not show a strong dependence on the different confinement as well as bulk conditions. This reduces the statistical error compared to the difference in the peak positions.

These S1 positions q_1 are shown in Figure 4A. A roughly linear behavior is found in all samples, with the slopes

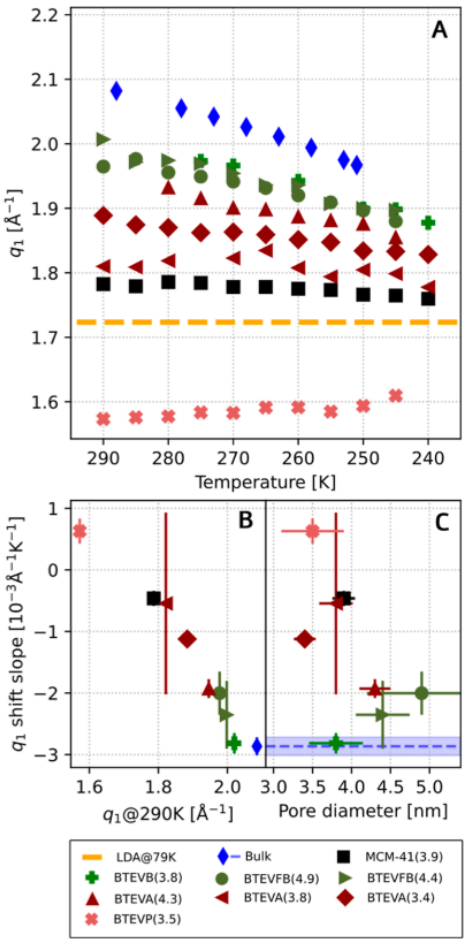


Figure 4. (A) Position of the first structure factor peaks in various materials over temperature. (B) The slope of the linearly fitted peak shift against the peak position at 290 K of the same fit. (C) The slope of the linearly fitted peak shift against the pore size.

depending on the type of porous material. At room temperature, bulk water shows the highest q_1, which then decreases the most throughout the cooling process. Next to the bulk water are the rather hydrophobic materials BTEVB and BTEVFB, the latter of which were measured with two different pore diameters of 4.9 and 4.4 nm. At lower q, we then find more hydrophilic samples including BTEVA with different pore diameters as well as MCM-41(3.9). These also show a smaller slope than bulk water and the more hydrophobic samples. BTEVP(3.5) shows a different behavior than the other samples with the lowest q_1 at room temperature, which then increases with lower temperatures. A shift of S1 to smaller q in water under confinement has consistently been reported in previous studies.[14,55,56]

Figure 4A also shows the q_1-value for low density amorphous ice (LDA), as measured by Mariedahl et al.[53] It provides a fitting reference when comparing structural features in this context, as it has a strongly tetrahedral structure without interstitials.[53,57] In our study, all samples seem to approach the value of LDA when cooling, including BTEVP(3.5). In this sample, S1 starts, in fact, at a lower q_1 than LDA and then rises upon cooling, thereby also approaching the value of LDA. Note also that water under confinement has a smaller q_1 than bulk water for all observed materials and temperatures.

Figure 4A suggests a correlation between the slope of the linearly fitted peak shift and the peak position at room temperature. This relationship is shown in Figure 4B. Here, a clear trend with regard to the material hydrophilicity is observed. At room temperature, q_1 is at lower values for hydrophilic samples, while the slopes of their S1 shifts are larger. Hydrophobic pores lead to larger q_1-values at room temperature, while the slopes are more negative.

Figure 4C shows the slope of the linearly fitted peak shift against the pore diameter. For individual samples, a trend of the slope deviating further from that of bulk water in smaller pores can be observed. This trend seems to be stronger between the hydrophilic pores than between the more hydrophobic ones. BTEVA(4.3) shows a slope closer to bulk water and the hydrophobic samples than that to BTEVA(3.8) and BTEVA(3.4). In the hydrophobic samples, no such trend can be observed. In fact, they seem to show a decrease of the slope for smaller pore diameters, notably even between BTEVFB(4.9) and BTEVFB(4.4), which differ only in pore size. However, due to the pore size distributions, fitting errors, and the small number of measured samples, one should be careful when interpreting this data.

In bulk water, a lower-q position of S1 is often attributed to a larger amount of tetrahedrally structured water.[51,58] While this may also contribute to this effect, this cannot fully be transferred to confined water, as interface and geometric effects become non-negligible in this case. A particularly interesting quantity that is altered under confinement conditions is the density of water. It has been agreed upon that layers with different densities form in water when confined in hydrophilic nanoporous material.[10−12,14,59,60] More molecules adsorb to the pore wall in this case, leading to a higher number density close to the interface and a lower density in the core of the pore. As discussed above, the average density of water throughout the whole pore cross section under confinement in MCM-41 is also considerably lower than that of bulk water.[14,59]

This effect could explain the material-dependent shift of S1, as it is most prominent in rather hydrophilic pores, with a strong wall−water interaction. As water confined in hydrophobic pores has a larger contact angle with the pore wall, they do not show this decreased density as strongly in comparison to bulk water, and therefore, we do not observe the S1 shift as strongly as in hydrophilic pores. Furthermore, for geometric reasons, the negative pressure could scale with smaller pore

https://doi.org/10.1021/acs.jpcc.3c06491
J. Phys. Chem. C 2024, 128, 499−507

diameters. This might lead to the effect being more pronounced in smaller pores than in larger ones, which is also reflected in the S1 shift that we observed. Surprisingly, the interplay of pore size and hydrophilicity seems to induce a very low density in liquid water confined in BTEVP(3.5), which would be even lower than that of LDA and especially low at room temperature. Note that while the density cannot completely be identified via the structure factor, a smaller density would certainly lead to smaller values of q_1[14] and is therefore in agreement with the data presented here, as well as previous studies.[14,55,56]

Pair Distribution Function. For completion, Figure 5A shows the structural factors at the highest and lowest studied

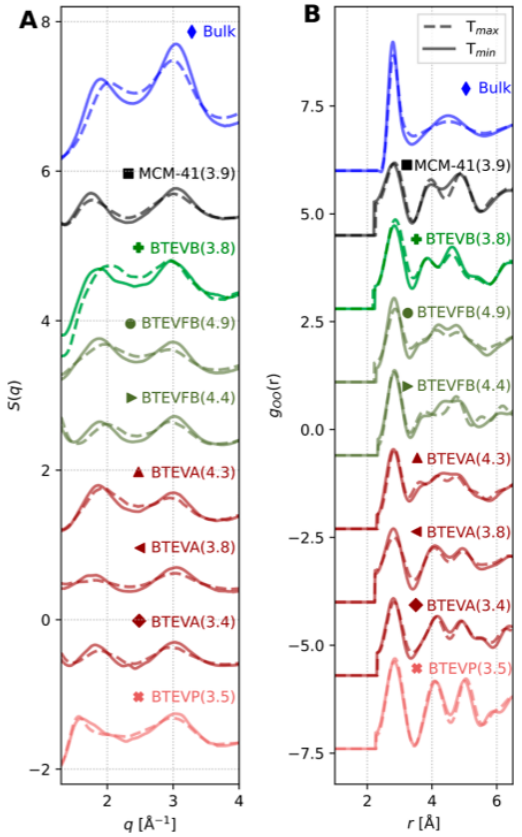


Figure 5. (A) Structure factor of water in the observed samples at the highest and lowest used temperature. The data for bulk water were measured by Pathak et al.[54] The curves are set 1 unit apart of each other. (B) The pair distribution functions at the same temperatures. $g_{OO}(r < 2.2$ Å) were set to zero, as the signal in this range comes from artifacts of the correlation. Bulk data are from Skinner et al.[61] The curves are set 1.7 units apart from each other.

temperatures. In Figure 5B, the computed pair distribution functions (PDFs) for water in the various PMO materials are plotted once at the highest studied temperature T_{max} and once at the lowest T_{min}. T_{max} and T_{min} for each sample are noted in the individual plots in Figure 6. For bulk water, T_{max} = 295.1 K and T_{min} = 254.1 K.[51]

Figure 5B reveals qualitative differences in the structure of confined water compared to that of bulk that are present in all

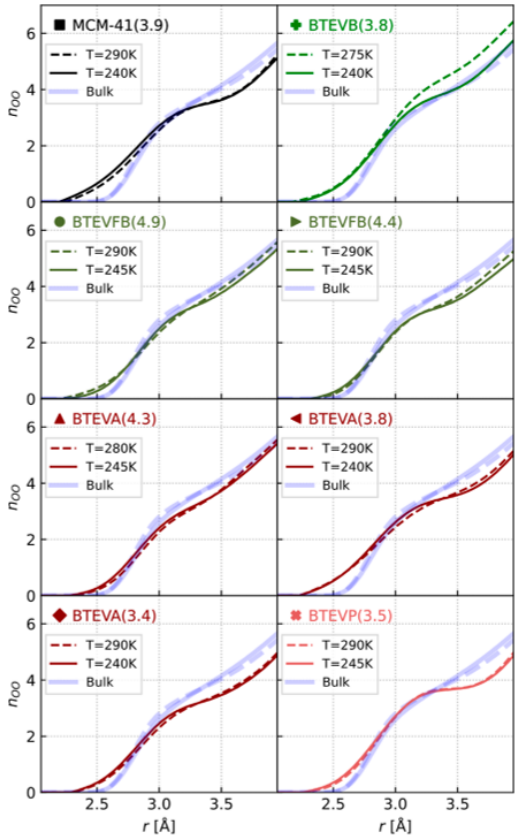


Figure 6. Running coordination number of water in the samples. Bulk data were calculated from the PDF obtained from Skinner et al.[61]

PMO materials. The most striking one is the splitting of the broad second neighbor peak of bulk water into several separate ones. In MCM-41(3.9), BTEVA(3.8), BTEVA(3.4), and BTEVP(3.5), two peaks are present in this region, while the rest of the samples cause three peaks.

The appearance of several peaks emerging in the region from 3.5 to 5 Å can be attributed to a more pronounced, albeit distorted, tetrahedrally bonded network, which has also been observed in previous studies for (hydrophilically) confined water.[14,15,17,59] It also has been argued that the interaction between the silanol groups in the pore wall and the confined water also contributes to the pair distribution function at a bond length of approximately 3.8 Å.[15,16] However, this effect does not seem to be reflected in all of our data.

Comparing the rather hydrophilic samples BTEVA(4.3), BTEVA(3.8), and BTEVA(3.4) shows a shoulder at 3.8 Å in BTEVA(4.3), which cannot be observed for the latter two. If the water−substrate interaction was a dominant effect in these pores, one would expect a more prominent contribution in smaller pores instead of larger ones. On the other hand, this peak is quite prominent in the more hydrophobic BTEVB(3.8). An explanation for this difference could be that in the hydrophobic samples more water molecules bind to the silanol groups, as they interact less with the functional groups. In contrast, in hydrophilic samples, the increased amount of interactions between the functional groups and the confined

https://doi.org/10.1021/acs.jpcc.3c06491
J. Phys. Chem. C 2024, 128, 499−507

water leads to fewer interactions with the silica in the pore wall. While the water−silanol interaction most likely contributes to the PDFs, we also propose another explanation that addresses the emergence of three peaks in materials with larger pores compared to only two in those with smaller ones.

While the broad peak in bulk water suggests a broad distribution of second-neighbor distances, the two peaks present in the previously mentioned samples would hint at two more discrete distances. The emergence of a third peak may indicate a more bulklike behavior in these materials, such that the number of possible second-neighbor bonding lengths is increased in comparison to the samples giving only two peaks. The results presented in Figure 5B are consistent with literature,[14,15,17,59] as two peaks are predominantly present in smaller and more hydrophilic pores and three peaks in larger, as well as more hydrophobic pores.

Running Coordination Number. The analysis of the pair distribution functions gave a first hint toward the presence of tetrahedral structuring in the confined water. To gain more insights into this, we take into account the interstitial molecules between the first and second neighbor peaks. These can be visualized by integrating the radial distribution function. The subsequent quantity is called the running coordination number n_{OO}.[14,53,54] The resulting curves for n_{OO} against the distance from an initial oxygen atom are shown in Figure 6, again at the highest and lowest temperatures for each sample. The curves for bulk water are also shown in blue for comparison. More or less pronounced plateaus are observed around 3.5 Å in all samples as well as in bulk water. A more strongly pronounced plateau can be attributed to more tetrahedral structuring, as it indicates less or no interstitial oxygen atoms between the first and second neighbor shells.[54] From this, we can derive another qualitative statement about the presence of tetrahedrally structured water in the various confining materials. The curves of BTEVA(3.8), BTEVA(3.4), and especially BTEVP(3.5) and MCM-41(3.9) show a strongly pronounced plateau, indicating a larger ratio of tetrahedral water when compared to bulk water. Water confined in the remaining materials shows a more bulk-like plateau, indicating a more disordered water structure in these materials. These results are again in agreement with the previously discussed findings that (hydrophilic) confinement supports the formation of a tetrahedrally structured hydrogen bond network.[14,15,17,59]

CONCLUSIONS

We observed that the structural behavior of water under confinement in PMOs is strongly influenced by the properties of the confining material. In particular, the shift of the first structure factor peak of water during cooling differs more strongly from that of bulk water in hydrophilic pores than in more hydrophobic pores. This effect can be attributed to a lower density of the confined water compared to bulk. We could also show that by lowering the pore diameter, this effect can be further amplified.

In the PDFs of water in the PMOs, a distinction can be observed between materials which lead to either two or three peaks in the region of 3.5 to 5.5 Å, i.e., the region of the second neighbor peak in the PDF of bulk water. While smaller pores give two distinct peaks, confinement in larger pores leads to three peaks or no clear peak structure at all. The presence of two peaks is attributed to the development of a distorted tetrahedral bonding structure,[14,15,59] while the presence of a third peak could hint at the restoration of more bulk-like conditions. Looking at the minimum between the first and second PDF peaks, as well as the running coordination number, we could furthermore observe a higher amount of tetrahedral structuring in smaller and more hydrophilic pores. In contrast, larger and more hydrophobic pores show a weaker development of tetrahedral structures. This is in agreement with conclusions from previous studies, which also observe that hydrophilic confinement supports tetrahedral structuring.[14,15,17]

We can conclude that by confinement in PMOs with varying pore diameters and pore wall chemistry, it is possible to tune fundamental properties of water, such as the density and amount of tetrahedral structuring. Further experimental and simulation studies would be beneficial to acquire a more in-depth understanding of these effects.

ASSOCIATED CONTENT

Supporting Information

The Supporting Information is available free of charge at https://pubs.acs.org/doi/10.1021/acs.jpcc.3c06491.

Synthesis of PMO precursors, PMOs, and MCM-41 including synthesis parameters, powder X-ray diffraction of porous materials, and porosity data of used materials (PDF)

AUTHOR INFORMATION

Corresponding Authors

Michael Fröba − *University of Hamburg, Institute of Inorganic and Applied Chemistry, 20146 Hamburg, Germany; The Hamburg Centre for Ultrafast Imaging, 22761 Hamburg, Germany*; Email: michael.froeba@uni-hamburg.de

Felix Lehmkühler − *Deutsches Elektronen-Synchrotron DESY, 22607 Hamburg, Germany; The Hamburg Centre for Ultrafast Imaging, 22761 Hamburg, Germany*; orcid.org/0000-0003-1289-995X; Email: felix.lehmkuehler@desy.de

Authors

Niels C. Gießelmann − *Deutsches Elektronen-Synchrotron DESY, 22607 Hamburg, Germany*; orcid.org/0009-0002-8139-4357

Philip Lenz − *University of Hamburg, Institute of Inorganic and Applied Chemistry, 20146 Hamburg, Germany; The Hamburg Centre for Ultrafast Imaging, 22761 Hamburg, Germany*

Sophia-Marie Meinert − *University of Hamburg, Institute of Inorganic and Applied Chemistry, 20146 Hamburg, Germany*

Tamás Simon − *University of Hamburg, Institute of Inorganic and Applied Chemistry, 20146 Hamburg, Germany*

Wonhyuk Jo − *Deutsches Elektronen-Synchrotron DESY, 22607 Hamburg, Germany; European XFEL, 22869 Schenefeld, Germany*

Nele N. Striker − *Deutsches Elektronen-Synchrotron DESY, 22607 Hamburg, Germany*; orcid.org/0000-0001-9429-0835

Complete contact information is available at: https://pubs.acs.org/10.1021/acs.jpcc.3c06491

Notes

The authors declare no competing financial interest.

■ ACKNOWLEDGMENTS

We acknowledge DESY (Hamburg, Germany), a member of the Helmholtz Association HGF, for the provision of experimental facilities. Parts of this research were carried out at PETRA III and we would like to thank Dr. Alexander Schökel and Dr. Martin Etter for assistance in using the P02.1 beamline.[47] Beamtime was allocated for proposals I-20200440 and I-20190201. This research was carried out in the framework of the city of Hamburg's state funded research project "Control of the special properties of water in nanopores" (LFF-FV68). It was furthermore supported by the Centre for Molecular Water Science (CMWS) in an Early Science Project and by the Cluster of Excellence "Advanced Imaging of Matter" of the Deutsche Forschungsgemeinschaft (DFG) (EXC 2056, Project 390715994).

■ REFERENCES

(1) Jähnert, S.; Vaca Chávez, F.; Schaumann, G.; Schreiber, A.; Schönhoff, M.; Findenegg, G. Melting and freezing of water in cylindrical silica nanopores. *Phys. Chem. Chem. Phys.* **2008**, *10*, 6039−6051.

(2) Deschamps, J.; Audonnet, F.; Brodie-Linder, N.; Schoeffel, M.; Alba-Simionesco, C. A thermodynamic limit of the melting/freezing processes of water under strongly hydrophobic nanoscopic confinement. *Phys. Chem. Chem. Phys.* **2010**, *12*, 1440−1443.

(3) Jelassi, J.; Castricum, H. L.; Bellissent-Funel, M.-C.; Dore, J.; Webber, J. B. W.; Sridi-Dorbez, R. Studies of water and ice in hydrophilic and hydrophobic mesoporous silicas: pore characterisation and phase transformations. *Phys. Chem. Chem. Phys.* **2010**, *12*, 2838−2849.

(4) Moore, E. B.; Allen, J. T.; Molinero, V. Liquid-ice coexistence below the melting temperature for water confined in hydrophilic and hydrophobic nanopores. *J. Phys. Chem. C* **2012**, *116*, 7507−7514.

(5) Thompson, W. H. Solvation dynamics and proton transfer in nanoconfined liquids. *Annu. Rev. Phys. Chem.* **2011**, *62*, 599−619.

(6) Reiter, G.; Deb, A.; Sakurai, Y.; Itou, M.; Krishnan, V.; Paddison, S. Anomalous ground state of the electrons in nanoconfined water. *Phys. Rev. Lett.* **2013**, *111*, 036803.

(7) Kapoor, K.; Patil, S.; Patil, S. Viscoelasticity and shear thinning of nanoconfined water. *Phys. Rev. E* **2014**, *89*, 013004.

(8) Munoz-Santiburcio, D.; Marx, D. Chemistry in nanoconfined water. *Chem. Sci.* **2017**, *8*, 3444−3452.

(9) Liang, C.; Rayabharam, A.; Aluru, N. Structural and Dynamical Properties of H2O and D2O under Confinement. *J. Phys. Chem. B* **2023**, *127*, 6532−6542.

(10) Gallo, P.; Ricci, M.; Rovere, M. Layer analysis of the structure of water confined in vycor glass. *J. Chem. Phys.* **2002**, *116*, 342−346.

(11) Gallo, P.; Rovere, M.; Chen, S.-H. Dynamic crossover in supercooled confined water: Understanding bulk properties through confinement. *J. Phys. Chem. Lett.* **2010**, *1*, 729−733.

(12) Soper, A. K. Density profile of water confined in cylindrical pores in MCM-41 silica. *J. Phys.: Condens. Matter* **2012**, *24*, 064107.

(13) Erko, M.; Wallacher, D.; Hoell, A.; Hauß, T.; Zizak, I.; Paris, O. Density minimum of confined water at low temperatures: a combined study by small-angle scattering of X-rays and neutrons. *Phys. Chem. Chem. Phys.* **2012**, *14*, 3852−3858.

(14) Soper, A. K. Radical re-appraisal of water structure in hydrophilic confinement. *Chem. Phys. Lett.* **2013**, *590*, 1−15.

(15) Smirnov, P.; Yamaguchi, T.; Kittaka, S.; Takahara, S.; Kuroda, Y. X-ray diffraction study of water confined in mesoporous MCM-41 materials over a temperature range of 223- 298 K. *J. Phys. Chem. B* **2000**, *104*, 5498−5504.

(16) Aso, M.; Ito, K.; Sugino, H.; Yoshida, K.; Yamada, T.; Yamamuro, O.; Inagaki, S.; Yamaguchi, T. Thermal behavior, structure, and dynamics of low-temperature water confined in mesoporous organosilica by differential scanning calorimetry, X-ray diffraction, and quasi-elastic neutron scattering. *Pure Appl. Chem.* **2012**, *85*, 289−305.

(17) Khoder, H.; Schaniel, D.; Pillet, S.; Bendeif, E.-E. X-ray scattering study of water confined in bioactive glasses: experimental and simulated pair distribution function. *Acta Crystallogr. A* **2020**, *76*, 589−599.

(18) Crupi, V.; Interdonato, S.; Longo, F.; Majolino, D.; Migliardo, P.; Venuti, V. A new insight on the hydrogen bonding structures of nanoconfined water: a Raman study. *J. Raman Spectrosc.* **2008**, *39*, 244−249.

(19) Malfait, B.; Moréac, A.; Jani, A.; Lefort, R.; Huber, P.; Fröba, M.; Morineau, D. Structure of water at hydrophilic and hydrophobic interfaces: Raman spectroscopy of water confined in periodic mesoporous (organo) silicas. *J. Phys. Chem. C* **2022**, *126*, 3520−3531.

(20) Inagaki, S.; Guan, S.; Ohsuna, T.; Terasaki, O. An ordered mesoporous organosilica hybrid material with a crystal-like wall structure. *Nature* **2002**, *416*, 304−307.

(21) Sayari, A.; Wang, W. Molecularly ordered nanoporous organosilicates prepared with and without surfactants. *J. Am. Chem. Soc.* **2005**, *127*, 12194−12195.

(22) Cornelius, M.; Hoffmann, F.; Fröba, M. Periodic mesoporous organosilicas with a bifunctional conjugated organic unit and crystal-like pore walls. *Chem. Mater.* **2005**, *17*, 6674−6678.

(23) Beretta, M.; Morell, J.; Sozzani, P.; Fröba, M. Towards peptide formation inside the channels of a new divinylaniline-bridged periodic mesoporous organosilica. *Chem. Commun.* **2010**, *46*, 2495−2497.

(24) Waki, M.; Mizoshita, N.; Ohsuna, T.; Tani, T.; Inagaki, S. Crystal-like periodic mesoporous organosilica bearing pyridine units within the framework. *Chem. Commun.* **2010**, *46*, 8163−8165.

(25) Bracco, S.; Beretta, M.; Cattaneo, A.; Comotti, A.; Falqui, A.; Zhao, K.; Rogers, C.; Sozzani, P. Dipolar rotors orderly aligned in mesoporous fluorinated organosilica architectures. *Angew. Chem., Int. Ed.* **2015**, *54*, 4773−4777.

(26) Martens, S.; Ortmann, R.; Brieler, F. J.; Pasel, C.; Joo Lee, Y.; Bathen, D.; Fröba, M. Periodic mesoporous organosilicas as adsorbents of toxic trace gases out of the ambient air. *Z. Anorg. Allg. Chem.* **2014**, *640*, 632−640.

(27) Mietner, J. B. Visiting Nanopores: The Great Potential of PMOs for Studying the Properties of Water in Nanopores of Different Polarity. Ph.D. Thesis, University of Hamburg: Germany, 2018.

(28) Mietner, B. J.; Fröba, M.; Valiullin, R. Water Transport in Periodic Mesoporous Organosilica Materials. *J. Phys. Chem. C* **2018**, *122*, 12673−12680.

(29) Jani, A.; Busch, M.; Mietner, J. B.; Ollivier, J.; Appel, M.; Frick, B.; Zanotti, J.-M.; Ghoufi, A.; Huber, P.; Fröba, M.; et al. Dynamics of water confined in mesopores with variable surface interaction. *J. Chem. Phys.* **2021**, *154*, 094505.

(30) Yang, Q.; Liu, J.; Zhang, L.; Li, C. Functionalized periodic mesoporous organosilicas for catalysis. *J. Mater. Chem.* **2009**, *19*, 1945−1955.

(31) Karimi, B.; Mirzaei, H. M.; Mobaraki, A. Periodic mesoporous organosilica functionalized sulfonic acids as highly efficient and recyclable catalysts in biodiesel production. *Catal. Sci. Technol.* **2012**, *2*, 828−834.

(32) Parambadath, S.; Mathew, A.; Jenisha Barnabas, M.; Ha, C.-S. A pH-responsive drug delivery system based on ethylenediamine bridged periodic mesoporous organosilica. *Microporous Mesoporous Mater.* **2015**, *215*, 67−75.

(33) Rao, K. M.; Parambadath, S.; Kumar, A.; Ha, C.-S.; Han, S. S. Tunable intracellular degradable periodic mesoporous organosilica hybrid nanoparticles for doxorubicin drug delivery in cancer cells. *ACS Biomater. Sci. Eng.* **2018**, *4*, 175−183.

(34) Inagaki, S.; Ohtani, O.; Goto, Y.; Okamoto, K.; Ikai, M.; Yamanaka, K.-i.; Tani, T.; Okada, T. Light harvesting by a periodic mesoporous organosilica chromophore. *Angew. Chem.* **2009**, *121*, 4102−4106.

(35) Takeda, H.; Ohashi, M.; Goto, Y.; Ohsuna, T.; Tani, T.; Inagaki, S. Light-Harvesting Photocatalysis for Water Oxidation Using Mesoporous Organosilica. *Chem.—Eur. J.* **2014**, *20*, 9130−9136.

(36) Croissant, J. G.; Cattoën, X.; Wong Chi Man, M.; Durand, J.-O.; Khashab, N. M. Syntheses and applications of periodic mesoporous organosilica nanoparticles. *Nanoscale* **2015**, *7*, 20318−20334.
(37) Mietner, J. B.; Brieler, F. J.; Lee, Y. J.; Fröba, M. Properties of water confined in periodic mesoporous organosilicas: nanoimprinting the local structure. *Angew. Chem., Int. Ed.* **2017**, *56*, 12348−12351.
(38) Malfait, B.; Jani, A.; Mietner, J. B.; Lefort, R.; Huber, P.; Fröba, M.; Morineau, D. Influence of pore surface chemistry on the rotational dynamics of nanoconfined water. *J. Phys. Chem. C* **2021**, *125*, 16864−16874.
(39) Bilo, M. Controlled Pore Glasses and Alginate Hydrogels as Form-Giving Matrices for Nanoporous Organosilicas. Ph.D. Thesis, University of Hamburg: Germany, 2019.
(40) Feng, J.; Zhang, C.; Li, Y.; Yang, M. Hyperbranched polymer based on triphenylamine and pyridine: Fluorescent chemosensors for palladium ions. *J. Appl. Polym. Sci.* **2011**, *121*, 217−225.
(41) Brunauer, S.; Emmett, P. H.; Teller, E. Adsorption of gases in multimolecular layers. *J. Am. Chem. Soc.* **1938**, *60*, 309−319.
(42) Landers, J.; Gor, G. Y.; Neimark, A. V. Density functional theory methods for characterization of porous materials. *Colloids Surf., A* **2013**, *437*, 3−32.
(43) Thommes, M.; Kaneko, K.; Neimark, A. V.; Olivier, J. P.; Rodriguez-Reinoso, F.; Rouquerol, J.; Sing, K. S. Physisorption of gases, with special reference to the evaluation of surface area and pore size distribution (IUPAC Technical Report). *Pure Appl. Chem.* **2015**, *87*, 1051−1069.
(44) Fried, D. I.; Bednarski, D.; Dreifke, M.; Brieler, F. J.; Thommes, M.; Fröba, M. Influence of the hydrophilic−hydrophobic contrast of porous surfaces on the enzymatic performance. *J. Mater. Chem. B* **2015**, *3*, 2341−2349.
(45) Thommes, M.; Mitchell, S.; Perez-Ramirez, J. Surface and pore structure assessment of hierarchical MFI zeolites by advanced water and argon sorption studies. *J. Phys. Chem. C* **2012**, *116*, 18816−18823.
(46) Thommes, M.; Morell, J.; Cychosz, K. A.; Fröba, M. Combining nitrogen, argon, and water adsorption for advanced characterization of ordered mesoporous carbons (CMKs) and periodic mesoporous organosilicas (PMOs). *Langmuir* **2013**, *29*, 14893−14902.
(47) Dippel, A.-C.; Liermann, H.-P.; Delitz, J. T.; Walter, P.; Schulte-Schrepping, H.; Seeck, O. H.; Franz, H. Beamline P02. 1 at PETRA III for high-resolution and high-energy powder diffraction. *J. Synchrotron Radiat.* **2015**, *22*, 675−687.
(48) Amann-Winkel, K.; Bellissent-Funel, M.-C.; Bove, L. E.; Loerting, T.; Nilsson, A.; Paciaroni, A.; Schlesinger, D.; Skinner, L. X-ray and neutron scattering of water. *Chem. Rev.* **2016**, *116*, 7570−7589.
(49) Juhás, P.; Davis, T.; Farrow, C. L.; Billinge, S. J. PDFgetX3: a rapid and highly automatable program for processing powder diffraction data into total scattering pair distribution functions. *J. Appl. Crystallogr.* **2013**, *46*, 560−566.
(50) Egami, T.; Billinge, S. J. *Underneath the Bragg peaks: Structural Analysis of Complex Materials*; Newnes, 2012. Chapter 5.
(51) Sellberg, J. A.; Huang, C.; McQueen, T. A.; Loh, N.; Laksmono, H.; Schlesinger, D.; Sierra, R.; Nordlund, D.; Hampton, C.; Starodub, D.; et al. Ultrafast X-ray probing of water structure below the homogeneous ice nucleation temperature. *Nature* **2014**, *510*, 381−384.
(52) Benmore, C.; Gallington, L. C.; Soignard, E. Intermediate range order in supercooled water. *Mol. Phys.* **2019**, *117*, 2470−2476.
(53) Mariedahl, D.; Perakis, F.; Späh, A.; Pathak, H.; Kim, K. H.; Camisasca, G.; Schlesinger, D.; Benmore, C.; Pettersson, L. G. M.; Nilsson, A.; et al. X-ray scattering and O−O pair-distribution functions of amorphous ices. *J. Phys. Chem. B* **2018**, *122*, 7616−7624.
(54) Pathak, H.; Späh, A.; Kim, K. H.; Tsironi, I.; Mariedahl, D.; Blanco, M.; Huotari, S.; Honkimäki, V.; Nilsson, A. Intermediate range O−O correlations in supercooled water down to 235 K. *J. Chem. Phys.* **2019**, *150*, 224506.
(55) Yoshida, K.; Yamaguchi, T.; Kittaka, S.; Bellissent-Funel, M.-C.; Fouquet, P. Thermodynamic, structural, and dynamic properties of supercooled water confined in mesoporous MCM-41 studied with calorimetric, neutron diffraction, and neutron spin echo measurements. *J. Chem. Phys.* **2008**, *129*, 054702.
(56) Kamitakahara, W. A.; Faraone, A.; Liu, K.-H.; Mou, C.-Y. Temperature dependence of structure and density for D2O confined in MCM-41-S. *J. Phys.: Condens. Matter* **2012**, *24*, 064106.
(57) Bowron, D.; Finney, J.; Hallbrucker, A.; Kohl, I.; Loerting, T.; Mayer, E.; Soper, A. The local and intermediate range structures of the five amorphous ices at 80K and ambient pressure: A Faber-Ziman and Bhatia-Thornton analysis. *J. Chem. Phys.* **2006**, *125*, 194502.
(58) Shi, R.; Tanaka, H. Direct evidence in the scattering function for the coexistence of two types of local structures in liquid water. *J. Am. Chem. Soc.* **2020**, *142*, 2868−2875.
(59) Mancinelli, R.; Imberti, S.; Soper, A.; Liu, K.; Mou, C.; Bruni, F.; Ricci, M. A. Multiscale approach to the structural study of water confined in MCM41. *J. Phys. Chem. B* **2009**, *113*, 16169−16177.
(60) Erko, M.; Wallacher, D.; Paris, O. Deformation mechanism of nanoporous materials upon water freezing and melting. *Appl. Phys. Lett.* **2012**, *101*, 181905.
(61) Skinner, L. B.; Benmore, C.; Neuefeind, J. C.; Parise, J. B. The structure of water around the compressibility minimum. *J. Chem. Phys.* **2014**, *141*, 214507.

https://doi.org/10.1021/acs.jpcc.3c06491
J. Phys. Chem. C 2024, 128, 499−507

5.4. Colossal Effect of Nanopore Surface Ionic Charge on the Dynamics of Confined Water

Armin Mozhdehei, **Philip Lenz**, Stella Gries, Sophia-Marie Meinert, Ronan Lefort, Jean-Marc Zanotti, Quentin Berrod, Markus Appel, Mark Busch, Patrick Huber*, Michael Fröba*, Denis Morineau.

Synopsis

In the water adsorption study, materials with a charged surface, such as the *N*-MBTEVP^{+}I^{-}-PMO, showed distinct effects on the adsorbed layer. In addition, water confined in the non-functionalized precursor (BTEVP-PMO) showed pronounced structural deviations compared to bulk water. To gain insight into the impact of surface charge on water dynamics, nanoconfined water in *N*-MBTEVP^{+}I^{-}-PMO was compared to that in its neutral counterpart (BTEVP-PMO) on picosecond to nanosecond timescales using quasielastic neutron scattering (QENS). The measurements were performed on the spectrometers SHARP and IN16B at the Institut Laue-Langevin (ILL) in Grenoble (France). The samples were prepared with different water filling degrees and measured at temperatures between 245 and 300 K.

Analysis of the QENS data for fully water-filled PMOs revealed a moderate influence of BTEVP-PMO on the diffusion coefficient compared to bulk water, particularly at higher temperatures. The residence time of water in BTEVP-PMO was found to be higher than in bulk water and in the more hydrophobic divinylbenzene-bridged PMOs, which can be attributed to the additional hydration site at the pyridine group of BTEVP-PMO in addition to the silanol groups. For water confined in the charged *N*-MBTEVP^{+}I^{-}-PMO, a significant slowdown of the dynamics was observed. Compared to bulk water, the residence time increased by approximately one order of magnitude, while the translational diffusion coefficient decreased by a factor of four. Furthermore, comparison of fully and partially filled PMOs revealed that the surface charge influences not only interfacial water but also water in the pore center.

The author of this PhD thesis, who is also a co-author of the publication (Philip Lenz), actively participated in the QENS measurements at the Institut Laue-Langevin, synthesized all PMO samples used in the study, and characterized them with respect to their porosity and structure. Furthermore, he was involved in the discussion of the observed dynamical behavior of water confined in the different PMOs.

THE JOURNAL OF PHYSICAL CHEMISTRY C
A JOURNAL OF THE AMERICAN CHEMICAL SOCIETY

pubs.acs.org/JPCC

Article

Colossal Effect of Nanopore Surface Ionic Charge on the Dynamics of Confined Water

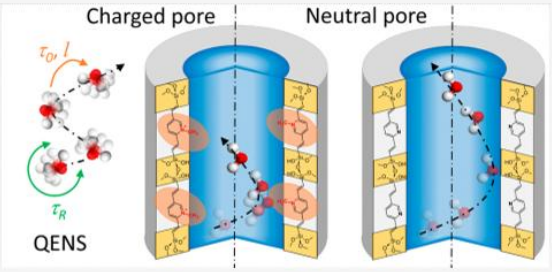
Armin Mozhdehei, Philip Lenz, Stella Gries, Sophia-Marie Meinert, Ronan Lefort, Jean-Marc Zanotti, Quentin Berrod, Markus Appel, Mark Busch, Patrick Huber,* Michael Fröba,* and Denis Morineau*

Cite This: J. Phys. Chem. C 2025, 129, 18311−18324

Read Online

ACCESS | Metrics & More | Article Recommendations | Supporting Information

ABSTRACT: Interfacial interactions significantly alter the fundamental properties of water confined in mesoporous structures with crucial implications for geological, physicochemical, and biological processes. Herein, we focused on the effect of changing the surface ionic charge of nanopores with comparable pore sizes (3.5−3.8 nm) on the dynamics of confined liquid water. The control of the pore surface ionicity was achieved by using two periodic mesoporous organosilicas (PMOs) containing either neutral or charged forms of a chemically similar bridging unit. The effect on the dynamics of water at the nanoscale was investigated in the temperature range 245−300 K, encompassing the glass transition by incoherent quasi-elastic neutron scattering (QENS). For both types of PMOs, the water dynamics revealed two distinct types of molecular motions: rapid local movements and translational jump diffusion. While the neutral PMO induces a moderate confinement effect, we show that the charged PMO drastically slows down water dynamics, reducing translational diffusion by a factor of 4 and increasing the residence time by an order of magnitude. Notably, by changing the pore filling values, we demonstrate that for charged PMOs, this effect extends beyond the interfacial layer of surface-bound water molecules to encompass the entire pore volume. Thus, our observation indicates a dramatic change in the long-range character of the interaction of water confined in nanopores with surface ionic charge compared to a simple change in hydrophilicity. This is relevant for the understanding of a broad variety of applications in (nano)technological phenomena and processes such as nanofiltration and membrane design.



Downloaded via UNIV HAMBURG on March 11, 2026 at 10:45:12 (UTC).
See https://pubs.acs.org/sharingguidelines for options on how to legitimately share published articles.

1. INTRODUCTION

Water is fundamental to life, and albeit a simple molecule, it exhibits unique and complex behavior that remains a subject of intense scientific investigations. Water's remarkable properties, such as its high heat capacity, anomalous density behavior, and complex hydrogen-bonding network, become even more pronounced when it is confined within small pores.[1−3] In this regard, the behavior of water confined in mesoporous materials has been extensively studied due to its implications in numerous scientific and industrial fields, such as capillarity-driven water transport,[4] catalysis,[5−7] energy storage,[8−11] nanofiltration,[12] and environmental remediation.[13] Unlike bulk water, water confined in nanoscale environments exhibits unique structural and dynamical properties due to spatial constraints, surface interactions, and changes in hydrogen-bond networks.[14−17] Studies by Gallo et al. and Debenedetti and Stillinger have shown that these properties are significantly altered under confinement, where the interactions between water molecules and the surrounding surfaces lead to deviations from bulk behavior.[18,19] In confined systems, water can form distinct layers with different structural and dynamic characteristics depending on its proximity to the pore walls. The molecules closest to the surface often exhibit reduced mobility due to stronger hydrogen-bonding interactions with surface functional groups, while molecules located toward the center of the pore may retain more bulk-like behavior.[20,21] As a whole, these studies indicate that the influence of nanoporous confinement on the water properties arises from the complex interplay of different effects, such as low-dimensionality, spatial restriction, and surface interaction.

Mesoporous silica materials, such as MCM-41 and SBA-15, and periodic mesoporous organosilicas (PMOs)[22] provide ideal model systems for exploring how confinement and surface chemistry (i.e., surface charge, surface polarity, hydrophilicity/hydrophobicity, and so forth) influence water dynamics. These materials are characterized by their tunable pore sizes, well-defined geometries, and versatile surface

Received: July 11, 2025
Revised: September 13, 2025
Accepted: September 18, 2025
Published: September 29, 2025



ACS Publications

© 2025 The Authors. Published by American Chemical Society

https://doi.org/10.1021/acs.jpcc.5c04787
J. Phys. Chem. C 2025, 129, 18311−18324

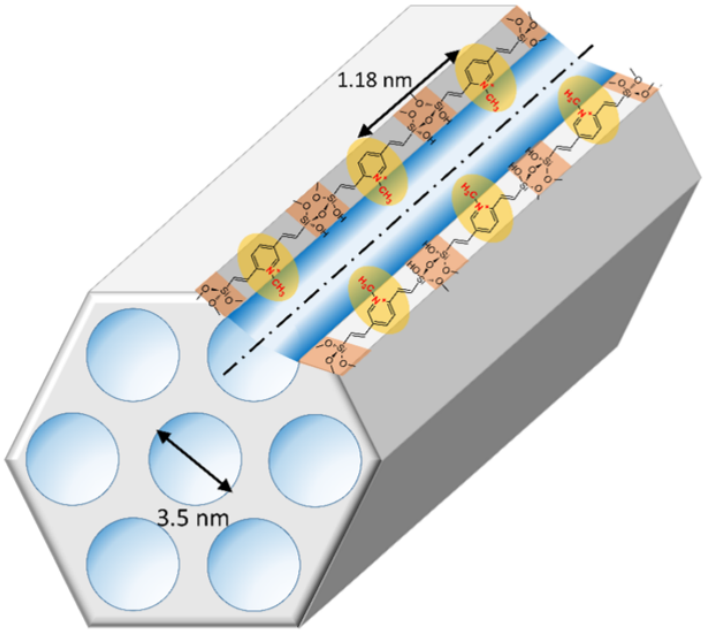


Figure 1. Illustration of the PMO DVMeP-PMO illustrating the hexagonal arrangement of monodisperse cylindrical pores (D = 3.5 nm) with a periodic repetition (c = 1.18 nm) of silica units (orange) and ionically charged divinyl-methylpyridinium units (yellow) along the pore axis.

chemistries, allowing researchers to systematically study the impact of surface interactions on confined water.[23−28] Jani et al., by doing quasi-elastic neutron scattering (QENS) measurements, demonstrated that modifying the hydrophilicity of the pore walls can significantly influence water mobility. In hydrophilic MCM-41, water molecules form strong hydrogen bonds with silanol groups on the surface, resulting in a slower diffusion and rotational dynamics. Conversely, hydrophobic PMOs, which contain organic bridging units like benzene, reduce surface water interactions, allowing water to behave more similarly to its bulk counterpart.[25] Moreover, Malfait et al. further expanded these findings by investigating the role of surface chemistry in shaping the rotational dynamics of water confined in PMOs. Using techniques such as Raman spectroscopy and dielectric relaxation spectroscopy, they revealed that water near hydrophilic surfaces tends to form a more structured hydrogen-bond network, whereas water near hydrophobic surfaces is less constrained and thus more dynamic.[29,30]

The complexity of water behavior in bulk and confined spaces increases when ions are present.[23,26,31,32] Previous studies have explored this phenomenon in aqueous electrolytic solutions confined to porous silica. The researchers demonstrated how cation−silica surface interactions affect water dynamics, finding that the type of ion (e.g., kosmotropic vs chaotropic) plays a significant role in determining water mobility within nanoconfined systems. Kosmotropic ions, such as Li^+, enhance water structuring near surfaces, thereby reducing diffusion rates, whereas chaotropic ions like Cs^+ have a lesser impact on water dynamics, allowing for faster molecular motion. These findings have significant implications for optimizing technologies like energy storage in batteries, fluid transport in nanofiltration, or electrosorption-induced actuation,[33,34] where electrolyte behavior under confinement is critical for performance.

Building on these foundational studies, the present work addresses a focused version of a broader question: how does confinement within ionically charged porous media influence water dynamics? To explore this in a controlled way, we used a model system of PMOs with identical pore structures but with either neutral or ionically charged inner surfaces. Using quasi-elastic neutron scattering (QENS), we systematically probe the translational dynamics of water confined in these two materials. Our findings reveal a pronounced effect of surface charge on water mobility, even beyond the 2−3 interfacial layers. Although limited to a single specific ionically charged PMO system, these results significantly expand the current understanding of confined water, which so far has been mainly based on neutral hydrophilic or hydrophobic surfaces.

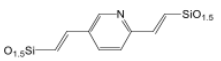
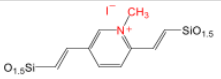
2. MATERIALS AND METHODS

2.1. Samples. Two different PMO powders with comparable porous geometry but different surface chemistries were prepared. The first one, termed DVP-PMO, is a divinylpyridine-bridged PMO, which presents an essentially neutral pore surface. The second one, referred to as DVMeP-PMO, is a divinyl-methylpyridinium-bridged PMO, which presents a positively charged pore surface induced by the presence of pyridinium cations. This charged porous material was derived from the postsynthetic modification of DVP-PMO using methyl iodide (MeI).

The structure of the two PMOs can be described as a regular hexagonal lattice of parallel and cylindrical channels, conforming to a honeycomb structure like MCM-41 porous silicas, as schematized in Figure 1. In contrast, the pore walls of the PMO's feature organic units bridging inorganic silica units, which alternate periodically along the main pore axis. The

https://doi.org/10.1021/acs.jpcc.5c04787
J. Phys. Chem. C 2025, 129, 18311−18324

Table 1. Structural Parameters of the Neutral (DVP-PMO) and Charged (DVMeP-PMO) Mesoporous Matrices

Name	Bridging unit name	Bridging unit	Periodic distance along the pore axis (nm) [a]	Pore volume ($cm^3.g^{-1}$) [b]	Specific Surface Area ($m^2.g^{-1}$) [b]	Pore diameter (nm)
DVP-PMO	Divinyl-pyridine		1.18	0.748	740	3.8
DVMeP-PMO	Divinyl-methyl pyridinium		1.18	0.518	704	3.5

[a]Evaluated from the (00*l*) Bragg reflections (see the Supporting Information). [b]Evaluated from the nitrogen physisorption isotherms (see the Supporting Information).

molecular-scale periodicity of the arrangement of organic/silica units along the pore axis is demonstrated by (00*l*) Bragg reflections, while, like for MCM-41, the hexagonal in-plan arrangement of porous channels is demonstrated by (*hk*0) Bragg reflections.

A detailed description of the synthesis methods, as well as the characterization methods that include powder X-ray diffraction and nitrogen physisorption experiments, is provided in the Supporting Information (Figures S1 and S2). Remarkably, the Bragg reflections observed by X-ray diffraction have no significant counterpart in the neutron scattering intensity, which is dominated by incoherent scattering of hydrogen atoms (Figure S3), except for the most intense (100) Bragg peak that is observable at the lowest Q-position of the QENS instrument. This is an asset for QENS experiments to separate the water and matrix contributions to the total scattering intensity of water-filled PMOs.

The structural parameters of the matrices are summarized in Table 1. Although differing in ionic charges, the two bridging units have a similar geometry, as confirmed by the same value of the repetition distance (1.18 nm) along the pore axis. Small differences in the porous geometry are reflected by a reduction of the pore volume, surface, and pore diameter by about 10% from 3.8 to 3.5 nm when comparing DVMeP-PMO to DVP-PMO. This is attributed to the presence of the additional methyl group and the counterion.

All matrices were first dried under vacuum at 120 °C for a minimum of 24 h. For the preparation of hydrated matrices, a consistent amount of mesoporous material was placed in a flat aluminum rectangular cell (1 mm thick) and positioned in a desiccator alongside a beaker containing a saturated aqueous solution of NaCl or $MgCl_2$. The resulting relative humidities (RH) were 33% for $MgCl_2$ and 75% for NaCl at 25 °C. The 75% RH exceeded the partial pressure for capillary condensation, ensuring the complete filling of the pore system, while the 33% RH is below the onset of capillary condensation, resulting in water being adsorbed onto the pore surfaces without filling the pore centers (partially filled condition). The samples were maintained in these constant humidity environments for 24 h to ensure equilibrium was reached. Afterward, the cells were sealed with indium wire to prevent water loss and maintain a stable hydration level throughout the neutron scattering experiments.

2.2. Quasi-elastic Neutron Scattering (QENS) Measurements. Quasi-elastic neutron scattering (QENS) experiments were performed on two different spectrometers, SHARP and IN16B at the Institut Laue-Langevin (ILL, Grenoble, France), to be able to probe a wide range of time scales, from ps to ns. Measurements were carried out on two different PMO powders with comparable pore geometry but different surface chemistries.

QENS methods allow measurement of the incoherent neutron scattering intensity $I(Q, \omega, T)$ as a function of momentum transfer Q, energy transfer $E = \hbar\omega$, and temperature T. The accessible length scale determined by Q is typically in the nanometer range. The accessible time scale is bounded between two limits determined by the energy resolution of the instrument δE and by its dynamical range ΔE. The latter two parameters can vary by orders of magnitude depending on the instrument. Finally, it should be noted that two complementary types of acquisition can be used: either a series of QENS spectra $I(Q, \omega)$ are acquired at fixed temperatures T, or the intensity is acquired at a fixed energy $\hbar\omega$ while the temperature is continuously ramped. The second approach can be applied either at zero energy transfer and denoted as elastic fixed window scan (EFWS) or at a fixed energy offset $\hbar\omega_{offset}$ and denoted as inelastic fixed window scan (IFWS). Bearing in mind that the instrumental energy resolution δE is finite, EFWS does not measure purely elastic scattering but rather the fraction of scattered intensity that appears at an energy lower than δE, i.e., $I\left(Q, \omega < \left(\frac{\delta E}{\hbar}\right), T\right)$. As such, it normally increases as the dynamics slows on cooling. Conversely, for IFWS, $I(Q, \omega_{offset}, T)$ should exhibit a maximum around the temperature at which the typical time of the sample dynamics coincides with the time scale selected by the energy offset.

The cold neutron time-focusing time-of-flight spectrometer SHARP was used with an incident wavelength of 5.12 Å, providing an energy resolution (δE) at the elastic peak of approximately 70 μeV (fwhm), corresponding to a typical time scale ($t = \hbar/\delta E$) of about 10 ps and covering a Q-range from 0.2 $Å^{-1}$ to 2.0 $Å^{-1}$. It is ideally suited to measuring the fast water translational and local (e.g., rotational) dynamics.

Complementing SHARP's setup, the neutron backscattering spectrometer IN16B at ILL provided a higher resolution (by about a factor of 100) suitable for slower translational dynamics. IN16B's backscattering configuration, using an unpolished Si(111) monochromator and analyzers, was set to an incident wavelength of 6.27 Å, giving an energy resolution of δE = 0.75 μeV and a time scale of around 1 ns. IN16B's measurements covered an energy transfer range ΔE of ±30 μeV and a Q-range between 0.19 $Å^{-1}$ and 1.84 $Å^{-1}$. IN16B's background chopper was operated in high signal-to-noise mode to enhance data quality.[35]

https://doi.org/10.1021/acs.jpcc.5c04787
J. Phys. Chem. C 2025, 129, 18311−18324

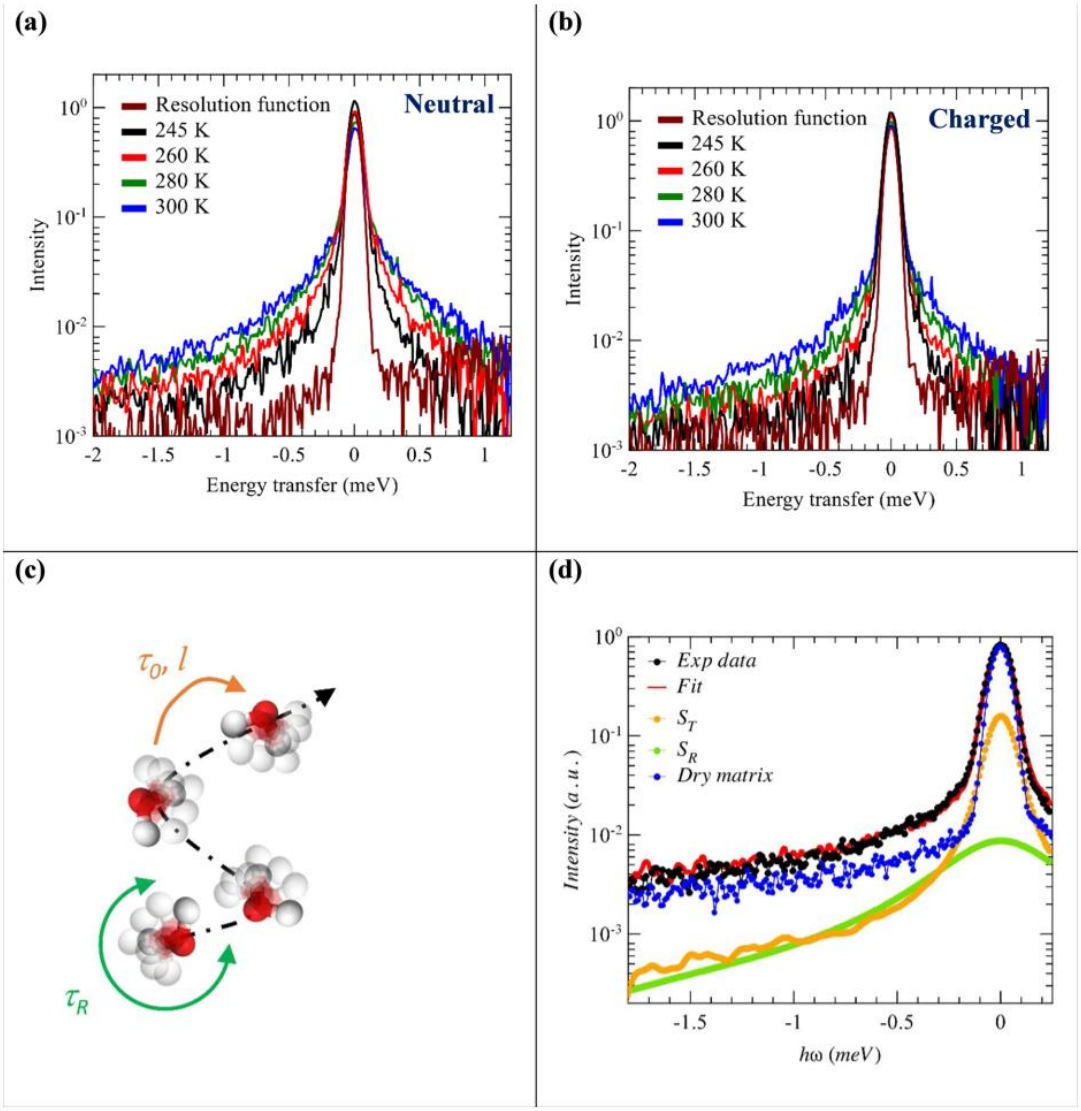


Figure 2. QENS spectra recorded on SHARP at Q = 1.5 Å^{-1} illustrate the temperature-dependent scattering intensity of water-filled (a) neutral DVP-PMO and (b) charged DVMeP-PMO. (c) Illustration of the water dynamics probed by QENS and modeled by the combination of a fast local rotation with associated correlation time τ_R and a slower jump translation diffusion with associated residence time τ_0 and jump length l. (d) Representative experimental (black) and fitted (red) scattering intensity $I(Q, \omega)$ curves at T = 280 K and Q = 1.5 Å^{-1}, modeled using two Lorentzian functions added to the dry matrices, for water-filled charged DVMeP-PMO acquired by SHARP.

In both cases, temperature control was achieved with an ILL cryofurnace. Measurements on water-filled PMOs were collected sequentially on cooling to different target temperatures: 300, 280, 260, and 245 K on SHARP and 278, 258, and 243 K on IN16B. On SHARP, both the ionically charged DVMeP-PMO and neutral DVP-PMO were studied after their porosity was completely filled with water at 75% RH. On IN16B, the study was focused on the ionically charged matrix DVMeP-PMO, at 33% and 75% RH, allowing a specific investigation of the effect of the filling fraction. Moreover, for water-filled DVMeP-PMO (75% RH), fixed window scans (FWS) were acquired in the temperature range 195−300 K on the elastic line with Doppler drive at rest (EFWS) and at the inelastic energy offset value of 3 μeV (IFWS).[36] EFWS and IFWS probe distinct dynamical regimes: EFWS quantifies the immobile fraction of water that corresponds to energy transfer smaller than δE (i.e., purely elastic contributions and motions with typical time exceeding 1 ns), while IFWS detects slow motions as their inverse typical time matches with the inverse offset-energy (e.g., translational diffusion). On both instruments, the quasi-elastic spectra of the corresponding dried porous samples were additionally recorded as references.

Data were processed using the MANTID software,[37] which applied corrections for detector efficiency and background contributions from the empty cell and spectrometer, to determine the scattering intensity $I(Q, \omega)$. The dynamic

https://doi.org/10.1021/acs.jpcc.5c04787
J. Phys. Chem. C 2025, 129, 18311−18324

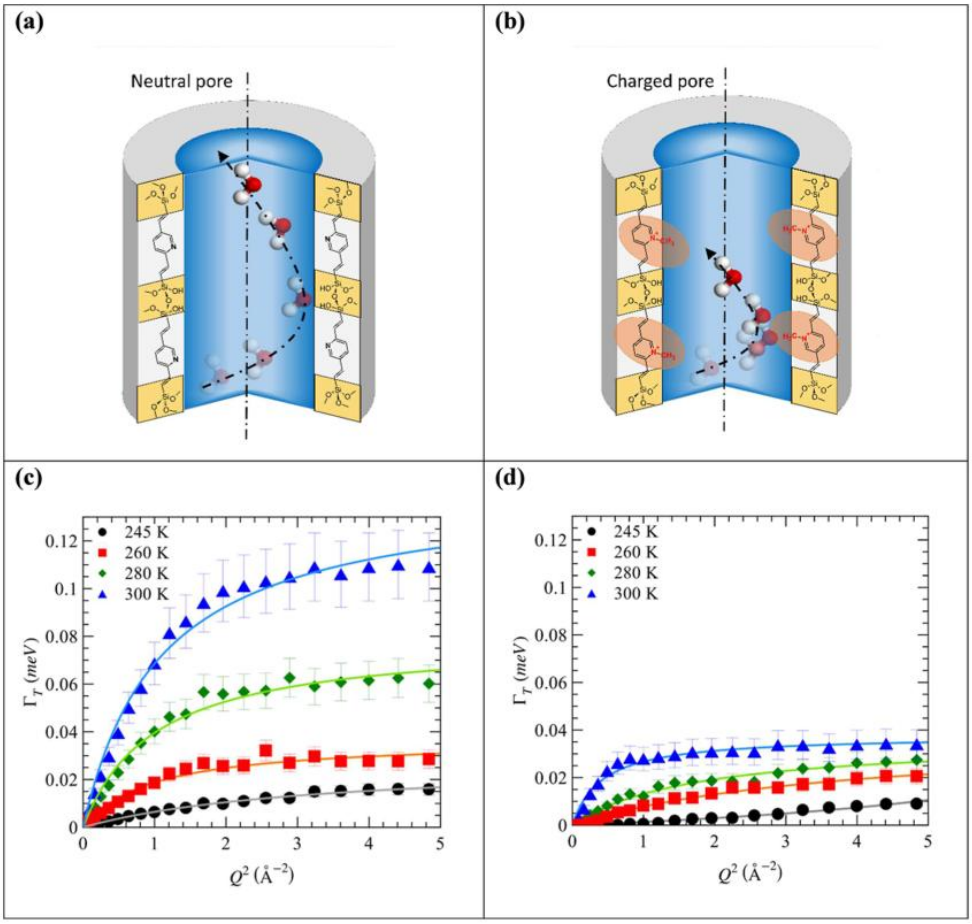


Figure 3. Illustration of the trajectory of water in (a) neutral DVP-PMO and (b) charged DVMeP-PMO, indicating the much longer residence time in the latter case, resulting in a significant slowdown of translational diffusion. Evolution of the half-width at half-maximum of the sharp Lorentzian (Γ_T) as a function of Q^2, obtained from the fitting of QENS spectra recorded on SHARP for water confined in (c) neutral DVP-PMO and (d) charged DVMeP-PMO at four different temperatures. The fits using the jump-diffusion model are shown as solid lines.

structure factor of confined water, $S^{water}(Q, \omega)$, was then fitted to the experimental intensity in the frequency domain using QENSH software from Laboratoire Léon Brillouin (LLB, Saclay, France), enabling detailed interpretation of the dynamic behavior under varied temperature and humidity conditions.

3. RESULTS AND DISCUSSION

3.1. Effect of the Surface Charge on the Water Dynamics—Neutron Time-of-Flight Study. We first consider the influence of the chemical nature of the PMO's pore surface (i.e., neutral vs charged) on the dynamics of water at full loading (i.e., 75% RH). Figure 2a–d illustrates the temperature dependence of neutron scattering intensity of the two different water-filled PMOs at a representative momentum transfer Q = 1.5 Å^{-1} for a selected range of energy transfer from −2 to +1.3 meV. From a qualitative point of view, as the temperature decreases from 300 to 245 K, the quasi-elastic line continuously sharpens. Since the width of quasi-elastic scattering is inversely related to the time scale of particle motion, this sharpening indicates that water dynamics slows down with cooling. Also, the absence of a sharp increment in the elastic signal confirms that the water remained in a liquid state across the studied temperature range. By comparing the two panels of Figure 2, it is evident that the water inside the ionically charged DVMeP-PMO has a sharper quasi-elastic line than that inside the neutral DVP-PMO, indicating slower water dynamics.

The scattering intensity of the water-filled matrix, $I^{water\ filled}(Q, \omega)$, was fitted at each individual Q by a model that was the sum of the scattering intensity from the matrix, corresponding to the experimental intensity of the dry matrix $I^{dry}(Q, \omega)$, and the scattering from the confined water convoluted by the instrumental resolution function $R(Q, \omega)$. A detailed description of the underlying theoretical model and the fitting procedure is provided as the Supporting Information.

In agreement with the approach of recent studies on confined water in MCM-41 and PMOs with different surface functionalities,[25] we found that the dynamic structure factor of water $S^{water}(Q, \omega)$ could be modeled by the combination of two distinct motions: a slow translational diffusion (T) and a

https://doi.org/10.1021/acs.jpcc.5c04787
J. Phys. Chem. C 2025, 129, 18311−18324

Table 2. Fit Parameters D_T, τ_0, and l Obtained by Fitting of $\Gamma_T(Q^2)$ Using the Jump-Diffusion Model for Data Acquired by SHARP

	neutral			charged			bulk		
T (K)	D_T (10^{-9} m^2/s)	τ_0 (ps)	l (Å)	D_T (10^{-9} m^2/s)	τ_0 (ps)	l (Å)	D_T (10^{-9} m^2/s)	τ_0 (ps)	l (Å)
245	0.13 ± 0.01	36 ± 2	1.7	0.03 ± 0.002			0.42	22.7	2.4
260	0.49 ± 0.06	27 ± 1.5	2.8	0.15 ± 0.01	41 ± 2	1.9	0.56	8.9	1.7
280	1.11 ± 0.09	13 ± 0.5	2.9	0.31 ± 0.02	32.5 ± 1.5	2.5	1.3	2.3	1.3
300	1.76 ± 0.13	7.0 ± 0.3	2.7	0.6 ± 0.15	20.5 ± 1	2.7	2.3	1.1	1.2

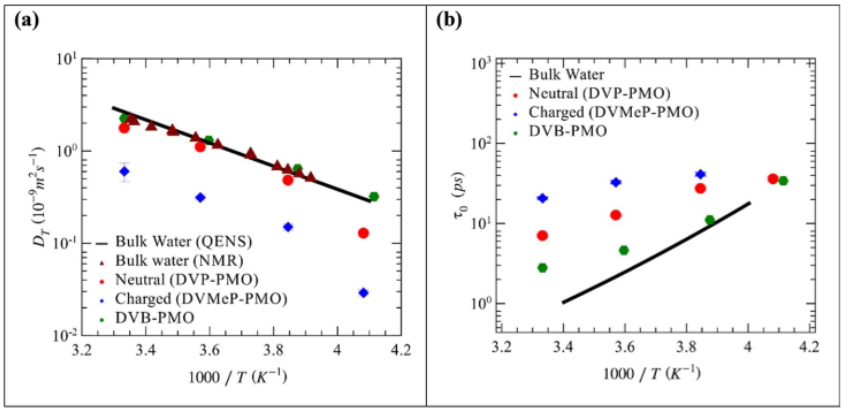


Figure 4. (a) Translational diffusion coefficient (D_T) of water and (b) residence time (τ_0) of water, evaluated from the fit of SHARP spectra using the jump-diffusion model, for water confined in neutral (red circle) and charged (blue diamond) PMOs as a function of the inverse temperature. For comparison, QENS data for bulk water from Teixeira et al.[38] and NMR diffusion coefficients from Price et al.[40] are presented alongside QENS data for DVB-PMO from Jani et al.[25] Adapted with permission from [Teixeira et al., 1985]. Copyright [1985] American Physical Society. Adapted from Price et al., 1999]. Copyright [1999] American Chemical Society.

faster local rotation-like motion (R). We defined $S_T(Q, \omega)$ and $S_R(Q, \omega)$ as the dynamic structure factors of these motions. The diffusive motion was modeled by a Lorentzian quasi-elastic term

$$S_T(Q, \omega) = L_T(Q, \omega) \quad (1)$$

while the second motion comprised both an elastic and an inelastic term due to its localized character

$$S_R(Q, \omega) = A(Q)\delta(\omega) + (1 - A(Q))L_R(Q, \omega) \quad (2)$$

The spectral widths of these two motions (HWHM) are noted as $\Gamma_T(Q)$ and $\Gamma_R(Q)$, respectively, and $A(Q)$ is the elastic incoherent structure factor (EISF) of the local dynamics.

The relative contribution of the broadest component (L_R) to $S^{water}(Q, \omega)$ was found to be negligible at low-Q, and even at room temperature, it could be determined accurately only for values of the transfer of momentum larger than Q = 1.2 Å^{-1}. This is fully consistent with the localized nature of the associated motion, leading to a large value of the corresponding EISF $A(Q)$, which eventually approaches unity at small values of Q. In this situation, the intensity of the quasi-elastic component (second term of eq 2) vanishes, and only the elastic term persists. The EISF is directly related to the spatial trajectory of the motion. In the classical model of water proposed by Teixeira et al., the local hydrogen dynamics are described as isotropic rotations around the oxygen atom. The associated EISF is given by $A_R(Q) = [j_0(QR_R)]^2$, where j_0 denotes the zeroth-order spherical Bessel function and R_R = 0.98 Å represents the length of the O−H bond.[38]

For water confined in neutral and charged PMOs, this classical model only showed good agreement with experimental data at high temperature (300 K) and in the high Q range (see Figure S5). By decreasing the temperature, the measured EISFs were consistently higher than this theoretical model, indicating that hydrogen trajectories are more spatially restricted than expected for free rotational motions. This means that the broad quasi-elastic line cannot be solely attributed to isotropic rotational diffusion but rather interpreted in terms of restricted rotation or librational motion. The associated correlation time, as determined by the inverse half-width at half-maximum (HWHM) of the broad Lorentzian component (Γ_R), is on the order of 1−3 ps (Figure S7), which is in line with previous studies on confined water.[25] Compared to DVP-PMO, the local dynamics of water filled in charged DVMeP-PMO appeared slower (Γ_R smaller by about a factor of 1.5−2) and spatially more restricted with larger EISF as illustrated in Figure S6. This can be related to the strengthening of the water surface interaction through hydrogen bonds and solvation in the ionically charged PMO compared to its neutral counterpart.

We now consider the most significant component of the dynamic structure factor in the studied range of temperature, energy, and transfer of momentum, which is the first Lorentzian term, $L_T(Q, \omega)$, attributed to translation dynamics, as sketched in Figure 3a,b. The temperature dependence of its HWHM(Γ_T) as a function of Q^2 is illustrated in Figure 3c,d. A direct visual comparison of the two panels obviously demonstrates that the water dynamics in the charged DVMeP-PMO is significantly reduced compared to those in

https://doi.org/10.1021/acs.jpcc.5c04787
J. Phys. Chem. C 2025, 129, 18311−18324

the water-filled neutral DVP-PMO. This striking slowdown induced by different surface chemistry is accompanied by a systematic reduction in mobility with decreasing temperature.

For most of the data, $\Gamma_T(Q^2)$ exhibits an initial linear evolution at low Q^2, followed by a deviation at higher Q^2 values upon reaching a plateau. In fact, the initial linear increase in $\Gamma_T(Q^2)$ with Q^2 reflects diffusive motion, which is in agreement with Fickian behavior and also consistent with the absence of an elastic term that would have indicated that diffusion was spatially restricted on these specific time and length scales. Conversely, in the high Q accessible range, $\Gamma_T(Q^2)$ deviated from Fickian behavior and reached a plateau. This indicates that translation motions are discontinuous at the molecular scale. This plateau is more pronounced in the charged PMO due to longer residence times, as expected from strong water−surface interactions. This behavior is consistent with previous findings regarding the water dynamics in nanoconfined media.[25,26,38] It is well-described by a jump-diffusion model, suggesting that the translational motion of water molecules is intermittently interrupted by localized residence times. To quantitatively describe this behavior, we fitted the data using the Singwi and Sjölander (SS) model, which assumes an exponential distribution of jump lengths.[39] According to this model, the Q^2-dependence of Γ_T is given by

$$\Gamma_T = \frac{D_T Q^2}{1 + D_T Q^2 \tau_0} \tag{4}$$

where τ_0 is the residence time between jumps and D_T is the translational diffusion coefficient.

The fitting parameters are summarized in Table 2. As shown in Figure 4a, the results in their Arrhenius plot indicate that across all temperatures, the diffusion coefficient D_T for water confined within neutral PMOs is only slightly smaller than that of bulk water, especially at 300 K (1.76×10^{-9} m^2/s vs 2.3×10^{-9} m^2/s). This moderated effect of confinement aligns with previous observations made for another nonionic PMO, denoted as DVB-PMO in Figure 4a, which presents a pore geometry comparable to DVP-PMO but a more hydrophobic character conveyed by divinylbenzene bridging units.[25] Moreover, Figure 4b shows that the residence time τ_0 is prolonged for water in neutral DVP-PMO compared to bulk water at the same temperature (7 ps vs 1.1 ps at 300 K for bulk water). This increase in residence time is slightly larger than previously reported for water confined in DVB-PMO. This difference is compatible with the existence of interfacial H-bonds between water and the pyridine group for DVP-PMO, which is absent for DVB-PMO.

From this viewpoint, the situation encountered for divinyl-pyridine shares a similarity with that reported for the hydrophilic divinyl-aniline-bridged PMO (DVA-PMO) by Jani et al.[25] In the latter case, it was found that the amino groups of the bridging units acted as secondary H-bonding sites for interfacial water molecules in addition to the silanols of the silica units. This was supported by the NMR observation of strong interfacial correlations between water and both silica and organic units.[28] Also, neutral PMOs prepared using divinyl-pyridine precursors possess a weakly basic surface due to the protonation equilibrium of pyridine groups ($pK_a \approx 5.2$ for pyridine). The partial protonation induces mild electrostatic interactions that have a minimal impact on water diffusion. Therefore, water confined in neutral DVP-PMO retains near-bulk translational diffusion, although it is slightly reduced compared to other neutral PMOs with a higher hydrophobic character, such as DVB-PMO.

A starkly different behavior is observed for water within the ionically charged DVMeP-PMO, where the diffusion coefficient is significantly reduced, approximately by a factor of 4 (i.e., $D_T = 0.6 \times 10^{-9}$ m^2/s at 300 K). More strikingly, the residence time is 1 order of magnitude longer for water confined in charged DVMeP-PMO (i.e., 20.5 ps at 300 K) than for bulk water. This slowdown is considerably larger than the confinement effects observed in the present study for neutral DVP-PMO and for many other water-filled PMOs and silicas with comparable pore size, whatever the hydrophilic character of their surface.[25] It is noteworthy that the 8% reduction in pore size between DVP-PMO (3.8 nm) and DVMeP-PMO (3.5 nm) cannot be considered as a significant reason for the observed slowdown. Indeed, in the QENS study on water confined in two neutral PMOs that presented a difference in pore size of 15%, namely, DVB-PMO (4.1 nm) and BP-PMO (3.5 nm), it was observed only a minor reduction of 10% in the diffusivity and an increase of 50% in the residence time.[25] Therefore, we can conclude that the ionic character of DVMeP-PMO compared to neutral DVP-PMO actually plays a crucial role in the observed slowdown.

The combination of the diffusion coefficient and the residence time can be used to evaluate the mean squared jump length $\langle l^2 \rangle$ that is expressed as

$$\langle l^2 \rangle = 6 D_T \tau_0 \tag{5}$$

The jump length values are in the range of 2 to 3 Å for both PMOs, with no systematic temperature dependence. This is about twice as large as that for bulk water, which suggests that the microscopic mechanism involved in jump diffusion is altered in confined geometry, possibly as a result of a disrupted H-bond network. The most striking observation is that the jump length has comparable values for the neutral and ionically charged PMO, despite very different values of the diffusion coefficient and the residence time. This scale is far smaller than the pore size (~3.5−3.8 nm), meaning that the observed motion reflects local rearrangements within a structured hydrogen-bond network, not long-range diffusion limited by the pore walls. In this picture, the jump itself likely corresponds to a displacement of a water molecule from one local site (i.e., basin) of attraction (a hydrogen-bonded configuration) to another. It suggests that the topology of these local sites does not change drastically between the neutral and charged environments. What differs significantly, however, is the residence time within each site (i.e., how long a water molecule remains in a given local configuration before making a jump). In the charged PMO, electrostatic interactions with the pyridinium groups deepen these sites or raise the energy barriers (i.e., activation energy) between them, leading to longer residence times and, therefore, a reduced diffusion coefficient. In contrast, the neutral PMO allows for more frequent transitions between sites, resulting in a faster diffusion.

In general, the jump-diffusion model predicts that the low-range diffusion coefficient is determined at the microscopic scale both by the typical length between two successive atomic jumps and the residence time that separates these two events. Within this theoretical framework, it can be deduced that the reduction in the translational diffusion of water within charged DVMeP-PMO is primarily due to the huge increase in the residence time. This is indicative of the enhanced electrostatic

https://doi.org/10.1021/acs.jpcc.5c04787
J. Phys. Chem. C 2025, 129, 18311−18324

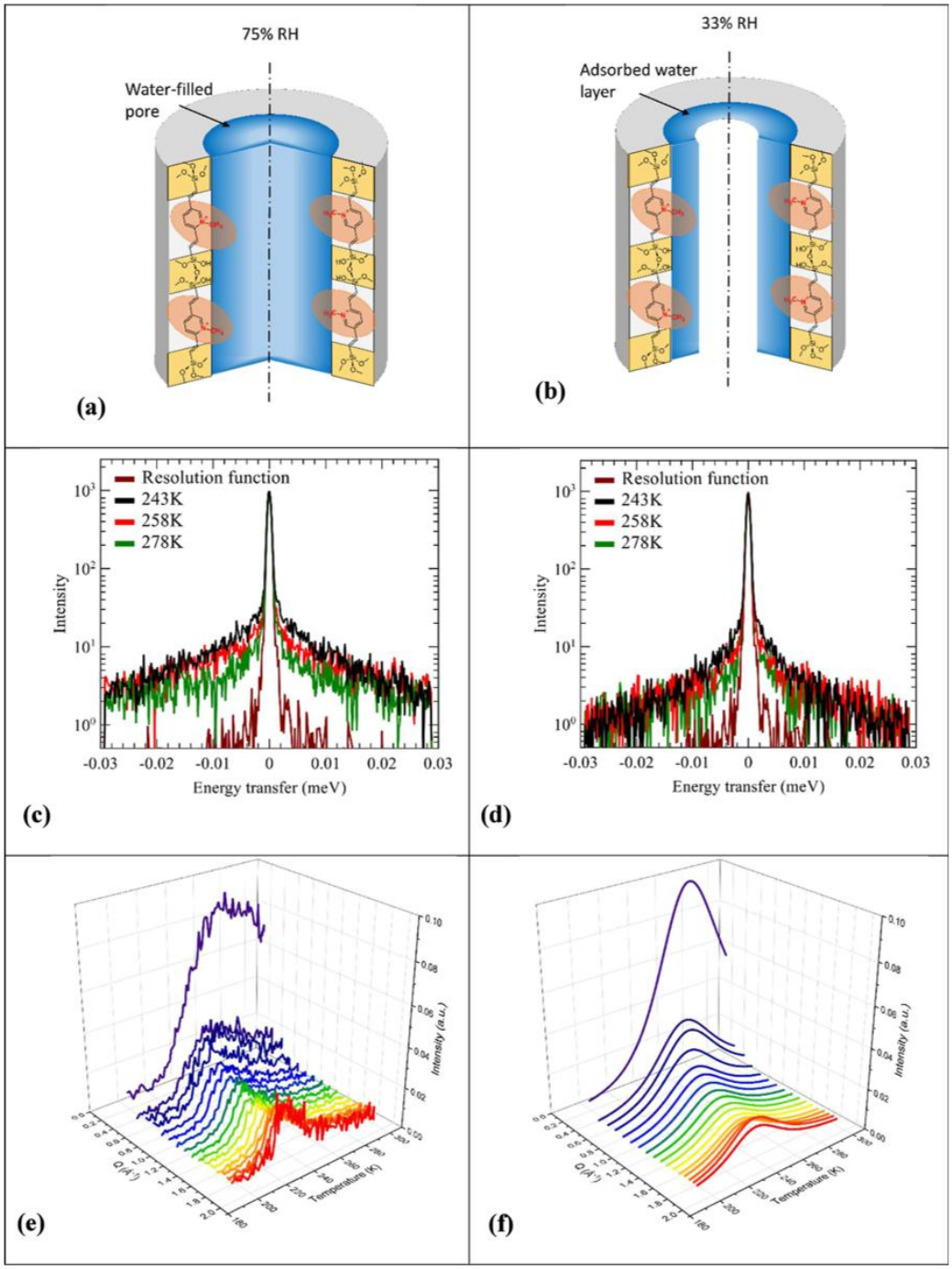


Figure 5. Illustration of (a) fully filled (75% RH) and (b) partially filled (33% RH) charged DVMeP-PMO. QENS spectra of (c) fully filled and (d) partially filled charged DVMeP-PMO recorded on IN16B at $Q = 1.5$ Å^{-1} and three different temperatures. Inelastic FWS (IFWS) for fully filled, charged DVMeP-PMO as a function of temperature and transfer of momentum for $Q \geq 0.3$ Å^{-1}. The experimental intensity (e) and to the corresponding fitted intensity (f).

interactions between the water molecules and the pyridinium groups and the counterion present on the surface of the DVMeP-PMO. On average, the surface charge is balanced by the counterions. However, on the molecular scale, one expects that the dissociation of the pyridinium and iodide ion pairs is enabled by the presence of water. As a result, highly polar and

https://doi.org/10.1021/acs.jpcc.5c04787
J. Phys. Chem. C 2025, 129, 18311−18324

positively charged surface areas are formed around pyridinium groups. They act as strong surface adsorbing sites that strengthen hydrogen bonding and alter the water dynamics. As for the iodine counterion, it is worth noting that a chaotropic effect can also be invoked. In fact, chaotropic ions are expected to weaken the hydrogen-bond network in water and increase the water dynamics.[26] Although the iodide counterion is chaotropic and is expected to promote increased water mobility, our results show a substantial reduction in translational diffusion. This suggests that the dominant factor is actually the strong electrostatic interaction between water and the pyridinium group present at the pore surface, which overcomes the chaotropic effect of the iodine counterion on the water dynamics. Indeed, the existence of ionically charged adsorption sites and the resulting strong electrostatic interactions can favor long-lived interfacial environments that differ from the hydrogen-bonding network of water found under normal conditions. Being more tightly bound to the charged surface, the water molecules exhibit a longer residence time and, therefore, reduced translational mobility.

Whether this conclusion can be generalized to other systems is an open question, which highlights the interest in investing further effort in the design of PMO with different chaotropic or kosmotropic counterions. Indeed, a different situation may be encountered for other counterions, resulting from a different balance between the respective effects of the water−pore and water−counterion interactions on water dynamics. The impact of counterion identity, particularly the hydration strength and polarizability, is an important variable that remains to be systematically addressed. While I^- was used in this study due to its synthetic accessibility via methyl iodide, future studies would explore Cl^-, Br^-, and OH^- to determine how counterions modulate confined water dynamics.

To place our findings in a broader framework on how confinement and surface charge influence phase behavior, it is also worth mentioning previous X-ray diffraction studies that investigated the effects of pore surface chemistry, and more specifically surface ionic charge, on confined ice and water structures in PMOs.[27,41] Importantly, those studies observed ice formation only at 230 K, which is fully consistent with our current observation that the dynamics measured by QENS at 243 K and above is characteristic of the liquid state.

Despite the different temperature ranges and, so, the different natures of the confined phase, this work also indicates that the structural behavior of confined water is shaped by the combined effects of surface chemistry and geometric confinement. Prior work has shown that in larger pores (e.g., d_p = 4.9 nm), stacking-disordered ice (Isd), comprising both hexagonal and cubic phases, can form under specific conditions. In contrast, the smaller pore sizes used here (d_p = 3.5−3.8 nm) impose stronger confinement that suppresses crystallization.[41] For charged PMOs, the high polarity and hydrogen-bonding capacity of pyridinium groups induce local structuring of confined water and deviations in the lattice order, even in the absence of ice formation. These effects are amplified by the smaller pore size in DVMeP-PMO (d_p = 3.5 nm). In neutral PMOs (d_p = 3.8 nm), weaker electrostatic interactions allow more bulk-like water behavior in the pore center, while the partially protonated pyridine groups still generate interfacial structuring near the walls. These observations underscore the role of surface functionalization, not just in modifying interfacial behavior but also in tuning the phase stability and dynamic regimes throughout the pore.

Moreover, a recent study investigating the OH-stretching band of water near graphene with varying surface charges revealed that water molecules at positively charged interfaces, similar to those in charged PMOs, exhibit significantly stronger hydrogen bonding.[42] This enhanced hydrogen-bonding network causes water molecules to bind more tightly to the solid surface, resulting in reduced mobility and increased interfacial structuring.

Our findings support the conclusion about the critical role of surface chemistry that was derived in previous studies of water-filled nonionic PMOs with variable hydrophilicity, but they also demonstrate the unique effect of ionic surface charge. Consequently, the question of the spatial extension of the surface charge effect on the water dynamics: Is it strictly limited to those water molecules that interact directly with the surface ions through adsorption, H-bonding, and solvation forces or does it spread over longer distances in the confined liquid? To address this issue, complementary QENS experiments with variable water loadings were performed on DVMeP-PMO.

3.2. Effect of the Filling Fraction on the Water Dynamics—Neutron Backscattering Study. To explore the water behavior near the charged surface in more detail, we studied the effect of varying the amount of adsorbed water in DVMeP-PMO by tuning the relative humidity. From the previous part, it is clear that the huge slowdown of the dynamics of water in charged PMOs makes such a systematic study, if possible, extremely challenging on SHARP. The energy resolution of the IN16B neutron backscattering spectrometer is about 2 orders of magnitude better than that of SHARP, but its dynamical range is also limited. This makes it unsuitable to study the water dynamics in the neutral PMO at the same temperatures, but it is ideally suited to focus on the case of ionically charged DVMeP-PMO. The selected values, 75% and 33% RH, are located, respectively, above and below the capillary condensation pressure. They made it possible to compare the dynamics of the water in the completely filled pore at 75% RH to the water adsorbed approximately two to three molecular layers on the surface of the pore at 33% RH, as illustrated in Figure 5a,b, respectively.

Figure 5c,d displays the temperature-dependent scattering intensity of IN16B spectra at a momentum transfer Q = 1.5 $Å^{-1}$ over an energy transfer range of −30 to +30 μeV for fully filled and partially filled charged PMOs, respectively. As the temperature decreases from 278 to 243 K, the quasi-elastic line continuously sharpens, a trend previously observed in the SHARP data. This sharpening reflects the slowing down of water dynamics at lower temperatures, as the narrowing of the quasi-elastic width indicates longer time scales of molecular motion. This interpretation is fully supported by the EFWS measured at 75% RH (Figure S9) that continuously increases on cooling from 280 to 190 K, with a sigmoidal shape centered at about 230 K. In the meantime, the inelastic fixed window scan (IFWS) measured at 3 μeV presents a single peak that covers the temperature range from 220 to 265 K at half-maximum intensity and that is centered around 235 K. Its maximum position shifts to a higher temperature as the value of the transfer of momentum decreases as illustrated in Figure 5e. This evolution reveals the dispersive nature of the associated dynamics, which is attributed to the Q-dependent onset of translational diffusion dynamics within the dynamical range fixed by the selected offset energy (3 μeV). It also demonstrates that below 200 K, the subsequent increase of

https://doi.org/10.1021/acs.jpcc.5c04787
J. Phys. Chem. C 2025, 129, 18311−18324

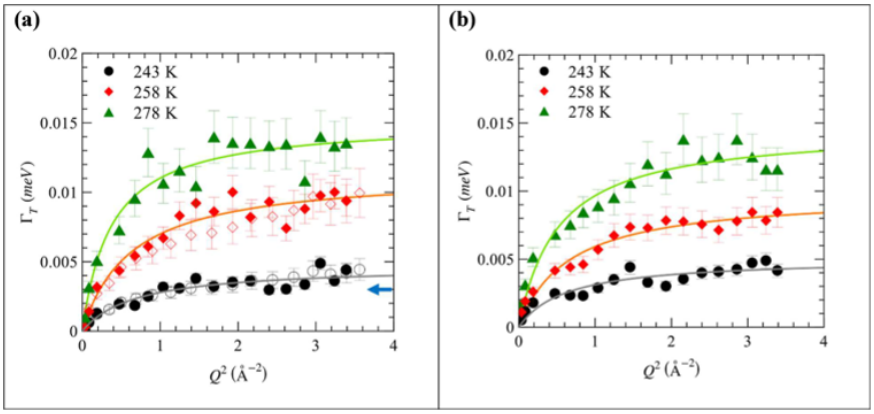


Figure 6. Evolution of the half-width at half-maximum of Lorentzian (Γ_T) as a function of Q^2 obtained from the fitting of QENS spectra recorded on IN16B for water confined in (a) fully filled and (b) partially filled charged PMOs at three different temperatures. The fits using the jump-diffusion model are shown as solid lines. The empty symbols represent the Γ_T value obtained through an inelastic fixed window scan (IFWS). The blue arrow in the left panel shows the energy offset of 3 μeV that was used for IFWS.

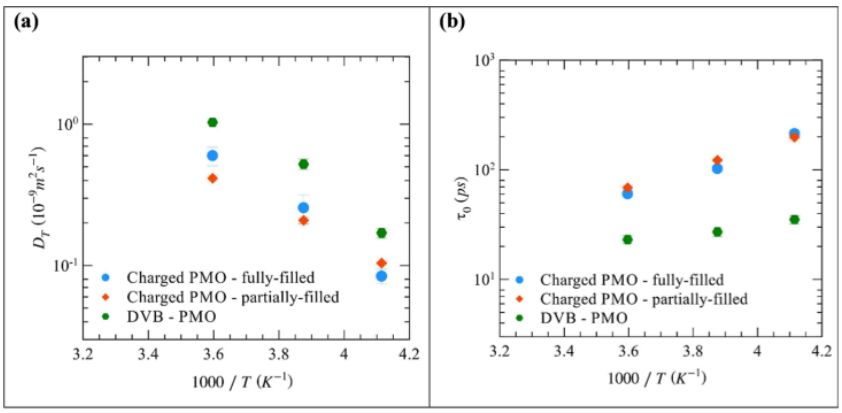


Figure 7. (a) Translational diffusion coefficient (D_T) and (b) residence time (τ_0) of water, evaluated from the fitting of IN16B spectra using the jump-diffusion model, for water confined in fully filled and partially filled charged DVMeP-PMO as a function of the inverse temperature. QENS data for D_T and τ_0 in DVB-PMO, as derived from Jani et al.,[25] are also included.

elastic intensity is not related to translational dynamics anymore but rather to localized modes (e.g., vibrations) that contribute to the Debye−Waller factor.

To quantitatively analyze the spectra, each spectrum was individually fitted at each Q-value using a model that incorporated a single Lorentzian function and a flat background (Figure S5). The procedure of fit and the theoretical model expressed in eq 6 are similar to those used for SHARP. The only exception concerns the second Lorentzian contribution $L_R(Q, \omega)$ that was related to the quasi-elastic component of the local rotational dynamics. According to the SHARP study, the width of $L_R(Q, \omega)$ considerably exceeds the dynamical window of IN16B. Therefore, it was replaced by a flat ω-independent background BG(Q).

The fitted incoherent scattering intensity can then be expressed as

$$I^{\text{fit}}_{\text{QENS}}(Q, \omega) = I^{\text{dry}}(Q, \omega) + R(Q, \omega) \otimes [A(Q)L_T(Q, \omega) + \text{BG}(Q)] \quad (6)$$

As a result, only the slower component related to translational dynamics was evaluated on IN16B.

Based on the same hypothesis, the IFWS was fitted by eq 7

$$I^{\text{fit}}_{\text{IFWS}}(Q, T) = A(Q)L_T(Q, \omega_{\text{offset}}) + \text{BG}(Q) \quad (7)$$

where $\hbar\omega_{\text{offset}}$ (=3 μeV) represents the offset energy, as illustrated in Figure 5f. Here, the temperature dependence of the line width $\Gamma(Q)$ of the Lorentzian function L_T was assigned to the Arrhenius law, yielding an activation energy E_a = 28.1 kJ mol^{-1} as expressed by eq 8. This value is in excellent agreement with the activation energy obtained from $I^{\text{fit}}_{\text{QENS}}$ and Figure 7a (E_a = 28.47 kJ mol^{-1}), demonstrating the consistency of both methods (QENS and IFWS) in describing the dynamical process.

$$\Gamma_{\text{IFWS}}(Q, T) = \Gamma_0(Q) \exp\left(\frac{-E_a}{k_B T}\right) \quad (8)$$

The line width (HWHM) of the quasi-elastic intensity measured on IN16B is shown in Figure 6a,b at three temperatures, 243, 258, and 278 K. It initially follows a

https://doi.org/10.1021/acs.jpcc.5c04787
J. Phys. Chem. C 2025, 129, 18311−18324

Table 3. Fit Parameters D_T, τ_0, and l Obtained by Fitting $\Gamma_T(Q^2)$ Using the Jump-Diffusion Model for Data Acquired by IN16B

	fully filled			partially filled		
T (K)	D_T (10^{-9} m^2/s)	τ_0 (ps)	l (Å)	D_T (10^{-9} m^2/s)	τ_0 (ps)	l (Å)
243	0.10 ± 0.01	213 ± 20	3.6	0.12 ± 0.002	206 ± 17	3.9
258	0.27 ± 0.06	102 ± 5.5	4.1	0.22 ± 0.01	132 ± 5	4.1
278	0.61 ± 0.09	60 ± 3	4.7	0.43 ± 0.02	73 ± 4	4.4

trend proportional to the square of the momentum transfer (Q^2) but gradually deviates from the linear slope at higher Q-values, as observed on SHARP. In certain cases, particularly at higher temperatures, the line width displays fluctuations rather than a smooth, monotonic increase. These fluctuations are attributed to statistical noise, more prominent at higher temperatures when the quasi-elastic broadening approaches the maximum energy transfer of 30 μeV on IN16B. At lower temperatures, the quasi-elastic intensity increases, and these fluctuations diminish as the line width sharpens.

From the fitting parameters of IFWS, the line widths $\Gamma_{IFWS}(Q, T)$ were independently evaluated at 243 and 258 K, as indicated by open symbols in Figure 6a. They showed excellent agreement with those evaluated from the QENS spectra. Such a comparison was elusive at 278 K because the quasi-elastic broadening systematically exceeds the selected energy offset indicated by the arrow in Figure 6a. This is also illustrated in Figure S9, which confirms that only the two lowest temperatures fall within the temperature range of the IFWS peak.

As for SHARP measurements, the line width data were fitted using a jump-diffusion model (eq 4). The resulting diffusion coefficients and residence times are presented in Figure 7a,b and summarized in Table 3. It should be noted that the values of the diffusion coefficient and residence times obtained on IN16B for the fully filled DVMeP-PMO systematically differ (by a factor of 1.8−2.5) from those measured on SHARP. This stems from the vastly different energy resolutions of the two spectrometers. SHARP, with a coarser resolution ($\delta E \approx 70$ μeV), captures faster dynamics and is thus sensitive to broader quasi-elastic features. IN16B, with a 2 orders of magnitude finer resolution ($\delta E \approx 0.75$ μeV), probes significantly slower motion and captures only the narrowest components of the dynamics. These differences reflect the time scale sensitivity of the instruments, with different limitations and not an inconsistency in the underlying physics. The impact of the instrument resolution is especially significant for water in charged DVMeP-PMO that exhibits a drastic slowdown compared to bulk water. Indeed, its quasi-elastic broadening (~10 μeV at 280 K and Q = 1 Å^{-1}) entered the elastic resolution of SHARP, while it was obviously not the case on IN16B. Note that the opposite situation was encountered for water in neutral DVP-PMO, with a quasi-elastic broadening (~40 μeV at 280 K and Q = 1 Å^{-1}) that was ideally suited for SHARP but would have exceeded the dynamical range of IN16B (E_{max} = ±30 μeV).

We compared in Figure 7 the diffusion coefficient and residence time values obtained on IN16B for water in charged DVMeP-PMO with those obtained on the same instrument for a water-filled nonionic DVB-PMO by Jani et al.[25] In agreement with the observation made for SHARP data, the diffusion coefficient D_T for water confined in the charged DVMeP-PMO is consistently lower than for water in the nonionic DVB-PMO. Also, the characteristic residence times (τ_0) are significantly higher in the charged matrices compared to the neutral systems. This confirms that the water molecules in charged DVMeP-PMO exhibit much slower diffusion due to stronger electrostatic interactions with the surface ionic groups.

The new insight provided by the experiments on IN16B concerns the effect of the filling ratio. In fact, the diffusive dynamics of water in the partially filled DVMeP-PMO (2−3 interfacial water at 33% RH) are slower than that of water in the same matrix at full loading (capillary-filled water at 75% RH). However, this additional slowdown is rather modest: at 278 K, the diffusion coefficient for water adsorbed at 33% RH has only been reduced by 30% compared with that for water in capillary-filled pores at 75% RH. Similarly, the increase in residence time is only about 22%. This observation made for charged PMOs contrasts sharply with the approximately 4× reduction in diffusivity observed between neutral and charged PMOs at full loading. It underscores that varying the interfacial layer thickness of water adsorbed in this specific DVMeP-PMO ionically charged matrix has a much smaller impact on the water dynamics than varying the nature of the pore surface (neutral vs charged) for a fully filled pore. Moreover, the huge slowdown effect induced by the surface charge is maintained over the entire temperature range studied, while its mild dependence on RH tends to disappear upon decreasing the temperature to 243 K, as shown in Figure 7.

This is an important indication that the huge impact of the ionic interaction on the water dynamics is not restricted to the adsorbed molecules located at the pore surface but affects the water molecules present in the entire pore volume. This can be explained by the long-range nature of the electrostatic interaction that remains significant over a distance that approaches the pore radius of 1.8 nm. The specific H-bonded structure adopted by water molecules can also play an important role in connecting the dynamics of the water molecules located in the pore center to those in direct interaction with the surface charged units. On cooling, the observed merging of water dynamics in partially and fully filled pores can also be interpreted by the H-bond network becoming stronger at low temperatures, so that the liquid volume that is influenced by the surface condition increases.

4. CONCLUSION

This work explored water confined in neutral and charged PMOs, revealing how surface chemistry (i.e., surface charge and its polarity) influences molecular dynamics. Using neutron scattering techniques (SHARP and IN16B), we demonstrated the distinct effects of divinylpyridine-based neutral PMOs and their methylated, ionically charged counterparts on water dynamics.

Comparing neutral and charged PMOs highlights the critical role of surface charge in modulating water dynamics, and the results provide detailed quantitative measurements of translational diffusion and residence times, offering insights into the crucial role of molecular interactions and electrostatic effects in modulating water mobility under confinement.

https://doi.org/10.1021/acs.jpcc.5c04787
J. Phys. Chem. C 2025, 129, 18311−18324

The most salient phenomenon is observed for the ionically charged PMO, which induces an extreme slowing of the water translational dynamics. Based on the jump-diffusion modeling of the QENS spectra, this decrease in the dynamics can be quantified as a reduction by a factor 4 of the diffusion coefficient and an increase by 1 order of magnitude of the residence time. Such a colossal slowdown can be attributed to the strong surface adsorption of water on the cationic pyridinium sites, which induces long-lived interfacial structures. This conclusion is supported by the fact that the mean jump length barely depends on the surface charge, which means that the reduction of the diffusion coefficient is solely a consequence of the much longer residence time.

Remarkably, the impact of the surface charge is not restricted to the dynamics of the adsorbed water molecules but affects the entire volume of the pore, with a pore size of 3.7 nm. This important conclusion can be derived from the high-resolution QENS study of PMO hydrated at different RH, which demonstrates a modest difference between the dynamics of the fully filled sample and the adsorbed liquid layer.

The dynamical properties of water confined in surface-charged PMOs are unusual and markedly different from what is currently known from neutral porous media. In the latter cases, water dynamics exhibits only a moderate slowdown, with the extent of the effect depending on the chemical nature of the pore surface. This phenomenon is traditionally attributed to varying degrees of hydrophobicity and hydrophilicity. In the present study, this is confirmed for water-filled DVP-PMO, which exhibits a hydrophilic character further enhanced by the partial protonation of the pyridine groups. Consequently, the confinement effect on the water dynamics exceeds the observations made in the literature for other neutral PMO, such as DVB-PMO, but it remains much smaller than that for the charged DVMeP-PMO.

These findings underscore the importance of tailoring surface chemistry to control water dynamics in confined systems. While this study provides valuable insights into water dynamics in neutral and charged PMOs, it also raises several questions warranting further investigation. For example, the role of different counterions and varying degrees of functionalization in modifying water dynamics within charged PMOs remains an open area of research, particularly at lower hydration levels, where water−ion interactions could dominate. Finally, integrating experimental data with molecular dynamics simulations, mapping hydration structure and dynamics near pyridinium-functionalized surfaces, could provide a more detailed atomistic view of water−surface interactions and help elucidate the mechanisms underlying the observed differences in diffusion and residence times. Such insights would enhance our ability to predict and design materials with the desired water transport properties.

■ ASSOCIATED CONTENT

Data Availability Statement

The raw data for this study were collected at the Institut Laue-Langevin (ILL) large-scale facility, and the data set will be publicly available after the embargo period (i.e., five years after conducting the experiments).[43,44] Data derived from these findings can be obtained from the corresponding author upon request.

Supporting Information

The Supporting Information is available free of charge at https://pubs.acs.org/doi/10.1021/acs.jpcc.5c04787.

PMO synthesis; structural characterization of divinylpyridine-bridged PMO and divinyl-methylpyridinium-bridged PMO; neutron structure factor of dry and capillary-filled PMOs; fitting procedure; EISF of the local quasi-elastic relaxation obtained from SHARP measurements; time scale of rotational and librational motions; Arrhenius fitting of the translational diffusion coefficient of water in neutral and charged PMOs; and elastic and inelastic FWS measured on IN16B (PDF)

■ AUTHOR INFORMATION

Corresponding Authors

Patrick Huber − *Institute for Materials and X-ray Physics, Hamburg University of Technology, 21073 Hamburg, Germany; Centre for X-ray and Nano Science CXNS, Deutsches Elektronen-Synchrotron DESY, 22603 Hamburg, Germany;* orcid.org/0000-0002-2126-9100; Email: patrick.huber@tuhh.de

Michael Fröba − *Institute of Inorganic and Applied Chemistry, University of Hamburg, 20146 Hamburg, Germany; The Hamburg Centre for Ultrafast Imaging, 22761 Hamburg, Germany;* orcid.org/0000-0001-6927-0509; Email: michael.froeba@uni-hamburg.de

Denis Morineau − *Institute of Physics of Rennes, UMR 6251, CNRS-University of Rennes, F-35042 Rennes, France;* orcid.org/0000-0002-8784-3021; Email: denis.morineau@univ-rennes.fr

Authors

Armin Mozhdehei − *Institute of Physics of Rennes, UMR 6251, CNRS-University of Rennes, F-35042 Rennes, France*

Philip Lenz − *Institute of Inorganic and Applied Chemistry, University of Hamburg, 20146 Hamburg, Germany; The Hamburg Centre for Ultrafast Imaging, 22761 Hamburg, Germany*

Stella Gries − *Institute for Materials and X-ray Physics, Hamburg University of Technology, 21073 Hamburg, Germany; Centre for X-ray and Nano Science CXNS, Deutsches Elektronen-Synchrotron DESY, 22603 Hamburg, Germany*

Sophia-Marie Meinert − *Institute of Inorganic and Applied Chemistry, University of Hamburg, 20146 Hamburg, Germany*

Ronan Lefort − *Institute of Physics of Rennes, UMR 6251, CNRS-University of Rennes, F-35042 Rennes, France*

Jean-Marc Zanotti − *Laboratoire Léon Brillouin, CEA, CNRS, Université Paris-Saclay, F-91191 Gif-sur-Yvette, France*

Quentin Berrod − *CNRS, CEA, Grenoble INP, IRIG, SyMMES, Université Grenoble Alpes, F-38000 Grenoble, France;* orcid.org/0000-0003-3254-1779

Markus Appel − *Institut Laue-Langevin, F-38042 Grenoble, France*

Mark Busch − *Institute for Materials and X-ray Physics, Hamburg University of Technology, 21073 Hamburg, Germany; Centre for X-ray and Nano Science CXNS, Deutsches Elektronen-Synchrotron DESY, 22603 Hamburg, Germany*

Complete contact information is available at: https://pubs.acs.org/10.1021/acs.jpcc.5c04787

Notes

The authors declare no competing financial interest.

■ ACKNOWLEDGMENTS

This research was carried out as part of the DFG-ANR collaborative project (ANR-23-CE29-0028) for which we express our gratitude. D.M. and A.M. acknowledge the funding by ANR-22-CE50-0002. We also thank the Institut Laue-Langevin and 2FDN (Fédération Française de Diffusion Neutronique) for providing neutron beam time (IN16B #6-07-90 and SHARP #CRG-2896), which was essential to this work. Scientific exchange and financial support of the Center for Molecular Water Science (CMWS), the research initiative "BlueMat: Water-Driven Materials" at Hamburg University of Technology, the Cluster of Excellence "Advanced Imaging of Matter" of the DFG (EXC 2056)—project ID 390715994, as well as of the city of Hamburg's state-funded research project "Control of the special properties of water in nanopores" (LFF-FV68), is also acknowledged.

■ REFERENCES

(1) Munoz-Santiburcio, D.; Marx, D. Chemistry in nanoconfined water. *Chem. Sci.* **2017**, *8* (5), 3444−3452.
(2) Jelassi, J.; Castricum, H. L.; Bellissent-Funel, M.-C.; Dore, J.; Webber, J. B. W.; Sridi-Dorbez, R. Studies of water and ice in hydrophilic and hydrophobic mesoporous silicas: pore characterisation and phase transformations. *Phys. Chem. Chem. Phys.* **2010**, *12* (12), 2838−2849.
(3) Moore, E. B.; Allen, J. T.; Molinero, V. Liquid-ice coexistence below the melting temperature for water confined in hydrophilic and hydrophobic nanopores. *J. Phys. Chem. C* **2012**, *116* (13), 7507−7514.
(4) Gruener, S.; Hofmann, T.; Wallacher, D.; Kityk, A. V.; Huber, P. Capillary rise of water in hydrophilic nanopores. *Phys. Rev. E: Stat., Nonlinear, Soft Matter Phys.* **2009**, *79* (6), 067301.
(5) Martínez-Edo, G.; Balmori, A.; Pontón, I.; Marti del Rio, A.; Sánchez-García, D. Functionalized ordered mesoporous silicas (MCM-41): Synthesis and applications in catalysis. *Catalysts* **2018**, *8* (12), 617.
(6) Khan, D.; Shaily. Synthesis and catalytic applications of organo-functionalized MCM-41 catalyst: A review. *Appl. Organomet. Chem.* **2023**, *37* (3), No. e7007.
(7) Singh, S.; Kumar, R.; Setiabudi, H. D.; Nanda, S.; Vo, D.-V. N. Advanced synthesis strategies of mesoporous SBA-15 supported catalysts for catalytic reforming applications: A state-of-the-art review. *Appl. Catal., A* **2018**, *559*, 57−74.
(8) Dündar-Tekkaya, E.; Yürüm, Y. Mesoporous MCM-41 material for hydrogen storage: A short review. *Int. J. Hydrogen Energy* **2016**, *41* (23), 9789−9795.
(9) Ehsani, A.; Bigdeloo, M.; Alamgholiloo, H.; Asgari, E.; Sheikhmohammadi, A.; Nazari, S.; Hashemzadeh, B.; Ghasemian, N. Ternary nanocomposite of TiO2-ZnO/MCM-41: synthesis and electrochemical performance in supercapacitors. *J. Energy Storage* **2022**, *50*, 104633.
(10) Tripathi, A. K.; Singh, R. K. Development of ionic liquid and lithium salt immobilized MCM-41 quasi solid-liquid electrolytes for lithium batteries. *J. Energy Storage* **2018**, *15*, 283−291.
(11) Bera, B.; Das, N. Synthesis of high surface area mesoporous silica SBA-15 for hydrogen storage application. *Int. J. Appl. Ceram. Technol.* **2019**, *16* (1), 294−303.
(12) Kadhim, R. J.; Al-Ani, F. H.; Alsalhy, Q. F. MCM-41 mesoporous modified polyethersulfone nanofiltration membranes and their prospects for dyes removal. *Int. J. Environ. Anal. Chem.* **2023**, *103* (4), 828−848.
(13) Costa, J. A. S.; de Jesus, R. A.; Santos, D. O.; Mano, J. F.; Romao, L. P.; Paranhos, C. M. Recent progresses in the adsorption of organic, inorganic, and gas compounds by MCM-41-based mesoporous materials. *Microporous Mesoporous Mater.* **2020**, *291*, 109698.
(14) Corti, H. R.; Appignanesi, G. A.; Barbosa, M. C.; Bordin, J. R.; Calero, C.; Camisasca, G.; Elola, M. D.; Franzese, G.; Gallo, P.; Hassanali, A.; et al. Structure and dynamics of nanoconfined water and aqueous solutions. *Eur. Phys. J. E* **2021**, *44*, 136.
(15) Chiavazzo, E.; Fasano, M.; Asinari, P.; Decuzzi, P. Scaling behaviour for the water transport in nanoconfined geometries. *Nat. Commun.* **2014**, *5* (1), 3565.
(16) Gonella, G.; Backus, E. H.; Nagata, Y.; Bonthuis, D. J.; Loche, P.; Schlaich, A.; Netz, R. R.; Kühnle, A.; McCrum, I. T.; Koper, M. T.; et al. Water at charged interfaces. *Nat. Rev. Chem.* **2021**, *5* (7), 466−485.
(17) Schlaich, A.; Kappler, J.; Netz, R. R. Hydration friction in nanoconfinement: From bulk via interfacial to dry friction. *Nano Lett.* **2017**, *17* (10), 5969−5976.
(18) Gallo, P.; Amann-Winkel, K.; Angell, C. A.; Anisimov, M. A.; Caupin, F.; Chakravarty, C.; Lascaris, E.; Loerting, T.; Panagiotopoulos, A. Z.; Russo, J.; et al. Water: A tale of two liquids. *Chem. Rev.* **2016**, *116* (13), 7463−7500.
(19) Debenedetti, P. G.; Stillinger, F. H. Supercooled liquids and the glass transition. *Nature* **2001**, *410* (6825), 259−267.
(20) Zanotti, J.-M.; Bellissent-Funel, M.-C.; Chen, S.-H. Relaxational dynamics of supercooled water in porous glass. *Phys. Rev. E: Stat. Phys., Plasmas, Fluids, Relat. Interdiscip. Top.* **1999**, *59* (3), 3084.
(21) Takahara, S.; Sumiyama, N.; Kittaka, S.; Yamaguchi, T.; Bellissent-Funel, M.-C. Neutron scattering study on dynamics of water molecules in MCM-41. 2. Determination of translational diffusion coefficient. *J. Phys. Chem. B* **2005**, *109* (22), 11231−11239.
(22) Hoffmann, F.; Cornelius, M.; Morell, J.; Fröba, M. Silica-based mesoporous organic-inorganic hybrid materials. *Angew. Chem., Int. Ed.* **2006**, *45* (20), 3216−3251.
(23) Baum, M.; Rieutord, F.; Juranyi, F.; Rey, C.; Rébiscoul, D. Dynamical and structural properties of water in silica nanoconfinement: impact of pore size, ion nature, and electrolyte concentration. *Langmuir* **2019**, *35* (33), 10780−10794.
(24) Takahara, S.; Nakano, M.; Kittaka, S.; Kuroda, Y.; Mori, T.; Hamano, H.; Yamaguchi, T. Neutron scattering study on dynamics of water molecules in MCM-41. *J. Phys. Chem. B* **1999**, *103* (28), 5814−5819.
(25) Jani, A.; Busch, M.; Mietner, J. B.; Ollivier, J.; Appel, M.; Frick, B.; Zanotti, J.-M.; Ghoufi, A.; Huber, P.; Fröba, M.; et al. Dynamics of water confined in mesopores with variable surface interaction. *J. Chem. Phys.* **2021**, *154* (9), 094505.
(26) Khoder, H.; Siboulet, B.; Ollivier, J.; Baus-Lagarde, B.; Rébiscoul, D. How Cation-Silica Surface Interactions Affect Water Dynamics in Nanoconfined Electrolyte Solutions. *J. Phys. Chem. C* **2024**, *128* (30), 12558−12565.
(27) Gießelmann, N. C.; Lenz, P.; Meinert, S.-M.; Simon, T.; Jo, W.; Striker, N. N.; Fröba, M.; Lehmkühler, F. Structure of Water under Confinement in Periodic Mesoporous Organosilicas Investigated by X-ray Scattering. *J. Phys. Chem. C* **2024**, *128* (1), 499−507.
(28) Mietner, J. B.; Brieler, F. J.; Lee, Y. J.; Fröba, M. Properties of water confined in periodic mesoporous organosilicas: nanoimprinting the local structure. *Angew. Chem., Int. Ed.* **2017**, *56* (40), 12348−12351.
(29) Malfait, B.; Moréac, A.; Jani, A.; Lefort, R.; Huber, P.; Fröba, M.; Morineau, D. Structure of water at hydrophilic and hydrophobic interfaces: Raman spectroscopy of water confined in periodic mesoporous (organo) silicas. *J. Phys. Chem. C* **2022**, *126* (7), 3520−3531.
(30) Malfait, B.; Jani, A.; Mietner, J. B.; Lefort, R.; Huber, P.; Fröba, M.; Morineau, D. Influence of pore surface chemistry on the rotational dynamics of nanoconfined water. *J. Phys. Chem. C* **2021**, *125* (30), 16864−16874.
(31) Ben Ishai, P.; Mamontov, E.; Nickels, J. D.; Sokolov, A. P. Influence of Ions on Water Diffusion; A Neutron Scattering Study. *J. Phys. Chem. B* **2013**, *117* (25), 7724−7728.
(32) Mamontov, E.; Cole, D. R.; Dai, S.; Pawel, M. D.; Liang, C.; Jenkins, T.; Gasparovic, G.; Kintzel, E. Dynamics of water in LiCl and CaCl2 aqueous solutions confined in silica matrices: A backscattering neutron spectroscopy study. *Chem. Phys.* **2008**, *352* (1−3), 117−124.

https://doi.org/10.1021/acs.jpcc.5c04787
J. Phys. Chem. C 2025, 129, 18311−18324

(33) Brinker, M.; Dittrich, G.; Richert, C.; Lakner, P.; Krekeler, T.; Keller, T. F.; Huber, N.; Huber, P. Giant electrochemical actuation in a nanoporous silicon-polypyrrole hybrid material. *Sci. Adv.* **2020**, *6* (40), No. eaba1483.
(34) Brinker, M.; Huber, P. Wafer-Scale Electroactive Nanoporous Silicon: Large and Fully Reversible Electrochemo-Mechanical Actuation in Aqueous Electrolytes. *Adv. Mater.* **2022**, *34* (1), 2105923.
(35) Appel, M.; Frick, B. Note: One order of magnitude better signal-to-noise ratio for neutron backscattering. *Rev. Sci. Instrum.* **2017**, *88* (3), 036105.
(36) Frick, B.; Combet, J.; Van Eijck, L. New possibilities with inelastic fixed window scans and linear motor Doppler drives on high resolution neutron backscattering spectrometers. *Nucl. Instrum. Methods Phys. Res., Sect. A* **2012**, *669*, 7−13.
(37) Arnold, O.; Bilheux, J.-C.; Borreguero, J.; Buts, A.; Campbell, S. I.; Chapon, L.; Doucet, M.; Draper, N.; Ferraz Leal, R.; Gigg, M.; et al. Mantid—Data analysis and visualization package for neutron scattering and μ SR experiments. *Nucl. Instrum. Methods Phys. Res., Sect. A* **2014**, *764*, 156−166.
(38) Teixeira, J.; Bellissent-Funel, M.-C.; Chen, S.-H.; Dianoux, A.-J. Experimental determination of the nature of diffusive motions of water molecules at low temperatures. *Phys. Rev. A: At., Mol., Opt. Phys.* **1985**, *31* (3), 1913.
(39) Singwi, K.; Sjölander, A. Diffusive motions in water and cold neutron scattering. *Phys. Rev.* **1960**, *119* (3), 863.
(40) Price, W. S.; Ide, H.; Arata, Y. Self-diffusion of supercooled water to 238 K using PGSE NMR diffusion measurements. *J. Phys. Chem. A* **1999**, *103* (4), 448−450.
(41) Gießelmann, N. C.; Lenz, P.; Meinert, S.-M.; Simon, T.; Bauer, R. P.; Jo, W.; Claas, S.; Köhn, C.; Striker, N. N.; Fröba, M.; et al. The structure of ice under confinement in periodic mesoporous organosilicas (PMOs). *J. Chem. Phys.* **2024**, *161* (3), 034508.
(42) Rashmi, R.; Balogun, T. O.; Azom, G.; Agnew, H.; Kumar, R.; Paesani, F. Revealing the Water Structure at Neutral and Charged Graphene/Water Interfaces through Quantum Simulations of Sum Frequency Generation Spectra. *ACS Nano* **2025**, *19* (4), 4876−4886
(43) Busch, M.; Appel, M.; Froeba, M.; Gries, S.; Huber, P.; Jani, A. Lenz, P.; Morineau, D.; Schwake, S.; Seydel, T. *Water Dynamics in Mesopores with a Periodic Distribution of Ionic Surface Charge*; Institu Laue-Langevin (ILL), 2021.
(44) Morineau, D.; Busch, M.; Froeba, M.; Gries, S.; Huber, P. Lenz, P.; Schwake, S.; Zanotti, J.-M. *Water Dynamics in Mesopores with a Periodic Distribution of Ionic Surface Charge*; Institut Laue-Langevin (ILL), 2021.

https://doi.org/10.1021/acs.jpcc.5c04787
J. Phys. Chem. C 2025, 129, 18311−18324

5.5. Periodic Mesoporous Organosilicas as Host Materials for Studying Surface Chemistry Effects on the Freezing and Melting Behavior of Nanoconfined Water

Philip Lenz, Uta Sazama, Michael Steiger*, Michael Fröba*

Synopsis

In confined spaces, water freezes at temperatures far below its bulk melting point, with reports suggesting that freezing may be entirely absent in pores smaller than 3 nm in diameter. In such nanometer-sized confinements, surface properties play an increasingly important role in determining the melting and freezing behavior. Besides pore size, the dimension of the non-freezable water layer, often referred to as the quasi-liquid layer, consisting of a thin layer of water between the solid wall and ice, also influences the phase transition temperature. Because different studies use a variety of materials, pore sizes (and methods for their determination), and experimental conditions, comparisons and interpretations are challenging, resulting in discrepancies regarding how and to what extent surface hydrophilicity influences the non-freezable water layer. To address this, the MCM-41 silicas and periodic mesoporous organosilicas with divinylbenzene-type bridging units, whose water–wall interactions and surface hydrophilicity were established in the preceding water vapor sorption study, were used to investigate the melting behavior of confined water by low-temperature DSC. While surface chemistry has only a minor effect on the melting point depression of water in pores with radii > 1.8 nm, distinct differences emerge for smaller pores. Materials with lower hydrophilicity exhibit a more pronounced decrease in melting transition temperature as pore size decreases. Using the Gibbs–Thomson relation, the non-freezable layer thickness and the affinity between water and the pore wall were derived. However, this approach has limitations, such as the assumption that the non-freezable layer thickness is independent of pore size. Therefore, different geometric calculation approaches for cylindrical pores were applied to determine the layer thickness and density. In general, more hydrophobic or charged PMOs, as well as materials with larger pores, exhibit thicker non-freezable water layers with a tendency toward lower density. Only in the more hydrophobic BTEVB-PMO, which lacks functional groups pointing toward the pore center, is the non-freezable water layer density higher than expected, indicating that hydrophobicity alone is not the sole determinant of *t*-layer properties.

THE JOURNAL OF PHYSICAL CHEMISTRY C
A JOURNAL OF THE AMERICAN CHEMICAL SOCIETY

Open Access
This article is licensed under CC-BY 4.0

pubs.acs.org/JPCC
Article

Periodic Mesoporous Organosilicas as Host Materials for Studying Surface Chemistry Effects on the Freezing and Melting Behavior of Nanoconfined Water

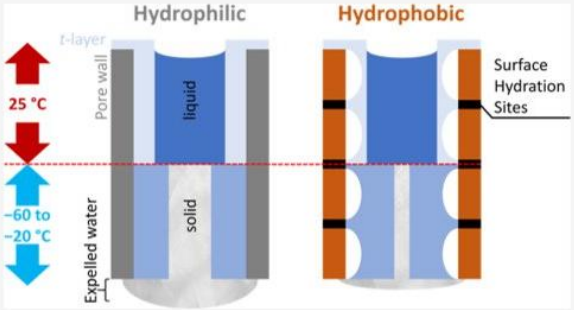
Philip Lenz, Uta Sazama, Michael Steiger,* and Michael Fröba*

Cite This: J. Phys. Chem. C 2025, 129, 20373−20386

Read Online

ACCESS | Metrics & More | Article Recommendations | Supporting Information

ABSTRACT: The impact of surface hydrophilicity on the freezing, melting, and nonfreezable layer of nanoconfined water remains debated. Variability in material types, pore sizes, surface functionality organization, and experimental conditions complicate direct comparisons and conclusions. To address this, periodic mesoporous organosilicas (PMOs) with a uniform divinylbenzene bridging unit were used. By fine-tuning hydrophilicity and pore sizes, confined water's phase behavior was studied via differential scanning calorimetry (DSC). Comparing gas-phase adsorption and incipient wetness as filling methods revealed an increased *t*-layer density with the latter. Surface hydrophilicity has little effect on melting point depression in larger pores but becomes increasingly influential as pore size decreases. The nonfreezable layer thickness was evaluated using the Gibbs−Thomson equation and geometric enthalpy-based calculations. In hydrophobic PMOs, water exhibited larger melting point depression, lower specific enthalpies, and thicker interfacial layers than in hydrophilic ones. In contrast, charged PMOs behaved differently: despite higher hydrophilicity, confined water exhibited a larger melting temperature depression, lower specific enthalpy, larger critical pore radius, and comparatively thicker *t*-layers, likely due to higher disorder of the hydrogen-bonding network close to the surface. Moreover, the *t*-layer density did not follow a simple trend based solely on hydrophilicity. These results highlight the complex interplay between pore size, surface chemistry, and interfacial water behavior, offering valuable insights into confined water properties and phase transitions.



1. INTRODUCTION

Water exhibits complex and unique behavior when confined within nanoscale pores, differing even more from bulk water, which itself shows anomalous properties.[1−4] In confinement, water exhibits changes in fundamental properties such as freezing and melting points,[2−9] density[2,10−14] and dielectric constant,[15−17] liquid water[18−20] and ice structure,[21−29] microphase separation behavior[30−32] and solvation capacity,[33] which can be exploited for chemistry in confined spaces.[34] One of the most notable effects is the depression of the freezing point, where confined water remains in a liquid-like state at temperatures where bulk water would freeze. This phenomenon, as well as other anomalies in phase transition, have implications for a wide range of applications, including environmental and geological sciences,[35−41] biological systems[42−45] and nanotribology,[46] where water often resides within pore structures.

In addition to pore size[2−9] and geometry,[47−51] surface chemistry/hydrophilicity influence the melting and freezing points, as well as the structure of ice and the nonfreezable water layer (often referred to as the quasi-liquid layer) between ice and pore walls.[52−59] However, the effect of surface hydrophilicity on melting point depression in confinement remains debated in the literature.[53] In various studies, a range of materials were investigated, including porous silica-based materials, their hydrophilic and hydrophobic functionalized counterparts, and porous carbons.[53−59] These studies report contradictory results regarding the influence of hydrophilicity on the phase transition temperature of confined water. For various materials with pore diameters r_p > 3 nm, it was observed that hydrophobic materials either exhibit higher melting points for confined water than hydrophilic ones or show a weak to negligible dependence on surface hydrophilicity. In contrast, Deschamps et al.[55] and Osta-Rangel[59] observed lower melting points for hydrophobic materials when comparing MCM-41 silica with hydrophobically functionalized MCM-41 at r_p < 3 nm.

Received: August 9, 2025
Revised: October 5, 2025
Accepted: October 23, 2025
Published: October 29, 2025



ACS Publications
© 2025 The Authors. Published by American Chemical Society

https://doi.org/10.1021/acs.jpcc.5c05595
J. Phys. Chem. C 2025, 129, 20373−20386

The range of surface chemistries in the investigated materials is limited, including hydrophilic silica materials like Vycor glass, MCM-41, and SBA-15, as well as surface-functionalized silica and porous carbons, such as mesoporous carbons and carbon nanotubes. To expand the hydrophilicity spectrum and investigate the effects of individual functional groups on confined water behavior, periodic mesoporous organosilicas (PMOs) offer an ideal system. Their versatile surface properties and high porosity make them well-suited for examining water behavior under confinement. These hybrid materials consist of a silica-based framework interconnected by organic bridging units, which can form crystal-like structures under specific synthesis conditions.[60−64] A key advantage of PMOs is their tunable pore dimensions and surface chemistry, which can be finely tuned by modifying the organic groups of the precursors. This adaptability makes them particularly suitable for investigating how confined water and ice respond to changes in surface polarity and pore size. PMOs have been used to study the structural, dynamic, and adsorption behavior of water, as well as its temperature-dependent properties under nanoconfinement.[14,20,65−70]

In our recent water vapor sorption study, we used PMOs to examine the effects of different surface functionalities on adsorption and condensation behavior. Additionally, we explored the relationship between material surface area as well as pore size with fundamental properties such as mean water density, adsorption layer thickness and adsorption layer density.[14] PMOs based on precursors such as 1,4-bis[(*E*)-2-(triethoxysilyl)vinyl]benzene (BTEVB),[61,62] 2,5-bis[(*E*)-2-(triethoxysilyl)vinyl]aniline (BTEVA),[64,71] 1,4-bis-(triethoxysilyl)benzene (BTEB),[60] 2,5-bis[(*E*)-2-(triethoxysilyl)vinyl]pyridine (BTEVP),[72] 2-chloro-1,4-((*E*)-2′-bis(triethoxysilyl)vinyl)benzene (BTEVClB),[14,70] *N*,*N*-dimethyl-2,5-bis((*E*)-2-(triethoxysilyl)vinyl)aniline (*N*,*N*-DMBTEVA)[14] and 1-methyl-2,5-bis((*E*)-2-(triethoxysilyl)-vinyl)pyridinium iodide (*N*-MBTEVP$^+$I$^-$)[14,70] were categorized according to their hydrophilicity, as shown in Figure 1. The same PMOs are used in this study. A summary of the hydrophilicity characteristics of PMOs from the previous study is provided in Table S3, including surface hydration site (SHS) densities, hydrophilicity indices derived from the inflection point of the desorption branch of water vapor sorption isotherms (HI_{id}), and contact angles. PMOs based on the precursors BTEVB, BTEVFB, and *N*,*N*-DMBTEVA showed lower SHS values (0.32−0.58 nm^{-2}) and higher contact angles (62−82°) compared to the more hydrophilic BTEVA- and BTEVP-PMOs, which exhibited SHS values of 0.65−1.3 nm^{-2} and contact angles of 44−59°. The most hydrophilic materials, BTEB- and *N*-MBTEVP$^+$I$^-$-PMOs as well as MCM-41 silica, displayed the highest SHS values (1.2−2.2 nm^{-2}) and the lowest contact angles (33−45°).

These PMOs were utilized to investigate how surface chemistry and pore diameter affect the structure and orientation of confined ice.[70] It was found that smaller and hydrophilic pores inducing greater deviations in the lattice constants of hexagonal ice compared to bulk. Additionally, cooling protocols were shown to significantly affect the resulting ice phases, with stepwise cooling favoring hexagonal contributions and continuous cooling leading to predominantly cubic-like ice.

The aim of this study is to employ a range of PMOs with varying surface chemistries and hydrophilicities (see Figure 1), as well as pore sizes between approximately 3 and 6 nm, to investigate whether and to what extent pore surface functionality affects the melting and freezing points of water in confinement. Additionally, three approaches for calculating *t*-layer thickness and two methods for determining its density are implemented and compared.

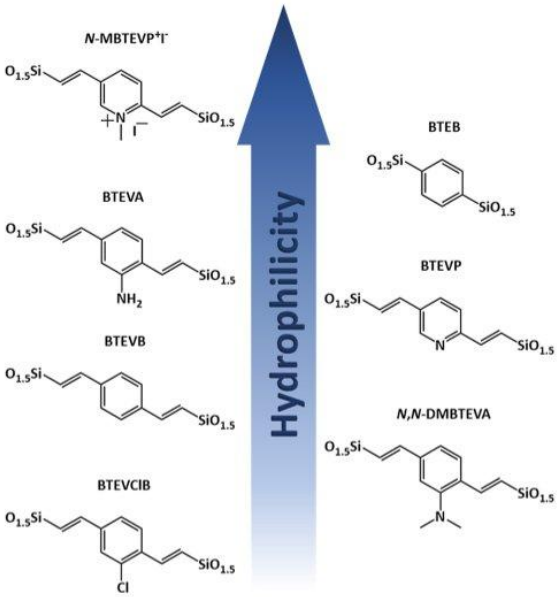


Figure 1. PMOs used, ranked by hydrophilicity as determined in our previous study.[14] Adapted and extended from [14]. 2025 American Chemical Society.

2. EXPERIMENTAL SECTION

2.1. Materials. The synthesis of the various PMOs and MCM-41 silicas was carried out using a soft-matter templating approach, employing cationic quaternary ammonium surfactants (C_nTAB) with alkyl chains of varying lengths (n). Pore sizes ranging from approximately 3 to 6 nm were achieved by adjusting the surfactant alkyl chain length within n = 12 to 20 or by adding *n*-hexane as a swelling agent.

The synthesis of PMO precursors and many PMOs and MCM-41 silicas is detailed in our previous work.[14] For materials not covered in that publication, or if a different batch was used, the synthesis procedures and characterizations are provided in the Supporting Information. The labeling of the different samples follows the same convention as in that work, consisting of the precursor used and the DFT-calculated pore size. For example, a BTEVB-PMO with a pore diameter of 3.8 nm is labeled as BTEVB_3.8.

2.2. Characterization Methods. X-ray powder diffraction (PXRD) patterns were recorded using a PANalytical X'Pert Pro PW3040/60 instrument with Cu Kα radiation to analyze the mesostructure and molecular ordering in the pore walls of the materials. Data evaluation was performed using OriginPro 2024 from OriginLab and X'Pert Highscore Plus from PANalytical.

Nitrogen physisorption measurements were conducted to characterize the porosities of the materials. Before measurement, samples were activated at 100 °C for 20 h under reduced pressure using a Quantachrome Masterprep degasser. The N_2 physisorption experiments were carried out at 77 K using a

https://doi.org/10.1021/acs.jpcc.5c05595
J. Phys. Chem. C 2025, 129, 20373−20386

Quantachrome Quadrasorb−SI−MP and Quadrasorb evo. The pore size distribution was calculated using density functional theory (DFT) with the kernel: N_2 on silica (cylindrical pores), nonlocal DFT (NLDFT) using the adsorption branch. Specific surface area was determined using the Brunauer−Emmett−Teller (BET) method within the p/p_0 range of 0.05−0.3.[73] In cases where the BET range intersected with the condensation step of the isotherms, the range was reduced to ensure measurements remained within the plateau region before condensation ($p/p_0 < 0.3$). Data analysis was performed using QuadraWin 6.0 software from Quantachrome.

To determine the melting and freezing temperatures of water within the porous materials, differential scanning calorimetry (DSC) measurements were conducted using DSC204F1 Phoenix ASC device (with a τ-sensor) from Netzsch, equipped with a liquid nitrogen cooling system. Approximately 2 mg of each sample was placed into a Concavus aluminum crucible (30 μL capacity). Two methods were employed to fill the samples with water: incipient wetness (IW) method and water vapor filling in the climate chamber (C).

For the IW-method, water was added based on the sample mass and pore volume determined from nitrogen physisorption, ensuring complete pore filling. However, this method often results in the presence of bulk water likely due to the lower density of water within the pores and measurement uncertainties associated with adding small amounts of water.[14]

In contrast, the water vapor filling method involved exposing the samples to water vapor in a Binder KMF 115 (E5.2) climate chamber maintained at 25 °C and 90% relative humidity for at least 24 h, allowing pore filling without bulk water formation.

After filling the samples with water, the crucibles were then sealed with aluminum lids using a Netzsch universal sealing press. DSC measurements were performed under a nitrogen atmosphere using heating−cooling cycles at rates of 3 and 10 K/min. For better comparability with literature,[6,9,65] improved signal separation, and more defined freezing signals, only the 3 K/min measurements were used for melting and freezing point determination. Lower heating rates are closer to the true transition temperature because thermal lag effects are reduced. Specifically, increasing the heating rate from 3 K/min to 10 K/min shifts the phase transition signals by roughly 1−3 K to higher temperatures across all samples. Both our data and previous DSC studies show that such rate variations affect the observed transition temperatures but not the integrated melting enthalpy, which remains unchanged in the range of 0.5−10 K/min.[74,75] Based on this experimental observation, and since both 3 and 10 K/min yielded identical enthalpies in our measurements, we included both rates in the enthalpy analysis, with baseline placement being the main source of uncertainty.

Cooling was achieved using liquid nitrogen in a nitrogen atmosphere. Calibration of temperature and heat flow was conducted under identical measurement conditions using a 6-point calibration with adamantane, water, indium, tin, bismuth, and zinc as reference materials.

Data analysis was carried out using Netzsch Proteus Thermal Analysis 8.0.3 and OriginPro 2024 software from OriginLab. A tangential baseline was used in the Netzsch software to determine the melting and freezing enthalpy. To minimize noise and reduce errors in the evaluation of enthalpies and phase transition temperatures, all DSC curves were smoothed using a factor of 6, with a maximum factor of 10 applied for smaller pores and weaker signals, prior to analysis in the Netzsch software. According to Netzsch, the smoothing process is based on established literature guidelines.[76]

3. RESULTS AND DISCUSSION

3.1. Material Characterization. Most materials in this study were previously examined in our recent water vapor sorption study.[14] Therefore, the synthesis and characterization of additional materials for this study are provided in the Supporting Information. Porosity data and hydrophilicity parameters of the materials from the previous water vapor study are also provided (see Table S3). The impact of iodomethane functionalization of BTEVP-PMOs to form *N*-MBTEVP$^+$I$^-$-PMOs on porosity for different pore sizes is summarized in Table S4.

3.2. Influence of Surface Chemistry on Water's Phase Transition Temperature and Enthalpy. The melting and freezing behavior of water confined in MCM-41 silica and various PMOs with hydrophilic, hydrophobic, and charged surface functionalities, with pore sizes between approximately 3 and 6 nm, was investigated calorimetrically. The DSC melting curves of water in samples filled using the C-method are presented in Figure S1, while those filled using the IW-method are displayed in Figure S2. Figure 2 provides an example of

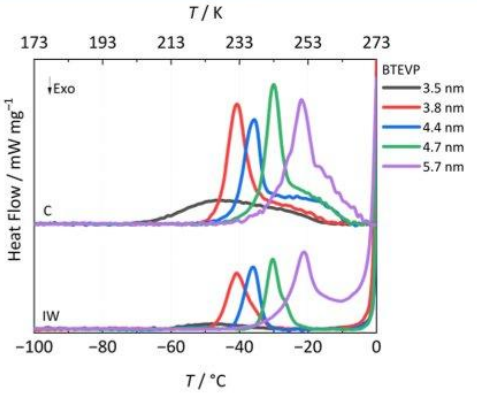


Figure 2. Baseline-corrected DSC melting curves of water in BTEVP-PMOs with varying pore diameters, filled using the IW- or the C-method. The DSC measurements were conducted at a heating rate of 3 K/min.

BTEVP-PMOs filled using both methods. When comparing the melting transitions of water within a specific pore size using both filling methods, the IW-method not only shows transitions of confined water but also displays bulk melting transitions at around 0 °C. This effect likely arises from the lower density of confined water, a correlation we identified for these samples in our recent work (see Table S3).[14] For all analyzed materials, the average density of confined water is lower than that of bulk water (0.997 g/cm^3). In more hydrophobic materials such as BTEVB or *N*,*N*-DMBTEVA, average densities are lower, ranging from 0.45 to 0.56 g/cm^3, whereas in hydrophilic materials such as MCM-41 silica or BTEB they range from 0.54 to 0.82 g/cm^3. Since the added water amount was calculated based on pore volume determined from nitrogen physisorption, and confined water

https://doi.org/10.1021/acs.jpcc.5c05595
J. Phys. Chem. C 2025, 129, 20373−20386

has a reduced density, the presence of bulk water is an expected result. Additionally, minor measurement errors in handling such small water quantities may contribute to this observation. When using the climate chamber method to fill PMOs with water, a shoulder appears adjacent to the pore melting transition. A sharper signal also emerges next to the freezing transitions of confined water in the cooling curves, with the enthalpy matching that of the shoulder in the melting transition (see Figure S3).

This phenomenon has also been observed in the literature and is described as expelled water.[77,78] The absence of this shoulder or signal in most melting and freezing curves of IW-filled samples suggests that, for the samples filled via C-method, water is partially displaced from the pores due to density changes during cooling (falling from the bulk liquid density of roughly 1.00 to 0.92 g/cm^3 as the temperature decreases from 280 K to the pore-size-dependent phase transition temperature), subsequently freezing outside the pores.[79] This process is schematically illustrated in Figure S4. Since only a small amount of water resides outside the pores and it maintains significant contact with the PMO particle surface, its melting and freezing temperatures differ from those of bulk water. Furthermore, pore melting may also initiate the melting of the water outside the pores. Assuming a bulk water melting enthalpy of 6.01 kJ/mol[80] the amount of water outside the pores can be calculated from the measured enthalpy (see Figure S5). As the melting temperature depression (ΔT) increases due to stronger confinement, the amount of outside water decreases significantly around ΔT = 30−40 K, then slightly increases as ΔT continues to rise for hydrophilic materials such as MCM-41 silica and BTEVA-PMOs, as well as the hydrophobic BTEVB-PMOs. In contrast, *N*,*N*-DMBTEVA-PMOs and charged *N*-MBTEVP$^+$I$^-$-PMOs show relatively constant behavior in the ΔT range of 30 to 60 K.

The pore size dependence of the melting point depression of water in MCM-41 silica and various PMOs, filled using the two previously mentioned methods, is presented in Figure 3 (top), while the freezing point depression is illustrated in Figure S6. Errors were not specified, as the experiments for both the melting and freezing processes are highly reproducible, with negligible error margins. For materials with larger pores (r_P > 1.8 nm), no significant influence of the surface chemistry on the melting transition temperature of confined water is observed, except for water in BTEVClB-PMOs, which exhibit a notably greater reduction in melting temperature when filled using both the C- and IW-methods. This lack of surface chemistry influence on confined water in larger pores aligns with previous studies.[53,56] When considering pore radii around 1.8 nm and smaller, a steeper slope is observed, particularly for hydrophobic materials like BTEVB and *N*,*N*-DMBTEVA. Hydrophilic materials such as MCM-41 silica, BTEVA-PMOs, BTEVP-PMOs, and BTEB-PMOs, show a shallower slope. This observation aligns with the findings of Deschamps et al.[55] and Osta-Rangel,[59] suggesting reduced ice crystal size in more hydrophobic materials. For a more detailed comparison of these results with our data, a common pore size definition is required. Since the BET-based pore size ($d_{P,BET}$) can be readily derived from the porosity data and was used in the study of Deschamps et al., we adopted this approach for comparison in Figure S7. The trend observed in this study agrees well with data of Deschamps, both showing a stronger melting-point depression in more hydrophobic materials. In contrast, the pronounced effects reported by

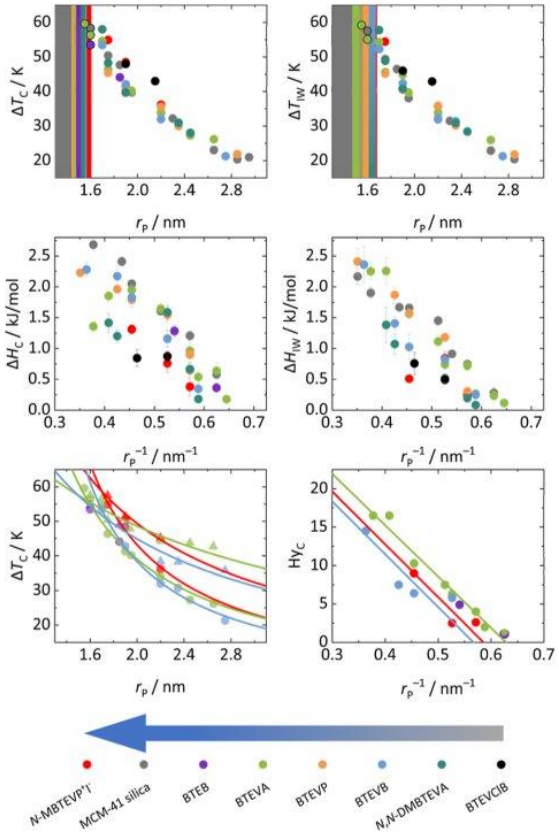


Figure 3. Top: pore size-dependent melting point depression of water confined in the pores of various MCM-41 silica and PMO materials, filled using the C-method (left) and the IW-method (right). Additionally, in the pore size regions where no melting or freezing transitions occur, are highlighted in the corresponding colors of the respective materials. Center: specific melting enthalpy of confined water in various materials plotted against the reciprocal pore radius, allowing the determination of the critical pore radius ($r_{P,cr,\Delta H}$) through extrapolation. The error bars mainly reflect deviations arising from the evaluation process. Bottom, left: the pore radius dependence of the melting points (circles) and freezing points (triangles) is displayed for *N*-MBTEVP$^+$I$^-$-PMOs, BTEB-PMOs, BTEVA-PMOs, and BTEVB-PMOs filled using the C-method. Additionally, Gibbs−Thomson fits for the melting and freezing points are shown as lines. Bottom, right: hysteresis plotted against the reciprocal pore radius, allowing for linear extrapolation. The arrow denotes increasing hydrophilicity of the materials.

Osta-Rangel for surface-modified MCM-41 silica are less evident when evaluated using $d_{P,BET}$. Hydrophobic materials like the BTEVB, *N*,*N*-DMBTEVA- and BTEVClB-PMOs on the other hand, show even stronger melting point reduction than the hydrophobically functionalized MCM-41 silica. This example highlights why quantitative comparisons across studies must be made with caution: differences in pore size determination methods and experimental parameters (e.g., heating rate, sample filling) complicate direct interpretation.

The effect of pore surface, which is only apparent in very small pores, can be attributed to the increasing ratio of the nonfreezable water layer to pore radius as pore size decreases. Additionally, DSC melting curves (see Figures S1 and S2)

https://doi.org/10.1021/acs.jpcc.5c05595
J. Phys. Chem. C 2025, 129, 20373−20386

Table 1. Critical Pore Radii ($r_{P,cr}$), for the C- and IW-Samples, Determined through Linear Fitting of the Specific Enthalpy (ΔH) and Hysteresis between Melting and Freezing Point (hy) of Confined Water

material	C-method		IW-method	
	$r_{P,cr,C,\Delta H}$/nm	$r_{P,cr,C,hy}$/nm	$r_{P,cr,IW,\Delta H}$/nm	$r_{P,cr,IW,hy}$/nm
N-MBTEVP$^+$I$^-$	1.61 ± 0.01	1.71 ± 0.10	1.68 ± 0.34	1.57 ± 0.07
MCM-41 silica	1.44 ± 0.02	1.57 ± 0.07	1.47 ± 0.04	1.57 ± 0.08
BTEB				
BTEVA	1.48 ± 0.04	1.60 ± 0.03	1.53 ± 0.03	1.57 ± 0.02
BTEVP	1.46 ± 0.09	1.65 ± 0.06	1.61 ± 0.06	1.61 ± 0.06
BTEVB	1.57 ± 0.06	1.76 ± 0.17	1.67 ± 0.07	1.92 ± 0.10
N,*N*-DM BTEVA	1.56 ± 0.10	1.62 ± 0.03	1.67 ± 0.02	1.66 ± 0.06
BTEVClB				

show broader and weaker signals for hydrophobic BTEVB and *N*,*N*-DMBTEVA-PMOs, as well as the charged *N*-MBTEV-P$^+$I$^-$-PMOs at a pore diameter of 3.4 nm, while hydrophilic materials like MCM-41 silica, BTEVA, and BTEB maintain well-defined signals down to approximately 3 nm.

The dependence of water's phase transition enthalpy on surface chemistry was examined using cyclical measurements conducted with both 3 and 10 K/min as heating/cooling rates. Despite strong agreement between the melting and freezing signals and both heating rates, including the satellites, uncertainties in the evaluation process result in errors in the reported data (see Figure 3, center). The specified enthalpies correspond to the water confined within the pores, with the bulk water contribution subtracted for IW-filled samples based on the bulk signal area and enthalpy. For samples filled in the climate chamber, total water content is directly used for enthalpy calculations if no satellite signals are present. Shoulder signals are treated as bulk, with pore-confined water determined as for IW-materials. Plotting the specific enthalpies against reciprocal pore radius reveals a linear progression that depends on the material class. Hydrophilic materials, including MCM-41 silica, BTEVA-PMOs, and, to a large extent, BTEVP-PMOs, show comparable specific enthalpies for confined water, which are higher than for hydrophobic materials. Assuming a bulk-like ice core within the pores, this indicates smaller ice cores in hydrophobic and charge samples, potentially due to a thicker nonfreezable water layer. The pore radius ($r_{P,cr,\Delta H}$) where $\Delta H = 0$, indicating no freezing, can be extrapolated from the linear trend. The determined values are presented in Table 1 and highlighted in Figure 3 (top) as zones, color-coded by material class to show the pore radius at which water freezing ceases. With increasing hydrophobicity, the specific enthalpy of fusion approaches zero at larger $r_{P,cr,\Delta H}$. For both filling methods (C/IW), the MCM-41 silica shows the lowest critical pore radius with 1.44 nm/1.47 nm, which is in a very good agreement with the results of Jähnert et al.,[9] while hydrophobic materials like BTEVB- and *N*,*N*-DMBTEVA-PMOs show with 1.56 nm/1.67 nm higher critical pore radii. Since the specific melting enthalpy of water in BTEVClB-PMOs is in the range of hydrophobic *N*,*N*-DMBTEVA-PMOs, a similar critical pore radius is expected.

Jähnert et al.[9] used Gibbs−Thomson fits to determine the pore size where confined water melts and freezes at the same temperature, below which no first-order phase transition occurs. Figure 3 (bottom, left) illustrates this approach applied to several PMOs. Using a modified approach with similar results but reduced errors, the data were extrapolated by plotting the hysteresis against r_p^{-1} (see Figure 3, bottom, right; or all other materials see Figure S8). With linear fits, the radii at which no hysteresis occurs between melting and freezing ($r_{P,cr,hy}$, listed in Table 1) were determined, revealing a trend consistent with $r_{P,cr,C,\Delta H}$. Despite its more hydrophilic nature, *N*-MBTEVP$^+$I$^-$-PMOs exhibits the largest values for all critical pore radii, except for $r_{P,cr,IW,hy}$. This result suggests a thicker *t*-layer, which aligns with findings from the water vapor sorption study for the adsorption layer.[14] The chaotropic nature and size of the surface ions (I$^-$/pyridinium$^+$), along with the hydrophobic methyl group extending into the pore, may induce changes in the water structure within the nonfreezable layer. The differences in functionalization degree among the charged PMOs, as shown in Table S4, where higher functionalization degrees (F) are observed for PMOs with larger pore radii (for d_P = 3.2 to 3.8 nm; F = 7% to 18%) could be a source of error. Moreover, the influence of the distribution of charged sites on the behavior of confined water cannot be ruled out and should be systematically investigated in future studies. The critical pore radius results align with experimental observations. For water in charged PMO with a pore diameter below 3.5 nm (Figure S1, *N*-MBTEVP$^+$I$^-$_3.2), no clear melting transition is observed. Since the critical pore diameter for the occurrence of a water−ice phase transition is around 3.3 nm, this explains the absence of a sharp water−ice transition in these pores. However, magnification of the DSC melting curve reveals a broad signal extending from −70 to −20 °C. This broad feature may originate from two contributions: (i) a continuous phase transition[5] of strongly confined water, and/or (ii) water expelled from the pores during freezing,[77,78] which remains near the external pore surface and exhibits a depressed melting temperature. If freezing does occur inside the pores close to the critical size, then even a small variation in pore diameter will strongly broaden the transition, because the Gibbs−Thomson relation links the melting/freezing point depression to ice core radius ($\Delta T \propto 1/r_c$). Thus, heterogeneity in pore size distribution near the critical regime can significantly smear out the transition signal. Such broadening is not exclusive to charged PMOs, but was also observed for BTEB_3.2 and BTEVP_3.5, indicating that it arises generally from the reduced dominance of the confined freezing signal at pore diameters close to the critical value. Further analysis would be required to determine the structural state of confined water close to its critical confinement limit, as in the sample *N*-MBTEVP$^+$I$^-$_3.2, and to clarify the melting behavior of water expelled to the external pore surface.

Due to limited data points, a detailed analysis of BTEB-PMOs is not feasible. However, their similarity to BTEVA-PMOs in temperature reduction and hysteresis behavior suggests comparable critical pore radii.

https://doi.org/10.1021/acs.jpcc.5c05595
J. Phys. Chem. C 2025, 129, 20373−20386

3.3. Nonfreezable Layer Thickness. In the previous section, an impact of pore size and surface chemistry on the measured parameters, including melting and freezing point depression, specific enthalpies, and hysteresis width, was observed. In smaller pores, the nonfreezable layer becomes more significant due to its increasing proportion relative to the pore radius. Its thickness directly affects the ice core size, influencing key variables such as melting temperature and enthalpy. The stronger melting point depression and lower specific enthalpies observed for PMOs with surface charges and higher hydrophobicity, particularly in smaller pores, suggest a smaller ice core or a thicker nonfreezable layer compared to hydrophilic materials. This section employs established methods from literature, along with modified approaches, to calculate the ice core size, nonfreezable layer thickness, and the density of confined water.

The group of Findenegg[6,9,57] used two methods to determine the nonfreezable layer thickness in cylindrical pores of ordered mesoporous silica, one based on the Gibbs–Thomson equation and the other on the extrapolation of relative melting enthalpy. By plotting the melting temperature depression (ΔT) against the pore radius (r_p), the Gibbs–Thomson constant (C_{GT}) and nonfreezable layer thickness (t) can be determined using the Gibbs–Thomson eq 1 for cylindrical pores.

$$\Delta T = \frac{C_{GT}}{(r_p - t)} \tag{1}$$

$$C_{GT} = \frac{2T_b(\gamma_{ws} - \gamma_{wl})v}{\Delta H_b} \tag{2}$$

The Gibbs–Thomson constant is given by eq 2, with the bulk water melting point (T_b), interfacial free energy wall–solid (γ_{ws}) and wall–liquid (γ_{wl}), molar volume of liquid water (v) and bulk melting enthalpy (ΔH_b).[6,81]

An example evaluation for water-filled MCM-41 silica samples is shown in Figure 4 (left), with data points from Jähnert et al.[9] marked as red circles. The data for MCM-41 silica, filled using both methods, are in good agreement with those from Jähnert et al.

Morishige and Kawano[5] applied a linearized Gibbs–Thomson equation to relate ΔT and $(r_p - t)^{-1}$. Using this plot (see Figure 4 (right)), the thickness of the nonfreezable layer ($t_{GT,lin}$) is determined by adjusting the t-value so that a linear fit passes through the origin, with the slope yielding the Gibbs–Thomson constant ($C_{GT,lin}$). The results from both methods are shown in Figure 5. A consistent trend emerges

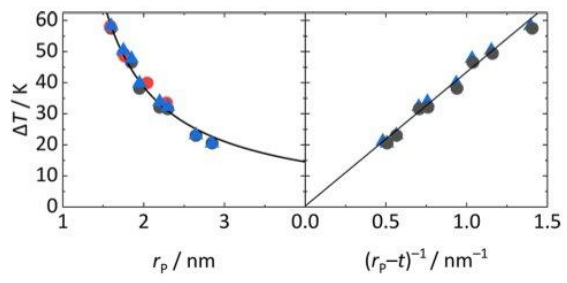


Figure 4. Melting point depression of water (ΔT) in MCM-41 silica filled with the IW-method (gray circles) and C-method (blue triangles) and the measured values by Jähnert et al.[9] (red circles), plotted against the pore radius (r_p) (left) and the reciprocal ice core radius (right), using a t-layer thickness of 0.89 nm.

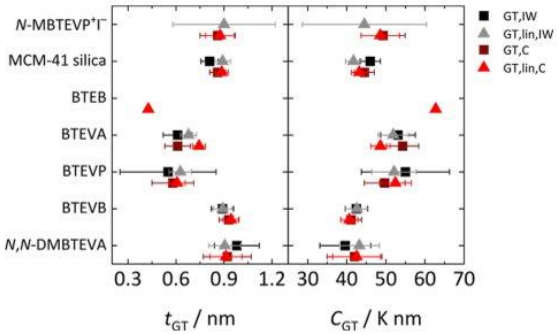


Figure 5. t-layer thickness (t_{GT}) and Gibbs–Thomson constant (C_{GT}) values, determined using the Gibbs–Thomson equation (squares) and its linearized form (triangles), are shown for various materials filled via the C (red shades) and IW (black shades) methods. The materials are arranged along the y-axis in order of increasing hydrophilicity.

across filling methods and evaluation approaches. Hydrophobic materials, such as BTEVB-PMOs and *N*,*N*-DMBTEVA-PMOs, have a larger t-layer (0.9–1 nm, while hydrophilic materials, like BTEVA-PMOs and BTEVP-PMOs, have a thinner layer (0.55–0.75 nm). The t-layer for BTEVP-PMOs is on average 0.07 nm smaller than for BTEVA-PMOs.

Smaller t-layers, around 0.43 nm, were calculated for the hydrophilic BTEB-PMOs, but this result should be interpreted cautiously due to the limited data points. The nonfreezable layer thickness aligns with earlier findings, explaining the steeper decrease in melting temperatures and larger critical pore radii in hydrophobic materials, which can be attributed to their thicker nonfreezable layer. Despite its hydrophilic nature, the charged PMOs exhibited a thicker nonfreezable layer, likely due to the influence of surface charges and functional groups, which will be further explored in later chapters. MCM-41 silica, with an average t-layer thickness of 0.86 nm, displays a higher thickness than expected, in contrast to the observations in Chapter 3.2. Using the literature value for C_{GT} for MCM-41 silicas (51.9 K nm)[9,57] and incorporating the data points from the literature, a t-layer thickness of 0.69 nm is obtained, aligning with the reported value of 0.66 nm[9].

For PMOs, C_{GT} values are lower in hydrophobic materials than in hydrophilic ones, suggesting higher γ_{wl} and/or lower γ_{ws}. This implies reduced liquid-wall affinity and slightly increased solid-wall affinity. Based on $\gamma_{ws} - \gamma_{wl} = \gamma_{sl}\cdot\cos(\theta)$, where γ_{sl} is the solid–liquid interfacial energy and θ is the ice/water contact angle ($\theta = 0°$ for complete wetting), stronger ice–liquid interactions are expected in hydrophobic pores. Conversely, larger C_{GT} values in hydrophilic materials indicate a preference for a liquid layer. Considering the onset of melting transition instead of signal maxima, reveals a similar trend, albeit with slightly higher t-layer and C_{GT} values (Figure S9). However, the differences between the various materials for the t-layer and C_{GT} are weaker. Since the Gibbs–Thomson equation does not account for influences from surface defects or different crystal phases,[82] as observed for water in PMOs,[70] and because PMOs, especially hydrophobic ones, exhibit alternating surface hydrophilicity (silica-organic bridge-silica),

https://doi.org/10.1021/acs.jpcc.5c05595
J. Phys. Chem. C 2025, 129, 20373–20386

the impact of this on the thickness of the liquid-like layer and C_{GT} remains unknown. Therefore, these results serve as rough comparative measures and should be interpreted with caution.

An alternative approach relies on melting and freezing enthalpy, offering an evaluation independent of the DSC peak shape. However, baseline misalignment can introduce significant errors, which were accounted for in all enthalpy-based calculations and represent the main source of the error bars. Jähnert et al.[9] employed a linear correlation between normalized melting enthalpy and reciprocal ice core radius to determine the *t*-layer, calculating a thickness of 0.6 nm for water in MCM-41 silica. In their calculation, the number density of water in the pores was used to determine the molar enthalpy of fusion for different pore sizes. Using the same method, we reproduced this result, obtaining 0.57 ± 0.02 nm (C type filling: 0.4 ± 0.02 nm). However, our water vapor sorption study[14] revealed that density varies with pore size and should be specified individually. Incorporating sample-specific densities, we obtained *t*-layer thicknesses of 0.3 ± 0.02 nm (IW-method) and 0.15 ± 0.02 nm (C-method) for MCM-41 silica. When applied to PMOs, this method yielded near-zero or even negative *t*-values, regardless of the filling method or density specification (averaged or individual). These unphysical results suggest that the approach is unsuitable for PMOs and will not be discussed further. The previously mentioned methods neglect the dependence of *t*-layer thickness on phase transition temperature and pore size, with studies indicating that smaller pores and lower temperatures lead to thinner nonfreezable layers.[52,83−89]

The *t*-layer can also be determined for individual samples using enthalpy-based calculations. Following the approach of Rother et al.[10,11] for evaluating adsorption layers in cylindrical pores, the ice core volume (V_c) is calculated using eq 3, from which the ice core radius (r_c) is derived (eq 4). The nonfreezable layer thickness t_{geo} is then obtained by subtracting r_c from the hydraulic radius (r_h) (see eq 5).

$$V_c = \frac{\Delta H_m}{\Delta H_T} \cdot \frac{1}{\rho_{ice}} \tag{3}$$

$$r_c = \sqrt{\frac{V_c r_h^2}{V_P m_S}} \tag{4}$$

$$t_{geo} = r_h - r_c \tag{5}$$

An alternative geometric approach uses the BET surface area (S_{BET}) from nitrogen physisorption to calculate the nonfreezable layer thickness ($t_{geo,BET}$) (see eq 6).

$$t_{geo,BET} = \frac{V_P m_S - V_c}{S_{BET} m_S} \tag{6}$$

where m_S represents the mass of the respective sample used in the DSC experiment, V_P is the pore volume obtained from nitrogen physisorption measurements, ΔH_m is the enthalpy of fusion of water in the pores in joules, and ρ_{ice} is the density of bulk ice (0.917 g/cm^3).[90] Additionally, the temperature-dependent melting enthalpy (ΔH_T) for ice Ih, as determined from the heat capacities of ice and supercooled water by Murphy and Koop,[91] was used. Results for the nonfreezable layer thickness, determined using the Rother method (eqs 4 and 5) and the BET surface approach (eq 6), show nearly linear behavior when plotting $t_{geo,BET}$ (Figure 6) and t_{geo} (Figure S10) against the relative pressure at the inflection point in the desorption branch of water vapor sorption isotherms ($(p/p_0)_{w,id}$). The position of $(p/p_0)_{w,id}$, as derived from the Kelvin equation,[14,92,93] provides insights into both the pore size and the surface hydrophilicity through the contact angle. As pore radii and contact angles increase, the inflection point shifts to higher relative pressures. In Figures 6 and S10, more hydrophobic materials, such as BTEVB- and *N*,*N*-DMBTEVA-PMOs, show greater nonfreezable layer thicknesses. A stronger linear trend is observed for materials filled via the climate chamber method, potentially due to differences at the pore entrances. In C-materials, water may escape from the pores during density changes, whereas in IW-materials, bulk ice blocks the pore entrances. Also, the pore-filling mechanism between water vapor sorption and the C-method is more comparable than with the IW-method. This phenomenon will be further discussed in subsequent sections. Notable deviations are particularly evident in the charged PMOs filled using the IW-method. *N*-MBTEVP$^+$I$^-$-PMOs exhibit comparatively larger *t*-layers. A similar but less pronounced trend emerges when comparing the nonfreezable layer thickness with the contact angle (θ), derived from the relative pressure at the inflection point of capillary condensation in the adsorption branch of the water vapor measurement (see Figure S11).

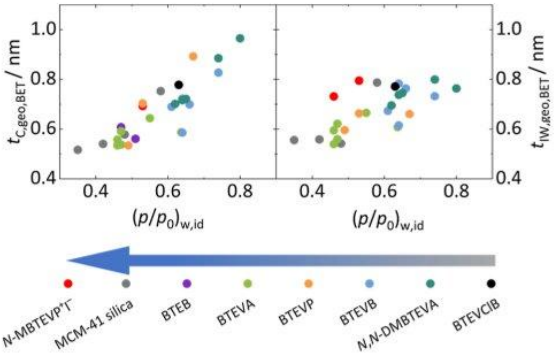


Figure 6. Dependence of *t*-layer thickness ($t_{geo,BET}$) on the relative pressure at the inflection point in the desorption branch of water vapor sorption isotherms for C-materials (left) and the IW-materials (right). The arrow denotes increasing hydrophilicity of the materials.

While the correlation is not as strong as in previous observations, it can still be seen that more hydrophilic materials, characterized by smaller contact angles, tend to exhibit smaller *t*-layers. No direct correlation with the surface hydration site density[14] was found. However, a trend suggests larger *t*-layers at lower SHS densities.

The pore radius dependence of the *t*-layer and the ratio of *t*-layer to pore radius (t/r_P) is shown in Figures 7 and S12. As pore size decreases and the reduced melting temperature increases, a decreasing trend is observed for both $t_{C,geo,BET}$ and $t_{IW,geo,BET}$. This trend aligns with expectations based on various studies in the literature.[52] While the *t*-layer decreases with pore size, its proportion relative to the pore radius increases, with a steeper gradient for IW- compared to C-materials.

More hydrophobic materials, such as *N*,*N*-DMBTEVA- and BTEVClB-PMOs, exhibit higher values for both the *t*-layer and the relative *t*-layer, especially in smaller pores. However, as pore radius increases, the differences between materials diminish. A similar trend is observed in the temperature dependence of the relative *t*-layer, with more hydrophobic

https://doi.org/10.1021/acs.jpcc.5c05595
J. Phys. Chem. C 2025, 129, 20373−20386

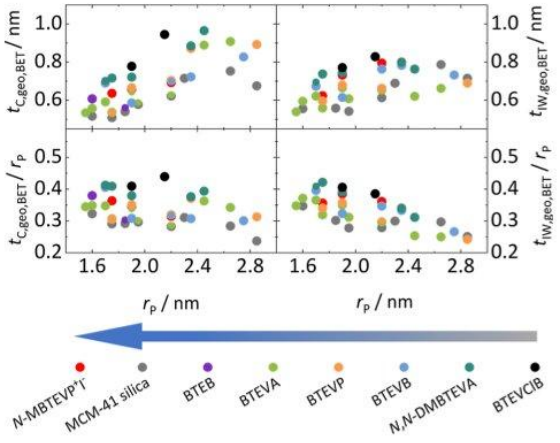


Figure 7. Pore size dependence of $t_{geo,BET}$ (top) and relative $t_{geo,BET}$ size (bottom) for C-materials (left) and IW-materials (right). The arrow denotes increasing hydrophilicity of the materials.

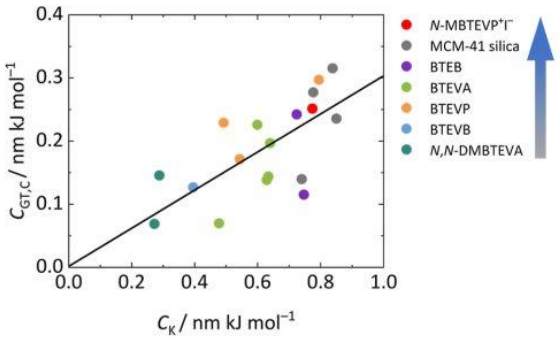


Figure 8. Plot of the Gibbs−Thomson constant ($C_{GT,C}$) against the Kelvin constant (C_K), with the black line representing a linear fit through the origin. The arrow denotes increasing hydrophilicity of the materials.

samples exhibit larger t/r_p ratio at greater melting temperature reduction (see Figure S13).

The temperature dependence of the nonfreezable layer of MCM-41 silica aligns well with both simulation and experimental literature studies on amorphous silica, which observed a *t*-layer of approximately 1 nm at 10 K (see Figure S14). Instead of the reported slope of −0.03 nm/K, we observe a slope of −0.01 ± 0.002 nm/K.[83,84] Similar values are observed for PMOs, suggesting that the slope is primarily temperature-dependent rather than influenced by surface chemistry.

There appears to be a relationship between the nonfreezable layer thickness and the adsorption layer thickness ($t_{a,WVS}$) determined from water vapor sorption (see Figure S15), with a stronger correlation observed between t_{geo} and $t_{a,WVS}$, both calculated using eqs 4 and (5). In general, the nonfreezable layer is roughly twice as thick as the adsorption layer, suggesting a reduced tendency of the surface to accommodate ice in its vicinity, likely due to a greater structural mismatch between ice and pore wall compared to liquid water and pore wall. The Gibbs−Thomson constant (C_{GT}) can be determined using ΔT, T_b, the radius of the ice core (r_{core}) and ΔH_b (eq 7). Similarly, the Kelvin constant (C_K) can be derived from $(p/p_0)_{w,id}$, the Kelvin radius (r_K), the ideal gas constant (R), and the temperature at which the water vapor sorption experiments were conducted (T_{WVS}) using eq 8. C_{GT} represents the product of the molar volume (v), γ_{sl} and $\cos(\theta)$ for temperature below the bulk melting transition, while C_K denotes the product of the surface tension at the liquid/gas interface within the confinement (γ_{gl}), the molar volume (v) and $\cos(\theta)$ at 25 °C.

$$C_{GT} = \Delta T \Delta H_b r_{core} \frac{1}{2T_b} = \gamma_{sl} v \cos(\theta) \tag{7}$$

$$C_K = \frac{1}{2} \ln\left(\frac{p}{p_0}\right) R T_{WVS} r_K = \gamma_{gl} v \cos(\theta) \tag{8}$$

Both C_K and $C_{GT,C}$ quantify the affinity between water and the pore wall. The near−linear relationship between $C_{GT,C}$ and C_K (see Figure 8) suggests a connection between capillary condensation pressure and liquid core radius (or adsorption layer thickness) to temperature reduction of melting transition and freezable core radius (or nonfreezable layer thickness), highlighting the similar influence of confinement and surface properties on water behavior in both situations.

Hydrophilic materials show higher values for the constant *C*, while hydrophobic materials fall in the lower range, a trend also observed for IW-materials. This behavior aligns with the C_{GT} trend from the Gibbs−Thomson fit (Figures 4 and 5).

In addition to the thicker *t*-layer, C_{GT} values in the frozen state are roughly half those of C_K. Assuming γ_{sl} = 31.7 mJ/m^2[29] and γ_{gl} = 71.69 mJ/m^2[94,95] remain constant under confinement across different materials and pore sizes, the γ_{gl}/γ_{sl} ratio of 2.26 could explain the nearly 2-fold higher C_K. In this context, the value of *C*, and consequently ΔT and r_{core}, for a given pore size are influenced by the contact angle.

A temperature- and surface-chemistry-dependent fraction of nonfreezable water relative to the total pore water is observed, ranging between 40% and nearly 100% (see Figure S16). As ΔT increases (due to a decreasing pore size), the nonfreezable water fraction rises. At the same melting temperature, hydrophobic materials show a higher fraction of liquid-like water, a trend particularly pronounced in IW-materials. Hydrophilic materials, such as MCM-41 silica, BTEVA- and BTEVP-PMOs, exhibit the lowest fraction, while more hydrophobic *N*,*N*-DMBTEVA-PMOs and charged PMOs show higher proportions of nonfreezable water. BTEVB- and BTEVClB-PMOs fall in an intermediate range between these two groups.

3.4. Non-Freezable Layer Density. Based on the results of the geometric *t*-layer calculation, the density (ρ_t) of the nonfreezable layer can be determined using the BET surface area and the mass of nonfreezable water (m_t), obtained from the mass of water in the pore (m_P) and core (m_C) in eq 9, and applied in eq 10.

$$m_t = m_P - \frac{\Delta H_m}{\Delta H_b} = m_P - m_C \tag{9}$$

$$\rho_t = \frac{m_t}{S_{BET} m_S t} \tag{10}$$

To ensure comparability with data from the water vapor sorption study,[14] the *t*-layer thickness derived from eq 5, is used to calculate ρ_t. In Figure 9, the calculated *t*-layer density of the samples filled via the climate chamber ($\rho_{C,t,geo}$) is plotted

https://doi.org/10.1021/acs.jpcc.5c05595
J. Phys. Chem. C 2025, 129, 20373−20386

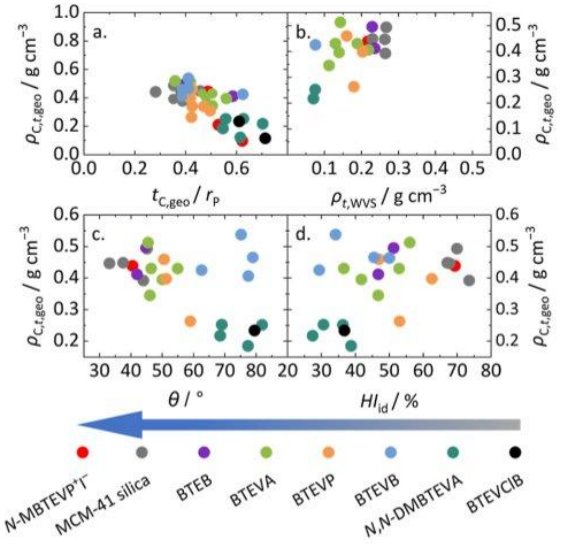


Figure 9. Plots of the nonfreezable layer density ($\rho_{C,t,geo}$) against (a). The relative *t*-layer thickness ($t_{C,geo}/r_P$), (b). Adsorption layer density ($\rho_{t,WVS}$), (c). Contact angle (θ), and (d). Hydrophilicity index (HI_{id}). The arrow denotes increasing hydrophilicity of the materials.

against $t_{C,geo}/r_P$, the average adsorption layer density from water vapor sorption ($\rho_{t,WVS}$), the contact angle (θ), and the hydrophilicity index (HI_{id}), which compares the relative pressure at the inflection point of desorption of water vapor sorption and nitrogen physisorption isotherms.

Consistent with the water vapor sorption study,[14] a clear trend emerges between the density and the relative *t*-layer thickness, where materials with thicker nonfreezable layers exhibit lower densities. A similar correlation was observed by Engemann et al.[83] in X-ray experiments for the nonfreezable layer between ice and SiO_2. They suggest that the average density reduction results from an increased possibility of fluctuations of the low-density liquid (LDL) phase in thicker layers, assuming an initial high-density liquid (HDL)-like phase. If a linear relationship between the relative $t_{C,geo}$ and the *t*-layer density, $\rho_{C,t,geo}$ would approach 1 g/cm^3 as $t_{C,geo}/r_P$ tends toward zero, similar to observations for water in PMOs at 25 °C.[14]

In our DSC experiments, hydrophobic samples generally exhibit lower densities and thicker *t*-layers. However, BTEVB-PMOs partially deviate from this trend, showing density and, in the case of C-filling, *t*-layer thickness values similar to more hydrophilic materials (Figures 9 and 7). A general correlation between $\rho_{C,t,geo}$ and $\rho_{t,WVS}$ is observed with respect to hydrophilicity. In contrast to water vapor sorption, where the water remains liquid within the pore center, the density of the *t*-layer in the presence of an ice core is approximately twice as high. This may result from molecular rearrangement or compaction of water near the pore wall, driven by the pressure from crystallization and expansion of the core water.[36,41,96] For IW-materials, the *t*-layer density is even higher. As shown in Figure S17, where $\rho_{IW,t,geo}/\rho_{C,t,geo}$ is plotted against $(p/p_0)_{w,id}$, hydrophobic materials like *N,N*-DMBTEVA- and BTEVClB-PMOs exhibit $\rho_{IW,t,geo}$ that are 2−5 times greater than $\rho_{C,t,geo}$. In contrast, more hydrophilic materials show only a slight, nearly constant increase in $\rho_{IW,t,geo}/\rho_{C,t,geo}$. For example, in MCM-41 silica, the ratio gradually rises from 1.4 to 1.8. The higher density in IW-materials could, as discussed in the previous chapter, result from pore closure by bulk ice formation, which traps the remaining water within the pores and limits its ability to escape during phase transitions. Consequently, the water in the nonfreezable layer may undergo restructuring and may occupy hydrophobic regions, explaining the significantly higher $\rho_{IW,t,geo}$ in more hydrophobic samples. However, this does not fully account for the BTEVB-PMOs. This consideration is further reinforced when the relative increase in specific pore water content per sample mass in IW-filled samples compared to C-filled ones ($\Delta_{rel}n_{s,P}$) is plotted against HI_{id} as shown in Figure S18. Despite the observed scatter, in highly hydrophilic materials ($HI_{id} \rightarrow 100\%$), the difference in specific pore water content approaches approximately 25%. However, in more hydrophobic samples, IW filling results in an increase of up to ~150% in specific pore water content, likely due to core water densification and/or migration to less favorable surface sites. The latter seems more probable, as surface hydrophilicity appears to govern the effect: in hydrophilic samples, the surface is nearly saturated with water, which limits additional water adsorption. Notably, this effect has no significant impact on *t*-layer thickness.

Figure 9(c,d) shows the effect of surface hydrophilicity, represented by the contact angle and hydrophilicity index, on *t*-layer density. Except for BTEVB-PMOs, more hydrophilic materials (MCM-41 silica, BTEVA-, BTEVP-, and BTEB-PMOs) exhibit higher nonfreezable layer densities than more hydrophobic ones (BTEVClB- and *N,N*-DMBTEVA-PMOs). While a correlation with surface hydration site density is evident for the adsorption layer density,[14] no such dependence is observed for the nonfreezable layer density. The BTEVP-PMO with $\rho_{C,t,geo}$ = 0.26 gcm^{-3} may be considered an outlier, although the overall scatter of all samples likely reflects dependencies on *t*-layer thickness and pore radius, highlighting the complex interplay of multiple parameters.

Assuming water molecules are confined near the surface hydration sites (SHS) rather than spread throughout the entire *t*-layer volume, the density $\rho_{t,SHS}$ can be calculated using eq 11. By applying the ratio of the silica bond length of 0.31 nm[97,98] to the repeating unit length d_{Ru}, the nonfreezable layer volume within the Si−O−Si unit can be estimated. Only the sites with hydration, represented by number of hydration sites per used sample amount (Nw), are considered, as not all Si−O−Si units contain silanol groups. For materials like BTEVP- and BTEVA-PMOs, where the pyridine nitrogen or the amino group serve as SHS, these groups and their associated volume are treated equivalently to Si−O−Si units. Given that MCM-41 silica is composed entirely of silica with d_{Silica} = 0.31 nm, this calculation would consider the entire *t*-layer volume, potentially underestimating the true value. Instead of being uniformly distributed, possibly forming clusters,[99,100] the expansion of which is unknown, preventing the calculation of the water density within these clusters.

$$\rho_{t,SHS} = \frac{m_t}{(V_P m_s - V_c)\frac{d_{Silica}}{d_{Ru}} N_w} \quad (11)$$

Figure 10 presents the calculated values for $\rho_{t,SHS}$ for both filling methods, plotted against the contact angle and the water density in the adsorption layer, as determined by water vapor sorption. For more hydrophilic materials filled using the C-

https://doi.org/10.1021/acs.jpcc.5c05595
J. Phys. Chem. C 2025, 129, 20373−20386

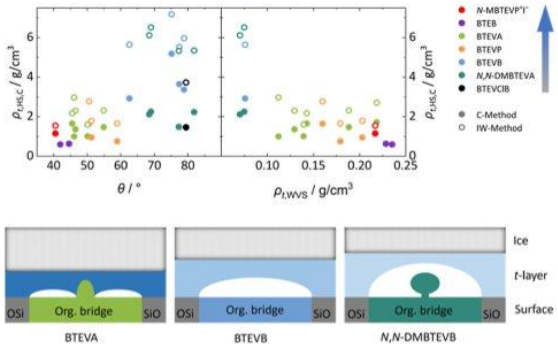


Figure 10. Plot of the SHS-normalized *t*-layer density ($\rho_{t,SHS}$) against the contact angle (θ) (top left) and against the adsorption layer density ($\rho_{t,WVS}$) (top right). Schematic representation of water distribution in the *t*-layer of PMOs with different surface functionalities (bottom), with darker blue shades indicating higher average *t*-layer densities.

method, such as BTEVA-, BTEVP-, BTEB-, and charged *N*-MBTEVP$^+$I$^-$-PMOs, the water density in the SHS region slightly exceeding 1 g/cm^3. This aligns with studies reporting higher surface water density than bulk water.[101−103] A simulation study observed a higher density (1.155 g/cm^3 at 210 K) in the interfacial layer of water between ice and a surface.[104] Engemann et al. reported a higher density of 1.2 g/cm^3 for the liquid film between ice and SiO_2 at approximately 256 K.[83]

Given that the $\rho_{t,SHS}$ values for hydrophobic samples such as BTEVB-, *N*,*N*-DMBTEVA-, and BTEVClB-PMOs range between 2 and 6 g/cm^3, significantly exceeding the density of bulk water, suggesting that water may accumulate beyond the defined volume of surface silanol groups. This supports the idea that water migrates into hydrophobic regions. When plotted against $\rho_{t,WVS}$ (see Figure 10, right), materials with lower adsorption layer densities at 25 °C show higher nonfreezable layer densities at lower temperatures. For IW-materials, a similar increase in density is observed, likely due to a redistribution of water molecules, particularly in hydrophobic materials.

In Figure 9, BTEVB-PMOs were observed to deviate from the hydrophilicity trend, exhibiting an average *t*-layer density higher than that of *N*,*N*-DMBTEVA-PMOs and comparable to the more hydrophilic materials. This may be explained by the schematic representation of a potential water constellation in the nonfreezable layer for different surfaces in Figure 10 (bottom). While the mean *t*-layer density of BTEVB- and BTEVA-PMOs is similar due to higher water content in the region of the organic bridge, $\rho_{t,SHS}$ is greater for BTEVB-PMOs, likely due to the lack of functional groups in the organic bridge compared to BTEVA-PMOs.

In contrast, the more hydrophobic *N*,*N*-DMBTEVA- and BTEVClB-PMOs do not exhibit this behavior. Both materials contain bulky functional groups in their organic bridges (with estimated vertical extensions of approximately 0.45 and 0.35 nm, and van der Waals volumes (assuming cylindrical geometry) of roughly 0.10 nm^3 and 0.034 nm^3, respectively) which may hinder the accumulation of water in these regions, thereby contributing to a lower average *t*-layer density. Given their $\rho_{C,t,BET}$ values of about 2 g/cm^3, it can be inferred that some water, though less than in BTEVB-PMOs, remains partially present in the organic bridge region. Only under conditions where water cannot escape from the pores during freezing, or when higher pressures exist in the pores, might the water-free space become filled, explaining the significant density difference between the IW- and C-methods for BTEVClB- and *N*,*N*-DMBTEVA-PMOs, as shown in Figure 10.

As observed in the water vapor sorption study,[14] the charged *N*-MBTEVP$^+$I$^-$-PMOs exhibit slightly different behavior compared to other materials. While hydrophilic materials generally show smaller *t*-layers with higher densities, the *N*-MBTEVP$^+$I$^-$-PMOs, despite their highly hydrophilic nature, display a tendentially larger *t*-layer coupled with a higher *t*-layer density. However, this density decreases significantly with decreasing pore size or increasing relative *t*-layer thickness. Since the densities (see Figure S17) or specific water amounts (see Figure S18) in the pores are comparable between the C and IW filling methods, the *t*-layer appears to be so densely packed that no additional water molecules can migrate into it, even when the pores are partially sealed by bulk ice in the IW filling method. The reason for this may be the chaotropic behavior of iodide, which probably also accumulates in less polar or hydrophilic surface regions, and to some extent also of the *N*-methylpyridinium bridge, potentially allowing water to migrate into more hydrophobic regions.[14,105−111]

In general, trends between nonfreezable layer density and parameters from water vapor sorption are observed, though fluctuations may result from competing effects of structural and interfacial properties. One explanation may be the assumption that the water core behaves like bulk water, leading to the use of bulk water densities. However, it was found that while core water density increases significantly with temperature after the melting transition, it remains independent of pore size at the melting transition temperature and matching the density of hexagonal ice.[79]

4. CONCLUSIONS

This study investigated the influence of pore size and surface chemistry on the melting and freezing behavior of confined water, using MCM-41 silica and PMOs with varying surface chemistries, emphasizing the role of hydrophilicity.

While discrepancies in literature exist regarding the effects of surface hydrophilicity on solid−liquid phase transitions, partly due to variability in material types, pore sizes, and experimental conditions (e.g., heating/cooling rates), PMOs offer an ideal platform to resolve these due to their uniform repeating unit length and chemically consistent base structure, allowing precise control over surface functionality.

PMOs with higher hydrophilicity, such as the charged *N*-MBTEVP$^+$I$^-$- or BTEB-PMOs with shorter repeating unit lengths, followed by hydrophilic materials like BTEVA- and BTEVP-PMOs, and hydrophobic Materials like BTEVB-, *N*,*N*-DMBTEVA-, and BTEVClB-PMOs, were used.

The porous materials were filled with water using two methods, the gas-phase method in a climate chamber and the incipient wetness method. While both methods resulted in similar melting point depressions and nonfreezable layer sizes, the IW-method led to higher *t*-layer densities (1.5−5 times higher) in hydrophobic materials. This is possibly due to a partially pore-blocking by bulk ice, which limits water displacement during cooling/freezing process and forces it into hydrophobic regions.

https://doi.org/10.1021/acs.jpcc.5c05595
J. Phys. Chem. C 2025, 129, 20373−20386

Surface hydrophilicity has no significant impact on melting point depression for pore radii larger than 1.8 nm, which is consistent with reports in the literature.[53,56] However, as the pore size decreases, the impact of surface chemistry becomes more pronounced. Hydrophobic materials, such as *N*,*N*-DMBTEVA- and BTEVB-PMOs, exhibit a stronger increase in ΔT with decreasing pore radius, lower freezing and specific melting enthalpies of pore water, and comparatively larger values for the calculated critical pore radius, suggesting a reduced ice core radius and a thicker *t*-layer. This aligns with observations in the literature regarding the impact of hydrophilicity on the *t*-layer.[52]

Various methods were applied to determine *t*-layer thickness, revealing thicker nonfreezable layers in materials with larger pores, greater hydrophobicity, and in charged PMOs. Nonfreezable layer densities were generally lower in hydrophobic materials, except for BTEVB-PMOs. The higher densities observed across all materials, compared to the adsorption layer density, may be explained by crystallization pressure, which could force water into hydrophobic regions.

Overall, surface effects appear to influence the melting and freezing behavior primarily in very small pores. The equilibrium state established between the ice core size, the thickness and density of the nonfreezable layer, and surface chemistry suggests that hydrophobicity alone is not the sole determinant of *t*-layer properties. Instead, as evidenced by the differences in nonfreezable layer density between BTEVB- and *N*,*N*-DMBTEVA- or BTEVClB-PMOs, as well as *N*-MBTEVP$^+$I$^-$-PMOs, the type and possibly the size of functional groups play a significant role. Further investigation into the influence of surface chemistry on surface water properties at lower temperatures with materials featuring pore diameters below 3 nm will require alternative techniques, as DSC experiments are unable to detect, or the liquid−solid phase transition may not occur, at temperatures below approximately −60 °C (213 K) based on the signal maximum or −80 °C (193 K) based on the signal onset.

■ ASSOCIATED CONTENT

Supporting Information

The Supporting Information is available free of charge at https://pubs.acs.org/doi/10.1021/acs.jpcc.5c05595.

MCM-41 silica and PMO synthesis protocols including reaction conditions; porosity data of different materials; DSC curves of water in MCM-41 silicas and different PMOs filled using the C- and IW-method; additional correlation of the nonfreezable layer (PDF)

■ AUTHOR INFORMATION

Corresponding Authors

Michael Steiger − *Institute of Inorganic and Applied Chemistry, University of Hamburg, 20146 Hamburg, Germany*; Email: michael.steiger@uni-hamburg.de

Michael Fröba − *Institute of Inorganic and Applied Chemistry, University of Hamburg, 20146 Hamburg, Germany; The Hamburg Centre for Ultrafast Imaging, 22761 Hamburg, Germany*; orcid.org/0000-0001-6927-0509; Email: michael.froeba@uni-hamburg.de

Authors

Philip Lenz − *Institute of Inorganic and Applied Chemistry, University of Hamburg, 20146 Hamburg, Germany; The Hamburg Centre for Ultrafast Imaging, 22761 Hamburg, Germany*

Uta Sazama − *Institute of Inorganic and Applied Chemistry, University of Hamburg, 20146 Hamburg, Germany*

Complete contact information is available at: https://pubs.acs.org/10.1021/acs.jpcc.5c05595

Notes

The authors declare no competing financial interest.

■ ACKNOWLEDGMENTS

This work is funded by the Cluster of Excellence "Advanced Imaging of Matter" of the Deutsche Forschungsgemeinschaft (DFG)—EXC 2056—project ID 390715994 and the DFG project FR1372/26-1. Scientific exchange and support of the Center for Molecular Water Science (CMWS) is also acknowledged. We would like to thank Isabelle Nevoigt for measuring our PXRDs and Sandra König for the nitrogen physisorption and water vapor sorption measurements.

■ REFERENCES

(1) Petrov, O. V.; Furó, I. NMR cryoporometry: Principles, applications and potential. *Prog. Nucl. Magn. Reson. Spectrosc.* **2009**, *54* (2), 97−122.

(2) Knight, A. W.; Kalugin, N. G.; Coker, E.; Ilgen, A. G. Water properties under nano-scale confinement. *Sci. Rep.* **2019**, *9* (1), 8246.

(3) Christenson, H. K. Confinement effects on freezing and melting. *J. Phys.: Condens. Matter* **2001**, *13* (11), R95−R133.

(4) Alba-Simionesco, C.; Coasne, B.; Dosseh, G.; Dudziak, G.; Gubbins, K. E.; Radhakrishnan, R.; Sliwinska-Bartkowiak, M. Effects of confinement on freezing and melting. *J. Phys.: Condens. Matter* **2006**, *18* (6), R15−R68.

(5) Morishige, K.; Kawano, K. Freezing and melting of water in a single cylindrical pore: The pore-size dependence of freezing and melting behavior. *J. Chem. Phys.* **1999**, *110* (10), 4867−4872.

(6) Schreiber, A.; Ketelsen, I.; Findenegg, G. H. Melting and freezing of water in ordered mesoporous silica materials. *Phys. Chem. Chem. Phys.* **2001**, *3* (7), 1185−1195.

(7) Sklari, S.; Rahiala, H.; Stathopoulos, V.; Rosenholm, J.; Pomonis, P. The influence of surface acid density on the freezing behavior of water confined in mesoporous MCM-41 solids. *Microporous Mesoporous Mater.* **2001**, *49* (1−3), 1−13.

(8) Webber, B.; Dore, J. Structural and dynamic studies of water in mesoporous silicas using neutron scattering and nuclear magnetic resonance. *J. Phys.: Condens. Matter* **2004**, *16* (45), S5449−S5470.

(9) Jähnert, S.; Vaca Chávez, F.; Schaumann, G. E.; Schreiber, A.; Schönhoff, M.; Findenegg, G. H. Melting and freezing of water in cylindrical silica nanopores. *Phys. Chem. Chem. Phys.* **2008**, *10* (39), 6039−6051.

(10) Rother, G.; Stack, A. G.; Gautam, S.; Liu, T.; Cole, D. R.; Busch, A. Water uptake by silica nanopores: Impacts of surface hydrophilicity and pore size. *J. Phys. Chem. C* **2020**, *124* (28), 15188−15194.

(11) Rother, G.; Gautam, S.; Liu, T.; Cole, D. R.; Busch, A.; Stack, A. G. Molecular structure of adsorbed water phases in silica nanopores. *J. Phys. Chem. C* **2022**, *126* (5), 2885−2895.

(12) Takei, T.; Mukasa, K.; Kofuji, M.; Fuji, M.; Watanabe, T.; Chikazawa, M.; Kanazawa, T. Changes in density and surface tension of water in silica pores. *Colloid Polym. Sci.* **2000**, *278* (5), 475−480.

(13) Thommes, M.; Morell, J.; Cychosz, K. A.; Fröba, M. Combining nitrogen, argon, and water adsorption for advanced characterization of ordered mesoporous carbons (CMKs) and periodic mesoporous organosilicas (PMOs). *Langmuir* **2013**, *29* (48), 14893−14902.

(14) Lenz, P.; Meinert, S.-M.; König, S.; Steiger, M.; Fröba, M. Influence of surface chemistry on t-layer dimension and density of

nanoconfined water by fine-tuning the functional groups of periodic mesoporous organosilica. *J. Phys. Chem. C* **2025**, *129* (27), 12536−12550.
(15) Fumagalli, L.; Esfandiar, A.; Fabregas, R.; Hu, S.; Ares, P.; Janardanan, A.; Yang, Q.; Radha, B.; Taniguchi, T.; Watanabe, K.; et al. Anomalously low dielectric constant of confined water. *Science* **2018**, *360* (6395), 1339−1342.
(16) Dufils, T.; Schran, C.; Chen, J.; Geim, A. K.; Fumagalli, L.; Michaelides, A. Origin of dielectric polarization suppression in confined water from first principles. *Chem. Sci.* **2024**, *15* (2), 516−527.
(17) Senapati, S.; Chandra, A. Dielectric constant of water confined in a nanocavity. *J. Phys. Chem. B* **2001**, *105* (22), 5106−5109.
(18) Weinberger, C.; Zysk, F.; Hartmann, M.; Kaliannan, N. K.; Keil, W.; Kühne, T. D.; Tiemann, M. The structure of water in silica mesopores − influence of the pore wall polarity. *Adv. Mater. Interfaces* **2022**, *9* (20), 2200245.
(19) Haug, T. C. V.; Hoffmann, F.; Tasova, M. N.; Heffels, R.; Fröba, M. IR spectroscopic studies on water confined in an isoreticular MOF series−influence of the metal and linker functionality. *Adv. Mater. Interfaces* **2025**, *12*, 2400847.
(20) Gießelmann, N. C.; Lenz, P.; Meinert, S.-M.; Simon, T.; Jo, W.; Striker, N. N.; Fröba, M.; Lehmkühler, F. Structure of water under confinement in periodic mesoporous organosilicas investigated by X-ray scattering. *J. Phys. Chem. C* **2024**, *128* (1), 499−507.
(21) Morishige, K.; Nobuoka, K. X-ray diffraction studies of freezing and melting of water confined in a mesoporous adsorbent (MCM-41). *J. Chem. Phys.* **1997**, *107* (17), 6965−6969.
(22) Takamuku, T.; Yamagami, M.; Wakita, H.; Masuda, Y.; Yamaguchi, T. Thermal property, structure, and dynamics of supercooled water in porous silica by calorimetry, neutron scattering, and NMR relaxation. *J. Phys. Chem. B* **1997**, *101* (29), 5730−5739.
(23) Baker, J. M.; Dore, J. C.; Behrens, P. Nucleation of ice in confined geometry. *J. Phys. Chem. B* **1997**, *101* (32), 6226−6229.
(24) Bellissent-Funel, M.-C.; Lal, J.; Bosio, L. Structural study of water confined in porous glass by neutron scattering. *J. Phys. Chem.* **1993**, *98* (5), 4246−4252.
(25) Morishige, K.; Uematsu, H. The proper structure of cubic ice confined in mesopores. *J. Chem. Phys.* **2005**, *122* (4), 44711.
(26) Mohammed, S.; Asgar, H.; Benmore, C. J.; Gadikota, G. Structure of ice confined in silica nanopores. *Phys. Chem. Chem. Phys.* **2021**, *23* (22), 12706−12717.
(27) Domin, K.; Chan, K.-Y.; Yung, H.; Gubbins, K. E.; Jarek, M.; Sterczynska, A.; Sliwinska-Bartkowiak, M. Structure of ice in confinement: Water in mesoporous carbons. *J. Chem. Eng. Data* **2016**, *61* (12), 4252−4260.
(28) Liu, E.; Dore, J. C.; Webber, J. B. W.; Khushalani, D.; Jähnert, S.; Findenegg, G. H.; Hansen, T. Neutron diffraction and NMR relaxation studies of structural variation and phase transformations for water/ice in SBA-15 silica: I. The over-filled case. *J. Phys.: Condens. Matter* **2006**, *18* (44), 10009−10028.
(29) Jażdżewska, M.; Śliwińska-Bartkowiak, M.; Domin, K.; Chudoba, D. M.; Beskrovnyi, A. I.; Neov, D. S.; Gubbins, K. E. Structure of ice confined in carbon and silica nanopores. *Bull. Mater. Sci.* **2019**, *42* (4), 184.
(30) Mhanna, R.; Abdel Hamid, A. R.; Dutta, S.; Lefort, R.; Noirez, L.; Frick, B.; Morineau, D. More room for microphase separation: An extended study on binary liquids confined in SBA-15 cylindrical pores. *J. Chem. Phys.* **2017**, *146* (2), 24501.
(31) Jani, A.. Nanostructuring of binary liquids and water by confinement in periodic mesoporous organosilicates. Ph.D. Thesis, University of Rennes, France, 2021.
(32) Malfait, B.; Pouessel, A.; Jani, A.; Morineau, D. Extension and limits of cryoscopy for nanoconfined solutions. *J. Phys. Chem. Lett.* **2020**, *11* (14), 5763−5769.
(33) Breynaert, E.; Houlleberghs, M.; Radhakrishnan, S.; Grübel, G.; Taulelle, F.; Martens, J. A. Water as a tuneable solvent: a perspective. *Chem. Soc. Rev.* **2020**, *49* (9), 2557−2569.
(34) Muñoz-Santiburcio, D.; Marx, D. Chemistry in nanoconfined water. *Chem. Sci.* **2017**, *8* (5), 3444−3452.
(35) Bartels-Rausch, T. Chemistry: Ten things we need to know about ice and snow. *Nature* **2013**, *494* (7435), 27−29.
(36) Scherer, G. W. Crystallization in pores. *Cem. Concr. Res.* **1999**, *29* (8), 1347−1358.
(37) Zhou, T.; Mirzadeh, M.; Pellenq, R. J.-M.; Bazant, M. Z. Freezing point depression and freeze-thaw damage by nanofluidic salt trapping. *Phys. Rev. Fluids* **2020**, *5* (12), 124201.
(38) Steiger, M.; Asmussen, S. Crystallization of sodium sulfate phases in porous materials: The phase diagram Na2SO4−H2O and the generation of stress. *Geochim. Cosmochim. Acta* **2008**, *72* (17), 4291−4306.
(39) Everett, D. H. The thermodynamics of frost damage to porous solids. *Trans. Faraday Soc.* **1961**, *57*, 1541−1551.
(40) Coussy, O. *Mechanics and physics of porous solids*; Wiley, 2010.
(41) Guo, J.; Sun, W.; Xu, Y.; Lin, W.; Jing, W. Damage mechanism and modeling of concrete in freeze−thaw cycles: A review. *Buildings* **2022**, *12* (9), 1317.
(42) Debenedetti, P. G. *Metastable liquids: Concepts and principles*; Princeton University Press, 1997.
(43) Storey, K. B.; Storey, J. M. Frozen and alive. *Sci. Am.* **1990**, *263*, 92−97.
(44) Brovchenko, I.; Oleinikova, A. *Interfacial and confined water*; Elsevier, 2008.
(45) Wisniewski, M.; Gusta, L.; Neuner, G. Adaptive mechanisms of freeze avoidance in plants: A brief update. *Environ. Exp. Bot.* **2014**, *99*, 133−140.
(46) Klein, J.; Kumacheva, E. Confinement-induced phase transitions in simple liquids. *Science* **1995**, *269* (5225), 816−819.
(47) Petrov, O.; Furó, I. A study of freezing-melting hysteresis of water in different porous materials. Part II: surfactant-templated silicas. *Phys. Chem. Chem. Phys.* **2011**, *13* (36), 16358−16365.
(48) Morishige, K.; Yasunaga, H.; Denoyel, R.; Wernert, V. Pore-blocking-controlled freezing of water in cagelike pores of KIT-5. *J. Phys. Chem. C* **2007**, *111* (26), 9488−9495.
(49) Morishige, K.; Yasunaga, H.; Uematsu, H. Stability of cubic ice in mesopores. *J. Phys. Chem. C* **2009**, *113* (8), 3056−3061.
(50) Morishige, K.; Yasunaga, H.; Matsutani, Y. Effect of pore shape on freezing and melting temperatures of water. *J. Phys. Chem. C* **2010**, *114* (9), 4028−4035.
(51) Alzaidi, A.; Schneider, D.; Kikkinides, E. S.; Valiullin, R. The spectrum of experimentally accessible states for melting and freezing transitions in mesoporous materials. *J. Chem. Phys.* **2024**, *161* (19), 194703.
(52) Emelyanenko, K. A.; Emelyanenko, A. M.; Boinovich, L. B. Review of the state of the art in studying adhesion phenomena at interfaces of solids with solid and liquid aqueous media. *Colloid J.* **2022**, *84* (3), 265−286.
(53) Morishige, K. Influence of pore wall hydrophobicity on freezing and melting of confined water. *J. Phys. Chem. C* **2018**, *122* (9), 5013−5019.
(54) Hirama, Y.; Takahashi, T.; Hino, M.; Sato, T. Studies of water adsorbed in porous vycor glass. *J. Colloid Interface Sci.* **1996**, *184* (2), 349−359.
(55) Deschamps, J.; Audonnet, F.; Brodie-Linder, N.; Schoeffel, M.; Alba-Simionesco, C. A thermodynamic limit of the melting/freezing processes of water under strongly hydrophobic nanoscopic confinement. *Phys. Chem. Chem. Phys.* **2010**, *12* (7), 1440−1443.
(56) Jelassi, J.; Castricum, H. L.; Bellissent-Funel, M.-C.; Dore, J.; Webber, J. B. W.; Sridi-Dorbez, R. Studies of water and ice in hydrophilic and hydrophobic mesoporous silicas: pore characterisation and phase transformations. *Phys. Chem. Chem. Phys.* **2010**, *12* (12), 2838−2849.
(57) Findenegg, G. H.; Jähnert, S.; Akcakayiran, D.; Schreiber, A. Freezing and melting of water confined in silica nanopores. *ChemPhysChem* **2008**, *9* (18), 2651−2659.
(58) Sliwinska-Bartkowiak, M.; Jazdzewska, M.; Huang, L. L.; Gubbins, K. E. Melting behavior of water in cylindrical pores: carbon

https://doi.org/10.1021/acs.jpcc.5c05595
J. Phys. Chem. C 2025, 129, 20373−20386

nanotubes and silica glasses. *Phys. Chem. Chem. Phys.* **2008**, *10* (32), 4909−4919.
(59) Osta-Rangel, O. Water confined in hydrophobic nanopores: Towards a new phase diagram. Ph.D. Thesis, University of Paris-Saclay, France, 2021.
(60) Inagaki, S.; Guan, S.; Ohsuna, T.; Terasaki, O. An ordered mesoporous organosilica hybrid material with a crystal-like wall structure. *Nature* **2002**, *416* (6878), 304−307.
(61) Sayari, A.; Wang, W. Molecularly ordered nanoporous organosilicates prepared with and without surfactants. *J. Am. Chem. Soc.* **2005**, *127* (35), 12194−12195.
(62) Cornelius, M.; Hoffmann, F.; Fröba, M. Periodic mesoporous organosilicas with a bifunctional conjugated organic unit and crystal-like pore walls. *Chem. Mater.* **2005**, *17* (26), 6674−6678.
(63) Hoffmann, F.; Cornelius, M.; Morell, J.; Fröba, M. Silica-based mesoporous organic-inorganic hybrid materials. *Angew. Chem., Int. Ed.* **2006**, *45* (20), 3216−3251.
(64) Beretta, M.; Morell, J.; Sozzani, P.; Fröba, M. Towards peptide formation inside the channels of a new divinylaniline-bridged periodic mesoporous organosilica. *Chem. Commun.* **2010**, *46* (14), 2495−2497.
(65) Aso, M.; Ito, K.; Sugino, H.; Yoshida, K.; Yamada, T.; Yamamuro, O.; Inagaki, S.; Yamaguchi, T. Thermal behavior, structure, and dynamics of low-temperature water confined in mesoporous organosilica by differential scanning calorimetry, X-ray diffraction, and quasi-elastic neutron scattering. *Pure Appl. Chem.* **2012**, *85* (1), 289−305.
(66) Mietner, J. B.; Brieler, F. J.; Lee, Y. J.; Fröba, M. Properties of water confined in periodic mesoporous organosilicas: Nanoimprinting the local structure. *Angew. Chem., Int. Ed.* **2017**, *56* (40), 12348−12351.
(67) Mietner, B. J.; Fröba, M.; Valiullin, R. Water transport in periodic mesoporous organosilica materials. *J. Phys. Chem. C* **2018**, *122* (24), 12673−12680.
(68) Malfait, B.; Jani, A.; Mietner, J. B.; Lefort, R.; Huber, P.; Fröba, M.; Morineau, D. Influence of pore surface chemistry on the rotational dynamics of nanoconfined water. *J. Phys. Chem. C* **2021**, *125* (30), 16864−16874.
(69) Jani, A.; Busch, M.; Mietner, J. B.; Ollivier, J.; Appel, M.; Frick, B.; Zanotti, J.-M.; Ghoufi, A.; Huber, P.; Fröba, M.; et al. Dynamics of water confined in mesopores with variable surface interaction. *J. Chem. Phys.* **2021**, *154* (9), 94505.
(70) Gießelmann, N. C.; Lenz, P.; Meinert, S.-M.; Simon, T.; Bauer, R. P. C.; Jo, W.; Claas, S.; Köhn, C.; Striker, N. N.; Fröba, M.; et al. The structure of ice under confinement in periodic mesoporous organosilicas (PMOs). *J. Chem. Phys.* **2024**, *161* (3), 34508.
(71) Martens, S.; Ortmann, R.; Brieler, F. J.; Pasel, C.; Joo Lee, Y.; Bathen, D.; Fröba, M. Periodic mesoporous organosilicas as adsorbents of toxic trace gases out of the ambient air. *Z. Anorg. Allg. Chem.* **2014**, *640* (3−4), 632−640.
(72) Waki, M.; Mizoshita, N.; Ohsuna, T.; Tani, T.; Inagaki, S. Crystal-like periodic mesoporous organosilica bearing pyridine units within the framework. *Chem. Commun.* **2009**, *46* (43), 8163−8165.
(73) Thommes, M.; Kaneko, K.; Neimark, A. V.; Olivier, J. P.; Rodriguez-Reinoso, F.; Rouquerol, J.; Sing, K. S. Physisorption of gases, with special reference to the evaluation of surface area and pore size distribution (IUPAC Technical Report). *Pure Appl. Chem.* **2015**, *87* (9−10), 1051−1069.
(74) Kittaka, S.; Ishimaru, S.; Kuranishi, M.; Matsuda, T.; Yamaguchi, T. Enthalpy and interfacial free energy changes of water capillary condensed in mesoporous silica, MCM-41 and SBA-15. *Phys. Chem. Chem. Phys.* **2006**, *8* (27), 3223−3231.
(75) Norinaga, K.; Kumagai, H.; Hayashi, J.; Chiba, T. Classification of water sorbed in coal on the basis of congelation characteristics. *Energy Fuels* **1998**, *12* (3), 574−579.
(76) Savitzky, A.; Golay, M. J. E. Smoothing and differentiation of data by simplified least squares procedures. *Anal. Chem.* **1964**, *36* (8), 1627−1639.
(77) Kittaka, S.; Urabe, T.; Tominaga, I. Expulsion of pore water from MCM-41 and SBA-16 and the enthalpy change of melting of water. *Adsorpt. Sci. Technol.* **2015**, *33* (9), 749−757.
(78) Thangswamy, M.; Maheshwari, P.; Dutta, D.; Bera, A. K.; Singh, M. N.; Sinha, A. K.; Yusuf, S. M.; Pujari, P. K. Evolution of confined ice nano structures at different levels of pore filling: a synchrotron based X-ray diffraction study. *Phys. Chem. Chem. Phys.* **2020**, *22* (25), 14309−14317.
(79) Erko, M.; Wallacher, D.; Hoell, A.; Hauss, T.; Zizak, I.; Paris, O. Density minimum of confined water at low temperatures: a combined study by small-angle scattering of X-rays and neutrons. *Phys. Chem. Chem. Phys.* **2012**, *14* (11), 3852−3858.
(80) Feistel, R.; Wagner, W. A new equation of state for H2O ice Ih. *J. Phys. Chem. Ref. Data* **2006**, *35* (2), 1021−1047.
(81) Faivre, C.; Bellet, D.; Dolino, G. Phase transitions of fluids confined in porous silicon: A differential calorimetry investigation. *Eur. Phys. J. B* **1999**, *7* (1), 19−36.
(82) Sparavigna, A. C. Water in pores: The Gibbs-Thomson effect. *SSRN* **2023**, 4349640.
(83) Engemann, S.; Reichert, H.; Dosch, H.; Bilgram, J.; Honkimäki, V.; Snigirev, A. Interfacial melting of ice in contact with SiO(2). *Phys. Rev. Lett.* **2004**, *92* (20), 205701.
(84) Uchida, S.; Fujiwara, K.; Shibahara, M. Structure of the water molecule layer between ice and amorphous/crystalline surfaces based on molecular dynamics simulations. *J. Phys. Chem. B* **2021**, *125* (33), 9601−9609.
(85) Shi, J.; Fulford, M.; Li, H.; Marzook, M.; Reisjalali, M.; Salvalaglio, M.; Molteni, C. Investigating the quasi-liquid layer on ice surfaces: a comparison of order parameters. *Phys. Chem. Chem. Phys.* **2022**, *24* (20), 12476−12487.
(86) Ishizaki, T.; Maruyama, M.; Furukawa, Y.; Dash, J. G. Premelting of ice in porous silica glass. *J. Cryst. Growth* **1996**, *163* (4), 455−460.
(87) Stapf, S.; Kimmich, R. Translational mobility in surface induced liquid layers investigated by NMR diffusometry. *Chem. Phys. Lett.* **1997**, *275* (3−4), 261−268.
(88) Petrov, O. V.; Vargas-Florencia, D.; Furó, I. Surface melting of octamethylcyclotetrasiloxane confined in controlled pore glasses: curvature effects observed by 1H NMR. *J. Phys. Chem. B* **2007**, *111* (7), 1574−1581.
(89) Zhu, X.; Vandamme, M.; Jiang, Z.; Brochard, L. Molecular simulation of the confined crystallization of ice in cement nanopore. *J. Chem. Phys.* **2023**, *159* (15), 154704.
(90) Ishikiriyama, K.; Todoki, M. Evaluation of water in silica pores using differential scanning calorimetry. *Thermochim. Acta* **1995**, *256* (2), 213−226.
(91) Murphy, D. M.; Koop, T. Review of the vapour pressures of ice and supercooled water for atmospheric applications. *Q. J. R. Meteorol. Soc.* **2005**, *131* (608), 1539−1565.
(92) Thomson, W. L. X. On the equilibrium of vapour at a curved surface of liquid. *Philos. Mag.* **1871**, *42* (282), 448−452.
(93) Cohan, L. H. Sorption hysteresis and the vapor pressure of concave surfaces. *J. Am. Chem. Soc.* **1938**, *60* (2), 433−435.
(94) Kocherbitov, V.; Alfredsson, V. Hydration of MCM-41 studied by sorption calorimetry. *J. Phys. Chem. C* **2007**, *111* (35), 12906−12913.
(95) David, R. O.; Fahrni, J.; Marcolli, C.; Mahrt, F.; Brühwiler, D.; Kanji, Z. A. The role of contact angle and pore width on pore condensation and freezing. *Atmos. Chem. Phys.* **2020**, *20* (15), 9419−9440.
(96) Zeng, Q.; Li, K. Quasi-liquid layer on ice and its effect on the confined freezing of porous materials. *Crystals* **2019**, *9* (5), 250.
(97) Nagasima, N. Structure analysis of silicon dioxide films formed by oxidation of silane. *J. Appl. Phys.* **1972**, *43* (8), 3378−3386.
(98) Pauly, T. R.; Petkov, V.; Liu, Y.; Billinge, S. J. L.; Pinnavaia, T. J. Role of framework sodium versus local framework structure in determining the hydrothermal stability of MCM-41 mesostructures. *J. Am. Chem. Soc.* **2002**, *124* (1), 97−103.

https://doi.org/10.1021/acs.jpcc.5c05595
J. Phys. Chem. C 2025, 129, 20373−20386

(99) Zhuravlev, L. T. The surface chemistry of amorphous silica. Zhuravlev model. *Colloids Surf. A Physicochem. Eng. Asp.* **2000**, *173* (1−3), 1−38.
(100) Schrader, A. M.; Monroe, J. I.; Sheil, R.; Dobbs, H. A.; Keller, T. J.; Li, Y.; Jain, S.; Shell, M. S.; Israelachvili, J. N.; Han, S. Surface chemical heterogeneity modulates silica surface hydration. *Proc. Natl. Acad. Sci. U.S.A.* **2018**, *115* (12), 2890−2895.
(101) Hartnig, C.; Witschel, W.; Spohr, E.; Gallo, P.; Ricci, M. A.; Rovere, M. Modifications of the hydrogen bond network of liquid water in a cylindrical SiO2 pore. *J. Mol. Liq.* **2000**, *85* (1−2), 127−137.
(102) Giovambattista, N.; Rossky, P. J.; Debenedetti, P. G. Effect of temperature on the structure and phase behavior of water confined by hydrophobic, hydrophilic, and heterogeneous surfaces. *J. Phys. Chem. B* **2009**, *113* (42), 13723−13734.
(103) Zhang, Y.; Faraone, A.; Kamitakahara, W. A.; Liu, K.-H.; Mou, C.-Y.; Leão, J. B.; Chang, S.; Chen, S.-H. Density hysteresis of heavy water confined in a nanoporous silica matrix. *Proc. Natl. Acad. Sci. U.S.A.* **2011**, *108* (30), 12206−12211.
(104) Sun, Q.; Xiao, D.; Zhang, W.; Mao, X. Quasi-water layer sandwiched between hexagonal ice and wall and its influences on the ice tensile stress. *Nanoscale* **2022**, *14* (36), 13324−13333.
(105) Zhao, H. Are ionic liquids kosmotropic or chaotropic? An evaluation of available thermodynamic parameters for quantifying the ion kosmotropicity of ionic liquids. *J. Chem. Technol. Biotechnol.* **2006**, *81* (6), 877−891.
(106) Lund, M.; Jungwirth, P. Patchy proteins, anions and the Hofmeister series. *J. Phys.: Condens. Matter* **2008**, *20* (49), 494218.
(107) Liu, L.; Kou, R.; Liu, G. Ion specificities of artificial macromolecules. *Soft Matter* **2017**, *13* (1), 68−80.
(108) Lee, E.; Choi, J.-H.; Cho, M. The effect of Hofmeister anions on water structure at protein surfaces. *Phys. Chem. Chem. Phys.* **2017**, *19* (30), 20008−20015.
(109) Assaf, K. I.; Nau, W. M. The chaotropic effect as an assembly motif in chemistry. *Angew. Chem., Int. Ed.* **2018**, *57* (43), 13968−13981.
(110) Bastos-González, D.; Pérez-Fuentes, L.; Drummond, C.; Faraudo, J. Ions at interfaces: the central role of hydration and hydrophobicity. *Curr. Opin. Colloid Interface Sci.* **2016**, *23*, 19−28.
(111) Gibb, C. L. D.; Gibb, B. C. Anion binding to hydrophobic concavity is central to the salting-in effects of Hofmeister chaotropes. *J. Am. Chem. Soc.* **2011**, *133* (19), 7344−7347.

https://doi.org/10.1021/acs.jpcc.5c05595
J. Phys. Chem. C 2025, 129, 20373−20386

5.6. The Structure of Ice under Confinement in Periodic Mesoporous Organosilicas (PMOs)

Niels C. Gießelmann, **Philip Lenz**, Sophia-Marie Meinert, Tamás Simon, Robert P. C. Bauer, Wonhyuk Jo, Sarah Claas, Christian Köhn, Nele N. Striker, Michael Fröba*, Felix Lehmkühler*

Synopsis

In the previous publication on ice confined in PMOs, the impact of pore size and surface chemistry on the solid–liquid phase transition temperature and enthalpy was studied using differential scanning calorimetry. To further investigate the structure of ice and the orientation of ice crystals inside these PMOs, X-ray scattering measurements were performed at the P02.1 and P03 beamlines of PETRA III at DESY in Hamburg (Germany).

Analysis of the ice structure in the various PMOs revealed an influence of both pore size and surface chemistry, with the confined ice exhibiting contributions from both hexagonal and cubic stacking sequences. Furthermore, an amorphous contribution was observed, which likely originates from the non-freezable layer at the pore surface. As in the DSC studies, the importance of the cooling protocol was confirmed, and the X-ray measurements further demonstrated its influence on the resulting ice structure. Additionally, the confined ice showed shifts in the lattice parameters of the hexagonal phase compared to bulk ice, depending on pore size and surface chemistry. Ice in hydrophilic materials or under stronger confinement showed the most pronounced deviations from bulk behavior, often observed as an elongation of the unit cell. The benzene-bridged BTEVB-PMO shows the strongest cubic-like contribution among the studied samples. X-ray cross-correlation analysis was used to investigate the orientation of ice crystals inside the pores of the various PMOs. Stronger correlations were found for materials with hydrophilic surface functionalization and appear to be connected to the observed lattice parameter shifts.

The author of this PhD thesis and co-author of this publication (Philip Lenz) actively participated in the measurements at PETRA III, synthesized the PMO samples used in the study, and characterized them with respect to their porosity, structure, and hydrophilicity. Furthermore, he wrote the section of the publication describing the material characteristics and was involved in the discussion of the observed structural behavior of ice confined in the different PMOs.

The Journal of Chemical Physics

RESEARCH ARTICLE | JULY 17 2024

The structure of ice under confinement in periodic mesoporous organosilicas (PMOs)

Special Collection: Water: Molecular Origins of its Anomalies

Niels C. Gießelmann ✉ ; Philip Lenz ; Sophia-Marie Meinert; Tamás Simon ; Robert P. C. Bauer; Wonhyuk Jo; Sarah Claas ; Christian Köhn ; Nele N. Striker ; Michael Fröba ✉ ; Felix Lehmkühler ✉

Check for updates

J. Chem. Phys. 161, 034508 (2024)
https://doi.org/10.1063/5.0216697

View Online
Export Citation

Articles You May Be Interested In

Dynamics of water confined in mesopores with variable surface interaction

J. Chem. Phys. (March 2021)

Water-modulated structure and dynamics in aqueous choline chloride-polyol deep eutectic solvents: Insights from molecular dynamic simulations

J. Chem. Phys. (December 2025)

11 March 2026 10:43:34



Zurich Instruments
Freedom to Innovate.
The New VHFLI 200 MHz Lock-in Amplifier.
Orchestrate pulses, triggers, and acquisition as the hub of your experiment.
Discover more – run every signal analysis tool, simultaneously.
Order now

AIP Publishing

The Journal of Chemical Physics ARTICLE pubs.aip.org/aip/jcp

The structure of ice under confinement in periodic mesoporous organosilicas (PMOs)

Cite as: J. Chem. Phys. 161, 034508 (2024); doi: 10.1063/5.0216697
Submitted: 30 April 2024 • Accepted: 30 June 2024 •
Published Online: 17 July 2024

View Online Export Citation CrossMark

Niels C. Gießelmann,[1,a] Philip Lenz,[2,3] Sophia-Marie Meinert,[2] Tamás Simon,[2] Robert P. C. Bauer,[1,4] Wonhyuk Jo,[1,5] Sarah Claas,[2] Christian Köhn,[2] Nele N. Striker,[1] Michael Fröba,[2,3,a] and Felix Lehmkühler[1,3,a]

AFFILIATIONS

[1] Deutsches Elektronen-Synchrotron DESY, Notkestr. 85, 22607 Hamburg, Germany
[2] Institute of Inorganic and Applied Chemistry, University of Hamburg, Martin-Luther-King-Platz 6, 20146 Hamburg, Germany
[3] The Hamburg Centre for Ultrafast Imaging, Luruper Chaussee 149, 22761 Hamburg, Germany
[4] Freiberg Center for Water Research, Technische Universität Bergakademie Freiberg, Winklerstraße 8, 09599 Freiberg, Germany
[5] European XFEL, Holzkoppel 4, 22869 Schenefeld, Germany

Note: This paper is part of the JCP Special Topic on Water: Molecular Origins of its Anomalies.
[a] **Authors to whom correspondence should be addressed:** niels.giesselmann@desy.de; michael.froeba@uni-hamburg.de; and felix.lehmkuehler@desy.de

ABSTRACT

We investigated the structure of ice under nanoporous confinement in periodic mesoporous organosilicas (PMOs) with different organic functionalities and pore diameters between 3.4 and 4.9 nm. X-ray scattering measurements of the system were performed at temperatures between 290 and 150 K. We report the emergence of ice I with both hexagonal and cubic characteristics in different porous materials, as well as an alteration of the lattice parameters when compared to bulk ice. This effect is dependent on the pore diameter and the surface chemistry of the respective PMO. Investigations regarding the orientation of hexagonal ice crystals relative to the pore wall using x-ray cross correlation analysis reveal one or more discrete preferred orientation in most of the samples. For a pore diameter of around 3.8 nm, stronger correlation peaks are present in more hydrophilically functionalized pores and seem to be connected to stronger shifts in the lattice parameters.

© 2024 Author(s). All article content, except where otherwise noted, is licensed under a Creative Commons Attribution (CC BY) license (https://creativecommons.org/licenses/by/4.0/). https://doi.org/10.1063/5.0216697

11 March 2026 10:43:34

I. INTRODUCTION

Liquid water is known to exhibit different equilibrium and dynamical properties in porous confinement compared to bulk.[1–4] One particular example is the lowering of the melting point, when confined in pores with diameters smaller than 100 nm.[5–8]

In addition, in its solid state, the properties of water are influenced by spatial restrictions. For instance, under confinement on a scale of nanometers, stacking-disordered ice I_{sd} is present in a stable form.[9–13] This phase, which represents the presence of both hexagonal and cubic domains, for example, is observable in micrometer-sized droplets or as a metastable phase from supercooled water.[14–20] Furthermore, several studies have shown a strong presence of amorphous phases, especially pre-melted liquid water at the interface between ice and the pore wall.[8,21–23]

While the influence of the pore size has been extensively studied, not much is known about the effect of a modified pore wall surface chemistry on the formation of ice. In the study at hand, we want to analyze this effect, using periodic mesoporous organosilicas (PMOs). These are a class of organosilica hybrid materials with cylindrical pores, possessing organic moieties, which are an intrinsic part of the pore wall. Due to the periodic arrangement and long-range ordering of the organic moieties in the pore walls, additional (00l) reflections parallel to the pore axis appear.[24,25] These organic moieties can furthermore be varied, which changes the surface chemistry and, therefore, the interactions between the pore walls and the confined material.[26–28] Using the advantages of both

© Author(s) 2024

hexagonally arranged cylindrical pores with narrow size distributions and different surface chemistries, PMOs can, therefore, be tuned to various intended applications, such as catalysis,[29,30] drug delivery,[31,32] or light harvesting.[24,33,34] Tuning the pore–water interaction and polarity of the pore wall has an influence on the structure and dynamics of water and ice confined in PMOs,[25,35,36] which is further investigated in this study.

Here, we take a closer look at the ice formed in different PMOs. We want to investigate how different pore–water interactions and a varying pore diameter influence the formation of ice inside the pores. A focus is set on the lattice parameters of the hexagonal component, when confined in PMOs with various pore diameters and surface chemistries, as well as the orientation of ice crystal in relation to the pore axis using x-ray scattering. The orientations are determined by the use of x-ray scattering with a nanofocused beam in combination with x-ray cross correlation analysis.[37,38]

II. METHODS

A. Samples and sample preparation

The porous materials used in this study, as well as their porosity data and the experiment in which they were measured, are presented in Table I. The chemical structures of the PMO precursors are given in the supplementary material.

The synthesis of the porous materials was performed following the description given in a previous publication.[28] The charge in BTEVP+ samples was introduced using a postsynthetic pathway. In this approach, the colorless BTEVP-PMO was exposed to a saturated iodomethane atmosphere at room temperature for two days in a sealed system. The yellowish powder was freed from iodomethane residues by keeping it open at room temperature for two days and then in vacuum (0.1 mbar) for 5 min. The synthesis parameters of the various samples are given in the supplementary material. Water was adsorbed into the pores by exposing the sample to water vapor inside a humidity chamber. The humidity was set to 90% relative humidity (RH) to ensure that no excess water is present outside the pores.

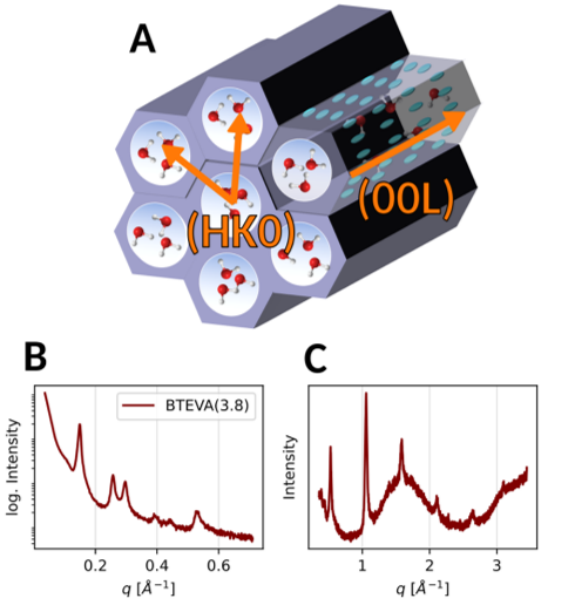


FIG. 1. (a) Sketch of a PMO material. The light blue ellipsoids represent the organic moieties. The arrows indicate the directions of the scattering planes of the (hk0) and (00l) reflections. In the following, small (b) and wide (c) angle scattering signals of BTEVA(3.8) are shown as an example.

TABLE I. List of porous materials used in the experiment. The precursors used for the PMO synthesis, the pore diameter d_P (where the uncertainty is given by the half width at half maximum of the pore size distribution), the pore volume at 90% relative pressure $V_{P,0.9}$, the organic unit periodicity d_{org}, and the experiment in which the sample was used (1 = P02.1, 2 = P03) are shown. * Two different batches of BTEVA(3.8) were used in the two experiments, but their properties did not show any notable differences.

		Precursor	d_p (nm)	$V_{P,0.9}$ (cm^3g^{-1})	d_{org} (nm)	Exp.
■	MCM-41(3.9)	MCM-41	3.9 ± 0.3	0.85	···	1
✚	BTEB(3.8)	BTEB	3.8 ± 1.1	1.26	0.76	1
	BTEVB(3.8)	BTEVB	3.8 ± 0.7	0.54	1.19	1, 2
●	BTEVFB(4.9)	BTEVFB	4.9 ± 1.4	0.83	1.20	1
▶	BTEVFB(4.4)	BTEVFB	4.4 ± 0.7	1.04	1.20	1
	BTEVFB(3.8)	BTEVFB	3.8 ± 0.4	0.61	1.18	2
▲	BTEVA(4.4)	BTEVA	4.3 ± 0.3	0.83	1.18	1
◀	BTEVA(3.8)	BTEVA	3.8 ± 0.4	0.67	1.18	1, 2*
◆	BTEVA(3.4)	BTEVA	3.4 ± 0.4	0.64	1.18	1
	BTEVP(3.8)	BTEVP	3.8 ± 0.7	0.87	1.19	2
✖	BTEVP(3.5)	BTEVP	3.5 ± 0.8	0.63	1.19	1
	BTEVP+(3.5)	BTEVP+	3.5 ± 0.5	0.47	1.18	2
●	BTEVP+(3.4)	BTEVP+	3.4 ± 0.6	0.60	1.18	1
	BTEVCl(3.8)	BTEVCl	3.8 ± 0.8	0.93	1.19	2

PMOs have a distinct x-ray scattering signal. Figures 1(b) and 1(c) show the small and wide angle signals of BTEVA(3.8). The peaks that are found in the small angle regime can mainly be attributed to the reflections from the distribution of the pores, i.e., (hk0), while those in the wide angle regime stem from the periodicity of the organic moieties, i.e., (00l). Note that the angle at the highest q (≈0.53 $Å^{-1}$) shown in Fig. 1(b) is the same as the peak at the lowest q shown in Fig. 1(c).

B. Experimental

The data presented here were obtained at two separate x-ray scattering experiments. The first was performed at the P02.1 beamline[39] at PETRA III (DESY, Hamburg, Germany) with a beam diameter of ~1 mm and at an energy of 60 keV. The powder samples were filled into glass capillaries with a diameter of 1.5 mm and a wall thickness of 10 μm (*Hilgenberg GmbH*). Scattering patterns were taken at temperatures between 290 and 150 K with an exposure time of 1 s. A Perkin Elmer XRD 1621 CN3 detector was used for

11 March 2026 10:43:34

© Author(s) 2024

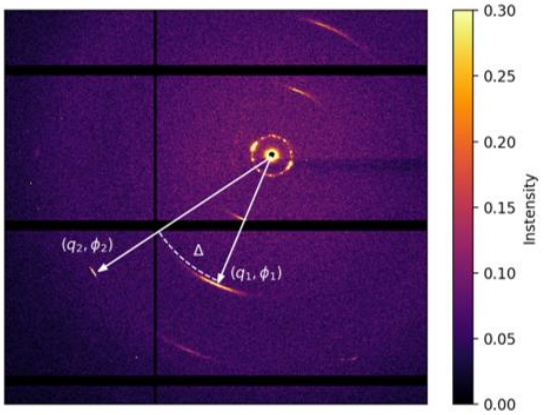


FIG. 2. Detector image of water-filled BTEVP(3.8) at 150 K with a visualization of the XCCA process. Here, q_1 is the value for the signal from the PMO at an angle ϕ_1 while q_2 is that of the (002) peak of the hexagonal ice at an angle $\phi_2 = \phi_1 + \Delta$.

capturing the patterns, which were azimuthally integrated to create the intensity curves presented later.

The second experiment, which was aimed at XCCA, was performed at the nanofocus endstation of the P03 beamline, also at PETRA III.[40,41] Here, the beamsize was ~250 × 350 nm^2 with a beam energy of 17.5 keV. The images were acquired by using an Eiger X 9M detector.

In both experiments, the temperature was controlled by a nitrogen cryostream surrounding the sample capillary. We estimated the error of the temperature conservatively to be about 5 K, which is implied in all the temperature data we measured. LaB_6 was used for geometry calibration in both experiments.

C. Lattice parameter analysis

In order to obtain the lattice parameters of the hexagonal ice, we located the peaks of the intensity $I(q)$ vs the momentum transfer q corresponding to the hexagonal ice by fitting them as Gaussians. We identified their Miller indices (hkl) by comparing them to bulk literature values.[42] A linear regression fit corresponding to Bragg's

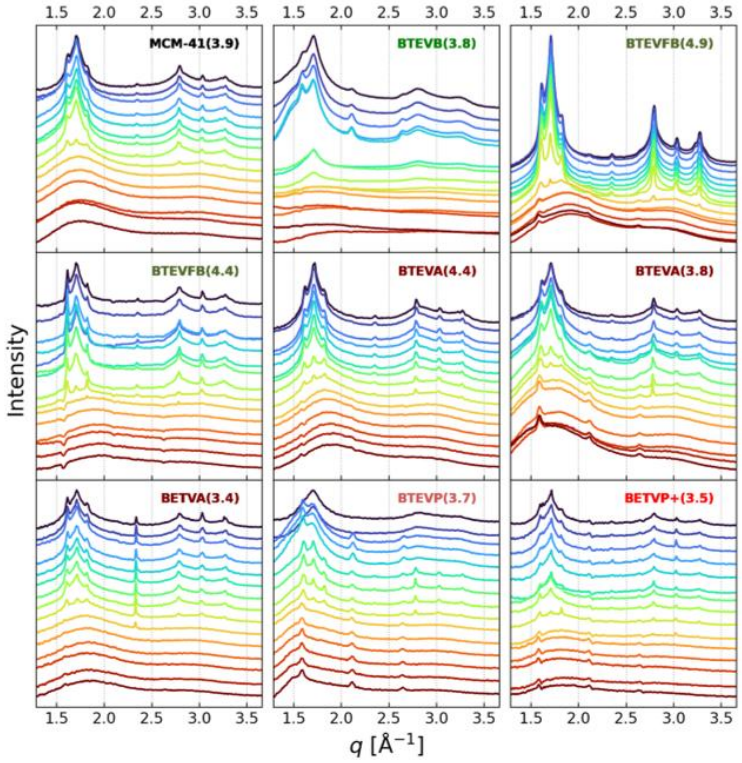


FIG. 3. X-ray diffraction signal of water in several different PMOs at temperatures between 290 (bottom, red) and 150 K (top, blue) in steps of 10 K.

11 March 2026 10:43:34

© Author(s) 2024

law was performed with the q values and the Miller indices of the hexagonal peaks,

$$\frac{q^2}{4\pi^2} = \frac{4}{3}\frac{h^2 + hk + k^2}{a^2} + \frac{l^2}{c^2}. \quad (1)$$

With this, it is then possible to compute the hexagonal lattice parameters a and c. Using the width of the peaks, the crystallite size L can be calculated using the Scherrer equation,[43,44]

$$L \approx \frac{K \cdot \lambda}{\Delta(2\theta) \cdot \cos\theta}, \quad (2)$$

where K is the Scherrer constant, λ is the x-ray wavelength, $\Delta(2\theta)$ the full width at half maximum of the peak after taking into account the instrument broadening, and θ is the Bragg angle of the diffraction peak. In the case of a cylindrical crystal, K depends on several factors, such as the aspect ratio of the cylinder and the Miller indices of the scattering plane.[45,46]

D. Ice crystal orientations

In order to analyze the orientation of ice crystals with respect to the pore axis, we employed x-ray cross correlation analysis (XCCA).[37,38,47–50] In this, the intensity $I(q_1, \phi)$ at q_1 and azimuthal angle ϕ is correlated with $I(q_2, \phi + \Delta)$ as

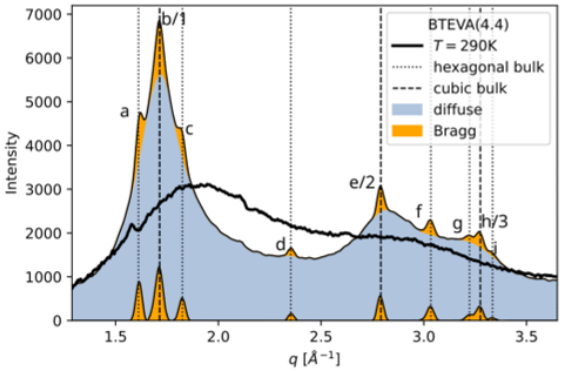
$$C(q_1, q_2, \Delta) = \frac{\langle I(q_1, \phi) I(q_2, \phi + \Delta)\rangle_\phi}{\langle I(q_1, \phi)\rangle \langle I(q_2, \phi)\rangle_\phi}. \quad (3)$$

If we now choose the q value related to the peaks from the PMO structure for q_1 [e.g., the (00l) peaks shown in Fig. 1] and those related to the ice structure as q_2 (cf. Fig. 2), the resulting correlation function $C(\Delta)$ gives us a statistical insight into common angles Δ between the scattering planes of the PMO and the ice crystallites (see discussion below).[48,49]

III. RESULTS

Figure 3 shows the azimuthally integrated x-ray scattering intensity of water confined in various PMOs at temperatures between 290 and 150 K. It was obtained by subtracting the signal of an empty PMO from that of its water-filled counterpart. In some samples, namely, BTEVFB(4.9), BTEVA(4.4), BTEVA(3.8), and BTEVP(3.5), this did not fully remove the signal from the empty PMO. Here, the remaining peaks at 1.7 A^{-1}, which stem from the periodicity of the functional groups in the pore wall, are visible. On the one hand, the reason for this were the fluctuations of the x-ray intensity during the measurement, which could not fully be compensated by normalization. On the other hand, the electron density difference is lower for water-filled pores, hence the PMO peaks are more prominent in empty (or air-filled) pores. In these cases, the (100) peak of hexagonal ice overlaps with the (003) PMO peak and was, therefore, not taken into account when determining the lattice constants discussed later.

In most samples, characteristics of both ice I_h-like, sharp Bragg peaks and more ice I_c-like, diffuse peaks are visible. Specifically, in the regions between 1.5 and 2.0 A^{-1} and between 2.5 and 3.5 A^{-1}, an overlay between a broad diffuse peak and the triplet characteristic for ice I_h is observed. This structural behavior of ice crystallization has been observed in previous simulation[51,52] and experimental[11,13,44] studies on water in nanopores. Figure 4 shows a separation of the diffuse and Bragg contributions, which are marked in blue and orange, respectively, for the example of BTEVA(4.4). The diffuse part also contains a contribution from liquid, non-freezing interfacial water, which is known to appear in nanopores.[8,51,52] This contribution is not shown in Fig. 4 as it is difficult to meaningfully separate it from the broad cubic-like contribution. The confined water in the same pore at room temperature is also plotted to visualize the general shape of this amorphous contribution. However, as shown in a previous study by us,[28] the first sharp diffraction peak of water grows and shifts to lower q values under confinement and even more during cooling, ending up closer to the first diffuse peak.



Hexagonal		Cubic	
Label	*hkl*	Label	*hkl*
a	100		
b	002	1	111
c	101		
d	102		
e	110	2	220
f	103		
g	200		
h	112	3	311
i	201		

FIG. 4. Diffuse and Bragg contributions to the integrated scattering pattern at T = 165 K are shown in blue and orange, respectively. $I(q)$ of the confined water at 290 K is plotted for comparison (black) as well as the peak locations for bulk cubic and hexagonal ice (dark gray). The bulk hexagonal peaks are also located at the same positions as the bulk cubic peaks. Twofold labeling indicates a coincidence of peaks from different contributors. The indexing of the marked peaks can be seen in the table underneath the figure.

The presence of both the diffuse and Bragg contributions suggest stacking-disordered ice I in the pore. The diffuse part implies small individual crystallites with a large number of stacking faults, while the Bragg contribution can probably be described as ice I_h with a large ratio of Φ_h to Φ_c according to Malkin *et al.*[20] Going forward, the Bragg contribution, therefore, will be referred to as the hexagonal contribution even though it does probably not represent pure ice I_h.

In order to estimate the sizes of individual crystallites, the Scherrer equation [Eq. (2)] can be applied, leading to values of 35–50 nm with no systematic difference between the samples. The

11 March 2026 10:43:34

© Author(s) 2024

values are rather vague, as the Scherrer constant K strongly depends on various factors, as mentioned in Sec. II. In this case, cylindrical crystallites are assumed, which generally leads to Scherrer constants $K > 0.9$. The number, therefore, only serves as an estimate of the order of magnitude of the crystallite size, not as an exact result. A more detailed discussion is given in the supplementary material. The crystallites of the diffuse constribution were calculated to be in the range of 1–2 nm. This is in agreement with the findings of Moore *et al.*,[51] stating that cubic ice domains in silica pores are in the range of only a couple of molecular layers. However, due to the discussed amorphous contribution, a precise determination is not possible.

Some of the studied samples stand out in this regard. BTEVFB(4.9) shows the previously discussed general structure but has much higher relative intensities of the (hexagonal) ice peaks. We connect this to its pore diameter, which is the largest of the measured samples at 4.9 nm. Therefore, the amount of ice present in the pore is larger than for the other materials, leading to a stronger scattering signal. In BTEVB(3.8) and BTEVP(3.5), one can see that the patterns differ at the five lowest temperatures. These lowest-temperature measurements were performed with a higher initial cooling rate than the standard procedure and with no equilibration steps being taken while cooling down to 180 K. In BTEVB(3.8), the (003) PMO peak at 1.7 A^{-1} is more visible in these temperatures while the overall structure is qualitatively the same as for the higher temperatures. In BTEVP(3.5), however, we observe no hexagonal ice peaks at those temperatures reached via the faster procedure. This suggests that the emerging ice structure is dependent on the cooling procedure. Specifically, a higher cooling rate without equilibration steps seems to hinder the formation of hexagonal ice. We also want to note that BTEVB(3.8) represents the only sample in which no hexagonal ice peaks were observed in both the standard measurement and the measurement with faster cooling.

A. Hexagonal structure

We will now take a closer look at the hexagonal contribution to the signal with a focus on the influence of the PMO confinement on its structure. Figure 5 shows the lattice constants for the hexagonal ice contributions inside the different PMOs, as well as those of bulk ice. The bulk ice values are based on the polynomial expression described by Röttger *et al.*[53,54] to describe the lattice constants of hexagonal ice over a wide temperature range sorted by pore size. While the measured samples follow the general trend as expected in bulk ice, some notable deviations are observed.

The left panel of Fig. 5 shows ice in the largest pores with diameters ≥4.4 nm. While the more hydrophilically amine-functionalized BTEVA(4.4) closely follows the lattice parameters of bulk ice, the two samples with the BTEVFB precursor do not follow this behavior. In BTEVFB(4.4), both a and c are larger than in bulk ice. Their ratio, however, is still similar to bulk ice. This is not the case for BTEVFB(4.9), where only c differs from bulk, implying an elongated hexagonal unit cell. This trend is also observable for MCM-41(3.9) in the middle panel. Similar to BTEVFB(4.9), hexagonal ice in MCM-41(3.9) seems to be elongated along its c direction. In

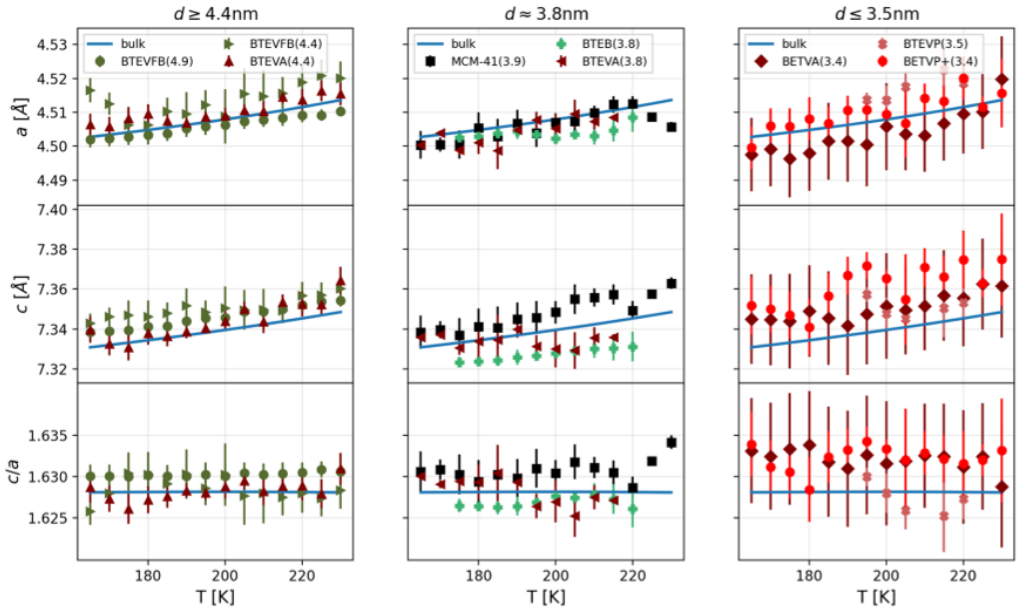


FIG. 5. Plots showing the lattice parameters a and c of hexagonal ice in various porous materials, as well as their ratio c/a. The three columns show the materials with decreasing pore diameters from left to right. Hydrophilic PMO samples are plotted in a shade of red, while more hydrophobic ones are a shade of green. MCM-41 is plotted in black. The lattice parameters of bulk ice are also plotted for comparison. The bulk values were calculated according to the work by Röttger *et al.*.[53,54]

11 March 2026 10:43:34

© Author(s) 2024

contrast, BTEB(3.8) gives a lower value for c and, consequently, also a lower value for the c/a ratio.

The smaller BTEVA(3.4) and BTEVP+(3.4) in the right panel show a stronger deviation from bulk than the ones previously discussed. Note that BTEVA(3.4) also particularly differs from its larger counterparts. While the ice in BTEVA(3.4) and BTEVA(3.8) structures similarly to bulk ice, in BETVA(3.4), it also shows an elongated hexagonal cell with c/a that is above that of bulk ice. This may indicate that a pore size effect only becomes relevant below 3.8 nm, at least in BTEVA-PMOs. However, it should be noted that BTEVA(3.4) has a larger error margin, potentially stemming from the lower amount of water adsorbed in the pore, which, in turn, gives a weaker scattering signal. The other sample with a pore diameter in this range, BTEVP+(3.4), supports a pore size-dependent deformation of the hexagonal structure as it shows the most elongated c parameter out of all materials. It should be noted here that due to its synthesis, a residual iodide ion is present in the BTEVP+-PMOs, which takes up additional space in the vicinity of a functional group. The c/a-ratio in BTEVP(3.5) is again more closely following that of bulk ice; however, we observe slightly larger lattice parameters for both a and c, suggesting an overall expanded unit cell, similar to BTEVFB(4.4).

B. Orientation of ice crystals in relation to the pore axis

The shifts in lattice parameters are most often not equal for a and c. This could be caused by a dependence of the lattice parameter shift on the orientation. Such dependence could stem from the pore wall chemistry. The interactions of water with the organic moieties could force the molecules into arrangements that would not be favorable under bulk conditions while hindering others that would. We shall now investigate the orientation of these hexagonal crystals relative to the pore axis to evaluate such dependence. In order to determine an orientational dependence, x-ray cross correlation analysis (XCCA) was conducted.[37,38,47,50,55] Following Eq. (3), an angular correlation is calculated between spots at two different q values.[48] We choose one q value to be the expected value for a (00l) periodicity of the functional groups of the PMO and the other that of hexagonal ice (see Fig. 2).

Figure 6 shows a selection of correlation functions in PMOs with 3.8 nm pore diameter. The correlations between the (002) peak of ice with both the (001) and (002) peaks of the PMOs are shown in the subfigures Figs. 6(a) and 6(b), respectively. The latter represent the periodicity of the functional groups in the pore walls and, therefore, the pore axis direction. Since $(001)_{PMO}$ and $(002)_{PMO}$ are parallel, both correlations should show the same qualitative features. Their equivalence can, therefore, be used as an additional indication if visible peaks are actual angular correlations or just artifacts, for example, from detector noise or background scattering. Note that the angles of the correlation peaks are statistical values that indicate a preferred orientation. Other orientations might also be present inside one pore. Therefore, the analysis is quite sensitive to the specific area where the scattering pattern was taken. In order to mitigate this, we measured at about 100 separate spots for each sample and performed background correlations, which are explained in further detail in the supplementary material.

The correlation functions in some materials show very clear peaks, while others do not. The presence of peaks implies that some materials lead to certain angles Δ between the (00l) axis of the ice crystals and the pore axis being more common than others. The absence of peaks can either mean the absence of ice crystals in these materials or random orientations of crystals with respect to the pore axis. For the hydrophilic samples (red), BTEVP+(3.5) shows a large peak at 180°, indicating a preferred orientation of the (00l) axis of the ice parallel to the pore axis. A second large peak can be seen at about 40°. BTEVP(3.8) shows a quite large peak at about 30° and some smaller ones at ~60°, 120°, and 150°. BTEVA(3.8) primarily shows a peak at 90°, albeit less pronounced than in BTEVP(3.8). In contrast, the more hydrophobic samples, BTEVB(3.8) also shows some quite pronounced peaks at 30°, 150°, and two peaks slightly above and below 90°, respectively. BTEVFB(3.8) only shows some weak peaks at 150°, 75°, and 30°, although the latter is only visible in the correlation with $(002)_{PMO}$. BTEVCl(3.8) does not show any peaks at all. As the latter two are rather hydrophobic materials, the data shown in Fig. 6 generally suggest stronger correlations between the pore and ice crystal orientation in hydrophilic compared to hydrophobic pores, with the exception of BTEVB(3.8). However, in those samples that show strong peaks [i.e., BTEVB(3.8), BTEVA(3.8), BTEVP(3.8), and BTEVP+(3.5)], no systematic dependence of the correlation angles Δ on the material properties can be determined at these pore diameters, but it is notable that BTEVP+(3.5) shows the largest peak of all the measured materials while also having the lowest pore diameter and volume.

Note that the absence of correlation peaks in BTEVFB(3.8) and BTEVCl(3.8) does not necessarily imply that no preferred orientations occur in these samples. Instead, it is also possible that the amount of averaged spots is too small in these cases and more data would be required to reach a convergence. In any case, if preferred orientations are present, they are much more weakly pronounced in comparison to the other samples.

C. Angular correlations and lattice parameters

Figure 7 compares the lattice constants (panel a) to the angular correlation functions (panel b) for the samples measured in both experiments. A striking observation is that BTEVP+(3.4), which showed a strong unit cell elongation along the c axis, also gives a strong correlation at 180°. This suggests that the elongated cells are often oriented along the pore axis. In addition, another strong peak at about 40° and a third smaller peak at about 140° are visible. BTEVA(3.8), which closely sticks to the bulk lattice parameters, seems to be mostly oriented orthogonal to the pore axis as can be seen from its correlation peak at 90°. Smaller peaks at around 15° and 165° are also present. The correlations in BTEVB(3.8), which is the only measured PMO to show exclusively cubic ice characteristics, have two strong, symmetric correlation peaks at 30° and 150° and, additionally, two smaller peaks at about 75° and 105°, which are also symmetric. BTEVP(3.5) shows a strong peak at 30° and generally has a similar profile to BTEVP+(3.5) with no correlation at 90° and an additional small peak at around 150°, symmetric to its large peak at 30°. Both of these materials have the same functional pyridine group, but in BTEVP+, this group possesses an additional positive charge, a methyl group and the iodide counterion mentioned before.

The obtained ice crystal orientations relative to the pore axis in these samples are shown in Fig. 7(c).

11 March 2026 10:43:34

© Author(s) 2024

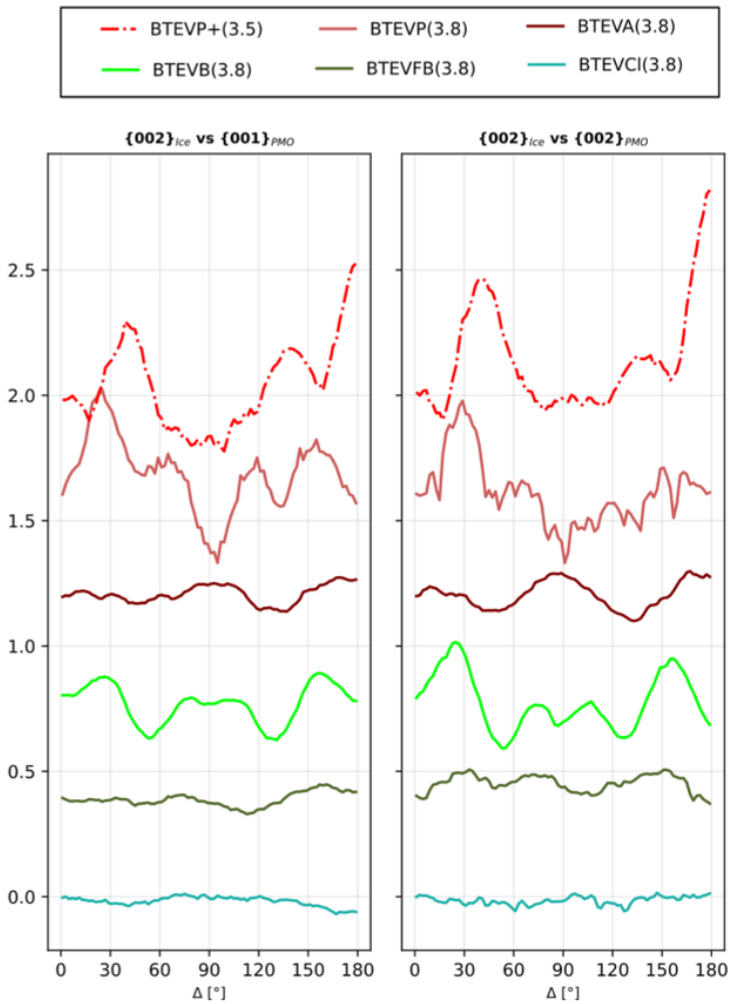


FIG. 6. Angular correlations between spots of the 002 signals of hexagonal ice and the 001 (panel a) and 002 (panel b) signals of various PMOs with a pore diameter of 3.8 nm.

IV. DISCUSSION

We investigated the structure of ice in periodic mesoporous organosilicas. We used x-ray scattering on powder samples in order to study confined ice with regard to its qualitative structure, as well as a more detailed analysis of the lattice constants of the hexagonal contributions. In order to analyze the orientation of the hexagonal crystallites relative to the pore axis, we used x-ray cross correlation analysis.

The overall structure, consisting of cubic, hexagonal, and amorphous contributions, which stem from the liquid layer at the pore wall,[13,51] is well in accordance with the literature.[8,11,13,44,51,52] Furthermore, we found indications that the structure is dependent on the way the sample is cooled. We consistently observed hexagonal contributions when lowering the temperature in a step-wise manner, while continuous cooling mostly led to pure cubic (or cubic-like) ice.

While previous studies did not report lattice constant shifts of the hexagonal phase in confinement,[13] we observe that they deviate from bulk ice in several of our measured samples. This effect depends on both the pore surface chemistry and the pore size of the confining material. All the hydrophobically functionalized materials discussed in this study, i.e., BTEVFB(4.9), BTEVFB(4.4) and BTEB(3.8), show a deviation from bulk

11 March 2026 10:43:34

© Author(s) 2024

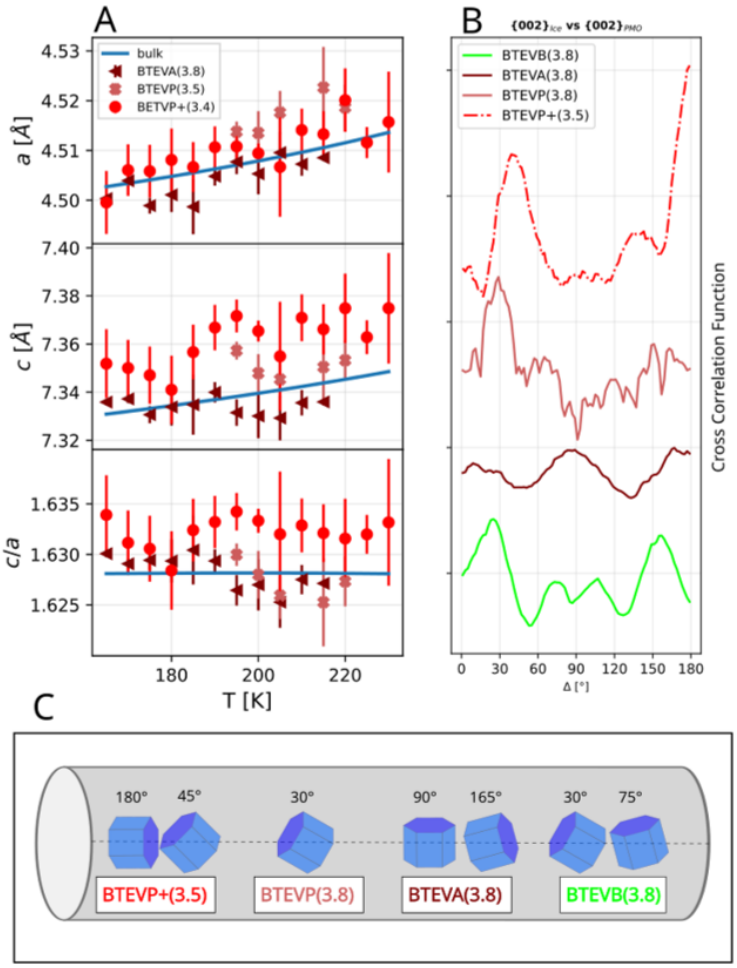


FIG. 7. (a) Lattice constants of materials for which XCCA was conducted. (b) Angular correlation curves for materials in panel (b). The correlations are for the angles between spots at q values identified for the (002) peak in hexagonal ice and the (002) peak of the periodicity of the organic moiety in the PMO. (c) A visualization of the most prominent angles Δ as shown in panel (b). The gray cylinder represents the pore, the black dashed line represents the pore axis, and the blue hexagonal prisms indicate the hexagonal crystallites.

properties, while in hydrophilic materials, this effect is mostly observable for small pore diameters ≤3.8 nm. These shifts, therefore, seem to be dependent on both the pore wall chemistry and especially the pore size as stronger shifts were observed in smaller pores [i.e., BTEVP(3.7), BTEVP+(3.5), and BTEVA(3.4)]. We most commonly observe an increased c/a ratio, meaning an elongation of the unit cell (see Fig. 5).

It is not clear what causes this change in the lattice constants relative to bulk ice. An explanation could be that the highly stacking-disordered cubic-like phase leads to connections with the hexagonal ice domains that would be unfavorable under bulk conditions, leading to the observed elongated [BTEVFB(4.9), MCM-41(3.9), BTEVA(3.4), and BTEVP+(3.4)], expanded [BTEVFB(4.4) and BTEVP(3.5)], or truncated [BTEB(3.8)] hexagonal unit cells. Notably, only BTEB(3.8) leads to a c/a smaller than bulk while also being the sample with the smallest d_{org} at only 0.76 nm (see Table I). This length describes the distance between the silicon atoms at either end of the organic moiety. With this, d_{org}/c in BTEB(3.8) is close to 1, while for all other PMOs, the ratio is closer to 1.5. While there is also the interfacial water between the pore wall and the ice, this indicates that the length of the organic moieties could play an important role in the development of ice in PMOs

11 March 2026 10:43:34

© Author(s) 2024

and seems to be a major factor in the observed lattice constant shift.

Cubic or stacking-disordered ice and an amorphous nonfreezing layer have consistently been reported in similar pores in various studies.[9,13,44,51] The broad peaks observed in our data are in agreement with the argumentation of Morishige and Uematsu[9] and Moore *et al.*,[51] which confirmed that cubic ice consists of small crystallites with a large number of stacking faults to such a degree that it is better described as stacking-disordered ice.[20]

The sharper ice I_h peaks that are observed in these systems were argued by Thangswamy *et al.*[44] to be, in fact, not hexagonal ice inside the pore but instead ice that crept out of the pore during crystallization, forming bulk crystallites outside the pore, as suggested by a calculated crystallite size that is considerably larger than the pore diameter.[44] This is also the case in our study with crystallite sizes calculated to be around 20–30 nm. However, we propose that the hexagonal contribution is, in fact, ice inside the pores. The sharpness of the corresponding peaks and the implied large crystallite size does not necessarily mean that they have to be outside the pore. Instead, they could be caused by crystallites grown along the pore axis with the crystallite size describing the length of a cylindrical crystallite. This way, it is, in principle, only limited by the length of the pore. This is supported by the fact that larger pores lead to larger hexagonal peaks, as in BTEVFB(4.9) or BTEVA(4.4) compared to smaller pores, such as BTEVP(3.5) or BTEVP+(3.4). Furthermore, we observe the previously discussed deviations in the lattice parameters of the hexagonal contributions from those of bulk ice.

X-ray cross correlation analysis suggests preferred orientations of the hexagonal contributions in several samples (see Figs. 6 and 7). For a pore diameter of about 3.8 nm, we find that stronger correlations tend to occur in more hydrophilic pores. When comparing the XCCA results to the lattice parameter shifts in specific samples (Fig. 7), more prominent correlations are found in samples that also exhibit larger lattice parameter shifts [e.g., BTEVP+(3.5)] or exclusively cubic-like ice [BTEVB(3.8)].

SUPPLEMENTARY MATERIAL

The supplementary material contains information on the synthesis and chemical structure of the PMOs, as well as their pore size distribution and adsorption and desorption curves. The estimation of the Scherrer constants is also discussed in further detail along with a more thorough explanation of the background correlations in the XCCA.

ACKNOWLEDGMENTS

We acknowledge DESY (Hamburg, Germany), a member of the Helmholtz Association HGF, for the provision of experimental facilities. Parts of this research were carried out at PETRA III, and we thank Dr. Alexander Schökel and Dr. Martin Etter for their assistance in using the P02.1 beamline[39] and Dr. Anton Davydok for assistance in using the nanofocus endstation at P03.[40,41] Beamtime was allocated for Proposal Nos. I-20200440, I-20190201 (P02.1), and I-20220503 (P03). This research was carried out in the framework of the city of Hamburg's state-funded research project "Control of the special properties of water in nanopores" (LFF-FV68). It was further supported by the Centre for Molecular Water Science (CMWS) in an Early Science Project and by the Cluster of Excellence Advanced Imaging of Matter of the Deutsche Forschungsgemeinschaft (DFG) (EXC 2056, Project No. 390715994).

AUTHOR DECLARATIONS

Conflict of Interest

The authors have no conflicts to disclose.

Author Contributions

Niels C. Gießelmann: Data curation (lead); Formal analysis (lead); Investigation (equal); Software (lead); Validation (equal); Visualization (lead); Writing – original draft (lead); Writing – review & editing (equal). **Philip Lenz**: Formal analysis (supporting); Investigation (equal); Resources (equal); Validation (equal); Visualization (equal); Writing – original draft (supporting); Writing – review & editing (equal). **Sophia-Marie Meinert**: Formal analysis (supporting); Investigation (equal); Validation (equal); Visualization (equal); Writing – original draft (supporting); Writing – review & editing (equal). **Tamás Simon**: Investigation (equal); Resources (equal); Validation (equal); Visualization (equal); Writing – review & editing (equal). **Robert P. C. Bauer**: Data curation (supporting); Formal analysis (supporting); Investigation (equal); Software (supporting); Writing – review & editing (equal). **Wonhyuk Jo**: Investigation (equal); Software (supporting); Writing – review & editing (equal). **Sarah Claas**: Resources (equal); Writing – review & editing (equal). **Christian Köhn**: Investigation (equal); Writing – review & editing (equal). **Nele N. Striker**: Investigation (equal); Writing – review & editing (equal). **Michael Fröba**: Conceptualization (equal); Funding acquisition (equal); Project administration (equal); Supervision (equal); Validation (equal); Writing – review & editing (equal). **Felix Lehmkühler**: Conceptualization (equal); Funding acquisition (equal); Investigation (equal); Project administration (equal); Software (equal); Supervision (equal); Validation (equal); Writing – review & editing (equal).

DATA AVAILABILITY

Raw data were generated at the large scale facility Deutsches Elektronen-Synchrotron DESY, Hamburg, Germany. Derived data supporting the findings of this study are available from the corresponding author upon reasonable request.

REFERENCES

[1] W. H. Thompson, "Solvation dynamics and proton transfer in nanoconfined liquids," Annu. Rev. Phys. Chem. **62**, 599–619 (2011).
[2] G. Reiter, A. Deb, Y. Sakurai, M. Itou, V. Krishnan, and S. Paddison, "Anomalous ground state of the electrons in nanoconfined water," Phys. Rev. Lett. **111**, 036803 (2013).
[3] K. Kapoor and S. Patil, "Viscoelasticity and shear thinning of nanoconfined water," Phys. Rev. E **89**, 013004 (2014).
[4] D. Munoz-Santiburcio and D. Marx, "Chemistry in nanoconfined water," Chem. Sci. **8**, 3444–3452 (2017).

11 March 2026 10:43:34

© Author(s) 2024

[5]S. Jähnert, F. V. Chávez, G. Schaumann, A. Schreiber, M. Schönhoff, and G. Findenegg, "Melting and freezing of water in cylindrical silica nanopores," Phys. Chem. Chem. Phys. **10**, 6039–6051 (2008).
[6]J. Deschamps, F. Audonnet, N. Brodie-Linder, M. Schoeffel, and C. Alba-Simionesco, "A thermodynamic limit of the melting/freezing processes of water under strongly hydrophobic nanoscopic confinement," Phys. Chem. Chem. Phys. **12**, 1440–1443 (2010).
[7]J. Jelassi, H. L. Castricum, M.-C. Bellissent-Funel, J. Dore, J. B. W. Webber, and R. Sridi-Dorbez, "Studies of water and ice in hydrophilic and hydrophobic mesoporous silicas: Pore characterisation and phase transformations," Phys. Chem. Chem. Phys. **12**, 2838–2849 (2010).
[8]E. B. Moore, J. T. Allen, and V. Molinero, "Liquid-ice coexistence below the melting temperature for water confined in hydrophilic and hydrophobic nanopores," J. Phys. Chem. C **116**, 7507–7514 (2012).
[9]K. Morishige and H. Uematsu, "The proper structure of cubic ice confined in mesopores," J. Chem. Phys. **122**, 044711 (2005).
[10]M. Jazdzewska, M. M. Śliwinska-Bartkowiak, A. I. Beskrovnyy, S. G. Vasilovskiy, S.-W. Ting, K.-Y. Chan, L. Huang, and K. E. Gubbins, "Novel ice structures in carbon nanopores: Pressure enhancement effect of confinement," Phys. Chem. Chem. Phys. **13**, 9008–9013 (2011).
[11]K. Domin, K.-Y. Chan, H. Yung, K. E. Gubbins, M. Jarek, A. Sterczynska, and M. Sliwinska-Bartkowiak, "Structure of ice in confinement: Water in mesoporous carbons," J. Chem. Eng. Data **61**, 4252–4260 (2016).
[12]D. W. Moreau, H. Atakisi, and R. E. Thorne, "Ice formation and solvent nanoconfinement in protein crystals," IUCrJ **6**, 346–356 (2019).
[13]S. Mohammed, H. Asgar, C. J. Benmore, and G. Gadikota, "Structure of ice confined in silica nanopores," Phys. Chem. Chem. Phys. **23**, 12706–12717 (2021).
[14]W. Kuhs, D. Bliss, and J. Finney, "High-resolution neutron powder diffraction study of ice I_c," J. Phys. Colloq. **48**, C1-631–C1-636 (1987).
[15]B. J. Murray, D. A. Knopf, and A. K. Bertram, "The formation of cubic ice under conditions relevant to earth's atmosphere," Nature **434**, 202–205 (2005).
[16]B. J. Murray and A. K. Bertram, "Formation and stability of cubic ice in water droplets," Phys. Chem. Chem. Phys. **8**, 186–192 (2006).
[17]T. Hansen, M. Koza, and W. Kuhs, "Formation and annealing of cubic ice: I. Modelling of stacking faults," J. Phys.: Condens.Matter **20**, 285104 (2008).
[18]T. Hansen, M. Koza, P. Lindner, and W. Kuhs, "Formation and annealing of cubic ice: II. Kinetic study," J. Phys.: Condens.Matter **20**, 285105 (2008).
[19]E. B. Moore and V. Molinero, "Is it cubic? Ice crystallization from deeply supercooled water," Phys. Chem. Chem. Phys. **13**, 20008–20016 (2011).
[20]T. L. Malkin, B. J. Murray, C. G. Salzmann, V. Molinero, S. J. Pickering, and T. F. Whale, "Stacking disorder in ice I," Phys. Chem. Chem. Phys. **17**, 60–76 (2015).
[21]S. Engemann, H. Reichert, H. Dosch, J. Bilgram, V. Honkimaki, and A. Snigirev, "Interfacial melting of ice in contact with SiO_2," Phys. Rev. Lett. **92**, 205701–206100 (2004).
[22]S. Schöder, H. Reichert, H. Schröder, M. Mezger, J. Okasinski, V. Honkimäki, J. Bilgram, and H. Dosch, "Radiation-induced premelting of ice at silica interfaces," Phys. Rev. Lett. **103**, 095502 (2009).
[23]M. Jażdżewska, M. Śliwińska-Bartkowiak, K. Domin, D. M. Chudoba, A. I. Beskrovnyi, D. S. Neov, and K. E. Gubbins, "Structure of ice confined in carbon and silica nanopores," Bull. Mater. Sci. **42**, 184 (2019).
[24]J. G. Croissant, X. Cattoën, M. W. C. Man, J.-O. Durand, and N. M. Khashab, "Syntheses and applications of periodic mesoporous organosilica nanoparticles," Nanoscale **7**, 20318–20334 (2015).
[25]J. B. Mietner, "Zu Gast in nanoporen: Das große potential von PMOs bei der untersuchung der Eigenschaften von Wasser in nanoporen unterschiedlicher polarität," Ph.D. thesis, Staats-und Universitätsbibliothek Hamburg Carl von Ossietzky, 2018.
[26]B. J. Mietner, M. Fröba, and R. Valiullin, "Water transport in periodic mesoporous organosilica materials," J. Phys. Chem. C **122**, 12673–12680 (2018).
[27]A. Jani, M. Busch, J. B. Mietner, J. Ollivier, M. Appel, B. Frick, J.-M. Zanotti, A. Ghoufi, P. Huber, M. Fröba, and D. Morineau, "Dynamics of water confined in mesopores with variable surface interaction," J. Chem. Phys. **154**, 094505 (2021).
[28]N. C. Gießelmann, P. Lenz, S.-M. Meinert, T. Simon, W. Jo, N. N. Striker, M. Fröba, and F. Lehmkühler, "Structure of water under confinement in periodic mesoporous organosilicas investigated by x-ray scattering," J. Phys. Chem. C **128**, 499–507 (2023).
[29]Q. Yang, J. Liu, L. Zhang, and C. Li, "Functionalized periodic mesoporous organosilicas for catalysis," J. Mater. Chem. **19**, 1945–1955 (2009).
[30]B. Karimi, H. M. Mirzaei, and A. Mobaraki, "Periodic mesoporous organosilica functionalized sulfonic acids as highly efficient and recyclable catalysts in biodiesel production," Catal. Sci. Technol. **2**, 828–834 (2012).
[31]S. Parambadath, A. Mathew, M. J. Barnabas, and C.-S. Ha, "A *p*H-responsive drug delivery system based on ethylenediamine bridged periodic mesoporous organosilica," Microporous Mesoporous Mater. **215**, 67–75 (2015).
[32]K. M. Rao, S. Parambadath, A. Kumar, C.-S. Ha, and S. S. Han, "Tunable intracellular degradable periodic mesoporous organosilica hybrid nanoparticles for doxorubicin drug delivery in cancer cells," ACS Biomater. Sci. Eng. **4**, 175–183 (2018).
[33]S. Inagaki, O. Ohtani, Y. Goto, K. Okamoto, M. Ikai, K.-i. Yamanaka, T. Tani, and T. Okada, "Light harvesting by a periodic mesoporous organosilica chromophore," Angew. Chem. **121**, 4102–4106 (2009).
[34]H. Takeda, M. Ohashi, Y. Goto, T. Ohsuna, T. Tani, and S. Inagaki, "Light-harvesting photocatalysis for water oxidation using mesoporous organosilica," Chem. - Eur. J. **20**, 9130–9136 (2014).
[35]J. B. Mietner, F. J. Brieler, Y. J. Lee, and M. Fröba, "Properties of water confined in periodic mesoporous organosilicas: Nanoimprinting the local structure," Angew. Chem., Int. Ed. **56**, 12348–12351 (2017).
[36]B. Malfait, A. Jani, J. B. Mietner, R. Lefort, P. Huber, M. Fröba, and D. Morineau, "Influence of pore surface chemistry on the rotational dynamics of nanoconfined water," J. Phys. Chem. C **125**, 16864–16874 (2021).
[37]R. P. Kurta, M. Altarelli, and I. A. Vartanyants, "Structural analysis by x-ray intensity angular cross correlations," Adv. Chem. Phys. **161**, 1–39 (2016).
[38]I. A. Zaluzhnyy, R. P. Kurta, M. Scheele, F. Schreiber, B. I. Ostrovskii, and I. A. Vartanyants, "Angular x-ray cross-correlation analysis (AXCCA): Basic concepts and recent applications to soft matter and nanomaterials," Materials **12**, 3464 (2019).
[39]A.-C. Dippel, H.-P. Liermann, J. T. Delitz, P. Walter, H. Schulte-Schrepping, O. H. Seeck, and H. Franz, "Beamline P02.1 at PETRA III for high-resolution and high-energy powder diffraction," J. Synchrotron Radiat. **22**, 675–687 (2015).
[40]A. Buffet, A. Rothkirch, R. Döhrmann, V. Körstgens, M. M. Abul Kashem, J. Perlich, G. Herzog, M. Schwartzkopf, R. Gehrke, P. Müller-Buschbaum, and S. V. Roth, "P03, the microfocus and nanofocus X-ray scattering (MiNaXS) beamline of the PETRA III storage ring: The microfocus endstation," J. Synchrotron Radiat. **19**, 647–653 (2012).
[41]C. Krywka, H. Neubauer, M. Priebe, T. Salditt, J. Keckes, A. Buffet, S. V. Roth, R. Doehrmann, and M. Mueller, "A two-dimensional waveguide beam for X-ray nanodiffraction," J. Appl. Cryst. **45**, 85–92 (2012).
[42]L. G. Dowell and A. P. Rinfret, "Low-temperature forms of ice as studied by x-ray diffraction," Nature **188**, 1144–1148 (1960).
[43]A. Patterson, "The Scherrer formula for x-ray particle size determination," Phys. Rev. **56**, 978 (1939).
[44]M. Thangswamy, P. Maheshwari, D. Dutta, A. Bera, M. Singh, A. K. Sinha, S. Yusuf, and P. K. Pujari, "Evolution of confined ice nano structures at different levels of pore filling: A synchrotron based X-ray diffraction study," Phys. Chem. Chem. Phys. **22**, 14309–14317 (2020).
[45]S. Lele and T. Anantharaman, "Influence of crystallite shape on particle size broadening of Debye–Scherrer reflections," Proc. Indian Acad. Sci. Sec. A **64**, 261–274 (1966).
[46]J. I. Langford and D. Louër, "Diffraction line profiles and Scherrer constants for materials with cylindrical crystallites," J. Appl. Cryst. **15**, 20–26 (1982).
[47]F. Lehmkühler, G. Grübel, and C. Gutt, "Detecting orientational order in model systems by X-ray cross-correlation methods," J. Appl. Cryst. **47**, 1315–1323 (2014).
[48]F. Lehmkühler, B. Fischer, L. Müller, B. Ruta, and G. Grübel, "Structure beyond pair correlations: X-ray cross-correlation from colloidal crystals," J. Appl. Cryst. **49**, 2046–2052 (2016).
[49]N. Mukharamova, D. Lapkin, I. A. Zaluzhnyy, A. André, S. Lazarev, Y. Y. Kim, M. Sprung, R. P. Kurta, F. Schreiber, I. A. Vartanyants, and M. Scheele, "Revealing grain boundaries and defect formation in nanocrystal superlattices by nanodiffraction," Small **15**, 1904954 (2019).

11 March 2026 10:43:34

© Author(s) 2024

[50]F. Schulz, I. Lokteva, W. J. Parak, and F. Lehmkühler, "Recent notable approaches to study self-assembly of nanoparticles with X-ray scattering and electron microscopy," Part. Part. Syst. Charact. **38**, 2100087 (2021).
[51]E. B. Moore, E. De La Llave, K. Welke, D. A. Scherlis, and V. Molinero, "Freezing, melting and structure of ice in a hydrophilic nanopore," Phys. Chem. Chem. Phys. **12**, 4124–4134 (2010).
[52]E. Stefanutti, L. Bove, G. Lelong, M. Ricci, A. Soper, and F. Bruni, "Ice crystallization observed in highly supercooled confined water," Phys. Chem. Chem. Phys. **21**, 4931–4938 (2019).
[53]K. Röttger, A. Endriss, J. Ihringer, S. Doyle, and W. Kuhs, "Lattice constants and thermal expansion of H_2O and D_2O ice I*h* between 10 and 265 K," Acta Crystallogr., Sect. B: Struct. Sci. **50**, 644–648 (1994).
[54]K. Röttger, A. Endriss, J. Ihringer, S. Doyle, and W. F. Kuhs, "Lattice constants and thermal expansion of H_2O and D_2O Ice I*h* between 10 and 265 K. Addendum," Acta Crystallogr., Sect. B: Struct. Sci. **68**, 91 (2012).
[55]F. Schulz, F. Westermeier, F. Dallari, V. Markmann, H. Lange, G. Grübel, and F. Lehmkühler, "Plasmonic supercrystals with a layered structure studied by a combined TEM-SAXS-XCCA approach," Adv. Mater. Interfaces **7**, 2000919 (2020).

11 March 2026 10:43:34

© Author(s) 2024

6. Discussion

In this work, the influence of surface chemistry on the behavior of confined water in PMOs was investigated. A broad set of PMOs with different surface functionalities was prepared, including several newly developed or optimized materials. MCM-41 silica samples were included as a reference to the literature and to benchmark the measurements. Water in its adsorbed, liquid, and solid states was probed by several analytical methods, with water vapor sorption as the central technique to resolve how water interacts with the pore walls, specifically how the wall chemistry governs water–surface affinity and the modes of adsorption, condensation, and desorption. Adsorption thermodynamics were assessed by the isosteric method, which evaluates adsorption energies from temperature-dependent isotherms via the Clausius–Clapeyron equation. This was complemented by a calorimetric method developed in this work that enables direct measurement of adsorption enthalpies. The low-temperature behavior was studied by DSC to determine melting and freezing transitions and the corresponding enthalpies.

To obtain a broad set of PMOs, literature-known BTEVB- and BTEVA-based PMOs were used. To expand their pore size range, synthesis parameters were adjusted and expanders were introduced. Although BTEVP-based PMOs were originally reported by Waki *et al.*,[162] the present work introduces substantial optimizations that yield a highly porous material with a narrow pore size distribution. By using iodomethane to functionalize BTEVA-PMOs *in situ* or BTEVP-PMOs post-synthetically, both the twice methylated *N*,*N*-DMBTEVA-PMOs and the surface-charged *N*-MBTEVP^{+}I^{-}-PMOs were obtained. Also newly introduced is the BTEVClB-PMO, whose precursor was originally developed by Bilo,[283] but for which no suitable PMO synthesis conditions had previously been identified. The main challenge was the low solubility of the precursor, which was resolved here by adding ethanol. Under optimized conditions (pH of 13.67, surfactant (C_{18}TAB) concentration of 0.105 mol L^{-1}, and reaction at 90 °C for 25 h), a BTEVClB-PMO with a pore diameter of 3.8 nm was successfully synthesized. Further studies are required to achieve other pore sizes, particularly below 3.8 nm, because, unlike for other PMOs, the synthesis conditions for BTEVClB-PMOs must be fully re-optimized when surfactants with different chain lengths are used to tune the pore size. This is likely caused by the higher hydrophobicity of the precursor, which alters its interaction with the surfactant and increases its affinity for the hydrophobic carbon chains. Still, extending the reaction time from 25 to 48 h or increasing the

temperature from 90 to 100 °C under otherwise identical conditions resulted in larger pores of about 4.3 nm.

Amide–acid functionalized PMOs based on the BTEVA and BTEPA frameworks were synthesized to introduce multifunctionality at the pore surface. Although the precursor modification of BTEPA and BTEVA with oxobutanoic acid or oxobut-2-enoic acid was successful, the final functionalization degree after PMO synthesis depends strongly on the synthesis conditions. Co-condensation of BTEPA-OBenA with BTEB at strong acidic conditions (pH ≈ −0.14) resulted, according to ^{1}H-NMR analysis, in a pronounced loss of amide–acid groups, yielding only about 1.5 % amide–acid functionalized BTEPA in the final material. However, the ratio of the two precursors used in the synthesis closely matched that found in the final PMO, consistent with all other co-condensation systems studied. Co-condensation of BTEPA-OBA with BTEB also showed a reduction in amide–acid content, but the remaining fraction was significantly higher (about 29 % amide–acid functionalized BTEPA), which is notable given that the structural difference between OBA and OBenA is essentially the presence of a double bond. Although both acids exhibit similar reactivity, maleic acid amides are known to be more susceptible to hydrolysis under acidic conditions.[284] Adjusting the synthesis parameters could increase the functionality degree but may also lead to an altered porosity of the resulting PMO. A post-synthetic route appears promising, as shown for BTEVA OBenA-PMOs, where the functionalization degree increased from 13 to 52%. The limitation here is pore size. If the pores are too small, transport of the modifying molecules becomes restricted due to functional groups near pore entrances and potential pore blocking. A pseudomorphic transformation approach, conducted under milder alkaline conditions, also proved effective, as demonstrated for BTEVA-OBA-PMOs. Owing to the amine functionality of the BTEVA precursor and the system’s ability to form highly ordered pores and pore walls, BTEVA-based PMOs provide an excellent platform for further surface modification. One example is the aspartic-acid-functionalized BTEVA-AA PMO.

In a separate approach, an aspartic-acid-derived precursor (BOC-BTEPSA) was co-condensed with BTEB under acidic conditions, and the protecting group was removed *in situ* to yield the corresponding PMO with an aspartic acid unit incorporated directly into the organic bridge. As observed for the other co-condensed PMOs, the precursor ratio used during synthesis was well reproduced in the final material composition. In

contrast to the OBA and OBenA functionalities, the aspartic acid bridge remained intact under these synthesis conditions, likely due to its two anchoring amide groups.

NMR techniques are well-suited for assessing chemical composition, precursor integrity, and the degree of hydrolysis. As PMOs are powders, solid-state NMR would normally be used, but it is time-consuming, yields broad signals, and was not available during this work. Instead, the PMOs were hydrolyzed in 1 M NaOD/D_2O solution over several days and subsequently analyzed by solution-state NMR. This approach allowed reliable determination of precursor integrity, identification of residual ethoxy groups through ethanol signals, and, for the modified PMOs, evaluation of the functionalization degree.

Water vapor sorption was used to quantify PMO hydrophilicity through several complementary parameters. A simple approach is to evaluate the relative pressure at which condensation or pore emptying occurs. However, because the position of condensation depends not only on surface hydrophilicity but also strongly on pore size, as described by the Kelvin Equation (1), comparisons require materials with similar pore diameters. To decouple hydrophilicity from pore size effects, several hydrophilicity metrics have been established. A commonly used descriptor of surface hydrophilicity is the contact angle, which can be calculated for porous materials using Equation (2). In addition to the Henry adsorption constant and the number of surface hydration sites, hydrophilicity indices such as HI_T and HI_{BET} can be used, as well as the HI_i developed in this work (see Equation (3)) can be used, which incorporates contact angle, pore radius, and adsorption-layer thickness data. When applied to PMOs and MCM-41 silica, all parameters follow a comparable trend, allowing the materials to be ranked by increasing hydrophilicity:

BTEVClB ≤ BTEVFB ≈ *N*, *N*-DMBTEVA ≈ BTEVB < BTEVP ≈ BTEVA < BTEB ≤ MCM-41 silica < *N*-MBTEVP$^+$I$^-$

Further, WVS measurements were conducted to determine the adsorption-layer thickness and density, calculated using the geometric approach of Rother *et al.*,[58,59] which they used to calculate the t_a-layer for water confined in MCM-41 silica. For PMOs, a correlation between HI_{id} and the ratio t_a/r_h was observed, where more hydrophobic materials tend to have a larger adsorption-layer-to-hydraulic-pore-radius ratio. In addition, a clear pore-size dependence was found, with increasing pore diameter leading to a decrease in t_a/r_h, reaching a minimum or plateau at pore

diameters of about 3–4 nm. For materials such as BTEVP-PMOs, the ratio t_a/r_h shows a slight increase beyond pore diameters of about 4 nm, appears to level off around 6 nm, and is likely to decrease again for even larger pores. This behavior may indicate a balance between geometric confinement and surface curvature.

The density of the adsorption layer is strongly affected by the density of surface hydration sites. Across all materials studied, covering a *SHS* range of 0.4–2.2 nm^{-2} (and up to 13 nm^{-2} for amide–acid PMOs), adsorption-layer densities increase with *SHS* from 0.07 to 0.27 g cm^{-3} and, in the case of amide–acid functionality, can even exceed the density of bulk water. This *SHS*-ρ_a correlation and the low-density values suggest that water preferentially accumulates near silanol groups while avoiding more hydrophobic regions. This is in agreement with observations reported by Kocherbitov *et al*.[205] and Rother *et al*.[58,59] for MCM-41 silica, and Mietner *et al*.[146] for PMOs. In this case, the calculated values for ρ_a do not represent the true microscopic water density, which has been indicated to be bulk-like or even slightly denser,[216,217] but rather the average water amount distributed over the entire adsorption-layer volume. The increased water density observed in amide–acid PMOs aligns with reports on hydration layers at protein surfaces.[281,282] This suggests that water beyond the primary adsorption layer may undergo structural rearrangement, resulting in a pore-core density exceeding that of bulk water. In addition, surface charges from deprotonated carboxylic acid groups and protonated amine groups promote the formation of tightly bound hydration layers around these sites.

By measuring water vapor sorption isotherms at different temperatures, ideally three isotherms with a temperature difference of 10 K,[155] the isosteric enthalpy can be determined via the Van't Hoff Plot and Clausius–Clapeyron relation (see Equation (10)). At very low surface coverage, clear differences emerge between hydrophilic materials, such as MCM-41 silica, BTEVA- and BTEVP-PMO, and more hydrophobic materials, such as BTEVB-, *N*,*N*-DMBTEVA- and BTEVClB-PMO. For hydrophobic PMOs, as in the case of *N*,*N*-DMBTEVA- and BTEVClB-PMOs, the absolute values of isosteric adsorption enthalpy show a steep increase until reaching the absolute bulk condensation enthalpy of (44 kJ mol^{-1}), indicating weak water–surface interactions at low coverage until water–water interactions dominate. In contrast, the hydrophilic materials exhibit an initial steep increase, reaching $|\Delta H_{a,st}|$ values up to 50 kJ mol^{-1}, reflecting stronger water–wall interactions. After adsorption of roughly 2–3 water molecules per hydration site, water–water interactions become

predominant and the enthalpy approaches the bulk value. A strong correlation between the average adsorption enthalpy, determined via the Henry constant, and *SHS* was observed, with a higher number of surface hydration sites leading to higher $|\Delta H_{a,K}|$. To obtain better-resolved data at low water coverage, and as a complementary method, the adsorption enthalpy was also measured by the direct calorimetric approach. Even hydrophobic materials possess silanol groups that act as hydration sites, so during the initial water–surface contact, a high adsorption energy similar to that of hydrophilic materials was observed. Once the most active sites were saturated, the adsorption energy dropped sharply, from roughly 80 kJ mol^{-1} to 12 kJ mol^{-1} for hydrophobic materials such as BTEVB-PMOs.

Taken together, the water sorption studies provide insight into possible adsorption mechanisms. From the perspective of the more hydrophobic PMOs, the observations suggest that adsorption may proceed as follows:

- High adsorption energies are observed upon first water contact due to energetically favored and accessible hydration sites, accompanied by a loss of degrees of freedom.
- As adsorption progresses, the absolute adsorption enthalpy sharply decreases while entropy increases, reflecting higher disorder. Water adsorption is less favorable than in hydrophilic materials, as indicated by the lower pore-volume-normalized slope of the adsorption area prior to capillary condensation ($s_{a,V}$).
- The combination of low $s_{a,V}$ and a larger critical cluster size (evident from the number of water molecules per *SHS* prior to capillary condensation (N_w/N_{SHS})) delays the condensation.
- Lower *SHS* densities (larger distances between hydration sites) favor the formation of larger water clusters before they overlap with neighboring clusters. Water avoids hydrophobic areas, contributing to a thicker adsorption layer with lower density. In addition, pore size influences the process: as the pore diameter decreases, the curvature increases, bringing water clusters spatially closer together and thus reducing the critical cluster size, thereby shifting the condensation to lower pressures.
- The desorption process occurs via a receding meniscus, which is assigned as the equilibrium step.[156,285,286] In contrast, the adsorption process depends on the formation of water clusters reaching a certain size, which appears to be relatively

temperature-independent, before condensation occurs. Nevertheless, the amount of water at the onset of condensation ($n_{o,a}$) and the endset of pore emptying ($n_{e,d}$) remain nearly identical. This suggests that after the core water has desorbed, new water clusters form and then shrink during desorption, as supported by the comparable slopes of cluster formation and evaporation.

Hydrophilic PMOs behave similarly to MCM-41 silica, which has already been extensively studied,[58,59,66,205,287] and differ from hydrophobic PMOs primarily in the stronger interactions and structuring of the adsorbed water, with indications that this structuring can extend partially into the liquid water core.[68]

Water structuring in the pores of PMOs with different pore diameters and surface chemistries was investigated by X-ray scattering at different temperatures. A correlation between surface hydrophilicity and the position of the first structure factor peak was observed. More hydrophilic samples, such as MCM-41 silica or BTEVA-PMOs, showed a shift of the first structure factor peak toward lower scattering vector values, approaching values reported for low-density amorphous ice, where lower scattering vector positions are associated with reduced density. Furthermore, the pair distribution functions reveal a clear deviation from bulk behavior. In bulk water, the second-neighbor region is represented by a single broad peak, whereas in hydrophilic PMOs this feature splits into two distinct peaks, indicating the formation of a more pronounced, though distorted, tetrahedral hydrogen-bond network. This observation is in agreement with literature findings.[99,288–290] In contrast, water confined in more hydrophobic materials, such as BTEVB- and BTEVFB-PMOs, shows a first structure factor peak closer to that of bulk water. The corresponding pair distribution functions for these materials exhibit up to three peaks in the second-neighbor region, indicating a more bulk-like or less tetrahedrally ordered structure. The BTEVP-PMO shows a distinctive effect on water structuring, with indications of enhanced tetrahedral structuring, which may be connected to the previously observed slight increase in t_a/r_h with increasing pore diameters between 4 and 6 nm. Combining the results from the WVS and the X-ray scattering study, a clear impact of surface chemistry on the properties of confined water becomes apparent. In general, more hydrophilic materials exhibit thinner and denser adsorption layers together with stronger tetrahedral structuring of nanoconfined water. In contrast, more hydrophobic PMOs tend to show weaker structural ordering and thicker, less dense adsorption layers. However, this trend should be understood as a general trend rather than a strict classification, as

specific functional groups and their associated surface interactions can significantly influence the behavior of confined water beyond a simple hydrophilic–hydrophobic distinction, as observed, for example, for BTEVP- and BTEVB-based materials.

Low-temperature DSC measurements were performed to investigate the impact of pore size and surface chemistry on the solid–liquid phase transition temperature, as well as on the dimensions and density of the non-freezable water layer. For water in the various PMOs, no effect of surface hydrophilicity on the melting point depression was observed for pores with diameters larger than 3.6 nm, consistent with literature reports.[97,141] With decreasing pore size, more hydrophobic materials, such as BTEVB- or *N*,*N*-DMBTEVA-PMO, exhibit a stronger depression of melting and freezing temperatures, accompanied by reduced specific phase transition enthalpies of pore water. These observations, along with the comparatively larger calculated critical pore radii, indicate the formation of smaller ice cores. Nonetheless, the transition behavior is influenced by a complex interplay between type and size of the surface functionality, pore size/ curvature, transition temperature and its enthalpy change, surface-functionality-dependent ice orientation (see Figure 5),[129] water density, and even the filling method (IW vs. C), making it difficult to establish a clear connection exclusively to surface hydrophilicity. The non-freezable layer thickness decreases with decreasing pore dimensions, so that the t_{nf}/r_P ratio is only slightly increasing. For hydrophobic materials, a Gibbs–Thomson constant of around 40 K nm was obtained, which is in good agreement with previous reports for water confined in mesoporous carbon xerogels (39 K nm).[269] Beyond the non-freezable water layer, the pore wall also has an impact on the freezable confined water, as shown by the X-ray scattering study.[129] In more hydrophilic materials, such as BTEVA-, BTEVP-, or even more pronounced in the charged *N*-MBTEVP$^+$I$^-$-PMO, or in smaller pores, greater changes in the lattice parameters of the hexagonal ice component were observed compared to bulk ice. These deviations were accompanied by stronger angular correlations in the X-ray cross-correlation analysis, indicating preferred orientations of the ice crystallites relative to the pore axis.

The results from WVS and low-temperature DSC studies indicate that surface chemistry similarly influences overall confined water behavior, but with phase-dependent sensitivity. For the vapor–liquid transition, surface-chemistry-dependent shifts in relative pressure are already evident at larger pore diameters (around 5 nm), whereas for the solid–liquid transition, surface effects become noticeable only at pore

diameters below approximately 3.6 nm. In both cases, hydrophobic materials lead to higher melting temperatures or higher relative pressures for capillary condensation of confined water, whereas more hydrophilic materials exhibit the opposite trend. This connection between surface effects is also reflected in the Kelvin and the Gibbs–Thomson constant, both of which quantify the affinity between water and the pore wall, with the C_{GT} values in the frozen state being almost half of C_K. In both water vapor sorption and melting, the *t*-layer dimensions, which are influenced by the surface chemistry, appear to play a decisive role in the respective phase transitions. This effect becomes more significant as the pore size decreases. In both cases, for a liquid core and a frozen core, the surface layer tends to be thicker and less dense in more hydrophobic materials. For frozen cores, however, t_{nf} or ρ_{nf} can be up to twice that of t_a or ρ_a. Although the non-freezable layer is denser, likely due to the crystallization pressure during freezing, its density remains below that of bulk liquid water for the same reason as the adsorption layer, namely the presence of cavities at hydrophobic sites. Due to the lower structuring of surface water[69,89,289] and the additional effect of crystallization pressure, these cavities become more accessible or are filled as water is forced into them, particularly for PMOs like BTEVB, which lack bulky functional groups that would hinder water approach. In addition, a greater structural mismatch between ice and the pore surface may further contribute to the increased thickness of the non-freezable layer.

Except for the amide–acid functionalized PMOs, the charged *N*-MBTEVP$^+$I$^-$-PMOs exhibited the highest hydrophilicity indices in many cases, with *SHS* and adsorption-layer densities comparable to, or exceeding, those of MCM-41 silica. Unlike the other materials, these charged PMOs showed a distinct behavior: the surface water layer was densely packed, likely due to the chaotropic properties of the iodide anion and, to a lesser extent, the *N*-methylpyridinium unit, which disrupts the water structure in the *t*-layer and enables adsorption even at hydrophobic sites.[291] Additionally, the iodide ion, due to its chaotropic nature, is likely located near the surface, either at cationic sites or even within hydrophobic regions, enabling water to be located there as the iodide's hydration shell.[291–295] In contrast to the general trend of thinner but denser *t*-layers in other systems, the charged PMOs displayed comparatively thick *t*-layers with higher average densities. In our recent quasielastic neutron scattering study,[199] the dynamics of water in *N*-MBTEVP$^+$I$^-$-PMOs were compared to those in the bulk state and in the neutral equivalent (BTEVP-PMO). A significant slowdown of water was

observed in *N*-MBTEVP^{+}I^{-}-PMOs relative to its bulk state, with the diffusion coefficient reduced by nearly fourfold and residence times increased by up to about twentyfold. Compared to the neutral BTEVP-PMO, the diffusion coefficient was roughly three times lower and the residence time notably longer. This slowdown can be attributed to stronger electrostatic interactions with the surface ionic groups, which lead to long-lasting structuring of water around the charged sites. There are also strong indications that the charged surface affects not only the interfacial water but also the pore core.

The effects of varying surface chemistries on water behavior can be rationalized by the role of the interfacial layer. In the adsorption regime, the pore surface directly governs water structuring and thus adsorption strength.[104,106] Even in pores containing a liquid core, the surface strongly influences the interfacial layer, as the core water in this state remains comparatively mobile[100] and disordered,[106] allowing it to adjust to surface interactions and to adopt surface-imposed structuring. In contrast, when the pore core is frozen, the situation is more constrained. The non-freezable layer is forced to mediate between two competing structural templates: the surface, which imposes its preferred ordering, and the ice core, which enforces its crystalline lattice. This competition likely explains why the interfacial layer in the liquid-core state achieves stronger ordering, whereas in the frozen-core state it becomes denser and structurally mixed, with weak hydrogen bonding and no indication of tetrahedral organization.[89] As a result, the *t*-layer in pores with an ice core can be significantly thicker than in those with a liquid core, reflecting the higher degree of structural frustration at the solid–surface interface. The surface layer size, often described in terms of the number of monolayers it comprises, does not depend solely on the amount of water but must also account for the cavity dimensions within that layer.

Future studies could further elucidate the relationship between surface chemistry and the structural and dynamic properties of confined water beyond a description based solely on hydrophilicity. Systematic variation of functional group type, size, and charge, together with counterion exchange in charged PMOs, could help to disentangle the effects of specific surface functionalities and, for charged systems, ion-specific effects on confined water. Comparing different counterions could provide further insight into the role of the ionic environment in confined water. Moreover, the structural and dynamic properties of the interfacial water layer in both the liquid- and solid-core states warrant further investigation, given its distinct deviations from bulk water and its particular sensitivity to surface chemistry.

7. References

[1] R. M. Lynden-Bell, S. C. Morris, J. D. Barrow, J. L. Finney, C. Harper, *Water and life; The unique properties of H_2O*, CRC Press, **2010**.

[2] F. Franks, Ed., *Water: A matrix of life*, The Royal Society of Chemistry, **2000**.

[3] T. C. Hansen, *Nat. Commun.* **2021**, *12*, 3161.

[4] K. Komatsu, *Crystallogr. Rev.* **2022**, *28*, 224–297.

[5] Y. Lei, X. Liu, Y. Yu, H. Niu, *The Innovation* **2025**, *6*, 100881.

[6] F. Della Pia, A. Zen, D. Alfè, A. Michaelides, *J. Chem. Phys.* **2022**, *157*, 134701.

[7] P. Gallo, K. Amann-Winkel, C. A. Angell, M. A. Anisimov, F. Caupin, C. Chakravarty, E. Lascaris, T. Loerting, A. Z. Panagiotopoulos, J. Russo, J. A. Sellberg, H. E. Stanley, H. Tanaka, C. Vega, L. Xu, L. G. M. Pettersson, *Chem. Rev.* **2016**, *116*, 7463–7500.

[8] M. Chaplin, *Anomalous properties of water*, https://water.lsbu.ac.uk/water/water_anomalies.html (accessed 2025-07-21).

[9] M. F. Chaplin, Structure and properties of water in its various states. In *Encyclopedia of water*:*Science, technology, and society,* First edition, P. A. Maurice, Ed., Wiley, **2020**, pp 1–19.

[10] A. Nilsson, L. G. M. Pettersson, *Nat. Commun.* **2015**, *6*, 8998.

[11] P. H. Poole, F. Sciortino, U. Essmann, H. E. Stanley, *Nature* **1992**, *360*, 324–328.

[12] O. Mishima, H. E. Stanley, *Nature* **1998**, *396*, 329–335.

[13] S. Sastry, P. G. Debenedetti, F. Sciortino, H. E. Stanley, *Phys. Rev. E* **1996**, *53*, 6144–6154.

[14] C. A. Angell, *Science* **2008**, *319*, 582–587.

[15] P. H. Poole, F. Sciortino, T. Grande, H. E. Stanley, C. A. Angell, *Phys. Rev. Lett.* **1994**, *73*, 1632–1635.

[16] R. J. Speedy, *J. Phys. Chem.* **1982**, *86*, 982–991.

[17] A. Nilsson, *J. Non-Cryst. Solids: X* **2022**, *14*, 100095.

[18] G. I. Likhtenshtein, Supercooled and supercritical water and ice. In *Biological Water: Physicochemical Aspects*, G. I. Likhtenshtein, Ed., Springer International Publishing, **2021**, pp 183–231.

[19] L. G. M. Pettersson, A Two-State Picture of Water and the Funnel of Life. In *Modern Problems of the Physics of Liquid Systems*, L. A. Bulavin, L. Xu, Eds., Springer Proceedings in Physics, Springer International Publishing, **2019**, pp 3–39.

[20] M. P. Andersson, *J. Mol. Liq.* **2023**, *383*, 122169.

[21] A. Nilsson, C. Huang, L. G. Pettersson, *J. Mol. Liq.* **2012**, *176*, 2–16.

[22] R. Shi, H. Tanaka, *J. Am. Chem. Soc.* **2020**, *142*, 2868–2875.

[23] I. Skarmoutsos, G. Franzese, E. Guardia, *J. Mol. Liq.* **2022**, *364*, 119936.

[24] Wikipedia, *Phase diagram*, https://en.wikipedia.org/wiki/Phase_diagram #/media/File:Phase_diagram_of_water.svg (accessed 2025-08-27).

[25] J. L. Miller, *Physics Today* **2018**, *71*, 18–20.

[26] H. R. Corti, G. A. Appignanesi, M. C. Barbosa, J. R. Bordin, C. Calero, G. Camisasca, M. D. Elola, G. Franzese, P. Gallo, A. Hassanali, K. Huang, D. Laria, C. A. Menéndez, J. M. M. de Oca, M. P. Longinotti, J. Rodriguez, M. Rovere, D. Scherlis, I. Szleifer, *Eur. Phys. J. E* **2021**, *44*, 136.

[27] S. Cerveny, F. Mallamace, J. Swenson, M. Vogel, L. Xu, *Chem. Rev.* **2016**, *116*, 7608–7625.

[28] M. Weigler, M. Brodrecht, G. Buntkowsky, M. Vogel, *J. Phys. Chem. B* **2019**, *123*, 2123–2134.

[29] A. Manka, H. Pathak, S. Tanimura, J. Wölk, R. Strey, B. E. Wyslouzil, *Phys. Chem. Chem. Phys.* **2012**, *14*, 4505–4516.

[30] F. Mallamace, M. Broccio, C. Corsaro, A. Faraone, D. Majolino, V. Venuti, L. Liu, C.-Y. Mou, S.-H. Chen, *PNAS* **2007**, *104*, 424–428.

[31] C. M. Burba, J. Janzen, *Thermochimica Acta* **2015**, *615*, 81–87.

[32] J. Meissner, A. Prause, G. H. Findenegg, *J. Phys. Chem. Lett.* **2016**, *7*, 1816–1820.

[33] E. Mamontov, D. R. Cole, S. Dai, M. D. Pawel, C. D. Liang, T. Jenkins, G. Gasparovic, E. Kintzel, *Chem. Phys.* **2008**, *352*, 117–124.

[34] M. Baum, D. Rébiscoul, F. Juranyi, F. Rieutord, *J. Phys. Chem. C* **2018**, *122*, 19857–19868.

[35] M. Baum, F. Rieutord, F. Juranyi, C. Rey, D. Rébiscoul, *Langmuir* **2019**, *35*, 10780–10794.

[36] R. Mancinelli, *J. Phys.: Condens. Matter* **2010**, *22*, 404213.

[37] P. Agre, D. Kozono, *FEBS Lett.* **2003**, *555*, 72–78.

[38] P. Agre, *Angew. Chem. Int. Ed.* **2004**, *43*, 4278–4290.

[39] P. Mentré, *J. Biol. Phys.* **2012**, *38*, 13–26.

[40] X. Wu, Z. Bao, B. Yuan, J. Wang, Y. Sun, H. Luo, S. Deng, *Microporous Mesoporous Mater.* **2013**, *180*, 114–122.

[41] S. Sircar, *Ind. Eng. Chem. Res.* **2006**, *45*, 5435–5448.

[42] N. Riaz, M. Sultan, T. Miyazaki, M. W. Shahzad, M. Farooq, U. Sajjad, Y. Niaz, *Int. Commun. Heat Mass Transfer* **2021**, *128*, 105594.

[43] K. Thu, A. Chakraborty, Y.-D. Kim, A. Myat, B. B. Saha, K. C. Ng, *Desalination* **2013**, *308*, 209–218.

[44] K. C. Ng, K. Thu, Y. Kim, A. Chakraborty, G. Amy, *Desalination* **2013**, *308*, 161–179.

[45] S. Mitra, K. Srinivasan, P. Kumar, S. S. Murthy, P. Dutta, *Energy Procedia* **2014**, *49*, 2261–2269.

[46] A. S. Alsaman, A. A. Askalany, K. Harby, M. S. Ahmed, *Energy* **2017**, *128*, 196–207.

[47] R. G. AbdulHalim, P. M. Bhatt, Y. Belmabkhout, A. Shkurenko, K. Adil, L. J. Barbour, M. Eddaoudi, *J. Am. Chem. Soc.* **2017**, *139*, 10715–10722.

[48] Y. Zhang, R. Wang, *Energy Storage Mater.* **2020**, *27*, 352–369.

[49] A. Frazzica, V. Brancato, V. Palomba, S. Vasta, Sorption Thermal Energy Storage. In *Recent advancements in materials and systems for thermal energy storage*, A. Frazzica, L. F. Cabeza, Eds., Green Energy and Technology, Springer International Publishing, **2019**, pp 33–54.

[50] A. W. Knight, N. G. Kalugin, E. Coker, A. G. Ilgen, *Sci. Rep.* **2019**, *9*, 8246.

[51] H. K. Christenson, *J. Phys.: Condens. Matter* **2001**, *13*, R95-R133.

[52] C. Alba-Simionesco, B. Coasne, G. Dosseh, G. Dudziak, K. E. Gubbins, R. Radhakrishnan, M. Sliwinska-Bartkowiak, *J. Phys.: Condens. Matter* **2006**, *18*, R15.

[53] K. Morishige, K. Kawano, *J. Chem. Phys.* **1999**, *110*, 4867–4872.

[54] A. Schreiber, I. Ketelsen, G. H. Findenegg, *Phys. Chem. Chem. Phys.* **2001**, *3*, 1185–1195.

[55] S. Sklari, H. Rahiala, V. Stathopoulos, J. Rosenholm, P. Pomonis, *Microporous Mesoporous Mater.* **2001**, *49*, 1–13.

[56] B. Webber, J. Dore, *J. Phys.: Condens. Matter* **2004**, *16*, S5449-S5470.

[57] S. Jähnert, F. Vaca Chávez, G. E. Schaumann, A. Schreiber, M. Schönhoff, G. H. Findenegg, *Phys. Chem. Chem. Phys.* **2008**, *10*, 6039–6051.

[58] G. Rother, A. G. Stack, S. Gautam, T. Liu, D. R. Cole, A. Busch, *J. Phys. Chem. C* **2020**, *124*, 15188–15194.

[59] G. Rother, S. Gautam, T. Liu, D. R. Cole, A. Busch, A. G. Stack, *J. Phys. Chem. C* **2022**, *126*, 2885–2895.

[60] T. Takei, K. Mukasa, M. Kofuji, M. Fuji, T. Watanabe, M. Chikazawa, T. Kanazawa, *Colloid Polym. Sci.* **2000**, *278*, 475–480.

[61] M. Thommes, J. Morell, K. A. Cychosz, M. Fröba, *Langmuir* **2013**, *29*, 14893–14902.

[62] P. Lenz, S.-M. Meinert, S. König, M. Steiger, M. Fröba, *J. Phys. Chem. C* **2025**, *129*, 12536–12550.

[63] L. Fumagalli, A. Esfandiar, R. Fabregas, S. Hu, P. Ares, A. Janardanan, Q. Yang, B. Radha, T. Taniguchi, K. Watanabe, G. Gomila, K. S. Novoselov, A. K. Geim, *Science* **2018**, *360*, 1339–1342.

[64] T. Dufils, C. Schran, J. Chen, A. K. Geim, L. Fumagalli, A. Michaelides, *Chem. Sci.* **2024**, *15*, 516–527.

[65] S. Senapati, A. Chandra, *J. Phys. Chem. B* **2001**, *105*, 5106–5109.

[66] C. Weinberger, F. Zysk, M. Hartmann, N. K. Kaliannan, W. Keil, T. D. Kühne, M. Tiemann, *Adv. Mater. Interfaces* **2022**, *9*, 2200245.

[67] T. C. V. Haug, F. Hoffmann, M. N. Tasova, R. Heffels, M. Fröba, *Adv. Mater. Interfaces* **2025**, *12*.

[68] N. C. Gießelmann, P. Lenz, S.-M. Meinert, T. Simon, W. Jo, N. N. Striker, M. Fröba, F. Lehmkühler, *J. Phys. Chem. C* **2024**, *128*, 499–507.

[69] K. Morishige, K. Nobuoka, *J. Chem. Phys.* **1997**, *107*, 6965–6969.

[70] T. Takamuku, M. Yamagami, H. Wakita, Y. Masuda, T. Yamaguchi, *J. Phys. Chem. B* **1997**, *101*, 5730–5739.

[71] J. M. Baker, J. C. Dore, P. Behrens, *J. Phys. Chem. B* **1997**, *101*, 6226–6229.

[72] M.-C. Bellissent-Funel, J. Lal, L. Bosio, *J. Chem. Phys.* **1993**, *98*, 4246–4252.

[73] K. Morishige, H. Uematsu, *J. Chem. Phys.* **2005**, *122*, 44711.

[74] S. Mohammed, H. Asgar, C. J. Benmore, G. Gadikota, *Phys. Chem. Chem. Phys.* **2021**, *23*, 12706–12717.

[75] K. Domin, K.-Y. Chan, H. Yung, K. E. Gubbins, M. Jarek, A. Sterczynska, M. Sliwinska-Bartkowiak, *J. Chem. Eng. Data* **2016**, *61*, 4252–4260.

[76] E. Liu, J. C. Dore, J. B. W. Webber, D. Khushalani, S. Jähnert, G. H. Findenegg, T. Hansen, *J. Phys.: Condens. Matter* **2006**, *18*, 10009–10028.

[77] M. Jażdżewska, M. Śliwińska-Bartkowiak, K. Domin, D. M. Chudoba, A. I. Beskrovnyi, D. S. Neov, K. E. Gubbins, *Bull. Mater. Sci.* **2019**, *42*, 184.

[78] R. Mhanna, A. R. Abdel Hamid, S. Dutta, R. Lefort, L. Noirez, B. Frick, D. Morineau, *J. Chem. Phys.* **2017**, *146*, 24501.

[79] A. Jani, Nanostructuring of binary liquids and water by confinement in periodic mesoporous organosilicates., Ph.D. Thesis, University of Rennes, France, **2021**.

[80] B. Malfait, A. Pouessel, A. Jani, D. Morineau, *J. Phys. Chem. Lett.* **2020**, *11*, 5763–5769.

[81] E. Breynaert, M. Houlleberghs, S. Radhakrishnan, G. Grübel, F. Taulelle, J. A. Martens, *Chem. Soc. Rev.* **2020**, *49*, 2557–2569.

[82] D. Muñoz-Santiburcio, D. Marx, *Chem. Sci.* **2017**, *8*, 3444–3452.

[83] Y. Wang, *Chem. Geol.* **2014**, *378-379*, 1–23.

[84] W. Thomson, *London Edinburgh Philos. Mag. & J. Sci.* **1871**, *42*, 448–452.

[85] L. H. Cohan, *J. Am. Chem. Soc.* **1938**, *60*, 433–435.

[86] S. Merchiori, A. Le Donne, J. D. Littlefair, A. R. Lowe, J.-J. Yu, X.-D. Wu, M. Li, D. Li, M. Geppert-Rybczyńska, L. Scheller, B. A. Trump, A. A. Yakovenko, P. Zajdel, M. Chorążewski, Y. Grosu, S. Meloni, *J. Am. Chem. Soc.* **2024**, *146*, 13236–13246.

[87] G. H. Findenegg, S. Jähnert, D. Akcakayiran, A. Schreiber, *ChemPhysChem* **2008**, *9*, 2651–2659.

[88] L. Xu, V. Molinero, *J. Phys. Chem. B* **2011**, *115*, 14210–14216.

[89] M. Erko, G. H. Findenegg, N. Cade, A. G. Michette, O. Paris, *Phys. Rev. B* **2011**, *84*, 104205.

[90] C. Zhang, Z. Liu, P. Deng, *Can. Geotech. J.* **2018**, *55*, 1144–1153.

[91] M. Wang, J. Wang, J. Jiang, *Adv. Theory Simul.* **2022**, *5*, 2100395.

[92] O. Petrov, I. Furó, *Phys. Chem. Chem. Phys.* **2011**, *13*, 16358–16365.

[93] K. Morishige, H. Yasunaga, R. Denoyel, V. Wernert, *J. Phys. Chem. C* **2007**, *111*, 9488–9495.

[94] K. Morishige, H. Yasunaga, H. Uematsu, *J. Phys. Chem. C* **2009**, *113*, 3056–3061.

[95] K. Morishige, H. Yasunaga, Y. Matsutani, *J. Phys. Chem. C* **2010**, *114*, 4028–4035.

[96] A. Alzaidi, D. Schneider, E. S. Kikkinides, R. Valiullin, *J. Chem. Phys.* **2024**, *161*, 194703.

[97] K. Morishige, *J. Phys. Chem. C* **2018**, *122*, 5013–5019.

[98] A. Lerbret, G. Lelong, P. E. Mason, M.-L. Saboungi, J. W. Brady, *Food Biophys.* **2011**, *6*, 233–240.

[99] A. K. Soper, *Chem. Phys. Lett.* **2013**, *590*, 1–15.

[100] A. Jani, M. Busch, J. B. Mietner, J. Ollivier, M. Appel, B. Frick, J.-M. Zanotti, A. Ghoufi, P. Huber, M. Fröba, D. Morineau, *J. Chem. Phys.* **2021**, *154*, 94505.

[101] B. Malfait, A. Moréac, A. Jani, R. Lefort, P. Huber, M. Fröba, D. Morineau, *J. Phys. Chem. C* **2022**, *126*, 3520–3531.

[102] P. Gallo, M. Rapinesi, M. Rovere, *J. Chem. Phys.* **2002**, *117*, 369–375.

[103] A. Tinti, G. Camisasca, A. Giacomello, *Philos. Trans. R. Soc. A* **2021**, *379*, 20200403.

[104] C. Xiao, P. Shi, W. Yan, L. Chen, L. Qian, S. H. Kim, *Colloids Interfaces* **2019**, *3*, 55.

[105] L. Chen, X. He, H. Liu, L. Qian, S. H. Kim, *J. Phys. Chem. C* **2018**, *122*, 11385–11391.

[106] D. B. Asay, S. H. Kim, *J. Phys. Chem. B* **2005**, *109*, 16760–16763.

[107] D. Argyris, D. R. Cole, A. Striolo, *J. Phys. Chem. C* **2009**, *113*, 19591–19600.

[108] H. Moon, R. P. Collanton, J. I. Monroe, T. M. Casey, M. S. Shell, S. Han, S. L. Scott, *J. Am. Chem. Soc.* **2022**, *144*, 1766–1777.

[109] H. Söngen, Y. Morais Jaques, L. Zivanovic, S. Seibert, R. Bechstein, P. Spijker, H. Onishi, A. S. Foster, A. Kühnle, *Phys. Rev. B* **2019**, *100*, 205410.

[110] P. A. Bonnaud, B. Coasne, R. J.-M. Pellenq, *J. Phys.: Condens. Matter* **2010**, *22*, 284110.

[111] L. Cheng, P. Fenter, K. L. Nagy, M. L. Schlegel, N. C. Sturchio, *Phys. Rev. Lett.* **2001**, *87*, 156103.

[112] S. Pintea, W. de Poel, A. E. F. de Jong, V. Vonk, P. van der Asdonk, J. Drnec, O. Balmes, H. Isern, T. Dufrane, R. Felici, E. Vlieg, *Langmuir* **2016**, *32*, 12955–12965.

[113] J. N. Israelachvili, Solvation, structural, and hydration forces. In *Israelachvili (Hg.) 2011 – Intermolecular and surface forces*, pp 341–380.

[114] J. N. Israelachvili, R. M. Pashley, *Nature* **1983**, *306*, 249–250.

[115] R. G. Horn, J. N. Israelachvili, *J. Chem. Phys.* **1981**, *75*, 1400–1411.

[116] T. Fukuma, Y. Ueda, S. Yoshioka, H. Asakawa, *Phys. Rev. Lett.* **2010**, *104*, 16101.

[117] S. Takahara, M. Nakano, S. Kittaka, Y. Kuroda, T. Mori, H. Hamano, T. Yamaguchi, *J. Phys. Chem. B* **1999**, *103*, 5814–5819.

[118] A. Faraone, L. Liu, C.-Y. Mou, P.-C. Shih, J. R. D. Copley, S.-H. Chen, *J. Chem. Phys.* **2003**, *119*, 3963–3971.

[119] S. Takahara, N. Sumiyama, S. Kittaka, T. Yamaguchi, M.-C. Bellissent-Funel, *J. Phys. Chem. B* **2005**, *109*, 11231–11239.

[120] M. Aso, K. Ito, H. Sugino, K. Yoshida, T. Yamada, O. Yamamuro, S. Inagaki, T. Yamaguchi, *Pure Appl. Chem.* **2012**, *85*, 289–305.

[121] M. Jazdzewska, M. M. Sliwinska-Bartkowiak, A. I. Beskrovnyy, S. G. Vasilovskiy, S.-W. Ting, K.-Y. Chan, L. Huang, K. E. Gubbins, *Phys. Chem. Chem. Phys.* **2011**, *13*, 9008–9013.

[122] D. W. Moreau, H. Atakisi, R. E. Thorne, *IUCrJ* **2019**, *6*, 346–356.

[123] C. G. Salzmann, B. J. Murray, *Nat. Mater.* **2020**, *19*, 586–587.

[124] E. B. Moore, E. de La Llave, K. Welke, D. A. Scherlis, V. Molinero, *Phys. Chem. Chem. Phys.* **2010**, *12*, 4124–4134.

[125] J. A. Hayton, M. B. Davies, T. F. Whale, A. Michaelides, S. J. Cox, *Faraday Discuss.* **2024**, *249*, 210–228.

[126] N. Zhao, S. Hu, C. Zhang, F. Li, R. Chen, *Colloids Surf. A Physicochem. Eng. Asp.* **2023**, *674*, 131851.

[127] S. Wang, L. Zhou, X. Du, *Int. J. Heat Mass Transf.* **2025**, *242*, 126871.

[128] M. Rescigno, M. Lucioli, F. G. Alabarse, U. Ranieri, B. Frick, B. Coasne, L. E. Bove, *J. Phys. Chem. B* **2023**, *127*, 4570–4576.

[129] N. C. Gießelmann, P. Lenz, S.-M. Meinert, T. Simon, R. P. C. Bauer, W. Jo, S. Claas, C. Köhn, N. N. Striker, M. Fröba, F. Lehmkühler, *J. Chem. Phys.* **2024**, *161*, 34508.

[130] M. Thangswamy, P. Maheshwari, D. Dutta, A. K. Bera, M. N. Singh, A. K. Sinha, S. M. Yusuf, P. K. Pujari, *Phys. Chem. Chem. Phys.* **2020**, *22*, 14309–14317.

[131] W. Zhu, Y. Li, H. Wang, Z. Chen, X. Liu, Z. Li, W. Zhao, X. C. Zeng, *J. Phys. Chem. B* **2025**, *129*, 5989–5997.

[132] I. Yasuda, K. Endo, N. Arai, K. Yasuoka, *Commun. Chem.* **2024**, *7*, 117.

[133] B. Malfait, A. Jani, J. B. Mietner, R. Lefort, P. Huber, M. Fröba, D. Morineau, *J. Phys. Chem. C* **2021**, *125*, 16864–16874.

[134] M. Weigler, M. Brodrecht, H. Breitzke, F. Dietrich, M. Sattig, G. Buntkowsky, M. Vogel, *Z. Phys. Chem.* **2018**, *232*, 1041–1058.

[135] J. Banys, M. Kinka, J. Macutkevic, G. Völkel, W. Böhlmann, V. Umamaheswari, M. Hartmann, A. Pöppl, *J. Phys.: Condens. Matter* **2005**, *17*, 2843–2857.

[136] J. Canivet, J. Bonnefoy, C. Daniel, A. Legrand, B. Coasne, D. Farrusseng, *New J. Chem.* **2014**, *38*, 3102–3111.

[137] M. Thommes, S. Mitchell, J. Pérez-Ramírez, *J. Phys. Chem. C* **2012**, *116*, 18816–18823.

[138] J. Deschamps, F. Audonnet, N. Brodie-Linder, M. Schoeffel, C. Alba-Simionesco, *Phys. Chem. Chem. Phys.* **2010**, *12*, 1440–1443.

[139] O. Osta-Rangel, Water confined in hydrophobic nanopores: Towards a new phase diagram, Ph.D. Thesis, University of Paris-Saclay, France, **2021**.

[140] Y. Hirama, T. Takahashi, M. Hino, T. Sato, *J. Colloid Interface Sci.* **1996**, *184*, 349–359.

[141] J. Jelassi, H. L. Castricum, M.-C. Bellissent-Funel, J. Dore, J. B. W. Webber, R. Sridi-Dorbez, *Phys. Chem. Chem. Phys.* **2010**, *12*, 2838–2849.

[142] F. Hoffmann, M. Cornelius, J. Morell, M. Fröba, *Angew. Chem. Int. Ed.* **2006**, *45*, 3216–3251.

[143] S. Inagaki, S. Guan, T. Ohsuna, O. Terasaki, *Nature* **2002**, *416*, 304–307.

[144] A. Sayari, W. Wang, *J. Am. Chem. Soc.* **2005**, *127*, 12194–12195.

[145] M. Cornelius, F. Hoffmann, M. Fröba, *Chem. Mater.* **2005**, *17*, 6674–6678.

[146] J. B. Mietner, F. J. Brieler, Y. J. Lee, M. Fröba, *Angew. Chem. Int. Ed.* **2017**, *56*, 12348–12351.

[147] U. Schubert, N. Hüsing, *Synthesis of inorganic materials*, 4th ed., Wiley-VCH, **2019**.

[148] C. J. Brinker, G. W. Scherer, *Sol-gel science: The physics and chemistry of sol-gel processing*, Academic Press, **1990**.

[149] K. Rurack; R. Martínez-Máñez, Eds., *The supramolecular chemistry of organic-inorganic hybrid materials*, Wiley, **2010**.

[150] S. Inagaki, S. Guan, Y. Fukushima, T. Ohsuna, O. Terasaki, *J. Am. Chem. Soc.* **1999**, *121*, 9611–9614.

[151] T. Asefa, M. J. MacLachlan, N. Coombs, G. A. Ozin, *Nature* **1999**, *402*, 867–871.

[152] B. J. Melde, B. T. Holland, C. F. Blanford, A. Stein, *Chem. Mater.* **1999**, *11*, 3302–3308.

[153] G. Park, M. Bilo, M. Fröba, Y. Jung, Y. J. Lee, *J. Phys. Chem. C* **2022**, *126*, 14693–14703.

[154] C. Schlumberger, M. Thommes, *Adv. Mater. Interfaces* **2021**, *8*, 2002181.

[155] J. Rouquerol, F. Rouquerol, P. Llewellyn, G. Maurin, K. Sing, *Adsorption by powders and porous solids: Principles, methodology and applications*, 2nd ed., Academic Press, **2013**.

[156] S. Lowell, J. E. Shields, M. A. Thomas, M. Thommes, *Characterization of porous solids and powders: Surface area, pore size and density*, Springer Netherlands, **2004**.

[157] M. Thommes, C. Schlumberger, *Annu. Rev. Chem. Biomol. Eng.* **2021**, *12*, 137–162.

[158] M. Thommes, K. Kaneko, A. V. Neimark, J. P. Olivier, F. Rodriguez-Reinoso, J. Rouquerol, K. S. Sing, *Pure Appl. Chem.* **2015**, *87*, 1051–1069.

[159] V. Meynen, P. Cool, E. F. Vansant, *Microporous Mesoporous Mater.* **2009**, *125*, 170–223.

[160] A.-H. Lu, D. Zhao, Y. Wan, *Nanocasting: A versatile strategy for creating nanostructured porous materials*, RSC nanoscience & nanotechnology, Vol. 11, Royal Society of Chemistry, **2010**.

[161] M. Beretta, J. Morell, P. Sozzani, M. Fröba, *Chem. Commun.* **2010**, *46*, 2495–2497.

[162] M. Waki, N. Mizoshita, T. Ohsuna, T. Tani, S. Inagaki, *Chem. Commun.* **2010**, *46*, 8163–8165.

[163] S. Martens, R. Ortmann, F. J. Brieler, C. Pasel, Y. Joo Lee, D. Bathen, M. Fröba, *Z. Anorg. Allg. Chem.* **2014**, *640*, 632–640.

[164] G. Gonella, E. H. G. Backus, Y. Nagata, D. J. Bonthuis, P. Loche, A. Schlaich, R. R. Netz, A. Kühnle, I. T. McCrum, M. T. M. Koper, M. Wolf, B. Winter, G. Meijer, R. K. Campen, M. Bonn, *Nat. Rev. Chem.* **2021**, *5*, 466–485.

[165] A. Horner, C. Siligan, A. Cornean, P. Pohl, *Faraday Discuss.* **2018**, *209*, 55–65.

[166] G. Smeulders, V. Meynen, A. Silvestre-Albero, K. Houthoofd, M. Mertens, J. Silvestre-Albero, J. A. Martens, P. Cool, *Mater. Chem. Phys.* **2012**, *132*, 1077–1088.

[167] B. Karimi, N. Ganji, O. Pourshiani, W. R. Thiel, *Prog. Mater. Sci.* **2022**, *125*, 100896.

[168] W. Zhang, H. Ma, J. Hua, W. Zhang, C. Guo, J. Wang, *J. Solid State Chem.* **2019**, *277*, 761–768.

[169] A. Kuschel, H. Sievers, S. Polarz, *Angew. Chem.* **2008**, *120*, 9655–9659.

[170] J. Wang, M. Zhou, C. Gu, W. Zhang, M. Lv, C. Guo, L. Sun, H. Zhang, *Mater. Lett.* **2017**, *193*, 299–304.

[171] F. K. Zandian, S. Balalaie, K. Amiri, H. Bagheri, *Anal. Chim. Acta* **2024**, *1290*, 342206.

[172] J. Wang, W. Zhang, C. Gu, W. Zhang, M. Zhou, Z. Wang, C. Guo, L. Sun, *Chem. Asian J.* **2017**, *12*, 3162–3171.

[173] W. Huybrechts, J. Lauwaert, A. de Vylder, M. Mertens, G. Mali, J. W. Thybaut, P. van der Voort, P. Cool, *Microporous Mesoporous Mater.* **2017**, *251*, 1–8.

[174] J. Morell, S. Chatterjee, P. J. Klar, D. Mauder, I. Shenderovich, F. Hoffmann, M. Fröba, *Chem. Eur. J.* **2008**, *14*, 5935–5940.

[175] E. Steinrücken, L. Diehl, T. Wissel, G. Buntkowsky, H. S. Varol, A. Andrieu-Brunsen, M. Vogel, *J. Chem. Phys.* **2025**, *162*, 84702.

[176] W. Whitnall, L. Cademartiri, G. A. Ozin, *J. Am. Chem. Soc.* **2007**, *129*, 15644–15649.

[177] A. A. Milischuk, B. M. Ladanyi, *J. Chem. Phys.* **2011**, *135*, 174709.

[178] P. Gallo, M. Rovere, S.-H. Chen, *J. Phys.: Condens. Matter* **2012**, *24*, 64109.

[179] N. Kuon, A. A. Milischuk, B. M. Ladanyi, E. Flenner, *J. Chem. Phys.* **2017**, *146*, 214501.

[180] S. Uchida, K. Fujiwara, M. Shibahara, *J. Phys. Chem. B* **2021**, *125*, 9601–9609.

[181] J. Shi, M. Fulford, H. Li, M. Marzook, M. Reisjalali, M. Salvalaglio, C. Molteni, *Phys. Chem. Chem. Phys.* **2022**, *24*, 12476–12487.

[182] X. Zhu, M. Vandamme, Z. Jiang, L. Brochard, *J. Chem. Phys.* **2023**, *159*, 154704.

[183] J.-B. Brubach, A. Mermet, A. Filabozzi, A. Gerschel, D. Lairez, M. P. Krafft, P. Roy, *J. Phys. Chem. B* **2001**, *105*, 430–435.

[184] S. Le Caër, S. Pin, S. Esnouf, Q. Raffy, J. P. Renault, J.-B. Brubach, G. Creff, P. Roy, *Phys. Chem. Chem. Phys.* **2011**, *13*, 17658–17666.

[185] R. Musat, J. P. Renault, M. Candelaresi, D. J. Palmer, S. Le Caër, R. Righini, S. Pommeret, *Angew. Chem. Int. Ed.* **2008**, *47*, 8033–8035.

[186] B. Baumgartner, J. Hayden, J. Loizillon, S. Steinbacher, D. Grosso, B. Lendl, *Langmuir* **2019**, *35*, 11986–11994.

[187] V. Crupi, S. Interdonato, F. Longo, D. Majolino, P. Migliardo, V. Venuti, *J. Raman Spectrosc.* **2008**, *39*, 244–249.

[188] E. W. Hansen, H. C. Gran, E. J. Sellevold, *J. Phys. Chem. B* **1997**, *101*, 7027–7032.

[189] K. Overloop, L. Vangerven, *J. Magn. Reson. A* **1993**, *101*, 179–187.

[190] E. W. Hansen, M. Stöcker, R. Schmidt, *J. Phys. Chem.* **1996**, *100*, 2195–2200.

[191] T. Ishizaki, M. Maruyama, Y. Furukawa, J. G. Dash, *Journal of Crystal Growth* **1996**, *163*, 455–460.

[192] C. Lederle, M. Sattig, M. Vogel, *J. Phys. Chem. C* **2018**, *122*, 15427–15434.

[193] K. Morishige, H. Iwasaki, *Langmuir* **2003**, *19*, 2808–2811.

[194] J. Dore, *Chem. Phys.* **2000**, *258*, 327–347.

[195] N. Floquet, J. Coulomb, N. Dufau, G. Andre, R. Kahn, *Phys. B: Condens. Matter* **2004**, *350*, 265–269.

[196] J.-M. Zanotti, M.-C. Bellissent-Funel, S.-H. Chen, *Phys. Rev. E* **1999**, *59*, 3084–3093.

[197] M. Bellissent-Funel, S. H. Chen, J. Zanotti, *Phys. Rev. E* **1995**, *51*, 4558–4569.

[198] M. Sliwinska-Bartkowiak, M. Jazdzewska, L. L. Huang, K. E. Gubbins, *Phys. Chem. Chem. Phys.* **2008**, *10*, 4909–4919.

[199] A. Mozhdehei, P. Lenz, S. Gries, S.-M. Meinert, R. Lefort, J.-M. Zanotti, Q. Berrod, M. Appel, M. Busch, P. Huber, M. Fröba, D. Morineau, *J. Phys. Chem. C* **2025**, *129*, 18311–18324.

[200] D. I. Fried, D. Bednarski, M. Dreifke, F. J. Brieler, M. Thommes, M. Fröba, *J. Mater. Chem. B* **2015**, *3*, 2341–2349.

[201] J. Swenson, S. Cerveny, *J. Phys.: Condens. Matter* **2015**, *27*, 33102.

[202] N. C. Giesselmann, X-ray scattering investigations of the structure of water and ice in periodic mesoporous organosilicas, Ph.D. Thesis, University of Hamburg, Germany, **2026**.

[203] J. Als-Nielsen, Des McMorrow, *Elements of modern X-ray physics*, 2nd ed., John Wiley & Sons, **2011**.

[204] M. J. Bée, *Quasielastic neutron scattering: Principles and applications in solid state chemistry, biology and materials science*, Adam Hilger, **1988**.

[205] V. Kocherbitov, V. Alfredsson, *J. Phys. Chem. C* **2007**, *111*, 12906–12913.

[206] R. O. David, J. Fahrni, C. Marcolli, F. Mahrt, D. Brühwiler, Z. A. Kanji, *Atmos. Chem. Phys.* **2020**, *20*, 9419–9440.

[207] J. I. Carrero, *ChemTexts* **2024**, *10*, 4.

[208] S. Brandani, E. Mangano, L. Sarkisov, *Adsorption* **2016**, *22*, 261–276.

[209] H. L. Nguyen, A. Darù, S. Chheda, A. Alawadhi, S. E. Neumann, L. Wang, X. Bai, M. Alawad, C. Borgs, J. Chayes, J. Sauer, L. Gagliardi, O. Yaghi, *ACS Cent. Sci.* **2025**, *11*, 665–671.

[210] B. C. Dallin, A. S. Kelkar, R. C. van Lehn, *Chem. Sci.* **2023**, *14*, 1308–1319.

[211] P. Lenz, U. Sazama, S. König, M. Steiger, M. Fröba, *J. Phys. Chem. C* **2026**, *130*, 3472–3485.

[212] I. G. Shenderovich, G. Buntkowsky, A. Schreiber, E. Gedat, S. Sharif, J. Albrecht, N. S. Golubev, G. H. Findenegg, H.-H. Limbach, *J. Phys. Chem. B* **2003**, *107*, 11924–11939.

[213] S. Saliba, P. Ruch, W. Volksen, T. P. Magbitang, G. Dubois, B. Michel, *Microporous Mesoporous Mater.* **2016**, *226*, 221–228.

[214] K. L. Miller, R. Lin, J. Hou, C. J. Kepert, D. M. D'Alessandro, M. B. Solomon, *Mater. Adv.* **2024**, *5*, 1868–1874.

[215] S. W. Rutherford, *Langmuir* **2025**, *41*, 20502–20515.

[216] M. Erko, D. Wallacher, A. Hoell, T. Hauss, I. Zizak, O. Paris, *Phys. Chem. Chem. Phys.* **2012**, *14*, 3852–3858.

[217] P. Gallo, M. A. Ricci, M. Rovere, *J. Chem. Phys.* **2002**, *116*, 342–346.

[218] I. I. Salame, T. J. Bandosz, *J. Colloid Interface Sci.* **1999**, *210*, 367–374.

[219] A. Matsumoto, T. Sasaki, N. Nishimiya, K. Tsutsumi, *Colloids Surf. A Physicochem. Eng. Asp.* **2002**, *203*, 185–193.

[220] A. Matsumoto, T. Sasaki, N. Nishimiya, K. Tsutsumi, *Langmuir* **2001**, *17*, 47–51.

[221] S. Furmaniak, M. Wiśniewski, K. Werengowska-Ciećwierz, A. P. Terzyk, K. Hata, P. A. Gauden, P. Kowalczyk, M. Szybowicz, *J. Phys. Chem. C* **2015**, *119*, 2703–2715.

[222] A. Cauvel, D. Brunel, F. Di Renzo, E. Garrone, B. Fubini, *Langmuir* **1997**, *13*, 2773–2778.

[223] D. B. Asay, A. L. Barnette, S. H. Kim, *J. Phys. Chem. C* **2009**, *113*, 2128–2133.

[224] M. A. Khan, K. Thu, S. Mitra, *Appl. Therm. Eng.* **2024**, *249*, 123289.

[225] L. Giraldo, P. Rodriguez-Estupiñán, J. C. Moreno-Piraján, *Processes* **2019**, *7*, 203.

[226] Y. Tian, J. Wu, *Langmuir* **2017**, *33*, 996–1003.

[227] A. Nuhnen, C. Janiak, *Dalton Trans.* **2020**, *49*, 10295–10307.

[228] F. H. M. Azahar, S. Mitra, A. Yabushita, A. Harata, B. B. Saha, K. Thu, *Appl. Therm. Eng.* **2018**, *143*, 688–700.

[229] F. R. Siperstein, C. Avendaño, J. J. Ortiz, A. Gil-Villegas, *AIChE Journal* **2021**, *67*, e17186.

[230] J. B. Ott, J. Boerio-Goates, Chapter 8 - The Equilibrium Condition Applied to Phase Equilibria. In *Chemical Thermodynamics: Principles and Applications*, J. B. Ott, J. Boerio-Goates, Eds., Academic Press, **2000**, pp 383–433.

[231] D. P. Broom, D. Book, Hydrogen storage in nanoporous materials. In *Advances in hydrogen production, storage and distribution*, A. Basile, A. Iulianelli, Eds., Woodhead Publishing/ Elsevier, **2014**, pp 410–450.

[232] Q. Xiao, Q. Tong, *Food Res. Int.* **2013**, *54*, 1605–1612.

[233] T. A. Shittu, F. Idowu-Adebayo, I. I. Adedokun, O. Alade, *NIFOJ* **2015**, *33*, 90–96.

[234] Cantrell, G. E. Ewing, *J. Phys. Chem. B* **2001**, *105*, 5434–5439.

[235] Y. Larher, *J. Colloid Interface Sci.* **1971**, *37*, 836–848.

[236] S. Poyet, S. Charles, *Cem. Concr. Res.* **2009**, *39*, 1060–1067.

[237] P. M. Frías-Ureña, M. Bárcena-Soto, V. Soto, K. Chávez, E. Orozco-Guareño, J. Badillo-Camacho, J. R. Robledo-Ortiz, I. Fernández-Cervantes, S. Gómez-Salazar, *ACS omega* **2025**, *10*, 11421–11438.

[238] S. Brunauer, P. H. Emmett, E. Teller, *J. Am. Chem. Soc.* **1938**, *60*, 309–319.

[239] T. Triyono, W. Trisunaryanti, O. Sidjabat, *SCOG* **2008**, *31*, 21–25.

[240] N. Lu, M. Khorshidi, *J. Geotech. Geoenviron. Eng.* **2015**, *141*, 4015032.

[241] H. Demir, M. Mobedi, S. Ülkü, *J. Therm. Anal. Calorim.* **2011**, *105*, 375–382.

[242] S. V. Ushakov, A. Navrotsky, *Appl. Phys. Lett.* **2005**, *87*, 164103.

[243] L. Mazeina, A. Navrotsky, *Chem. Mater.* **2007**, *19*, 825–833.

[244] S. Hayun, T. Y. Shvareva, A. Navrotsky, *J. Am. Ceram. Soc.* **2011**, *94*, 3992–3999.

[245] D. Gouvêa, S. V. Ushakov, A. Navrotsky, *Langmuir* **2014**, *30*, 9091–9097.

[246] H. Binder, B. Kohlstrunk, H. H. Heerklotz, *Chem. Phys. Lett.* **1999**, *304*, 329–335.

[247] T. Muangthong-on, J. Wannapeera, H. Ohgaki, K. Miura, *Energy Fuels* **2017**, *31*, 10691–10698.

[248] C. Wang, Y. Zhang, J. Wang, Y. Fan, Y. Tang, *Combust. Sci. Technol.* **2024**, *196*, 1957–1972.

[249] Y. Cui, S. Gao, R. Zhang, L. Cheng, J. Yu, *Polymers* **2020**, *12*, 98.

[250] H. Yang, K. Jayaatmaja, X. Qiu, M. Fan, M. Dejam, S. P. Tan, H. Adidharma, *J. Phys. Chem. C* **2023**, *127*, 21980–21988.

[251] H. Kim, H. J. Cho, S. Narayanan, S. Yang, H. Furukawa, S. Schiffres, X. Li, Y.-B. Zhang, J. Jiang, O. M. Yaghi, E. N. Wang, *Sci. Rep.* **2016**, *6*, 19097.

[252] T. Li, H. Tian, X. Xiao, P. Cheng, Q. Zhou, Q. Wei, *Mar. Pet. Geol.* **2017**, *86*, 858–873.

[253] M. Bilal, M. Sultan, T. Morosuk, W. Den, U. Sajjad, M. M. Aslam, M. W. Shahzad, M. Farooq, *Int. Commun. Heat Mass Transf.* **2022**, *133*, 105961.

[254] H. Kim, S. Yang, S. R. Rao, S. Narayanan, E. A. Kapustin, H. Furukawa, A. S. Umans, O. M. Yaghi, E. N. Wang, *Science* **2017**, *356*, 430–434.

[255] S. Ülkü, *J. Heat. Recov. Syst.* **1986**, *6*, 277–284.

[256] H. Demir, M. Mobedi, S. Ülkü, *Renew. Sustain. Energy Rev.* **2008**, *12*, 2381–2403.

[257] S. Saren, S. Mitra, T. Miyazaki, K. C. Ng, K. Thu, *J. Therm. Anal. Calorim.* **2023**, *148*, 3059–3071.

[258] M. S. Akhtar, S. Ali, W. Zaman, *Molecules* **2024**, *29*, 4317.

[259] Y.-S. Wang, X.-J. Zhang, Y.-Q. Ba, T.-Y. Li, G.-P. Hao, A.-H. Lu, *Research* **2022**, *2022*, 9780864.

[260] A. H. Farmahini, D. S. Sholl, S. K. Bhatia, *J. Am. Chem. Soc.* **2015**, *137*, 5969–5979.

[261] R. Schmidt, E. W. Hansen, M. Stoecker, D. Akporiaye, O. H. Ellestad, *J. Am. Chem. Soc.* **1995**, *117*, 4049–4056.

[262] S. Kittaka, S. Ishimaru, M. Kuranishi, T. Matsuda, T. Yamaguchi, *Phys. Chem. Chem. Phys.* **2006**, *8*, 3223–3231.

[263] G. W. H. Höhne, W. F. Hemminger, H.-J. Flammersheim, *Differential scanning calorimetry*, 2., revised and enl. ed., Springer, **2003**.

[264] C. Faivre, D. Bellet, G. Dolino, *Eur. Phys. J. B* **1999**, *7*, 19–36.

[265] J. Riikonen, J. Salonen, V.-P. Lehto, *J. Therm. Anal. Calorim.* **2011**, *105*, 811–821.

[266] S. Schöder, H. Reichert, H. Schröder, M. Mezger, J. S. Okasinski, V. Honkimäki, J. Bilgram, H. Dosch, *Phys. Rev. Lett.* **2009**, *103*, 95502.

[267] S. Engemann, H. Reichert, H. Dosch, J. Bilgram, V. Honkimäki, A. Snigirev, *Phys. Rev. Lett.* **2004**, *92*, 205701.

[268] K. A. Emelyanenko, A. M. Emelyanenko, L. B. Boinovich, *Colloid J.* **2022**, *84*, 265–286.

[269] L. Kořená, V. Slovák, S. L. Flores-López, A. Arenillas, *Thermochim. Acta* **2025**, 180128.

[270] K. Ishikiriyama, M. Todoki, *Thermochimica Acta* **1995**, *256*, 213–226.

[271] D. M. Murphy, T. Koop, *Q. J. R. Meteorol. Soc.* **2005**, *131*, 1539–1565.

[272] E. B. Moore, J. T. Allen, V. Molinero, *J. Phys. Chem. C* **2012**, *116*, 7507–7514.

[273] Y. Zhang, H. R. Lashgari, Y. Di, K. Sepehrnoori, *Fuel* **2017**, *197*, 575–582.

[274] F.-X. Coudert, A. Boutin, A. H. Fuchs, *Commun. Chem.* **2021**, *4*, 106.

[275] T. Wang, H. Iriawan, J. Peng, R. R. Rao, B. Huang, D. Zheng, D. Menga, A. Aggarwal, S. Yuan, J. Eom, Y. Zhang, K. McCormack, Y. Román-Leshkov, J. Grossman, Y. Shao-Horn, *Chem. Rev.* **2025**, *125*, 1420–1467.

[276] J. Monroe, M. Barry, A. DeStefano, P. Aydogan Gokturk, S. Jiao, D. Robinson-Brown, T. Webber, E. J. Crumlin, S. Han, M. S. Shell, *Annu. Rev. Chem. Biomol. Eng.* **2020**, *11*, 523–557.

[277] W. Song, C. Lang, Y. Shen, M. Kumar, *Annu. Rev. Mater. Res.* **2018**, *48*, 57–82.

[278] M. Barboiu, *Angew. Chem. Int. Ed.* **2012**, *51*, 11674–11676.

[279] A. Abdelrasoul, H. Doan, A. Lohi, *Biomimetic and bioinspired membranes for new frontiers in sustainable water treatment technology*, IntechOpen, **2017**.

[280] D.-D. Su, M. Barboiu, *Coordination Chemistry Reviews* **2024**, *515*, 215973.

[281] D. I. Svergun, S. Richard, M. H. Koch, Z. Sayers, S. Kuprin, G. Zaccai, *PNAS* **1998**, *95*, 2267–2272.

[282] N. Smolin, R. Winter, *J. Phys. Chem. B* **2004**, *108*, 15928–15937.

[283] M. Bilo, Controlled pore glasses and alginate hydrogels as form-giving matrices for nanoporous organosilicas, Ph.D. Thesis, University of Hamburg, Germany, **2019**.

[284] G. T. Hermanson, Functional targets for bioconjugation. In *Bioconjugate Techniques,* 3rd ed., G. T. Hermanson, Ed., Elsevier, **2013**, pp 127–228.

[285] P. A. Monson, *Langmuir* **2008**, *24*, 12295–12302.

[286] J. Landers, G. Y. Gor, A. V. Neimark, *Colloids Surf. A: Physicochem. Eng. Asp.* **2013**, *437*, 3–32.

[287] E.-P. Ng, S. Mintova, *Microporous Mesoporous Mater.* **2008**, *114*, 1–26.

[288] P. Smirnov, T. Yamaguchi, S. Kittaka, S. Takahara, Y. Kuroda, *J. Phys. Chem. B* **2000**, *104*, 5498–5504.

[289] H. Khoder, D. Schaniel, S. Pillet, E. E. Bendeif, *Acta Crystallogr., Sect. A: Found. Adv.* **2020**, *76*, 589–599.

[290] R. Mancinelli, S. Imberti, A. K. Soper, K. H. Liu, C. Y. Mou, F. Bruni, M. A. Ricci, *J. Phys. Chem. B* **2009**, *113*, 16169–16177.

[291] H. Zhao, *J. Chem. Technol. Biotechnol.* **2006**, *81*, 877–891.

[292] M. Lund, P. Jungwirth, *J. Phys.: Condens. Matter* **2008**, *20*, 494218.

[293] L. Liu, R. Kou, G. Liu, *Soft Matter* **2016**, *13*, 68–80.

[294] E. Lee, J.-H. Choi, M. Cho, *Phys. Chem. Chem. Phys.* **2017**, *19*, 20008–20015.

[295] K. I. Assaf, W. M. Nau, *Angew. Chem. Int. Ed.* **2018**, *57*, 13968–13981.

[296] Institut für Arbeitsschutz der Deutschen Gesetzlichen Unfallversicherung, *GESTIS-Stoffdatenbank*, Can be found under gestis.dguv.de (accessed 11.11.25).

[297] Sigma-Aldrich, Can be found under sigmaaldrich.com (accessed 11.11.25).

[298] J. H. Shin, S. S. Park, M. Selvaraj, C.-S. Ha, *J. Porous Mater.* **2012**, *19*, 29–35.

[299] A. Galarneau, H. Cambon, F. Di Renzo, R. Ryoo, M. Choi, F. Fajula, *New J. Chem.* **2003**, *27*, 73–79.

[300] S. Dhawan, M. B. Bijesh, V. Haridas, *Polymer* **2018**, *138*, 218–228.

[301] A. Galarneau, J. Iapichella, K. Bonhomme, F. Di Renzo, P. Kooyman, O. Terasaki, F. Fajula, *Adv. Funct. Mater.* **2006**, *16*, 1657–1667.

[302] J. B. Mietner, Visiting nanopores: The great potential of PMOs for studying the properties of water in nanopores of different polarity, Ph.D. Thesis, University of Hamburg, Germany, **2018**.

[303] P. R. Sultane, T. B. Mete, R. G. Bhat, *Tetrahedron Lett.* **2015**, *56*, 2067–2070.

[304] R. B. Merrifield, *J. Am. Chem. Soc.* **1963**, *85*, 2149–2154.

[305] V. Vinayagam, S. K. Sadhukhan, D. V. Botla, R. R. Chittem, S. R. Kasu, T. V. Hajay Kumar, *J. Org. Chem.* **2024**, *89*, 5665–5674.

8. Appendix

8.1. List of Chemicals Used in This Work

All chemicals used in this thesis are listed in Table S1, including safety information such as GHS pictograms and hazard and precautionary statements.

Table S1: Safety information for the substances used in this work according to the GHS classification.[296,297]

Substance (CAS Registry Number)	GHS Pictograms	Hazard Statements	Precautionary Statements
(3-Aminopropyl)-triethoxysilane (919-30-2)		302, 314, 317	261, 270, 280, 301+312, 303+361+353, 305+351+338
(R)-2-amino-N^1,N^4-bis(3-(triethoxysilyl)propyl)succinamide / -PMO	–	–	–
1,4-bis(triethoxysilyl)benzene / -PMO	–	–	–
1,4-bis[(*E*)-2-(triethoxysilyl)vinyl]benzene / -PMO	–	–	–
1,4-Dibromo-2-chlorobenzene (3460-24-0)		315, 319, 335	261, 305, 338, 351
1,4-Dibromobenzene (106-37-6)		315, 319, 335, 410	261, 264, 271, 273, 302+352, 305+351+338
1,4-Dioxane (123-91-1)		225, 319, 335, 350	202, 210, 233, 240, 305+351+338, 308+313

Table S1: Safety information for the substances used in this work according to the GHS classification.[296,297]

Substance (CAS Registry Number)	GHS Pictograms	Hazard Statements	Precautionary Statements
1-methyl-2,5-bis((*E*)-2-(triethoxysilyl)vinyl)pyridinium iodide / -PMO	–	–	–
2,5-Bis((trimethylsilyl)ethynyl)pyridine (172883-67-9)	–	–	–
2,5-bis[(*E*)-2-(triethoxysilyl)-vinyl]aniline / -PMO	–	–	–
2,5-bis[(*E*)-2-(triethoxysilyl)-vinyl]aniline-4-oxobut-2-enoic / -PMO	–	–	–
2,5-bis[(*E*)-2-(triethoxysilyl)-vinyl]aniline-4-oxo-butanoic acid / -PMO	–	–	–
2,5-bis[(*E*)-2-(triethoxysilyl)-vinyl]pyridine / -PMO	–	–	–
2,5-Dibromoaniline (3638-73-1)		302+312+332, 315, 317, 319, 335	261, 280, 301+312, 302+352+312, 304+340+321, 305+351+338
2,5-Diethynylpyridine (137000-75-0)		315, 319	264, 280, 302+353+337+313, 305+351+338, 362+364, 332+313

Table S1: Safety information for the substances used in this work according to the GHS classification.[296,297]

Substance (CAS Registry Number)	GHS Pictograms	Hazard Statements	Precautionary Statements
2,5-Diiodopyridine (116195-81-4)		302, 315, 317, 318, 334, 335	261, 280, 305+351+338, 342+311
2-chloro-1,4-((*E*)-2′-bis(triethoxysilyl)vinyl)benzene / -PMO	–	–	–
4-(bis(3-(triethoxysilyl)propyl)-amino)-4-oxobut-2-enoic / -PMO	–	–	–
4-(bis(3-(triethoxysilyl)propyl)-amino)-4-oxobutanoic acid / -PMO	–	–	–
Aceton (67-64-1)		225, 319, 336	210, 233, 240, 241, 242, 305+351+338
Acetonitrile (75-05-8)		225, 302+312+332	210, 280, 301+312, 303+361+353, 304+340+312, 305+351+338
Ammonia solution (25 wt%) (7664-41-7)		314, 335, 410	261, 271, 273, 280, 303+361+353, 305+351+338
Bis(3-(triethoxysilyl)propyl)-amine (13497-18-2)		314	280, 305+351+338, 310

Table S1: Safety information for the substances used in this work according to the GHS classification.[296,297]

Substance (CAS Registry Number)	GHS Pictograms	Hazard Statements	Precautionary Statements
Bis(triphenylphosphine)-palladium(II) dichloride (13965-03-2)		317, 413	261, 272, 273, 280, 302+352, 333+313
Bis(tri-*tert*-butylphosphine)-palladium(0) (53199-31-8)	Not a hazardous substance.		
Celite 545 (68855-54-9)		372	260, 264, 270, 314, 501
Charcoal Activated (7440-44-0)	Not a hazardous substance.		
Chloro(1,5-cyclooctadiene)rhodium(I) dimer (12092-47-6)		319	264, 280, 305+351+338, 337+313
Chloroform-d (865-49-6)		302, 315, 319, 331, 336, 351, 361d, 372	202, 301+312, 302+352, 304+340+311, 305+351+338, 308+313
Copper(I) iodide (7681-65-4)		302, 315, 317, 318, 410	273, 280, 301+312+330, 302+352, 305+351+338+310
Decyltrimethylammonium bromide (2082-84-0)		315, 319, 335	261, 264, 271, 280, 302+352, 305+351+338
Deuterium oxide (7789-20-0)	Not a hazardous substance.		

Table S1: Safety information for the substances used in this work according to the GHS classification.[296,297]

Substance (CAS Registry Number)	GHS Pictograms	Hazard Statements	Precautionary Statements
Dichloromethane (75-09-2)		315, 319, 336, 351	201, 261, 264, 302+352, 305+351+338
Dicyclohexylcarbodiimide (538-75-0)		302, 311, 317, 318	261, 264, 280, 301+312, 302+352, 305+351+338
Diisopropylamine (108-18-9)		225, 302, 331, 314, 335, 412	210, 273, 280, 303+361+353, 304+340+310, 305+351+338, 403+235
Dimethyl sulfoxide-d_6 (2206-27-1)	Not a hazardous substance.		
Dimethylacetamide (127-19-5)		312+332, 319, 360D	202, 280, 302+352+312, 304+340+312, 305+351+338, 308+313
Dodecyltrimethylammonium bromide (1119-94-4)		301, 315, 319, 410	264, 270, 273, 301+310, 302+352, 305+351+338
Ethanol (64-17-5)		225, 319	210, 233, 240, 241, 242, 305+351+338

Table S1: Safety information for the substances used in this work according to the GHS classification.[296,297]

Substance (CAS Registry Number)	GHS Pictograms	Hazard Statements	Precautionary Statements
Ethyl acetate (141-78-6)		225, 319, 336	210, 233, 240, 241, 242, 305+351+338
Hexadecyltrimethylammonium Bromide (57-09-0)		302, 315, 318, 335, 373, 410	273, 280, 301+312, 302+352, 305+351+338, 314
Hydrochloric acid (37 wt%) (7647-01-0)		290, 314, 335	234, 261, 271, 280, 303+361+353, 305+351+338
Iodomethane (74-88-4)		301+331, 312, 315, 335, 351	201, 208, 301+310, 302+352, 304+340, 311
Magnesium powder (7439-95-4)		228, 251, 261	210, 223, 231+232, 235, 240, 403+235
Maleic Anhydride (108-31-6)		302, 314, 317, 334, 372	260, 280, 301+312, 303+361+353, 304+340+310, 305+351+338
MCM-41 silica (7631-86-9)	Not a hazardous substance.		

Table S1: Safety information for the substances used in this work according to the GHS classification.[296,297]

Substance (CAS Registry Number)	GHS Pictograms	Hazard Statements	Precautionary Statements
Methanol (67-56-1)		225, 301+311+331, 370	210, 233, 280, 301+310, 303+361+353, 304+340+311
N-(tert-Butoxycarbonyl)-L-aspartic Acid (13726-67-5)	Not a hazardous substance.		
N,*N*-Dicyclohexylmethylamine (7560-83-0)		302, 314	270, 280, 301+312+330, 331, 303+361+353, 305+351+338
N,*N*-dimethyl-2,5-bis((*E*)-2-(triethoxysilyl)vinyl)aniline / -PMO	–	–	–
N,*N*-Dimethylformamide (68-12-2)		226, 312+332, 319, 360D	210, 280, 303+361+353, 304+340+312, 305+351+338, 308+313
N^2-((benzyloxy)carbonyl)-N^4-(2,5-bis((*E*)-2-(triethoxysilyl)vinyl)phenyl)-L-asparagine (PMO)	–	–	–
N-Carbobenzoxy-L-aspartic anhydride (4515-23-5)	Not a hazardous substance.		

Table S1: Safety information for the substances used in this work according to the GHS classification.[296,297]

Substance (CAS Registry Number)	GHS Pictograms	Hazard Statements	Precautionary Statements
n-Heptane (142-82-5)		225, 304, 315, 336, 410	210, 233, 273, 301+310, 303+361+353, 331
n-Hexane (110-54-3)		225, 304, 315, 336, 361f, 372, 411	202, 210, 273, 301+310, 303+361+353, 331
N-Hydroxysuccinimide (6066-82-6)		315, 318	264, 280, 302+352, 305+351+338, 332+313, 362+364
Nitric acid (65 wt%) (7697-37-2)		272, 290, 314, 331	210, 220, 280, 303+361+353, 304+340+310, 305+351+338
Octadecyltrimethylammonium bromide (1120-02-1)		302, 315, 317, 318, 410	261, 273, 280, 301+312, 302+352, 305+351+338
Pluronic P123 (9003-11-6)	Not a hazardous substance.		
Pluronic F-127 (9003-11-6)	Not a hazardous substance.		

Table S1: Safety information for the substances used in this work according to the GHS classification.[296,297]

Substance (CAS Registry Number)	GHS Pictograms	Hazard Statements	Precautionary Statements
Potassium hydroxide (1 M) (1310-58-3)		290, 302, 314	234, 260, 280, 301+312, 303+361+353, 305+351+338
Sodium chloride (7647-14-5)	Not a hazardous substance.		
Sodium deuteroxide (40 wt%) (14014-06-3)		314	280, 305+351+338, 310
Sodium hydroxide (1310-73-2)		290, 314	234, 260, 280, 303+361+353, 304+340+310, 305+351+338
Succinic Anhydride (108-30-5)		302, 314, 317, 334	280, 301+330+331, 303+361+353, 304+340, 305+351+338, 310
Tetradecyltrimethyl-ammonium bromide (1119-97-7)		302, 315, 318, 335, 373, 410	273, 280, 301+312, 302+352, 305+351+338, 314
Tetraethyl orthosilicate (78-10-4)		226, 332, 319, 335	210, 261, 280, 304+340, 305+351+338

Table S1: Safety information for the substances used in this work according to the GHS classification.[296,297]

Substance (CAS Registry Number)	GHS Pictograms	Hazard Statements	Precautionary Statements
Tetrahydrofuran (109-99-9)		225, 302, 319, 335, 336, 351	210, 280, 301+312+330, 305+351+338, 370+378, 403+235
Tetrakis(triphenylphosphine)-palladium(0) (14221-01-3)		302	264, 270, 301+312, 501
Toluene (108-88-3)		225, 315, 361d, 336, 373, 304, 412	202, 210, 273, 301+310, 303+361+353, 331
Triethoxysilane (998-30-1)		226, 302, 330, 315, 318	210, 280, 301+312, 303+361+353, 304+340+310, 305+351+338
Triethoxyvinylsilane (78-08-0)		226	210

Table S1: Safety information for the substances used in this work according to the GHS classification.[296,297]

Substance (CAS Registry Number)	GHS Pictograms	Hazard Statements	Precautionary Statements
Triethylamine (121-44-8)		225, 301+311+331, 314, 335	210, 280, 301+312, 303+361+353, 304+340+310, 305+351+338+ 310
Trimethylsilylacetylene (1066-54-2)		225, 315, 319	210, 233, 240, 241, 303+361+353, 305+351+338
Triphenylphosphine (603-35-0)		302, 317, 318, 372	260, 280, 301+312, 302+352, 305+351+338, 314
Water (7732-18-5)	Not a hazardous substance.		

8.2. Supporting Information for "Influence of Surface Chemistry on *t*-Layer Dimension and Density of Nanoconfined Water by Fine-Tuning the Functional Groups of Periodic Mesoporous Organosilicas"

Supporting Information for

Influence of Surface Chemistry on *t*-Layer Dimension and Density of Nanoconfined Water by Fine-Tuning the Functional Groups of Periodic Mesoporous Organosilica

Philip Lenz[a,b], Sophia-M. Meinert[a], Sandra König[a], Michael Steiger[a,] and Michael Fröba[a,b,]**

AFFILIATIONS:

[a] Institute of Inorganic and Applied Chemistry, University of Hamburg, Martin-Luther-King-Platz 6, 20146 Hamburg, Germany

[b] The Hamburg Centre for Ultrafast Imaging, Luruper Chaussee 149, 22761 Hamburg, Germany

E-mail: michael.steiger@uni-hamburg.de and michael.froeba@uni-hamburg.de

Chemicals

All reagents and solvents used for the precursor and PMO synthesis were purchased from commercial suppliers (*abcr*, *Merck*, *Sigma-Aldrich*, *TCI*, *Fisher Scientific*). The surfactants C_{20}TAB and C_{22}TAB were prepared according to the literature.[1]

Precursor synthesis

The synthesis of the BTEVB[1,2], BTEVA[1], BTEVFB[2,3], BTEVClB[2], BTEB[1] and BTEVP[4] precursors as well as MCM-41 silica[5] was conducted according to the specified synthesis protocols.

PMO synthesis

General PMO synthesis procedure:

The corresponding surfactant type was first dissolved in an aqueous NaOH solution at 31 °C for 30 minutes.[a)] Then the solution was stirred for an additional 30 minutes at room temperature before the precursor was added. The reaction mixture was stirred for 20 hours at room temperature, followed by hydrothermal treatment.[b)] After cooling to room temperature, the product was filtered and washed with 200 mL of demineralized water and 50 mL of ethanol. The surfactant was removed by soxhlet extraction using a 37 *m*% ethanol-HCl solution (*V*/*V*; 98:2). Finally, the product was dried at 80 °C. Table S1 details the exact compositions, as well as the temperature and duration of the hydrothermal treatment for the various precursors used.

[a)] For the synthesis of BTEVClB-PMOs, absolute ethanol (17 molar equivalents relative to the precursor) was added as a co-solvent before introducing the precursor, to enhance its solubility.

[b)] For the synthesis of *N*,*N*-DMBTEVA-PMOs, an additional step was included: after cooling to room temperature, iodomethane (3.8 molar equivalents relative to the precursor) was added to the product mixture and stirred for 5 minutes. Following this, the hydrothermal treatment was repeated.

N-MBTEVP^{+}I^{-}-PMOs via post-synthetic approach:

The functionalization of BTEVP to *N*-MBTEVP^{+}I^{-} occurs via the gas phase. In a sealed 30 mL system, BTEVP-PMO was stored with 1 mL of iodomethane for two days at room temperature. To prevent direct contact between the PMO and liquid iodomethane, they were kept in separate containers within the vessel. The container is then left open for few days at room temperature and then the remaining unreacted iodomethane is removed under reduced pressure (approx. 0.03 mbar) for 30 min.

Table S1: PMO synthesis conditions, including amounts (n) of the precursor (P), of sodium hydroxide (NaOH) and of the respective surfactant (S), the volumes of water (V_{water}), as well as the temperature (T_{ht}) and duration (t_{ht}) of the hydrothermal treatment for each PMO type, along with the resulting pore size (d_P).

PMO Type	d_P / nm	n_P / mmol	n_{NaOH} / mmol	Surfactant type	n_S / mmol	V_{water} / mL	T_{ht} / °C	t_{ht} / h
BTEB	3.2	4.1	14	C_{14}TAB	4.1	40	95	24
	3.7	4.1	14	C_{16}TAB	4.2	40	95	24
BTEVA	2.9	3.4	18	C_{12}TAB	6.8	40	95	24
	3.1	3.4	18	C_{12}TAB	5.5	40	95	24
	3.2	1.1	6.0	C_{12}TAB	1.8	13	95	24
	3.4	1.1	6.0	C_{12}TAB	2.3	13	95	24
	3.5	3.4	18	C_{14}TAB	4.2	40	95	24
	3.7	3.4	18	C_{16}TAB	4.2	40	95	24
	3.8	7.7	35	C_{16}TAB	8.4	80	95	24
BTEVP	3.5	2.0	7.5	C_{10}TAB	2.1	20	95	27
	3.8	2.9	14	C_{14}TAB	3.1	30	95	24
	4.4	2.9	14	C_{16}TAB	3.1	30	95	24
	4.7	0.7	3.4	C_{18}TAB	0.86	7.5	95	24
	5.7	0.7	3.4	C_{20}TAB	0.86	7.5	95	24
BTEVB	3.4	3.3	36	C_{14}TAB	4.9	40	95	12
	3.8	9.9	108	C_{18}TAB	15	120	95	12
	4.4*	2.6	29	C_{18}TAB	3.9	32	95	12
	4.7*	1.3	14	C_{18}TAB	2.0	16	95	12
	5.5	1.3	15	C_{20}TAB	2.0	16	95	12
N,*N*-DM BTEVA	3.4	3.4	18	C_{14}TAB	4.2	40	95	24
	3.5	3.4	18	C_{16}TAB	4.2	40	95	24
	3.8	3.4	18	C_{18}TAB	4.2	40	95	24
	4.7	1.7	9	C_{20}TAB	2.1	20	95	24
	4.9	1.7	9	C_{22}TAB	2.1	20	95	24
BTEVFB	2.6	1.8	12.8	C_{12}TAB	2.8	21	80	24
	3.5	0.6	3.9	C_{14}TAB	1.1	7.1	80	24
	3.8	3.6	26	C_{18}TAB	5.5	42	80	24
	4.7**	0.6	4.3	C_{20}TAB	0.93	7.0	80	24
BTEVClB	3.8	1.4	6.9	C_{18}TAB	1.5	15	90	25
	4.3	1.4	6.9	C_{18}TAB	1.5	15	90	48

* Before adding the precursor, *n*-hexane (5.8 molar equivalents relative to the precursor) was introduced as a swelling agent additive for the synthesis.

** Before adding the precursor, 0.1 mL mesitylene was introduced as a swelling agent additive for the synthesis.

PMO characterization

The purity of the different PMOs was assessed using ^{1}H-NMR and IR spectroscopy. The IR spectrum matches well with previously published data on similar PMOs. For ^{1}H-NMR analysis, the PMOs were dissolved in a 1 M NaOD/D_2O solution. Although the BTEVP-PMOs did not fully dissolve, they were analyzed after filtration. Figure S1 shows the ^{1}H-NMR spectra exemplarily for each PMO class. All NMRs of the different PMOs show signals at 0.8 and 3.2 ppm which can be assigned to residual ethanol present in low concentrations (1–5%).[6] Only the BTEB has a higher ethanol content of 13%.

For the BTEVB-PMOs, as with all other PMOs, no surfactant residues were detected. Additionally, no traces of the pore expander *n*-hexane were observed in the BTEVB_4.4 sample.

The FT-IR spectra of BTEVA-, BTEVB-, BTEB-PMOs are consistent with literature values. The ^{1}H-NMR results further confirm the high purity of these PMOs.[2,7,8]

The pyridine-based PMOs synthesized in this study exhibit a particularly well-defined arrangement of organic units within the pore walls, along with a high degree of pore ordering (see Figure S4 and Figure S6). The ^{1}H-NMR of the BTEVP precursor and the FT-IR spectrum of the BTEVP-PMO agree with literature data.[9] The ^{1}H-NMR signals of the BTEVP-PMO were successfully assigned. Additionally, a second species was identified in which one of the two vinyl groups is absent. Two further multiplets appear at 2.45–2.35 ppm and 0.36–0.30 ppm. Since these signals were not observed in the NMR analysis of the precursor and the FT-IR spectra of both the precursor and PMO align with literature data, it is assumed that a reaction involving the vinyl group and NaOD occurred during the dissolution of the PMO. This reaction appears to be very sensitive to slight deviations in the pH, as the product-to-second-species ratio is not consistently

reproducible. This is evident when comparing the BTEVP-PMO with the *N*-MBTEVP^{+}I^{-}-PMO, where the proportion of the product relative to the second species is higher than in the BTEVP-PMO (see Figure S1). For *N*-MBTEVP^{+}I^{-}-PMO, successful methylation of the nitrogen can be confirmed by the presence of signals at 3.94 ppm in the ^{1}H-NMR spectrum. Additionally, since all protons of the divinylpyridine bridging unit are present, further methylation at other sites of the organic component can be excluded. From the integral of the methyl proton signal in the ^{1}H-NMR spectrum, the degree of methylation is estimated to be at least 18%. This value could be higher, as it was observed that the methyl-pyridine bond in the NaOD/D_2O solution breaks over time. The TG-DTA-MS analysis further confirms partial methylation. Instead of the expected 38% mass loss, only 7% was observed, corresponding to a degree of functionalization of approximately 18%.

The comparison of FT-IR spectra between BTEVA- and *N*,*N*-DMBTEVA-PMO (Figure S2, top) indicates successful methylation. Unlike the BTEVA-PMO, the *N*,*N*-DMBTEVA-PMO displays a single band at 3431 cm^{-1}, attributed to silanol groups or adsorbed water, confirming the absence of N-H stretching vibrations. Additionally, bands in the range of 2990–2780 cm^{-1}, as well as at 1454 cm^{-1} and 1290 cm^{-1}, are exclusive to the methylated sample, corresponding to CH_3 valence, deformation, rocking vibrations, and asymmetric CCN stretching vibrations.[10] A double methylation can be confirmed through ^{1}H-NMR and thermogravimetric analysis.

BTEVClB-PMOs, which we recently introduced for the first time[11], exhibit high purity as confirmed by ^{1}H-NMR (Figure S1). The measured FT-IR spectrum (Figure S3) confirms their structural integrity, and, in contrast to all other PMOs, displays a distinctive band at 692 cm^{-1}, characteristic of C-Cl stretching vibrations.[10] The mass loss observed in the thermogravimetric analysis aligns with the expected values.

Fluorinated PMOs were also obtained in high purity. The ^{19}F-NMR results are consistent with the literature[2] and confirm the integrity of the fluorine within the PMO (see Figure S1). The IR band at 1253 cm^{-1} is characteristic of aromatic fluorine compounds, while the band at 703 cm^{-1} corresponds to aromatic C-F stretching and ring deformation vibrations.[10]

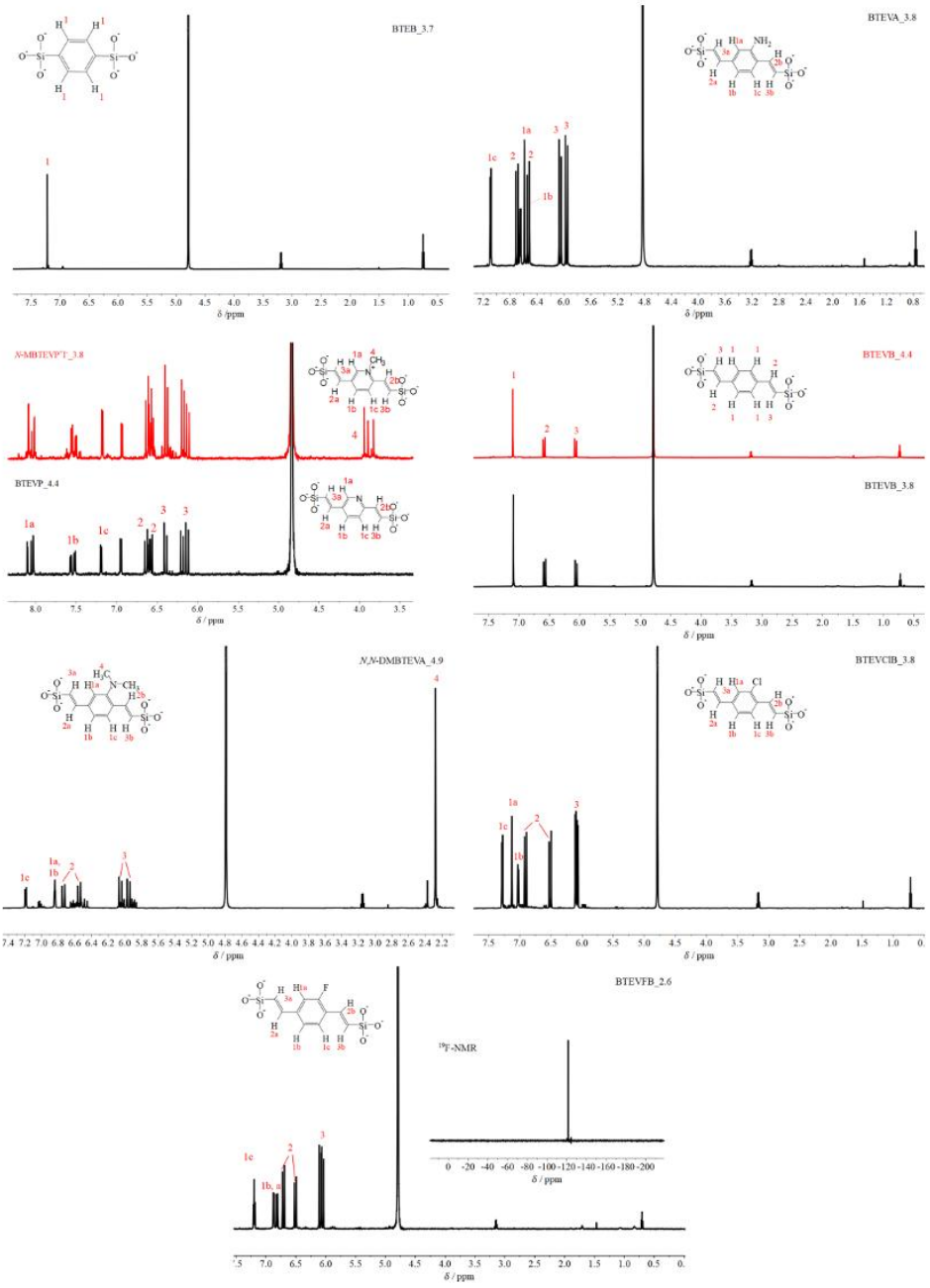


Figure S1. ^{1}H-NMR of the different PMOs dissolved in a 1 M NaOD/D_2O solution. ^{19}F-NMR is given for the BTEVFB-PMO.

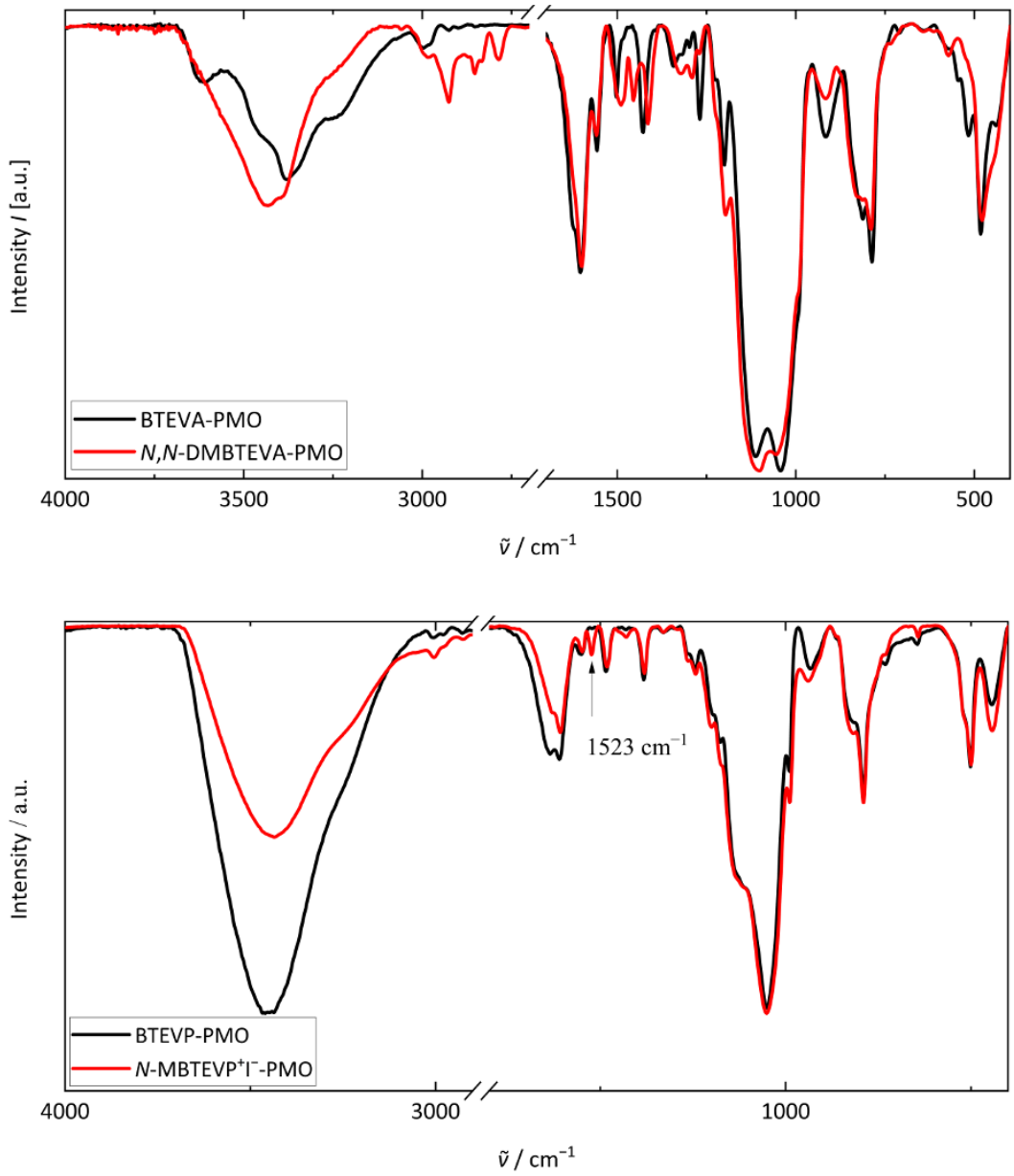


Figure S2. Comparison of FT-IR spectra (KBr-disc) between non-methylated (black line) and methylated PMO (red line) species.

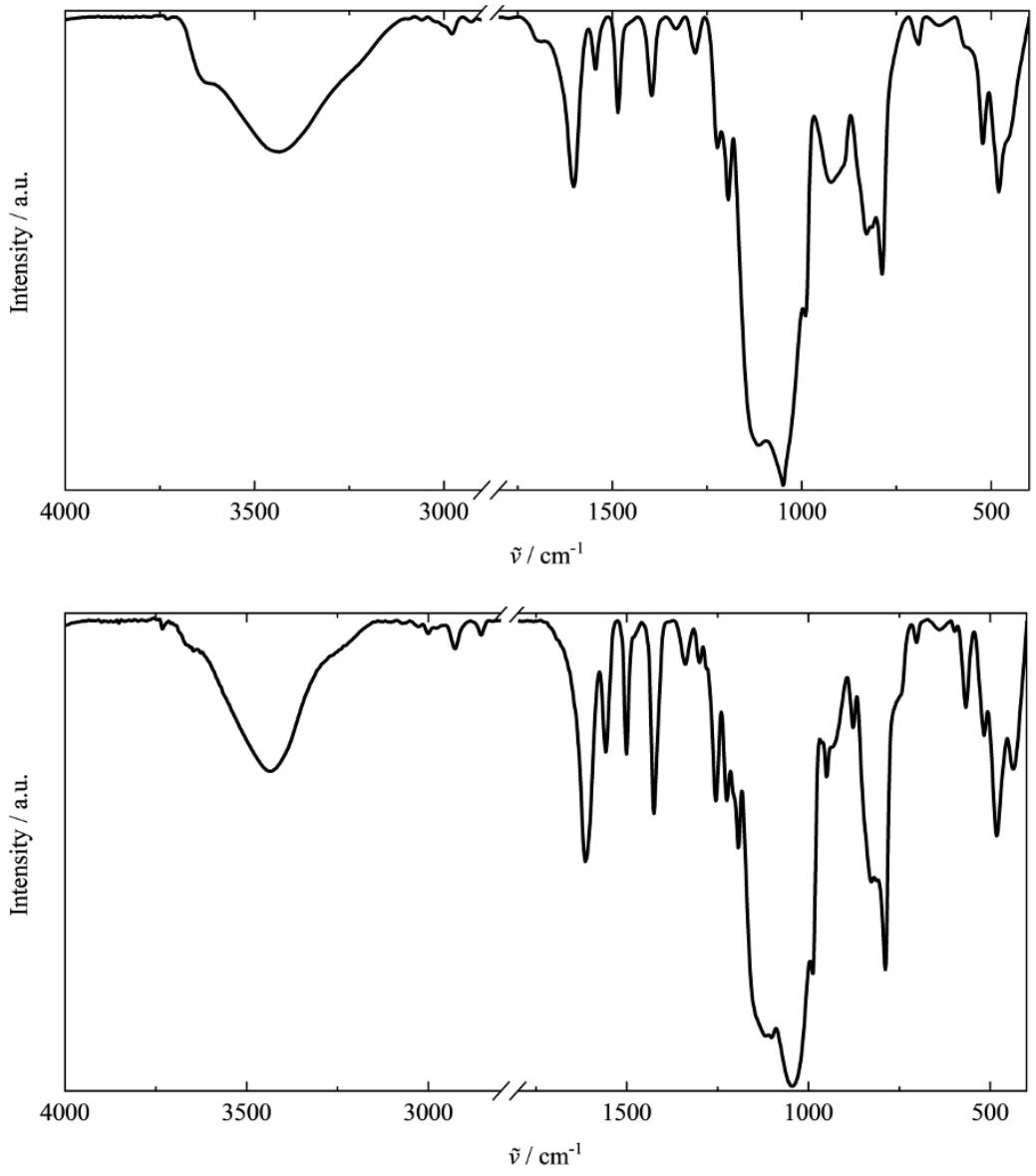


Figure S3. FT-IR spectra (KBr-disc) of BTEVClB-PMO (top), BTEVFB-PMO (bottom).

BTEB-PMO:

^{1}H-NMR (600 MHz, 1 M NaOD/ D_2O, 25 °C): δ [ppm] = 7.22 (s, 4H).

Further signals: δ [ppm] = 3.19 (*q*, J = 7.1 Hz), 0.74 (t, J = 7.1 Hz).

FT-IR (KBr-disc): $\tilde{\nu}$ [cm^{-1}] = 3435, 1630, 1385, 1164, 1061, 918, 810, 761, 563, 519, 434.

BTEVA-PMO:

^{1}H-NMR (600 MHz, 1 M NaOD/ D_2O, 25 °C): δ [ppm] = 7.09 (d, ^{3}J = 8.1 Hz, 1H), 6.70 (d, ^{3}J = 19.1 Hz, 1H), 6.65 (dd, $^{3,4}J$ = 8.0, 1.7 Hz, 1H), 6.59 (d, ^{3}J = 1.7 Hz, 1H), 6.53 (d, ^{3}J = 19.3 Hz, 1H), 6.06 (d, ^{3}J = 19.3 Hz, 1H), 5.96 (d, ^{3}J = 19.1 Hz, 1H). Further Signals: δ [ppm] = 3.22 (q, ^{3}J = 7.1 Hz), 0.77 (t, ^{3}J = 7.1 Hz).

FT-IR (KBr-disc): $\tilde{\nu}$ [cm^{-1}] = 3613, 3379, 3238, 1602, 1556, 1502, 1427, 1269, 1199, 1112, 1043, 916, 812, 787, 517, 482.

BTEVP-PMO:

^{1}H-NMR (600 MHz, 1 M NaOD/ D_2O, 25 °C): δ [ppm] = 8.10 (d, ^{3}J = 2.2 Hz, 1H), 7.57 (dd, $^{3,4}J$ = 8.3, 2.2 Hz, 1H), 7.19 (d, ^{3}J = 8.3 Hz, 1H), 6.64 (d, ^{3}J = 19.3 Hz, 1H), 6.58 (d, ^{3}J = 19.3 Hz, 1H), 6.40 (d, ^{3}J = 19.3 Hz, 1H), 6.19 (d, ^{3}J = 19.3 Hz, 1H). Further Signals: δ [ppm] = 8.06 (s), 8.03 (d, ^{3}J = 2.2 Hz), 7.52 (dd, ^{3}J = 8.3, 2.3 Hz), 6.95 (d, ^{3}J = 8.3 Hz), 6.60 (d, ^{3}J = 19.3 Hz), 6.13 (d, ^{3}J = 19.4 Hz), 3.20 (q, ^{3}J = 7.1 Hz), 2.45–2.35 (m), 1.52 (s), 0.75 (t, ^{3}J = 7.1 Hz), 0.36–0.30 (m).

FT-IR (KBr-disc): $\tilde{\nu}$ [cm^{-1}] = 3444, 1637, 1610, 1551, 1485, 1382, 1244, 1051, 989, 789, 501, 442.

***N*-MBTEVP^{+}I^{-}-PMO:**

^{1}H-NMR (600 MHz, 1 M NaOD/ D_2O, 25 °C): δ [ppm] = 8.04 (d, J = 2.2 Hz, 1H), 7.51 (dd, J = 8.4, 2.3 Hz, 1H), 7.13 (d, J = 8.3 Hz, 1H), 6.58 (d, J = 19.3 Hz, 1H), 6.54 (d, ^{3}J = 19.3 Hz, 1H), 6.34 (d, ^{3}J = 19.3 Hz, 1H), 6.14 (d, ^{3}J = 19.3 Hz, 1H), 3.89 (s, 0.9 H). Further Signals: δ [ppm] = 7.97 (d, ^{3}J = 2.3 Hz), 7.46 (dd, $^{3,4}J$ = 8.2, 2.3 Hz), 6.89 (d, ^{3}J = 8.2 Hz), 6.52 (d, ^{3}J = 19.3 Hz), 6.07 (d, ^{3}J = 19.4 Hz), 3.85 (s), 3.78 (s), 2.36–2.31 (m), 0.29–0.24 (m).

FT-IR (KBr-disc): $\tilde{\nu}$ [cm^{-1}] = 3435, 1631, 1608, 1548, 1523, 1481, 1381, 1244, 1051, 989, 788, 499, 442.

TG-DTA-MS:

Theoretical mass loss: CH_3I = 38%; C_9H_7N = 34% Theoretical residual mass: Si_2O_3 = 28%

Experimental mass loss: CH_3I = 7%; C_9H_7N = 43% Theoretical residual mass: Si_2O_3 = 50%

BTEVB-PMO:

^{1}H-NMR (600 MHz, 1 M NaOD/ D_2O, 25 °C): δ [ppm] = 7.10 (s, 4H), 6.59 (d, ^{3}J = 19.3 Hz, 2H), 6.07 (d, ^{3}J = 19.3 Hz, 2H). Further Signals: δ [ppm] = 3.18 (q, ^{3}J = 7.1 Hz), 0.73 (t, ^{3}J = 7.1 Hz).

FT-IR (KBr-disc): $\tilde{\nu}$ [cm^{-1}] = 3425, 1604, 1556, 1508, 1412, 1332, 1294, 1230, 1198, 1051, 989, 813, 777, 501, 446.

***N*,*N*-DMBTEVA-PMO:**

^{1}H-NMR (600 MHz, 1 M NaOD/ D_2O, 25 °C): δ [ppm] = 7.19 (d, ^{3}J = 8.5 Hz, 1H), 6.84 (dd, ^{3}J = 4.4, 2.7 Hz, 2H), 6.74 (d, ^{3}J = 19.2 Hz, 1H), 6.55 (d, ^{3}J = 19.3 Hz, 1H), 6.06 (d, ^{3}J = 19.3 Hz, 1H), 5.96 (d, ^{3}J = 19.1 Hz, 1H), 2.28 (s, 6H). Further Signals: δ [ppm] = 3.15 (q, ^{3}J = 7.1 Hz), 0.71 (t, ^{3}J = 7.1 Hz).

FT-IR (KBr-disc): $\tilde{\nu}$ [cm^{-1}] = 3431, 2983, 2925, 2852, 2785, 1599, 1558, 1489, 1454, 1414, 1323, 1290, 1198, 1101, 1055, 917, 788, 478.

TG-DTA-MS:

Theoretical mass loss: $C_{12}H_{13}N$ = 62% Theoretical residual mass: Si_2O_3 = 38%

Experimental mass loss: $C_{12}H_{13}N$ = 65% Theoretical residual mass: Si_2O_3 = 35%

BTEVClB-PMO:

^{1}H-NMR (600 MHz, 1 M NaOD/ D_2O, 25 °C): δ [ppm] = 7.28 (d, ^{3}J = 8.3 Hz, 1H), 7.13 (d, ^{3}J = 1.7 Hz, 1H), 7.02 (dd, $^{3,4}J$ = 8.1, 1.8 Hz, 1H), 6.91 (d, ^{3}J = 19.2 Hz, 1H), 6.51 (d, ^{3}J = 19.2 Hz, 1H), 6.10 (d, ^{3}J = 7.4 Hz, 1H), 6.07 (d, ^{3}J = 7.5 Hz, 1H). Further signals: δ [ppm] = 3.17 (q, ^{3}J = 7.1 Hz), 0.72 (t, ^{3}J = 7.1 Hz).

FT-IR (KBr-disc): $\tilde{\nu}$ [cm^{-1}] = 3432, 1602, 1544, 1485, 1396, 1280, 1223, 1193, 1116, 1049, 989, 922, 829, 787, 692, 523, 480.

Theoretical mass loss: $C_{10}H_7Cl$ = 61% Theoretical residual mass: Si_2O_3 = 39%

Experimental mass loss: $C_{10}H_7Cl$ = 56% Theoretical residual mass: Si_2O_3 = 44%

BTEVFB-PMO:

^{1}H-NMR (600 MHz, 1 M NaOD/ D_2O, 25 °C): δ [ppm] = 7.20 (t, ^{3}J = 8.2 Hz, 1H), 6.87 (dd, ^{3}J = 8.2, 1.6 Hz, 1H), 6.81 (dd, $^{3,4}J$ = 12.5, 1.7 Hz, 1H), 6.71 (d, ^{3}J = 19.5 Hz, 1H), 6.51 (d, ^{3}J = 19.2 Hz, 1H), 6.09 (d, v = 19.4 Hz, 1H), 6.05 (d, ^{3}J = 19.3 Hz, 1H). Further signals: δ [ppm] = 3.15 (q, ^{3}J = 7.1 Hz), 0.70 (t, ^{3}J = 7.1 Hz).

^{19}F-NMR (600 MHz, 1 M NaOD/ D_2O, 25 °C): δ [ppm] = −121.45 (dd, $^{3,4}J$ = 12.2, 8.2 Hz, 1F)

FT-IR (KBr-disc): $\tilde{\nu}$ [cm^{-1}] = 3437, 1614, 1558, 1501, 1425, 1339, 1300, 1256, 1225, 1194, 1103, 1045, 989, 950, 876, 827, 789, 702, 567, 516, 482, 436.

Some PMOs with pores smaller than 3.5 nm show only one reflection in the PXRD, which indicates an ordering of the pores but does not allow an exact statement of the pore structure. This may be due to the fact that the pore structure is not very pronounced when using surfactants with shorter carbon chains or the given synthesis condition, in other words the hexagonal pore structure is less perfectly ordered. As pore diameter decreases, the pore size distribution has a greater impact on the overall pore structure. Even slight tilting of hexagonally arranged pores can extinguish the (110) and (200) reflections, leaving only the (100) reflection visible while preserving the hexagonal arrangement. Using BTEVP_3.5 as an example, it can be shown that only one reflection can be seen in the PXRD, while the hexagonal pore order can be recognized in the TEM image (Figure S5).

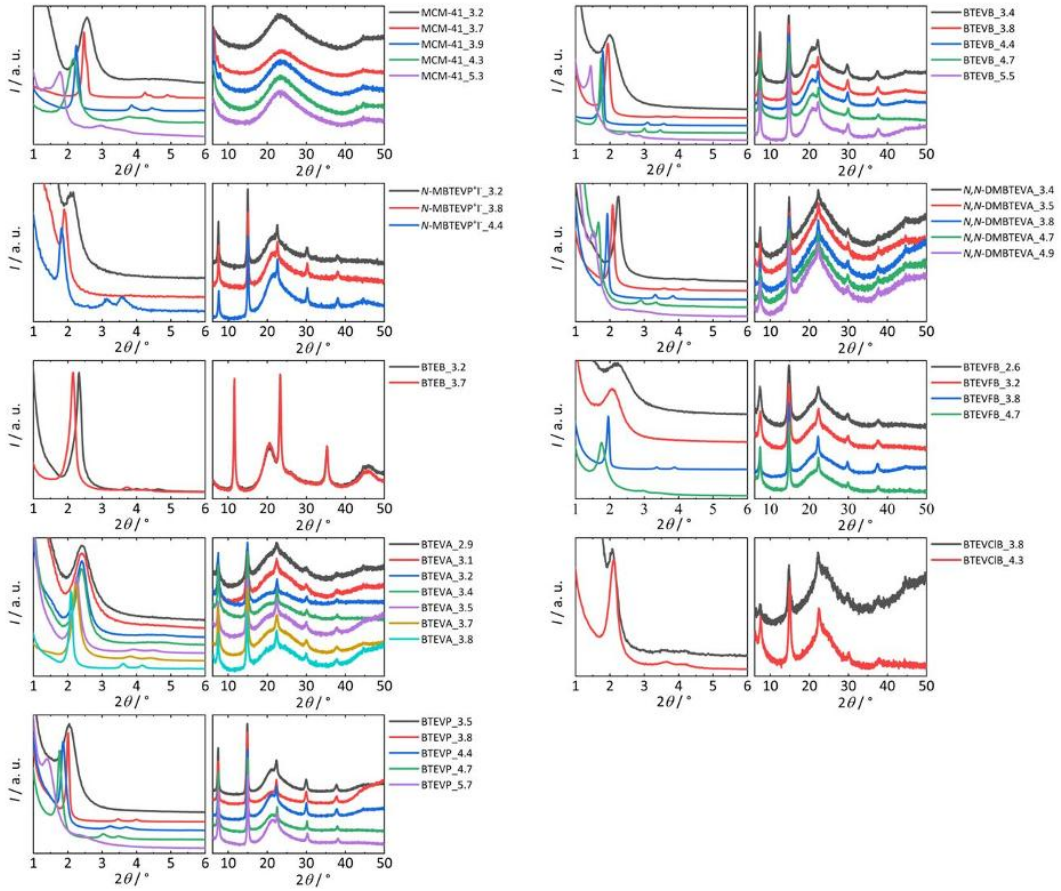


Figure S4. Normalized X-ray powder diffractograms of MCM-41 silica and various PMOs, shown in the ranges of 1 to 6° 2 θ and 6 to 50° 2θ.

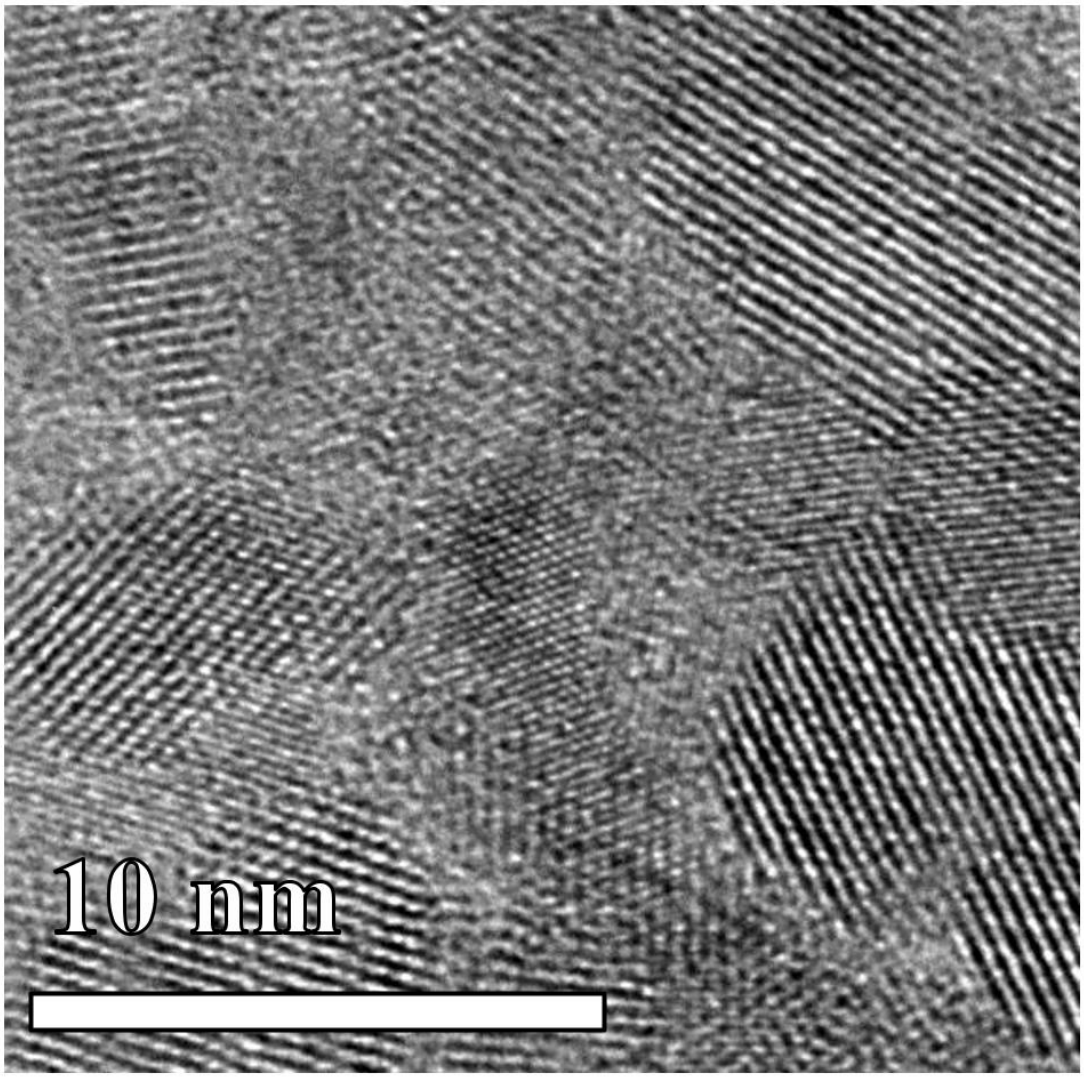


Figure S5. HRTEM image of BTEVP_3.5.

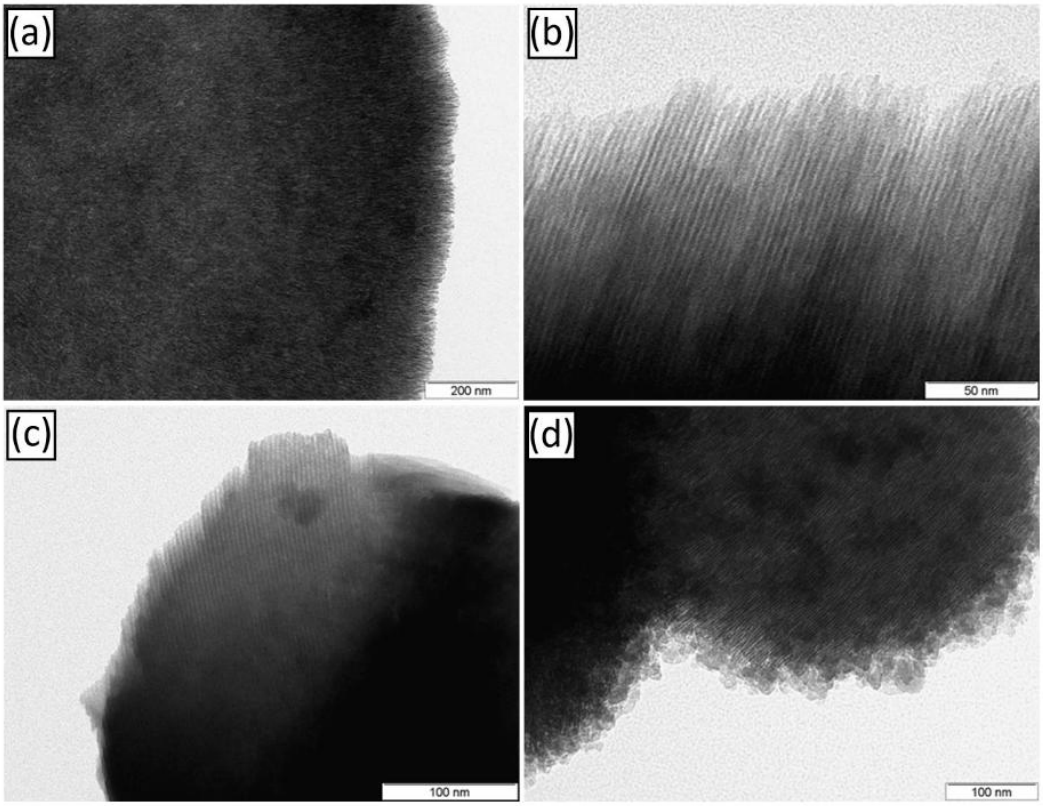


Figure S6. HRTEM images of BTEVP_3.8, displaying the pore structure. (a) and (b) side views of the pore channels, illustrating the material's high degree of pore ordering and structural integrity. After methylation, the pore integrity remains intact as shown in (c) and (d).

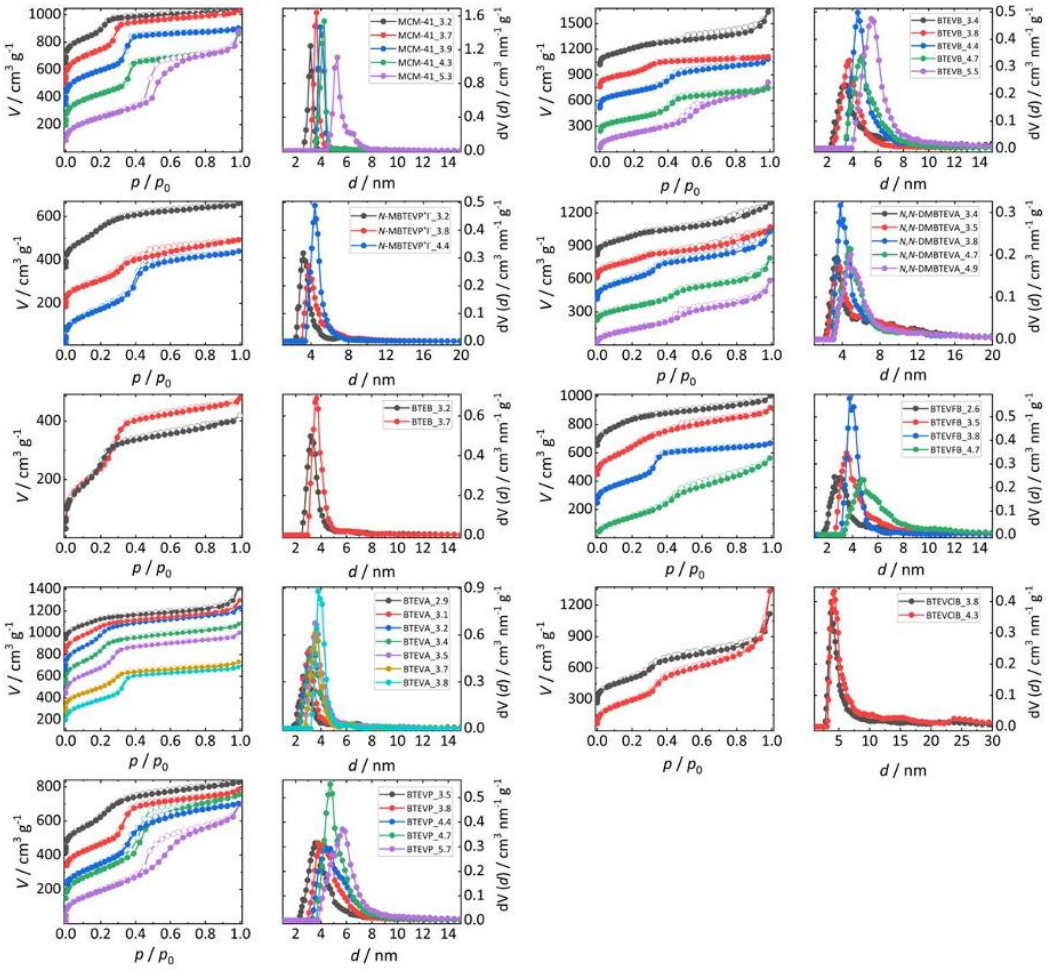


Figure S7. Nitrogen physisorption isotherms at 77 K, showing the adsorption branch (filled circles) and desorption branch (hollow circles), along with the corresponding pore size distribution curves on the right (calculated using the kernel: N_2 at 77 K on silica, cylindr. Pores. NLDFT at adsorptions branch) for MCM-41 silica and various PMOs. The isotherms are shifted vertically along the Y-axis by a constant value, which differs for each material class.

Table S2. The nitrogen physisorption analysis provides the pore diameter (d_P), hydraulic radius (r_h), pore volume at relative pressures of 0.8 ($V_{P,n,0.8}$) and 0.9 ($V_{P,n,0.9}$), specific BET surface area (S_{BET}), isotherm inflection points of the adsorption ($(p/p_0)_{n,ia}$) and desorption branch ($(p/p_0)_{n,id}$), along with PXRD analysis results for the periodicity of the repetition unit (d_{RU}), the (100) reflection (d_{100}), and the calculated pore wall thickness (d_W).

PMO Type	d_P / nm	r_h / nm	$V_{P,n,0.8}$ / cm^3/g	$V_{P,n,0.9}$ / cm^3/g	S_{BET} / m^2/g	$(p/p_0)_{n,ia}$	$(p/p_0)_{n,id}$	d_{RU} / nm	d_{100} / nm	d_W / nm
N-MBTEVP$^+$I$^-$	3.2	1.1	0.453	0.459	836	0.170	0.174	1.18	4.20	1.65
	3.8	1.9	0.491	0.470	520	0.315	0.450	1.17	4.64	1.56
	4.4	1.9	0.650	0.659	670	0.399	0.397	1.17	4.84	1.19
MCM-41 silica	3.2	1.2	0.644	0.650	1034	0.212	0.212	-	3.45	0.78
	3.7	1.5	0.840	0.855	1118	0.280	0.280	-	3.57	0.42
	3.9	1.7	0.895	0.902	1071	0.343	0.345	-	3.94	0.65
	4.3	1.7	0.874	0.974	1026	0.363	0.360	-	4.09	0.42
	5.3	2.4	1.10	1.13	911	0.533	0.479	-	5.00	0.47
BTEB	3.2	1.3	0.588	0.608	882	0.205	0.202	0.764	3.8	1.19
	3.7	1.5	0.693	0.704	903	0.273	0.273	0.762	4.10	1.03
BTEVA	2.9	1.2	0.538	0.574	894	-	0.115	1.19	3.66	1.33
	3.1	1.1	0.667	0.694	1181	0.159	0.156	1.19	3.66	1.13
	3.2	1.3	0.821	0.844	1258	0.194	0.190	1.18	3.66	1.03
	3.4	1.4	0.812	0.833	1179	0.198	0.130	1.18	3.67	0.84
	3.5	1.4	0.865	0.883	1256	0.267	0.257	1.19	3.91	1.01
	3.7	1.4	0.675	0.692	949	0.275	0.275	1.18	3.96	0.87
	3.8	1.6	0.817	0.830	1005	0.330	0.323	1.19	4.21	1.06
BTEVP	3.5	1.3	0.561	0.634	851	0.225	0.217	1.19	4.35	1.52
	3.8	2.0	0.740	0.703	740	0.330	0.329	1.19	4.40	1.28
	4.4	2.3	0.731	0.750	630	0.365	0.367	1.19	4.75	1.08
	4.7	1.9	0.800	0.968	834	0.435	0.425	1.18	5.04	1.12
	5.7	2.4	0.872	0.912	739	0.570	0.470	1.17	6.36	1.64
BTEVB	3.4	1.5	0.590	0.641	779	0.190	0.190	1.20	4.44	1.73
	3.8	1.5	0.525	0.544	682	0.279	0.271	1.20	4.56	1.47
	4.4	2.0	0.791	0.812	790	0.400	0.400	1.20	4.95	1.32
	4.7	2.2	0.701	0.715	624	0.411	0.411	1.20	5.08	1.17
	5.5	2.4	1.01	1.07	840	0.549	0.500	1.2	6.19	1.65
N,*N*-DM BTEVA	3.4	1.4	0.525	0.633	726	0.202	0.176	1.19	3.93	1.14
	3.5	1.6	0.520	0.614	658	0.245	0.233	1.19	4.24	1.40
	3.8	1.7	0.681	0.754	801	0.326	0.325	1.20	4.57	1.48
	4.7	2.0	0.598	0.659	592	0.437	0.430	1.19	5.34	1.47
	4.9	2.1	0.606	0.657	578	0.470	0.444	1.19	5.82	1.82
BTEVFB	2.6	1.2	0.528	0.548	861	0.150	0.140	1.20	3.87	1.87
	3.5	1.6	0.700	0.726	897	0.209	0.220	1.19	4.21	1.36
	3.8	1.7	0.683	0.700	812	0.326	0.320	1.20	4.51	1.41
	4.7	2.1	0.686	0.776	639	0.424	0.430	1.19	5.81	1.12
BTEVClB	3.8	1.8	0.872	0.934	990	0.305	0.287	1.20	4.30	1.65
	4.3	2.0	1.13	1.24	1145	0.343	0.337	1.17	4.18	0.53

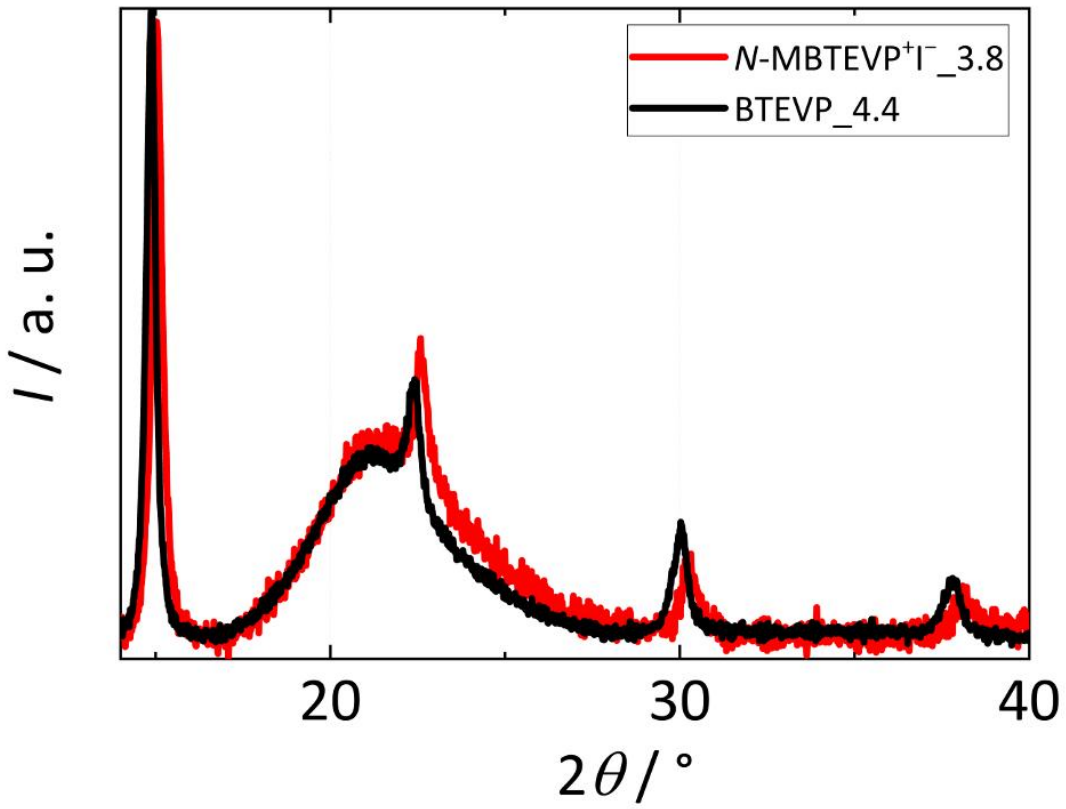


Figure S8. Normalized X-ray powder diffractograms of the charged *N*-MBTEVP^{+}I^{-} and the corresponding unfunctionalized BTEVP-PMO.

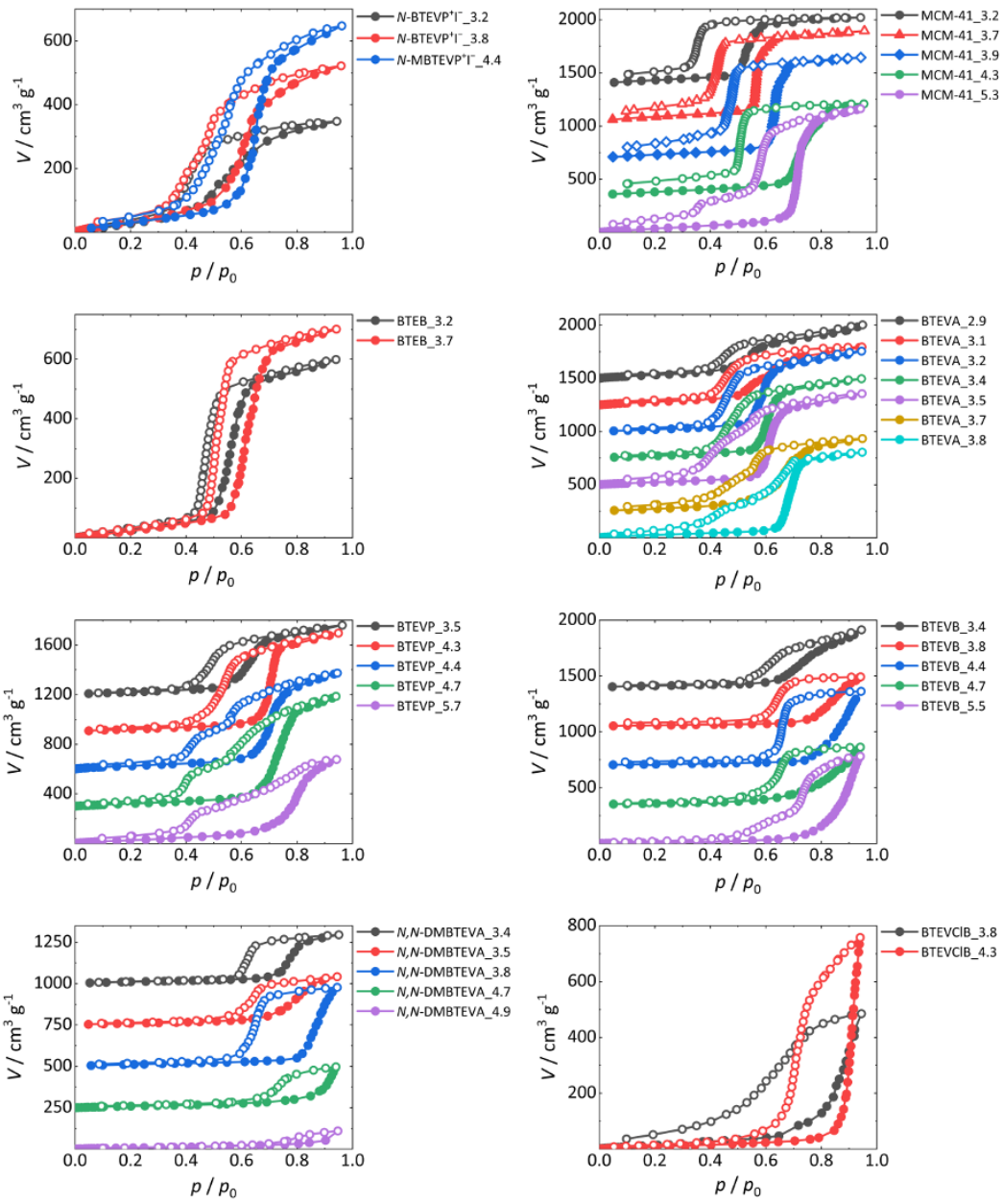


Figure S9. Water vapor sorption isotherms at 25 °C of the adsorption branch (filled circles) and desorption branch (hollow circles) from MCM-41 silica and different PMOs. The isotherms are shifted vertically along the Y-axis by a constant value, which differs for each material class.

Table S3. Water vapor sorption analysis for different material classes with varying pore diameters (d_P) includes the specific amount of water in a fully filled pore ($n_{s,w,f}$), specific BET surface area ($S_{BET,w}$), adsorbed water volume before capillary condensation (V_{wa}), volume of water adsorbed during capillary condensation ($V_{pc,w}$), pore volume at a relative pressure of 0.9 ($V_{P,w,0.9}$), inflection points for capillary condensation ($(p/p_0)_{w,ia}$) and pore emptying ($(p/p_0)_{w,id}$), specific amounts at the onset ($n_{o,d}$) and endset ($n_{e,d}$) of pore emptying, and the slope in the linear range of the adsorption isotherm before capillary condensation (s_a).

PMO Type	d_P / nm	$n_{s,w,f}$ / mmol/g	$S_{BET,w}$ / m^2/g	V_{wa} / cm^3/g	$V_{pc,w}$ / cm^3/g	$V_{P,w,0.9}$ / cm^3/g	$(p/p_0)_{w,ia}$	$(p/p_0)_{w,id}$	$n_{o,d}$ / mmol/g	$n_{e,d}$ / mmol/g	s_a / mmol/g
N-MBTEVP$^+$I$^-$	3.2	14.4	156	56.5	243	0.274	0.57	0.42	13.9	2.96	6.20
	3.8	19.6	143	74.6	331	0.408	0.60	0.46	17.6	3.40	5.90
	4.4	25.5	126	77.3	452	0.500	0.65	0.53	23.4	3.84	5.00
MCM-41 silica	3.2	25.7	161	72.2	486	0.497	0.54	0.35	26.3	6.61	6.35
	3.7	35.8	184	92.6	691	0.670	0.57	0.42	33.5	8.40	7.01
	3.9	39.0	160	86.6	787	0.753	0.64	0.48	38.1	9.99	6.32
	4.3	38.3	151	93.5	724	0.679	0.75	0.52	35.8	9.25	6.29
	5.3	50.2	169	109	955	0.915	0.72	0.58	45.2	10.9	6.86
BTEB	3.2	23.9	162	66.8	448	0.470	0.56	0.47	22.3	2.96	5.84
	3.7	30.2	159	70.9	551	0.553	0.62	0.51	26.8	3.10	5.73
BTEVA	2.9	16.2	131	66.7	250	0.369	0.54	0.46	14.8	3.43	5.65
	3.1	20.4	133	63.8	371	0.423	0.60	0.46	21.3	3.33	5.38
	3.2	29.3	109	52.1	556	0.586	0.59	0.46	25.7	2.78	5.20
	3.4	30.1	103	56.7	572	0.587	0.61	0.47	27.0	2.87	4.89
	3.5	34.4	102	63.1	633	0.669	0.61	0.47	32.3	4.00	4.45
	3.7	28.3	129	67.2	519.5	0.532	0.67	0.51	26.5	4.17	
	3.8	34.1	101	68.0	654	0.635	0.69	0.55	32.4	6.44	4.07
BTEVP	3.5	22.7	92	49.4	389	0.427	0.64	0.49	18.3	2.07	3.88
	3.8	31.6	91	60.2	612	0.619	0.70	0.53	27.9	2.65	3.80
	4.4	31.3	104	69.9	564	0.599	0.70	0.53	28.8	3.66	4.28
	4.7	35.8	105	66.2	679	0.680	0.74	0.57	34.0	3.68	4.36
	5.7	30.2	111	83.3	619	0.509	0.80	0.67	30.2	4.36	4.58
BTEVB	3.4	17.3	52	32.7	303	0.359	0.72	0.61	14.7	1.65	2.17
	3.8	-	34	25.9	-	0.311	0.85	0.64	-	2.05	1.39
	4.4	-	42	33.3	-	-	0.9	0.66	-	2.33	1.73
	4.7	-	45	32.7	-	-	-	0.64	-	1.76	1.87
	5.5	-	34	28.8	-	-	0.91	0.74	-	1.93	1.69
N,*N*-DM BTEVA	3.4	13.2	42	30.4	221	0.225	0.77	0.62	11.6	1.19	1.66
	3.5	13.1	41	31.5	228	0.222	0.78	0.64	11.7	1.40	1.65
	3.8	-	44	37.6	445	-	0.87	0.65	19.4	1.87	2.16
	4.7	-	40	34.6	-	-	0.93	0.74	-	1.54	1.60
	4.9	-	31	27.0	-	-	-	0.80	-	1.15	1.25
BTEVFB	2.6	15.4	55	32.0	276	0.319	0.67	0.53	13.5	1.54	2.13
	3.5	25.8	40	29.6	501	0.467	0.78	0.58	23.2	1.37	1.71
	3.8	-	24	71.1	-	-	0.90	0.68	-	1.20	1.35
	4.7	-	43	67.3	-	-	-	0.71	-	1.36	1.67
BTEVClB	3.8	-	55	52.9	-	-	0.89	0.63	-	-	2.82
	4.3	-	40	33.5	-	-	0.91	0.71	-	1.77	1.70

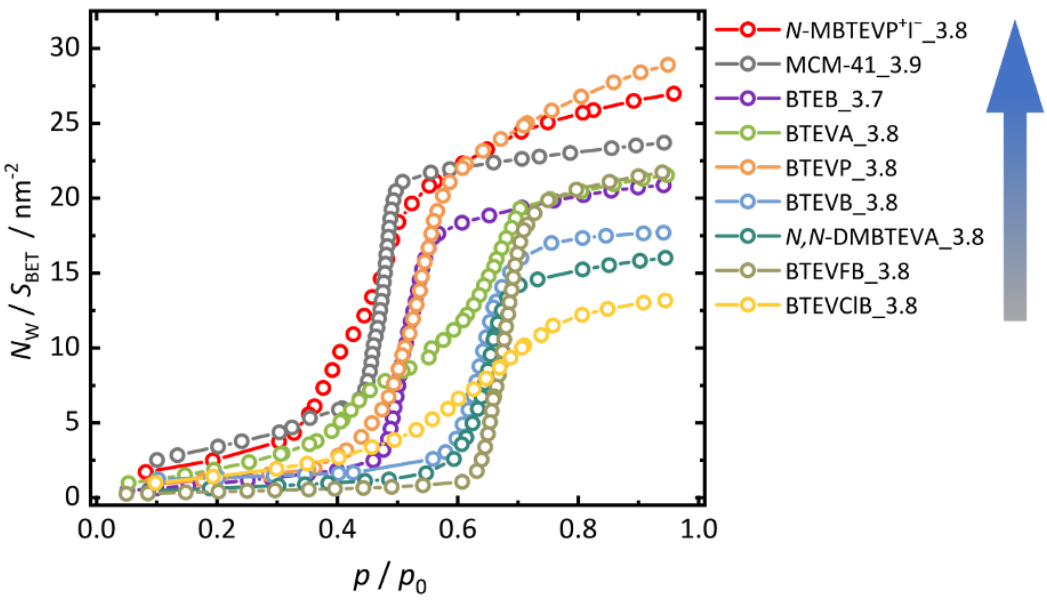


Figure S10. Desorption branch of water vapor sorption measurement at 25 °C of MCM-41 silica and various PMOs with a pore diameter of about 3.8 nm. The isotherms were normalized with the specific BET surface area of the respective materials to show the number of water molecules per surface unit at a certain relative pressure. An arrow in the legend denotes the order of increasing hydrophilicity for the listed materials.

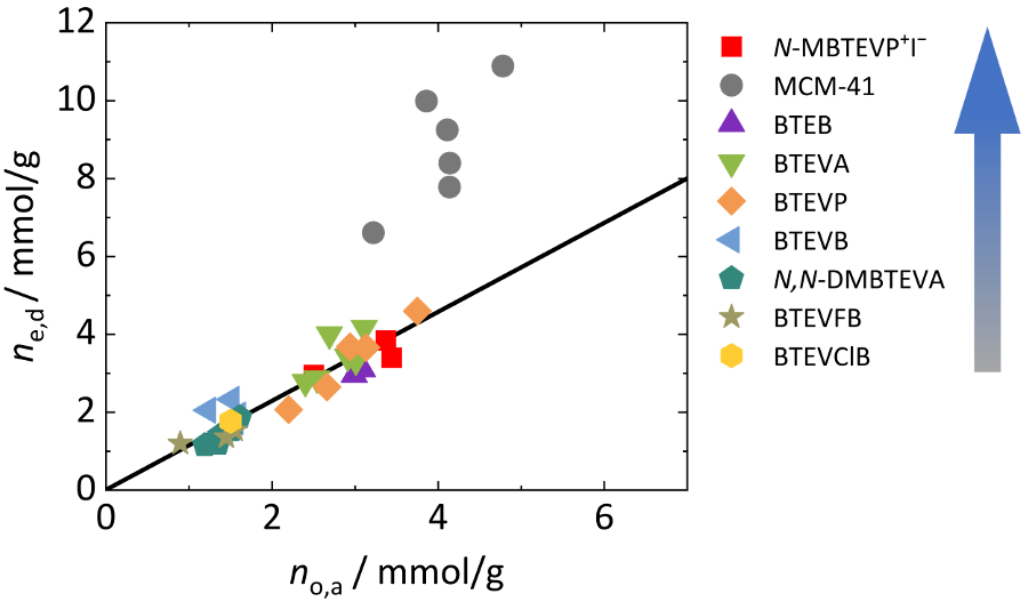


Figure S11. Comparison of the specific amount of water adsorbed at the onset of adsorption before capillary condensation ($n_{o,a}$) and at the end of the pore emptying step ($n_{e,d}$). Linear fit (black line) of the various PMOs (excluding MCM-41 silica). An arrow in the legend denotes the order of increasing hydrophilicity for the listed materials.

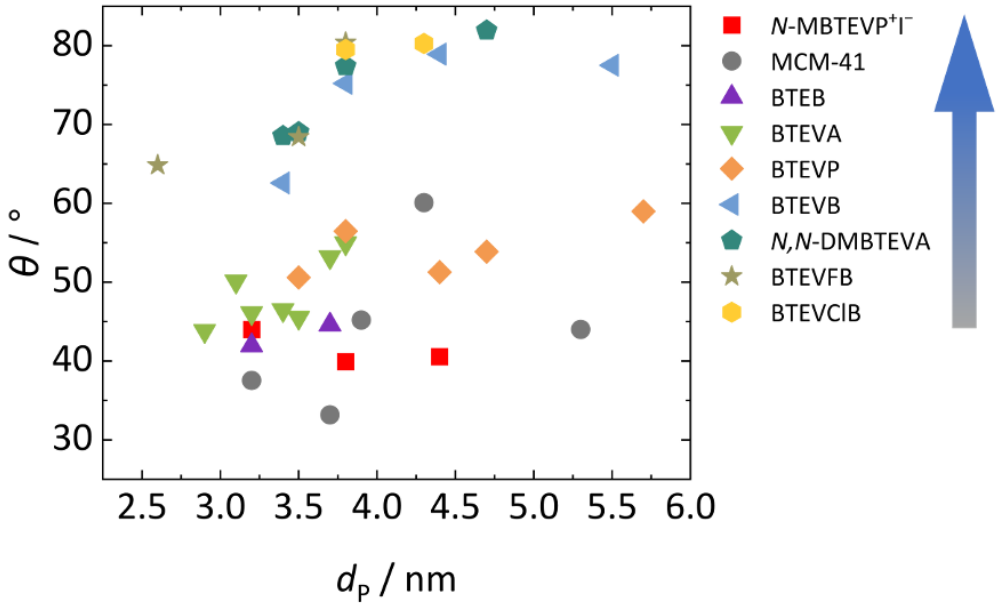


Figure S12. Pore size dependence of the contact angle of water within the confinement of various PMOs and MCM-41 silica. An arrow in the legend denotes the order of increasing hydrophilicity for the listed materials.

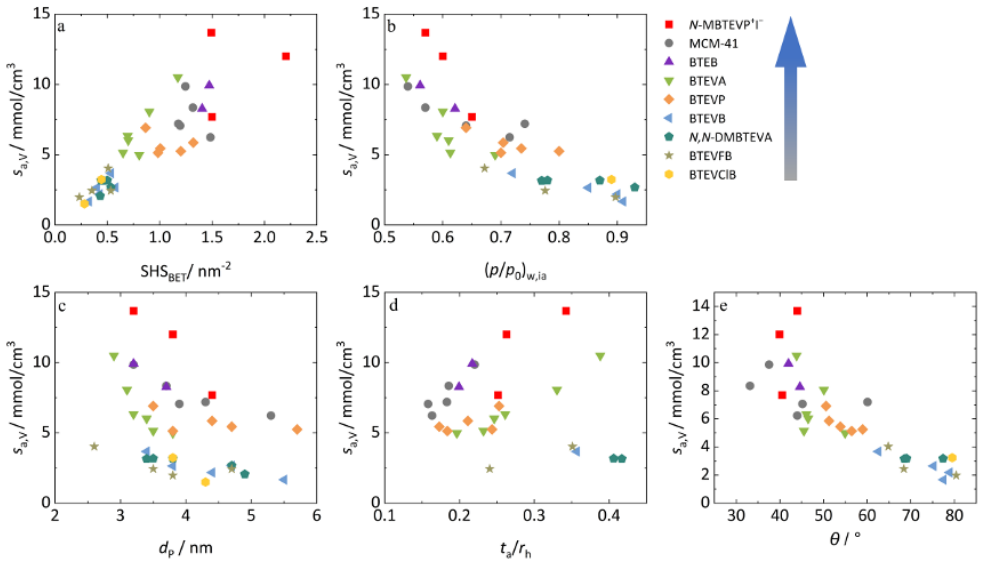
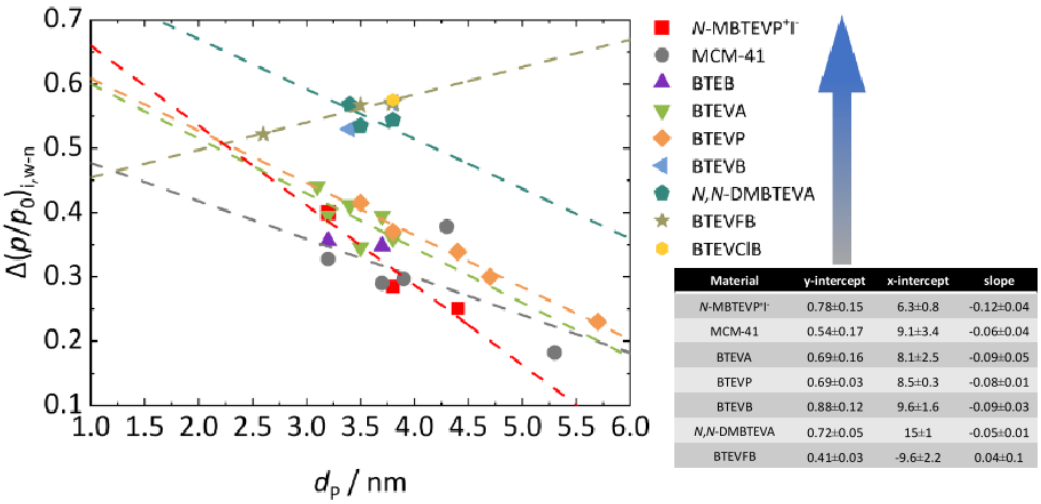


Figure S13. Relationship between the volume-normalized, relative pressure-dependent water uptake quantity ($s_{a,V}$) and a: surface hydration sites, b: the relative pressure of the inflection point of the capillary condensation, c: pore diameter, d: relative adsorption layer size and e: contact angle. An arrow in the legend denotes the order of increasing hydrophilicity for the listed materials.



Material	y-intercept	x-intercept	slope
N-MBTEVP$^+$I$^-$	0.78±0.15	6.3±0.8	-0.12±0.04
MCM-41	0.54±0.17	9.1±3.4	-0.06±0.04
BTEVA	0.69±0.16	8.1±2.5	-0.09±0.05
BTEVP	0.69±0.03	8.5±0.3	-0.08±0.01
BTEVB	0.88±0.12	9.6±1.6	-0.09±0.03
N,N-DMBTEVA	0.72±0.05	15±1	-0.05±0.01
BTEVFB	0.41±0.03	-9.6±2.2	0.04±0.1

Figure S14. Dependence of the difference between the relative pressures at the inflection points of capillary condensation in water vapor sorption isotherms and nitrogen physisorption isotherms ($\Delta(p/p_0)_{i,w-n}$) on pore diameter (d_P). The table provides the parameters of the corresponding linear fit curves (dashed lines). An arrow in the legend denotes the order of increasing hydrophilicity for the listed materials.

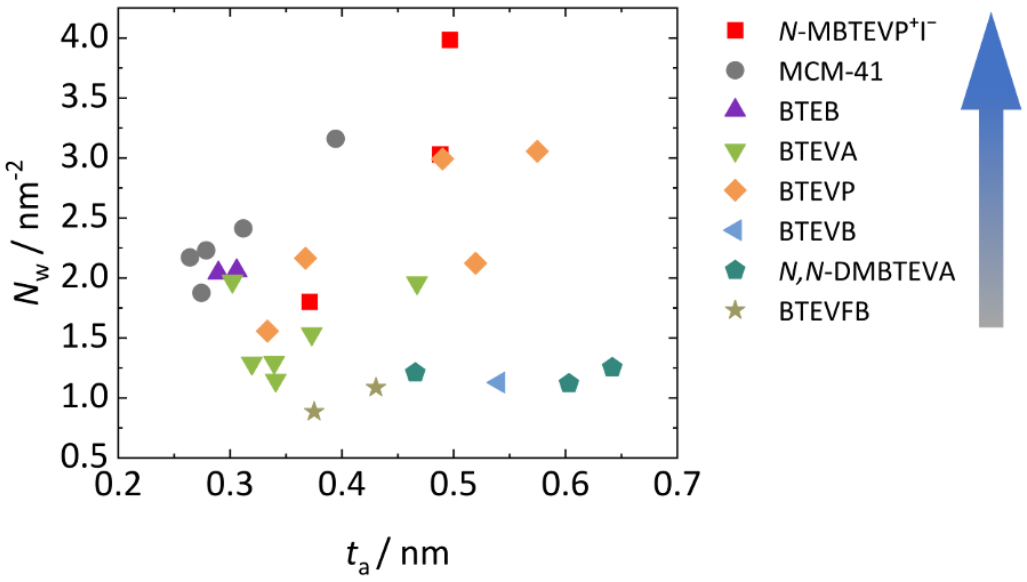


Figure S15. Number of water molecules per square nanometer for a given adsorption layer thickness. An arrow in the legend denotes the order of increasing hydrophilicity for the listed materials.

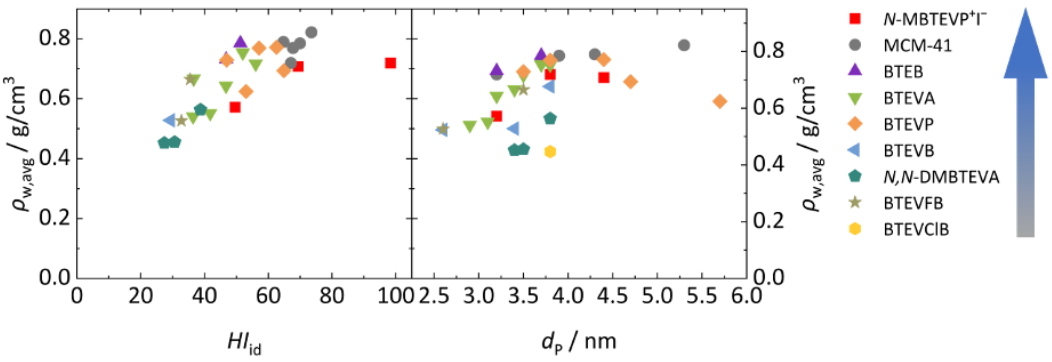


Figure S16. Relationship between the average density and the hydrophilicity index HI_{id} (left), and the pore diameter (right). An arrow in the legend denotes the order of increasing hydrophilicity for the listed materials.

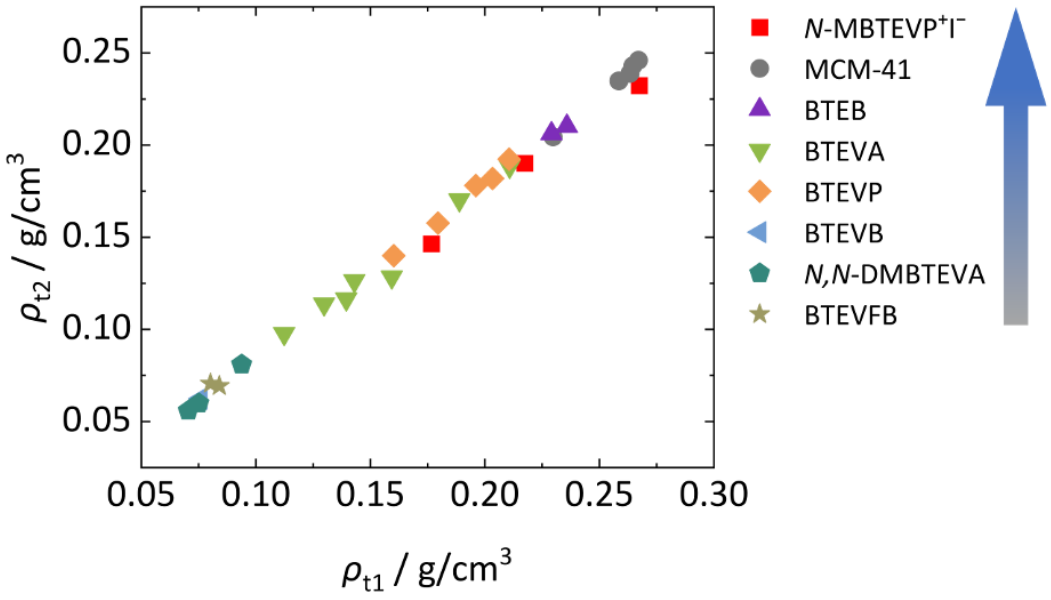


Figure S17. Comparison of adsorption layer density calculated from liquid pore volume using water vapor sorption and nitrogen physisorption (ρ_{t1}) with adsorption layer density calculated from specific BET surface area and *t*-layer size (ρ_{t2}). An arrow in the legend denotes the order of increasing hydrophilicity for the listed materials.

In Table S4 SHS_B was calculated by norming the SHS by the value of a BTEVB-PMO with a pore diameter of 3.8 nm. Using the d_{RU} values from X-ray measurements and assuming a Si–Si distance of 0.31 nm[12,13] $RUHS_B$ can be calculated.

Table S4. Normalized to BTEVB, the relative surface hydration sites (SHS_B) and relative hydration sites per repeat unit ($RUHS_B$) and the relative adsorption layer density ($\rho_{t,MB}$). All the materials presented have a pore diameter of 3.8 nm.

Material	SHS_B	$RUHS_B$	$\rho_{t,MB}$*
BTEVFB	0.6	0.6	-
N,*N*-DMBTEVA	1.1	1.1	1
BTEVClB	1.1	1.1	-
BTEVA	2.0	2.0	2.0
BTEVP	2.5	2.5	2.1
MCM-41 silica	3	0.8	2.9
BTEB	3.5	2.2	2.4
N-MBTEVP$^+$I$^-$	5.5	5.4	2.9

* The relative adsorption layer density was determined by normalizing to *N*,*N*-DMBTEVA-PMO, as no density could be determined for BTEVB-PMO and their densities generally do not differ greatly.

Table S5. Impact of methylation on BTEVP-PMO porosity, structure and the behavior of water confined within its pores. The degree of functionalization, based on the NMR analysis (FC_{NMR}), is also quantified.

	Δd_P / nm	Δd_{RU} / nm	Δd_{100} / nm	Δd_{wall} / nm	Δt_a / nm	$\Delta t_a / r_h$	$\Delta \rho_t$ / g/cm^3	$\Delta \rho_{w,avg}$/ g/cm^3	Fc_{NMR} / %
N-MBTEVP$^+$I$^-$_3.2	−0.3	−0.01	−0.15	+0.13	+0.04	+0.09	+0.02	−0.16	7
N-MBTEVP$^+$I$^-$_3.8	−0.6	−0.02	−0.11	+0.48	+0.01	+0.05	+0.07	−0.05	18
N-MBTEVP$^+$I$^-$_4.4	-	−0.03	−0.15	-	-	-	-	-	-

REFERENCES

(1) Mietner, J. B. Visiting nanopores: The great potential of PMOs for studying the properties of water in nanopores of different polarity. Ph.D. Thesis, University of Hamburg, Germany, 2018.

(2) Bilo, M. Controlled pore glasses and alginate hydrogels as form-giving matrices for nanoporous organosilicas. Ph.D. Thesis, University of Hamburg, Germany, 2019.

(3) Bracco, S.; Beretta, M.; Cattaneo, A.; Comotti, A.; Falqui, A.; Zhao, K.; Rogers, C.; Sozzani, P. Dipolar rotors orderly aligned in mesoporous fluorinated organosilica architectures. *Angew. Chem. Int. Ed.* **2015**, *54* (16), 4773–4777. DOI: 10.1002/anie.201412412.

(4) Gießelmann, N. C.; Lenz, P.; Meinert, S.-M.; Simon, T.; Jo, W.; Striker, N. N.; Fröba, M.; Lehmkühler, F. Structure of water under confinement in periodic mesoporous organosilicas investigated by X-ray scattering. *J. Phys. Chem. C* **2024**, *128* (1), 499–507. DOI: 10.1021/acs.jpcc.3c06491.

(5) Jähnert, S. Study of pure substances in periodic mesoporous silica material with thermophysical methods and in-situ small-angle X-ray-diffraction. Ph.D. Thesis, Technical University of Berlin, Germany, 2008.

(6) Thomé, A. G.; Schroeter, F.; Bottke, P.; Wittayakun, J.; Roessner, F. Facile determination of the degree of modification of ordered mesoporous silica by liquid phase NMR. *Microporous Mesoporous Mater.* **2019**, *274*, 342–346. DOI: 10.1016/j.micromeso.2018.08.034.

(7) Beretta, M.; Morell, J.; Sozzani, P.; Fröba, M. Towards peptide formation inside the channels of a new divinylaniline-bridged periodic mesoporous organosilica. *Chem. Commun.* **2010**, *46* (14), 2495–2497. DOI: 10.1039/B923485C.

(8) Cornelius, M.; Hoffmann, F.; Fröba, M. Periodic mesoporous organosilicas with a bifunctional conjugated organic unit and crystal-like pore walls. *Chem. Mater.* **2005**, *17* (26), 6674–6678. DOI: 10.1021/cm051935n.

(9) Waki, M.; Mizoshita, N.; Ohsuna, T.; Tani, T.; Inagaki, S. Crystal-like periodic mesoporous organosilica bearing pyridine units within the framework. *Chem. Commun.* **2010**, *46* (43), 8163–8165. DOI: 10.1039/C0CC01944E.

(10) Socrates, G. *Infrared and raman characteristic group frequencies*:*Tables and charts*, 3. ed., repr. as paperback; Wiley, 2010.

(11) Gießelmann, N. C.; Lenz, P.; Meinert, S.-M.; Simon, T.; Bauer, R. P. C.; Jo, W.; Claas, S.; Köhn, C.; Striker, N. N.; Fröba, M.; et al. The structure of ice under confinement in periodic mesoporous organosilicas (PMOs). *J. Chem. Phys.* **2024**, *161* (3). DOI: 10.1063/5.0216697.

(12) Pauly, T. R.; Petkov, V.; Liu, Y.; Billinge, S. J. L.; Pinnavaia, T. J. Role of framework sodium versus local framework structure in determining the hydrothermal stability of MCM-41 mesostructures. *J. Am. Chem. Soc.* **2002**, *124* (1), 97–103. DOI: 10.1021/ja0118183.

(13) Nagasima, N. Structure analysis of silicon dioxide films formed by oxidation of silane. *J. Appl. Phys.* **1972**, *43* (8), 3378–3386. DOI: 10.1063/1.1661723.

8.3. Synthesis of Bifunctional Amide–Acid PMOs

8.3.1. BTEPA-Based PMOs

Synthesis of the precursors 4-(bis(3-(triethoxysilyl)propyl)amino)-4-oxobutanoic acid (BTEPA-OBA) and 4-(bis(3-(triethoxysilyl)propyl)amino)-4-oxobut-2-enoic acid (BTEPA-OBenA)

The synthesis was performed using the Schlenk method under a nitrogen atmosphere. By adding bis(3-triethoxysilylpropyl)amine (BTEPA) to a solution of either maleic anhydride (MA) or succinic anhydride (SA) in 1,4-dioxane (molar ratio 1:1:70; BTEPA:MA or SA:dioxane) and stirring for 24 h at room temperature, BTEPA-OBenA or BTEPA-OBA was obtained, respectively (see Figure S1).

The ^{1}H-NMR spectra of BTEPA-OBenA and BTEPA-OBA are shown in Figure S2 and Figure S3, respectively. Both NMR and IR analyses confirm the successful synthesis of both precursors. The IR spectra of BTEPA-OBenA and BTEPA-OBA show characteristic bands for the carboxylic acid groups at 1719 cm^{-1} and 1732 cm^{-1}, respectively, and for the amide groups at 1623 cm^{-1} and 1647 cm^{-1}.

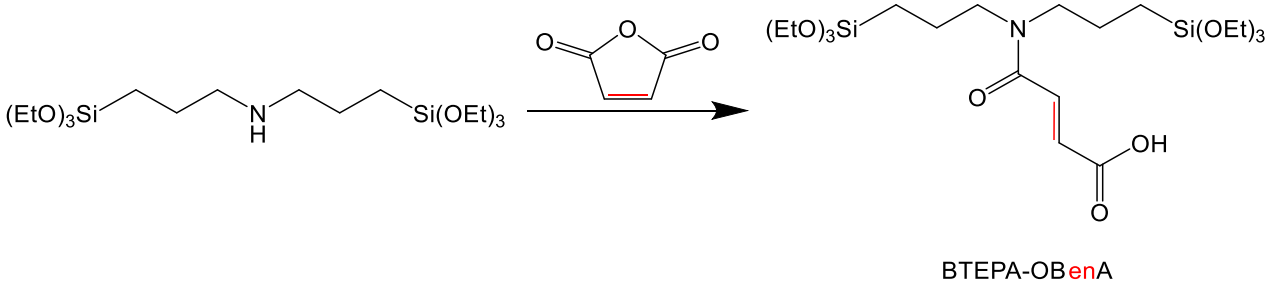


Figure S1: Synthetic routes for BTEPA-OBenA and BTEPA-OBA.

BTEPA-OBenA:

^{1}H-NMR (300 MHz, DMSO-d$_6$, 25 °C): *δ* [ppm] = 12.82 (s, 1H, COO**H**), 6.71 (d, ^{3}J = 12.1 Hz, 1H, =C**H**-), 5.93 (d, ^{3}J = 12.1 Hz, 1H, =C**H**-), 3.75 (q, ^{3}J = 7.0 Hz, 6H, O-**CH$_2$**´-CH$_3$), 3.73 (q, ^{3}J = 7.0 Hz, 6H, O-**CH$_2$**´´-CH$_3$), 3.28–3.12 (m, 4H, N-**CH$_2$**-), 1.66–1.41 (m, 4H, N-CH$_2$-**CH$_2$**), 1.15 (t, ^{3}J =7.0 Hz, 9H, O-CH$_2$-**CH$_3$**´), 1.14 (t, ^{3}J =7.0 Hz, 9H, O-CH$_2$-**CH$_3$**´´), 0.59–0.41 (m, 4H, -**CH$_2$**-Si).

Further signals: *δ* [ppm] = 3.6 (1,4-Dioxane).

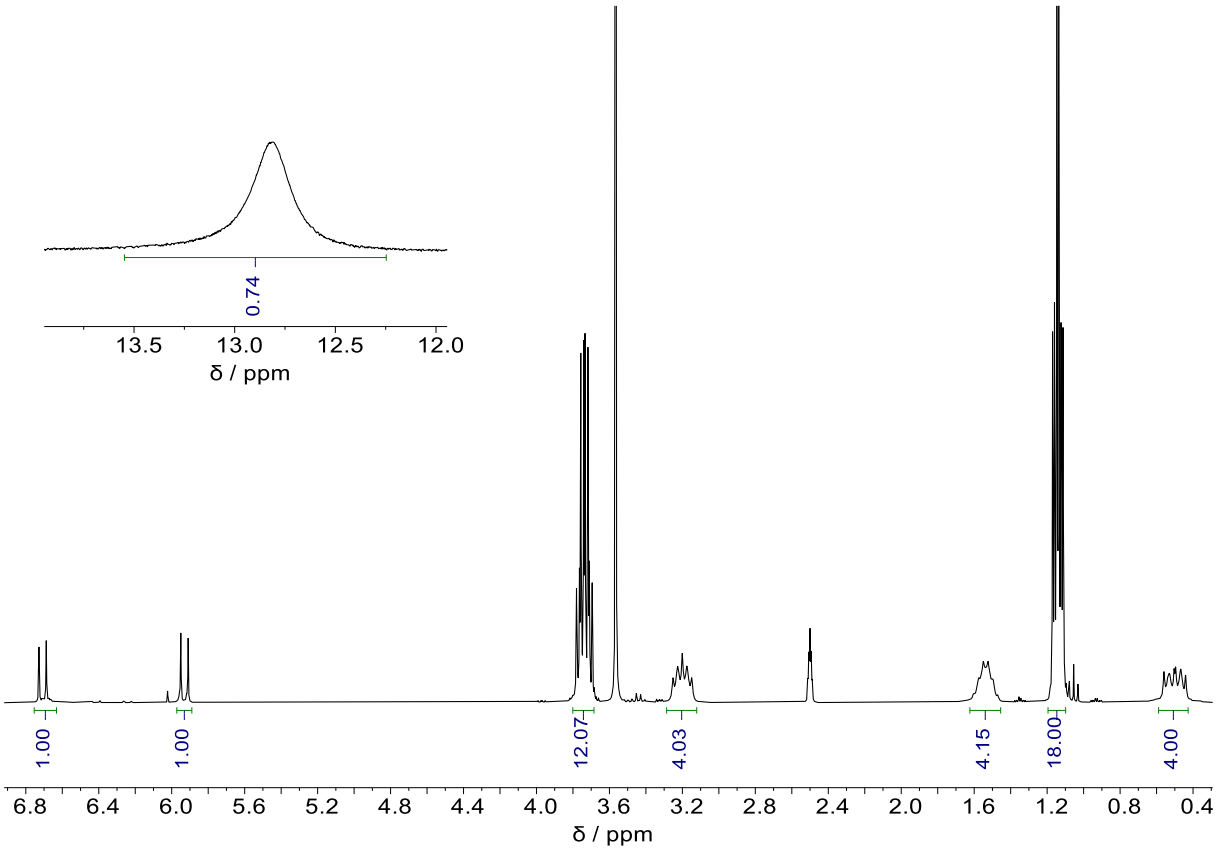


Figure S2: ^{1}H-NMR spectrum of BTEPA-OBenA in DMSO-d_6.

^{13}C {^{1}H}-NMR (75 MHz, DMSO-d_6, 25 °C): 166.1 (C´=O), 165.9 (C´´=O), 137.5 (=CH-), 124.4 (=CH-), 57.74 (O-**C´H$_2$**-CH$_3$), 57.71 (O-**C´´H$_2$**-CH$_3$), 50.3 (N-**C´H$_2$**-), 47.0 (N-**C´´H$_2$**-), 21.8 (N-CH$_2$-**C´H$_2$**), 20.4 (N-CH$_2$-**C´´H$_2$**), 18.18 (O-CH$_2$-**C´H$_3$**), 18.18 (O-CH$_2$-**C´´H$_3$**), 7.31 (-**C´H$_2$**-Si), 6.97 (-**C´´H$_2$**-Si).

Further signals: δ [ppm] = 66.4 (1,4-Dioxane).

FT-IR (KBr-disc): $\tilde{\nu}$ [cm^{-1}] = 3467, 2975, 2929, 2890, 2765, 2738, 1892, 1719, 1623, 1565, 1512, 1486, 1440, 1391, 1369, 1294, 1264, 1224, 1193, 1169, 1075, 958, 850, 781, 624, 461.

BTEPA-OBA:

^{1}H-NMR (300 MHz, DMSO-d_6, 25 °C): δ [ppm] = 11.87 (s, 1H, COO**H**), 3.76 (q, ^{3}J = 7.0 Hz, 6H, O-**CH$_2$**´-CH$_3$), 3.74 (q, ^{3}J = 7.0 Hz, 6H, O-**CH$_2$**´´-CH$_3$), 3.30–3.11 (m, 4H, N-**CH$_2$**-), 2.58–2.45 (m, 2H, **CH´$_2$**-C=O), 2.46–2.38 (m, 2H, **CH´´$_2$**-C=O), 1.66–1.40 (m, 4H, N-CH$_2$-**CH´$_2$**), 1.15 (t, ^{3}J =7.0 Hz, 9H, O-CH$_2$-**CH$_3$**´), 1.14 (t, ^{3}J =7.0 Hz, 9H, O-CH$_2$-**CH$_3$**´´), 0.61–0.41 (m, 4H, -**CH$_2$**-Si).

Further signals: δ [ppm] = 3.6 (s, 1,4-Dioxane).

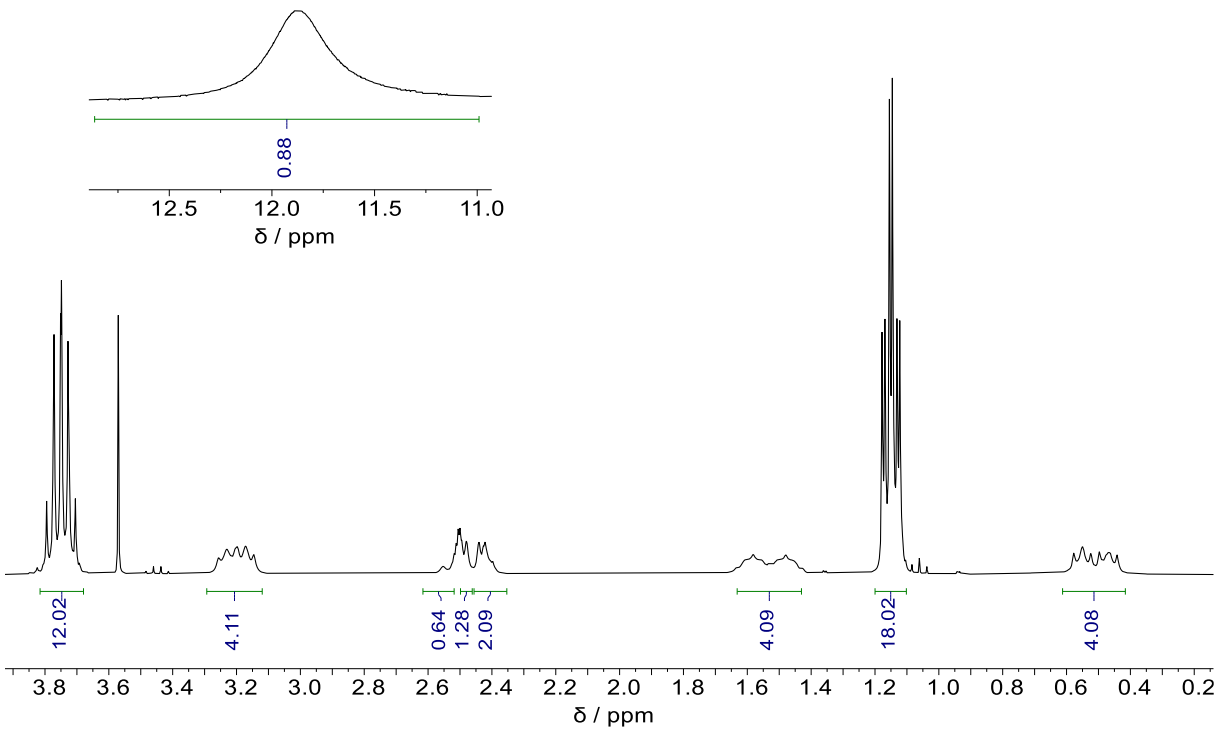


Figure S3: ^{1}H-NMR spectrum of BTEPA-OBA in DMSO-d_6.

^{13}C {^{1}H}-NMR (75 MHz, DMSO-d_6, 25 °C): 174.0 (C´=O), 170.3 (C´´=O), 57.8 (O-**C´H$_2$**-CH$_3$), 57.7 (O-**C´´H$_2$**-CH$_3$), 49.6 (N-**C´H$_2$**-), 48.1 (N-**C´´H$_2$**-), 29.1 (**C´H$_2$**-C=O), 27.4 (**C´´H$_2$**-C=O), 22.1 (N-CH$_2$-**C´H$_2$**), 20.9 (N-CH$_2$-**C´´H$_2$**), 18.1 (O-CH$_2$-**CH$_3$**), 7.3(-**C´H$_2$**-Si), 7.0 (-**C´´H$_2$**-Si).

Further signals: *δ* [ppm] = 66.4 (1,4-Dioxane).

FT-IR (KBr-disc): 2975, 2928, 2886, 2735, 1732, 1647, 1623, 1558, 1483, 1442, 1425, 1412, 1391, 1295, 1258, 1228, 1165, 1103, 1080, 957, 789, 472, 459.

Synthesis of BTEPA-OBA- and BTEPA-OBenA-based PMO via co-condensation with 1,4-bis-(triethoxysilyl)-benzene (BTEB)

This synthesis is based on a slightly modified version of a reported procedure.[298]

The block copolymer P123 ($1.5 \cdot 10^{-2}$ mmol) and sodium chloride (5.3 mmol) were dissolved in a solution of 0.367 mL hydrochloric acid (37 wt%) and 2.8 mL of demineralized water under stirring at 35 °C for 1 h. The precursor compounds were then added in the molar ratios given in Table S2, and the solution was stirred for 24 h at 40 °C, during which precipitation occurred. The resulting mixture was subsequently

hydrothermally treated at 80 °C for 24 h. The solid product was filtered and washed with 200 mL of demineralized water, followed by 50 mL of ethanol. Finally, the surfactant was removed by Soxhlet extraction using an ethanol/HCl (37 wt%) solution (98:2 *V*/*V*), and the resulting material was dried at 80 °C to yield a colorless powder.

Table S2: Molar amounts of precursors used for co-condensation.

Content of amide–acid precursor / %	$n_{\text{BTEPA-OBenA/ -OBA}}$ / mmol	n_{BTEB} / mmol
100%	0.83	0
80%	0.66	0.17
60%	0.50	0.33
50%	0.41	0.41
37%	0.30	0.52
20%	0.17	0.66
0%	0	0.83

BTEPA-OBenA PMOs:

The porosity and structural order of the PMOs were characterized by X-ray diffraction and nitrogen physisorption measurements (Figure S4), and the key parameters are summarized in Table S9. Due to the larger pore diameters (d_P = 5.9–8.2 nm) and thicker pore walls (d_w = 6.0–9.9 nm), both increasing with higher BTEPA-OBenA precursor content, the reflections in the normalized X-ray powder diffractograms (1–4° 2θ, Figure S4a) shift toward lower 2θ angles and are partially obscured in the background. To resolve this, small-angle X-ray scattering (SAXS) measurements were performed (Figure S4c and d), revealing well-defined reflection patterns. The pore walls show a certain ordering, as indicated by the broad reflections in the range of 5–15° 2θ. The PMO synthesized solely from BTEPA-OBenA shows an average repeating-unit length (d_{RU}) of 1.13 nm with an HWHM of 0.15. With decreasing BTEPA-OBenA content and increasing BTEB fraction, the d_{RU} gradually approaches the value typical for BTEB-bridged PMOs (d_{RU} = 0.78 nm). Based on ^{1}H-NMR measurements (Figure S5), the determined content of incorporated BTEPA + BTEPA-OBenA is plotted against d_{RU} in Figure S6. At around 60 %, d_{RU} changes most significantly, possibly due to weaker intermolecular interactions between BTEPA species at lower concentrations. With further reduction, the BTEB bridges dominate

the structure, likely forcing the more flexible BTEPA species into a folded configuration. The precursor ratio also affects interactions with the surfactant during synthesis, resulting in variations in pore diameter, as seen from nitrogen physisorption data (Figure S4e and f). Increasing BTEPA-OBenA content yields larger pores, thicker walls, and reduced specific surface areas. In addition to the main mesopores, the material contains smaller pores (approximately 3–7 nm), which result from the use of P123 as a surfactant, known to generate secondary pores that interconnect the primary cylindrical channels through the pore walls.[299] Furthermore, the desorption branch of all samples, except the 100 % specimen, exhibits an abrupt step at relative pressures of 0.44–0.48, characteristic of cavitation-induced desorption of nitrogen at 77 K within ink-bottle-type pores having neck diameters smaller than 6 nm.[158]

The ^{1}H-NMR (Figure S5) and IR analyses (Figure S7) indicate a pronounced loss of the OBenA functionality during synthesis, likely caused by the harsh acidic conditions (pH ≈ −0.14), leading to partial amide bond cleavage. The fraction of OBenA-functionalized species decreases from 1.5 % to 0.4 % with decreasing precursor content in the synthesis (Table S9).

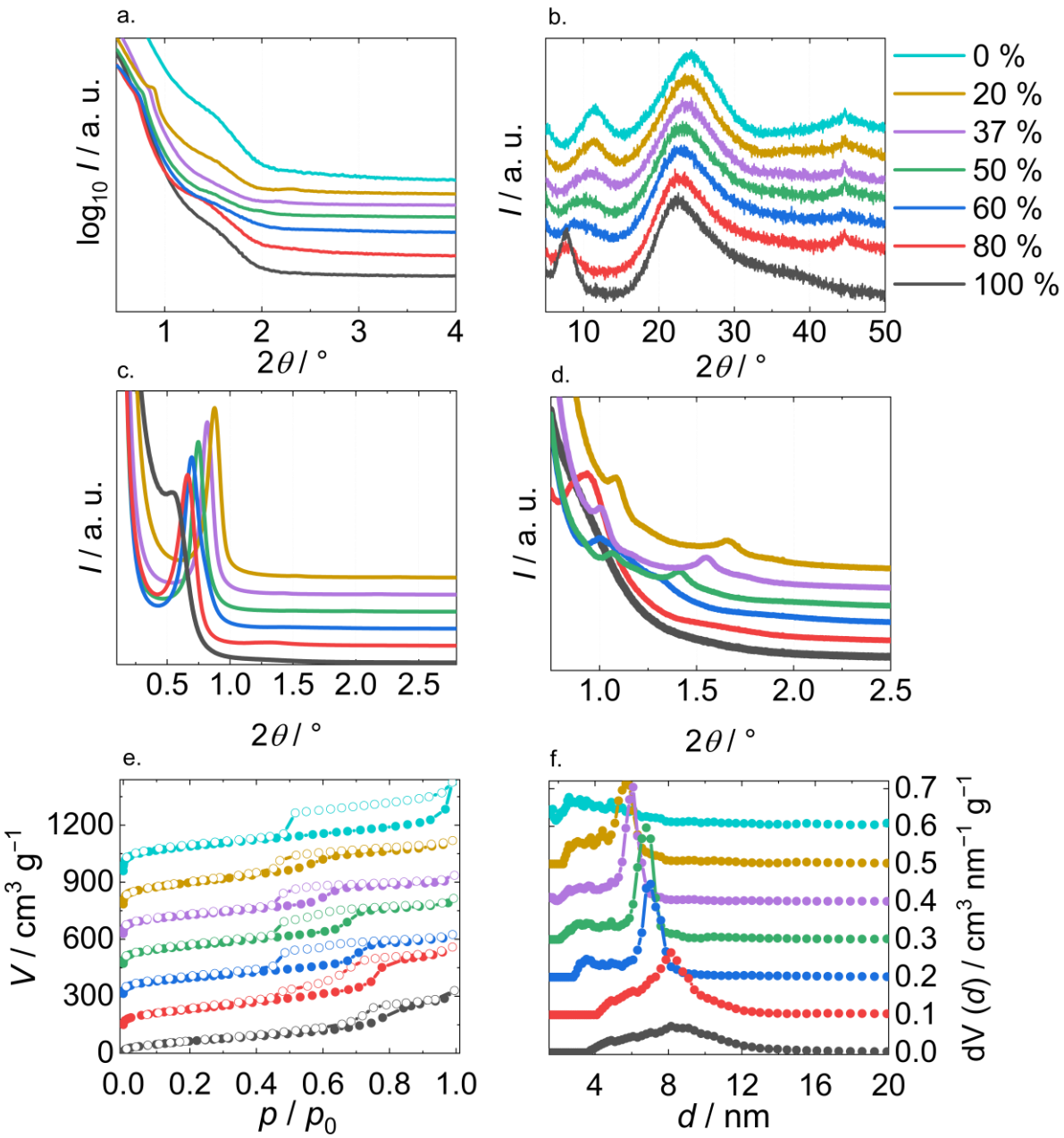


Figure S4: Porosity characterization of pure as well as co-condensed PMOs synthesized with different ratios of amide-acid precursor, using the BTEPA-OBenA and BTEB as precursor: a. normalized X-ray powder diffractograms in the range 0.5–4° 2θ, b. 5–50° 2θ, c. small-angle X-ray scattering with d. an inset showing the range 0.5–2.5° 2θ, e. nitrogen physisorption isotherms at 77 K, showing the adsorption branch (filled circles) and desorption branch (hollow circles), and f. the corresponding pore size distribution curves, calculated using the NLDFT kernel: N_2 at 77 K on silica, cylindr. pores, at adsorption branch. The isotherms (e.) are shifted vertically along the Y-axis by a value of 150 $cm^3\,g^{-1}$ and the pore size distributions (f.) by a value of 0.1 $cm^3\,nm^{-1}\,g^{-1}$.

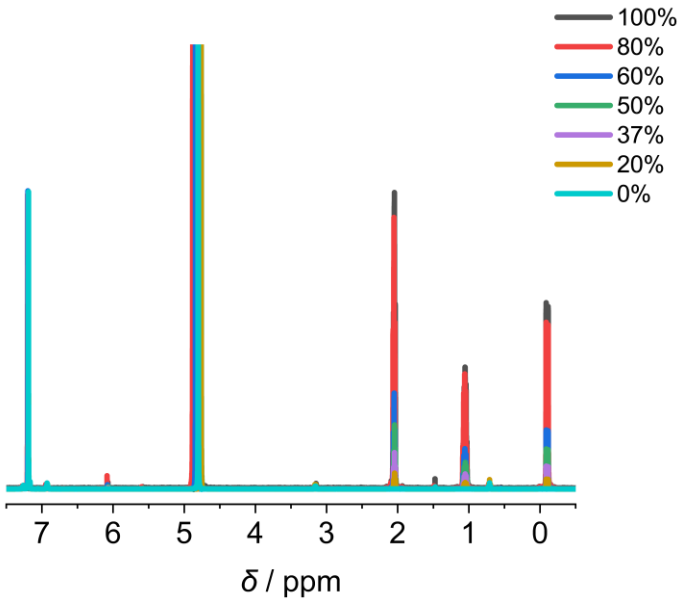


Figure S5: ^{1}H-NMR (600 MHz) spectra of PMOs synthesized with different BTEPA-OBenA precursor contents in co-condensation with BTEB. The resulting materials were dissolved in 1 M NaOD/D_2O.

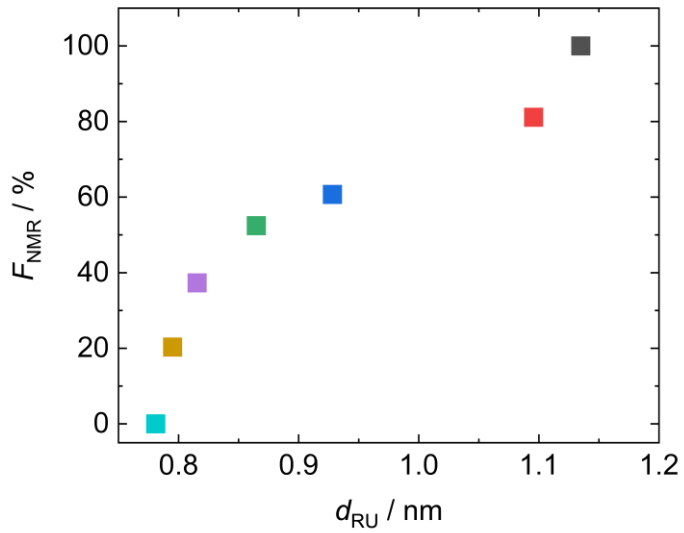


Figure S6: Dependence of the average PMO repeating-unit length (d_{RU}), derived from the (00l) reflection, on the BTEPA-OBenA content in the co-condensate, as determined by ^{1}H-NMR analysis.

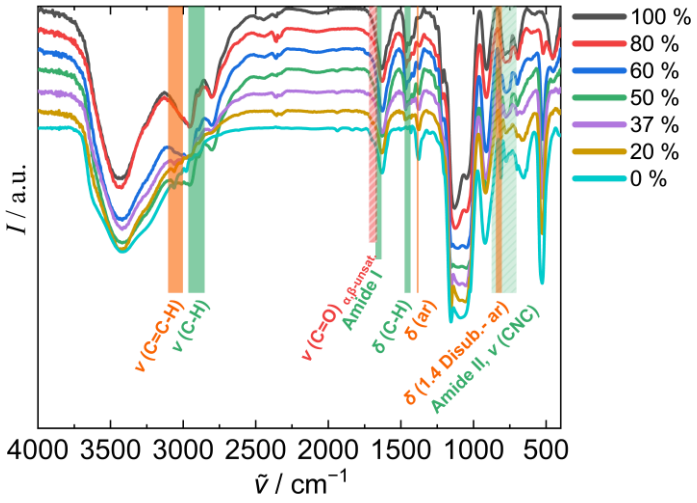


Figure S7: FT-IR spectra (KBr-disc) of PMOs synthesized with different BTEPA-OBenA precursor contents in co-condensation with BTEB.

Thermogravimetric analysis coupled with differential thermal analysis and mass spectrometry (TGA-DTA-MS) was used to characterize the co-condensed materials. The relative mass loss of surface-adsorbed water ($\Delta(m_w\, m_0^{-1})$), determined from the percentage mass change in the temperature range 30–150 °C, and the relative mass loss of the organic bridge combustion ($\Delta(m_{org}\, m_0^{-1})$), normalized to the mass at 150 °C to exclude adsorbed water content, were evaluated. In addition, the temperature at the combustion onset (T_{on}), endset (T_{end}), and the temperature at which 50 % of $\Delta(m_{org}\, m_0^{-1})$ is reached (T_{50}) were determined. The actual content of the amide–acid bridge was estimated for each individual sample (iPMO) based on $\Delta(m_{org}\, m_0^{-1})$ using the following equation:

$$\frac{m_{org}}{m_0} = \frac{f_1\, M_{1,org} + f_2\, M_{2,org}}{f_1\, M_{1,tot} + f_2\, M_{2,tot}} = \frac{f_1\, M_{1,org} + (1 - f_1)\, M_{2,org}}{f_1\, M_{1,tot} + (1 - f_1)\, M_{2,tot}} \qquad \text{(S1)}$$

with the fraction of component i (f_i), the molar mass of the organic bridge ($M_{i,org}$), and the molar mass of the total repeating unit ($M_{i,tot}$) of component i. Since ^{1}H-NMR analysis indicated that the OBenA content is considerably lower than the unfunctionalized BTEPA bridge, two limiting cases were assumed for the calculation: not functionalized BTEPA (nf) and completely functionalized BTEPA-OBenA (cf). As the experimentally measured $\Delta(m_{org}\, m_0^{-1})_{i,exp}$ of the homopolymeric materials (e.g., 100 % or 0 %) deviate from theoretical values, the experimental relative mass loss was used to determine the effective molar mass of the homopolymeric PMO (hpPMO) according to the relation:

$$M_{i,org} = \left(\frac{m_{org}}{m_0}\right)_{i,exp} M_{i,tot} \quad \text{(S2)}$$

By inserting Equation (S2) into Equation (S1), the fractions f_1 and f_2 were calculated. All parameters obtained from TGA-DTA-MS analysis are summarized in Table S3.

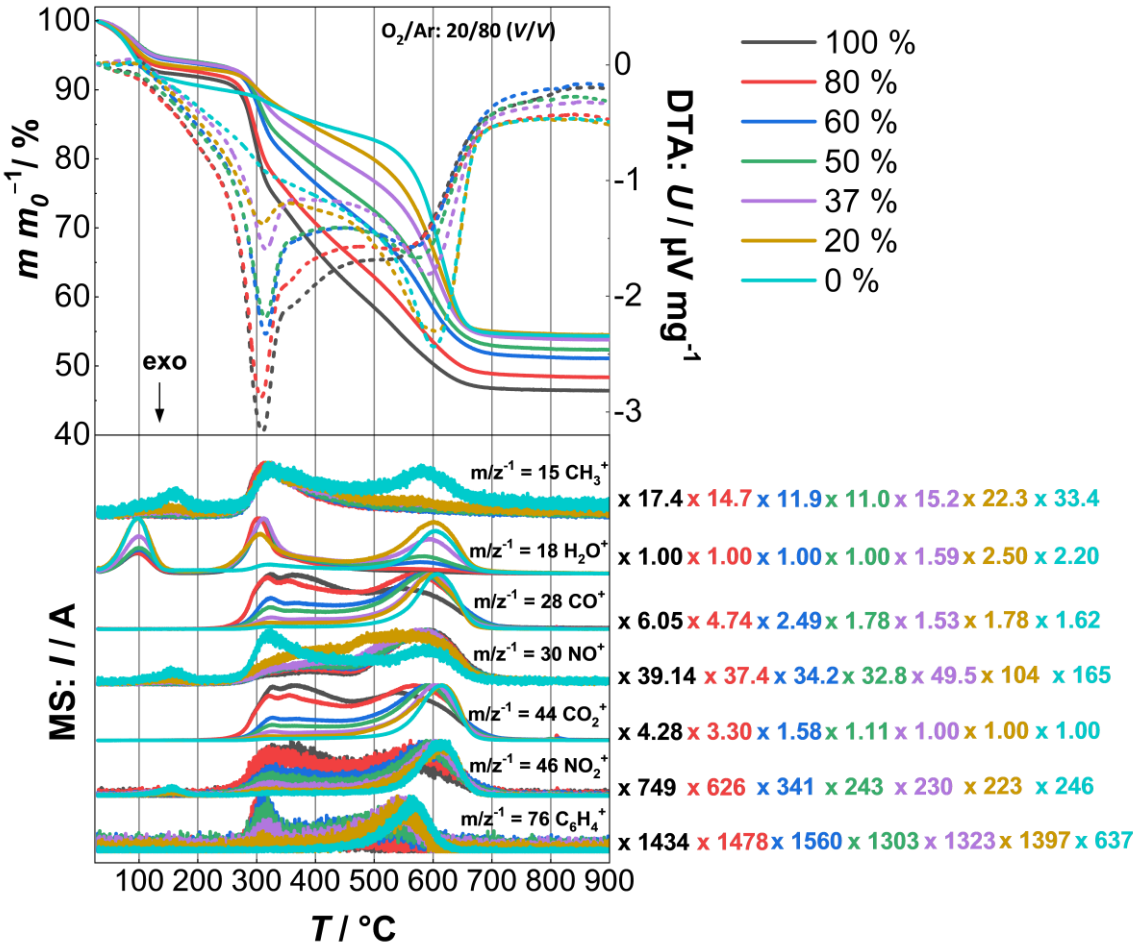


Figure S8: TGA-DTA-MS analysis of PMOs synthesized with different BTEPA-OBenA precursor contents in co-condensation with BTEB. Measurements were performed at a heating rate of 10 $Kmin^{-1}$ under an O_2/Ar atmosphere (20/80 (*V*/*V*)).

Similar to the ^{1}H-NMR results, the TGA-DTA-MS analysis indicates a lower OBenA content of about 4 % in the 100 % sample. Elemental analysis (EA) was further employed to determine the nitrogen, carbon, and hydrogen contents. Comparison of the theoretical compositions of BTEPA and BTEPA-OBenA with the experimental values yields an average functionalization degree of 24 %, which is higher than the estimates from NMR and TGA-DTA-MS. Deviations between theoretical and experimental data can result from variations in condensation degree (e.g., remaining ethoxy groups, which increase with BTEB content up to about 5 %) or from impurities.

Therefore, effective amounts of N, C, H, and Si_2O_3 as the remaining fraction in EA, calculated as $F(Si_2O_3)= 100 - F(N + C + H)$ were determined for both homopolymeric PMOs (100 % and 0 %) and normalized to the effective molar amount of Si_2O_3. Based on these two effective homopolymers, the composition of the co-condensed materials was derived (see Table S4). Across all three methods (NMR, TGA-DTA-MS, and EA), the content of the BTEPA species used in synthesis is roughly consistent with the actual amount incorporated into the resulting PMO. Due to the different assumptions made for TGA-DTA-MS and EA analysis, the NMR results represent a direct and more reliable measure of the material composition. Nevertheless, NMR-based quantification may be affected by undissolved residues that remain on the filter and are thus not analyzed, or by partial cleavage or side reactions during dissolution. In the latter case, side products may still be detected as long as they are not highly volatile.

The thermal stability was evaluated from the onset temperature of the TGA curve. As shown in Figure S8 (and summarized in Table S3), the co-condensed materials (20–80 %) exhibit two distinct mass-loss steps. The first step, at around $T_{on,1}$ = 277 °C, can be attributed to decomposition of the BTEPA bridge, whose relative mass loss decreases with increasing BTEB content. The second step corresponds to the decomposition of the benzene bridge, which becomes more pronounced at higher BTEB fractions. While the first step occurs at similar temperatures (272 and 280 °C), the second onset temperature, as well as T_{50} (temperature at 50 % organic mass loss) and the endset temperature, where all organic species are oxidized and mainly SiO_2 remains, shift to higher values with increasing BTEB content. The higher stability likely results from improved π–π stacking interactions between benzene bridges, which become less disrupted with decreasing incorporation of the more flexible BTEPA units.

Given the low OBenA content, a post-synthetic functionalization after PMO synthesis could potentially increase the overall functionalization degree. Additional experiments (not included in this thesis) have shown that using the unfunctionalized BTEPA precursor under identical synthesis conditions results in materials with significantly lower pore order and a non-uniform pore size distribution. This suggests that the maleic acid moiety, probably hydrolyzed during PMO synthesis, acts as a mediator in the formation process.

Table S3: Extracted data from TGA-DTA-MS analysis, including the relative mass loss of surface-adsorbed water in the range 30–150 °C ($\Delta(m_w\, m_0^{-1})$), the relative mass loss of the organic bridge combustion excluding adsorbed water content ($\Delta(m_{org}\, m_0^{-1})$), the functionalization degree (F), calculated directly from $\Delta(m_{org}\, m_0^{-1})$ for individual samples (iPMO) or based on the relative mass loss of homopolymeric PMOs (hpPMO) under the assumptions of no functionalization (nf) and complete functionalization (cf). Combustion temperatures were determined from the onsets ($T_{on,1}$, $T_{on,2}$) and endset (T_{end}), as well as the temperature at which $\Delta(m_{org}\, m_0^{-1})$ reaches 50 % (T_{50}).

BTEPA-OBenA precursor content	$\Delta(m_w\, m_0^{-1})$ / %	$\Delta(m_{org}\, m_0^{-1})$ / %	F iPMO/ hpPMO [nf (cf)] / %	$T_{on,1}$ ($T_{on,2}$) / °C	T_{50}	T_{end} / °C
100 %	7.52	49.7	96 (4)	274 (-)	378	643
80 %	6.81	48.1	88 (17) / 80 (73)	275 (521)	399	645
60 %	5.70	45.8	52 (10) / 54 (44)	280 (538)	453	648
50 %	5.39	44.7	34 (5) / 41 (32)	280 (542)	485	646
37 %	5.52	43.0	11 (2) / 24 (18)	279 (556)	536	648
20 %	6.39	41.8	0 (0) / 11 (8)	272 (555)	563	650
0 %	8.43	40.7	-	- (542)	592	649

Table S4: Results of elemental analysis (N, C, H) for materials synthesized with different BTEPA-OBenA precursor contents, and the calculated fraction of BTEPA species (F_{hpPMO}) based on the results of the homopolymeric PMOs.

BTEPA-OBenA precursor content	N / %	C / %	H / %	F_{hpPMO} / %
100 %	5.10	26.82	6.72	100 (24)*
80 %	4.52	29.00	6.21	80
60 %	3.51	30.42	5.46	57
50 %	3.04	31.34	5.43	50
37 %	2.21	32.72	4.84	30
20 %	1.33	33.87	4.62	16
0 %	0.00	34.79	4.36	0

*Calculated amount of functionalized BTEPA-OBenA.

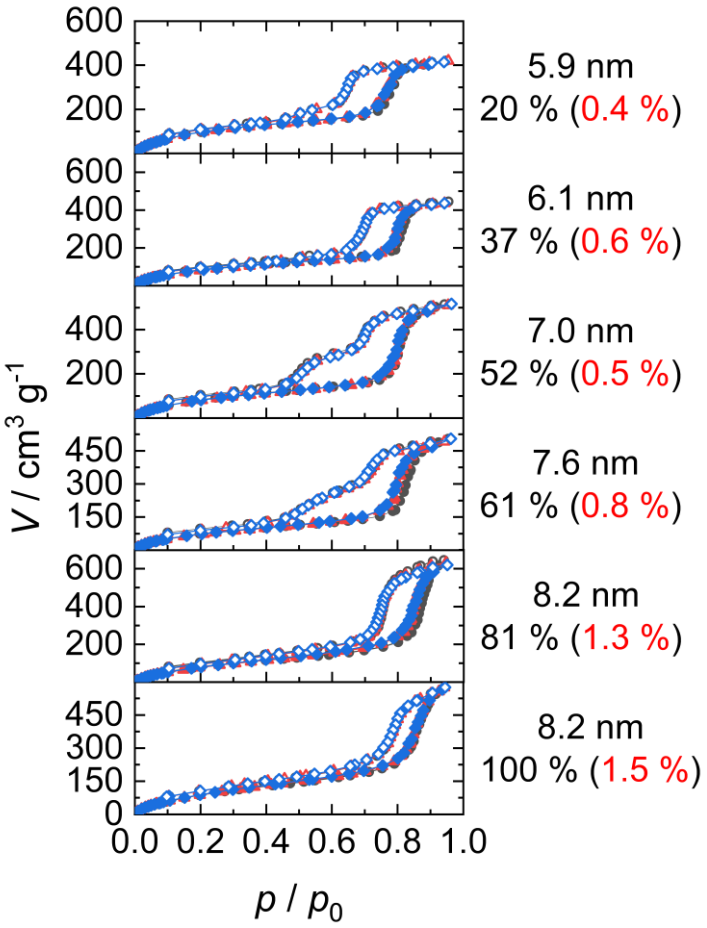


Figure S9: Water vapor sorption isotherms at 25 °C showing the adsorption branch (filled circles) and desorption branch (hollow circles) for PMOs co-condensed with BTEB and BTEPA-OBenA precursors at different ratios. Also shown are the corresponding pore diameters, determined from nitrogen physisorption using NLDFT, and the total percentage of combined species (functionalized and non-functionalized), with the percentage of the BTEPA-OBenA-derived fraction given in brackets, both determined by ^{1}H NMR analysis.

BTEPA-OBA PMOs:

The porosity and structural order of the BTEPA-OBA PMOs were characterized by X-ray diffraction and nitrogen physisorption measurements (Figure S10), with key parameters summarized in Table S9. Data for the 0 % (pure BTEB-based) sample were taken from the previous BTEPA-OBenA analysis and, except for the (00l) reflection and d_{RU} evaluation, are not provided here. Similar to the BTEPA-OBenA samples, the (100) reflection is partially obscured by the background of the X-ray powder diffractograms, and therefore only SAXS data are shown (Figure S10a). In contrast to the highly ordered co-condensed materials, the 100 % sample measured by PXRD shows no distinct reflections. The broad (00l) reflections in the range of 5–15° 2θ (Figure S10b) and the corresponding d_{RU} values (Figure S12) vary with the BTEPA-OBA fraction used in the synthesis in a manner similar to that observed for the co-condensed BTEPA-OBenA PMOs. Nitrogen physisorption isotherms and the corresponding pore size distributions (Figure S10c, d) show a reduction in pore diameter from 6.8 to 5.7 nm with decreasing BTEPA-OBA content. This trend mirrors that of the BTEPA-OBenA series, though with generally smaller pore diameters. As previously reported for the BTEPA-OBenA–BTEB PMOs, smaller secondary pores are also present, likely connecting the main pore channels. The desorption branch shows features typical of cavitation-controlled desorption.

From the ^{1}H-NMR analysis (Figure S11), the combined content of BTEPA and BTEPA-OBA was determined (Table S9) and found to be consistent with the synthesis ratios. The functionalization degree of OBA, ranging between 13 and 19 %, is roughly ten times higher than that of OBenA, indicating higher resistance of the OBA amide linkage toward acid hydrolysis. More pronounced amide and carboxylic acid bands in the IR spectra (Figure S13) and supporting TGA-DTA-MS data (Figure S14, Table S5) further confirm the higher functionalization degree for OBA. The thermal stability follows the same trend as described for the BTEPA-OBenA-based PMOs.

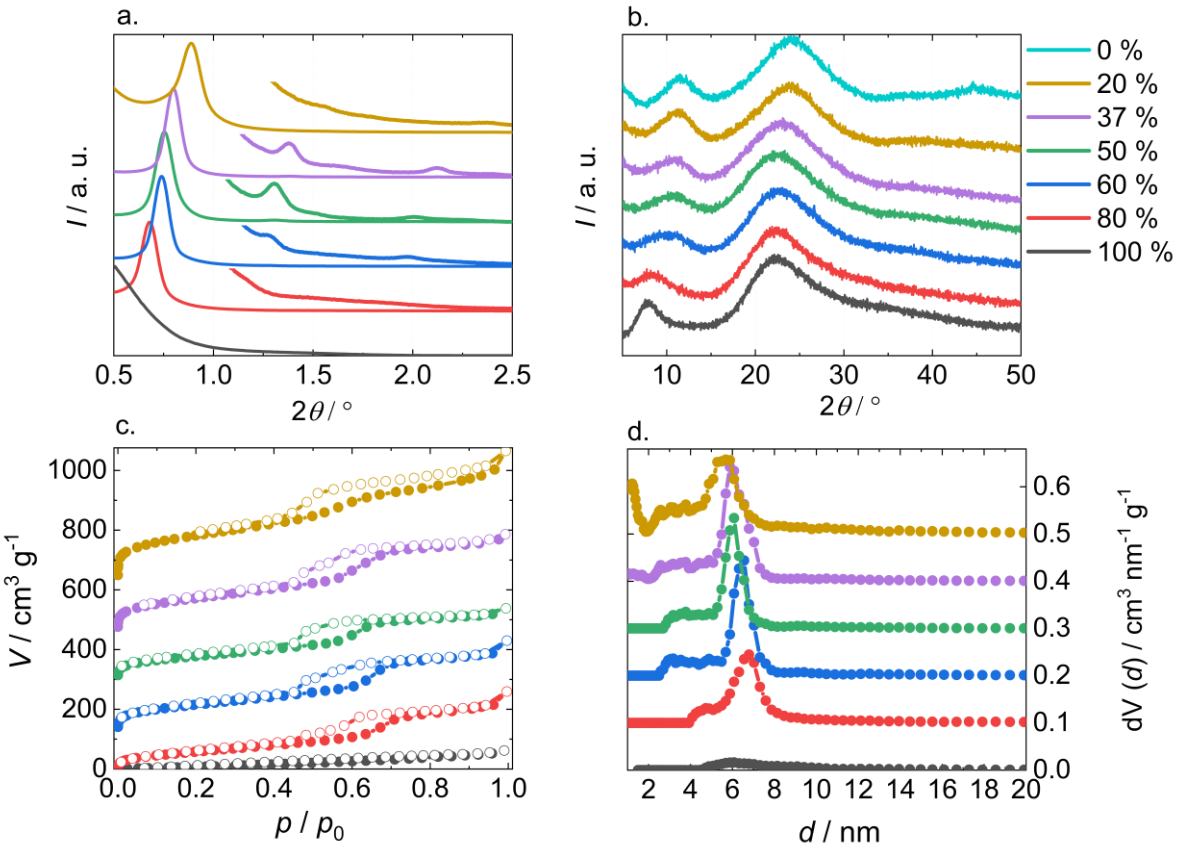


Figure S10: Porosity characterization of pure as well as co-condensed PMOs synthesized with different ratios of amide-acid precursor, using the BTEPA-OBA and BTEB as precursor: a. normalized small-angle X-ray scattering (SAXS) with insets and X-ray powder diffractogram of 100 % sample, b. normalized X-ray powder diffractograms in the range 5–50° 2θ, c. nitrogen physisorption isotherms at 77 K, showing the adsorption branch (filled circles) and desorption branch (hollow circles), and d. the corresponding pore size distribution curves, calculated using the NLDFT kernel: N_2 at 77 K on silica, cylindr. pores, at adsorption branch. The isotherms (c.) are shifted vertically along the Y-axis by a value of 125 cm^3g^{-1} and the pore size distributions (d.) by a value of 0.1 $cm^3nm^{-1}g^{-1}$.

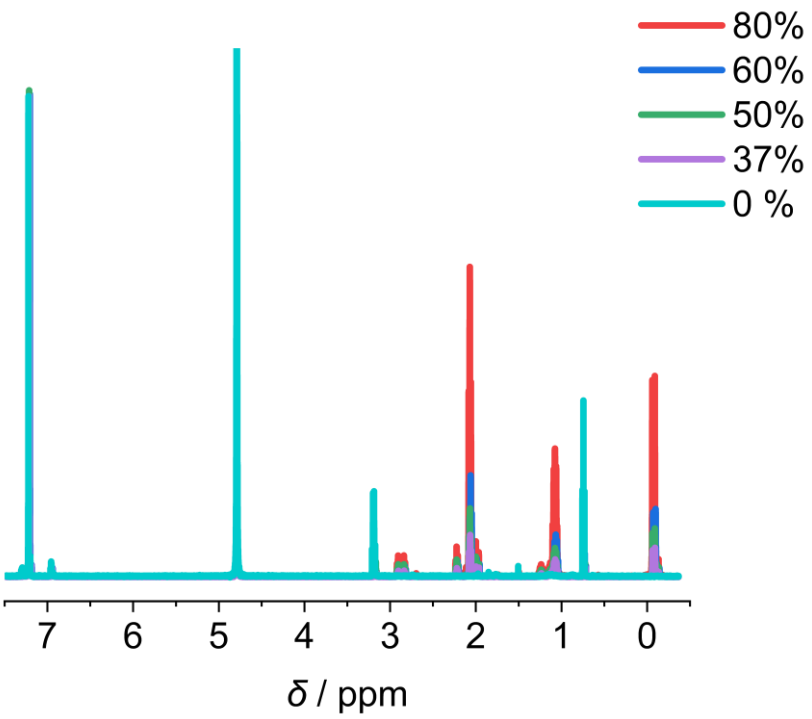


Figure S11: ^{1}H-NMR (600 MHz) spectra of PMOs synthesized with different BTEPA-OBA precursor contents in co-condensation with BTEB. The resulting materials were dissolved in 1 M NaOD/D_2O.

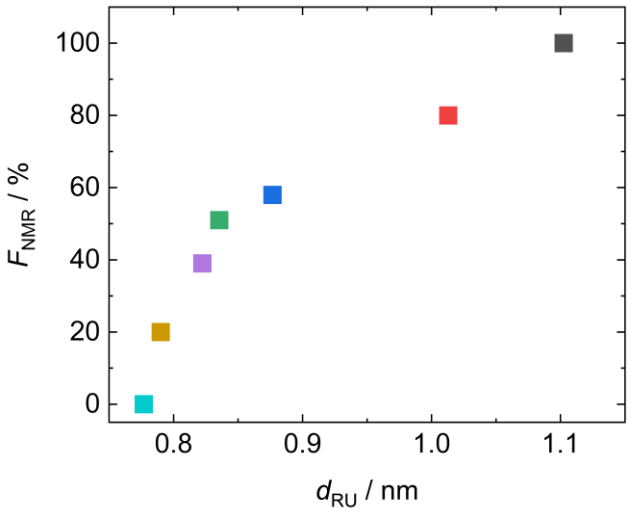


Figure S12: Dependence of the average PMO repeating-unit length (d_{RU}), derived from the (00l) reflection, on the BTEPA-OBA content in the co-condensate, as determined by ^{1}H-NMR analysis.

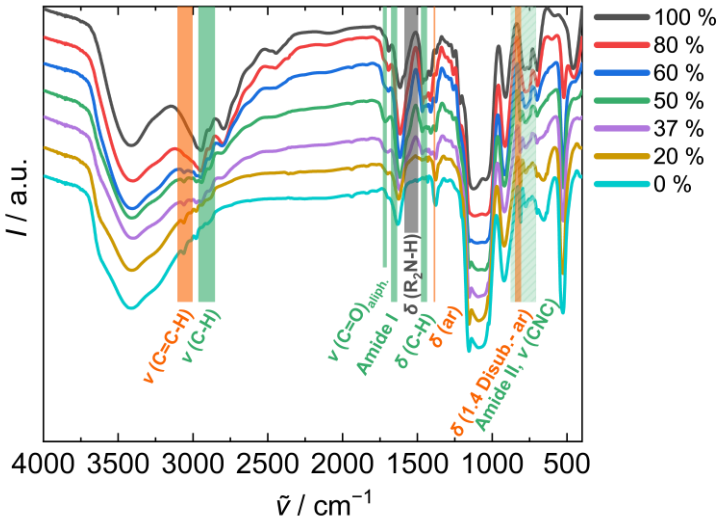


Figure S13: FT-IR spectra (KBr-disc) of PMOs synthesized with different BTEPA-OBA precursor contents in co-condensation with BTEB.

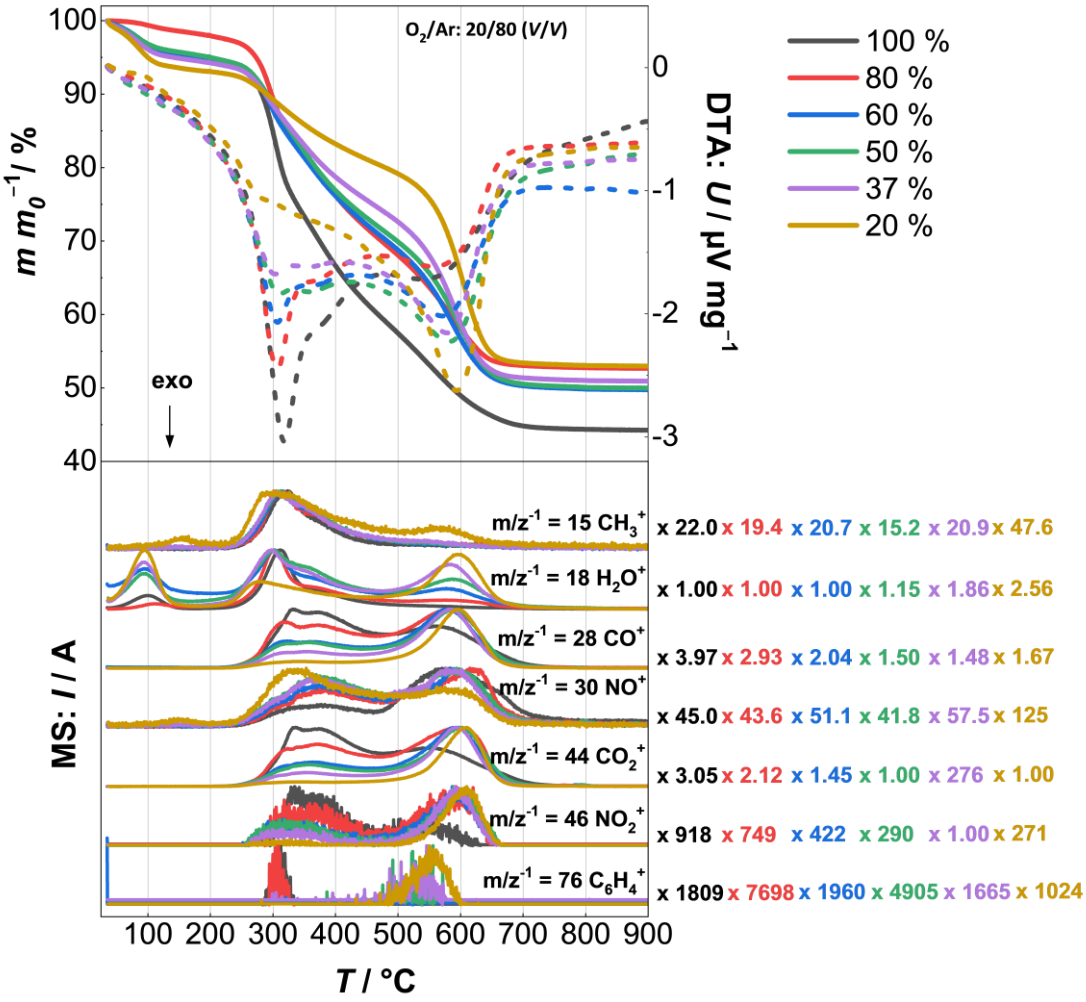


Figure S14: TGA-DTA-MS analysis of PMOs synthesized with different BTEPA-OBA precursor contents in co-condensation with BTEB. Measurements were performed at a heating rate of 10 $Kmin^{-1}$ under an O_2/Ar atmosphere (20/80 (*V*/*V*)).

Table S5: Extracted data from TGA-DTA-MS analysis, including the relative mass loss of surface-adsorbed water in the range of 30–150 °C ($\Delta(m_w\, m_0^{-1})$), the relative mass loss of the organic bridge combustion excluding adsorbed water content ($\Delta(m_{org}\, m_0^{-1})$), the functionalization degree (F), calculated directly from $\Delta(m_{org}\, m_0^{-1})$ for individual samples (iPMO) or based on the relative mass loss of homopolymeric PMOs (hpPMO) under the assumptions of no functionalization (nf) and complete functionalization (cf). Combustion temperatures were determined from the onsets ($T_{on,1}$, $T_{on,2}$) and endset (T_{end}), as well as the temperature at which $\Delta(m_{org}\, m_0^{-1})$ reaches 50 % (T_{50}).

BTEPA-OBA precursor content	**$\Delta(m_w\, m_0^{-1})$ / %**	**$\Delta(m_{org}\, m_0^{-1})$ / %**	**F iPMO/ hpPMO [nf (cf)] / %**	**$T_{on,1}$ ($T_{on,2}$) / °C**	**T_{50}**	**T_{end} / °C**
100 %	4.86	53.4	80 (20) / -	276 (-)	377	645
80 %	1.42	46.6	64 (12) / 43 (34)	271 (538)	405	643
60 %	4.40	47.9	85 (16) / 54 (44)	267 (543)	444	640
50 %	4.07	47.8	84 (16) / 53 (43)	263 (551)	455	646
37 %	4.91	46.3	59 (11) / 41 (32)	260 (548)	496	635
20 %	6.20	43.4	16 (3) / 19 (14)	256 (562)	568	641
0 %	8.43	40.7	0 / -	- (542)	592	649

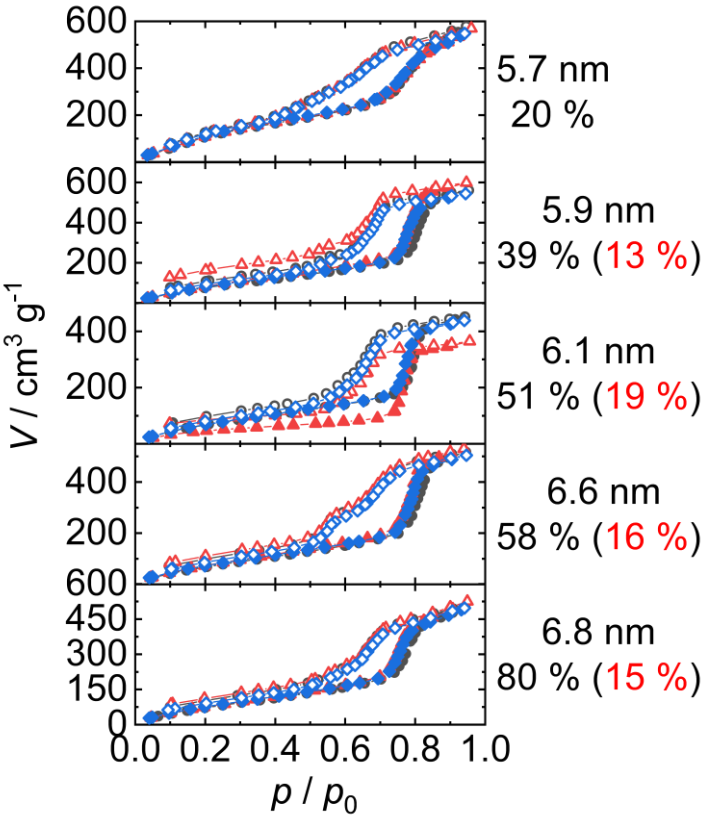


Figure S15: Water vapor sorption isotherms at 25 °C showing the adsorption branch (filled circles) and desorption branch (hollow circles) for PMOs co-condensed with BTEB and BTEPA-OBA precursors at different ratios. Also shown are the corresponding pore diameters, determined from nitrogen physisorption using NLDFT, and the total percentage of combined species (functionalized and non-functionalized), with the percentage of the BTEPA-OBA-derived fraction given in brackets, both determined by ^{1}H NMR analysis.

8.3.2. Aspartic-Acid-Based PMOs

Synthesis of the BOC-protected precursor (R)-2-amino-N1,N4-bis(3-(triethoxysilyl)propyl)succinamide (BOC-BTEPSA)

The synthesis procedure is based on a protocol described in the literature.[300] The synthesis was performed using the Schlenk technique under a nitrogen atmosphere. *N*-BOC-L-aspartic acid (4.20 g, 18.0 mmol) was dissolved in 20 mL of dry dichloromethane and cooled in an ice bath for 20 min. Subsequently, *N*-hydroxysuccinimide (3.11 g, 27.0 mmol), dicyclohexylcarbodiimide (5.58 g, 27.1 mmol), (3-aminopropyl)triethoxysilane (6.00 g, 27.1 mmol), and 3.80 mL triethylamine were added in this order, after which the ice bath was removed. The reaction mixture was stirred for 19 h at room temperature. The resulting suspension was filtered, and the filtrate was washed twice with saturated aqueous NH_4Cl, $NaHCO_3$, and NaCl solutions. The organic phase was collected, dried over $MgSO_4$, and the solvent was removed under reduced pressure (10 mbar) at 50 °C. The product

was obtained as a colorless solid (7.73 g, yield: 67 %). The ^{1}H-NMR spectrum of BOC-BTEPSA is shown in Figure S17.

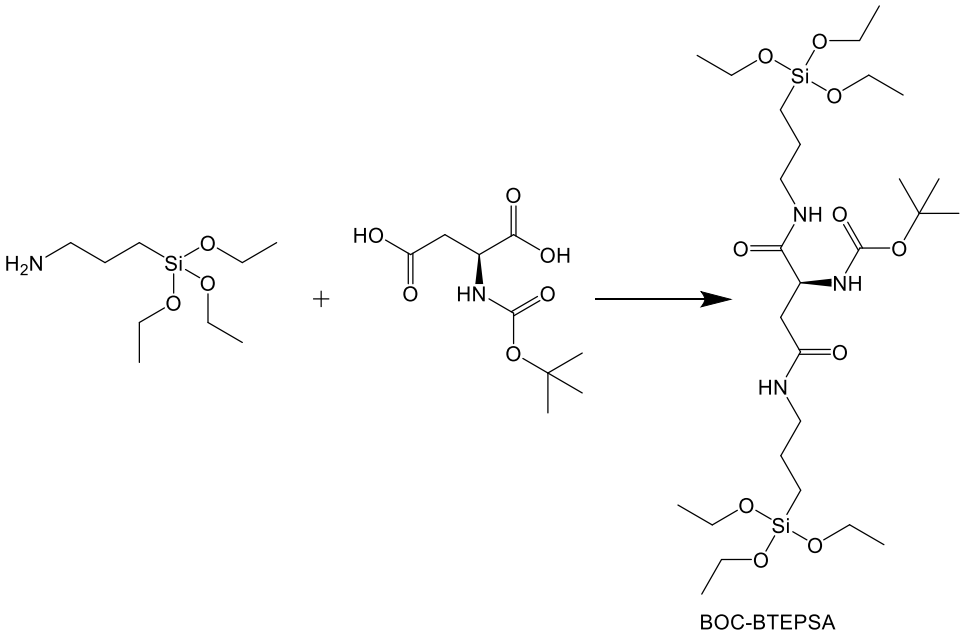


Figure S16: Synthetic route for the preparation of BOC-BTEPSA.

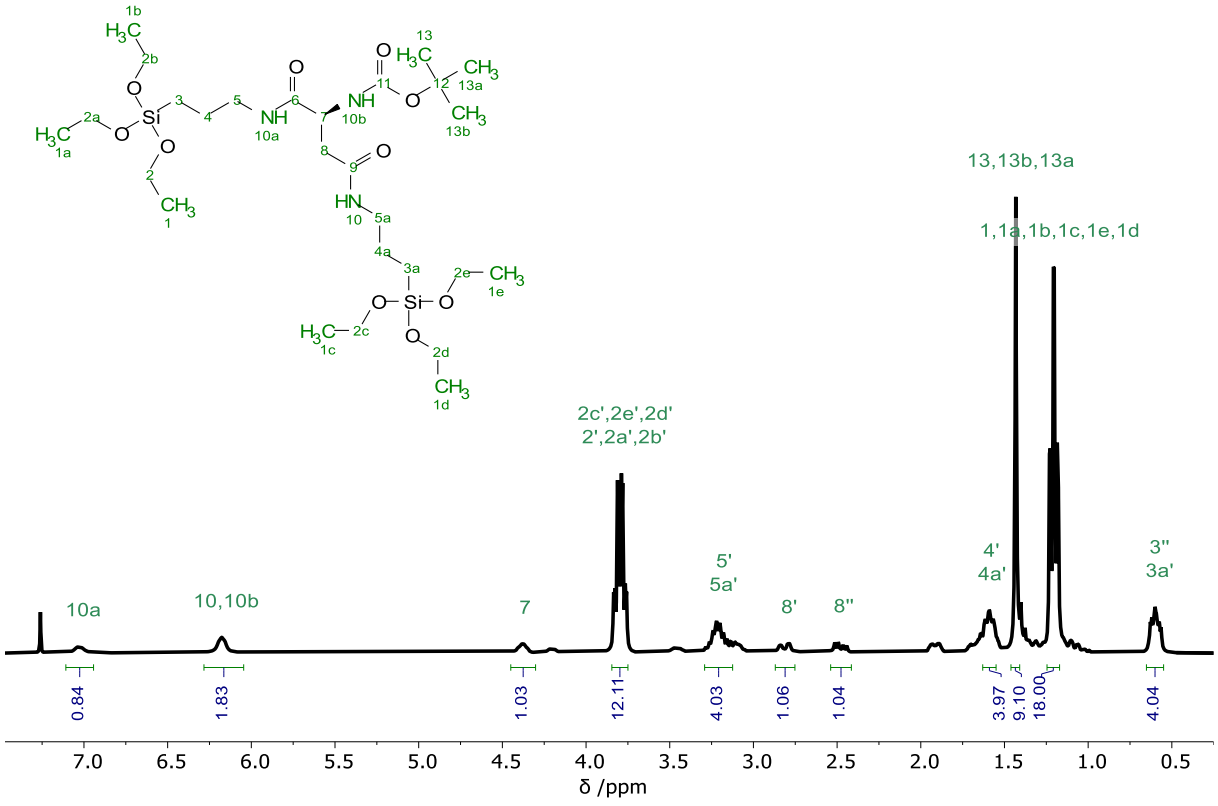


Figure S17: ^{1}H-NMR spectrum of BOC-BTEPSA.

^{1}H-NMR (300 MHz, $CDCl_3$, 25 °C): δ [ppm] = 7.03 (s, 1H), 6.18 (s, 2H), 4.46 – 4.31 (m, 1H), 3.80 (qd, *J* = 7.0, 2.3 Hz, 12H), 3.34 – 3.03 (m, 4H), 2.81 (dd, *J* = 15.3, 3.9 Hz, 1H), 2.48 (dd, *J* = 15.1, 6.4 Hz, 1H), 1.59 (p, *J* = 8.0, 6.9 Hz, 4H), 1.43 (s, 9H), 1.21 (td, *J* = 7.0, 1.8 Hz, 18H), 0.64 – 0.54 (m, 4H).

^{13}C {^{1}H}-NMR (75 MHz, $CDCl_3$, 25 °C): δ [ppm] = 171.08 (C6, C7), 80.23 (C12), 58.59+58.51 (C2), 49.24 (C7), 42.15+42.05 (C5), 37.98 (C8), 28.43 (C13), 23.01+22.82(C4), 18.41 (C1), 7.87+7.70 (C3).

FT-IR (KBr-disc): $\tilde{\nu}$ [cm^{-1}] = 3312, 2975, 2930, 2886, 1692, 1646, 1556, 1528, 1439, 1392, 1369, 1348, 1321, 1277, 1252, 1168, 1104, 1079, 1025, 957, 860, 790, 680, 659, 470.

Synthesis of BOC-BTEPSA-based PMO via co-condensation with BTEB

The synthesis of co-condensed PMOs using the precursors BOC-BTEPSA and BTEB at different ratios follows the procedure described for the BTEPA-OB(en)A-PMO synthesis (see Table S2). The only deviation was for the 60 % sample, where a molar BOC-BTEPSA–BTEB ratio of 0.50:0.29 was used, corresponding to a BOC-BTEPSA content of 63 %.

A variant of this material employing a Fmoc-protected BTEPSA precursor and TEOS as co-condensate has been reported elsewhere.[170]

The porosity and structural order of the PMOs were characterized by X-ray diffraction and nitrogen physisorption measurements (Figure S18), with key parameters summarized in Table S9. Data for the 0 % (pure BTEB-based) sample were taken from the previous BTEPA-OBenA analysis, and, except for the (00l) reflection and d_{RU} evaluation, are not provided here.

From the PXRD patterns in the range of 0.7–3.2° 2θ (Figure S18a), the materials synthesized using precursor ratios between 37 and 60 % exhibit highly ordered hexagonal pores, while samples outside this range show no distinct reflections. In the wide-angle region (5–50° 2θ, Figure S18b), the shift between the 100 % and 0 % samples is relatively small (from 10.01 to 11.33° 2θ), indicating that the repetition units of BTEPSA organize much more similarly to those of BTEB than BTEPA does.

Nitrogen physisorption isotherms and corresponding pore size distributions (Figure S18c, d) show increased porosity and type IV(a) isotherms,[158] typical for cylindrical mesoporous materials, only for samples containing 20–60 % BTEPSA. In contrast to the co-condensed PMOs presented in the previous chapter, no clear trend in pore diameter (ranging from 5.9–6.8 nm) with BTEPSA content is observed. The pore volume and specific BET surface area, however, tend to increase from 0.259 to 0.37 $cm^3\ g^{-1}$ and 222 to 450 $m^2\ g^{-1}$, respectively, with decreasing BTEPSA content. Samples with 20, 37, and 60 % BTEPSA contain an additional fraction of smaller mesopores (2–6 nm), which likely interconnect the main cylindrical pores through the pore walls and cause desorption effects characteristic of ink-bottle pores. The 50 % sample, however, lacks these secondary pores and therefore shows no indication of pore blocking or cavitation. Additionally, the absence of these interconnecting pores explains its smaller pore volume (0.244 $cm^3\ g^{-1}$) and specific BET surface area (168 $m^2\ g^{-1}$).

Due to limited sample quantities, not all materials could be characterized by every method. Those with higher porosity and pore order were, however, fully analyzed with respect to composition. From the ^{1}H-NMR spectra (Figure S19) of the 37–60 % samples, BTEPSA contents of 43, 55, and 60 % were determined, indicating that the incorporated fractions roughly reflect the synthesis compositions. TGA-DTA-MS analysis (Figure S22, Table S6) confirmed this trend. The results further show that the conditions favor co-condensation of both precursors but do not allow the formation of a pure BTEPSA PMO.

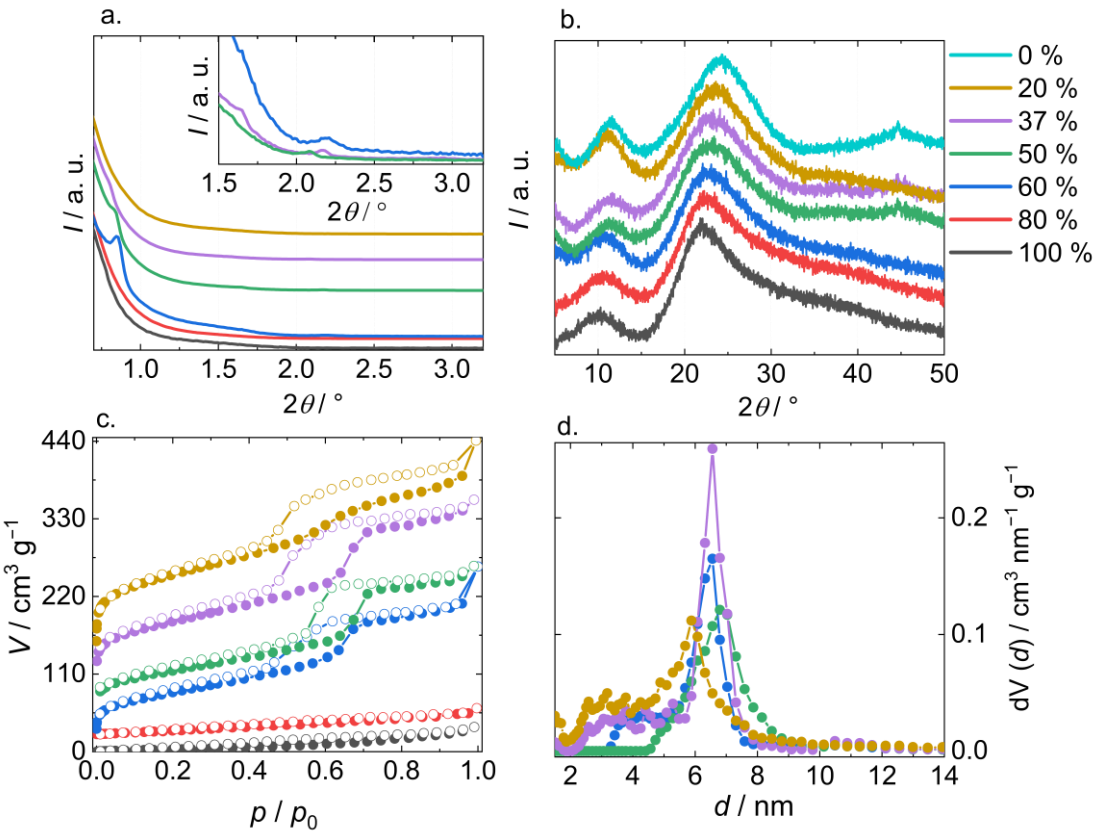


Figure S18: Porosity characterization of pure as well as co-condensed PMOs synthesized with different ratios of amide-acid precursor, using BOC-BTEPSA and BTEB as precursor: a. normalized X-ray powder diffractograms in the range 0.7–3.2° 2θ with an inset showing the range 1.5–3.5° 2θ, b. 5–50° 2θ, c. nitrogen physisorption isotherms at 77 K, showing the adsorption branch (filled circles) and desorption branch (hollow circles), and d. the corresponding pore size distribution curves, calculated using the NLDFT kernel: N_2 at 77 K on silica, cylindr. pores, at adsorption branch. The isotherms (c.) are shifted vertically along the Y-axis by a value of 25 cm^3g^{-1}.

The absence of the BOC-protecting group signals in the ^{1}H-NMR spectra indicates successful deprotection under the acidic synthesis conditions. In the IR spectra (Figure S21), the characteristic amide bands are clearly visible and increase in intensity with higher BTEPSA content, confirming the integrity of the amide functionality. As observed for the previous co-condensed materials, the TGA curves (Figure S22) show two distinct mass-loss steps. The first, at a lower temperature, corresponds to the decomposition of the BTEPSA bridge, which is thermally less stable than the amide–acid co-condensates (BTEPA-OBA or BTEPA-OBenA). This is followed by the decomposition of the BTEB bridge.

Despite applying the co-condensation approach, modified synthesis conditions were tested to obtain a homopolymeric BTEPSA-PMO. None of the syntheses performed under acidic conditions using surfactants such as P123, cetylpyridinium chloride, or F127 resulted in the formation of a porous BTEPSA-PMO. The long and flexible

BTEPSA bridge likely lacks sufficient rigidity to maintain the ordered PMO structure and may collapse during surfactant or solvent removal. Attempts using a pseudomorphic transformation[301] approach with CTAB at pH 13.75–14 led to the complete removal of the organic bridge, leaving behind a purely siliceous mesoporous material.

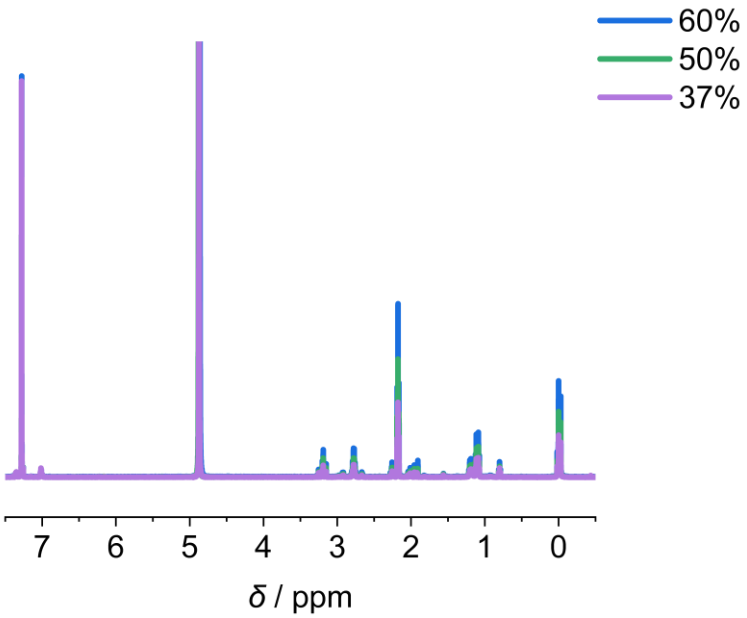


Figure S19: ^{1}H-NMR (600 MHz) spectra of PMOs synthesized with different BOC-BTEPSA precursor contents in co-condensation with BTEB. The resulting materials were dissolved in 1 M NaOD/D_2O.

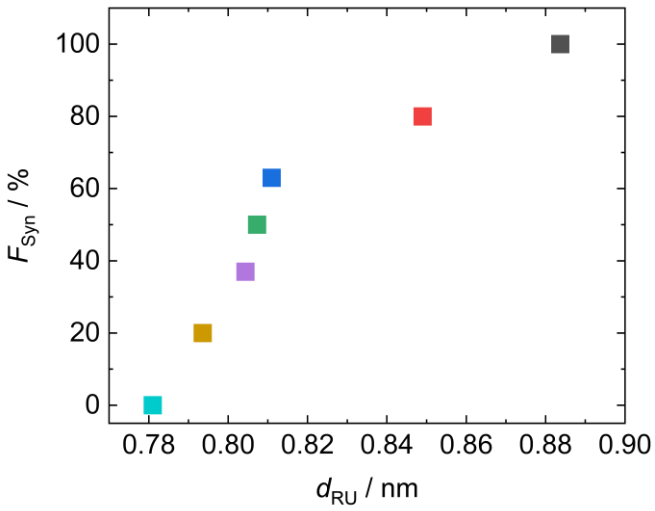


Figure S20: Dependence of the average PMO repeating-unit length (d_{RU}), derived from the (00l) reflection, on the used BOC-BTEPSA precursor contents (F_{Syn}) in co-condensation with BTEB.

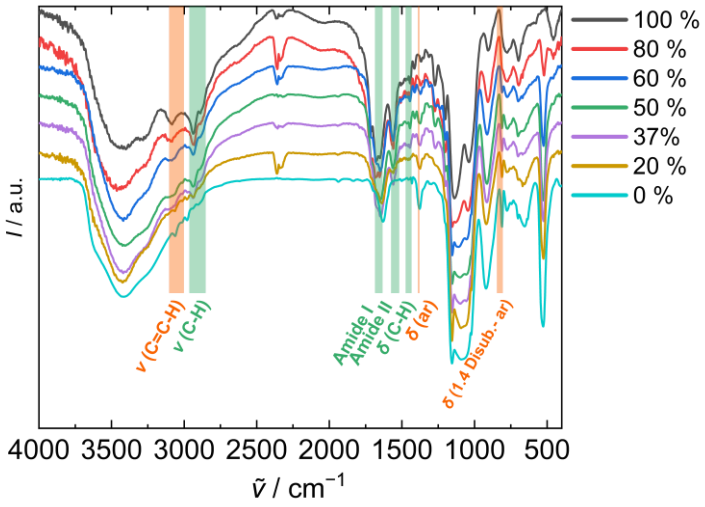


Figure S21: FT-IR spectra (KBr-disc) of PMOs synthesized with different BOC-BTEPSA precursor contents in co-condensation with BTEB.

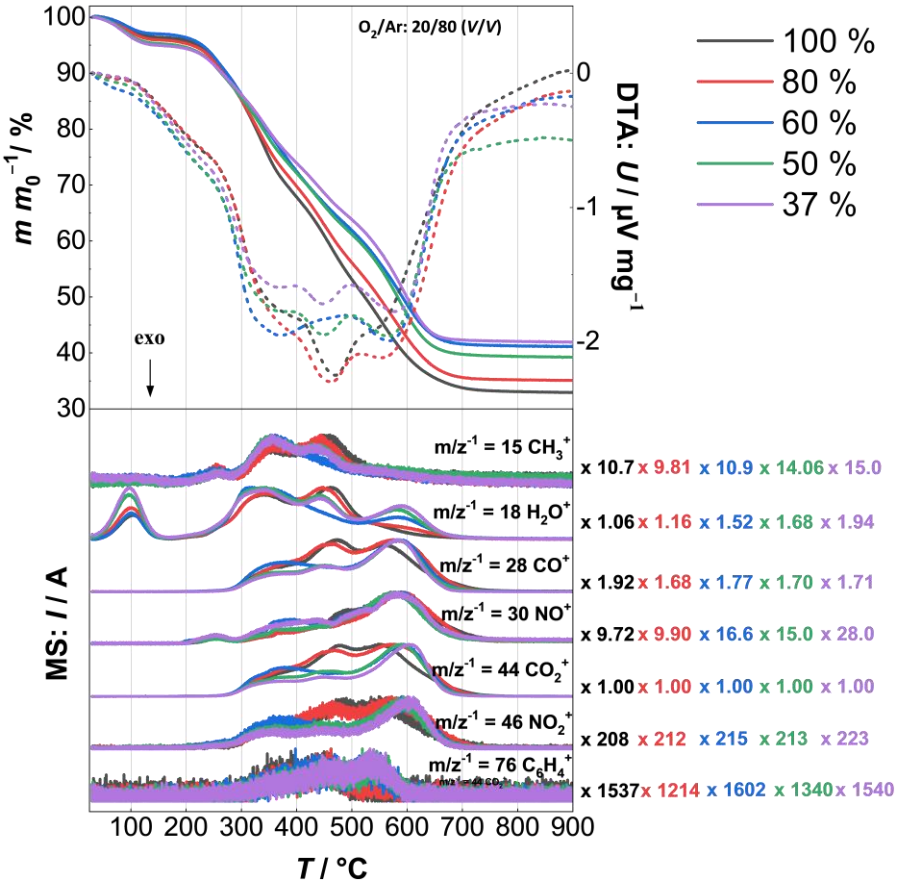


Figure S22: TGA-DTA-MS analysis of PMOs synthesized with different BOC-BTEPSA precursor contents in co-condensation with BTEB. Measurements were performed at a heating rate of 10 $Kmin^{-1}$ under an O_2/Ar atmosphere (20/80 (*V*/*V*)).

Table S6: Extracted data from TGA-DTA-MS analysis, including the relative mass loss of surface-adsorbed water in the range 30–150 °C ($\Delta(m_w\, m_0^{-1})$), the relative mass loss of the organic bridge combustion excluding adsorbed water content ($\Delta(m_{org}\, m_0^{-1})$), the functionalization degree (F), calculated directly from $\Delta(m_{org}\, m_0^{-1})$ for individual samples (iPMO) or based on the relative mass loss of homopolymeric PMOs (hpPMO) under the assumptions of complete deprotection (cd) and with the BOC protection group remaining (BOC). Combustion temperatures were determined from the onsets ($T_{on,1}$, $T_{on,2}$) and endset (T_{end}), as well as the temperature at which $\Delta(m_{org}\, m_0^{-1})$ reaches 50 % (T_{50}).

BOC-BTEPSA precursor content	$\Delta(m_w\, m_0^{-1})$ / %	$\Delta(m_{org}\, m_0^{-1})$ / %	F iPMO/ hpPMO [cd (BOC)] / %	$T_{on,1}$ ($T_{on,2}$) / °C	T_{50}	T_{end} / °C
100 %	3.55	65.8	100 (0)	228 (-)	426	635
80 %	4.03	63.4	76 (44) / 84 (80)	228 (536)	432	649
60 %	3.01	57.6	48 (30) / 54 (47)	228 (541)	428	644
50 %	4.69	58.8	53 (31) / 59 (53)	227 (543)	442	640
37 %	4.97	55.8	40 (23) / 46 (39)	227 (454)	450	640
20 %	-	-	-	-	-	-
0 %	8.43	40.7	0 / -	542	592	649

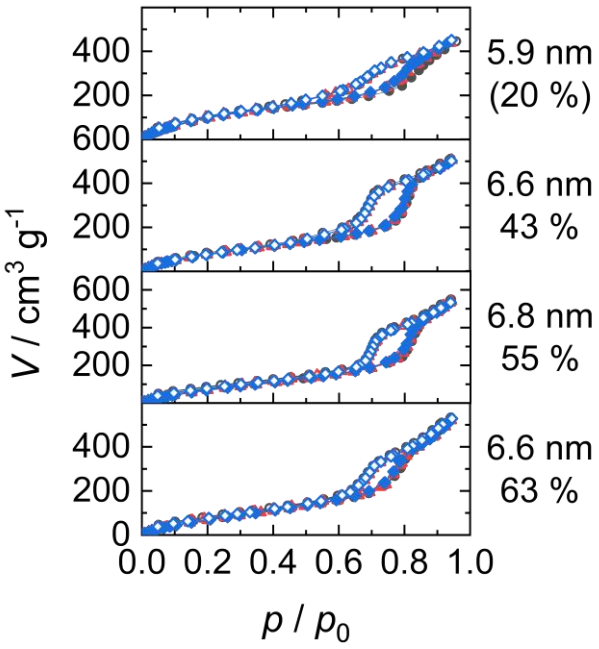
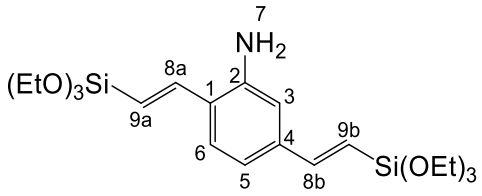


Figure S23: Water vapor sorption isotherms at 25 °C showing the adsorption branch (filled circles) and desorption branch (hollow circles) for PMOs co-condensed with BTEB and BOC-BTEPSA precursors at different ratios. Also shown are the corresponding pore diameters, determined from nitrogen physisorption using NLDFT, and the content of BTEPSA, as determined by ^{1}H NMR analysis. The value in brackets corresponds to the precursor amount used for synthesis, provided due to insufficient sample quantity for NMR characterization.

8.3.3. BTEVA-Based Bifunctional Amide–Acid PMOs

Purification of BTEVA precursor

For functionalization, the BTEVA precursor must be of high purity. Therefore, after synthesizing the BTEVA precursor according to the procedure reported in the literature,[302] purification was performed by column chromatography (*n*-hexane/ethyl acetate = 4:1). High purity is only relevant for the precursor functionalization, since during PMO synthesis, any remaining impurities are removed or washed out, as evident from the NMR spectra of hydrolyzed BTEVA-PMOs.[62] A comparison of the ^{1}H- and ^{13}C-NMR spectra of the crude and purified precursor is shown in Figure S24. Based on the purified BTEVA NMR spectra and additional 2D NMR measurements, a clear signal assignment can be made:



^{1}H-NMR (600 MHz, DMSO-d$_6$, 25 °C): δ [ppm] = 7.37 (d, J = 8.1 Hz, 1H, H6), 7.29 (d, J = 19.1 Hz, 1H, H9a), 6.97 (d, J = 19.2 Hz, 1H, H9b), 6.84 (d, J = 1.8 Hz, 1H, H3), 6.77 (dd, J = 8.1, 1.7 Hz, 1H, H5), 6.08 (d, J = 19.2 Hz, 1H, H8a), 5.99 (d, J = 19.1 Hz, 1H, H8b), 5.27 (s, 2H, H7), 3.81+3.80 (q, J = 7.0 Hz, 12H, CH$_3$-C**H**$_2$-O), 1.19+1.18 (t, J = 7.0 Hz, 18H, **C**H$_3$-CH$_2$-O).

^{13}C {^{1}H}-NMR (75 MHz, DMSO-d$_6$, 25 °C): δ [ppm] = 148.46 (C9b), 146.54 (C2), 143.49 (C9a), 137.97 (C4), 126.29 (C6), 122.38 (C1), 117.35 (C8a), 116.29 (C8b), 115.19 (C5), 114.41 (C3), 57.92+57.87 (CH$_3$-**C**H$_2$-O), 18.18+18.16 (**C**H$_3$-CH$_2$-O).

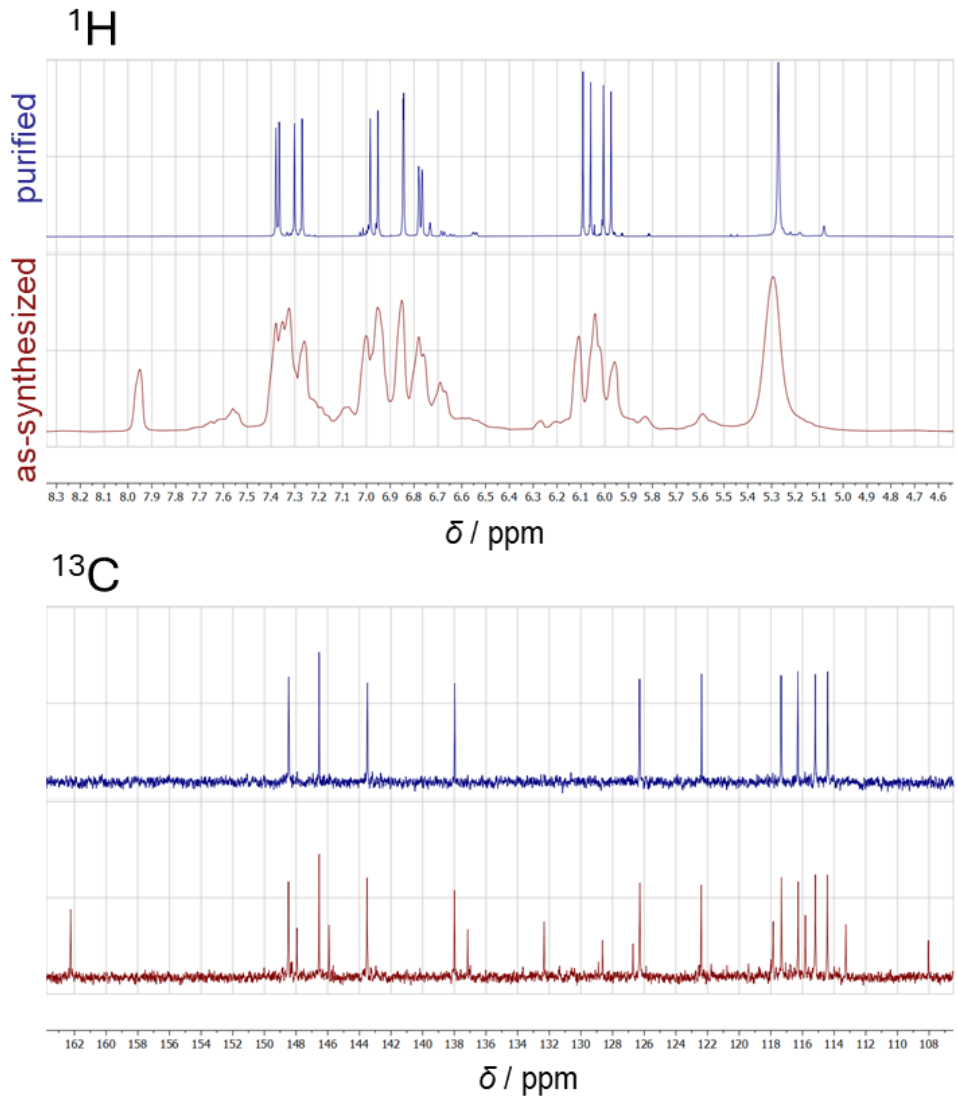
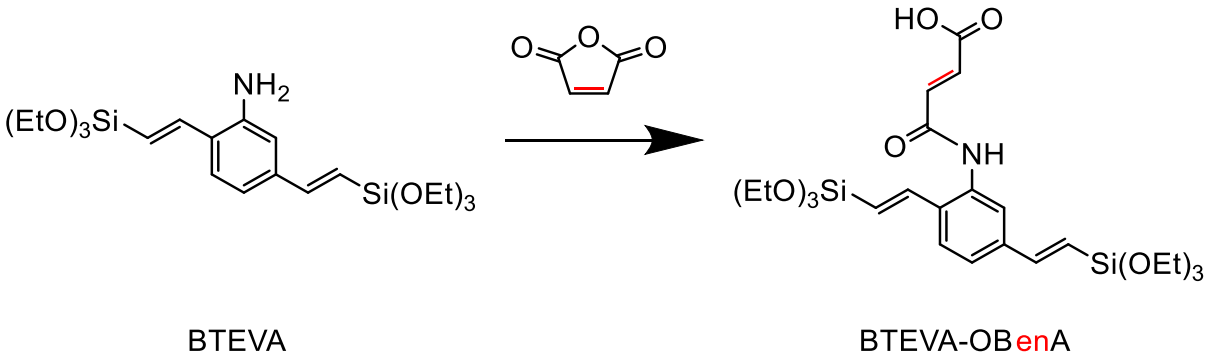


Figure S24: Comparison of the ^{1}H-NMR and ^{13}C-NMR spectra of BTEVA before and after purification by column chromatography (*n*-hexane/ethyl acetate = 4:1), recorded in DMSO-d_6 at 25 °C.

Synthesis of BTEVA-OBA and -OBenA precursor

The synthesis of BTEVA-OBA, -OBenA follows the procedure described for the BTEPA-OB(en)A precursor synthesis.



BTEVA BTEVA-OBenA

Figure S25: Synthetic routes for BTEVA-OBenA and BTEVA-OBA.

BTEVA-OBenA:

^{1}H-NMR (300 MHz, DMSO-d$_6$, 25 °C): 13.35 (s, 1H), 10.32 (s, 1H), 7.78 (d, *J* = 8.2 Hz, 1H), 7.57 – 7.42 (m, 2H), 7.26 (d, *J* = 19.3 Hz, 1H), 7.11 (d, *J* = 19.4 Hz, 1H), 6.57 (d, *J* = 12.2 Hz, 1H), 6.35 (d, *J* = 12.1 Hz, 1H), 6.27 (d, *J* = 19.3 Hz, 1H), 6.26 (d, *J* = 19.3 Hz, 1H), 3.81+3.80 (q, *J* = 7.0 Hz, 12H), 1.19+1.17 (td, *J* = 7.0 Hz, 18H).

^{13}C {^{1}H}-NMR (75 MHz, DMSO-d$_6$, 25 °C): 166.50 (C13), 164.27 (C10), 147.13 (C9b), 142.90 (C9a), 137.75 (C2), 134.88 (C4), 132.80 (C1), 131.64 (C11), 130.99 (C12), 126.02 (C6), 125.21 (C3), 124.90 (C5), 120.19+119.43 (C8a+8b), 58.01 (CH_3-**C**H_2-O), 18.19 (**C**H_3-CH_2-O).

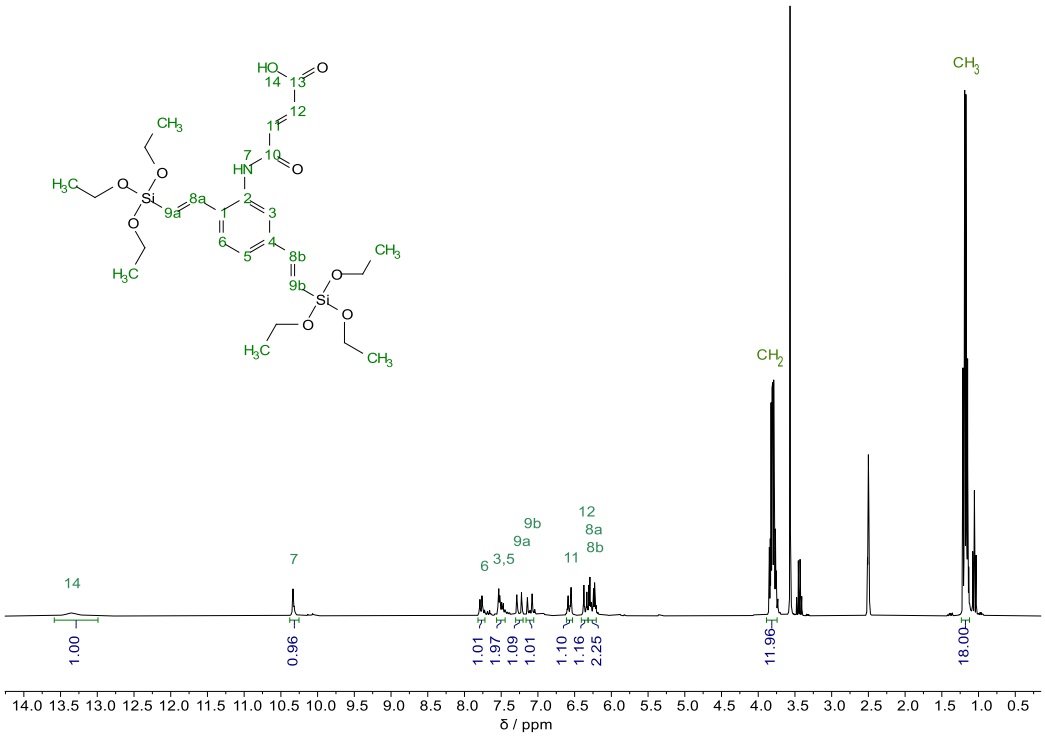


Figure S26: ^{1}H-NMR spectrum of BTEVA-OBenA in DMSO-d_6.

FT-IR (KBr-disc): $\tilde{\nu}$ [cm^{-1}] = 3441, 3274, 2976, 2928, 2891, 1711, 1631, 1603, 1562, 1541, 1484, 1391, 1296, 1259, 1218, 1197, 1167, 1105, 1078, 992, 960, 889, 831, 796, 609, 519, 475.

BTEVA-OBA:

^{1}H-NMR (300 MHz, DMSO-d_6, 25 °C): 12.13 (s, 1H), 9.76 (s, 1H), 7.73 (d, *J* = 8.7 Hz, 1H), 7.49 – 7.41 (m, 2H), 7.26 (d, *J* = 19.4 Hz, 1H), 7.09 (d, *J* = 19.3 Hz, 1H), 6.23 (d, *J* = 19.2 Hz, 1H), 3.81 (qd, *J* = 7.0, 0.5 Hz, 13H), 2.56 (dd, *J* = 14.8, 5.5 Hz, 3H), 1.18 (t, *J* = 7.0 Hz, 18H).

Further signals: *δ* [ppm] = 3.57 (1,4-Dioxane).

^{13}C {^{1}H}-NMR (75 MHz, DMSO-d_6, 25 °C): 173.68 (C13), 170.57 (C10), 147.26 (C9b), 143.21 (C9a), 137.60 (C2), 135.87 (C4), 132.72 (C1), 125.87 (C6), 125.39 (C5), 124.18 (C3), 119.54+119.06 (C8a+8b), 57.98(CH_3-**C**$\mathbf{H_2}$-O), 18.18 (**C**$\mathbf{H_3}$-CH_2-O).

Further signals: *δ* [ppm] = 66.35 (1,4-Dioxane).

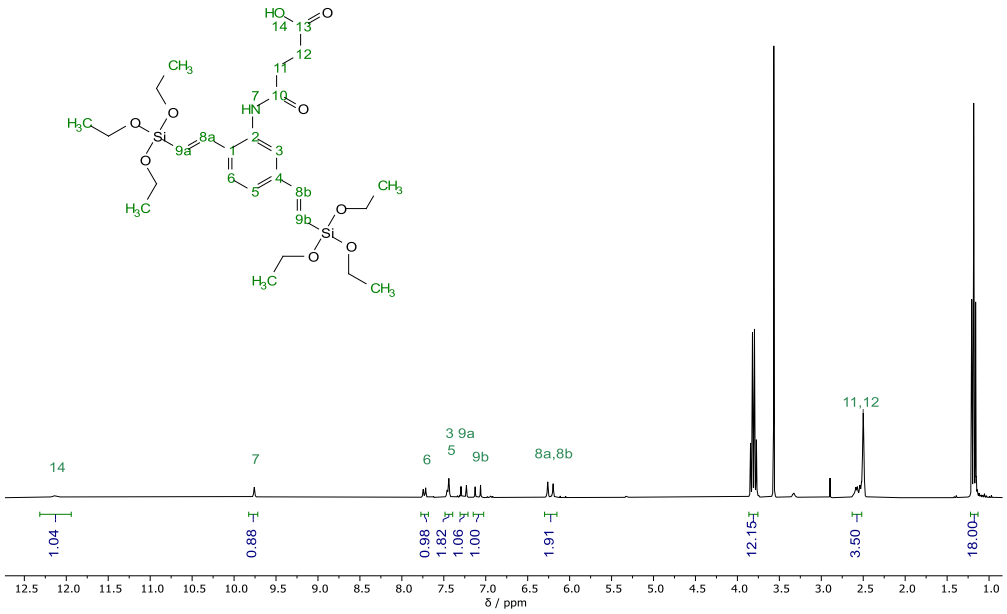


Figure S27: ^{1}H-NMR spectrum of BTEVA-OBA in DMSO-d_6.

FT-IR (KBr-disc): $\tilde{\nu}$ [cm^{-1}] = 3448, 3229, 3190, 2976, 2886, 1730, 1650, 1607, 1563, 1537, 1485, 1424, 1391, 1346, 1294, 1260, 1242, 1168, 1104, 1079, 988, 960, 831, 769, 666, 507, 481.

Synthesis of BTEVA-OBA-, BTEVA-OBenA-, and Cbz-BTEVA–aspartic acid (AA)-based PMOs

BTEVA-OBenA-PMO:

PMO synthesis:

The surfactant C_{16}TAB (0.343 g, 0.941 mmol) and NaOH (0.203 g, 5.07 mmol) were dissolved in demineralized water at 31 °C for 30 min. Then the solution was stirred for an additional 30 min at room temperature before the BTEVA-OBenA precursor (0.500 g, 0.878 mmol) was added. The reaction mixture was stirred for 20 h at room temperature, followed by hydrothermal treatment at 95 °C for 24 h. After cooling to room temperature, the product was filtered and washed with 200 mL of demineralized water and 50 mL of ethanol. The surfactant was removed by Soxhlet extraction using a 37 wt% ethanol-HCl solution (*V*/*V*; 98:2). Finally, the product was dried at 80 °C.

The resulting PMO exhibits a hexagonally ordered pore structure with a crystal-like pore wall organization, a narrow pore size distribution, and a pore diameter of 3.8 nm (see Figure S28, Table S10). Based on NMR and TGA-MS analyses, the

functionalization degree was estimated to be between 13 % and 18 %. The infrared spectra (Figure S29) also show a reduction in the characteristic OBenA bands (e.g., the carboxylic acid band) after synthesis. Together, these results indicate that the alkaline synthesis conditions led to partial cleavage of the amide bond, resulting in a reduced functionalization degree. To improve the degree of functionalization, optimization of the synthesis parameters, such as lowering the pH or reducing the synthesis temperature, should be considered.

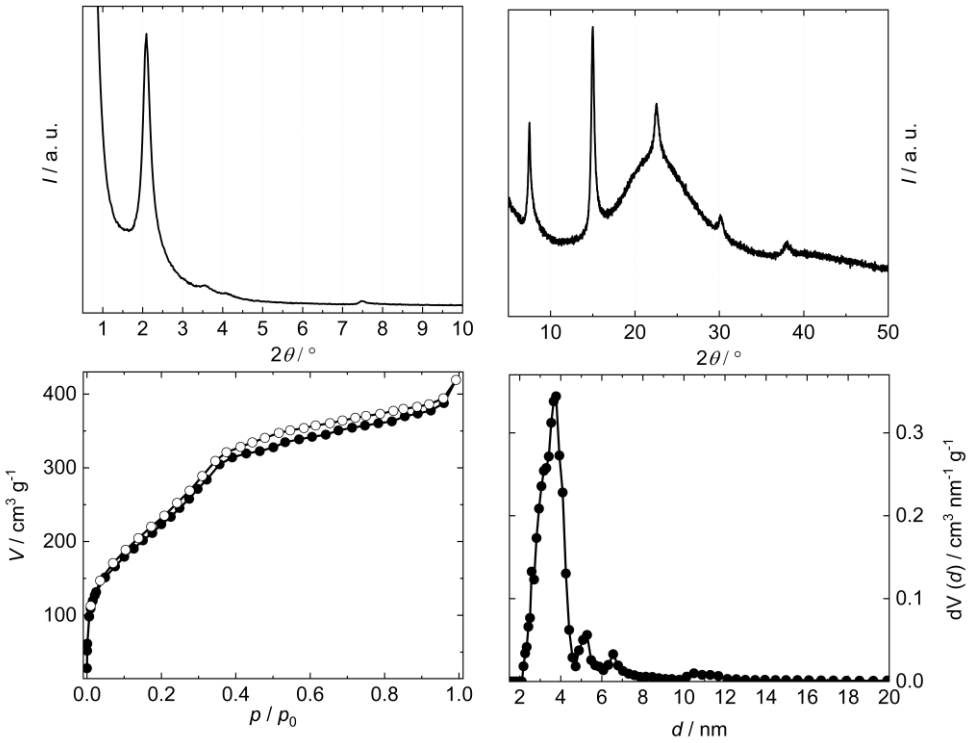


Figure S28: Normalized X-ray powder diffractograms in the range 0.5–10° 2θ (top, left) and 5–50° 2θ (top, right), nitrogen physisorption isotherm at 77 K (bottom, left), showing the adsorption branch (filled circles) and desorption branch (hollow circles), as well as the corresponding pore size distribution curve of a BTEVA-OBenA-PMO (bottom, right), calculated using the NLDFT kernel: N_2 at 77 K on silica, cylindr. pores, at adsorption branch.

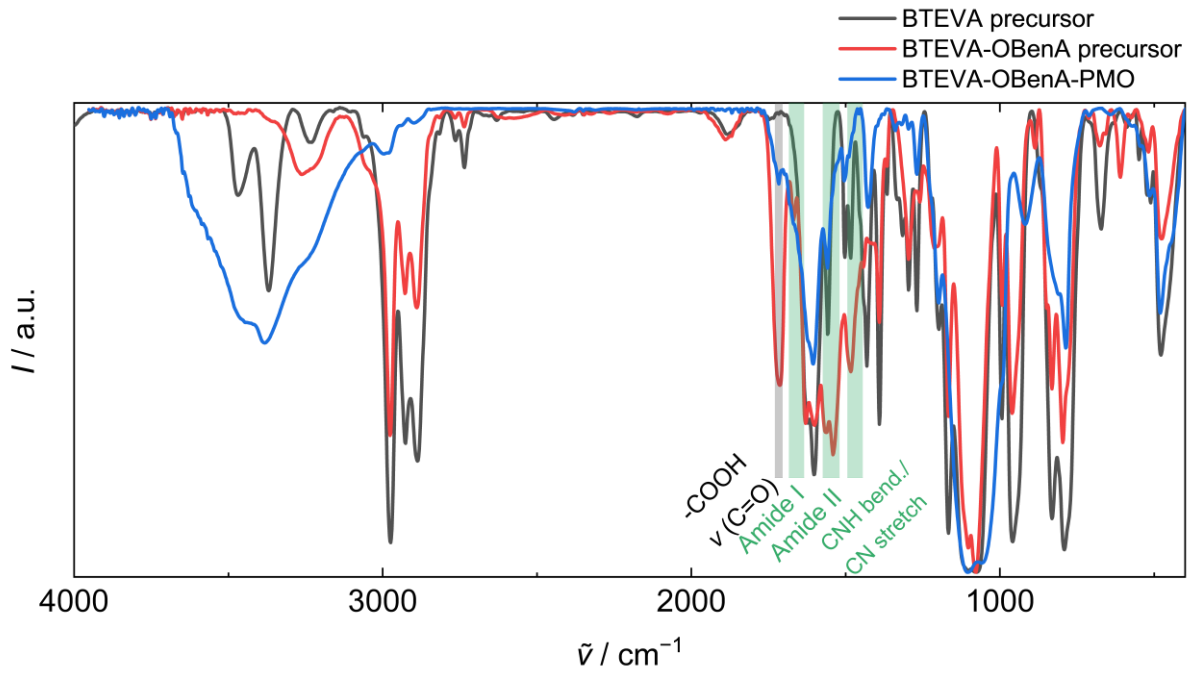


Figure S29: Comparison of the FT-IR spectra (KBr disc) of BTEVA-OBenA-PMO, the corresponding precursor, and the unfunctionalized BTEVA precursor.

Post-synthetic functionalization:

The synthesis was carried out using the Schlenk technique under a nitrogen atmosphere. For the functionalization, maleic anhydride (0.951 g, 9.70 mmol) was dissolved in 2.4 mL of 1,4-dioxane and added to the BTEVA-PMO (200 mg) samples with pore diameters of 3.2 nm or 4.4 nm. The suspension was stirred at room temperature overnight. The resulting solid was collected by filtration, washed thoroughly with 1,4-dioxane, and dried overnight under ambient conditions and subsequently at 80 °C.

Both resulting PMOs exhibit ordered mesopores and a crystal-like arrangement of the organic bridging units within the pore walls, along with narrow pore-size distributions centered at 3.1 and 4.1 nm (see Figure S30, Table S10). Due to the post-synthetic functionalization, the pore diameters decreased by 0.1 nm and 0.3 nm relative to the initial values of 3.2 and 4.4 nm, respectively. From the ^{1}H-NMR spectra of the PMOs dissolved in 1 M NaOD/ D_2O, two species were identified. The dominant signals correspond to the unfunctionalized BTEVA-PMO, while a second set of signals can be attributed to the BTEVA-OBenA species, showing downfield shifts (higher ppm), particularly for the protons of the trisubstituted benzene ring. Additionally, free maleic acid was detected, likely resulting from partial cleavage of the amide bond under the

alkaline dissolution conditions. The IR spectra (Figure S32) confirmed both material integrity and successful functionalization, showing characteristic bands for carboxylic acid and amide groups with higher intensities compared to materials synthesized by the conventional PMO route. Functionalization degrees determined from ^{1}H-NMR and TGA-DTA-MS (Figure S33, Table S7) both indicate higher functionalization for the sample with the larger pore diameter. Based on NMR, functionalization degrees F_{NMR} of 52 % and 40 % were obtained for samples with pore diameters of 4.1 nm and 3.2 nm, respectively. TGA-DTA-MS analysis of the BTEVA-OBenA-PMOs revealed two distinct mass-loss steps: the first ($T_{on,1}$ ≈ 155 °C) likely corresponding to the OBenA component, and the second ($T_{on,2}$ ≈ 410 °C) associated with the BTEVA organic framework decomposition. The increased amounts of surface-adsorbed water observed for the functionalized PMOs indicate enhanced hydrophilicity.

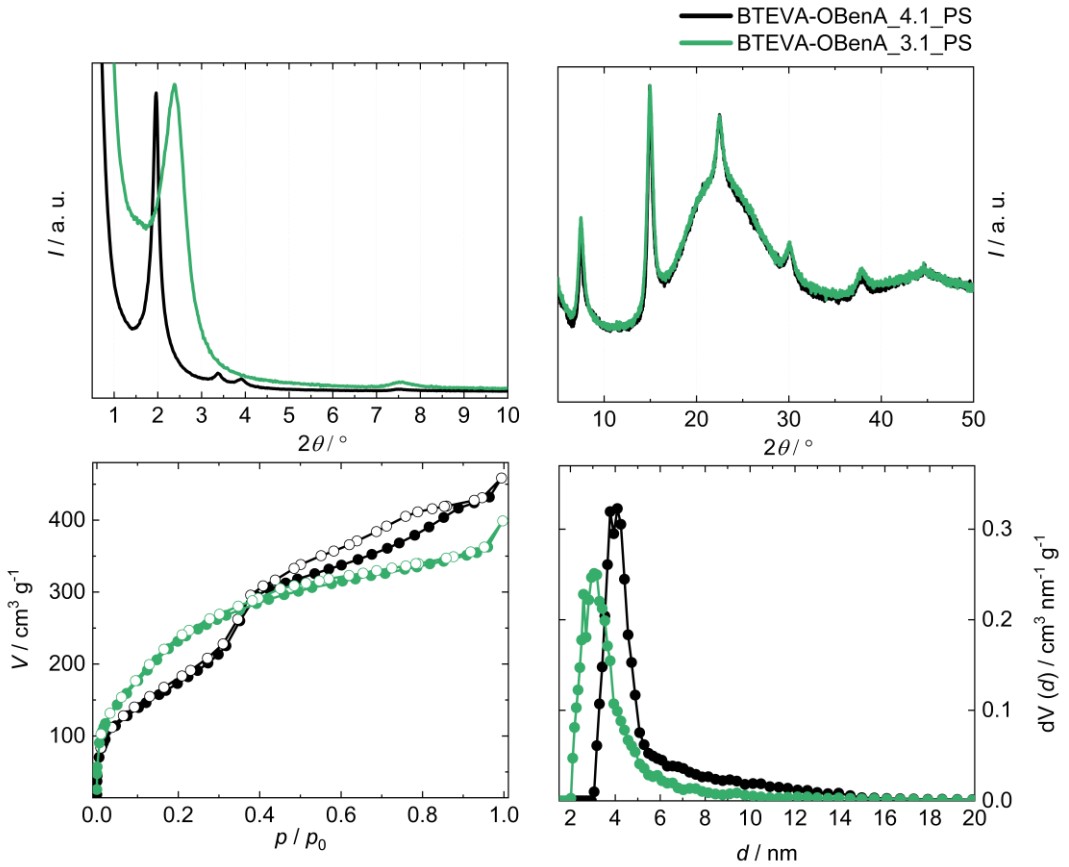


Figure S30: Normalized X-ray powder diffractograms in the range 0.5–10° 2θ (top, left) and 5–50° 2θ (top, right), nitrogen physisorption isotherms at 77 K (bottom, left), showing the adsorption branch (filled circles) and desorption branch (hollow circles), as well as the corresponding pore size distribution curves of the post-synthetic functionalized BTEVA-OBenA-PMOs (bottom, right), calculated using the NLDFT kernel: N_2 at 77 K on silica, cylindr. pores, at adsorption branch.

^{1}H-NMR (600 MHz, 1M NaOD/D_2O, 25 °C): 7.24 (d, *J* = 8.2 Hz, 1H, H6), 6.85 (dd, *J* = 8.2 Hz, 1.2 Hz, 1H, H5), 6.67 (m, 1H, H3), 6.63+6.54 (d, *J* = 19.3+19.4 Hz, 2H, H8a+b), 6.03+5.97 (d, *J* = 19.4+19.4 Hz, 2H, H9a+b), 5.79+5.75 (d, *J* = 12.2+12.2 Hz, 2H, H11+12).

Further signals: *δ* [ppm] = 5.59 (s, Maleic acid).

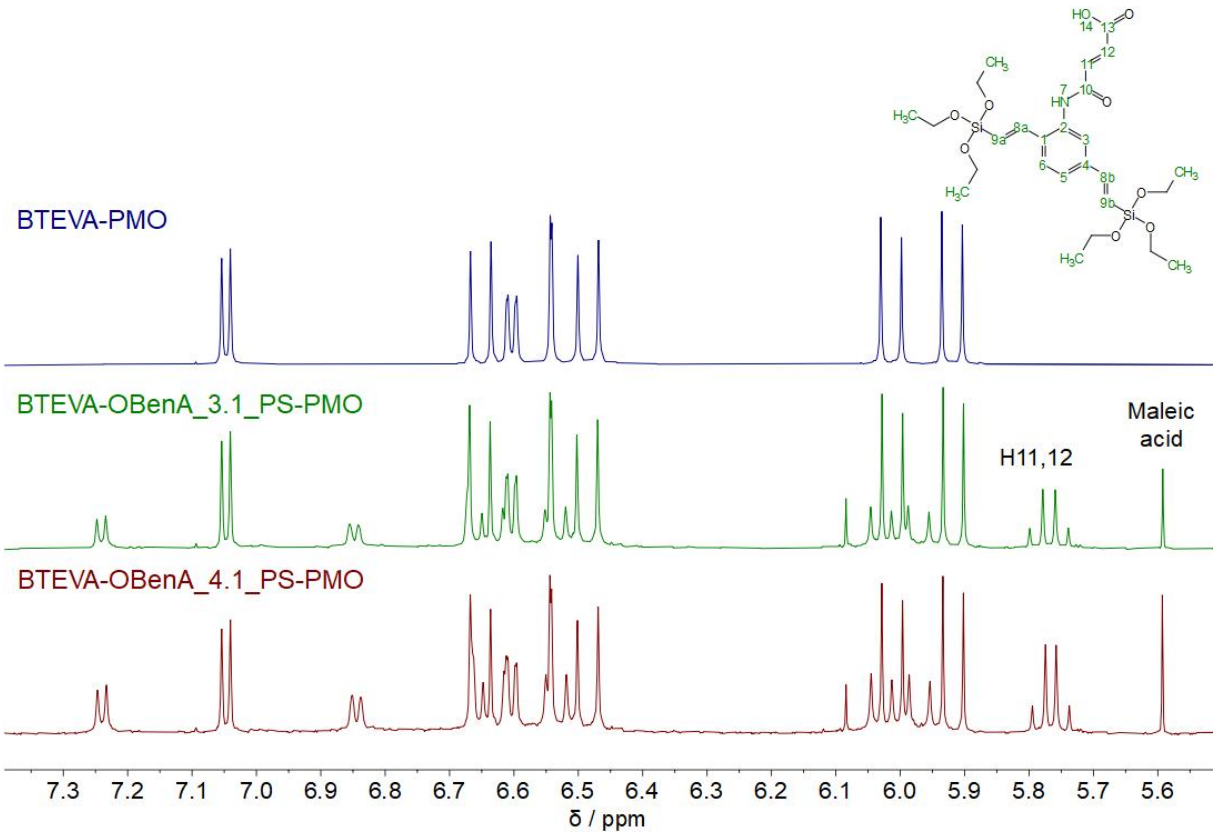


Figure S31: Comparison of the ^{1}H-NMR (600 MHz) spectra of BTEVA-PMO and post-synthetically functionalized BTEVA-OBenA-PMOs with two different pore diameters (3.1 and 4.1 nm). All materials were dissolved in 1 M NaOD/D_2O.

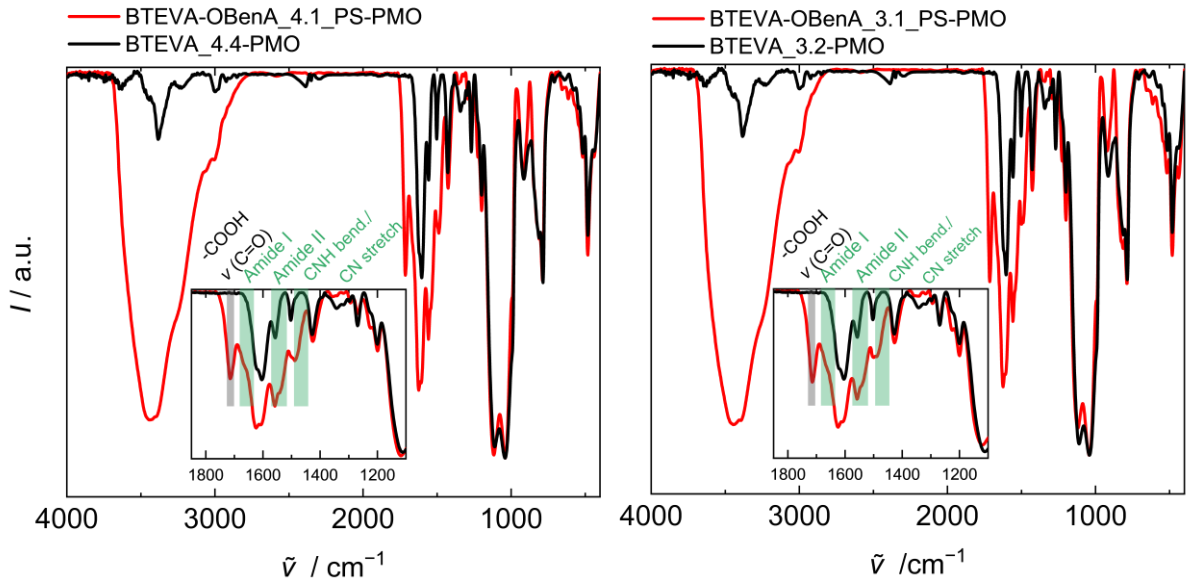


Figure S32: Comparison of the FT-IR spectra (KBr disc) of BTEVA-PMO and its post-synthetically functionalized forms (BTEVA-OBenA-PMOs) with pore diameters of 4.1 nm (left) and 3.1 nm (right). Insets highlight the relevant spectral regions and bands.

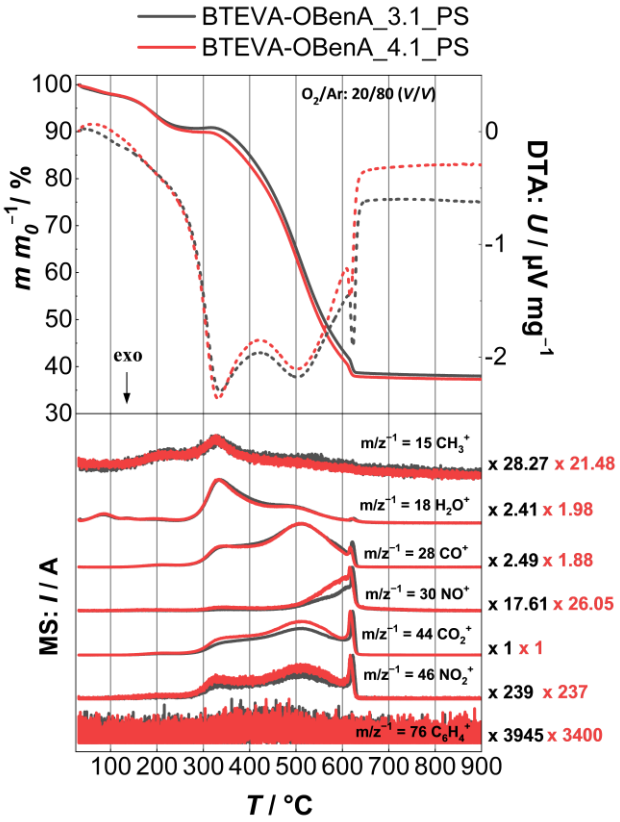


Figure S33: TGA-DTA-MS analysis of BTEVA-OBenA-PMOs with pore diameters of 4.1 nm and 3.1 nm functionalized via post-synthetic approach. Measurements were performed at a heating rate of 10 Kmin^{-1} under an O_2/Ar atmosphere (20/80 (*V*/*V*)).

Table S7: Extracted data from TGA-DTA-MS analysis, including the relative mass loss of surface-adsorbed water in the range 30–150 °C ($\Delta(m_w\, m_0^{-1})$), the relative mass loss of the organic bridge combustion excluding adsorbed water content ($\Delta(m_{org}\, m_0^{-1})$), and the functionalization degree (F), calculated directly from $\Delta(m_{org}\, m_0^{-1})$ considering the mass loss of the unfunctionalized BTEVA-PMO precursor (P), as well as the functionalization degree derived from the mass loss between 150–300 °C attributed to the OBenA moiety (FA). Combustion temperatures were determined from the onsets ($T_{on,1}$, $T_{on,2}$) and endset (T_{end}), as well as the temperature at which $\Delta(m_{org}\, m_0^{-1})$ reaches 50 % (T_{50}).

Sample	$\Delta(m_w\, m_0^{-1})$ / %	$\Delta(m_{org}\, m_0^{-1})$ / %	F_P (F_{FA}) / %	$T_{on,1}$ ($T_{on,2}$) / °C	T_{50}	T_{end} / °C
BTEVA_3.2	2.26	52.85	0	- (424)	511	626
BTEVA_4.4	1.95	53.11	0	- (419)	507	620
BTEVA-OBenA_3.1_PS	3.17	60.67	50 (25)	152 (407)	492	626
BTEVA-OBenA_4.1_PS	3.23	61.43	53 (28)	160 (406)	486	623

BTEVA-OBA:

PMO synthesis:

C_{16}TAB (0.686 g, 1.88 mmol) and NaOH (0.324 g, 8.11 mmol) were dissolved in demineralized water at 31 °C for 30 min. The solution was then stirred for an additional 30 min at room temperature before the BTEVA-OBA precursor (1.00 g, 1.75 mmol) was added. The reaction mixture was stirred for 20 h at room temperature, followed by hydrothermal treatment at 95 °C for 24 h. After cooling to room temperature, the product was filtered and washed with 200 mL of demineralized water and 50 mL of ethanol. The surfactant was removed by Soxhlet extraction using a 37 wt% ethanol-HCl solution (*V*/*V*; 98:2). Finally, the product was dried at 80 °C.

Based on the porosity characteristics shown in Figure S34, the synthesis of PMOs using the BTEVA-OBA precursor requires further optimization to achieve higher pore ordering, a narrower pore-size distribution, and a crystal-like pore wall arrangement. Adjustments to the synthesis parameters, such as increasing the pH to neutralize the carboxylic acid or modifying the surfactant concentration, should be considered to improve the structural quality of the material.

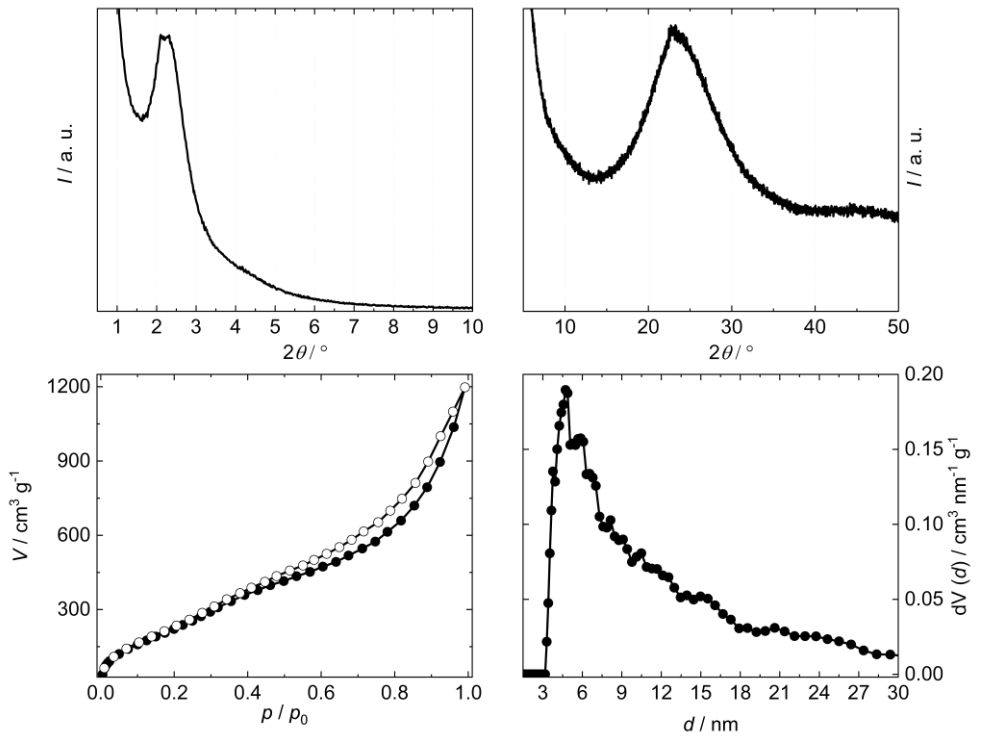


Figure S34: Normalized X-ray powder diffractograms in the range 0.5–10° 2θ (top, left) and 5–50° 2θ (top, right), nitrogen physisorption isotherm at 77 K (bottom, left), showing the adsorption branch (filled circles) and desorption branch (hollow circles), as well as the corresponding pore size distribution curve of the BTEVA-OBA-PMO (bottom, right), calculated using the NLDFT kernel: N_2 at 77 K on silica, cylindr. pores, at adsorption branch.

Post-synthetic functionalization:

The synthesis was carried out using the Schlenk technique under a nitrogen atmosphere. For the functionalization, succinic anhydride (52.6 mg, 0.526 mmol) was dissolved in 2.5 mL of 1,4-dioxane and added to the BTEVA-PMO (100 mg) with a pore diameter of 4.4 nm. The suspension was stirred at room temperature overnight, after which the solid was filtered, washed with 1,4-dioxane, and dried first overnight under ambient conditions and subsequently at 80 °C.

Using the post-synthetic approach, the material remains highly porous, with ordered pores and a narrow pore-size distribution (see Figure S35). A comparison of the BTEVA-PMO with the post-synthetically treated material shows no major spectral differences, apart from a weak band at 1721 cm^{-1} indicating the presence of –COOH groups, suggesting a low degree of functionalization. Increasing the succinic anhydride concentration, reaction temperature, or reaction time could enhance the extent of functionalization.

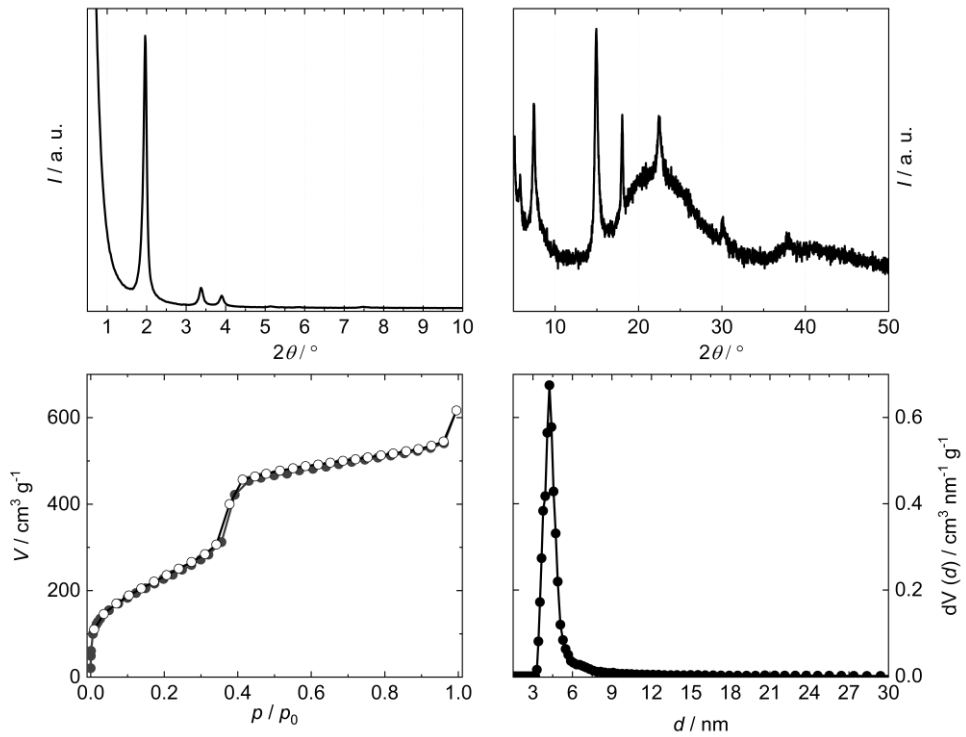


Figure S35: Normalized X-ray powder diffractograms in the range 0.5–10° 2θ (top, left) and 5–50° 2θ (top, right), nitrogen physisorption isotherm at 77 K (bottom, left), showing the adsorption branch (filled circles) and desorption branch (hollow circles), as well as the corresponding pore size distribution curve of the post-synthetic functionalized BTEVA-OBA-PMO (bottom, right), calculated using the NLDFT kernel: N_2 at 77 K on silica, cylindr. pores, at adsorption branch.

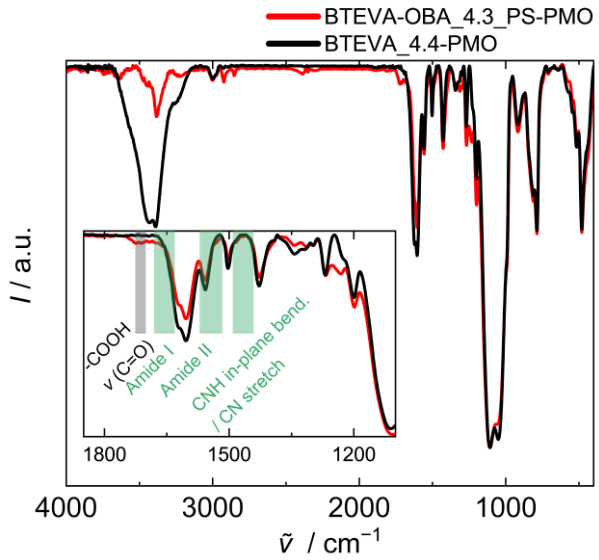


Figure S36: Comparison of the FT-IR spectra (KBr disc) of BTEVA-PMO and its post-synthetically functionalized form (BTEVA-OBA-PMOs) with pore diameters of 4.3 nm. The inset highlights the relevant spectral region and characteristic bands.

Pseudomorphic transformation:

Since neither the classical soft-templated PMO synthesis nor the post-synthetic functionalization yielded the desired material porosity and functionalization, a pseudomorphic transformation approach[301] was applied, which restructures a preformed silica framework through controlled dissolution–reprecipitation while preserving its macroscopic morphology. For this, the precursor was first hardened by adding 0.16 µL of HCl (37 wt%) to a solution containing BTEVA-OBA (200 mg, 0.373 mmol), 1.25 mL of THF, and 20 µL of demineralized water. The mixture was left to stand in a closed vessel at room temperature for three days. The resulting solid was then exposed to air for four days and subsequently dried at 80 °C for two days, yielding a beige, brittle monolithic material that did not exhibit the porosity typical of PMOs.

To induce pseudomorphic transformation, the solidified BTEVA-OBA (200 mg) was coarsely ground and added to 8.4 mL of an aqueous 0.1 M NaOH / 0.2 M C_{16}TAB solution. The suspension was stirred for several minutes and then hydrothermally treated at 120 °C for four days. After cooling to room temperature, the product was filtered and washed with 200 mL of demineralized water, followed by 50 mL of ethanol. The surfactant was removed by suspending the material in a solution of 11 mL of HCl (37 wt%) and 30 mL of ethanol, followed by heating in a closed vessel at 50 °C for 24 h. After filtration, washing with ethanol, and drying at 60 °C overnight, small beige granules were obtained.

The pseudomorphic transformation successfully introduced hexagonally ordered pores with a comparably narrow pore size distribution and a main pore diameter of 4.3 nm (see Figure S37, Table S10) into the previously hardened, low-porosity material. In addition, the initially amorphous framework was reorganized such that the resulting material exhibits a crystal-like arrangement of the organic bridging units within the pore walls. From the ^{1}H-NMR analysis (Figure S38), two species were identified, one of which corresponds to the functionalized BTEVA-OBA unit and the other to the unfunctionalized BTEVA species, likely formed by cleavage of the amide bond during either the acidic hardening step or the subsequent alkaline pseudomorphic transformation. The IR spectrum (Figure S39) confirms the presence of characteristic bands of the amide–acid compound.

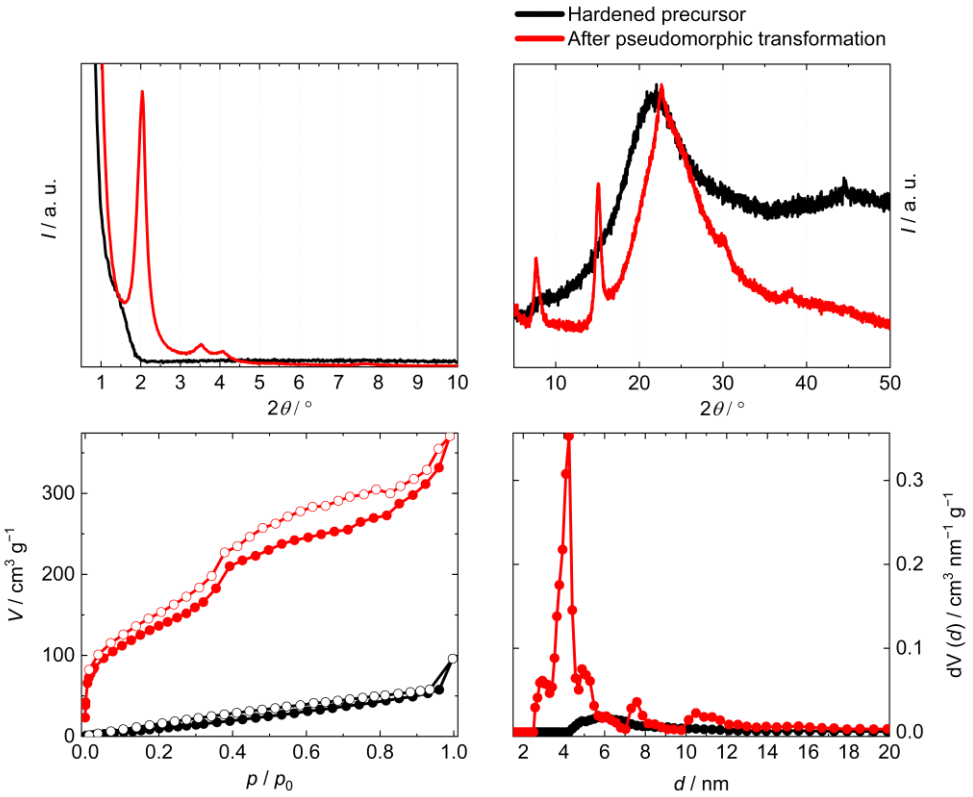


Figure S37: Comparison of the low-porous hardened precursor and the resulting PMO after pseudomorphic transformation: Normalized X-ray powder diffractograms in the ranges 0.5–10° 2θ (top, left) and 5–50° 2θ (top, right), nitrogen physisorption isotherms at 77 K (bottom left) showing the adsorption branch (filled circles) and desorption branch (hollow circles), and the corresponding pore size distribution curves (bottom right), calculated using the NLDFT kernel: N_2 at 77 K on silica, cylindr. pores, at adsorption branch.

^{1}H-NMR (600 MHz, 1 M NaOD/D_2O, 25 °C): 7.20 (d, J = 8.2 Hz, 1H, H6), 6.83 (dd, J = 8.1, 1.2 Hz, 1H, H5), 6.58 (m, 1H, H3), 6.54+6.50 (d, J = 19.4+19.3 Hz, 2H, H8a+b), 5.99+5.94 (d, J = 19.3, 19.3 Hz, 2H, H9a+b), 2.13-2.08 + 1.95-1.90(m, 2H, H11+12).

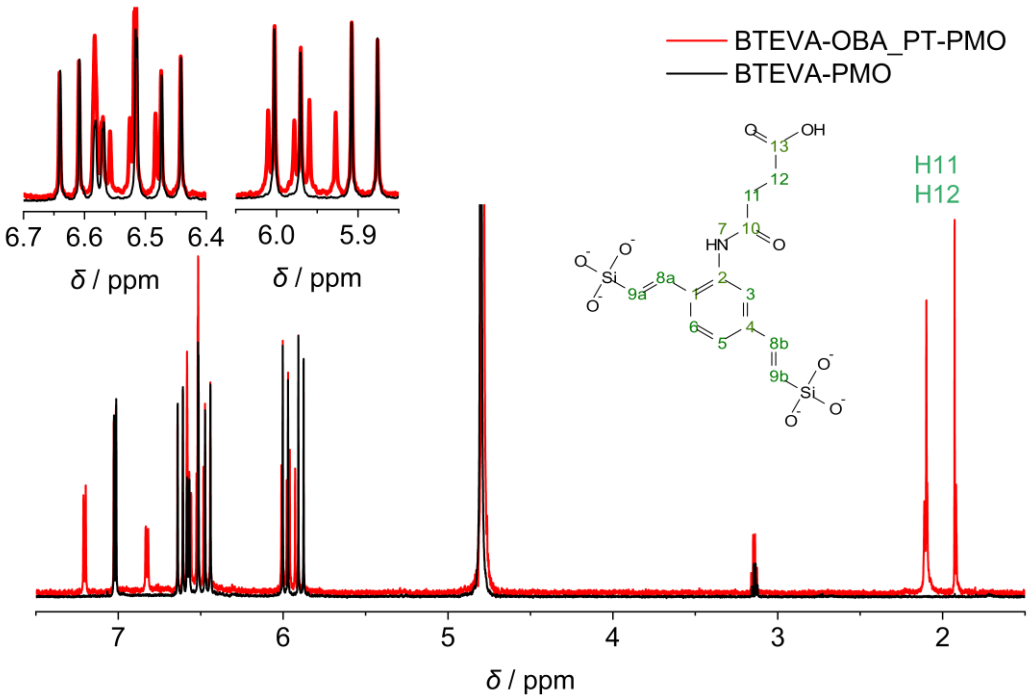


Figure S38: ^{1}H-NMR (600 MHz) spectra of BTEVA- and BTEVA-OBA_PT-PMOs. The materials were dissolved in 1 M NaOD/D_2O.

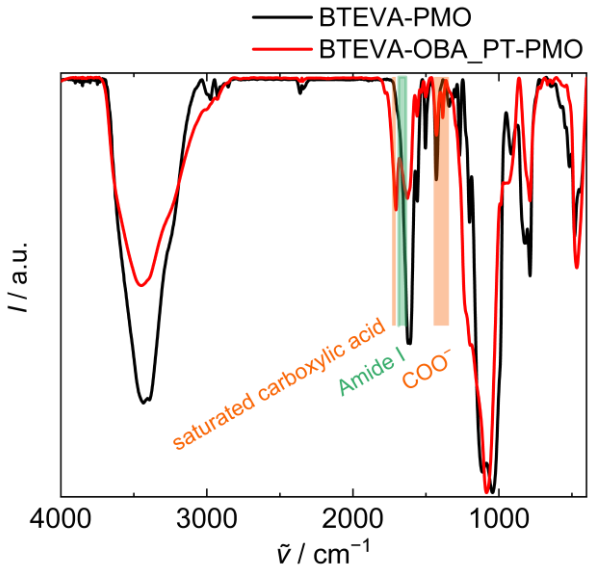


Figure S39: Comparison of the FT-IR spectra (KBr disc) of BTEVA- and BTEVA-OBA_PT-PMO.

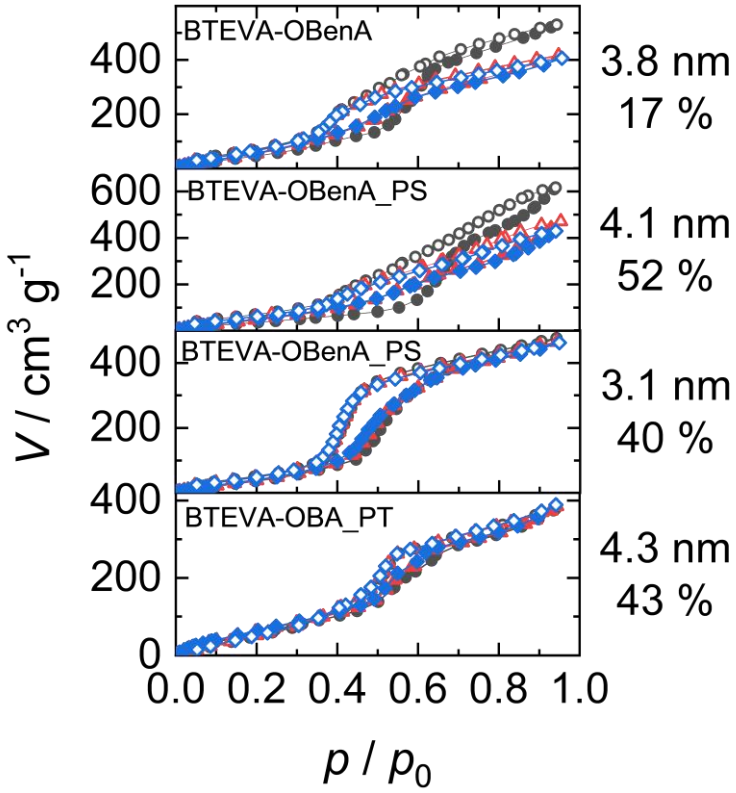
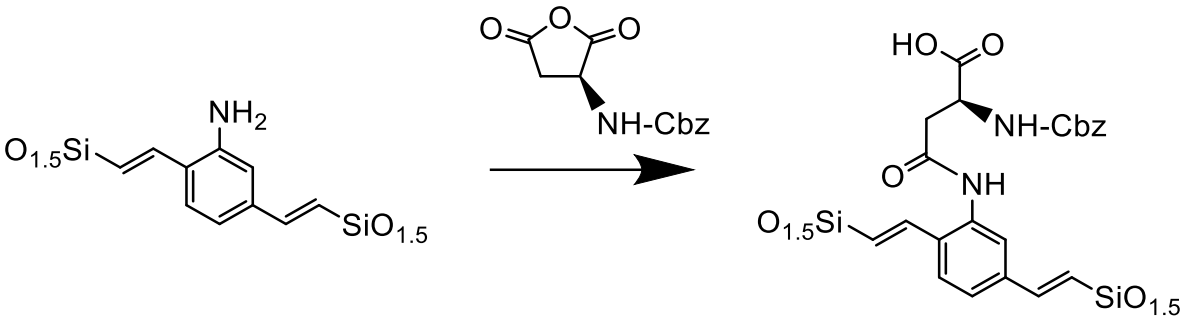


Figure S40: Water vapor sorption isotherms at 25 °C showing the adsorption branch (filled circles) and desorption branch (hollow circles) for different BTEVA based amide-acid PMOs. Also shown are the corresponding pore diameters, determined from nitrogen physisorption using NLDFT, and the functionalization degree, as determined by ^{1}H NMR analysis.

BTEVA-AA-PMO:

Post-synthetic functionalization:



BTEVA-PMO BTEVA-AA-PMO

Figure S41: Synthetic route for BTEVA-AA-PMO.

The synthesis was carried out using the Schlenk technique under a nitrogen atmosphere. For the functionalization, Cbz-L-aspartic acid anhydride (0.941 g, 3.78 mmol) was dissolved in 4 mL of 1,4-dioxane and added to the BTEVA-PMO (81.3 mg). The suspension was stirred at room temperature overnight, after which the solid was filtered, washed with 1,4-dioxane, and dried overnight under ambient conditions and subsequently at 80 °C. A yellow powder was obtained.

The porosity and structural order of the pristine BTEVA- and the functionalized BTEVA-AA-PMOs were characterized by X-ray diffraction and nitrogen physisorption measurements (Figure S42), with key parameters summarized in Table S10. The post-synthetic functionalization resulted in a reduction of the pore diameter from 4.1 to 3.4 nm, as well as decreases in pore volume and specific surface area from 1.08 to 0.551 $cm^3\ g^{-1}$ and from 1242 to 792 $m^2\ g^{-1}$, respectively. The (100) reflection is shifted by +0.03° 2θ and the (001) reflection by +0.13° 2θ, indicating a contraction of the repetition unit length by 0.021 nm and of the pore center-to-center distance by 0.07 nm, accompanied by an increase in pore wall thickness of 0.63 nm.

From the ^{1}H NMR analysis (Figure S43), a BTEVA:BTEVA-AA ratio of 1:0.5 was determined. The IR spectrum (Figure S44) confirms the structural integrity of the PMO. TGA-DTA-MS measurements (see Figure S45, Table S8) show thermal stability up to 408–419 °C. In contrast to previously observed amide–acid-functionalized BTEVA-PMOs, the BTEVA-AA sample does not exhibit a distinct two-step decomposition process but instead shows a continuous mass loss until complete degradation of the

organic BTEVA framework. The removal of Cbz-protecting groups using commonly employed metal-catalyzed hydrogenolytic conditions[303] is challenging due to the subsequent need to separate two powders. Alternative approaches are therefore recommended, such as treatment with HBr[304] or a recently introduced mild deprotection method using 1,1,1,3,3,3-hexafluoroisopropanol in combination with $AlCl_3$.[305] Additionally, protecting groups like BOC, which can be successfully removed *in situ* under acidic synthesis conditions, may be used. Overall, BTEVA- and BTEVP-based PMOs show great potential for incorporating biofunctional groups, as shown for alanine-functionalized BTEVA.[161] Their straightforward synthesis, high yields, crystal-like pore wall structure, and highly ordered pores with narrow pore size distribution make them suitable for a wide variety of applications.

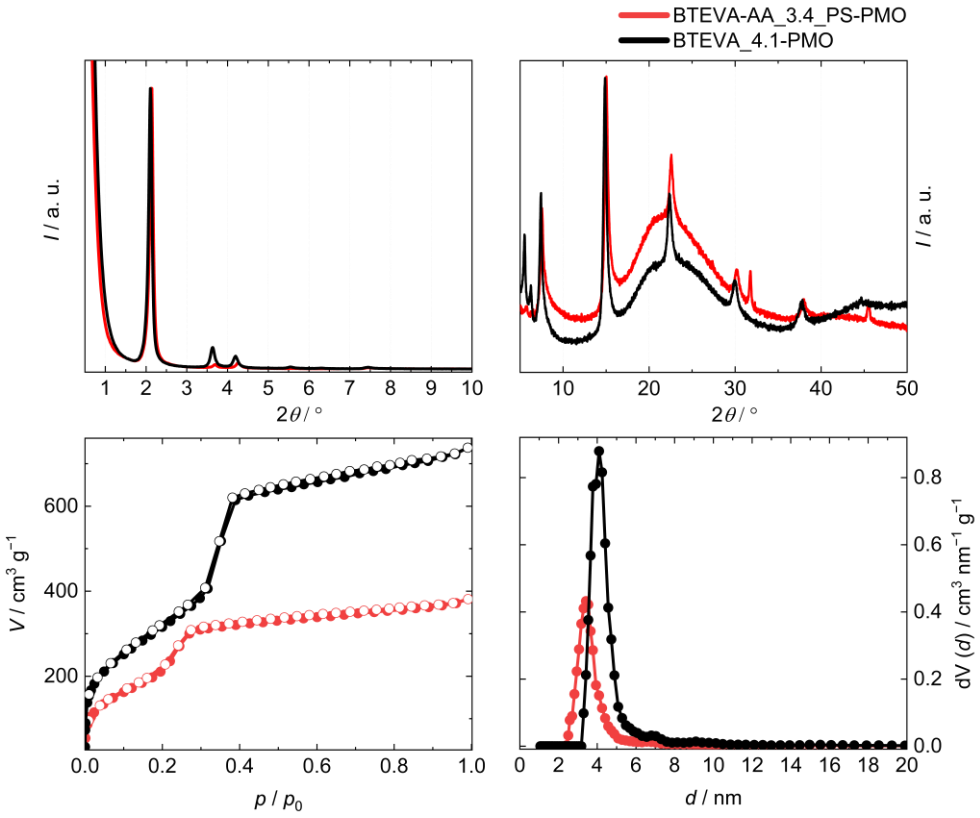


Figure S42: Comparison of the BTEVA-PMO and its post synthetically functionalized form (BTEVA-AA-PMO): Normalized X-ray powder diffractograms in the ranges 0.5–10° 2θ (top, left) and 5–50° 2θ (top, right), nitrogen physisorption isotherms at 77 K (bottom left) showing the adsorption branch (filled circles) and desorption branch (hollow circles), and the corresponding pore size distribution curves (bottom right), calculated using the NLDFT kernel: N_2 at 77 K on silica, cylindr. pores, at adsorption branch.

^{1}H-NMR (300 MHz, 1M NaOD/D_2O, 25 °C): 7.23 (d, *J* = 8.2 Hz, 1H, H6), 6.99 (d, *J* = 2.4 Hz, 1H, H3), 6.95 (dd, *J* = 8.1, 1.7 Hz, 1H, H5), 6.69+6.54 (d, *J* = 19.2 Hz, *J* = 19.3 Hz, 2H, H8a+b), 6.06+ (d, *J* = 19.3 Hz, *J* = 19.2 Hz, 2H, H9a+b), 3.91–3.87 (m, 1H, H12), 6.10-5.98 (m, 2H, H11).

Further signals: δ [ppm] = 7.02 (s, Cbz protecting group), 4.16 (s, Cbz protecting group).

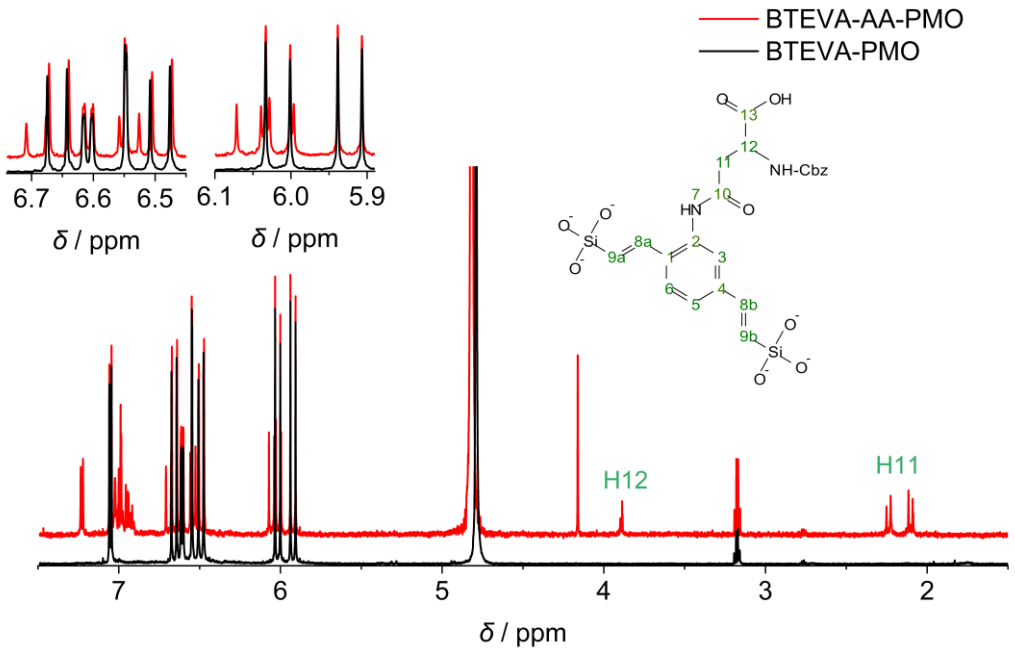


Figure S43: ^{1}H-NMR (600 MHz) spectra of BTEVA- and BTEVA-AA-PMOs. The materials were dissolved in 1 M NaOD/D_2O.

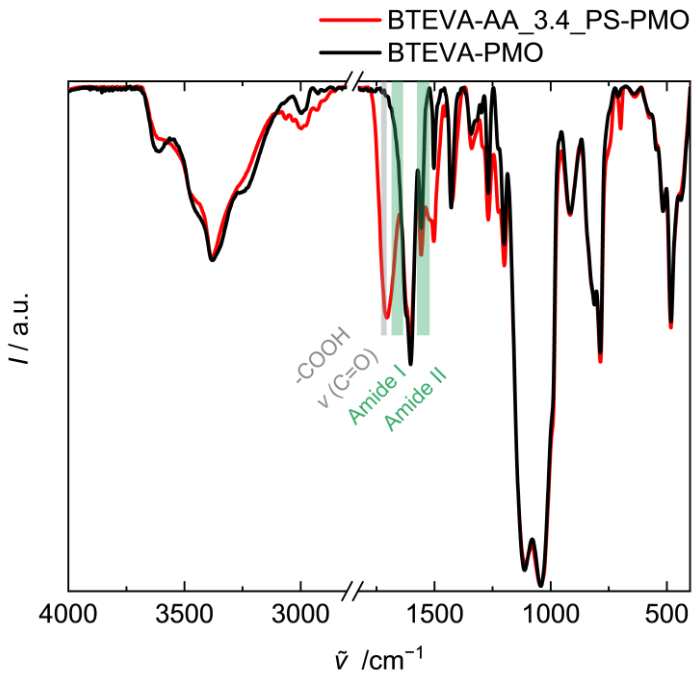


Figure S44: Comparison of the FT-IR spectra (KBr disc) of BTEVA- and BTEVA-AA_PS-PMO.

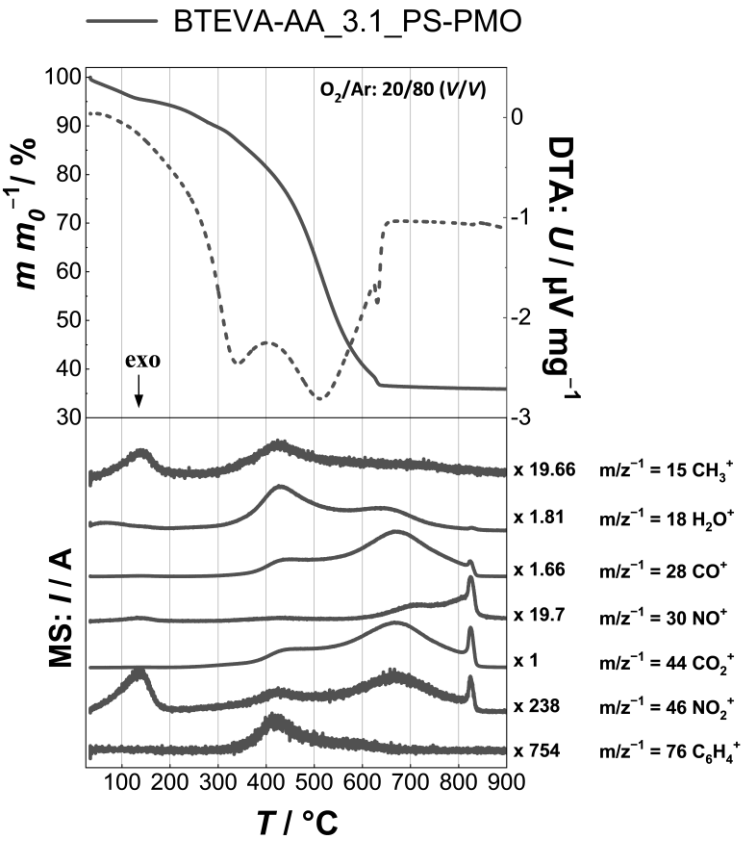


Figure S45: TGA-DTA-MS analysis of BTEVA-AA_PS-PMOs with a pore diameter of 3.1 nm. Measurements were performed at a heating rate of 10 Kmin^{-1} under an O_2/Ar atmosphere (20/80 (*V*/*V*)).

Table S8: Extracted data from TGA-DTA-MS analysis, including the relative mass loss of surface-adsorbed water in the range 30–150 °C ($\Delta(m_w\, m_0^{-1})$), the relative mass loss of the organic bridge combustion excluding adsorbed water content ($\Delta(m_{org}\, m_0^{-1})$), and the functionalization degree (*F*), calculated from $\Delta(m_{org}\, m_0^{-1})$ considering the mass loss of the unfunctionalized BTEVA-PMO precursor (P) and using the effective molar mass of its organic bridge of 130.73 g mol^{-1}, under the assumptions of complete deprotection (cd) and with the Cbz protection group remaining (Cbz). Combustion temperatures were determined from the onset (T_{on}) and endset (T_{end}), as well as the temperature at which $\Delta(m_w\, m_0^{-1})$ reaches 50 % (T_{50}).

	BTEVA-AA_PS
$\Delta(m_w\, m_0^{-1})$ / %	4.72
$\Delta(m_{org}\, m_0^{-1})$ / %	62.3
$F_{cd,(CbZ)}$ / %	53 (25)
T_{on} / °C	408–419
T_{50} / °C	493
T_{end} / °C	636

8.3.4. Porosity Characteristics of Bifunctional Amide–Acid PMOs

Table S9: Characteristics of BTEB:amide–acid co-condensed PMOs, including the percentage of the respective amide–acid precursor used for synthesis (CC), the co-condensate content determined by NMR (F_{NMR}), and the remaining amide–acid functionality (AAF), as well as the pore diameter (d_P), pore volume (V_P), specific BET surface area (S_{BET}), and pore wall thickness (d_W).

PMO	*CC* / %	F_{NMR} (F_{AAF}) / %	d_P / nm	V_P / $cm^3\,g^{-1}$	S_{BET} / $m^2\,g^{-1}$	d_w / nm
BTEPA-OBenA	100	100 (1.5)	8.2	0.428	259	9.9
	80	81 (1.3)	8.2	0.431	238	7.5
	60	60 (0.8)	7.6	0.371	300	7.5
	50	52 (0.5)	7	0.402	386	6.8
	40	37 (0.6)	6.1	0.442	375	6.4
	20	20 (0.4)	5.9	0.447	531	6.0
	0	0 (0)	1.2 + 2.4–7.6	0.455	676	-
BTEPA-OBA	100	-	-	0.063	74	-
	80	80 (15)	6.8	0.292	224	8.3
	60	58 (16)	6.6	0.377	327	7.2
	50	51 (19)	6.1	0.317	283	7.4
	37	39 (13)	5.9	0.454	433	6.9
	20	-	5.7	0.520	650	5.8
BOC-BTEPSA	100	-	-	0.031	19	-
	80	-	-	0.036	63	-
	60	60	6.6	0.259	222	-
	50	55	6.8	0.244	168	-
	37	43	6.6	0.341	304	-
	20	-	5.9	0.37	450	-

Table S10: Characteristics of functionalized BTEVA-PMOs, including the functionalization degree determined by NMR (F_{NMR}), pore diameter (d_P), pore volume (V_P), specific BET surface area (S_{BET}), and pore wall thickness (d_W).

PMO	F_{NMR} / %	d_P / nm	V_P / cm^3 g^{-1}	S_{BET} / m^2 g^{-1}	d_W / nm
BTEVA-OBenA	17	3.8	0.561	874	1.1
BTEVA-OBenA_PS	52	4.1	0.604	688	1.1
	40	3.1	0.525	875	1.2
BTEVA-OBA	-	4.8	1.02	930	-
BTEVA-OBA_PS	-	4.3	0.794	872	0.89
BTEVA-OBA_PT	43	4.3	0.422	502	0.69
Cbz-BTEVA-AA_PS	33	3.4	0.551	792	1.4

The characterization methods and parameters used for analyzing the bifunctional amide–acid PMOs and for the subsequent investigation of confined water follow the protocols described in the publications cited in this dissertation.[62]

8.4. Supporting Information for "The Role of Fine-Tuned Surface Functionality on Adsorption Thermodynamics of Nanoconfined Water within Periodic Mesoporous Organosilicas"

Supporting Information for

The Role of Fine-Tuned Surface Functionality on Adsorption Thermodynamics of Nanoconfined Water within Periodic Mesoporous Organosilicas

Philip Lenz[a,b], Uta Sazama[a], Sandra König[a], Michael Steiger[a,] and Michael Fröba[a,b,]**

AFFILIATIONS

[a] Institute of Inorganic and Applied Chemistry, University of Hamburg, Martin-Luther-King-Platz 6, 20146 Hamburg, Germany

[b] The Hamburg Centre for Ultrafast Imaging, Luruper Chaussee 149, 22761 Hamburg, Germany

E-mail: michael.steiger@uni-hamburg.de and michael.froeba@uni-hamburg.de

Chemicals

All used reagents and solvents for the synthesis of the precursors and PMOs were purchased from commercial suppliers (*abcr*, *Merck*, *Sigma-Aldrich*, *TCI*, *Fisher Scientific*).

MCM-41 silica and PMO synthesis

The synthesis of most materials used in this study has been described in detail previously.[1] The synthesis composition of the new sample introduced here is provided in Table S1 and follows the procedure outlined in our recent study.

Table S1. PMO synthesis conditions, including amounts (n) of the precursor (P), of sodium hydroxide (NaOH) and of the respective surfactant (S), the volumes of water (V_w), as well as the temperature (T_{ht}) and duration (t_{ht}) of the hydrothermal treatment for each PMO type, along with the resulting pore size (d_P).

PMO Type	d_P / nm	n_P / mmol	n_{NaOH} / mmol	Surfactant type	n_S / mmol	V_w / mL	T_{ht} / °C	t_{ht} / h
BTEVA	4.4	3.4	18	C_{18}TAB	4.2	40	95	24
BTEVP	2.9	2.0	7.5	C_{10}TAB	2.1	20	95	24
BTEVClB*	3.8	1.4	7.0	C_{18}TAB	1.5	15	90	25

*Absolute ethanol (1.4 mL) was added during surfactant dissolution.

PMO characterization

Porosity was characterized using nitrogen physisorption and powder X-ray diffraction (PXRD). While most materials were previously detailed[1], only the characteristics of newly introduced samples are discussed herein. A comprehensive summary of all material characteristics is provided in Table S2. Slight deviations from previously introduced samples are attributed to the use of materials synthesized in a different batch, even though following identical protocols.

Table S2: Nitrogen physisorption analysis yielded pore diameter based on NLDFT (d_P), pore volume (V_P), specific BET surface area (S_{BET}). Furthermore, surface hydration site density (SHS) was determined from water vapor sorption measurements at 25 °C.

Material	d_P / nm	V_P / cm^3g^{-1}	S_{BET} / m^2g^{-1}	SHS_{25}
MCM-41	3.2	0.644	1034	1.24
	3.7	0.840	1118	1.32
	5.3	1.10	911	1.48
BTEVA	2.9	0.538	894	1.17
	3.8	0.901	1158	1.17
	4.4	1.51	1150	0.57
BTEVP	2.9	0.396	695	1.92
	3.8	0.855	979	0.86
	3.8*	0.649	783	1.01
	4.3	0.763	785	1.32
BTEVB	3.4	0.590	779	0.53
	3.8	0.638	752	0.45
	4.4	0.791	790	0.42
N,*N*-DMBTEVA	3.8	0.647	808	0.67
BTEVClB	3.8	1.02	1122	0.44
	3.7*	0.780	1053	0.69

* Sample used for the isosteric method.

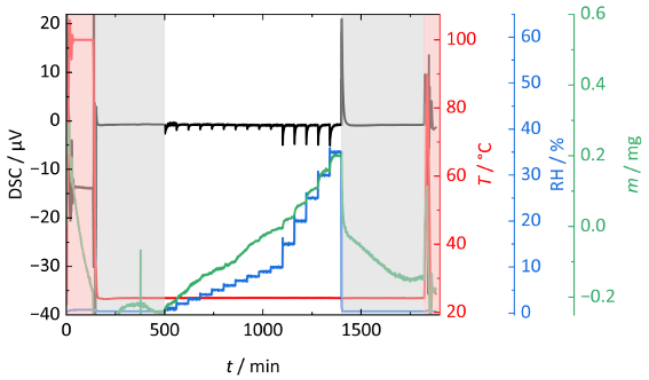


Figure S1. Exemplary raw simultaneous DSC-TGA adsorption measurement in the humidity range of 0–35% RH on BTEVP-PMO with a pore diameter of 3.8 nm. Red areas indicate the activation step at elevated temperatures; gray areas represent equilibrium phases at 0 % RH.

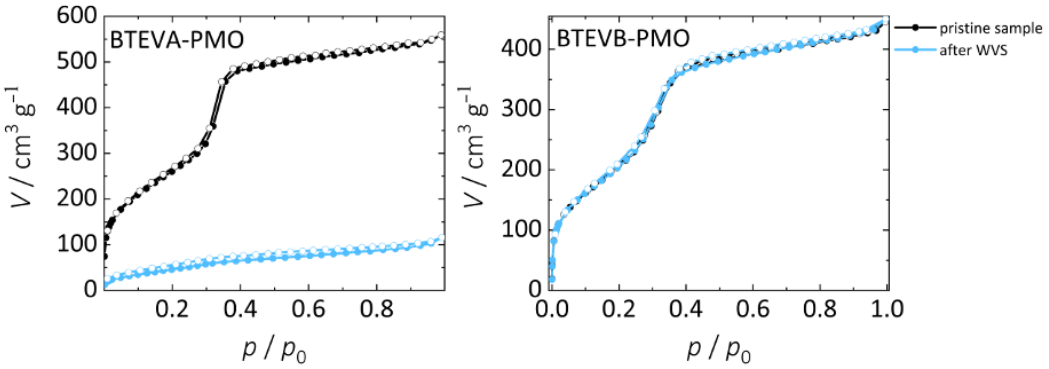


Figure S2. Nitrogen physisorption isotherms of hydrophilic BTEVA-PMO and hydrophobic BTEVB-PMO (both with a pore size of 3.8 nm), recorded before and after exposure to water vapor (WVS). Filled symbols indicate the adsorption branch, open symbols the desorption branch.

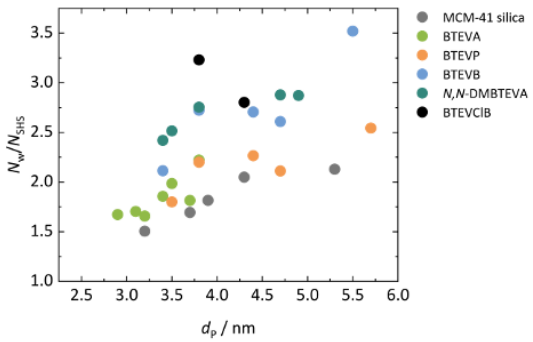


Figure S3. Influence of pore diameter (d_P) on the number of water molecules per surface hydration site (N_W/N_{SHS}). Datapoints are sourced from our previous publication.[1]

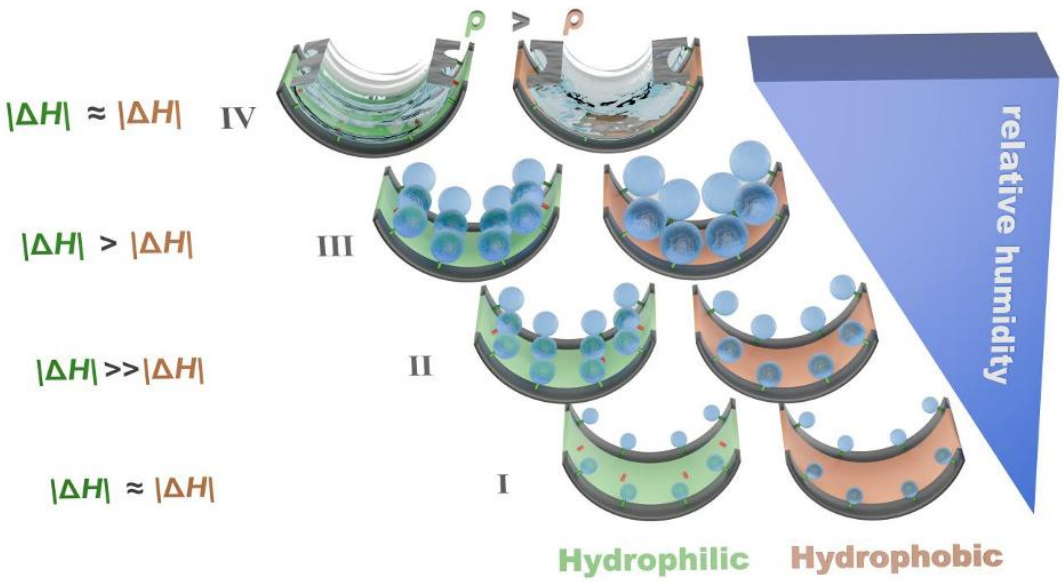


Figure S4. Schematic illustration of water adsorption on curved hydrophilic and hydrophobic surfaces at different relative humidities (RH) and filling stages. I. At low RH, water adsorbs at energetically favorable hydration sites. II. On hydrophilic surfaces, water further adsorbs on secondary sites; on hydrophobic surfaces, water aggregates begin to grow. III. Water aggregates grow until they reach a certain size for condensation (hydrophobic) or until neighboring aggregates interact (hydrophilic), leading to IV. the formation of a continuous water film and eventual capillary condensation. The gray areas represent the PMO silica backbone, with green sticks indicate silanol groups. Organic bridging units are shown in color: orange for hydrophobic, green for hydrophilic, and red indicating additional polar functional groups.

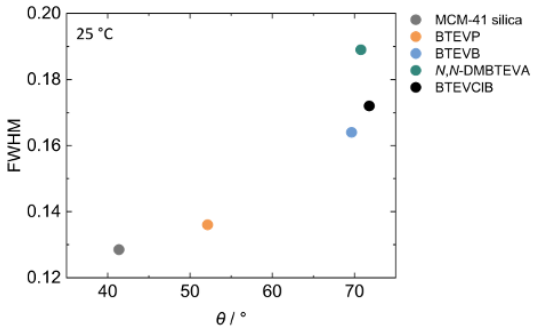


Figure S5. Adsorption-desorption hysteresis (FWHM) plotted against contact angle (θ).

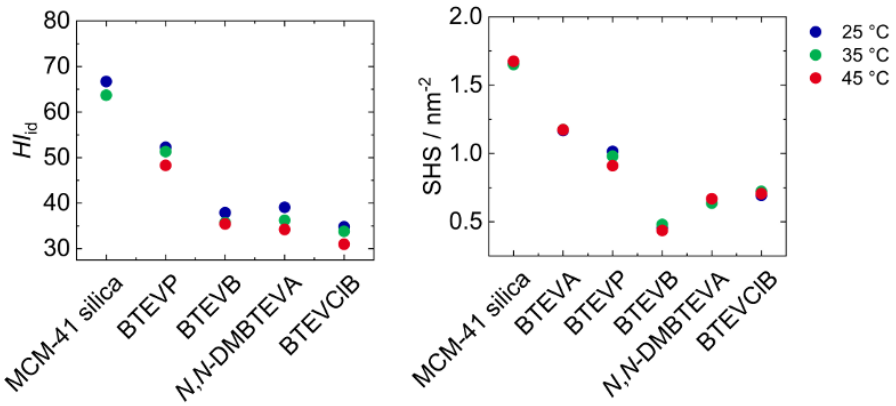


Figure S6. Material-specific and temperature-dependent behavior of HI_{id} (left) and surface hydration site (SHS) density (right).

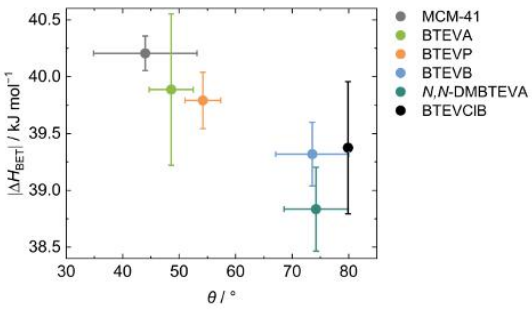


Figure S7. Plot of absolute values of adsorption enthalpy of the first water layer ($|\Delta H_{BET}|$, calculated from BET-constant from water vapor sorption isotherms at 25 °C) against contact angle (θ). Mean values are sourced from our previous publication.[1]

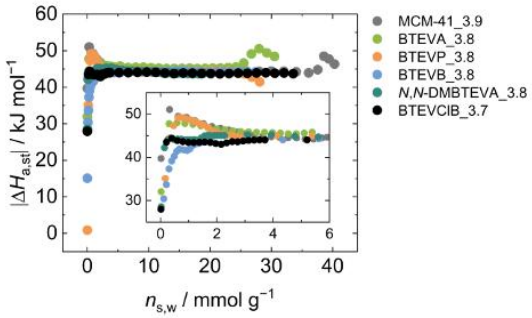


Figure S8. Isosteric enthalpy of adsorption (absolute value of $\Delta H_{a,st}$) against specific adsorbed water amount ($n_{s,w}$). An inset showing the $n_{s,w}$ range of 0–6 is provided.

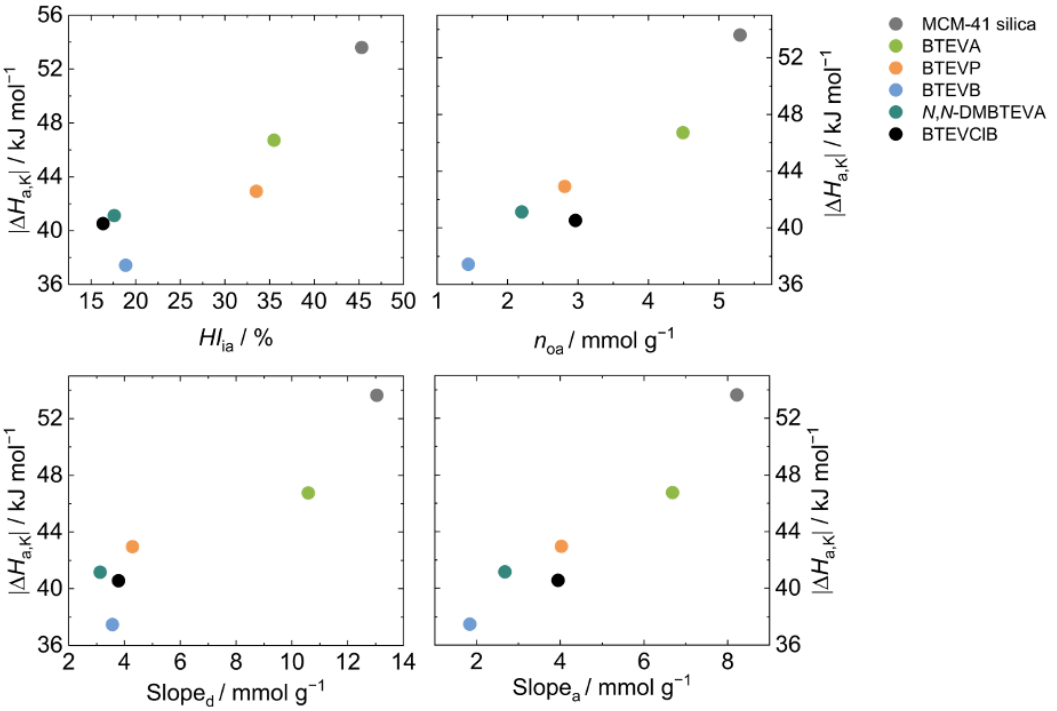


Figure S9. Plot of the material-dependent water adsorption enthalpy (absolute value of $\Delta H_{a,K}$), determined from Henry's constant, against: (a) the hydrophilicity index (HI_{ia}); (b) the specific water amount at the onset of capillary condensation (n_{oa}); (c) the slope of the desorption branch after pore emptying ($slope_d$); and (d) the slope of the adsorption branch prior to capillary condensation ($slope_a$).

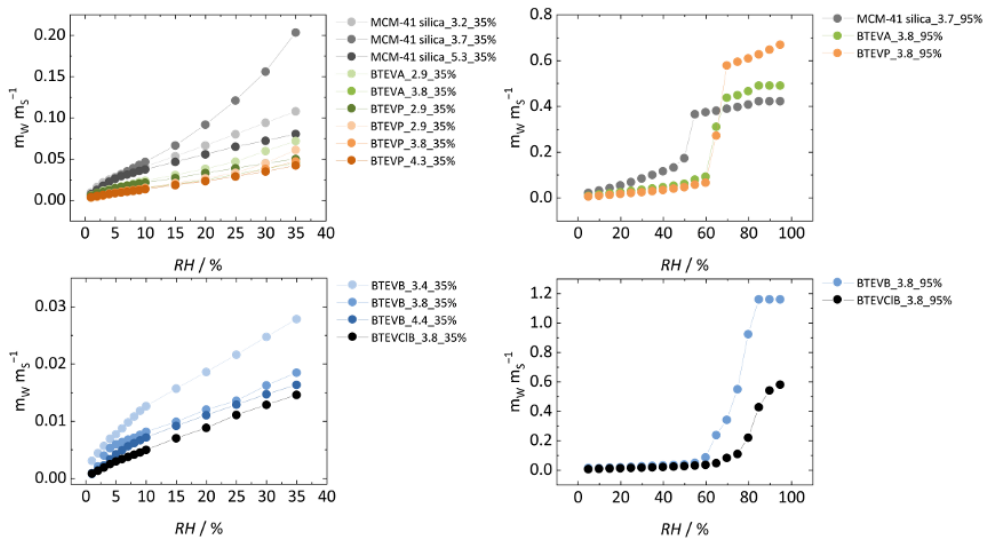


Figure S10. Adsorption isotherms as a plot of the adsorbed water mass per sample mass ($m_w\ m_s^{-1}$) at varying relative humidity (RH). These data were determined from DSC-TGA measurements, spanning the range of 0−35% RH (left) and 0−95% RH (right) for hydrophilic materials (top) and hydrophobic materials (bottom).

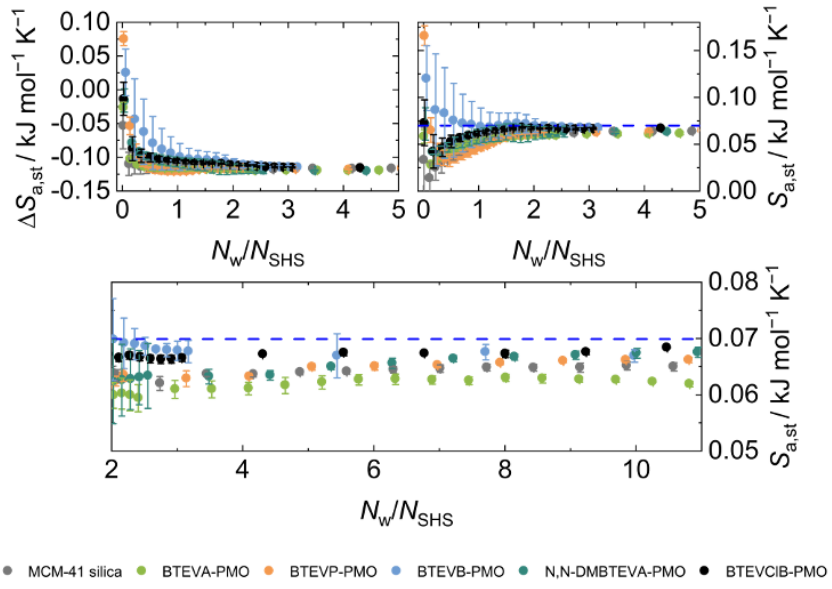


Figure S11. Plot of the isosteric entropy change ($\Delta S_{a,st}$) due to adsorption (left) and the absolute entropy ($S_{a,st}$), calculated according to the method of Cantrell et al.[2] (right), against the number of water molecules per surface hydration site (N_w/N_{SHS}). The inset (bottom) shows an enlarged view of the higher-coverage region. The blue dashed line represents the bulk value of 69.9 J mol^{-1} K^{-1} at 298.15 K.[2]

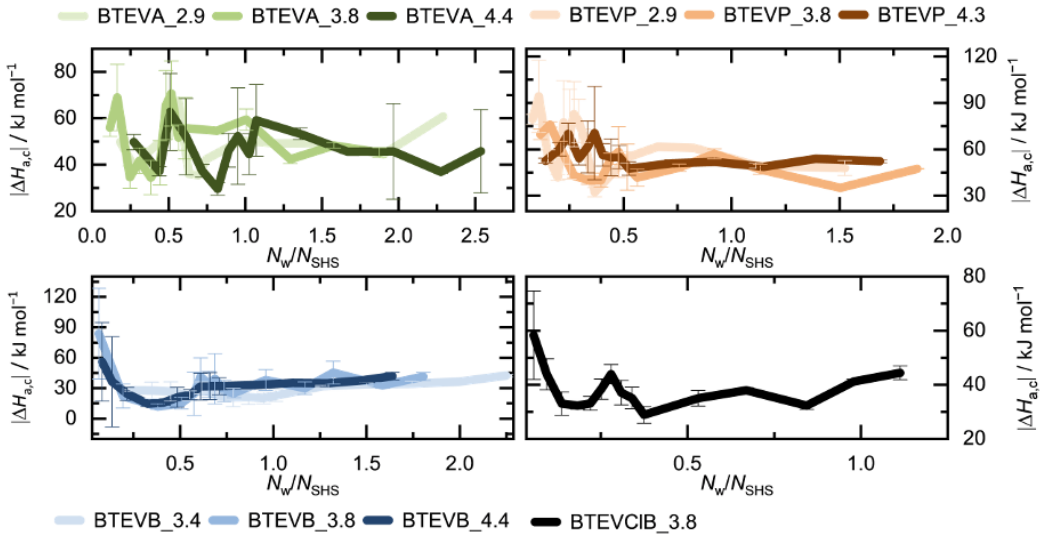


Figure S12. Calorimetrically determined absolute values of adsorption enthalpy ($\Delta H_{a,c}$) of water in various materials with differing pore sizes, plotted against the number of water molecules per surface hydration site (N_w/N_{SHS}).

REFERENCES

(1) Lenz, P.; Meinert, S.-M.; König, S.; Steiger, M.; Fröba, M. Influence of surface chemistry on t-layer dimension and density of nanoconfined water by fine-tuning the functional groups of periodic mesoporous organosilicas. *J. Phys. Chem. C* **2025**, *129* (27), 12536–12550. DOI: 10.1021/acs.jpcc.5c02277.

(2) Cantrell; Ewing, G. E. Thin film water on muscovite mica. *J. Phys. Chem. B* **2001**, *105* (23), 5434–5439. DOI: 10.1021/jp004305b.

8.5. Supporting Information for "Structure of Water under Confinement in Periodic Mesoporous Organosilicas Investigated by X-ray Scattering"

The Structure of Water Under Confinement in Periodic Mesoporous Organosilicas Investigated by X-Ray Scattering - Supporting Information

Niels C. Gießelmann,[†] Philip Lenz,[‡,¶] Sophia-Marie Meinert,[‡] Tamás Simon,[‡] Wonhyuk Jo,[†,§] Nele N. Striker,[†] Michael Fröba,[*,‡,¶] and Felix Lehmkühler[*,†,¶]

†*Deutsches Elektronen-Synchrotron DESY, Notkestr. 85, 22607 Hamburg, Germany*

‡*University of Hamburg, Institute of Inorganic and Applied Chemistry, Martin-Luther-King-Platz 6, 20146 Hamburg, Germany*

¶*The Hamburg Centre for Ultrafast Imaging, Luruper Chaussee 149, 22761 Hamburg, Germany*

§*European XFEL, Holzkoppel 4, 22869 Schenefeld, Germany*

E-mail: michael.froeba@uni-hamburg.de; felix.lehmkuehler@desy.de

Synthesis of porous materials

Precursor synthesis The synthesis of the BTEVB,[1,2] BTEVA[1] and BTEVFB[2,3] precursors and their reaction to the corresponding PMOs were carried out according to the given synthesis instructions. The synthesis of the BTEVP precursor is a modified form of literature synthesis.[4] Deviating from the three-step literature synthesis, the second step, the preparation of 2,5-diethynylpyridine, was carried out in a modified version of the given literature synthesis.[5] To a solution of 2.31 g (8.49 mmol) of 2,5-bis(trimethylsilylethynyl)pyridine and 23.0 mL of methanol (98 *m*%), 9.20 mL of an aqueous 1 M KOH solution was added and stirred for 1 h at room temperature. The product mixture was then filtered and washed with diethyl ether. The filtrate was washed three times with 200 mL of demineralized water and once with 200 mL of a saturated NaCl solution. The aqueous phases were washed three times with 100 mL of diethyl ether. The combined organic phases were dried over $MgSO_4$ and solvent was removed under reduced pressure. The product was purified by column chromatography (*n*-hexane/ethyl acetate = 3:1). The product is a colorless to slightly yellowish solid. Yield: 0.96 g (7.6 mmol), 90 % based on 2,5-bis(trimethylsilylethynyl)pyridine).

PMO synthesis The corresponding surfactant was dissolved in an aqueous NaOH solution at 31 °C for 30 min. Subsequently, the solution was stirred for another 30 min at room temperature and then the respective precursor was added. The reaction mixture was stirred for 20 h at room temperature and then hydrothermally treated. After cooling to room temperature, the product mixture was filtered and washed with 200 mL demineralized water and 50 mL ethanol. The surfactant was removed via Soxhlet extraction using an ethanol-HCl 37 *m*% solution (*V*:*V*; 98:2). The product was dried at 80 °C. Table S1 gives the exact compositions and the temperature and duration of hydrothermal treatment for the various precursors used.

Synthesis of MCM-41 For the synthesis of MCM-41, 60 mL of demineralized water and 5.6 mL of aqueous ammonia (25 *m*%) were added to 4.38 g (12 mmol) hexadecyltrimethylammonium-

bromid (C_{16}TAB) and dissolved by stirring at 35 °C. After cooling to room temperature, 5.00 mL (22.6 mmol) of tetraethyl orthosilicate were added and stirred for 2 h at room temperature. The reaction mixture was hydrothermally treated at 95 °C for 72 h. The colorless precipitate was filtered, washed with 200 mL of demineralized water and 50 mL ethanol. An ethanol-based Soxhlet extratraction was performed for three days. After drying at 65 °C for 16 h, calcination was carried out for 6 h at 550 °C (heating rate 1 K min^{-1}). A colorless powder was obtained.

Table S1: Shown are the amounts (n) of the precursor (P), of sodium hydroxide (NaOH) and of the respective surfactant (S), as well as the volumes of water ($V_{\mathbf{water}}$) used for the syntheses of the respective PMO. In addition, the temperature ($T_{\mathbf{ht}}$) and duration of the hydrothermal treatment ($t_{\mathbf{ht}}$) are given.

Sample	n_{P} [mmol]	n_{NaOH} [mmol]	**Surfactant type**	n_{S} [mmol]	V_{water} [mL]	T_{ht} [°C]	t_{ht} [h]
BTEVB(3.8)	9.90	108	C_{18}TAB	14.8	120	95	12
BTEVFB(4.9)	3.40	22.4	C_{18}TAB	4.70	40	95	24
BTEVFB(4.4)	1.78	12.8	C_{18}TAB	2.77	21	80	24
BTEVA(4.3)	3.52	18.8	C_{18}TAB	4.19	40	80	24
BTEVA(3.8)	6.82	36.0	C_{16}TAB	8.34	80	95	24
BTEVA(3.4)	3.52	18.8	C_{14}TAB	4.17	40	80	24
BTEVP(3.5)	1.95	7.50	C_{10}TAB	2.09	20	95	27

Structure of the porous materials

To investigate the materials regarding their mesostructure and molecular ordering within the pore walls, X-ray powder diffractograms (PXRD) were recorded with the *PANalytical X'Pert Pro PW3040/60* (Cu-Kα radiation λ = 0.154 178 nm). The evaluation was performed using *Origin 2023* and *X'Pert Highscore Plus*. The reflections in the q-range of 0.05 to 0.4 Å^{-1} of the powder XRD in Figure S1 (left) indicate a periodic arrangement of the pores of MCM-41 and the PMOs. In addition, the PMOs show reflection patterns in the 0.4 to 3.5 Å^{-1} range of the PXRD (see Figure S1, right), suggesting a crystal-like arrangement at the molecular level in the pore walls.[3,4,6–10] Note that the diffraction curve of BTEVP(3.5) we do not show the second and third peaks in the low-q region. These describe reflections of the (110) and (200) planes in the crystal-

like lattice of the pores. From this we can conclude that there might be irregularities in the arrangement of the pores towards each other as small angles between them may lead to a broadening or even vanishing of these peaks. Since the pores are not interconnected, this does however not touch upon the argumentation of this study and the confined water should not be affected by this issue. The conclusions should still be valid in the case of BTEVP(3.5), as the larger-q region suggests a periodicity of the organic bridges in the pore wall. Therefore the interaction between the water and the pore wall can be studied as described in the main manuscript.

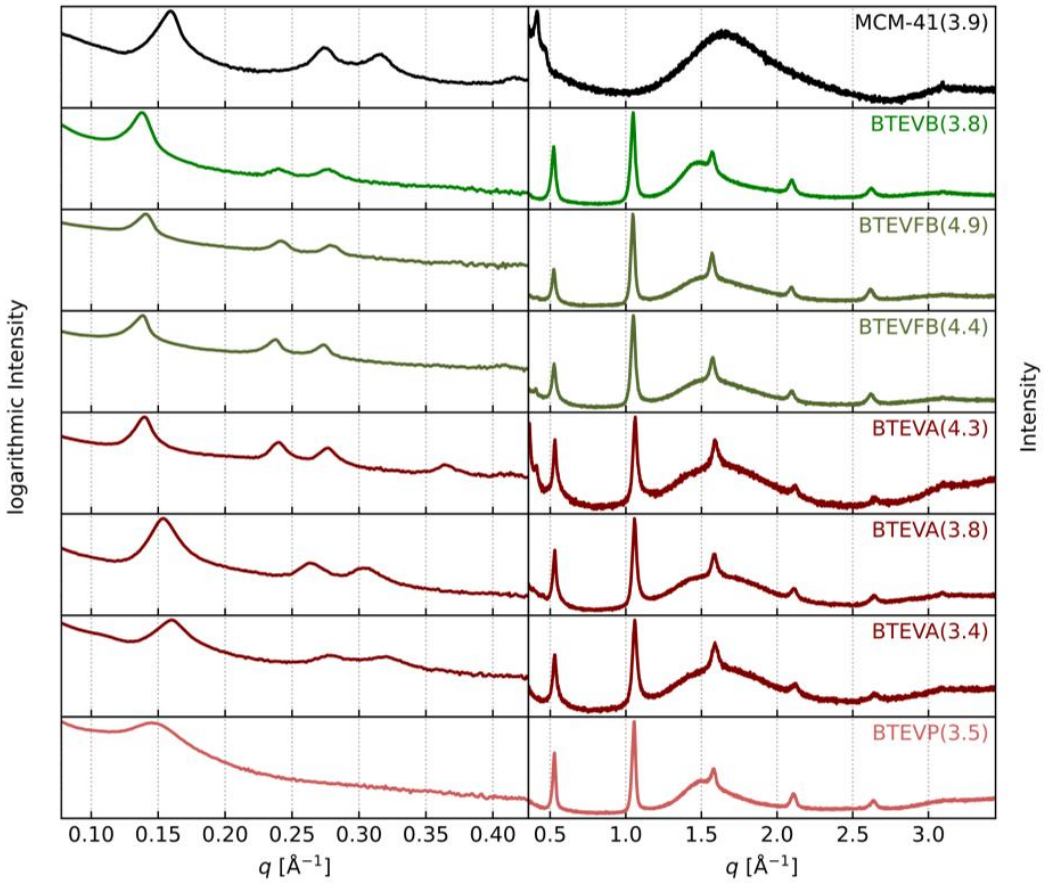


Figure S1: Normalized X-ray powder diffractograms of the various samples in the q-ranges from 0.08 to 0.42 $Å^{-1}$ on the left and 0.36 to 3.44 $Å^{-1}$ on the right. The y-axis in the small-q area is in logarithmic scale to better visualize the (110) and (200) peaks.

Porosity data

Table S2: Shown are the pore diameter determined from the peak maximum (d_P), the mean pore diameter ($d_{P,avg}$), the half-width of the pore size distribution curve (HWHM), the pore volume at a relative pressure of 0.9 ($V_{P,0.9}$), the BET surface area (S_{BET}), periodicity of the organic units in the pore wall (d_{org}), the interplanar d-spacing (d_{100}), and the pore wall width (d_W).

Sample	d_P [nm]	$d_{P,avg}$ [nm]	***HWHM*** [nm]	$V_{P,0.9}$ [cm^3g^{-1}]	S_{BET} [m^2g^{-1}]	d_{org} [nm]	d_{100} [nm]	d_W [nm]
MCM-41(3.9)	3.9	3.9	0.29	0.85	956	-	3.95	0.66
BTEVB(3.8)	3.8	3.8	0.69	0.54	762	1.19	4.56	1.47
BTEVFB(4.9)	4.9	5.3	1.4	0.83	632	1.20	4.47	0.26
BTEVFB(4.4)	4.4	4.5	0.69	1.04	976	1.20	4.54	0.84
BTEVA(4.3)	4.3	4.3	0.28	0.83	966	1.18	4.50	0.90
BTEVA(3.8)	3.7	3.7	0.43	0.67	948	1.18	4.09	1.0
BTEVA(3.4)	3.4	3.4	0.40	0.64	929	1.18	3.92	1.1
BTEVP(3.5)	3.5	3.7	0.80	0.63	851	1.19	4.35	1.5

References

(1) Mietner, J. B. Visiting nanopores: The great potential of PMOs for studying the properties of water in nanopores of different polarity. Ph.D. thesis, Universität Hamburg-Doctoral dissertation, 2018.

(2) Bilo, M. Controlled pore glasses and alginate hydrogels as form-giving matrices for nanoporous organosilicas. Ph.D. thesis, Staats-und Universitätsbibliothek Hamburg Carl von Ossietzky, 2019.

(3) Bracco, S.; Beretta, M.; Cattaneo, A.; Comotti, A.; Falqui, A.; Zhao, K.; Rogers, C.; Sozzani, P. Dipolar rotors orderly aligned in mesoporous fluorinated organosilica architectures. *Angewandte Chemie International Edition* **2015**, *54*, 4773–4777.

(4) Waki, M.; Mizoshita, N.; Ohsuna, T.; Tani, T.; Inagaki, S. Crystal-like periodic mesoporous organosilica bearing pyridine units within the framework. *Chemical communications* **2010**, *46*, 8163–8165.

(5) Feng, J.; Zhang, C.; Li, Y.; Yang, M. Hyperbranched polymer based on triphenylamine and pyridine: Fluorescent chemosensors for palladium ions. *Journal of Applied Polymer Science* **2011**, *121*, 217–225.

(6) Inagaki, S.; Guan, S.; Ohsuna, T.; Terasaki, O. An ordered mesoporous organosilica hybrid material with a crystal-like wall structure. *Nature* **2002**, *416*, 304–307.

(7) Sayari, A.; Wang, W. Molecularly ordered nanoporous organosilicates prepared with and without surfactants. *Journal of the American Chemical Society* **2005**, *127*, 12194–12195.

(8) Cornelius, M.; Hoffmann, F.; Fröba, M. Periodic mesoporous organosilicas with a bifunctional conjugated organic unit and crystal-like pore walls. *Chemistry of materials* **2005**, *17*, 6674–6678.

(9) Beretta, M.; Morell, J.; Sozzani, P.; Fröba, M. Towards peptide formation inside the channels of a new divinylaniline-bridged periodic mesoporous organosilica. *Chemical communications* **2010**, *46*, 2495–2497.

(10) Martens, S.; Ortmann, R.; Brieler, F. J.; Pasel, C.; Joo Lee, Y.; Bathen, D.; Fröba, M. Periodic mesoporous organosilicas as adsorbents of toxic trace gases out of the ambient air. *Zeitschrift für anorganische und allgemeine Chemie* **2014**, *640*, 632–640.

8.6. Supporting Information for "Colossal Effect of Nanopore Surface Ionic Charge on the Dynamics of Confined Water"

Colossal Effect of Nanopore Surface Ionic Charge on the Dynamics of Confined Water

Armin Mozhdehei[1], Philip Lenz[2,3], Stella Gries[4,8], Sophia-Marie Meinert[2], Ronan Lefort[1], Jean-Marc Zanotti[5], Quentin Berrod[6], Markus Appel[7], Mark Busch[4,8], Patrick Huber[4,8,*], Michael Fröba[2,3,*], Denis Morineau[1,*]

1. Institute of Physics of Rennes, CNRS-University of Rennes, UMR 6251, F-35042 Rennes, France.
2. Institute of Inorganic and Applied Chemistry, University of Hamburg, 20146 Hamburg, Germany.
3. The Hamburg Centre for Ultrafast Imaging, Luruper Chaussee 149, 22761 Hamburg, Germany
4. Institute for Materials and X-ray Physics, Hamburg University of Technology, Hamburg 21073, Germany
5. Université Paris-Saclay, Laboratoire Léon Brillouin, CEA, CNRS, F-91191 Gif-sur-Yvette, France
6. Univ. Grenoble Alpes, CNRS, CEA, Grenoble INP, IRIG, SyMMES, F-38000 Grenoble, France
7. Institut Laue-Langevin, F-38042 Grenoble, France
8. Centre for X-ray and Nano Science CXNS, Deutsches Elektronen-Synchrotron DESY, 22603 Hamburg, Germany.

Email addresses: *patrick.huber@tuhh.de, *michael.froeba@uni-hamburg.de, denis.morineau@univ-rennes.fr

Supporting information

1. PMO synthesis

The precursor 2,5-bis[(E)-2-(triethoxysilyl)vinyl]pyridine (BTEVP) was synthesized following literature protocols.[1]

For the synthesis of PMO, 3.1 mmol trimethyltetradecylammonium bromide and 14 mmol of NaOH were dissolved in 30 mL water at 31°C for 30 minutes. The solution was then stirred for an additional 30 minutes at room temperature before adding 2.9 mmol of the precursor. The reaction mixture was stirred for 20 hours at room temperature, followed by hydrothermal treatment at 95 °C for 24 hours. After cooling to room temperature, the product was filtered and washed with 200 mL of demineralized water and 50 mL of ethanol. The surfactant was removed by soxhlet extraction using a 37 m% ethanol-HCl solution (V/V; 98:2). Finally, the product was dried at 80°C.

Functionalization of BTEVP with MeI via gas-phase: In a sealed 30 mL system, BTEVP-PMO was exposed to 1 mL of iodomethane vapor for two days at room temperature. The vessel was then opened and left at room temperature for a few days before removing residual iodomethane under reduced pressure for 30 min.

2. Structural characterization of Divinyl Pyridine Bridged PMO

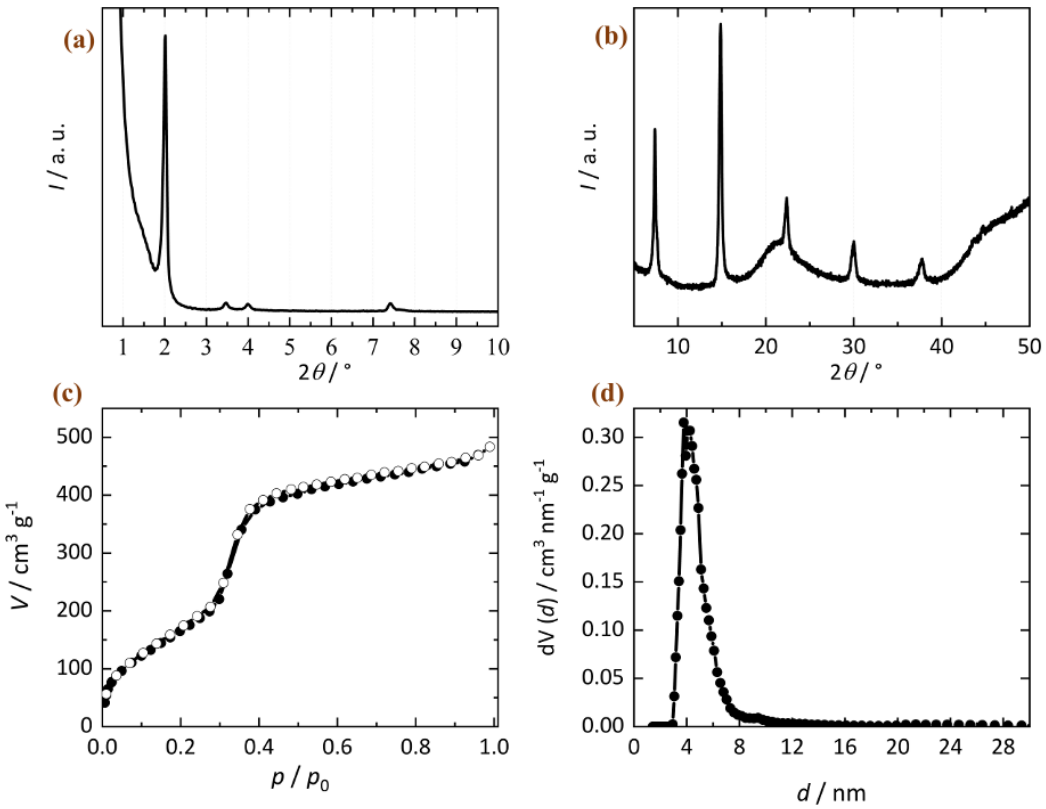


Fig. S1. Normalized X-ray powder diffractograms of Divinyl Pyridine bridged PMO (DVP-PMO) in the ranges of (a) 0.5 to 10° 2θ and (b) 5 to 50° 2θ. The Bragg reflections at angles 2θ = 2°, 3.46°, and 4° can be indexed (100), (110), and (200). They illustrate the 2D triangular lattice of the parallel pores. The Bragg reflections at angles 2θ = 7.5°, 15°, 22.5°, 30°, and 37.5° labelled (00l) illustrate the 1D periodic repetition of silica and organic bridging units along the pore axis. (c) Nitrogen physisorption isotherm, and (d) pore size distribution curves (calculated using the NLDFT kernel for N_2 at 77 K on silica, assuming cylindrical pores, based on the adsorption branch).

3. Structural characterization of Divinyl-methyl Pyridinium Bridged PMO

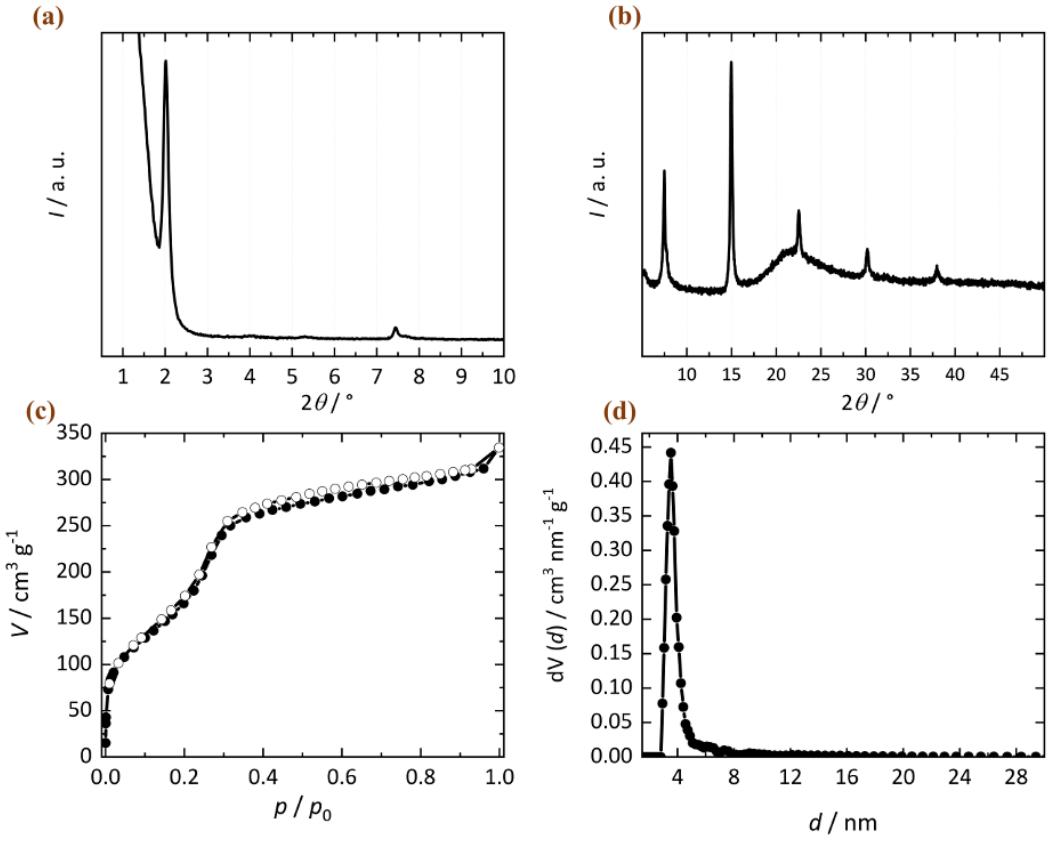


Fig. S2. Normalized X-ray powder diffractograms of Divinyl-Methyl Pyridinium bridged PMO (DVMeP-PMO) in the ranges of (a) 0.5 to 10° 2θ and (b) 5 to 50° 2θ. The Bragg reflections at angles 2θ = 1.9°, 3.45°, and 3.8° can be indexed (100), (110), and (200). They illustrate the 2D triangular lattice of the parallel pores. The Bragg reflections at angles 2θ = 7.5°, 15°, 22.5°, 30°, and 37.5° labelled (00l) illustrate the 1D periodic repetition of silica and organic bridging units along the pore axis. (c) Nitrogen physisorption isotherm, and (d) pore size distribution curves (calculated using the NLDFT kernel for N_2 at 77 K on silica, assuming cylindrical pores, based on the adsorption branch).

4. Neutron structure factor of dry and capillary filled PMO

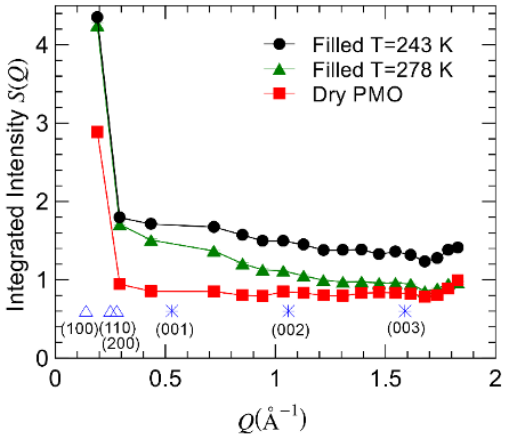


Fig. S3. Q-dependence of the neutron scattering intensity integrated over the entire accessible range of energy $S(Q) = \int_{-\omega_{max}}^{\omega_{max}} S(Q,\omega)d\omega$ *acquired on IN16B for water-filled charged PMO and dry charged PMO. The position of the Bragg reflections of the PMO evaluated by X-Ray diffraction are indicated by open triangles for (hk0) indexes and stars for (00l) indexes.*

5. Fitting procedure

The scattering intensity of water-filled matrix $I^{water\ filled}(Q,\omega)$ can be separated into two contributions arising from the matrix and the confined water, respectively. The third hypothetical water-matrix cross correlation term can be essentially neglected in this study because it exists only in the coherent scattering part, which is a minority given the mostly incoherent character of the water scattering cross-section. The essentially elastic scattering intensity of the matrix was evaluated experimentally from the measurement of the dry PMO $I^{dry}(Q,\omega)$, leading to Eq. S1.

$$I^{water\ filled}(Q,\omega) = I^{dry}(Q,\omega) + I^{water}(Q,\omega) \quad \text{(S1)}$$

The experimental scattering intensity of water corresponds to the incoherent dynamic structure factor of water $S(Q,\omega)$ convoluted by the instrumental resolution function $R(Q,\omega)$, which was measured with a vanadium sample, as written in Eq. S2 where $\otimes$ indicates a convolution in ω.

$$I^{water\ filled}(Q,\omega) = I^{dry}(Q,\omega) + R(Q,\omega) \otimes S^{water}(Q,\omega) \quad (2)$$

Each spectrum was successfully fitted at each individual Q using Eq. S2, where $S^{water}(Q,\omega)$ was modelled by the sum of two Lorentzian functions:

$$S^{water}(Q,\omega) = I_1 L_T(Q,\omega) + I_2 L_R(Q,\omega) \quad (3)$$

A simpler model assuming a single Lorentzian function provided unsatisfactory fits, while the addition of a third component (such as a Lorentzian or a purely elastic Dirac function) was found unnecessary. The four obtained fitted parameters were thus the two Lorentzian intensities I_1 and I_2 and, their spectral widths (HWHM) $\Gamma_T(Q)$ and $\Gamma_R(Q)$.

Following the approach of recent studies on confined water in MCM-41 and PMOs with different surface functionality,[2] we attribute the sharp and broad quasi-elastic components to two distinct dynamics: translational diffusion (T) and local rotation-like motion (R), respectively. We defined $S_T(Q,\omega)$ and $S_R(Q,\omega)$ the dynamic structre factors of these motions. A quasielastic Lorentzian term is expected for a diffusive motion

$$S_T(Q,\omega) = L_T(Q,\omega) \quad (S4)$$

while the second motion comprises both an elastic and an inelastic term due to its localized character

$$S_R(Q,\omega) = A(Q)\,\delta(\omega) + \big(1 - A(Q)\big)L_R(Q,\omega) \quad (S5)$$

$A(Q)$ is the elastic incoherent structure factor (EISF) of the local dynamics.

Provided that the two types of motions are independent, the dynamic structure factor of water writes as

$$S^{water}(Q,\omega) = K\,[S_T(Q,\omega) \otimes S_R(Q,\omega)] \quad (S6)$$

Here, K is a scaling factor that accounts for the reduction in scattering intensity caused by inelastic vibrational modes, commonly described by the Debye-Waller factor. By considering that the two motions are well-separated in time, the final expression for the dynamic structure factor of water obtained by combining Eqs. S4-S6 expresses as follows:

$$S^{water}(Q,\omega) = K[A(Q)\,L_T(Q,\omega) + (1 - A(Q))\,L_R(Q,\omega)] \quad (S7)$$

From a comparison between Eq. S3 and S7, it appears that the parameters derived from the fit of Eq. S2 to the experimental spectra allow to evaluate the EISF of the localized motion with $A(Q) = \frac{I_1}{I_1+I_2}$ as well as the spectral widths of the two quasielastic contributions $\Gamma_T(Q)$ and $\Gamma_R(Q)$.

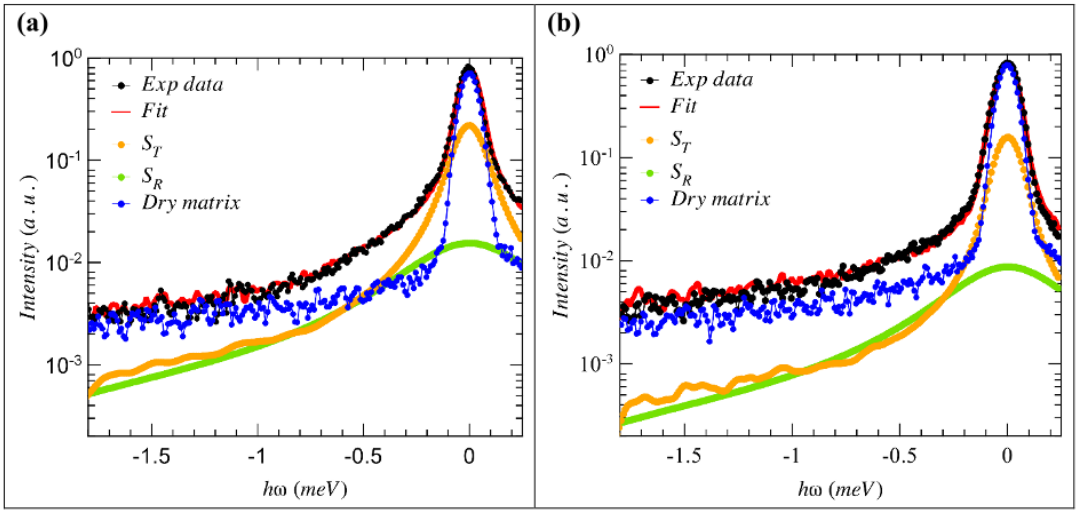


Fig. S4. Representative experimental (black) and fitted (red) S(Q,ω) curves at T = 280 K and Q = 1.5 Å^{-1}, modeled using two Lorentzian functions added to the dry matrices, for water-filled (a) neutral DVP-PMO and (b) charged DVMeP-PMO acquired by SHARP.

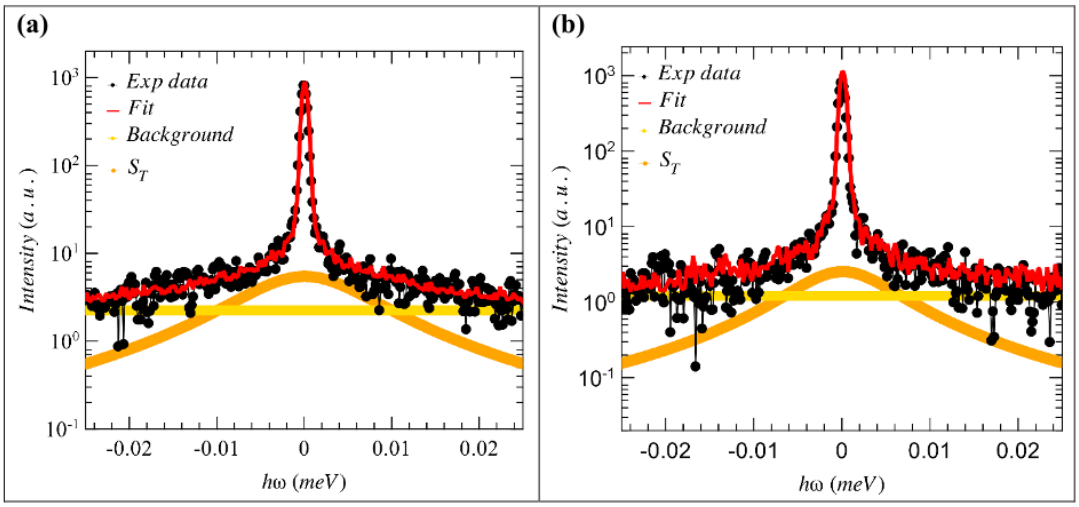


Fig. S5. Representative neutron backscattering experimental (IN16B) and fitted S(Q,ω) curves at T = 278 K and Q = 1.62 Å^{-1}, modeled using a Lorentzian with a flat background, for (a) fully-filled and (b) partially-filled charged DVMeP-PMO acquired by IN16B.

6. Elastic Incoherent Structure Factor (EISF) of the local quasi-elastic relaxation obtained from SHARP measurements

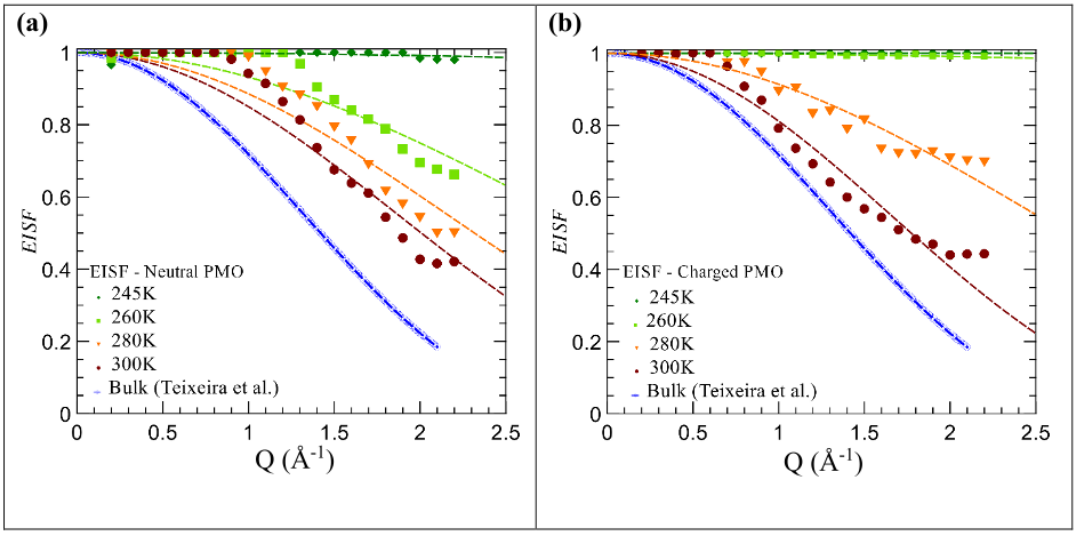


Fig. S6. Elastic Incoherent Structure Factor (EISF) of the local quasi-elastic relaxation (symbols) obtained from SHARP measurements at four different temperatures for water confined in (a) neutral DVP-PMO and (b) charged DVMeP-PMO. The blue dashed line represents the EISF for isotropic rotation of hydrogens around the oxygen atom, assumed to be temperature-independent within the same temperature range, as derived from Teixeira et al..[3]

7. Timescale of rotational and librational motions

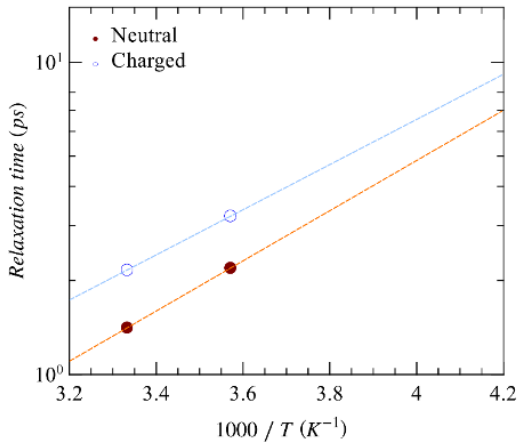


Fig. S7. Timescale of rotational and librational motions (i.e., relaxation time) for the water in neutral and charged PMOs.

8. Arrhenius fitting of the translational diffusion coefficient of water in neutral and charged PMOs

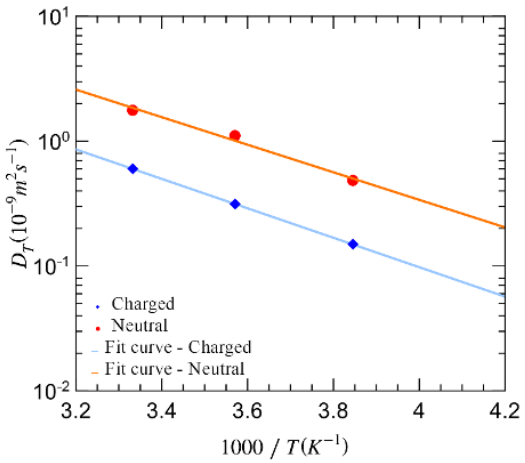


Fig. S8. Arrhenius fitting of the translational diffusion coefficient of water in neutral and charged PMOs, yielding activation energies of 21.1 kJ/mol and 22.6 kJ/mol, respectively.

9. Elastic and Inelastic Fixed Window Scans on IN16B with a 3μeV Energy Offset in the 300K–195K Temperature Range

The Elastic and Inelastic Fixed Window Scans (EFWS and IFWS) measurement was performed on fully-filled charged PMO (DVMeP-PMO). The data were processed using Mantid scripts, and the IFWS were fitted assuming that the dynamic structure factor could be described by a single Lorentzian. The width of this Lorentzian was modeled with an Arrhenius temperature dependence, corresponding to a relaxation time with the same behavior. This model was chosen based on the assumption that, given the high energy resolution of IN16B, only translational motion would contribute within its observation window. The scans were fitted independently for each *Q*-value, except the activation energy that was fitted as a *Q*-independent global parameter.

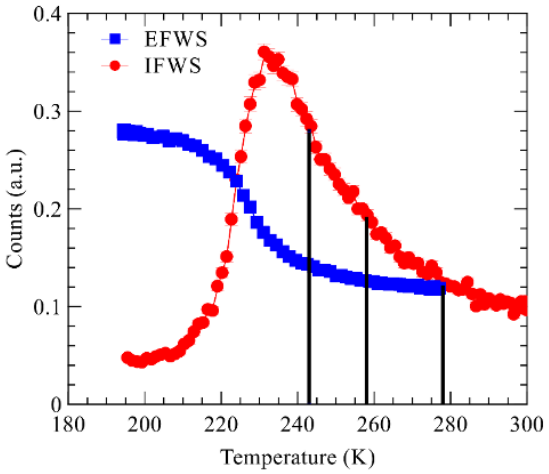


Fig. S9. Illustration of Elastic and Inelastic Fixed Window Scans (EFWS and IFWS) measured for fully filled, charged PMO (DVMeP-PMO) summed over all the scattering angles. The black lines indicate the temperatures at which the spectra were acquired.

Reference:

(1) Waki, M.; Mizoshita, N.; Ohsuna, T.; Tani, T.; Inagaki, S. Crystal-like periodic mesoporous organosilica bearing pyridine units within the framework. *Chemical Communications* **2010**, *46* (43), 8163–8165.
(2) Jani, A.; Busch, M.; Mietner, J. B.; Ollivier, J.; Appel, M.; Frick, B.; Zanotti, J.-M.; Ghoufi, A.; Huber, P.; Fröba, M. Dynamics of water confined in mesopores with variable surface interaction. *The journal of chemical physics* **2021**, *154* (9).
(3) Teixeira, J.; Bellissent-Funel, M.-C.; Chen, S.-H.; Dianoux, A.-J. Experimental determination of the nature of diffusive motions of water molecules at low temperatures. *Physical Review A* **1985**, *31* (3), 1913.

8.7. Supporting Information for "Periodic Mesoporous Organosilicas as Host Materials for Studying Surface Chemistry Effects on the Freezing and Melting Behavior of Nanoconfined Water"

Supporting Information for

Periodic Mesoporous Organosilicas as Host Materials for Studying Surface Chemistry Effects on the Freezing and Melting Behavior of Nanoconfined Water

Philip Lenz[a,b], Uta Sazama[a], Michael Steiger[a,] and Michael Fröba[a,b,*]*

AFFILIATIONS

[a] Institute of Inorganic and Applied Chemistry, University of Hamburg, Martin-Luther-King-Platz 6, 20146 Hamburg, Germany

[b] The Hamburg Centre for Ultrafast Imaging, Luruper Chaussee 149, 22761 Hamburg, Germany

E-mail: michael.steiger@uni-hamburg.de and michael.froeba@uni-hamburg.de

Chemicals

All reagents and solvents used for the precursor and PMO synthesis were purchased from commercial suppliers (*abcr*, *Merck*, *Sigma-Aldrich*, *TCI*, *Fisher Scientific*). The surfactants C_{20}TAB and C_{22}TAB were prepared according to the literature.[1]

MCM-41 silica synthesis

The synthesis of MCM-41 silica was performed following the specified protocols, using CTAB with alkyl chain lengths ranging from C12 to C22.[2]

PMO synthesis

The following section presents the synthesis and characterization of materials that were not included in the water vapor sorption study[3] but were additionally utilized in this study.

General PMO synthesis procedure:

The corresponding surfactant type was first dissolved in an aqueous NaOH solution at 31°C for 30 minutes.[a)] Then the solution was stirred for an additional 30 minutes at room temperature before the precursor was added. The reaction mixture was stirred for 20 hours at room temperature and then subjected to hydrothermal treatment. After cooling to room temperature, the product mixture was filtered and washed with 200 mL of demineralized water and 50 mL of ethanol. The surfactant was removed by Soxhlet extraction using a 37 m% ethanol-HCl solution (V/V; 98:2). Finally, the product was dried at 80°C. Table S1 details the exact compositions, as well as the temperature and duration of the hydrothermal treatment for the various precursors used.

[a)] For the synthesis of BTEVClB-PMOs, absolute ethanol (17 molar equivalents relative to the precursor) was added as a co-solvent before introducing the precursor, to enhance its solubility.

Table S1: PMO synthesis conditions, including amounts (n) of the precursor (P), of sodium hydroxide (NaOH) and of the respective surfactant (S), the volumes of water (V_w), as well as the temperature (T_{ht}) and duration (t_{ht}) of the hydrothermal treatment for each PMO type, along with the resulting pore size (d_P).

PMO Type	d_P / nm	n_P / mmol	n_{NaOH} / mmol	Surfactant type	n_S / mmol	V_w / mL	T_{ht} / °C	t_{ht} / h
BTEVA	3.9	3.4	18	C_{16}TAB	4.2	40	95	24
	4.4	3.4	18	C_{18}TAB	4.2	40	95	24
	4.9*	1.3	7	C_{16}TAB	1.6	16	95	24
	5.3	3.4	18	C_{20}TAB	4.2	40	95	24
BTEVP	4.7	0.7	3.4	C_{18}TAB	0.8	7.5	95	24
BTEVClB	4.3	1.4	7	C_{18}TAB	1.5	15	100	25

* Before adding the precursor, 1 ml of *n*-hexane was introduced as a swelling agent additive for the synthesis.

PMO characterization

The porosity of the materials was characterized through nitrogen physisorption and powder X-ray diffraction (P-XRD). The results are shown in Table S2. Since most of the materials characterized in our previous study[3] are also used in this work, the corresponding porosity, hydrophilicity values and water densities are provided in Table S3. The degree of functionalization and its impact on porosity during the transition from BTEVP- to *N*-MBTEVP^{+}I^{-}–PMO are shown in Table S4 for different pore sizes.

Table S2: The nitrogen physisorption analysis provides the pore diameter (d_P), hydraulic radius (r_h), pore volume at relative pressures of 0.8 ($V_{P, n, 0.8}$), specific BET surface area (S_{BET}), along with PXRD analysis results for the periodicity of the repetition units (d_{RU}), the (100) reflection (d_{100}), and the calculated pore wall thickness (d_W).

Material	d_P / nm	r_h / nm	$V_{P, n, 0.8}$ / cm^3/g	S_{BET} / m^2/g	d_{RU} / nm	d_{100} / nm	d_W / nm
MCM-41 silica	3.5	1.4	0.794	1126	-	3.52	0.56
	4.4	1.9	1.04	1069	-	4.27	0.53
	4.6	2.2	0.906	808	-	4.39	0.47
	5.7	2.5	0.754	601	-	5.53	0.69
BTEVA-PMO	3.9	1.7	0.929	1125	1.19	4.23	0.98
	4.4	1.9	0.884	909	1.18	4.48	0.77
	4.9	2.4	1.37	1155	1.18	5.39	1.32
	5.3	2.2	0.601	536	1.19	5.39	0.92
BTEVP-PMO	4.7	2.3	0.990	859	1.18	4.99	1.06
BTEVClB-PMO	4.3	2.0	1.07	1071	1.19	4.25	0.61
N-MBTEVP^{+}I^{-}	3.8	1.9	0.304	394	1.18	4.60	1.51

Table S3: Contact angle (θ), hydrophilicity index based on the relative pressure at the inflection point of pore emptying (HI_{id}), surface hydration site (SHS) density, and average water density inside the porous materials, with pore diameter (d_P), specific BET surface area (S_{BET}) and pore volume (V_P), for the samples used in this study. The data are taken from our previous work.[3]

Material	d_P / nm	S_{BET} / m^2/g	V_P / cm^3/g	θ / °	HI_{id}	SHS / nm^{-2}	$\rho_{water, ave}$ / g/cm^3
N-MBTEVP$^+$I$^-$	3.2	836	0.453	44.0	49.6	1.49	0.57
	3.8*	520	0.456	40.0	49.6	2.21	0.72
	4.4	670	0.594	40.5	69.3	1.50	0.71
MCM-41 silica	3.2	1034	0.644	37.5	67.1	1.25	0.72
	3.7	1118	0.840	33.2	67.8	1.32	0.77
	3.9	1071	0.895	45.2	70.0	1.20	0.79
	5.3	911	1.10	44.0	73.5	1.48	0.82
BTEB-PMO	3.2	882	0.588	42.0	46.8	1.47	0.73
	3.7	903	0.693	44.6	51.3	1.41	0.79
BTEVA-PMO	2.9	894	0.538	43.8	36.4	1.17	0.54
	3.1	1181	0.667	50.1	41.8	0.90	0.55
	3.2	1258	0.821	46.1	46.8	0.69	0.64
	3.4	1179	0.812	46.5	36.6	0.70	0.67
	3.5	1256	0.865	45.5	56.0	0.65	0.72
	3.8	1005	0.817	55.0	52.9	0.80	0.75
BTEVP-PMO	3.5	851	0.561	50.6	46.9	0.86	0.73
	4.4	750	0.731	51.3	62.6	1.32	0.77
	5.7	739	0.872	59.0	53.0	1.20	0.62
BTEVB-PMO	3.4	779	0.590	62.6	29.4	0.53	0.53
	3.8	682	0.525	75.2	34.2	0.40	-
	4.4	790	0.791	78.9	45.5	0.43	-
	4.7	624	0.701	-	50.0	0.58	-
	5.5	840	1.01	77.5	-	0.32	-
N,*N*-DMBTEVA	3.4	726	0.525	68.5	27.4	0.46	0.45
	3.5	658	0.520	69.0	30.6	0.50	0.46
	3.8	801	0.681	77.4	38.7	0.44	0.56
	4.7	592	0.598	81.9	36.3	0.53	-
	4.9	578	0.606	-	-	0.43	-
BTEVClB	3.8	990	0.872	79.51	36.8	0.44	-

* Sample was used specifically for investigating IW-filled samples.

Table S4: Comparison of functionalized *N*-MBTEVP^{+}I^{-}-PMO with pore size (d_P) and functionalization degree (determined by NMR (F_{NMR}) and TG-DTA-MS (F_{TDM})) with the initial BTEVP-PMO (i). The impact of functionalization on material characteristics is expressed as ratios of pore volume ($V_P/V_{P,i}$), pore size ($d_P/d_{P,i}$) and, BET surface area ($S_{BET}/S_{BET,i}$).

d_P / nm	$V_P/V_{P,i}$	$d_P/d_{P,i}$	$S_{BET}/S_{BET,i}$	F_{NMR} (F_{TDM})/ %
3.2	0.81	0.91	0.99	7 (-)
3.5	0.65	0.92	0.71	10 (15)
3.8	0.62	0.86	0.69	18 (18)

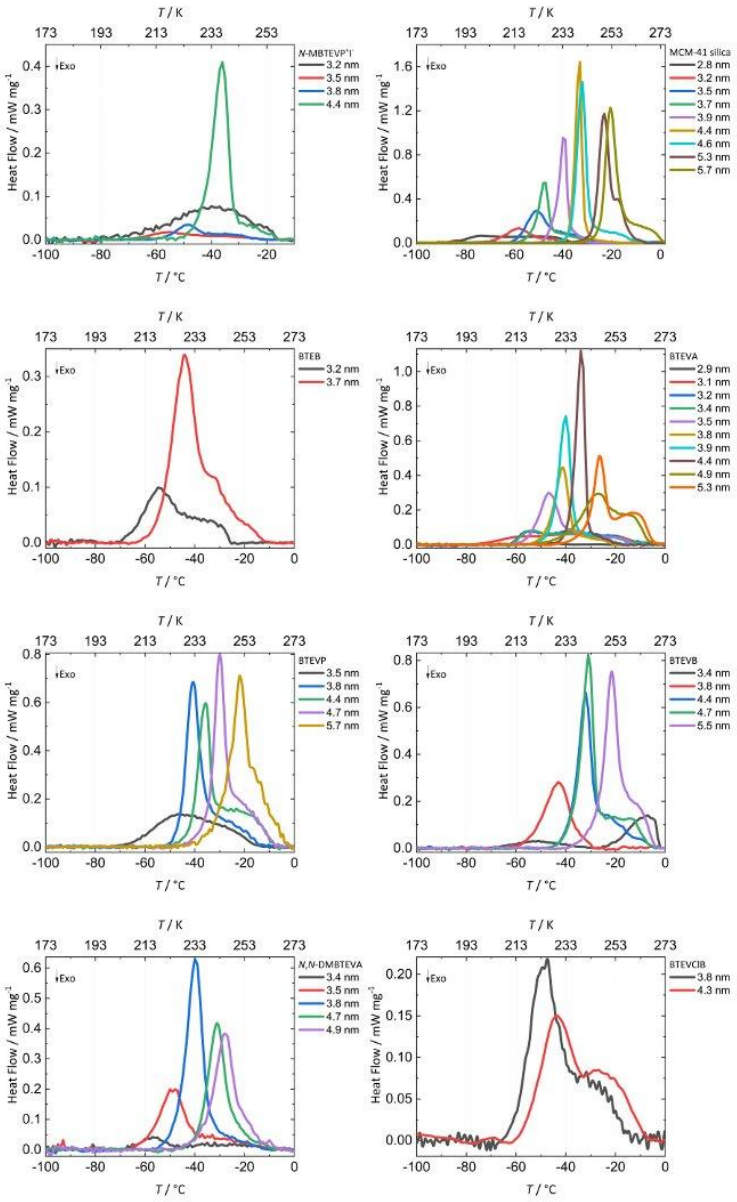


Figure S1: Baseline-corrected DSC curves of water in MCM-41 silicas and different PMOs with varying pore diameters, filled using the C-method. The heat flux values correspond to the total water content in each measurement. The DSC measurements were conducted at a heating rate of 3 K/min.

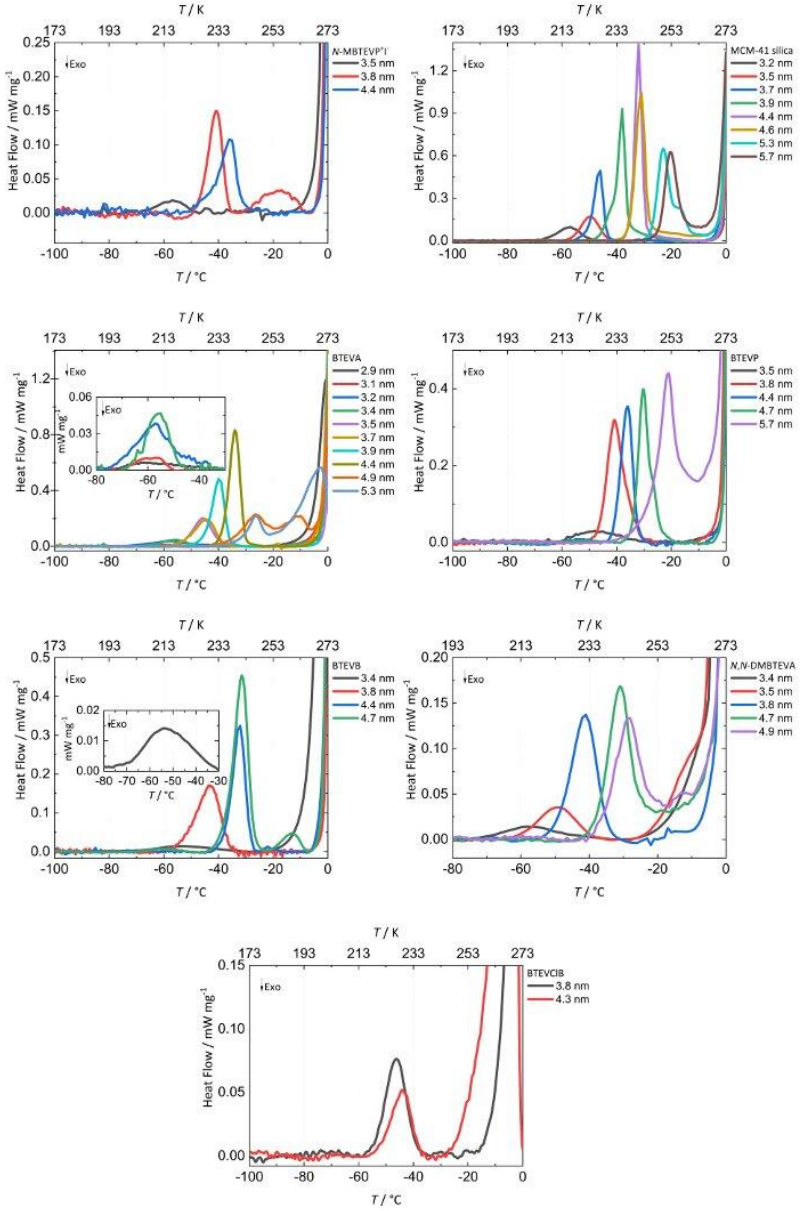


Figure S2: Baseline-corrected DSC curves of water in MCM-41 silicas and different PMOs with varying pore diameters, filled using the IW-method. The heat flux values correspond to the total water content in each measurement. The DSC measurements were conducted at a heating rate of 3 K/min.

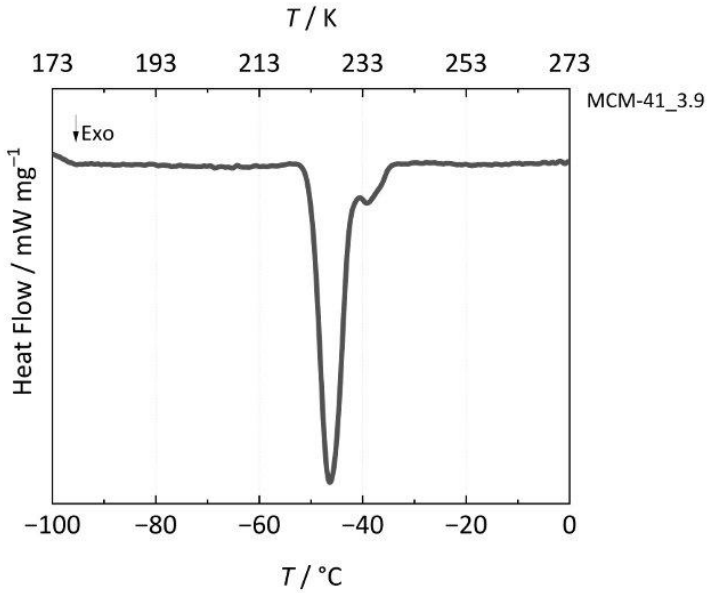


Figure S3: Baseline-corrected DSC cooling curves of water in MCM-41_3.9 with a cooling rate of 3 K/min. The heat flux values correspond to the total water content in each measurement.

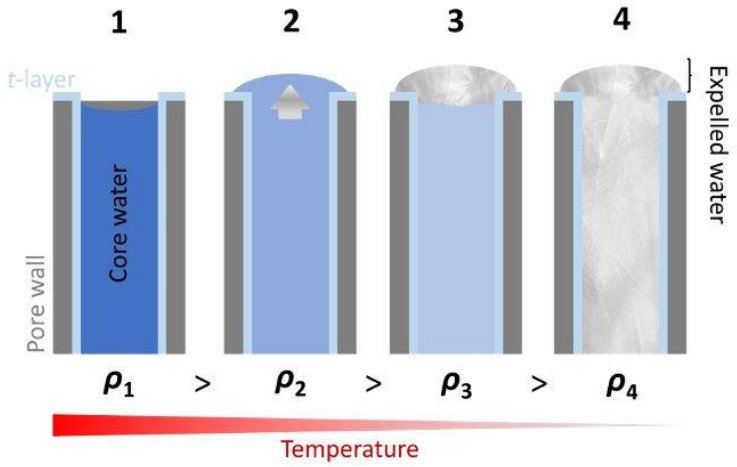


Figure S4: Schematic illustration of the process of water expulsion during cooling due to density decrease. State 1: sample after water filling, 2: water expulsion from the pores due to density decrease at lower temperatures, 3: freezing of expelled water and 4: freezing of core water inside the pores.

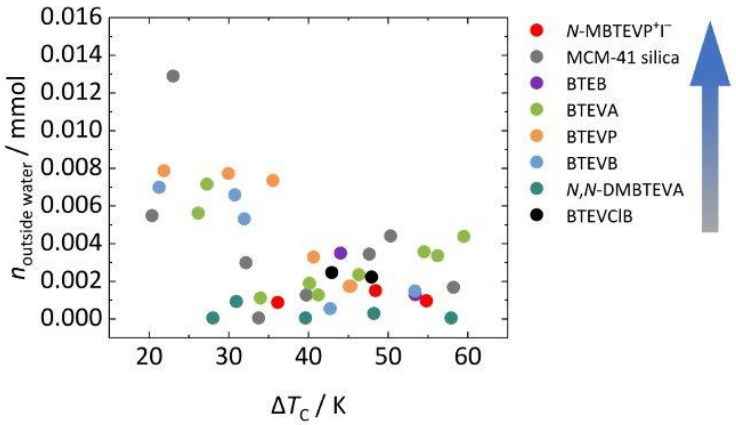


Figure S5: Dependence of the amount of water outside the pores ($n_{\text{outside water}}$) on the melting temperature depression for C-materials (ΔT_C). The arrow denotes increasing hydrophilicity of the materials.

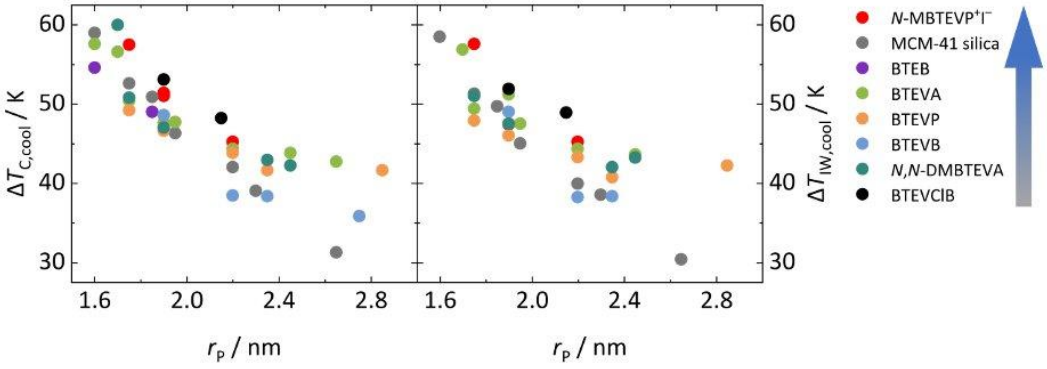


Figure S6: Pore radius dependent freezing point depression (ΔT_{cool}) of water confined in the pores of various MCM-41 silica and PMOs, filled using the C-method (left) and the IW-method (right). The arrow denotes increasing hydrophilicity of the materials.

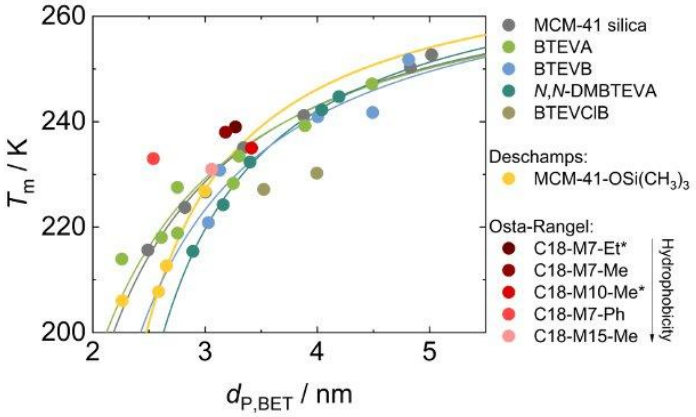


Figure S7: Pore-size-dependent melting temperature of water confined in different materials, including hydrophobized MCM-41 reported by Deschamps et al.[4] and Osta-Rangel[5], hydrophilic materials such as unfunctionalized MCM-41 silica and BTEVA-PMOs, as well as hydrophobic BTEVB-, BTEVClB-, and *N*,*N*-DMBTEVA-PMOs. For comparison, the BET-derived pore size ($d_{P,BET} = 4\ V_P / S_{BET}$) was used for all materials. The lines represent Gibbs–Thomson fits. Following the approach of Deschamps et al., the melting transition temperature of the smallest pore size in their dataset was excluded from the fit.

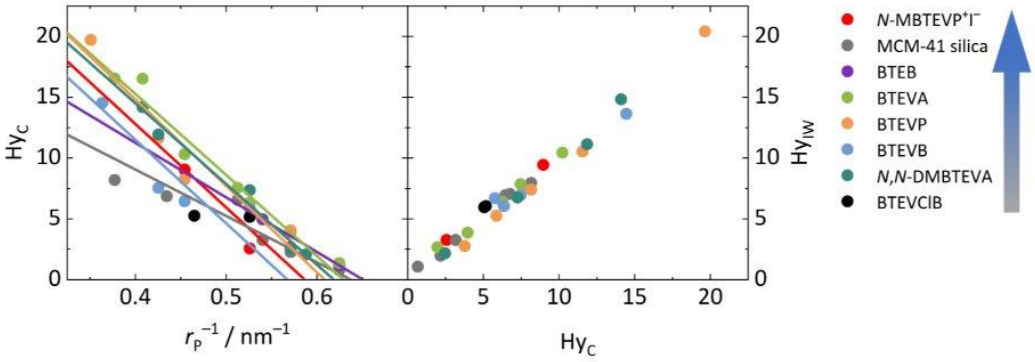


Figure S8: Linear relationship between the hysteresis between melting and freezing transition and the reciprocal pore radius (r_P^{-1}) for C-materials (left) and the correlation of the hysteresis (Hy) for IW- and the C-materials (right). The arrow denotes increasing hydrophilicity of the materials.

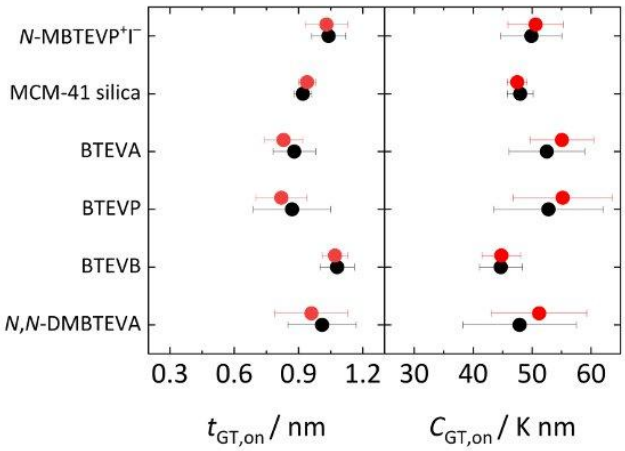


Figure S9: The *t*-layer thickness ($t_{GT,on}$) and Gibbs–Thomson constant ($C_{GT,on}$) values for C-materials, determined from the onset of the melting transition using the Gibbs–Thomson equation (black shades) and its linearized form (red shades). The materials are arranged along the y-axis in order of increasing hydrophilicity.

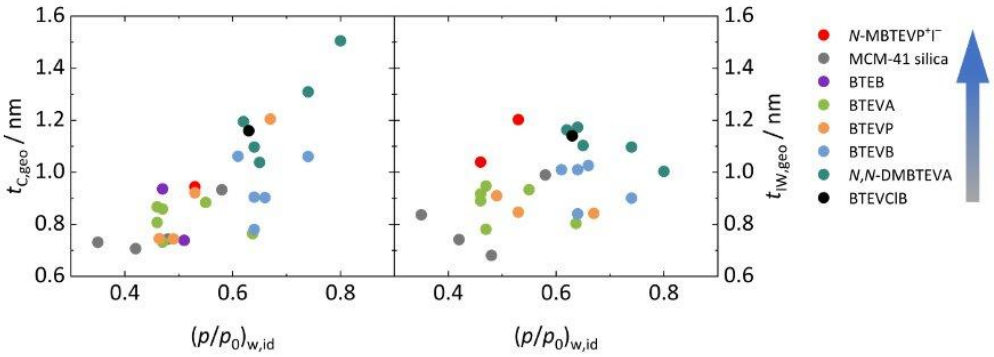


Figure S10: Relationship between the relative pressure at the inflection point in the desorption branch of water vapor sorption isotherms ($(p/p_0)_{w,id}$) and the *t*-layer thickness (t_{geo}) for C-materials (left) and IW-materials (right). The arrow denotes increasing hydrophilicity of the materials.

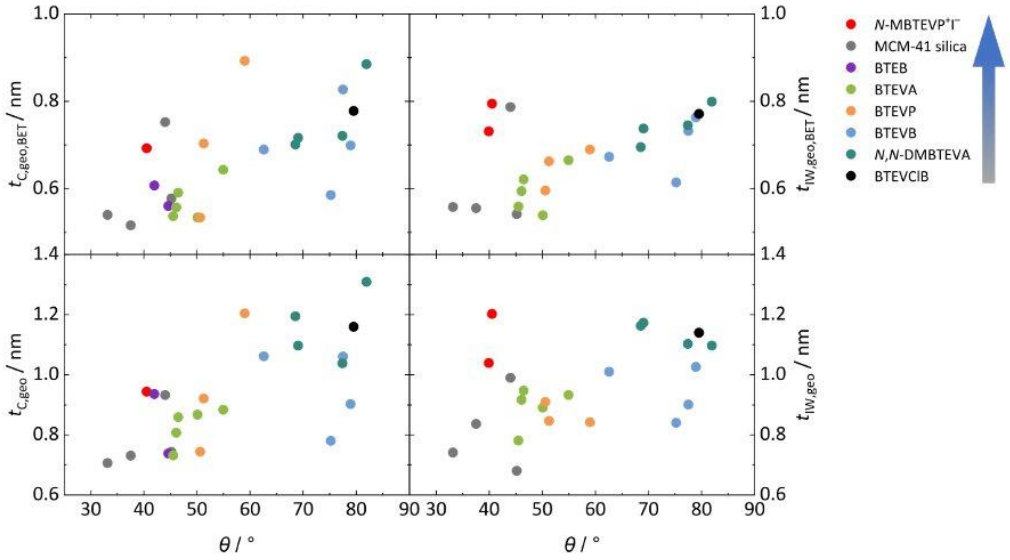


Figure S11: Influence of the contact angle (θ) on the t-layer thicknesses $t_{geo,BET}$ (top) and t_{geo} (bottom) for C-materials (left) and IW-materials (right). The arrow denotes increasing hydrophilicity of the materials.

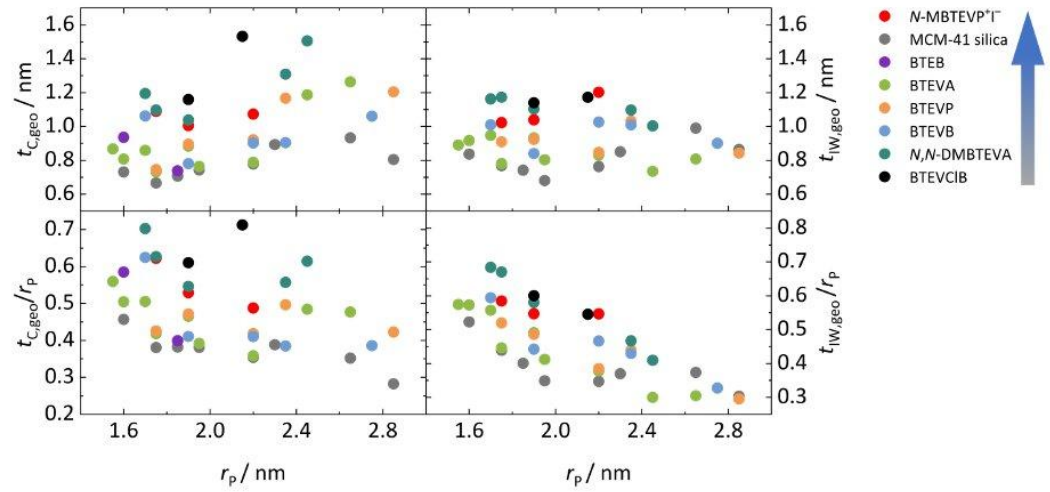


Figure S12: Pore radius dependence of the t-layer thickness (t_{geo}) (top) and relative thickness (t_{geo}/r_P) (bottom) for C-materials (left) and IW-materials (right). The arrow denotes increasing hydrophilicity of the materials.

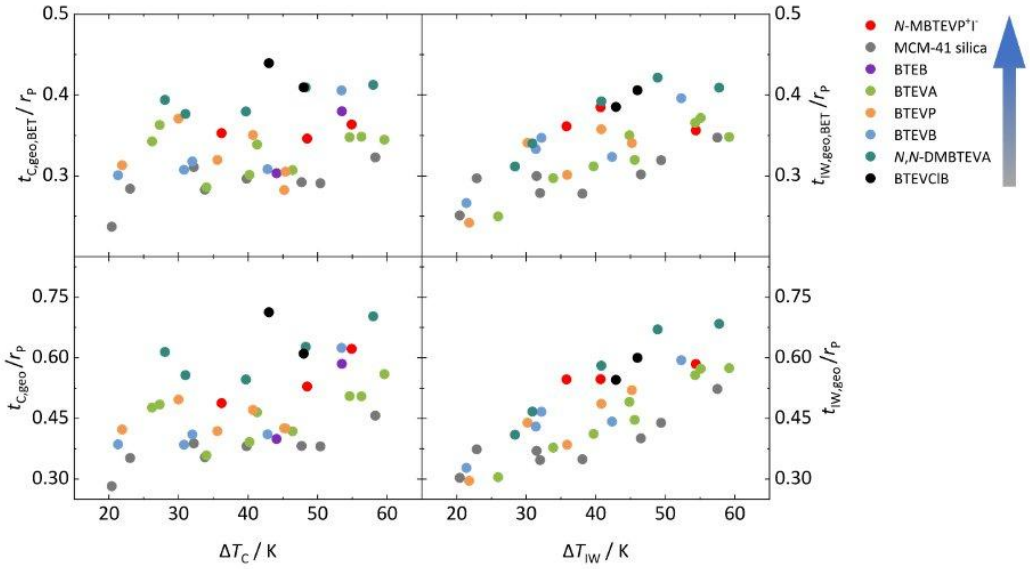


Figure S13: Influence of the melting temperature depression (ΔT) on the relative t-layer thicknesses $t_{geo,BET}/r_P$ (top) and t_{geo}/r_P (bottom) for C-materials (left) and IW-materials (right). The arrow denotes increasing hydrophilicity of the materials.

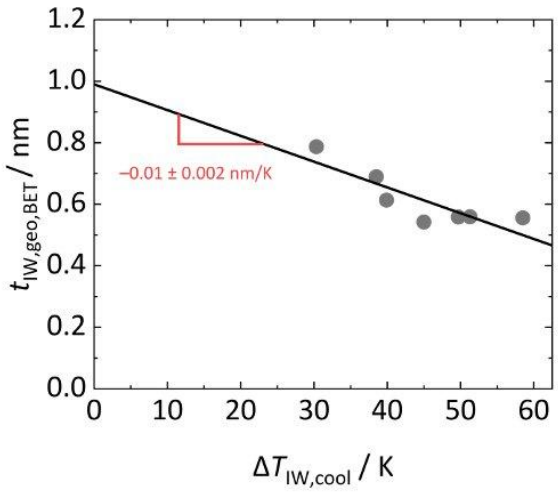


Figure S14: Linear fit of t-layer thickness ($t_{geo,BET}$) versus the freezing temperature depression, illustrated using MCM-41 silicas filled via the IW-method.

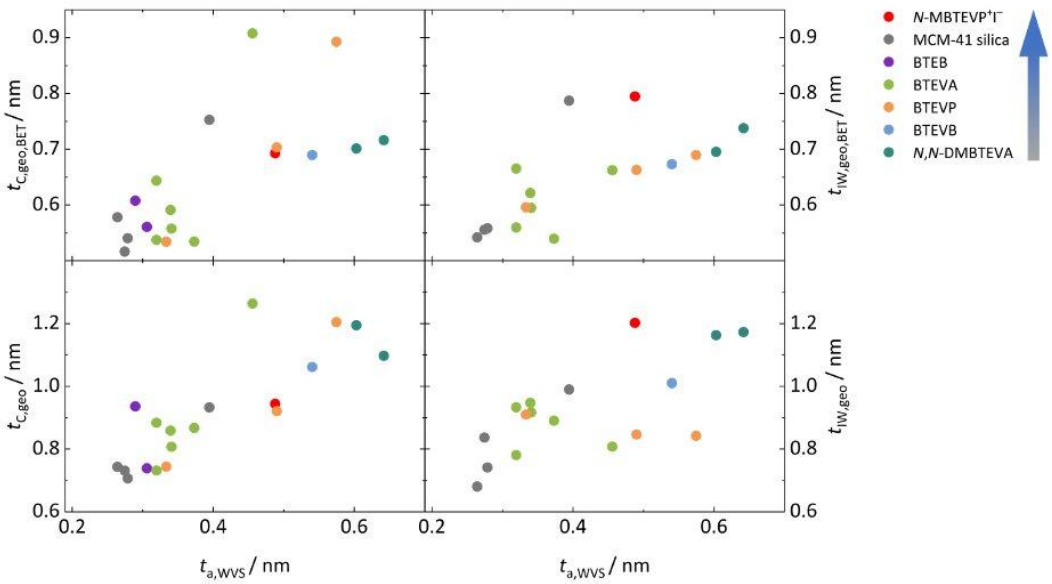


Figure S15: Plot of the adsorption layer thickness ($t_{a,WVS}$) against the non-freezable layer thicknesses t_{geo} (bottom) and $t_{geo,BET}$ (top) for C-materials (left) and IW-materials (right). The arrow denotes increasing hydrophilicity of the materials.

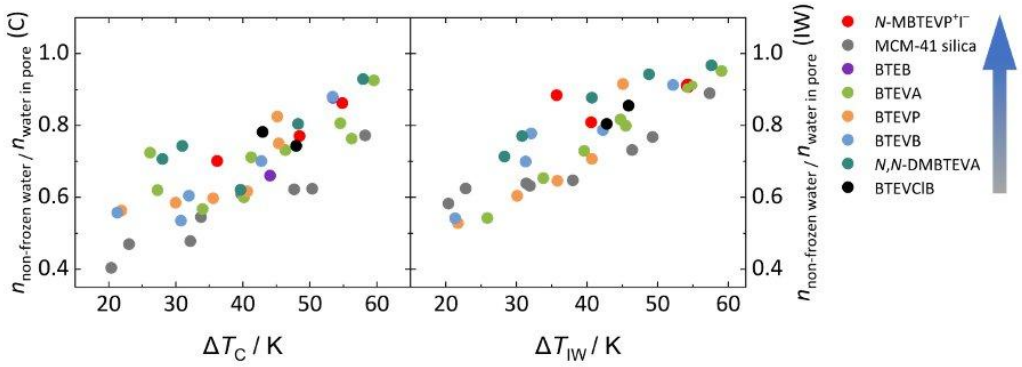


Figure S16: Plot of the non-frozen water fraction ($n_{non\text{-}frozen\ water}/n_{water\ in\ pore}$) against the melting temperature depression for C-materials (left) and IW-materials (right). The arrow denotes increasing hydrophilicity of the materials.

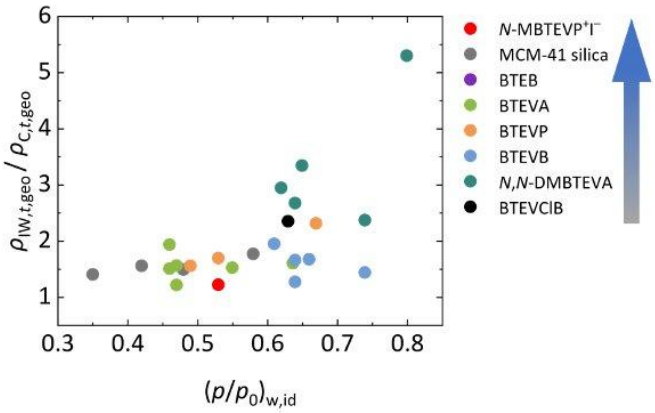


Figure S17: Plot of the density ratio between the IW- and C-filling methods ($\rho_{IW,t,geo} / \rho_{C,t,geo}$) against the relative pressure at the inflection point of the desorption branch of the water vapor sorption isotherm ($(p/p_0)_{w,id}$). The arrow denotes increasing hydrophilicity of the materials.

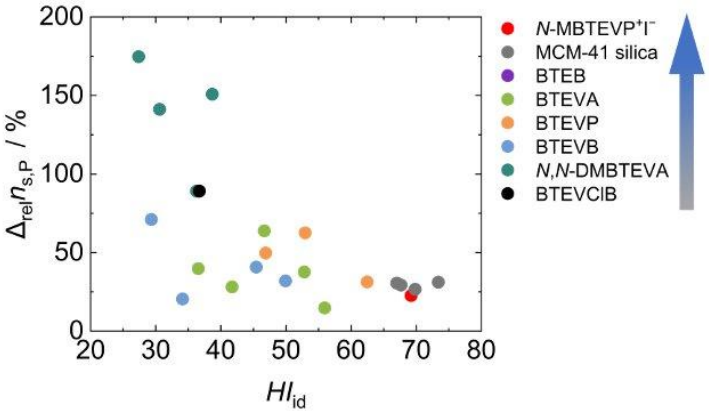


Figure S18: Plot of the relative increase in specific pore water content [$\Delta_{rel} n_{s,P} = (n_{s,P,IW} - n_{s,P,C})(n_{s,P,C})^{-1}$] for C- and IW-materials against the hydrophilicity index (HI_{id}). The arrow denotes increasing hydrophilicity of the materials.

REFERENCES

(1) Mietner, J. B. Visiting nanopores: The great potential of PMOs for studying the properties of water in nanopores of different polarity. Ph.D. Thesis, University of Hamburg, Germany, 2018.

(2) Jähnert, S. Study of pure substances in periodic mesoporous silica material with thermophysical methods and in-situ small-angle x-ray-diffraction. Ph.D. Thesis, Technical University of Berlin, Germany, 2008.

(3) Lenz, P.; Meinert, S.-M.; König, S.; Steiger, M.; Fröba, M. Influence of surface chemistry on t-layer dimension and density of nanoconfined water by fine-tuning the functional groups of periodic mesoporous organosilica. *J. Phys. Chem. C* **2025**, *129* (27), 12536–12550. DOI: 10.1021/acs.jpcc.5c02277.

(4) Deschamps, J.; Audonnet, F.; Brodie-Linder, N.; Schoeffel, M.; Alba-Simionesco, C. A thermodynamic limit of the melting/freezing processes of water under strongly hydrophobic nanoscopic confinement. *Phys. Chem. Chem. Phys.* **2010**, *12* (7), 1440–1443. DOI: 10.1039/B920816J.

(5) Osta-Rangel, O. Water confined in hydrophobic nanopores: Towards a new phase diagram. Ph.D. Thesis, University of Paris-Saclay, France, 2021.

8.8. Supporting Information for "The Structure of Ice under Confinement in Periodic Mesoporous Organosilicas (PMOs)"

The Structure of Ice Under Confinement in Periodic Mesoporous Organosilicas (PMOs) - Supporting Information

Niels C. Gießelmann,[1] Philip Lenz,[2,3] Sophia-Marie Meinert,[2] Tamás Simon,[2] Robert P. C. Bauer,[1,4] Wonhyuk Jo,[5,1] Sarah Claas,[2] Christian Köhn,[2] Nele N. Striker,[1] Michael Fröba,[2,3,a)] and Felix Lehmkühler[1,3,b)]

[1)] *Deutsches Elektronen-Synchrotron DESY, Notkestr. 85, 22607 Hamburg, Germany*

[2)] *University of Hamburg, Institute of Inorganic and Applied Chemistry, Martin-Luther-King-Platz 6, 20146 Hamburg, Germany*

[3)] *The Hamburg Centre for Ultrafast Imaging, Luruper Chaussee 149, 22761 Hamburg, Germany*

[4)] *Freiberg Center for Water Research, Technische Universität Bergakademie Freiberg, Winklerstraße 8, 09599 Freiberg, Germany*

[5)] *European XFEL, Holzkoppel 4, 22869 Schenefeld, Germany*

[a)] Electronic mail: michael.froeba@uni-hamburg.de

[b)] Electronic mail: felix.lehmkuehler@desy.de

S1. SYNTHESIS OF POROUS MATERIALS

The synthesis of the porous materials was performed following the description given in a previous paper.[1] However, BTEB(3.8) and the BTEVP+-samples were not used in this previous study. The BTEB precursor was synthesized follwing the instructions of Shea et al.[2] For the preparation of the sample, surfactant/NaOH solution was dissolved exclusively at room temperature for 30 min and its purification was carried out by the exclusive use of ethanol in the soxhlet extraction. The product was then dried at 60 °C. In the BTEVP+ samples, the charge was introduced using a postsynthetic pathway. In this approach, the colorless BTEVP-PMO was exposed to a saturated iodomethane atmosphere at room temperature for two days in a sealed system. The yellowish powder was freed from iodomethane residues by keeping it open at room temperature for two days and then in vacuum (0.1 mbar) for 5 minutes. The chemical structures of all used precursors are shown in Fig. S1.

Sample	n_P [mmol]	n_{NaOH} [mmol]	**Surfactant type**	n_S [mmol]	V_{water} [mL]	T_{ht} [°C]	t_{ht} [h]
BTEB(3.8)	4.10	14.0	C_{16}TAB	4.1	40	95	27
BTEVB(3.8)	9.90	108	C_{18}TAB	14.7	120	95	12
BTEVFB(4.9)	3.40	22.4	C_{18}TAB	4.7	40	95	24
BTEVFB(4.4)	1.78	12.8	C_{18}TAB	2.8	21	80	24
BTEVFB(3.8)	3.56	36.0	C_{18}TAB	5.5	42	80	24
BTEVA(4.3)	3.52	18.8	C_{18}TAB	4.2	40	80	24
BTEVA(3.8)	6.82	36.0	C_{16}TAB	8.3	80	95	24
BTEVA(3.4)	3.52	18.8	C_{14}TAB	4.2	40	80	24
BTEVP(3.8)	2.92	13.6	C_{14}TAB	3.1	30	95	24
BTEVP(3.5)	1.95	7.50	C_{10}TAB	2.1	20	95	27
BTEVP+(3.5)	-	-	-	-	-	-	-
BTEVP+(3.4)	-	-	-	-	-	-	-
BTEVCl(3.8)	1.43	6.91	C_{18}TAB	1.5	15	90	25

TABLE S1: Shown are the amounts (n) of the precursor (P), of sodium hydroxide (NaOH) and of the respective surfactant (S), as well as the volumes of water (V_{water}) used for the syntheses of the respective PMO. In addition, the temperature (T_{ht}) and duration of the hydrothermal treatment (t_{ht}) are given. The samples printed in italics were only used in the XCCA experiment.

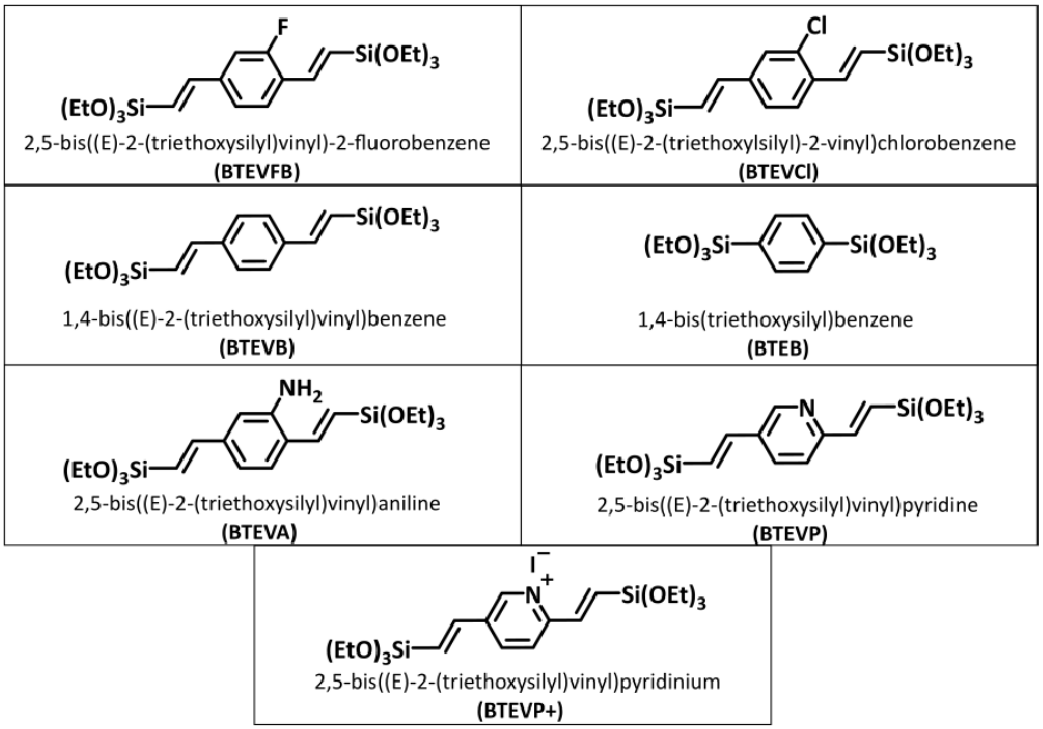


FIG. S1: The structural formulae of the used precursors.

S2. N_2 PHYSISORPTION

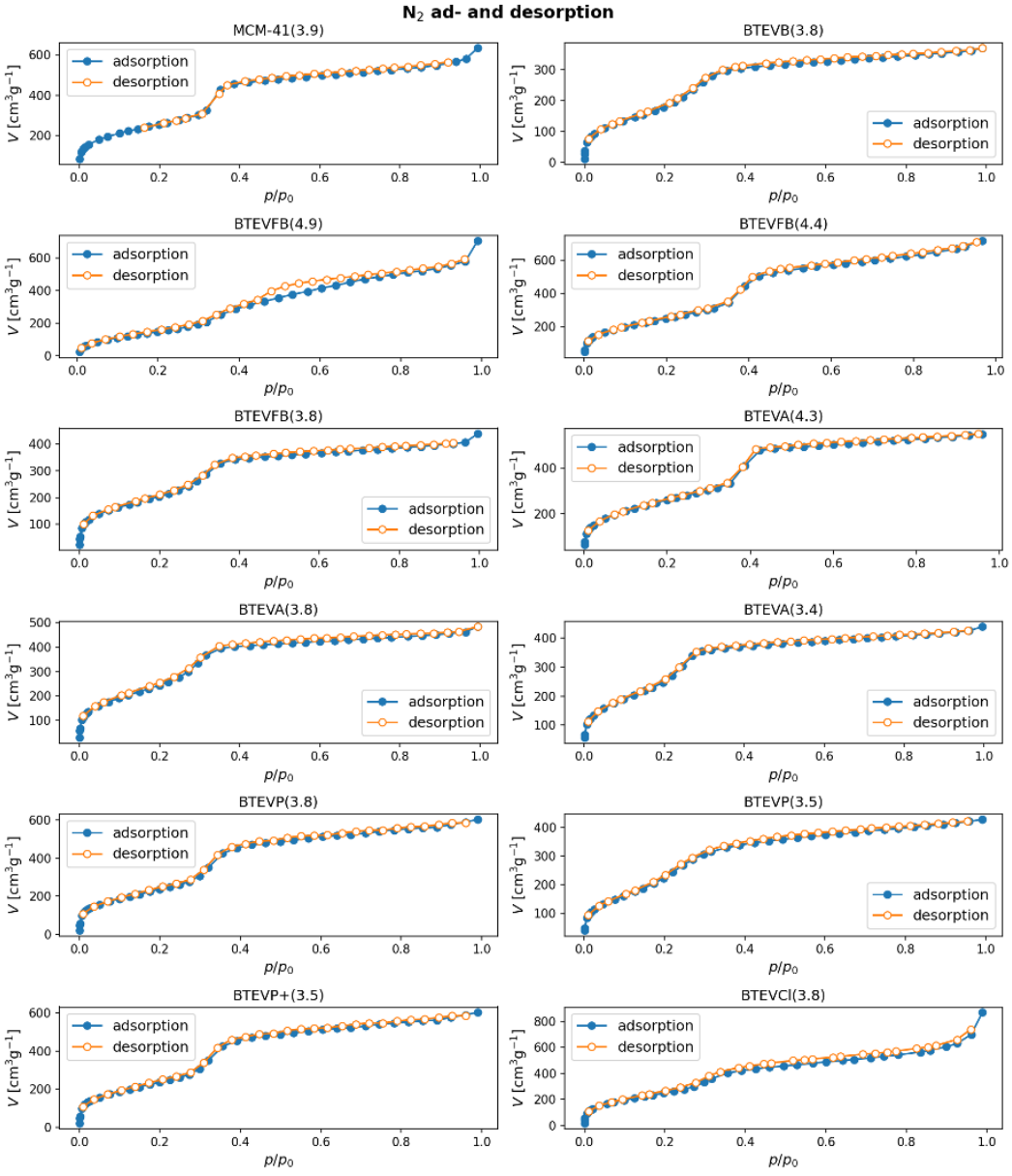


FIG. S2: N_2 ad- and desorption isotherms of the measured materials.

S3. PORE SIZE DISTRIBUTIONS

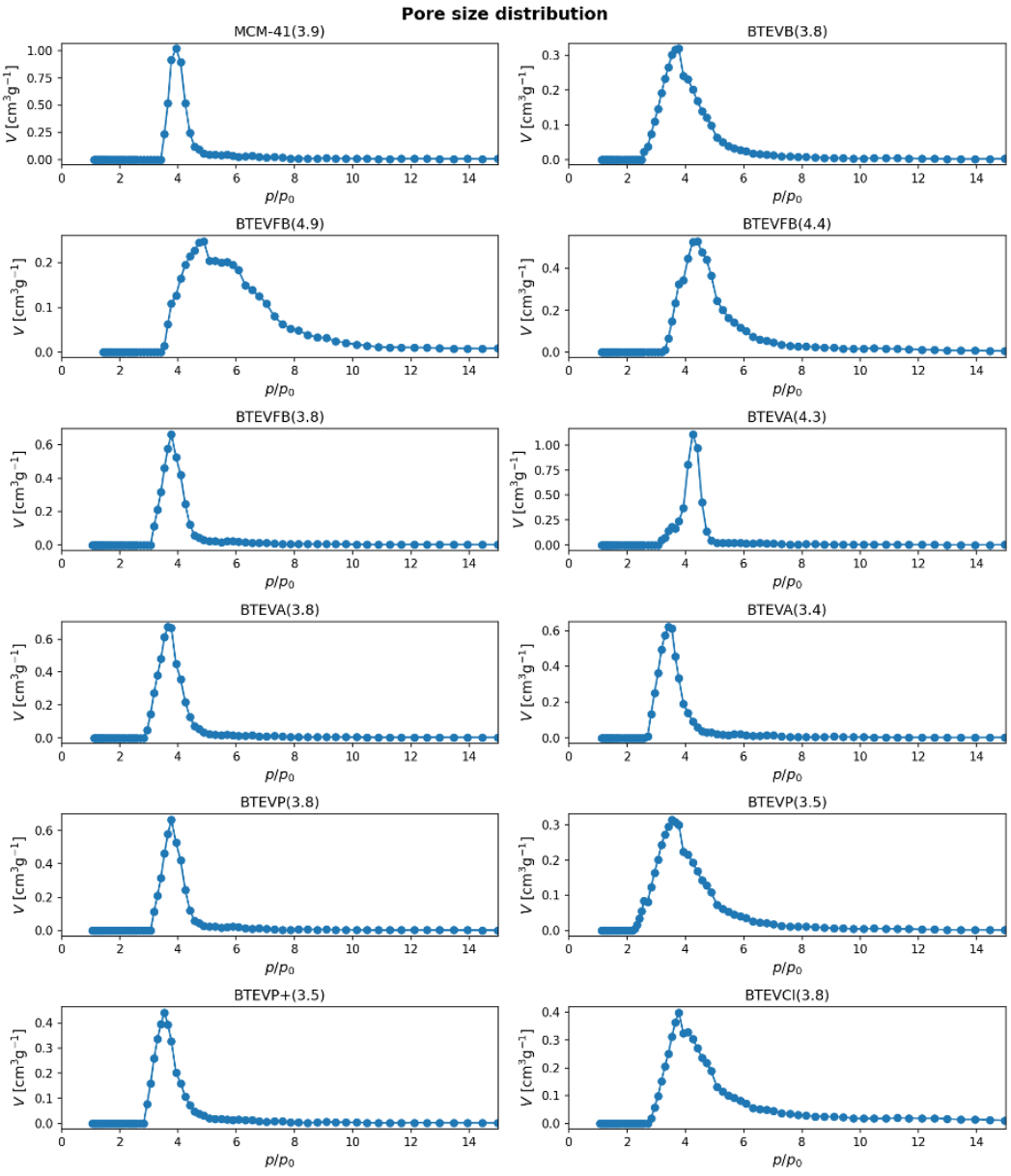


FIG. S3: Pore size distributions of the measured meaterials determined by DFT.[3–5]

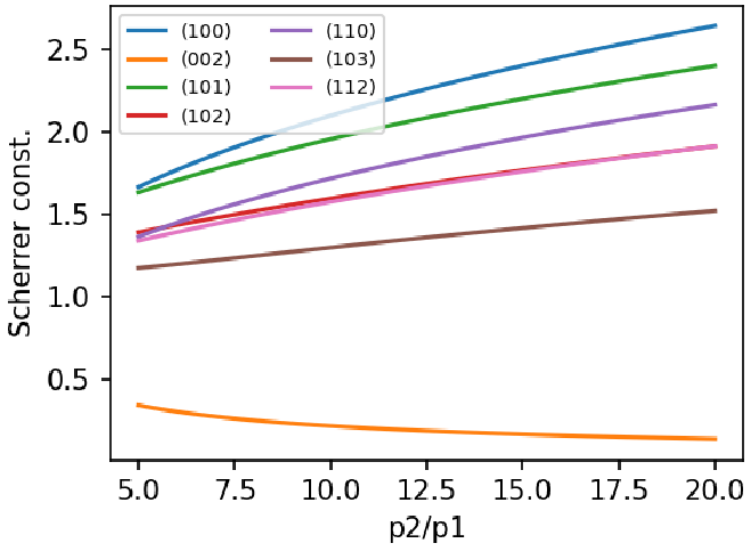


FIG. S4: Scherrer constant of a cylindrical crystal plotted against p_2/p_1 for different Miller indices.

S4. SCHERRER CONSTANT OF NON-ISOTROPIC CRYSTALLITES

As mentioned in the main text, the Scherrer constant K, which is needed to calculate the size of crystallites from their Bragg peaks, is strongly dependent on the shape of the crystals in question.[6,7] In this study, cylindrical crystals are assumed in the pores. In this case, K can be described according to Lele and Anantharaman[6] as

$$K = d\frac{2\rho\sigma\sqrt{(h^2+k^2)}+\sqrt{\pi}l}{\sqrt{\pi}\rho^{\frac{2}{3}}\sigma a} \tag{1}$$

with d being the distance between two scattering planes, $\rho = p_2/p_1$ the ratio between the square root of the base area of the cylinder (p_2) and its height p_1, $\sigma = \frac{c}{a}$ the ratio between the crystals lattice parameters and hkl the Miller indices.

This equations requires knowledge of the dimensions of the cylindrical crystal in order to determine the Scherrer constant. As we want to use K in order to calculate the size of the crystal, a precise result can therefore not be obtained in this case. In order to estimate the order of magnitude of the crystallite size, we assume an aspect ratio of the cylinders of 10, meaning that the height of the cylinder is ten time higher than its diameter. σ was calculated

using the lattice constants discussed later on in the study. Fig. S4 shows the dependence of K on $p_2/p_1 = \rho$ for different Miller indices and with the lattice constants of BTEVA(4.4). It shows that while it chenges with ρ, the order of magnitude stays similar. As the crystallite size depends linearly on K, the same should hold true for its calculation.

S5. XCCA EXPERIMENT AND ANALYSIS

After cooling to 150 K, 105 images were taken for each sample. These were recorded in 5 rows (scans) of 21 images each (see Fig. S5**B**). Consequently, each image was taken at a different spot. Fig. S5**A** shows all the signals recorded at 150 K, using BTEVP(3.8) as an example. In scans 11 and 12, one can see a couple of ice peaks that are larger than the others, for example in their respective upper-most plots. These probably come from bulk ice that formed outside of the pores, inside or outside the capillary. The measurements with these bulk ice peaks were not used in the cross correlations in order to ensure that only confined ice was analyzed.

Furthermore, background correlations were calculated to remove artificial correlations, for example from background scattering or noise on the detector. To achieve this, the correlation function was computed for images that are not related to each other *i.e.* that were taken at different positions and averaged. For example, the (002) PMO peak from spot 1 was correlated with the (002) ice peaks at positions 2 through 105 (cf. Fig. S5**B**). The resulting correlation functions were then averaged to obtain the background correlation and were subtracted from the correlation from spot 1. Fig. S6 shows the uncorrected and corrected correlation functions, as well as the background correlation for the example of BTEVP+(3.5). It shows that the background correlation constitutes the main contribution to the amplitude of the uncorrected correlation function. The stark drop in amplitude after correction is reasonable, as all scattered intensity not coming from a Bragg peak is removed with the background correlation, leading to comparably low average amplitudes in the corrected function.

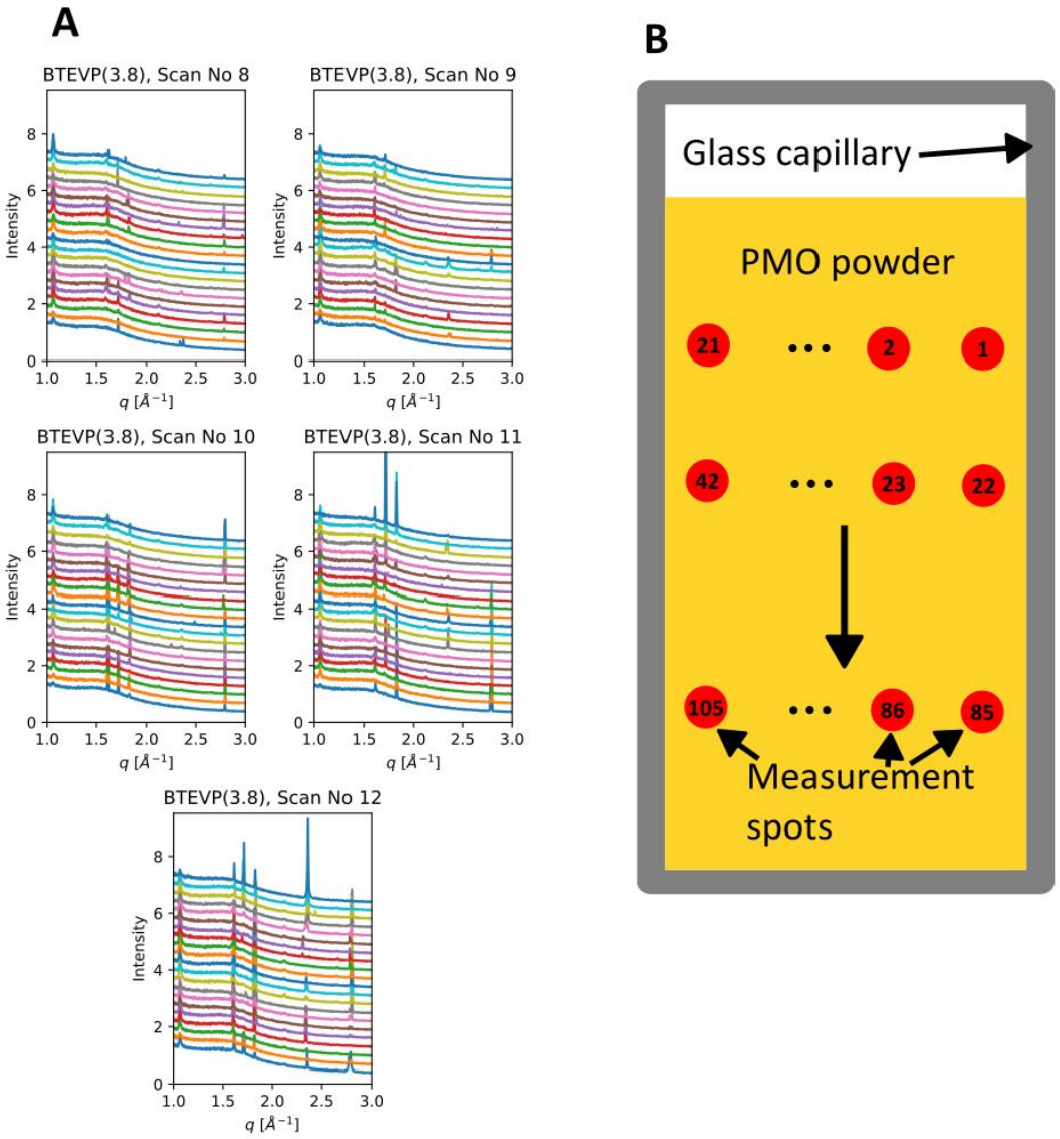


FIG. S5: **A** Individual nanofocus XRD signals in BTEVP(3.8). Each subfigure represents one row in which measurements were taken. In each row, 21 images were recorded. **B** Visualization of the arrangement of the measured spots. 105 locations were measured in 5 rows of 21 spots each. The perspective of the sketch is such that the reader looks into the direction of the beam.

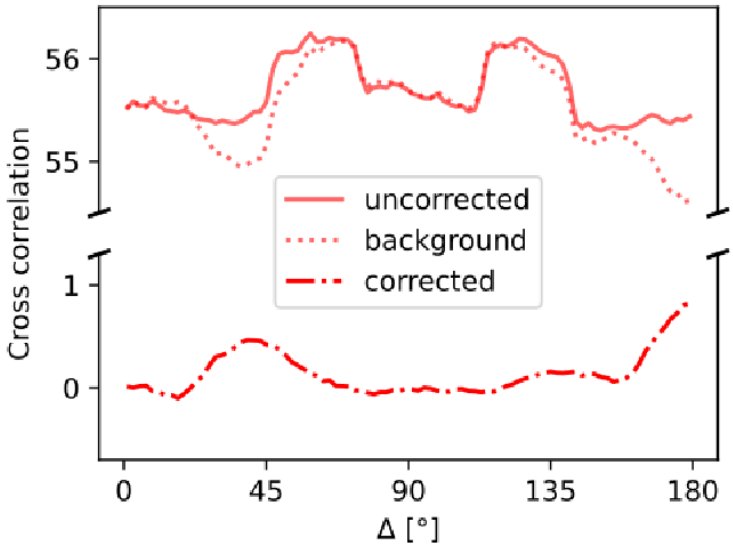


FIG. S6: The uncorrected (solid) and corrected (dash-dotted) average correlation functions, as well as the calculated background correlation (dotted) of BTEVP+(3.5) are shown as an example of the effect of background correlation subtraction.

REFERENCES

[1]Gießelmann, N. C.; Lenz, P.; Meinert, S.-M.; Simon, T.; Jo, W.; Striker, N. N.; Fröba, M.; Lehmkühler, F. *J. Phys. Chem. C* **2023**, *128*, 499–507.

[2]Shea, K.; Loy, D.; Webster, O. *J. Am. Chem. Soc.* **1992**, *114*, 6700–6710.

[3]Brunauer, S.; Emmett, P. H.; Teller, E. *J. Am. Chem. Soc.* **1938**, *60*, 309–319.

[4]Landers, J.; Gor, G. Y.; Neimark, A. V. *Colloids Surf. A* **2013**, *437*, 3–32.

[5]Thommes, M.; Kaneko, K.; Neimark, A. V.; Olivier, J. P.; Rodriguez-Reinoso, F.; Rouquerol, J.; Sing, K. S. *Pure and applied chemistry* **2015**, *87*, 1051–1069.

[6]Lele, S.; Anantharaman, T. Influence of crystallite shape on particle size broadening of Debye-Scherrer reflections. Proc. Natl. Acad. Sci. India A. 1966; pp 261–274.

[7]Langford, J. I.; Louër, D. *J. Appl. Cryst.* **1982**, *15*, 20–26.

9. Acknowledgment

Mein besonderer Dank gilt Herrn Prof. Dr. Michael Fröba für die Aufnahme in seinen Arbeitskreis und die damit verbundene Möglichkeit, an einem spannenden, komplexen und aktuellen Thema an der Schnittstelle von hybriden porösen Materialien, Confinement-Effekten und Wasser zu forschen. Ich danke ihm für die mir gewährten Freiheiten bei der Durchführung dieser Arbeit, das entgegengebrachte Vertrauen sowie die zahlreichen fachlichen Diskussionen und die daraus resultierenden Impulse. Auch Herr Prof. Dr. Michael Steiger war an diesen fachlichen Diskussionen beteiligt, wofür ich ihm ebenso wie für die Übernahme der Co-Betreuung meiner Arbeit herzlich danke.

Ich möchte mich zudem bei Herrn Prof. Dr. Tobias Beck und Herrn Prof. Dr. Matthias Thommes für die Übernahme der Begutachtung meiner Dissertation sowie bei Herrn Prof. Dr. Alf Mews und Herrn Prof. Dr. Simone Mascotto für die Mitwirkung in der Prüfungskommission bedanken.

Uta und Sandra danke ich für die Durchführung der Messungen sowie für die ausführliche Einweisung in die kalorimetrischen Messmethoden und die Gasadsorption. Darüber hinaus danke ich beiden für den regelmäßigen wissenschaftlichen Austausch, für Gespräche jenseits fachlicher Themen sowie für viele wertvolle Anregungen, die diese Arbeit maßgeblich vorangebracht haben. Uta danke ich zusätzlich für ihr außergewöhnliches Engagement bei der Realisierung der DSC-TGA-MHG-Anlage zur kalorimetrischen Messung, die einen wesentlichen Beitrag zu dieser Arbeit geleistet hat.

Isabelle Nevoigt danke ich für die zahlreichen PXRD-Messungen, Birgit Alpers und dem ZEA-Team für die Durchführung der Elementaranalytik, Dr. Andreas Meyer für die SAXS-Messungen, Elke Woelken für die REM-Aufnahmen sowie Dr. Charlotte Ruhmlieb, Andrea Köppen und Robert Schön für die TEM-Aufnahmen.

Für die praktische Unterstützung bei der Bearbeitung verschiedener Forschungsprojekte danke ich Tugce Oruc im Rahmen ihrer Bachelorarbeit sowie Alexander Busler, Björn Person und Andja Çela im Rahmen ihrer Projektpraktika.

Tamás danke ich für die fachliche Begleitung während meiner Bachelor- und insbesondere meiner Masterarbeit sowie für die zahlreichen Anregungen und den wissenschaftlichen Austausch während meiner Promotion.

Meinen Arbeitskolleginnen Sophia und Tabea danke ich für die angenehme Arbeitsatmosphäre im Büro. Darüber hinaus danke ich Sophia, Tabea, Patrick, Christian und Tamás für den fachlichen Austausch sowie für die gemeinsamen Abende, die meine Promotionszeit bereichert haben. Besonders danken möchte ich Sophia für den nahezu täglichen wissenschaftlichen und privaten Austausch, für die sehr gute Laboratmosphäre, insbesondere in der Weihnachtszeit, und für die gegenseitige Unterstützung. Allen aktuellen und ehemaligen Mitgliedern des Arbeitskreises Fröba danke ich für die stets hilfsbereite und freundschaftliche Zusammenarbeit.

Dem Exzellenzcluster CUI: AIM der Deutschen Forschungsgemeinschaft (DFG ─ EXC 2056 ─ ID 390715994) danke ich für die Organisation der Summer und Winter Schools, die mir spannende Einblicke in interdisziplinäre Forschung ermöglicht haben, sowie für die zahlreichen Begegnungen mit interessanten Menschen und die vielen unvergesslichen gemeinsamen Abende.

Mein Dank gilt meiner Familie für ihre uneingeschränkte Unterstützung in allen Lebenslagen. Ich danke meiner Schwester Julia sowie insbesondere meinen Eltern, Vera und Gleb, die mich während meines Studiums unterstützt und mir auch in schwierigen Zeiten Rückhalt gegeben haben. Ganz besonders danke ich meiner Frau Manon, die mich während meines Studiums immer motiviert und mir durch die Übernahme eines großen Teils der Kinderbetreuung ermöglicht hat, mich auf diese Arbeit zu konzentrieren. Meinem Sohn Sascha und meiner Tochter Liana danke ich für die vielen gemeinsamen schönen Momente und dafür, dass sie mich täglich zum Lächeln bringen.

10. Declaration on Oath

Eidesstattliche Versicherung:

Hiermit versichere ich an Eides statt, die vorliegende Dissertationsschrift selbst verfasst und keine anderen als die angegebenen Hilfsmittel und Quellen benutzt zu haben. Sofern im Zuge der Erstellung der vorliegenden Dissertationsschrift generative Künstliche Intelligenz (gKI) basierte elektronische Hilfsmittel verwendet wurden, versichere ich, dass meine eigene Leistung im Vordergrund stand und dass eine vollständige Dokumentation allerverwendeten Hilfsmittel gemäß der Guten wissenschaftlichen Praxis vorliegt. Ich trage die Verantwortung für eventuell durch die gKI generierte fehlerhafte oder verzerrte Inhalte, fehlerhafte Referenzen, Verstöße gegen das Datenschutz- und Urheberrecht oder Plagiate.

Affidavit:

I hereby declare and affirm that this doctoral dissertation is my own work and that I have not used any aids and sources other than those indicated. If electronic resources based on generative artificial intelligence (gAI) were used in the course of writing this dissertation, I confirm that my own work was the main and value-adding contribution and that complete documentation of all resources used is available in accordance with good scientific practice. I am responsible for any erroneous or distorted content, incorrect references, violations of data protection and copyright law or plagiarism that may have been generated by the gAI.

Hamburg, 02.10.2026



Ort, den | City, date

Unterschrift | Signature